Development and Studies of New Magnetic Core@Shell Nanostructures



A thesis submitted to the School of Chemistry, Trinity College Dublin
for the degree of Doctor of Philosophy

by

Garret Dee

Under the supervision of Professor Yurii Gun'ko

2022 Trinity College Dublin

Table of Contents

Acknowledgements and Declaration ..... **i**

Summary ..... **ii**

Abbreviations ..... **v**

1 Introduction **1**

1.1 Nanomaterials 1

1.2 Magnetic Materials and their Properties 2

1.3 Spinel Ferrites 8

1.4 Magnetic Nanoparticles 9

1.5 Methods of Synthesis of Magnetic Nanoparticles 11

1.5.1 Coprecipitation Synthesis 11

1.5.2 Thermal Decomposition Synthesis 12

1.5.3 Hydrothermal and Solvothermal Synthesis 13

1.5.4 Microemulsion Synthesis 14

1.5.5 Other Methods 16

1.6 Functionalisation of MNPs 16

1.6.1 Stabilisation and Protection 16

1.6.2 Catalytic Shells 18

1.6.3 Other Shells or Functionalisation Approaches 20

1.6.4 Applications of MNPs and their Composites 21

1.7 Boron Nitride Nanosheets (BNNS) Nanocomposites and Applications 23

1.8 Aims of the Project 26

1.9 References 28

2 Experimental **40**

2.1 Materials, Equipment and General Procedures 40
2.1.1 Starting Materials and Solvents 40
2.1.2 Small Lab Equipment used in the Synthesis and Processing of Materials 41
2.1.3 General Procedures 42
2.1.4 General Sample Preparation for Characterisation 42
2.2 Experimental Protocols for Chapter 3 43
2.2.1 Preparation of Magnetite MNPs by Coprecipitation (Fe_3O_4) 43
2.2.2 Preparation of Manganese Ferrite MNPs by Coprecipitation ($MnFe_2O_4$) 43
2.2.3 Preparation of Cobalt Ferrite MNPs by Coprecipitation ($CoFe_2O_4$) 44
2.2.4 Preparation of Copper Ferrite MNPs by Coprecipitation ($CuFe_2O_4$) 44
2.2.5 Preparation of Manganese Ferrite MNPs by Polyol ($MnFe_2O_4$) 44
2.2.6 Preparation of Magnetite MNPs by Polyol (Fe_3O_4) 45
2.3 Experimental Protocols for Chapter 4 45
2.3.1 Preparation of Citrate Stabilised Magnetite MNPs (Fe_3O_4@citrate) 45
2.3.2 Preparation of Citrate Stabilised Manganese Ferrite MNPs ($MnFe_2O_4$@citrate) 46
2.3.3 Preparation of Silica Nanoparticles (SiO_2) 46
2.3.4 Preparation of Core@Shell Magnetite@Silica MNPs (Fe_3O_4@SiO_2) 46
2.3.5 Preparation of Core@Shell Manganese Ferrite@Silica MNPs ($MnFe_2O_4$@SiO_2) 47
2.4 Experimental protocols for Chapter 5 47
2.4.1 Preparation of Manganese Dioxide Nanoparticles (MnO_2) 47
2.4.2 Preparation of Manganese Ferrite@Manganese Dioxide core@shell MNPs ($MnFe_2O_4$@MnO_2) 48
2.4.3 Preparation of Cerium Dioxide Nanoparticles (CeO_2) 48
2.4.4 Preparation of Manganese Ferrite@Silica@Cerium Dioxide MNPs ($MnFe_2O_4$@SiO_2@CeO_2) 49

2.5 Experimental Protocols for Chapter 6 49
2.5.1 Procedure for Catalytic Oxidation of Benzyl Alcohol to Benzaldehyde 49
2.5.2 Procedure for Catalytic Oxidation of Benzyl Alcohol to Benzylidene Alinine 50
2.5.3 Procedure for Glue Inhibition and Reactivation Testing 50
2.5.4 Procedure for Dye Removal Testing 50
2.6 Experimental Protocols for Chapter 7 51
2.6.1 Preparation of Boron Nitride Nanosheets (BNNS) 51
2.6.2 Preparation of Sodium Ethoxide (EtONa) 51
2.6.3 Transfer of BNNS from Water to Ethylene Glycol 51
2.6.4 Preparation of Boron Nitride Nanosheets Magnetite Nanocomposites (BNNS-Fe_3O_4) 52
2.6.5 Preparation of Boron Nitride Nanosheets Cobalt Ferrite Nanocomposites (BNNS-$CoFe_2O_4$)52
2.6.6 Preparation of Boron Nitride Nanosheets - Magnetic Nanoparticle Nanocomposite Membranes 52
2.6.7 Testing of the Membrane for Extraction of Dye 53
2.6.8 Testing of the Membrane for Magnetic Nanoparticle Filtration 53
2.7 Instrumentation and Techniques used for Characterisation 54
2.7.1 Electron Microscopy 54
2.7.2 Vibrating Sample Magnetometer (VSM) 56
2.7.3 Fourier Transform Infrared (FTIR) Spectroscopy 57
2.7.4 Nuclear Magnetic Resonance (NMR) 58
2.7.5 Ultraviolet-Visible Spectroscopy (UV-vis) 60
2.7.6 Dynamic Light Scattering (DLS) 61
2.7.7 Zeta Potential 62
2.7.8 X-ray Diffraction (XRD) 64

2.8 References 67

3 Synthesis of the Magnetic Core Nanoparticles 69

3.1 Introduction 69

3.2 Aims 70

3.3 Results and Discussion 71

3.3.1 Preparation of Magnetite NMPs (Fe_3O_4) by Coprecipitation 71

3.3.2 Preparation of Manganese Ferrite MNPs ($MnFe_2O_4$) by Coprecipitation 84

3.3.3 Preparation of Cobalt Ferrite MNPs ($CoFe_2O_4$) by Coprecipitation 90

3.3.4 Preparation of Copper Ferrite MNPs ($CuFe_2O_4$) by Coprecipitation 98

3.3.5 Preparation of Manganese Ferrite MNPs ($MnFe_2O_4$) by Polyol Method 103

3.3.6 Preparation of Magnetite MNPs (Fe_3O_4) by Polyol Method 117

3.4 Conclusion 120

3.5 References 121

4 Stabilisation and Protection of the Magnetic Cores 125

4.1 Introduction 125

4.2 Aims 126

4.3 Results and Discussion 127

4.3.1 Preparation of Citrate Stabilised Magnetite MNPs 127

4.3.2 Preparation of Citrate Stabilised Manganese Ferrite MNPs 133

4.3.3 Preparation of SiO_2 Nanoparticles 138

4.3.4 Preparation of SiO_2 shell on Magnetite Core MNPs 140

4.3.5 Preparation of SiO_2 shell on Manganese Ferrite Core MNPs 148

4.4 Conclusions 155

4.5 References 156

5 Coating of MNPs with Catalytic Shells 159

5.1 Introduction 159

5.2 Aims 160
5.3 Results and Discussion 161
5.3.1 Preparation of MnO_2 Nanoparticles 161
5.3.2 Preparation of MnO_2 Shell on MNP Cores 163
5.3.3 Preparation of CeO_2 Nanoparticles 174
5.3.4 Preparation of CeO_2 shell on MNP Cores 176
5.4 Conclusions 187
5.5 References 188
6 Testing the core@shell MNPs in Applications 191
6.1 Introduction 191
6.2 Aims 192
6.3 Results and Discussion 193
6.3.1 Testing of $MnFe_2O_4@MnO_2$ Nanostructures in Catalytic Oxidation of Benzyl Alcohol to Benzaldehyde 193
6.3.2 Testing of $MnFe_2O_4@SiO_2@CeO_2$ Nanostructures in Catalytic Oxidation of Benzyl Alcohol to Benzaldehyde 197
6.3.3 Testing of $Fe_3O_4@SiO_2@CeO_2$ for Catalytic Oxidation of Benzyl Alcohol to Benzaldehyde 198
6.3.4 Testing of $MnFe_2O_4@SiO_2@CeO_2$ for Catalytic Conversion of Benzyl Alcohol to Benzylidene Aniline 199
6.3.5 Testing of $MnFe_2O_4@MnO_2$ in the Activation of an Anaerobic Glue Formulation 201
6.3.6 Testing of $MnFe_2O_4@MnO_2$ for Methylene Blue Dye Removal 204
6.3.7 Testing of $MnFe_2O_4@MnO_2$ for Methyl Orange Dye Removal 211
6.3.8 Testing of $MnFe_2O_4@MnO_2$ for Rhodamine B Dye Removal 213
6.3.9 Testing of $MnFe_2O_4@SiO_2@CeO_2$ for Methylene Blue Dye Removal 214
6.4 Conclusions 216

6.5 Reference 217

7 Boron Nitride - Magnetic Nanoparticle Composites 220

7.1 Introduction 220

7.2 Aims 221

7.3 Results and Discussion 222

7.3.1 Preparation of BNNS 222

7.3.2 Preparation of BNNS-Fe_3O_4 Nanocomposites 224

7.3.3 Preparation of BNNS-$CoFe_2O_4$ Nanocomposites 229

7.3.4 Testing the Membranes for Filtration Applications 236

7.4 Conclusions 243

7.5 References 244

8 Conclusion and Future Work 246

8.1 Conclusions 246

8.2 Future Work 249

Appendix 251

A.1 Supplementary Information 251

A.2 List of Figures 258

A.3 List of Tables 266

Acknowledgements and Declaration

Acknowledgements

I would like to thank all the members of the Gun'ko group for their help and tutelage during the time I have been with the group while doing this research project. I am especially grateful for the guidance, advice and help given by Yurii and Finn, which without their expert help I would not have been able to complete this project in the allotted time nor have been able to produce the eloquent scientific style required for this thesis. I would like to express my gratitude to Professor Yurii Gun'ko for giving me the opportunity to pursue this PhD and who oversaw the direction of the project. Finally, I would like to thank the IRC for the funding that enabled me to do this work.

Declaration

This thesis is submitted for the degree of Doctor of Philosophy of the University of Dublin, Trinity College. I declare that all work contained in this report is entirely my own and has not been submitted before for any other degree or examination, to this or any other university. References are given to the works of others where appropriate and for material that I considered not to be common knowledge in this area. Permission is granted so that the University Library may lend or copy this thesis upon request. This permission covers only single copies made for study purposes, subject to normal conditions of acknowledgement.

_____

Garret Dee

Summary

The main goal of this work is to develop magnetic core@shell nanoparticles and to explore potential applications for these nanocomposites. These applications include magnetically extractable and recyclable catalysts, magnetically extractable and recyclable dye and pollutant absorbents, as well as magnetic inhibitors with a view to magnetic activation of a chemical reaction. Nanocomposites with magnetic nanoparticles will also be explored with a view to the development of new recyclable water filtration membranes.

Chapter 1 presents the introduction and an overview of the subject of nanomaterials, magnetism and magnetic nanoparticles. An overview of the current state of the art for magnetic nanomaterials synthesis is described. Then the functionalisation of these magnetic nanoparticles is discussed with some pertinent examples from the literature mentioned. The current and potential applications of magnetic nanoparticles are outlined. Finally, a brief overview of boron nitride based nanomaterials and their applications are presented, and the aims of this project are formulated.

Chapter 2 will give the details of the experimental procedures and techniques, which are used for synthesis and characterisation of the materials. The lab equipment and general procedures are described. The synthetic protocols for the creation of the various magnetic nanoparticles, the functionalisation of these particles, the boron nitride nanosheet – magnetic nanoparticle nanocomposites and the procedures for testing these nanomaterials in a variety of applications are presented. This chapter presents details of the characterisation techniques that were used to study the nanomaterials with a summary of the theory behind each technique and the specific instrument used.

Chapter 3 describes the syntheses and optimisation for the production of a variety of bare magnetic nanoparticles and the outcomes of these syntheses, with variations discussed. Two synthetic methods are the focus of this chapter and several different bare magnetic nanoparticles are produced by these two methods. The outcomes of the characterisations of the nanoparticles are discussed and how these characterisation results guided the next stages of the project or any variations to try to improve the outcomes of the protocols.

Chapter 4 is focused on the stabilisation and protection of the magnetic cores presented in chapter 3. The work in this chapter is a necessary step for further functionalisation, coating and optimisation of the nanoparticles. Full characterisation of the particles at this stage and the changes to the particles as observed with the characterisation are discussed in detail.

Chapter 5 describes the further functionalisation of the magnetic cores described in chapter 3 and 4 with catalytic shells of MnO_2 and CeO_2. Some optimisation of the method for coating the magnetic nanoparticle cores with the shell material will be done here and the outcomes discussed. These catalytic shell materials are also made separately for testing in the same applications as the core@shell material. The characterisation of the core@shell particles and the shell on its own will be discussed in detail, explaining how these results guided the optimisation process.

Chapter 6 describes how the particles reported in chapter 5 were tested for a variety of applications. These applications include oxidation of benzyl alcohol to benzaldehyde, which is a standard oxidation testing reaction in the literature. The outcomes of the catalysis will be characterised to give percent conversions to quantify the effectiveness of the catalysts. The manganese dioxide coated manganese ferrite magnetic nanoparticles will also be tested for inhibition of a free radical initiated polymerisation reaction. The polymerisation can be initiated by magnetic removal of the nanoparticles and the proposed mechanism of inhibition will be discussed. The MnO_2 coated particles are also to be tested for removal of several organic dye pollutants from water. The particles can be magnetically extracted and recycled. The efficacy and recyclability of the core@shell nanoparticles will be discussed.

Chapter 7 discusses the synthesis, characterisation and testing of a boron nitride – magnetic nanocomposite where the magnetic component is on the surface of the BN nanosheets. A novel synthetic approach is introduced here, which gives excellent coverage on the 2D boron nitride nanosheets. These nanocomposites are used to produce nanofiltration membranes that can be recycled through magnetic inductive heating. The nanocomposites are tested for removal of organic dye pollutant from water with UV-vis analysis quantifying the removal. The nanocomposites are also tested for filtration of magnetic nanoparticles and the results are discussed.

Finally, Chapter 8 provides the conclusions of the entire work and outlines the main achievements of the research. This chapter also includes details for recommended future directions to continue the work here.

We believe that the project contributed to the development of a number of very interesting magnetic nanocomposite materials with a range of potential applications.

Abbreviations

˚C	Degrees Celsius	**AU**	Arbitrary units
BN	Boron Nitride	**BNNS**	Boron Nitride Nanosheets
cm^{-1}	wavenumbers	**DLS**	Dynamic Light Scattering
EDX	Energy-dispersive X-ray	**FTIR**	Fourier Transform Infrared
mg / g	milligrams / grams	**IR**	Infrared
M	Magnetisation	**MB**	Methylene blue
H_c	Coercivity	**mL / L**	millilitres / litres
mmol	millimoles	**mM**	millimolar
MNP	Magnetic nanoparticle	**MNPs**	Magnetic nanoparticles
MO	Methyl Orange	**MP H_2O**	Millipore water
M_s	Saturation magnetisation	**M_r**	Magnetic Remanence
NMR	Nuclear Magnetic Resonance	**MHz**	MegaHertz
nm	nanometres	**PVDF**	Polyvinlyidene fluoride
PDI	Polydispersity Index	**RB**	Rodamine B
RBF	Round Bottom Flask	**mT / T**	milliTesla / Tesla
SEM	Scanning Electron Microscopy	**TEOS**	Tetraethyl orthosilicate
TEM	Transmission Electron Microscopy	**UV-vis**	Ultraviolet-visible
VSM	Vibrating Sample Magnetometer	**UV**	Ultraviolet
XRD	X-Ray Diffraction		

1 Introduction

1.1 Nanomaterials

Nanomaterials are materials that have at least one of their three dimensions below 0.1 micron (100 nm)[1]. Nanoscience deals with objects that have at least one dimension below this scale. For 2D materials, such as graphene we have the thickness in the nano-range, for 1D materials, such as nanowires the thickness and width are in the nano-range, while for 0D materials, such as nanoparticles the height, width and thickness are all in the nano-range. A 10 nm^3 nanoparticle of NaCl will consists of a lattice with approximately 45000 ordered atoms, whereas a macroscopic crystal of NaCl or a grain of salt 1 mm^3 that can be seen with the unaided eye consist of a lattice of approximately 4.48 x 10^{19} ordered atoms.

Nanomaterials can be produced by two main methods, which are the top-down approach or the bottom-up approach. In the top-down approach, bulk material is broken up into smaller parts to produce nano-sized material. Top-down methods include milling[2], laser pyrolysis, spray pyrolysis[3] and arc discharge[4]. Bottom-up approaches involve controlled growth using the techniques of chemistry. Bottom-up approaches include coprecipitation[5], sol-gel processing[6], synthesis by reduction[7], hydrothermal synthesis[8], solvothermal synthesis[9], thermal decomposition[10] and microemulsions[11]. It should be noted that these are not exhaustive lists. The top-down approaches are sometimes known as physical methods while the bottom-up approaches are known as chemical methods.

Nanoscience is a multidisciplinary area that encompasses different fields of chemistry, physics, materials science, engineering and biology. What makes nanoscience a separate discipline is the fact that the nanoscaled version of a material can exhibit different properties from the bulk material. The scaling of properties with size and the manifestation of new properties with size are important concepts of nanoscience. For example, a nanoscaled material will consist of more surface atoms than interior atoms. This is easily understood because for a spherical particle the surface area is dependent on r^2 while the volume is dependent on r^3, so as the object get smaller r^3 decreases faster than r^2. This is known as the surface area to volume ratio. Another important example is how the viscous force applied to an object scales with

size. This concept is captured in the Reynolds Number (R_e), which is a ratio of the inertial force to viscous force.

$$R_e = \frac{Inertial\ force}{Viscous\ force} = \frac{\rho v L}{\mu}$$

Where ρ is the density of the fluid, v is the velocity, L is the characteristic length, which for a sphere can be taken as the radius and μ is the viscosity of the fluid. From this equation, it can be seen that as L gets smaller the inertial force get smaller and the viscous force begins to dominate. Then other factors then come into play, such as the thermal energy of the medium[12]. The small nanosize results in the manifestation of new effects including quantum confinement observed in light emitting semiconducting nanoparticles (quantum dots) and plasmonic properties which are most known for gold and silver nanoparticles.

Another important property to note related to the surface area to volume ratio is the surface energy and the edge energy[13]. In a solid or liquid, the surface is intrinsically less energetically favourable than the interior bulk of a material. The surface energy is related to the amount of surface atoms compared to the bulk. As a macroscopic material becomes a nanomaterial the surface area increases and so too the surface energies. These effects become important in catalysis as the surface atoms are responsible for the catalytic reactions. A surface can be made up of a variety of atomic packing configurations, with the {111], {110} and {100} surfaces known as low index surfaces, being the most common as these surfaces have the lowest energy[13]. A high index surface, such as a {400} surface, will have more steps and kinks, and will thereby have a higher energy than a low index surfaces. High index surfaces and edge atoms are known to have stronger catalytic effect than low index surfaces[14].

1.2 Magnetic Materials and their Properties

Materials may be classified by their response to an applied external magnetic field as diamagnetic, paramagnetic, ferromagnetic, antiferromagnetic and ferrimagnetic, as outlined below (Figure 1-1).

A diamagnetic material has no net magnetic moment when there is no applied field and has a very weak magnetic moment in the direction opposite to an applied field when a field is

present. This means that a diamagnetic material is very weakly expelled from a magnetic field and so will have a small negative magnetic susceptibility, where the magnetic susceptibility is a constant that indicates the degree of magnetisation of a material in response to an applied magnetic field.

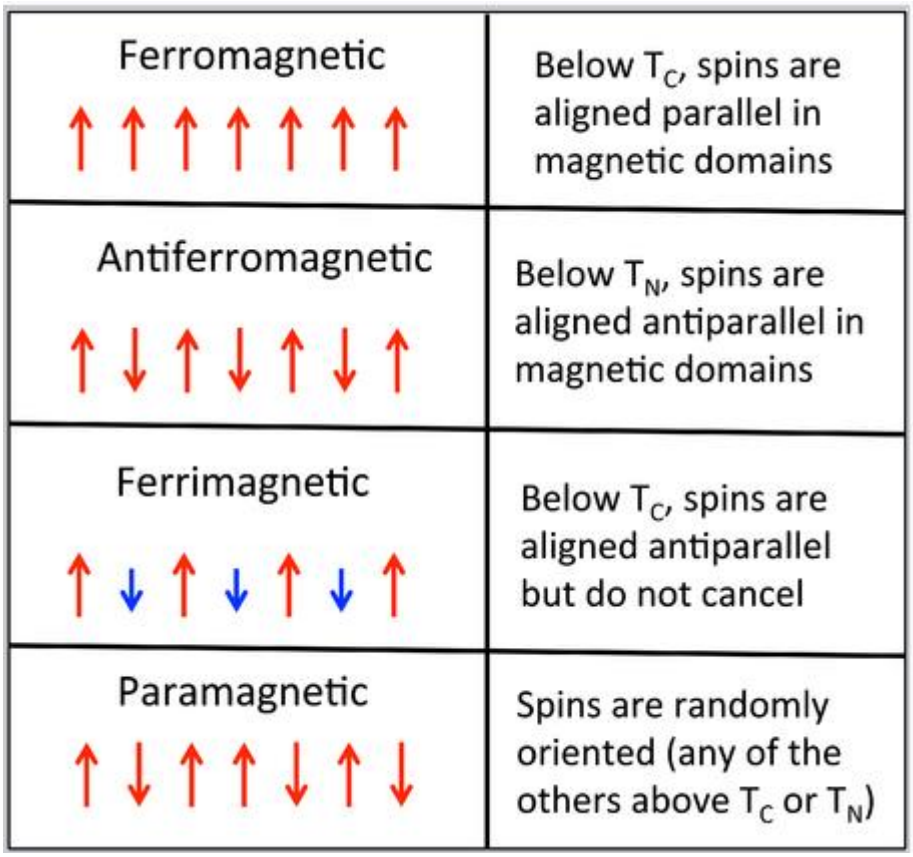


Figure 1-1: Types of magnetism[15].

A paramagnetic material has no net magnetic moment when there is no applied field and has a weak magnetic moment in the same direction to an applied field when a field is present. Paramagnetic materials are attracted towards a magnetic field and so have a positive magnetic susceptibility. Paramagnetism arises from unpaired electrons in the material, which are randomly orientated but can align in the presence of a magnetic field thereby enforcing it. Each electron in an atom possesses a spin magnetic moment, which in turn possesses an orbital magnetic moment. Below a certain characteristic temperature (the Néel or Curie temperature) paramagnetic materials may undergo a transition to a magnetically ordered state becoming ferromagnetic or ferrimagnetic (below the Curie temperature) and antiferromagnetic (below the Néel temperature). Below these temperatures, these substances have a domain structure when they are in this magnetically ordered state.

Ferromagnetic materials contain unpaired electrons, which will align in the presence of a magnetic field but these materials have a tendency for the electron to align parallel to each other in the absence of a magnetic field as well. Ferromagnetic materials have a much larger magnetic susceptibility than paramagnetic materials. Above their Curie temperature, these materials are paramagnetic but below this temperature, the unpaired electrons align spontaneously. The alignment of the electrons creates domains of magnetically ordered states. Initially the domains may be disordered pointing in different directions but in the presence of a magnetic field some these domains will align in the direction of the magnetic field, with the degree of alignment dependent on the strength of the external field. Upon removal of the external magnetic field, the domains will remain aligned and the material will retain a magnetic moment. To remove this retained magnetism an external magnetic field in the opposite direction must be applied.

Antiferromagnetic materials contain unpaired electrons but the spins are aligned in opposite directions and the magnitudes of their magnetisations are equal. It results in a close to zero net magnetic moment in the presence of an external magnetic field and zero magnetic moment with no magnetic field. Above the Néel temperature for these materials, the aligned electrons become randomly orientated and the material becomes paramagnetic.

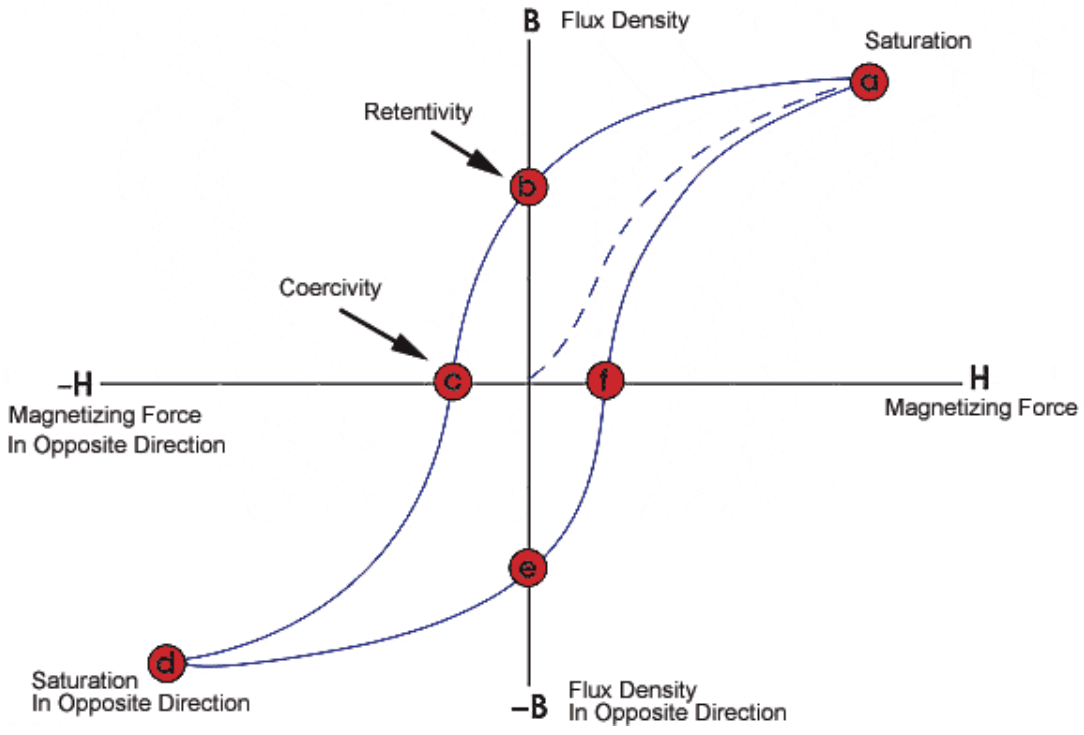


Figure 1-2: General hysteresis loop showing magnetic saturation (a, d) and coercivity (c, f)[16]**.**

Ferrimagnetic materials also possess opposed spins alignment, but the magnitude of magnetic moments pointing in one direction differs from those pointing in the opposite direction. This creates a considerable net magnetic moment but is still lower than that for ferromagnetic material. These materials can also retain some magnetism after the removal of the magnetic field and display paramagnetic behaviour above their Curie temperature.

A plot of applied field (magnetising force, **H**) against the induced magnetic moment (**B** or **M**) is known as a hysteresis loop and is a basic characterisation parameter for a magnetic sample. A plot of a general hysteresis loop can be see above (Figure 1-2).

For ferromagnetic and ferrimagnetic materials, when exposed to a strong external magnetic field (Magnetising Force, **H**), then the material may retain some magnetisation (Retentivity, **b** or **e**) after the magnetic field is removed. To remove this retained magnetism a magnetising force must be applied in the opposite direction. The strength of this field needed to return the material to a non-magnetic state (Coercivity, **c** or **f**) is related to whether the material is a "soft" or "hard" magnetic material. This concept is outlined in the diagram below (Figure 1-3). Soft and hard magnetic materials can have high values of saturation magnetisation but soft materials have low coercivity, while hard materials have high coercivity. For a soft magnetic material, a small field in the opposite direction will demagnetise the material whereas for a hard magnetic material a larger field is needed.

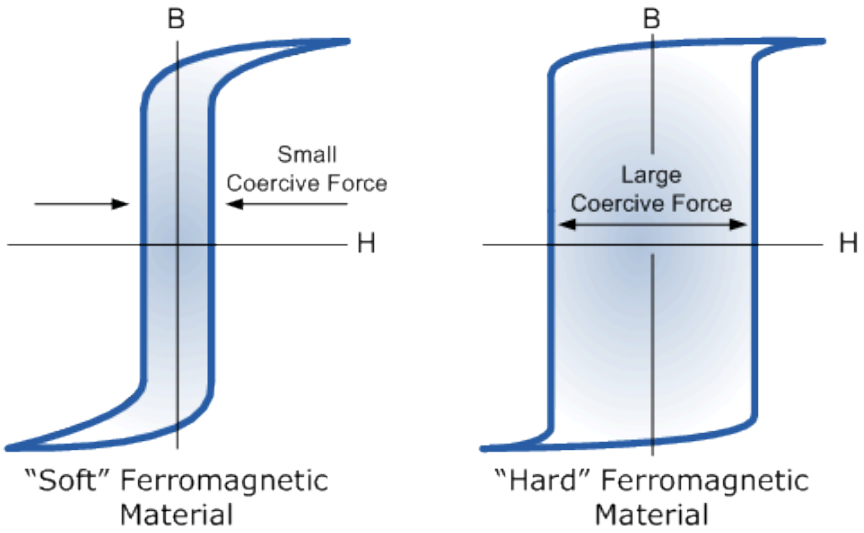


Figure 1-3: Hysteresis loops for a soft and hard magnetic material[17]**.**

The reason these effects happen is to do with what are known as magnetic domains. These small areas of the bulk material have uniform alignment below the Curie temperature. Domain

theory states that a given material can have a domain up to a maximum size before it splits into several separate domains to reduce the magnetostatic energy[18]. If enough of these domains point in the one direction then the material will have a magnetic moment (coercivity and remnant magnetisation). When all domains point in the direction of the eternal field, the material reaches saturation. These domains are not fixed in size or shape, they change size and shape under the influence of an external magnetising force.

With this domain concept, we can imagine a particle of a size equivalent to the maximum domain size for that material. If the particle is just a few atoms larger, the domain will split (to reduce the magnetostatic energy) into a multidomain particle. These domains cannot be aligned in the same direction and so after removal of a magnetising force the total coercivity will not be as large as for a single domain particle. A single domain particle will have uniform alignment of its magnetic field in one direction after removal of a magnetising force thereby having a larger coercivity. Now it should be understood that the largest coercivity possible for a material is from a collection of maximum sized single domain particles.

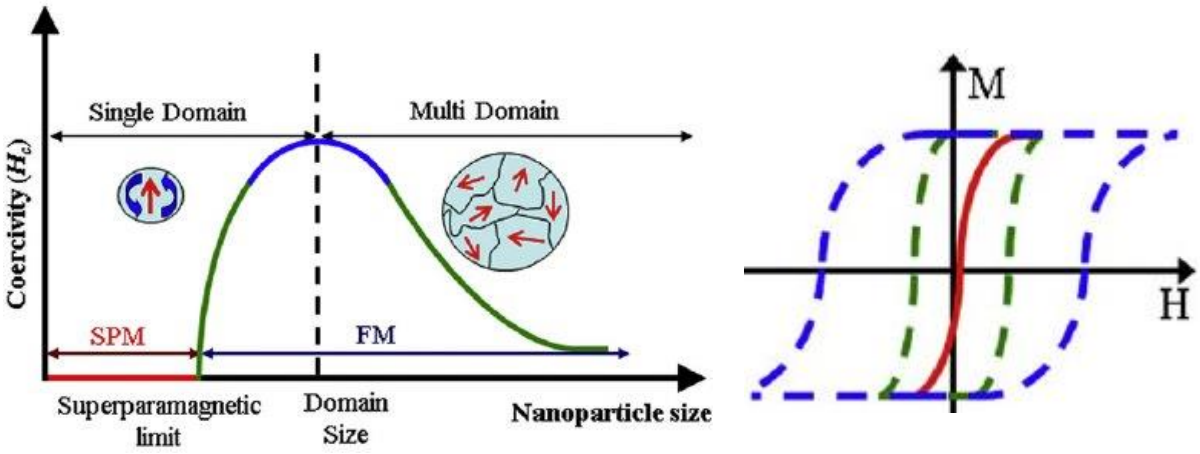


Figure 1-4: The qualitative behaviour of the size-dependent coercivity of magnetic particles. The magnetic behaviour of superparamagnetic (SPM) nanoparticles is demonstrated by the solid line, while ferromagnetic (FM) particles are presented by dashed lines in the hysteresis loops. Here H denotes the applied magnetic field strength and M is the measured magnetisation[19]**.**

We know that temperature affects the magnetism of a bulk material (above the Curie temperature the material becomes paramagnetic). In the single domain scale (the nanoscale), temperature also has an effect parallel to the Curie temperature effect. For a single domain particle at room temperature, the thermal perturbations may be enough to cause the particle to lose its remnant magnetisation. It is in effect paramagnetic but the particle is affected by a magnetic field as much at the bulk material at that temperature. This is the superparamagnetic

state. In the superparamagnetic state, the material does not retain any remnant magnetisation once the magnetising force is removed but has high susceptibility to external magnetic fields, which is explained in the diagram above (Figure 1-4).

Theoretically, any magnetic material can be made superparamagnetic by reducing the size of the material to below the single domain limit where superparamagnetic behaviour will emerge[18]. The single domain size (d_c) can be estimated as follows

$$d_c \approx 18\frac{\sqrt{AK_{eff}}}{\mu_0 M_s^2}$$

Where K_{eff} is the anisotropy constant, A is the exchange constant, μ_0 represents vacuum permeability and M_s is the saturation magnetisation for the bulk material. Superparamagnetic behaviour emerges below the d_c. The magnetic anisotropy energy per particle, which is responsible for holding the magnetic moment along certain directions, is expressed as

$$E(\theta) = K_{eff} V sin^2\theta$$

Where V is the particle volume and θ is the angle between the magnetisation and the easy axis (the easiest directions to magnetise a material, which are 180° apart corresponding to N and S). There is an energy barrier $K_{eff}V$ that separates the two directions of magnetisation. With decreasing particle size, V decreases until the energy from thermal perturbations, k_BT, become significant. When $k_BT > K_{eff}V$ the magnetisation will spontaneously flip direction and so the material will show no remanence[20]. In this state, which is directly related to the size of the particle (V), the particle is in a superparamagnetic state.

We understand that nanoparticles will randomly flip the direction of their magnetisation due to thermal energy. The average time to perform such a flip is called the Néel relaxation time (τ) and is expressed as

$$\tau = \tau_0 exp\left(\frac{K_{eff}V}{k_BT}\right)$$

Where τ_0 is the length of time characteristic of the material known as the attempt time, k_B is the Boltzmann constant and T is the temperature. The temperature where the thermal perturbations are enough to flip the direction of a particle of a given size is known as the

blocking temperature (T_B) and is dependent on the time window of the measurement. The blocking temperature depends on the effective anisotropy constant, the size of the particles and the experimental measuring time[20]. The table below (Table 1-1) shows the changing relaxation times with changing temperature and size. As can be seen below, depending on the time window of the measurement, the defined blocking temperature can change.

Table 1-1: Néel relaxation times for cobalt particles of different sizes and at different temperatures[18]**.**

Radius of Co particle (nm)	Temperature (K)	Relaxation time
3.5	260	332 s
3.5	300	10 s
3.5	340	0.6 s
3.5	380	76 ms
3	300	1.9 ms
4	300	223 h
5	300	1 $x10^{12}$ y

1.3 Spinel Ferrites

The spinel group of minerals have a general formula of $\mathbf{AB_2X_4}$ where **X** is an anion (typically S or O) and the **A** and **B** are cations. The **X** atoms form a face centred cubic lattice with the **A** and **B** atoms occupying the tetrahedral and octahedral holes respectively. One face centred cubic lattice unit contains 8 tetrahedral and 4 octrahedral sites. In a normal spinel, 1/8 of the tetrahedral holes will have **A** cations and 1/2 of the octahedral holes will have **B** cations. In an inverse spinel, the cations rearrange to reduce the crystal field stabilisation energy so that 1/8 of the tetrahedral holes will have **B** cations, 1/4 of the octahedral holes will have **B** cations and 1/4 of the octahedral holes will have **A** cations. A 3D graphical representation of a normal spinel structure is shown below (Figure 1-5).

Metal oxide ferrites belong to the spinel group with most being inverse spinel structures. Fe_3O_4, $CoFe_2O_4$, $MnFe_2O_4$, and $CuFe_2O_4$ are all inverse spinels.

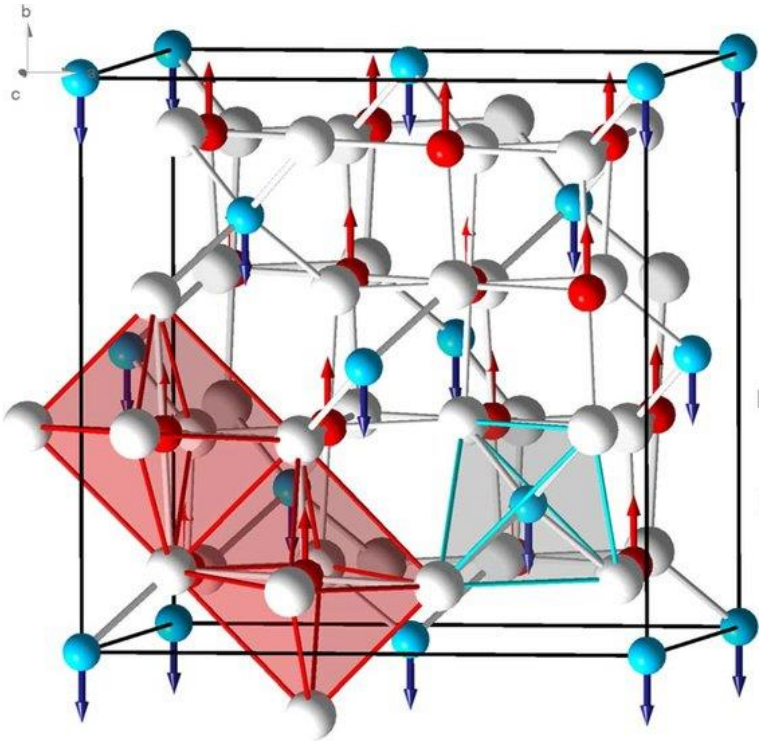


Figure 1-5: Normal spinel structure showing red balls as the B octahedral sites and blue balls as the A tetrahedral sites and white balls as the FCC lattice of oxygen atoms[21]**.**

1.4 Magnetic Nanoparticles

Magnetic nanoparticles are nano-sized materials, which can be manipulated using external magnetic fields. Although there are many various magnetic materials, only some of them have strong magnetic moments in the absence of a magnetic field at room temperature[18].

One of the most important parameters of a magnetic nanomaterial is its level of magnetic saturation in an external magnetic field. It is desirable that it will reach saturation quickly in a relatively low field and that it saturation magnetisation be high. The next parameter that is important is the level of coercivity or remnant magnetisation left in the material after removal of the external magnetic field. This remnant magnetisation can be removed by simply making the ensemble of nanoparticles smaller to create a collection of superparamagnetic particles. Along with these two properties, saturation magnetisation and coercivity, another factor that must be taken into account is the chemical properties and stability of the magnetic nanomaterial. The type of nanoparticle needed in an application will dependent on the final use of the nanocomposite.

As an example, we can look at a magnetic material, cobalt ferrite ($CoFe_2O_4$). Cobalt ferrite is a hard magnetic material with high remnant magnetisation and high coercivity. In magnetic media tape, coercivity is important for retention of the information. Single domain particles at the limit of size before spontaneous, multi-domain reorganisation takes place to reduce the magnetostatic energy, have the highest coercivity. These are desirable for information storage as these particles embedded in a polymer matrix will retain information and not change state unless a large external field is experienced. This type of composite material was used for magnetic recording in audio cassette tapes[22].

On the other side if cobalt ferrite particles were to be used in a core@shell structure catalyst, superparamagnetic behaviour would be desirable to prevent agglomeration and expose the catalyst, while the smaller size would increase surface area to enable a more efficient catalysis[23]. A high saturation reached quickly in a low field would be desirable also for recovery of the catalyst. Therefore, the smaller size superparamagnetic state of cobalt ferrite would be desirable.

Table 1-2: Various magnetic materials showing the saturation magnetisation (σ_s), Curie temperature (T_C) and structure (the most common crystal structure of the material).

Name	Composition	σ_s at 293 K	Structure	Tc (K)
Iron	Fe	218	Cubic	1044
Cobalt	Co	161	Hexagonal	1360
Nickel	Ni	55	Cubic	631
Magnetite	Fe_3O_4	92	Cubic	860
Maghemite	γ-Fe_2O_3	82	Cubic	985
Hematite	α-Fe_2O_3	0.5	Hexagonal	960
Manganese ferrite	$MnFe_2O_4$	77	Cubic	573
Cobalt ferrite	$CoFe_2O_4$	82	Cubic	1073
Nickel Ferrite	$NiFe_2O_4$	51	Cubic	858
Awaruite	Ni_3Fe	120	Cubic	893
Wairauite	CoFe	235	Cubic	1259

For the synthesis of Magnetic Nanoparticles (MNPs) there are many protocols in the literature[20] with new useful concepts still being published[24]. The real power of MNP come with modification of the bare particles. By creating magnetic core@shell structures or by

creation of nanostructures with MNPs as part of the framework, the magnetic properties of the nanoparticle will be added to the properties of the other material in the nanocomposite. Such modifications are generally called functionalisation of the MNPs[20].

The table above (Table 1-2) lists some common magnetic materials. It should be noted that apart from the single metal NP, these lists are not exhaustive. Each of these types have their own advantages and disadvantages. The metal oxide ferrites are one of the most common type used for MNPs because of their ease of synthesis.

1.5 Methods of Synthesis of Magnetic Nanoparticles

1.5.1 Coprecipitation Synthesis

The preparation of magnetite nanoparticles by coprecipitation can be traced back to 1869[25] and it is a well-established method for creating magnetite. The coprecipitation method involves the mixing of Fe(ll) and Fe(lll) ions in stoichiometric amounts in aqueous media, followed by the addition of a base (NaOH, NH_4OH) to precipitate out the Fe_3O_4 according to the equation:

$$Fe^{2+} + 2\ Fe^{3+} + 8OH^- \rightarrow Fe_3O_4 \downarrow + 4H_2O$$

In fact, this approach is highly adaptable to the synthesis of a range of MNPs of the magnetic ferrite family, Fe_3O_4[26], $CoFe_2O_4$[27], $CuFe_2O_4$[28] or $MnFe_2O_4$[29] as examples. The magnetic ferrites have the general formula MFe_2O_4 where M is a metal ion such as Co^{2+}, Mn^{2+}, Cu^{2+}, Ni^{2+}, Zn^{2+} or Fe^{2+}. The initial iron salts for magnetite production are usually the chlorides, $FeCl_2.4H_2O$ and $FeCl_3.6H_2O$, although other salts are sometimes used as well. Research has showed that using NH_4OH as the base to initiate precipitation has the effect of producing more uniform particles[5]. The magnetite can be transformed to maghemite in a number of ways, from heating the magnetite in air[30] to a more controlled oxidation in solution using HNO_3 and $Fe(NO_3)_3$[31]. Magnetite can slowly be oxidised to maghemite without considerable loss of magnetism. Sometimes, magnetite samples might contain some maghemite and so researchers frequently use terms such as iron oxide nanoparticles (ION) or superparamagnetic iron oxide nanoparticles (SPIONs).

Considerable research has been focused on optimizing the conditions for controlled synthesis of MNPs by coprecipitation. Examination of changing parameters in the reaction such as the types of salts used[32], the types of base used[5], the concentration of the salts[33], the pH[34], the ionic strength of the reaction solution[33], reaction temperature[34], reaction time[34], presence of oxygen, post reaction aging and addition rates of reactants have been carried out to optimize the synthesis and to examine the effects on the quality of the particles produced in relation to size, shape and magnetic properties.

Furthermore, additions to the initial reaction mixture of surfactants, polyelectrolytes or other reagents to modify the surface chemistry and control the nucleation process to affect the final size of the particle have also been performed[35][20][36].

1.5.2 Thermal Decomposition Synthesis

Thermal decomposition is a synthetic method used to prepare various magnetic and non-magnetic metals, metal alloys and metal oxides, including the magnetic ferrites. It involves the high temperature decomposition of a precursor, usually a metal-organic precursors, in a high boiling point nonpolar solvent (Figure 1-6). The solvent usually contains stabilising ligands that add to the surface of the particle and control the nucleation process and growth rate to give high quality particles of narrow size distribution. A typical example for the preparation of magnetic iron oxide nanoparticles would be using Fe(lll)-oleate as the metal-organic precursor, 1-octadecene as the high boiling point solvent and oleic acid as the stabilising ligand in a reaction vessel heated to 320 °C to give the spherical monodisperse MNPs[37]. Many modifications have been done to this basic procedure to give control over outcomes such as size, morphology and surface chemistry. Thermal decomposition of the organometallic precursor, such as $Fe(CO)_5$ gives elemental iron MNPs[38]. These type of procedures have been successful in synthesising highly monodisperse MNPs with excellent size control. The main factors that affect the size and shape of the particles include the solvent used, the decomposition temperature, the stabilising ligands and their ratio to the metal precursors and the reaction time[39].

Thermal decomposition leads to high quality particles, but the particles that result are normally hydrophobic and not soluble in water, which may be necessary for further

modification of the MNPs. Therefore, post synthesis modification such as ligand exchange or ligand modification have been explored so the MNPs can be used in aqueous medium [40]. Although this synthetic method produces high quality particles, the limiting factor is that the reaction mixture must be heated to very high temperatures, which can be dangerous and energy demanding. Organic solvents are used and sometimes this chemistry produces environmentally unfriendly waste products. In addition, the need for post synthesis modification means multistep reaction protocols, which are undesirable. This also limits the scalability of this approach. The reaction method is well established though and proven to give reliable results.

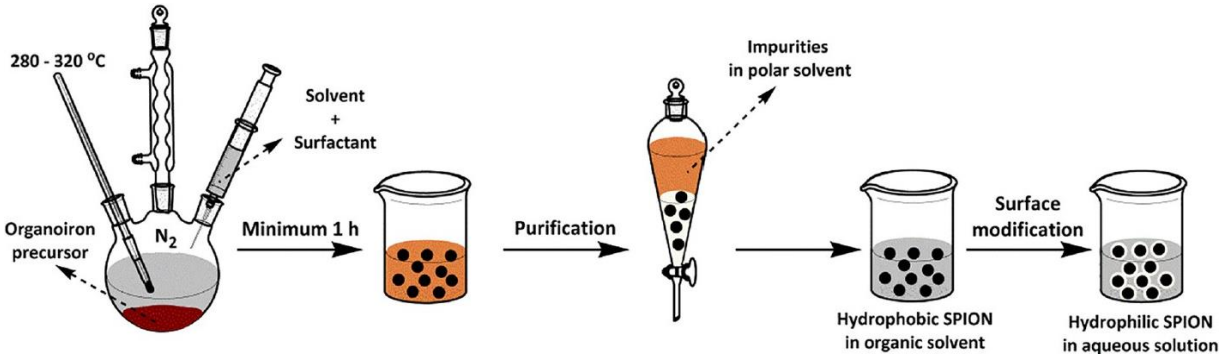


Figure 1-6: Thermal decomposition synthesis basic procedure[41].

1.5.3 Hydrothermal and Solvothermal Synthesis

Hydrothermal synthesis involves the production of MNPs in autoclaves or pressure vessels at high temperatures (>100 °C) and high pressures (>100 atm) in water. Solvothermal synthesis requires the same procedure but using a solvent other than water, such as ethylene glycol, and higher temperatures usually (>200 °C). The high temperatures and pressures of this method can produce high quality nanocrystals of the material being synthesised. The high temperatures and pressures induce rapid nucleation and growth leading to the formation of small sized nanoparticles with good size distribution and high crystallinity. Metal oxides are frequently produced by this method, so it is a way to prepare the magnetic nanoparticles of Fe_3O_4, Fe_2O_3, $CoFe_2O_4$, $MnFe_2O_4$ and other magnetic ferrites (Figure 1-7). Unlike thermal decomposition, this method is not used to produce pure metal or metal alloys. This is because the process either involves hydrolysis and oxidation, or neutralisation of mixed metal hydroxides, as steps in the synthetic pathway to the metal oxide[42].This method can be used

to control the sizes, shapes and composition of the produced MNPs. Both non-coated MNPs [8] and coated MNPs [43] can be prepared by this method.

The solvothermal reactions are still poorly understood from a mechanistic point of view, especially for the non-aqueous versions, making it difficult to develop a theoretical framework and so modification is difficult. Also monitoring of the reaction as it progresses is difficult as the reaction takes place inside a sealed high-pressure vessel. Work has been done to further the understanding of the mechanistic principles[44] and research is still trying to elucidate this process more. A lot of work has been done by this technique to give control over the MNPs produced by studying changes in the experimental conditions such as the types of the solvent[45], the reaction time[44], the ratio of stabilisers to reactants[9], different stabilisers[45], the reactant concentration and the reaction temperature[8].

Once the reaction is completed, the reaction vessel is cooled and the product is separated and washed to yield the required MNPs. The use of high-pressure vessel makes this type of synthesis difficult and the reaction usually takes several hours. In addition, the reaction is not as scalable as other methods due to the high pressures involved but this is a proven method to synthesis high quality magnetic crystals with good control over size and shape.

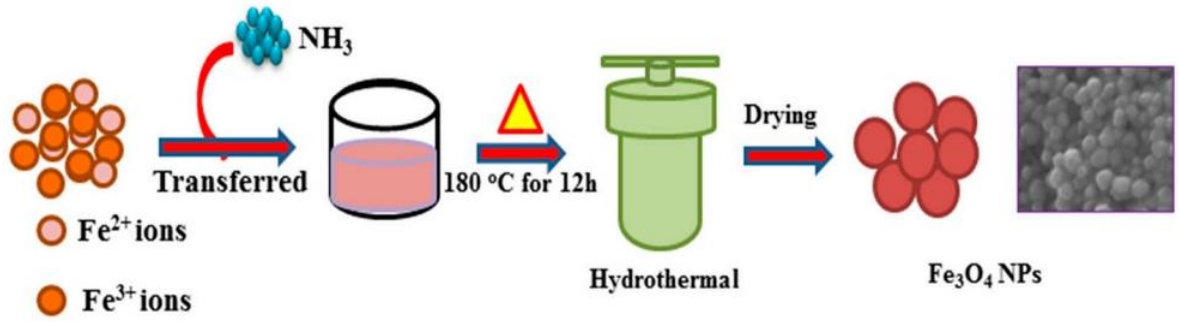


Figure 1-7: Hydrothermal synthesis concept showing the pressure vessel[46].

1.5.4 Microemulsion Synthesis

The microemulsion method is another way to synthesis various MNPs. This method involves the creation of a thermodynamically stable mixture of two immiscible liquids that are isotropic. The two liquids are usually a polar and nonpolar solvent (water and oil). These immiscible liquids are transformed into an emulsion by the addition of a surfactant molecule, a molecule that has a hydrophilic part and a hydrophobic part, to create microdomains of one

of the liquids stabilised by a monolayer of the surface-active molecule. Depending on which liquid is in excess, a water in oil (w/o) or an oil in water (o/w) emulsion will be created. For the water in oil emulsion there will be microdomains of water surrounded by the surfactant in a continuous oil phase (reverse micelles) and for the oil in water emulsion it will be the opposite (normal micelles). The thermodynamic stability is a dynamic one where the microdomains are in continual collisions, coalescing and breaking apart again. The ratio of oil to water to surfactant affects the size of the micelles formed and the microemulsion will have stability over a compositional range of the oil-water-surfactant ensemble. A third type of emulsion known as bicontinuous is where neither liquid is in excess and so individual microdomains are not created.

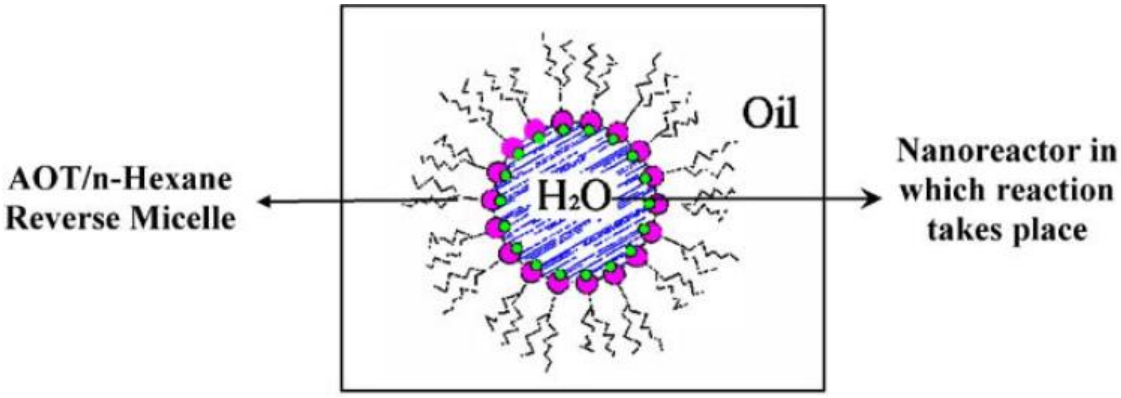


Figure 1-8: Schematic presentation of the structure of reverse micelles formed by dissolving the surfactant AOT in n-hexane. The inner core of the reverse micelle is hydrophilic and can dissolve water-soluble compounds. The size of these inner aqueous droplets can be modulated by controlling the parameter w/o (w/o = [water]/ [surfactant])[47].

For the preparation of spinel type MNPs, w/o is the usual method used (Figure 1-8). The synthesis usually involves mixing two w/o microemulsions containing the reactants (the metal precursors and precipitating base) to form the MNPs [48]. Since the formation of the microdomains are a self-assembly process, the water containing the metal ions, the oil and surfactant can be mixed and allowed to stabilise. Then later the precipitating base can be added to the solution, this will enter the microdomains and cause the MNPs to form[49]. In effect, the walls of the microdomain, created by the surfactant, create individual nano-sized reaction vessels. By varying the reaction conditions, size control of the final particles can be obtained[50]. Several types of magnetic ferrites can be synthesised by this method including Fe_3O_4[48], $MnFe_2O_4$[51] and $CoFe_2O_4$[50]. Many variations of this basic concept have been applied for MNP synthesis. Microemulsion techniques are known to have lower yields than

other methods like coprecipitation and the particles size and shape can vary widely. In addition, scaling up this method can be difficult.

1.5.5 Other Methods

Apart for the main chemical methods mentioned above, there are many other methods to synthesise MNPs. These include milling[2], arc discharge[4], sol-gel processing[6], synthesis by reduction[7], sonochemical[52], combustion[53], flow injection[54], supercritical fluid techniques[35], microwave methods[55], spray pyrolysis[56], laser pyrolysis and microbial methods[57]. Each of these syntheses have their own advantages and disadvantages. The properties of interest from a synthesis include, size of nanoparticle, monodispersity of the sample, crystallinity, magnetic properties such as saturation magnetisation and coercivity, shape and aspect ratio of particles and surface chemical composition after synthesis. The choice of synthesis or formulation of a new method are based on the final application of the MNPs. These factors have to be taken into consideration when designing a synthetic protocol.

1.6 Functionalisation of MNPs

Magnetic nanoparticles are not very useful on their own with few applications for bare MNPs. Nanocomposites, such as core@shell structures present a major interest and found most applications. Functionalisation and coating of MNPs can involve a number of steps to produce a MNP nanocomposite ready for application. Usually one of the first steps in functionalisation of bare MNPs is stabilisation[58] and/or protection[59] of the magnetic core so the other functionalisation can be done afterwards. In the case of metal nanoparticles (Fe, Co, Ni), these nanoparticles are readily oxidised in air so protection is necessary. Other functionalisation would be attachment of catalytic shells[60] or encasement in another material for targeted drug delivery[61].

1.6.1 Stabilisation and Protection

Stabilisation of MNPs is important to prevent the particles aggregation and flocculating out of solution. Stabilisation can be done by adding a surfactant to the particles to prevent

agglomeration by electrostatic or steric means. The best-known example of stabilisation of MNPs in solution are ferrofluids[20]. Ferrofluids are liquids that are responsive to magnetic fields and can be made in either water or oil. In aqueous solution the metal oxide ferrites can be coated with citric acid to form a stabilising surface layer on the MNPs, with numerous examples in the literature[62][63][64][26]. This method stabilises the MNPs in water because of induced electrostatic repulsion between the nanoparticles functionalised with citrate groups. This is because of the binding of the carboxylate group to the surface of the MNP. To create a stabilised metal oxide ferrite in a non-polar solvent, oleic acid is a common choice[37]. This surfactant again binds to the MNP through the carboxylate while the long chain then causes steric repulsion of the MNPs so they do not aggregate. The common attribute is that a carboxylic acid group is present as it binds strongly to the surface of the metal oxide ferrites. Another group that has been found to bind strongly the surface of these class of MNPs are the catechol group[65][66]. So using these groups as part of an organic molecule, one can cause that molecule to bind to a MNP to create functionalised MNPs.

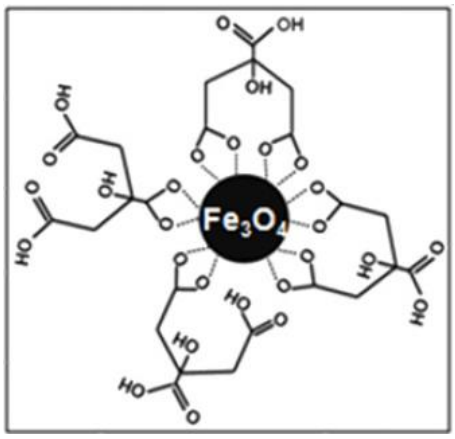


Figure 1-9: Iron oxide MNP showing citric acid binding to surface to create a monolayer[63].

Another common class of surfactants are polymers and polyelectrolytes such as polypyrrole[67], polyaniline[68], polyvinylpyrrolidone[69], polystyrene sulfonate[67], and polyethyleneimine[70] to name just a few. Copolymers, which are polymers made up from more than one type of monomer can also be used[71][72] giving a huge range of surface modification possibilities. Dextran, which is a natural sugar polymer, has been used to coat magnetite as both are biocompatible[73]. These types of stabilised MNP have been approved for clinical usage as MRI contrast agents[74]. They have also been explored as potential drug delivery systems[72][73].

Single molecule and polymer surfactants are good for stabilisation and further functionalisation but offer little protection to the core MNP from chemical attack. Silica coating MNPs is a known method to protect the core from chemical attack[64]. One of the most common examples for the ferrite oxides is the encapsulation in a layer of SiO_2 [75][76], which could then be reduced with H_2 to create a pure metal MNP core of α-Fe[77]. Various protocols for the tuning of the SiO_2 shell are in the literature[78][64][79]. Reasons for adding a SiO_2 layer to a MNP is that the SiO_2 protects the magnetic core, while further functionalisation is possible. Organic molecules can easily be attached by using 3-aminopropyl triethoxysilane. The free amino group can be reacted with another organic molecule (peptide coupling) before or after the silica attachment, where hydroxyl groups on the silica coat of the MNP attack and displace the ethoxy groups (silanisation) of the triethoxysilane group, to produce a range of desired outcome[80]. Silica is good for protection of the core in low pH solution, but silica itself partially dissolves at high pH.

Other protection strategies include precious metal coatings such as gold[81] or platinum[82]. These coatings are unreactive to high and low pH and gold can be further functionalised with molecules containing thiol group to further functionalise the MNP nanocomposite. With their low reactivity, coating of the MNPs precious metals is a difficult task at the metal tends not to adhere readily to the surface of MNPs directly. Various strategies have been employed to enable coating of MNPs with precious metals though, including pre-coating them with polymers and gold seeds[81] or by repeated deposition of gold seeds to build up a gold shell[83].

Carbon coatings have also been employed to protect MNP cores as it has a higher chemical stability[20], however particles are often obtained as agglomerated clusters which is not ideal. This is because of the lack of effective synthetic methods and a low degree of understanding of the formation mechanism behind carbon coating. As such, there is ongoing research to form carbon-coated nanoparticles in isolated form.

1.6.2 Catalytic Shells

The catalyst speeds up chemical reactions enabling the process to finish within a reasonable time and with high yields. The correct choice of reagents, catalyst and solvents can minimize

the environmental impact and reduce waste and costs[84]. In terms of catalysts, two types are defined, homogeneous and heterogeneous catalyst. Homogeneous catalyst are catalysts that are in the same phase as the reagents whereas heterogeneous catalysts are in a different phase (usually on a solid support)[85].

The advantages of homogeneous catalysts are that they have high rates of conversion, can be highly selective, have high catalytic activity due to all catalytic sites being available and it is possible to modify the catalyst for chemo-, regio- and enantio- selectivity. The major disadvantage is that they are difficult to remove from the reaction mixture. Heterogeneous catalyst have the advantage of being easier to remove from the reaction mixture but suffer from lower rates, lower selectivities and activities due to not all site being available to the reaction mixture[86].

Nanoparticles are known to be a bridge between these two types of catalysts[86]. Nanoparticles form colloidal suspensions in the reaction medium (not in the same phase), yet have high surface areas, which lead to higher activity and rates. MNPs as described previously, modified with a suitable catalyst on the surface and which are attracted in a magnetic field, are seen as a possible solution for the easy recovery and recycling of the catalyst and thereby a greener purification of the product. To date this technology has not been realised fully due to reduction in activity of the catalyst with recycling[80], which may be because of poisoning of the catalyst and because of leaching of the catalyst from the surface into the solvent.



Figure 1-10: The two Ni-based catalysts attached to the silica shell of the MNP[87]**.**

One of the most explored areas for catalytic shells is with homogeneous catalysts attached, usually to a silica coated MNPs because of the relative ease of covalently attaching the catalyst to the silica surface, with many reviews on this topic in the literature[88][80][60]. One example from 2010 a group from Korea created a magnetically recyclable catalyst bound to the silica shell (Figure 1-10). Initially the silica coated MNPs were prepared, and then an imidazolinyl-functionalised triethoxysilane was attached to the surface, as the ethoxysilane groups hydrolysed and condensed on to the silica surface. Further reactions were done to convert the

imidazole ring to the Ni-catalyst, with two different catalysts created. The catalysts were both N-heterocyclic carbene-nickel (NHC-Ni) complexes, which can be used to form C-S bonds. Both catalysts performed well with one showing >90% yield for the formation of aryl sulphides from the reaction of thiophenol with aryl halides. Various ring substituents on the precursors having electron-donating and electron-withdrawing character were investigated[87].

Organocatalysts contain no metal centres and are therefore considered to be more environmentally friendly. In addition, organocatalysts do not need the strict anhydrous or inert conditions that metal catalysts need and the catalyst will not leach metal[80]. In one study a group attached a 4-N,N-dimethylaminopyridine catalyst to an MNPs silica shell. The catalyst demonstrated thirty recycles without loss of catalytic activity in a variety of acylation reactions[89]. The same group showed in another paper that the support particle for the attached catalyst can have an influence on the reaction in some cases and therefore cannot always be considered inert[75].

There are other examples in the literature where enzymes were linked to MNPs in order to add magnetic functionality and so enable easy recovery and recycling[90][91]. Enzyme separation after reaction and efficient recovery and reuse of costly enzymes poses a problem and so facile recovery is desirable[80].

1.6.3 Other Shells or Functionalisation Approaches

Other inorganic materials have also been used for coating of MNPs, such as MnO_2[92], TiO_2[93] and various other oxides and metals[94]. It is also been shown to be possible to create multi shell structures with a magnetic core[95]. It is conceivable that with the correct protocols it would be possible to create a core@shell structure from any MNP and almost any other material. Apart from core@shell it has also been shown that other structures can be created using MNP as part of the framework[96] thereby giving a magnetic response of the structure. Finding synthetic methods to create these core@shell structures and other nanocomposites incorporating MNP, so as to expand the body of knowledge currently available is one of the very important goals of nanoparticles research.

1.6.4 Applications of MNPs and their Composites

MNPs and their nanocomposites have a range of applications in various areas of science and technology. For example, stabilised MNPs were researched by NASA as a way to guide propulsion fluids in a zero gravity environment, which led to the ferrofluid industry[97]. Ferrofluids, which are stabilised MNPs in a carrier fluid, are used in electronic devices such as hard drives to form liquid seals[98], in loudspeakers to dissipate heat and dampen the movement[99] and in research to image magnetic domain structures[100].

MNPs have found application as MRI contrast agents with many examples of coated iron oxide MNPs being approved for human usage, such as Resovist®, Feridex® and GastroMARK®. Other types of MNP have been researched such as metal alloys, like FeCo[101], but they have issues with toxicity due to presence of heavy metals. Iron oxide based MRI contrast agents have a number of issues such as they darken the region in the MRI image and so it can be confused with other artefacts (haemorrhage, calcification). In addition, the high magnetic moments of MNP can distort the surrounding image making it unclear[102], it can take longer to process the image when using current iron oxide MNP contrast agents and large MNPs (>60 nm) can be slow to clear from body therefore there is risk of long-term toxicity[103]. Therefore recent research has been around a MNP based contrast agent composed of ultra-small iron oxide MNP (<5 nm)[104]. This type of iron oxide based CA remove some of the issues with MNP contrast agents such as being ultra-small they have lower magnetisation tending towards paramagnetism (not superparamagnetic) and so do not distort the image, they are cleared from the body faster, they have positive contrast and so brighten the image rather than darken it and the process time is faster. Iron oxide based contrast agents are considered safe, as Fe is essential to the body. Research continues in this area with advances being made for iron oxide being used as a dual contrast agent, to both darken and brighten the image as needed, in clinical settings[105].

MNPs have also being researched as drug delivery agents. The magnetic functionality of a MNP nanocomposite means that magnetically guided targeted drug delivery is possible with many examples of this research in the literature[106][61]. Traditional routes for treatment in most cases involve administration of a drug to the whole body. This brings problems where higher doses have to be used to be effective at the diseased region as the drug is diffused throughout the whole body and furthermore the drug may be toxic to healthy regions causing undesired

side effects. MNP with their guidance capability using an external magnetic field bring the possibility to deliver drug payloads to the specific site. Dextran related MNP have already been approved as MRI agents (Feridex®, Resovist®) and dextran-coated MNP can be used as drug delivery agents because drug molecules can be noncovalently retained in the polymeric organic coating. Examples of this include one study where an anti-cancer drug loaded dextran coated MNP was magnetically guided to the tumour with drug release activated by the pH of the cancer cells [73]. In another study, cross-linked dextran MNP modified with carboxylate groups from a commercial source (Nanomag®) loaded with the anti-cancer drug Mitoxantrone were used in treatment of a metastasized tumour in a human patient. The treatment successfully caused a reduction in the size of the tumours by up to 90% [106]. In all cases the loading of the drug and magnetic guidance to the site of the tumour gave less side effects with greater levels of drug accumulation at the tumour site than if the free drug had been used alone [107]. Despite these excellent examples and several other clinical trials in this field, to the best of our knowledge none resulted in FDA approval or commercialisation[108].

Hyperthermia is a cancer therapy based on the localised increase in body temperature resulting in either killing cancer cells or sensitising them to enable other treatments (e.g. chemotherapy). Hyperthermia treatment can be carried out by irradiation with light, microwave, focused ultrasound, radiofrequency ablation, or by electromagnetic induction heating of MNPs to transfer thermal energy to cancerous tissues. The use of MNPs to heat the tumours under an Alternating Magnetic Field (AMF) was first reported in 1957 by Gilchrist[109]. Since then there were very significant developments in this area, particularly associated with the rapid development of the nanomaterials area and the wide introduction of MNPs. MNPs can be magnetically guided to a tumour site and then magnetic inductive heating of the MNPs results in the local temperature elevation of tumour tissues killing cancer cells [110]. Different types of various magnetic nanomaterials have been applied for magnetic hyperthermia therapy. These include metal (Fe, Co, and Ni)[111], metal alloy nanoparticles (FeCo, FePt, CoPt, and FePd)[112], iron oxide based nanoparticles (Fe_3O_4, and Fe_2O_3)[113][114], ferrite nanoparticles ($MnFe_2O_4$, $NiFe_2O_4$, and $ZnFe_2O_4$)[115][116] and various core-shell magnetic nanostructures ($Fe@Fe_3O_4$ and $CoFe_2O_4@MnFe_2O_4$)[117][118].

MNP nanocomposites, such as core@shell structures, have been investigated as recyclable catalysts with extensive research done in this area. For example, one group developed a Pd

nanoparticles supported on carbon coated magnetic nanobeads which showed higher activity than commercial Pd/C, with excellent recyclability[119]. Another catalyst was reported which involved a ruthenium metal centre coordinated to a phenyl ring and to 1,3,5-triaza-7-phosophatricyclo-[3.3.1.1.]-decane, known as RAPTA. RAPTA functionalised silica coated MNPs were utilised for a series of reactions including the hydration of nitriles to nitroamides, the isomerisation of allylic alcohols to ketones, and the cycloisomerisation of Z-enynols to furans. In each case the reactions were conducted over several catalytic cycles with the catalytic MNPs being recycled with conversion rates of over 90% in most cases[120]. The area of easily recycled catalysts using magnetic removal from solution is an exciting area with much potential but unfortunately this area has not moved beyond research with no commercial magnetically retrievable catalysts available to date.

MNPs have also been explored for use in separation, such as pollutant removal from water including organic[92] and heavy metal ions[121], for the chiral resolution of amino acids enantiomers[122] and for separation of biological molecules[123].

MNPs have previously been used in magnetic media tapes for data storage[124]. Research continues in this area with Nanostructured Magnetic Thin Films for use in large capacity hard disk drives being the current area of interest[125].

1.7 Boron Nitride Nanosheets (BNNS) Nanocomposites and Applications

Hexagonal boron nitride (h-BN) is a layered 2D material analogous to graphite[126]. BN possess a much higher chemical and thermal stability than graphene[127]. BN also has high mechanical strength, is electrically insulating and is an excellent lubricant. BN can be prepared as various nanomaterials such as 2D nanosheets[128], 1D nanotubes[129], 0D nano-particles[130] and nanofibers[131] (Figure 1-11). Bulk layered BN can be exfoliated to give boron nitride nanosheets (BNNS) similar to how graphene can be made from graphite[132]. These nanostructures have high surface areas. All these properties make BN nanomaterials excellent candidates for potential applications such as hydrogen storage, catalysis and contaminant removal.

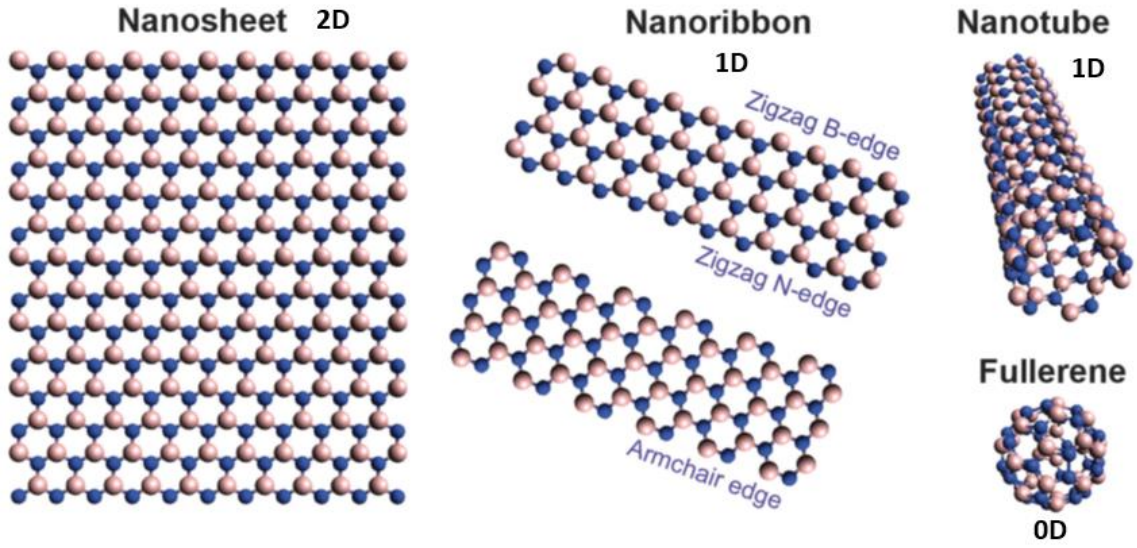


Figure 1-11: Structural models of 2D, 1D and 0D BN nanostructures[133].

For contaminant removal from water there are many approaches including coagulation, precipitation, filtration and sorption. Sorption has shown higher effectiveness for low concentration removal than the other methods, while being environmental friendly. BN has been shown to absorb a wide range of pollutants. Sorption can also be used for pre-concentrating pollutants prior to other treatments. The primary factor in determining the magnitude of sorption onto adsorbents is surface area. Theoretical calculations have shown that porous BN structures can have a surface area of up to 4800 m^2g^{-1}[134]. This makes BN an excellent candidate for water remediation. To date BN has been prepared that has a calculated surface area of up to 1900 m^2g^{-1}[135].

BN nanomaterials, nanocomposites and functionalised BN have been shown to remove heavy metal ions from waste water, such as As(V), Cu(II), Cr(III), Pb(II), Co(II) and Cd(II)[136][137][138][139], with high efficiencies. Various BN nanostructures have also been shown to remove many organic dye pollutants from water too such as Methylene Blue, Congo Red, Basic Yellow 1, Rhodamine B and Malachite Green[137][140][138]. For example, it was shown that the removal of an organic dye (MB) is favoured over the removal of a metal ion (Cu(II)) for BN[137] and further work has demonstrated that organic molecules with more aromatic rings are extracted more efficiently from solution than other organic molecules[141]. Studies have shown that the main process for metal ion removal is electrostatic interaction, while for the aromatic organic molecules there was π-π interactions with the sp^2 hybridised BN surface[134] with a schematic of these process below (Figure 1-12). One study reported

an incredible removal efficiency of 13973 mg g^{-1} for MB, which is almost 14 times the mass of BN used[140]. Other molecules that have been removed from wastewater included psychoactive drugs[141] and proteins[142], which often lead to biofouling of membranes.

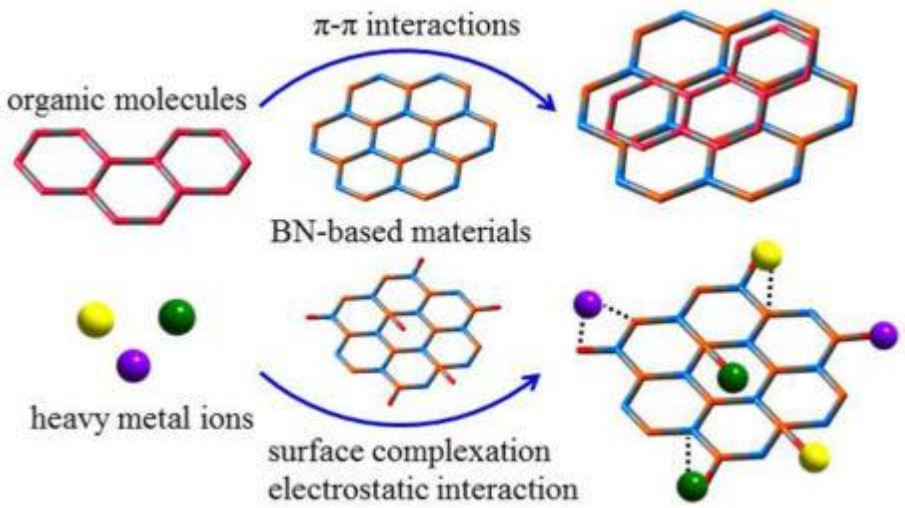


Figure 1-12: Schematic of the interaction mechanism of pollutants with BN-based materials[143]**.**

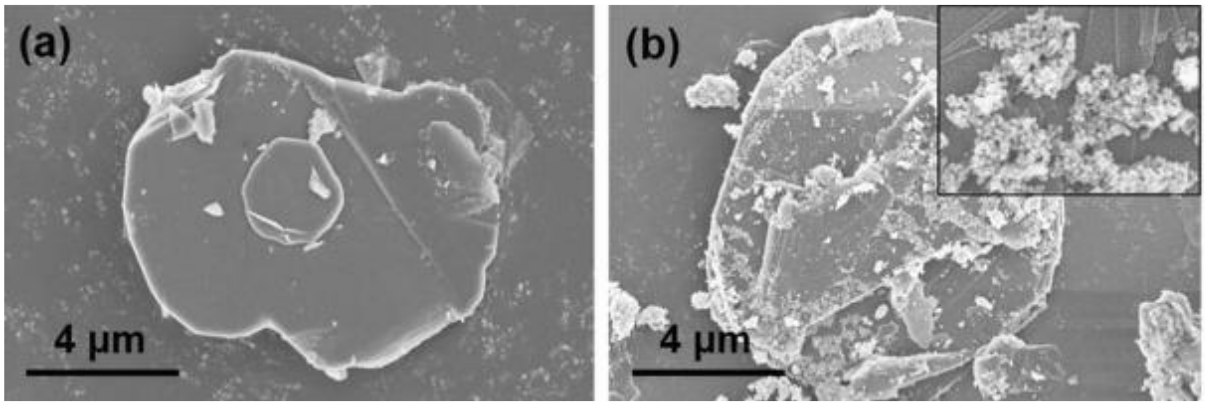


Figure 1-13: Raw BN (a) and BN with Fe_3O_4 on surface (b)[144]**.**

BN coated with MNPs are a relatively new topic with not so many papers on the subject. For example, BN surface has been functionalised with iron oxide[121] and cobalt ferrite[145] and these have been used in application such as toxic heavy metal ion removal from water[136][121], enhancing the thermal conductivity of an interfacial material when used in composite[144][146] and as an electromagnetic wave-absorbing composite[147]. In one of these studies, a hydroxide functionalised BN particles were used for attachment of the Fe_3O_4 with PVP, and then these were processed into a polymer coated Fe_3O_4-BN composite to be used in an epoxy filler for testing. The magnetic functionality enabled particle re-orientation in the epoxy matrix as it was cured. The polymer coated Fe_3O_4-BN composite layer enhanced

the thermal and mechanical properties of the epoxy filler with the chemically introduced outer polymer layer preventing problems during particle alignment[144].

1.8 Aims of the Project

As has been described, MNPs are materials that have already found applications in a variety of sectors and have potential uses in a number of field and so research continues to realise these potential. The main goal of this project is to develop new magnetic core@shell nanoparticle materials and other MNP based nanocomposites. These will be then tested for a number of potential applications, including magnetically retrievable recyclable catalysts, reaction inhibitors and removal of pollutants from water. Our research and technical objectives include:

1. Development of the synthesis of a variety of ferrite based MNPs by the coprecipitation technique and optimisation of nanomaterials with a view to improving the monodispersity index and morphology of the samples, while retaining good magnetic properties
2. Exploration of a solvothermal type reaction in polyol medium but without the need for a high-pressure vessel with the view to gaining some control over the size of the particles produced and maintaining the monodispersity of the sample.
3. Development of the functionalisation of selected MNPs to stabilise and protect the cores with a view to prepare the particles for further functionalisation with catalytic materials or other more useful shells.
4. Functionalisation of MNP cores with manganese dioxide on the surface of to create core@shell structures. Optimisation of the synthesis by trying a few modifications and characterising the outcomes of the process.
5. Functionalisation of MNP cores with cerium dioxide on the surface to create core@shell structures. Again, optimisation of the synthesis by trying a few modifications and characterising the outcomes to get an understanding of the process.
6. Testing of selected core@shell structures in catalysis for oxidation reactions, for use as a magnetically removable glue inhibitor and for water remediation with pollutant removal.

7. Development of BNNS-MNP nanocomposites and using these for removal of organic dyes with a view to creating a magnetically recyclable nanofiltration membrane.
8. Characterisation of the MNPs and the core@shell structures by various instrumental techniques such as TEM, SEM, FTIR, VSM, XRD, DLS and zeta potential.

The project is expected to result in a number of magnetic nanocomposite materials with a range of potential applications.

1.9 References

1 C. Buzea, I. I. Pacheco and K. Robbie, *Biointerphases*, 2007, **2**, MR17--MR71. https://doi.org/10.1116/1.2815690

2 A. M. Gabay, N. G. Akdogan, M. Marinescu, J. F. Liu and G. C. Hadjipanayis, *J. Phys. Condens. Matter*, 2010, **22**, 164213. https://doi.org/10.1088/0953-8984/22/16/164213

3 J. N. Wang, L. Zhang, F. Yu and Z. M. Sheng, *J. Phys. Chem. B*, 2007, **111**, 2119–2124. https://doi.org/10.1021/jp0674118

4 R. Fernández-Pacheco, M. Arruebo, C. Marquina, R. Ibarra, J. Arbiol and J. Santamaría, *Nanotechnology*, 2006, **17**, 1188–1192. https://doi.org/10.1088/0957-4484/17/5/004

5 W. S. Peternele, V. Monge Fuentes, M. L. Fascineli, J. Rodrigues Da Silva, R. C. Silva, C. M. Lucci and R. Bentes De Azevedo, *J. Nanomater.*, 2014, **2014**, 1–11. https://doi.org/10.1155/2014/682985

6 M. V. López-Ramón, M. A. Álvarez, C. Moreno-Castilla, M. A. Fontecha-Cámara, Á. Yebra-Rodríguez and E. Bailón-García, *J. Colloid Interface Sci.*, 2018, **511**, 193–202. https://doi.org/10.1016/j.jcis.2017.09.117

7 K.-C. Huang and S. H. Ehrman, *Langmuir*, 2007, **23**, 1419–1426. https://doi.org/10.1021/la0618364

8 J. Wang, J. Sun, Q. Sun and Q. Chen, *Mater. Res. Bull.*, 2003, **38**, 1113–1118. https://doi.org/10.1016/S0025-5408(03)00129-6

9 Y. Tian, B. Yu, X. Li and K. Li, *J. Mater. Chem.*, 2011, **21**, 2476–2481. https://doi.org/10.1039/c0jm02913k

10 R. Hufschmid, H. Arami, R. M. Ferguson, M. Gonzales, E. Teeman, L. N. Brush, N. D. Browning and K. M. Krishnan, *Nanoscale*, 2015, **7**, 11142–11154. https://doi.org/10.1039/c5nr01651g

11 C. N. R. N. R. Rao, P. J. J. Thomas and G. U. U. Kulkarni, *Nanocrystals: Synthesis, Properties and Applications*, Springer, 2007. https://doi.org/10.1017/CBO9781107415324.004

12 E. L. Wolf, *Nanophysics and Nanotechnology*, Wiley, 2006. https://doi.org/10.1002/9783527618972

13 G. Cao, *Nanostructures and Nanomaterials*, Imperial College Press, 2004. https://doi.org/10.1142/p305

14 Y. Xia, X. Xia and H. C. Peng, *J. Am. Chem. Soc.*, 2015, **137**, 7947–7966. https://doi.org/10.1021/jacs.5b04641

15 Types of Magnetism, https://chem.libretexts.org/Bookshelves/Inorganic_Chemistry/Book%3A_Introduction_to_Inorganic_Chemistry/06%3A_Metals_and_Alloys-_Structure_Bonding_Electronic_and_Magnetic_Properties/6.08%3A_Ferro-_Ferri-_and_Antiferromagnetism

16 Hysteresis Loop - labeled, https://www.nde-ed.org/Physics/Magnetism/HysteresisLoop.xhtml

17 Hard/Soft Hystersis Loops, https://www.electronics-tutorials.ws/electromagnetism/magnetic-hysteresis.html

18 J. M. D. D. Coey, *Magnetism and magnetic materials*, Cambridge University Press, Cambridge, 2010, vol. 9780521816. https://doi.org/10.1017/CBO9780511845000

19 M. Mehrmohammadi, K. Y. Yoon, M. Qu, K. P. Johnston and S. Y. Emelianov, *Nanotechnology*, 2011, **22**, 045502. https://doi.org/10.1088/0957-4484/22/4/045502

20 A.-H. Lu, E. L. Salabas and F. Schüth, *Angew. Chemie Int. Ed.*, 2007, **46**, 1222–1244. https://doi.org/10.1002/anie.200602866

21 V. G. Harris, A. Geiler, Y. Chen, S. D. Yoon, M. Wu, A. Yang, Z. Chen, P. He, P. V. Parimi, X. Zuo, C. E. Patton, M. Abe, O. Acher and C. Vittoria, *J. Magn. Magn. Mater.*, 2009, **321**, 2035–2047. https://doi.org/10.1016/j.jmmm.2009.01.004

22 K. Maaz, A. Mumtaz, S. K. Hasanain and A. Ceylan, *J. Magn. Magn. Mater.*, 2007, **308**, 289–295. https://doi.org/10.1016/j.jmmm.2006.06.003

23 M. Kooti and M. Afshari, *Sci. Iran.*, 2012, **19**, 1991–1995. https://doi.org/10.1016/j.scient.2012.05.005

24 A. S. Drozdov, V. Ivanovski, D. Avnir and V. V. Vinogradov, *J. Colloid Interface Sci.*, 2016, **468**, 307–312. https://doi.org/10.1016/j.jcis.2016.01.061

25 J. Lefort, *Comptes Rendus Acad. Sci. Paris*, 1869, **69**, 179

26 S. Riaz, M. Bashir and S. Naseem, *IEEE Trans. Magn.*, , DOI:10.1109/TMAG.2013.2277614. https://doi.org/10.1109/TMAG.2013.2277614

27 Y. A. Gromova, V. G. Maslov, M. A. Baranov, R. Serrano-García, V. A. Kuznetsova, F. Purcell-Milton, Y. K. Gun'Ko, A. V. Baranov and A. V. Fedorov, *J. Phys. Chem. C*, 2018, **122**, 11491–11497. https://doi.org/10.1021/acs.jpcc.8b00829

28 A. K. Arora and Ritu, *Int. J. Chem. Sci.*, 2013, **11**, 1571–1581

29 T. Kodama, M. Ookubo, S. Miura and Y. Kitayama, *Mater. Res. Bull.*, 1996, **31**, 1501–1512. https://doi.org/10.1016/S0025-5408(96)00146-8

30 I. H. . H. M. van Oorschot and M. . J. Dekkers, *Earth Planet. Sci. Lett.*, 1999, **167**, 283–295. https://doi.org/10.1016/S0012-821X(99)00033-3

31 S. P. Schwaminger, D. Bauer, P. Fraga-García, F. E. Wagner and S. Berensmeier, *CrystEngComm*, 2017, **19**, 246–255. https://doi.org/10.1039/c6ce02421a

32 M. Răcuciu, D. E. Creangă and A. Airinei, *Eur. Phys. J. E*, 2006, **21**, 117–121. https://doi.org/10.1140/epje/i2006-10051-y

33 I. Malinowska, Z. Ryżyńska, E. Mrotek, T. Klimczuk and A. Zielińska-Jurek, *J. Nanomater.*, 2020, **2020**, 1–12. https://doi.org/10.1155/2020/9046219

34 C. Blanco-Andujar, D. Ortega, Q. A. Pankhurst and N. T. K. Thanh, *J. Mater. Chem.*, 2012, **22**, 12498. https://doi.org/10.1039/c2jm31295f

35 A. S. Teja and P.-Y. Koh, *Prog. Cryst. Growth Charact. Mater.*, 2009, **55**, 22–45. https://doi.org/10.1016/j.pcrysgrow.2008.08.003

36 N. V. S. Vallabani and S. Singh, *3 Biotech*, 2018, **8**, 1–23. https://doi.org/10.1007/s13205-018-1286-z

37 J. Park, K. An, Y. Hwang, J. Park, H. Noh, J. Kim, J. Park, N. Hwang and T. Hyeon, *Nat. Mater.*, 2004, **3**, 891–895. https://doi.org/10.1038/nmat1251

38 H. Shao, H. S. Lee, Y. Huang, I. Y. Ko and C. O. Kim, *IEEE Trans. Magn.*, 2005, **41**, 3388–3390. https://doi.org/10.1109/TMAG.2005.855206

39 T. Hyeon, *Chem. Commun.*, 2003, **3**, 927–934. https://doi.org/10.1039/b207789b

40 T. Zhang, J. Ge, Y. Hu and Y. Yin, *Nano Lett.*, 2007, **7**, 3203–3207. https://doi.org/10.1021/nl071928t

41 S. M. Dadfar, K. Roemhild, N. I. Drude, S. von Stillfried, R. Knüchel, F. Kiessling and T. Lammers, *Adv. Drug Deliv. Rev.*, 2019, **138**, 302–325. https://doi.org/10.1016/j.addr.2019.01.005

42 L. H. Reddy, J. L. Arias, J. Nicolas and P. Couvreur, *Chem. Rev.*, 2012, **112**, 5818–5878. https://doi.org/10.1021/cr300068p

43 H. Cai, X. An, J. Cui, J. Li, S. Wen, K. Li, M. Shen, L. Zheng, G. Zhang and X. Shi, *ACS Appl. Mater. Interfaces*, 2013, **5**, 1722–1731. https://doi.org/10.1021/am302883m

44 A. Bunge, A. S. Porav, G. Borodi, T. Radu, A. Pîrnău, C. Berghian-Grosan and R. Turcu, *J. Mater. Sci.*, 2019, **54**, 2853–2875. https://doi.org/10.1007/s10853-018-3030-9

45 S. Xuan, Y. X. J. Wang, J. C. Yu and K. C. F. Leung, *Chem. Mater.*, 2009, **21**, 5079–5087. https://doi.org/10.1021/cm901618m

46 B. Govindan, B. S. Latha, P. Nagamony, F. Ahmed, M. A. Saifi, A. H. Harrath, S. Alwasel, L. Mansour and E. H. Alsharaeh, *Nanomaterials*, , DOI:10.3390/nano7060138. https://doi.org/10.3390/nano7060138

47 A. K. Gupta and M. Gupta, *Biomaterials*, 2005, **26**, 3995–4021. https://doi.org/10.1016/j.biomaterials.2004.10.012

48 K. M. Lee, C. M. Sorensen, K. J. Klabunde and G. C. Hadjipanayis, *IEEE Trans. Magn.*, 1992, **28**, 3180–3182. https://doi.org/10.1109/20.179751

49 J. Lee, Y. Lee, J. K. Youn, H. Bin Na, T. Yu, H. Kim, S.-M. Lee, Y.-M. Koo, J. H. Kwak, H. G. Park, H. N. Chang, M. Hwang, J.-G. Park, J. Kim and T. Hyeon, *Small*, 2008, **4**, 143–152. https://doi.org/10.1002/smll.200700456

50 N. Moumen and M. P. Pileni, *J. Phys. Chem.*, 1996, **100**, 1867–1873.

https://doi.org/10.1021/jp9524136

51 C. Liu, B. Zou, A. J. Rondinone and Z. J. Zhang, *J. Phys. Chem. B*, 2000, **104**, 1143–1145. https://doi.org/10.1021/jp993552g

52 S. I. Nikitenko, Y. Koltypin, O. Palchik, I. Felner, X. N. Xu and A. Gedanken, *Angew. Chemie*, 2001, **113**, 4579–4581. https://doi.org/10.1002/1521-3757(20011203)113

53 M. Houshiar, F. Zebhi, Z. J. Razi, A. Alidoust, Z. Askari, Z. Jafari, A. Alidoust, Z. Askari, Z. J. Razi, A. Alidoust and Z. Askari, *J. Magn. Magn. Mater.*, 2014, **371**, 43–48. https://doi.org/10.1016/j.jmmm.2014.06.059

54 G. Salazar-Alvarez, M. Muhammed and A. A. Zagorodni, *Chem. Eng. Sci.*, 2006, **61**, 4625–4633. https://doi.org/10.1016/j.ces.2006.02.032

55 F. N. Sayed and V. Polshettiwar, *Sci. Rep.*, 2015, **5**, 9733. https://doi.org/10.1038/srep09733

56 A.-H. Lu, X.-Q. Zhang, Q. Sun, Y. Zhang, Q. Song, F. Schüth, C. Chen and F. Cheng, *Nano Res.*, 2016, **9**, 1460–1469. https://doi.org/10.1007/s12274-016-1042-9

57 M. Amiri, M. Salavati-Niasari and A. Akbari, *Adv. Colloid Interface Sci.*, 2019, **265**, 29–44. https://doi.org/10.1016/j.cis.2019.01.003

58 M. A. Dheyab, A. A. Aziz, M. S. Jameel, O. A. Noqta, P. M. Khaniabadi and B. Mehrdel, *Sci. Rep.*, 2020, **10**, 1–8. https://doi.org/10.1038/s41598-020-67869-8

59 J. Liu, S. Z. Qiao, Q. H. Hu and G. Q. Max Lu, *Small*, 2011, **7**, 425–443. https://doi.org/10.1002/smll.201001402

60 J. Govan and Y. Gun'ko, *Nanomaterials*, 2014, **4**, 222–241. https://doi.org/10.3390/nano4020222

61 K. El-Boubbou, *Nanomedicine*, 2018, **13**, 929–952. https://doi.org/10.2217/nnm-2017-0320

62 D. Singh, R. K. Gautam, R. Kumar, B. K. Shukla, V. Shankar and V. Krishna, *J. Water Process Eng.*, 2014, **4**, 233–241. https://doi.org/10.1016/j.jwpe.2014.10.005

63 S. Nigam, K. C. Barick and D. Bahadur, *J. Magn. Magn. Mater.*, 2011, **323**, 237–243.

https://doi.org/10.1016/j.jmmm.2010.09.009

64 J. Zou, Y. G. Peng and Y. Y. Tang, *RSC Adv.*, 2014, **4**, 9693–9700. https://doi.org/10.1039/c3ra47043a

65 E. Amstad, T. Gillich, I. Bilecka, M. Textor and E. Reimhult, *Nano Lett.*, 2009, **9**, 4042–4048. https://doi.org/10.1021/nl902212q

66 O. Gleeson, R. Tekoriute, Y. K. Gun'ko and S. J. Connon, *Chem. - A Eur. J.*, 2009, **15**, 5669–5673. https://doi.org/10.1002/chem.200900532

67 S. Stafford, C. Garnier and Y. K. Gun'Ko, *Nanomaterials*, 2018, **8**, 1044. https://doi.org/10.3390/NANO8121044

68 H. Gu, Y. Huang, X. Zhang, Q. Wang, J. Zhu, L. Shao, N. Haldolaarachchige, D. P. Young, S. Wei and Z. Guo, *Polymer (Guildf).*, 2012, **53**, 801–809. https://doi.org/10.1016/j.polymer.2011.12.033

69 A. Alabresm, S. Mirshahghassemi, G. T. Chandler, A. W. Decho and J. Lead, *Environ. Sci. Nano*, 2017, **4**, 1859–1865. https://doi.org/10.1039/C7EN00257B

70 L. L. Félix, M. A. Rodriguez Martínez, D. G. Pacheco Salazar and J. A. Huamani Coaquira, *RSC Adv.*, 2020, **10**, 41807–41815. https://doi.org/10.1039/D0RA08872B

71 H. Y. Zhu, X. D. Song, X. R. Yang, C. J. Cheng, H. R. Yu and H. H. Zhang, *J. Mater. Sci.*, 2019, **54**, 2960–2974. https://doi.org/10.1007/s10853-018-3072-z

72 L. E. Euliss, S. G. Grancharov, S. O'Brien, T. J. Deming, G. D. Stucky, C. B. Murray and G. A. Held, *Nano Lett.*, 2003, **3**, 1489–1493. https://doi.org/10.1021/nl034472y

73 M. Peng, H. Li, Z. Luo, J. Kong, Y. Wan, L. Zheng, Q. Zhang, H. Niu, A. Vermorken, W. Van De Ven, C. Chen, X. Zhang, F. Li, L. Guo and Y. Cui, *Nanoscale*, 2015, **7**, 11155–11162. https://doi.org/10.1039/c5nr01382h

74 V. F. Cardoso, A. Francesko, C. Ribeiro, M. Bañobre-López, P. Martins and S. Lanceros-Mendez, *Adv. Healthc. Mater.*, 2018, **7**, 1–35. https://doi.org/10.1002/adhm.201700845

75 O. Gleeson, G.-L. Davies, A. Peschiulli, R. Tekoriute, Y. K. Gun'ko and S. J. Connon, *Org.*

Biomol. Chem., 2011, **9**, 7929. https://doi.org/10.1039/c1ob06110k

76 E. Rampazzo, E. Brasola, S. Marcuz, F. Mancin, P. Tecilla and U. Tonellato, *J. Mater. Chem.*, 2005, **15**, 2687. https://doi.org/10.1039/b502052b

77 P. Tartaj and C. J. Serna, *J. Am. Chem. Soc.*, 2003, **125**, 15754–15755. https://doi.org/10.1021/ja0380594

78 D. Yang, J. Hu and S. Fu, *J. Phys. Chem. C*, 2009, **113**, 7646–7651. https://doi.org/10.1021/jp900868d

79 Y. H. Deng, C. C. Wang, J. H. Hu, W. L. Yang and S. K. Fu, *Colloids Surfaces A Physicochem. Eng. Asp.*, 2005, **262**, 87–93. https://doi.org/10.1016/j.colsurfa.2005.04.009

80 R. Dalpozzo, *Green Chem.*, 2015, **17**, 3671–3686. https://doi.org/10.1039/C5GC00386E

81 E. A. Kwizera, E. Chaffin, X. Shen, J. Chen, Q. Zou, Z. Wu, Z. Gai, S. Bhana, R. Oconnor, L. Wang, H. Adhikari, S. R. Mishra, Y. Wang and X. Huang, *J. Phys. Chem. C*, 2016, **120**, 10530–10546. https://doi.org/10.1021/acs.jpcc.6b00875

82 Q. He, Z. Wu, L. Zeng and C. Huang, *Sensors Mater.*, 2012, **24**, 233. https://doi.org/10.18494/SAM.2012.760

83 J. L. Lyon, D. A. Fleming, M. B. Stone, P. Schiffer and M. E. Williams, *Nano Lett.*, 2004, **4**, 719–723. https://doi.org/10.1021/nl035253f

84 D. J. Cole-Hamilton, *Science (80-.).*, 2003, **299**, 1702–1706. https://doi.org/10.1126/science.1081881

85 S. Shylesh, V. Schünemann and W. R. Thiel, *Angew. Chemie Int. Ed.*, 2010, **49**, 3428–3459. https://doi.org/10.1002/anie.200905684

86 V. Polshettiwar and R. S. Varma, *Green Chem.*, 2010, **12**, 743–754. https://doi.org/10.1039/b921171c

87 H.-J. Yoon, J.-W. Choi, H. Kang, T. Kang, S.-M. Lee, B.-H. Jun and Y.-S. Lee, *Synlett*, 2010, **2010**, 2518–2522. https://doi.org/10.1055/s-0030-1258545

88 R. B. Nasir Baig, M. N. Nadagouda and R. S. Varma, *Coord. Chem. Rev.*, 2015, **287**, 137–156. https://doi.org/10.1016/j.ccr.2014.12.017

89 C. Ó Dálaigh, S. A. Corr, Y. Gun'ko and S. J. Connon, *Angew. Chemie Int. Ed.*, 2007, **46**, 4329–4332. https://doi.org/10.1002/anie.200605216

90 V. Polshettiwar and R. S. Varma, *Tetrahedron*, 2010, **66**, 1091–1097. https://doi.org/10.1016/j.tet.2009.11.015

91 R. B. Nasir Baig and R. S. Varma, *Green Chem.*, 2012, **14**, 625. https://doi.org/10.1039/c2gc16301b

92 Y. Zhai, J. Zhai, M. Zhou and S. Dong, *J. Mater. Chem.*, 2009, **19**, 7030. https://doi.org/10.1039/b912767d

93 A. Hasanpour, M. Niyaifar, H. Mohammadpour and J. Amighian, *J. Phys. Chem. Solids*, 2012, **73**, 1066–1070. https://doi.org/10.1016/j.jpcs.2012.04.003

94 R. Ghosh Chaudhuri and S. Paria, *Chem. Rev.*, 2012, **112**, 2373–2433. https://doi.org/10.1021/cr100449n

95 J. Chen, Y. G. Wang, Z. Q. Li, C. Wang, J. F. Li and Y. J. Gu, *J. Phys. Conf. Ser.*, 2009, **152**, 012041. https://doi.org/10.1088/1742-6596/152/1/012041

96 K. V. Lepik, A. R. Muslimov, A. S. Timin, V. S. Sergeev, D. S. Romanyuk, I. S. Moiseev, E. V. Popova, I. L. Radchenko, A. D. Vilesov, O. V. Galibin, G. B. Sukhorukov and B. V. Afanasyev, *Adv. Healthc. Mater.*, 2016, **5**, 3182–3190. https://doi.org/10.1002/adhm.201600843

97 NASA ferrofluid beginings, https://www.nasa.gov/feature/glenn/2021/history/novel-rocket-fuel-spawned-ferrofluid-industry

98 K. van der Wal, R. A. J. van Ostayen and S. G. E. Lampaert, *Tribol. Int.*, 2020, **150**, 106372. https://doi.org/10.1016/j.triboint.2020.106372

99 Ferrofluid in speakers, https://secure.aes.org/forum/pubs/conventions/?elib=2877

100 C. D. Mee, *Proc. Phys. Soc. Sect. A*, 1950, **63**, 922–922. https://doi.org/10.1088/0370-

1298/63/8/122

101 W. S. Seo, J. H. Lee, X. Sun, Y. Suzuki, D. Mann, Z. Liu, M. Terashima, P. C. Yang, M. V. McConnell, D. G. Nishimura and H. Dai, *Nat. Mater.*, 2006, **5**, 971–976. https://doi.org/10.1038/nmat1775

102 J. W. M. M. Bulte and D. L. Kraitchman, *NMR Biomed.*, 2004, **17**, 484–499. https://doi.org/10.1002/nbm.924

103 L. Gu, R. H. Fang, M. J. Sailor and J. H. Park, *ACS Nano*, 2012, **6**, 4947–4954. https://doi.org/10.1021/nn300456z

104 Z. Shen, A. Wu and X. Chen, *Mol. Pharm.*, 2017, **14**, 1352–1364. https://doi.org/10.1021/acs.molpharmaceut.6b00839

105 J. Estelrich, M. J. Sánchez-Martín and M. A. Busquets, *Int. J. Nanomedicine*, 2015, **10**, 1727–1741. https://doi.org/10.2147/IJN.S76501

106 M. G. Krukemeyer, W. Wagner, M. Jakobs and V. Krenn, *Nanomedicine*, 2009, **4**, 875–882. https://doi.org/10.2217/nnm.09.73

107 M. G. Krukemeyer, V. Krenn, M. Jakobs and W. Wagner, *J. Surg. Res.*, 2012, **175**, 35–43. https://doi.org/10.1016/j.jss.2011.01.060

108 P. M. Price, W. E. Mahmoud, A. A. Al-Ghamdi and L. M. Bronstein, *Front. Chem.*, , DOI:10.3389/fchem.2018.00619. https://doi.org/10.3389/fchem.2018.00619

109 R. K. Gilchrist, R. Medal, W. D. Shorey, R. C. Hanselman, J. C. Parrott and C. B. Taylor, *Ann. Surg.*, 1957, **146**, 596–606. https://doi.org/10.1097/00000658-195710000-00007

110 A. Akbarzadeh, M. Samiei and S. Davaran, *Nanoscale Res. Lett.*, 2012, **7**, 144. https://doi.org/10.1186/1556-276X-7-144

111 L. M. Lacroix, N. Frey Huls, D. Ho, X. Sun, K. Cheng and S. Sun, *Nano Lett.*, 2011, **11**, 1641–1645. https://doi.org/10.1021/nl200110t

112 M. Da Yang, C. H. Ho, S. Ruta, R. Chantrell, K. Krycka, O. Hovorka, F. R. Chen, P. S. Lai and C. H. Lai, *Adv. Mater.*, 2018, **30**, 1802444. https://doi.org/10.1002/adma.201802444

113 Y. Yang, X. Liu, Y. Lv, T. S. Herng, X. Xu, W. Xia, T. Zhang, J. Fang, W. Xiao and J. Ding, *Adv. Funct. Mater.*, 2015, **25**, 812–820. https://doi.org/10.1002/adfm.201402764

114 R. Chen, M. G. Christiansen and P. Anikeeva, *ACS Nano*, 2013, **7**, 8990–9000. https://doi.org/10.1021/nn4035266

115 X. L. Liu, C. T. Ng, P. Chandrasekharan, H. T. Yang, L. Y. Zhao, E. Peng, Y. B. Lv, W. Xiao, J. Fang, J. B. Yi, H. Zhang, K. H. Chuang, B. H. Bay, J. Ding and H. M. Fan, *Adv. Healthc. Mater.*, 2016, **5**, 2092–2104. https://doi.org/10.1002/adhm.201600357

116 J. H. Lee, J. T. Jang, J. S. Choi, S. H. Moon, S. H. Noh, J. W. Kim, J. G. Kim, I. S. Kim, K. I. Park and J. Cheon, *Nat. Nanotechnol.*, 2011, **6**, 418–422. https://doi.org/10.1038/nnano.2011.95

117 V. Vilas-Boas, F. Carvalho and B. Espiña, *Molecules*, 2020, **25**, 1–30. https://doi.org/10.3390/molecules25122874

118 P. Das, M. Colombo and D. Prosperi, *Colloids Surfaces B Biointerfaces*, 2019, **174**, 42–55. https://doi.org/10.1016/j.colsurfb.2018.10.051

119 Q. M. Kainz, R. Linhardt, R. N. Grass, G. Vilé, J. Pérez-Ramírez, W. J. Stark and O. Reiser, *Adv. Funct. Mater.*, 2014, **24**, 2020–2027. https://doi.org/10.1002/adfm.201303277

120 S. E. García-Garrido, J. Francos, V. Cadierno, J.-M. Basset and V. Polshettiwar, *ChemSusChem*, 2011, **4**, 104–111. https://doi.org/10.1002/cssc.201000280

121 R. S. Bangari, V. K. Yadav, J. K. Singh and N. Sinha, *ACS Omega*, 2020, **5**, 10301–10314. https://doi.org/10.1021/acsomega.9b04295

122 K. N. Jayaprabha and P. A. Joy, *RSC Adv.*, 2015, **5**, 22117–22125. https://doi.org/10.1039/c4ra16044d

123 W. Wu, C. Z. Jiang and V. A. L. Roy, *Nanoscale*, 2016, **8**, 19421–19474. https://doi.org/10.1039/C6NR07542H

124 Jones, D.; Manquen, D. (2008). "Chapter 28. Magnetic Recording and Playback". Handbook for Sound Engineers, Fourth Edition. Focal Press / Elsevier. ISBN 9780240809694.

125 J.-W. Liao, H.-W. Zhang and C.-H. Lai, in *Magnetic Nanomaterials - Fundamentals, Synthesis and Applications*, Wiley-VCH Verlag GmbH & Co. KGaA, Weinheim, Germany, 2017, pp. 439–472. https://doi.org/10.1002/9783527803255.ch14

126 H. Ribeiro, P. von Cardoso Randow, D. N. Vilela, M. Adriane Luciano and L. Maria de Andrade, *Recent Adv. Boron-Containing Mater.*, 2020, **i**, 13. https://doi.org/10.5772/intechopen.80849

127 J. Yu, L. Qin, Y. Hao, S. Kuang, X. Bai, Y.-M. Chong, W. Zhang and E. Wang, *ACS Nano*, 2010, **4**, 414–422. https://doi.org/10.1021/nn901204c

128 T. Sainsbury, A. Satti, P. May, Z. Wang, I. McGovern, Y. K. Gun'ko and J. Coleman, *J. Am. Chem. Soc.*, 2012, **134**, 18758–18771. https://doi.org/10.1021/ja3080665

129 J. Wu and L. Yin, *ACS Appl. Mater. Interfaces*, 2011, **3**, 4354–4362. https://doi.org/10.1021/am201008n

130 C. Tang, Y. Bando, Y. Huang, C. Zhi and D. Golberg, *Adv. Funct. Mater.*, 2008, **18**, 3653–3661. https://doi.org/10.1002/adfm.200800493

131 Y. Qiu, J. Yu, J. Rafique, J. Yin, X. Bai and E. Wang, *J. Phys. Chem. C*, 2009, **113**, 11228–11234. https://doi.org/10.1021/jp901267k

132 J. N. Coleman, M. Lotya, A. O'Neill, S. D. Bergin, P. J. King, U. Khan, K. Young, A. Gaucher, S. De, R. J. Smith, I. V. Shvets, S. K. Arora, G. Stanton, H. Y. Kim, K. Lee, G. T. Kim, G. S. Duesberg, T. Hallam, J. J. Boland, J. J. Wang, J. F. Donegan, J. C. Grunlan, G. Moriarty, A. Shmeliov, R. J. Nicholls, J. M. Perkins, E. M. Grieveson, K. Theuwissen, D. W. McComb, P. D. Nellist and V. Nicolosi, *Science (80-.).*, 2011, **331**, 568–571. https://doi.org/10.1126/science.1194975

133 A. Pakdel, Y. Bando and D. Golberg, *Chem. Soc. Rev.*, 2014, **43**, 934–959. https://doi.org/10.1039/C3CS60260E

134 J. Dai, X. Wu, J. Yang and X. C. Zeng, *J. Phys. Chem. Lett.*, 2014, **5**, 393–398. https://doi.org/10.1021/jz4026535

135 Q. Weng, X. Wang, Y. Bando and D. Golberg, *Adv. Energy Mater.*, 2014, **4**, 1301525. https://doi.org/10.1002/aenm.201301525

136 R. Chen, C. Zhi, H. Yang, Y. Bando, Z. Zhang, N. Sugiur and D. Golberg, *J. Colloid Interface Sci.*, 2011, **359**, 261–268. https://doi.org/10.1016/j.jcis.2011.02.071

137 X. Zhang, G. Lian, S. Zhang, D. Cui and Q. Wang, *CrystEngComm*, 2012, **14**, 4670. https://doi.org/10.1039/c2ce06748j

138 J. Li, X. Xiao, X. Xu, J. Lin, Y. Huang, Y. Xue, P. Jin, J. Zou and C. Tang, *Sci. Rep.*, 2013, **3**, 3208. https://doi.org/10.1038/srep03208

139 F. Liu, J. Yu, X. Ji and M. Qian, *ACS Appl. Mater. Interfaces*, 2015, **7**, 1824–1832. https://doi.org/10.1021/am507491z

140 Q. Li, T. Yang, Q. Yang, F. Wang, K.-C. Chou and X. Hou, *Ceram. Int.*, 2016, **42**, 8754–8762. https://doi.org/10.1016/j.ceramint.2016.02.114

141 D. Liu, W. Lei, S. Qin, K. D. Klika and Y. Chen, *Phys. Chem. Chem. Phys.*, 2016, **18**, 84–88. https://doi.org/10.1039/C5CP06399J

142 Y. Lin, T. V. Williams, T.-B. Xu, W. Cao, H. E. Elsayed-Ali and J. W. Connell, *J. Phys. Chem. C*, 2011, **115**, 2679–2685. https://doi.org/10.1021/jp110985w

143 A. Gupta, T. Sakthivel and S. Seal, *Prog. Mater. Sci.*, 2015, **73**, 44–126. https://doi.org/10.1016/j.pmatsci.2015.02.002

144 K. Kim, H. Ju and J. Kim, *Polymer (Guildf).*, 2016, **91**, 74–80. https://doi.org/10.1016/j.polymer.2016.03.066

145 Q. Zhang, Z. Li, X. Li, L. Yu, Z. Zhang and Z. Wu, *Nano*, 2019, **14**, 1950063. https://doi.org/10.1142/S1793292019500632

146 M. Salehirad, M. M. Alavi Nikje and L. Ahmadian-Alam, *Ind. Eng. Chem. Res.*, 2018, **57**, 1803–1814. https://doi.org/10.1021/acs.iecr.7b03540

147 W. Ye, Q. Sun, X. Long and Y. Cai, *RSC Adv.*, 2020, **10**, 11121–11131. https://doi.org/10.1039/d0ra00785d

2 Experimental

2.1 Materials, Equipment and General Procedures

2.1.1 Starting Materials and Solvents

Iron(lll) chloride hexahydrate, reagent grade ≥98%, **Iron(ll) chloride tetrahydrate**, p.a. ACS reagent, **Cobalt(ll) chloride hexahydrate**, reagent grade ≥98%, **Potassium Permanganate**, ACS reagent >99%, **Ethylene Glycol**, anhydrous 98%, **Tetraethyl orthosilicate**, reagent grade 98%, **HMTA**, reagent grade 99%, **Aniline**, reagent grade, **Methylene Blue**, reagent grade, **Rhodamine B**, reagent grade, **Methyl Orange**, reagent grade, **Ethanol**, HPLC grade, **Boron Nitride**, reagent grade, **Citric Acid**, 99%, **Trisodium Citrate dihydrate**, >99% ACS reagent, were supplied by Sigma-Aldrich. **Hydrazine Hydrate**, reagent grade, **Copper(ll) tetrafluoroborate**, reagent grade, **tert-butyl peroxybenzoate**, Luperox® P, 98%, **Triethylene glycol dimethacrylate**, 95%, were supplied by Aldrich. **Ammonia Solution 25%,** analytical reagent grade, **Sodium Hydroxide**, reagent grade, were supplied by Fisher Scientific. **Manganese(ll) Chloride**, reagent ACS, **Benzaldehyde**, reagent grade 99%, **Ammonium Chloride,** 99% grade, **Sulphuric Acid**, 95-97%, **Copper(ll) chloride dehydrate,** reagent grade, were supplied by Riedel-de Haen. **Sodium Acetate**, extra pure >99%, Durapore® 0.45 µm **PVDF membrane** was supplied by Merck. **Ethylenediamine**, >99%, was supplied by Merck-Schuchardt. **Benzyl Alcohol**, 98+% extra dry, was supplied by Acros Organics. **Cerium(III) Nitrate Hexahydrate**, extra pure 99.5%, was supplied by Fluka. **Toluene**, HPLC grade, was supplied by Honeywell.

Millipore water was obtained using a Synergy 185 Millipore filtration system equipped with a 0.22 µm filter that was filtering distilled water. Technical grade solvents (Ethanol, Methanol and Acetone) were supplied by TCD solvent stores.

2.1.2 Small Lab Equipment used in the Synthesis and Processing of Materials

Heating with magnetic stirring was performed using a Sigma-Aldrich MSC Basic S46 Heating Mantle with integrated magnetic stirring, equipped with a Sigma-Aldrich IKA ETS D4 Temperature controller.

Heating with mechanical stirring was performed using a Sigma-Aldrich MSC Basic S46 hot plate (from which the magnetic stirring element had been removed), equipped with a Sigma-Aldrich IKA ETS D4 Temperature controller. The mechanical stirrer was an IKA Stirrer with a PTFE paddle.

The sonic bath used for ultrasonic agitation was a Wise Clean WUC-A03H operating at 40 kHz with 124 W output capable of heating up to 85 °C.

The vacuum pump used for degassing and the vacuum oven was an Edwards RV5 Rotary Vane Pump capable of a vacuum of 0.2 Pa in high vacuum mode.

The oven used for drying was a Binder FED115, which has an accurate temperature controlled heating range from +10 °C above ambient to 300 °C.

The vacuum oven was a Gallenkamp Vacuum Oven OVA03100 with an Edwards RV5 Rotary Vane Pump attached capable of heating samples up to 200 °C under vacuum.

The furnace was an Elite Model BMF11/7 equipped with a EuroTherm 2416 digital controller capable of heating to 1100 °C.

Magnetic Extraction was done using two types of neodymium magnets; a rectangular magnet with 32.3 kg pull[1] and a round magnet with 81 kg pull[2], both supplied by first4magnets.com.

2.1.3 General Procedures

Degassing of water and other solvents

The liquid to be degassed was place in a RBF and connected to a Schlenk line. The solution was put under vacuum until it boiled while sonicating. The solution was allowed to boil gently for 1 minute. Then the solution was flashed with argon to atmospheric pressure. This process was repeated 5-10 times depending on the volume of liquid. Once degassed the container with the liquid was sealed under argon and only opened with argon flowing over it.

2.1.4 General Sample Preparation for Characterisation

Dry Sample Preparation (FTIR, VSM, XRD)

For dry sample characterisation, the product was extracted from the storage solution (by magnet or by centrifuging) and was left to dry overnight in an oven (70 °C) or dried in a vacuum oven at 80 °C. The dried product was broken up to a powder using a glass rod. If necessary the powder was ground with an Agate mortar and pestle. This powder was used for characterisation.

Wet Sample Preparation (TEM, SEM)

For TEM sample preparations approx. 1-2 mg of the material stored in solution was sonicated in 1-1.5 mL EtOH to disperse to create a solution that was semi-transparent. Then approximately 15 µL (1 drop) of this solution was dropped onto a TEM grid on filter paper, covered and left to dry. This TEM grid could then be used for getting TEM and SEM images.

Wet Sample Preparation (DLS, Zeta Potential)

For DLS approximately 1-2 mg of the material stored in solution was sonicated in 2-3 mL of MP H_2O to create a solution that was semi-transparent while for Zeta Potential it was sonicated in 2-3 mL of the pH adjusted MP H_2O. These solutions could then be used for DLS and Zeta Potential measurements.

2.2 Experimental Protocols for Chapter 3

2.2.1 Preparation of Magnetite MNPs by Coprecipitation (Fe_3O_4)

The Fe_3O_4 MNPs were prepared according to the previously reported procedures that was modified by us [3][4].

NH_4Cl (0.30 g, 5.6 mmol) was dissolved in MP H_2O (150 mL) and the solution was degassed and put under argon. Stock (25%) ammonia solution (40 mL, 581 mmol) was added and the solution was set up for mechanical stirring under argon and heated to 90 °C. Separately $FeCl_2.4H_2O$ (0.86 g, 4.3 mmol) and $FeCl_3.6H_2O$ (2.33 g, 8.6 mmol) were dissolved in degassed MP H_2O (50 mL) under argon. The iron solution was added dropwise to the ammonia solution using a pressure equalised dropping funnel with argon flow down the dripping funnel. The solution was left stirring for 2 hours under argon at 90 °C. After this, the solution was allowed to cool to RT and then the product was magnetically extracted. The product was washed with MP H_2O (100 mL), MeOH (2 x 100 mL) and acetone (100 mL). The product was stored in EtOH for further use.

2.2.2 Preparation of Manganese Ferrite MNPs by Coprecipitation ($MnFe_2O_4$)

The $MnFe_2O_4$ MNP were prepared according to a modified procedure[5].

NH_4Cl (0.15 g, 2.8 mmol) was dissolved in MP H_2O (75 mL) and the solution was degassed and put under argon. Stock (25%) ammonia solution (20 mL, 290 mmol) was added and the solution was set up for mechanical stirring under argon and heated to 90 °C. Separately $MnCl_2.4H_2O$ (0.43 g, 2.2 mmol) and $FeCl_3.6H_2O$ (1.17 g, 4.3 mmol) were dissolved in degassed MP H_2O (25 mL) under argon. The metal ion solution was added to the ammonia solution using a pressure equalised dropping funnel with argon flow down the dropping funnel. The solution was left stirring for 2 hours under argon at 90 °C. The solution was allowed to cool to RT and then the product was magnetically extracted. The product was washed with MP H_2O (100 mL), MeOH (2 x 100 mL) and acetone (100 mL). The product was stored in EtOH for further use.

2.2.3 Preparation of Cobalt Ferrite MNPs by Coprecipitation ($CoFe_2O_4$)

The $CoFe_2O_4$ NP were prepared according to a previously reported procedures that were modified by us [6][7].

Hydrazine (2 mL, 50% solution)) and stock (25%) ammonia solution (4 mL, 58 mmol) were added to degassed MP H_2O (150 mL). The solution was set up for mechanical stirring and heated to 90 °C. Separately $CoCl_2{\cdot}6H_2O$ (1.01 g, 4.3 mmol) and $FeCl_3{\cdot}6H_2O$ (2.30 g, 8.5 mmol) were dissolved in degassed MP H_2O (25 mL). The metal ion solution was added to the ammonia solution using a pressure equalised dropping funnel open to air. The solution was left stirring for 2 hours open to air at reflux. The solution was cooled to RT. The cobalt ferrite product were extracted using a strong Nd-based magnet. The product was washed with MP H_2O (100 mL), MeOH (2 x 100 mL) and acetone (100 mL). The product was stored in EtOH for further use.

2.2.4 Preparation of Copper Ferrite MNPs by Coprecipitation ($CuFe_2O_4$)

The $CuFe_2O_4$ NP were prepared according to a modified procedure[8].

$CuCl_2{\cdot}6H_2O$ (0.36 g, 2.1 mmol) and $FeCl_3{\cdot}6H_2O$ (1.13 g, 4.2 mmol) were dissolved in degassed MP H_2O (75 mL) under argon. The solution was mechanically stirred with heating to 90 °C. NaOH solution (1 M) was added to bring the solution to pH 12. The solution was mechanically stirred with heating at reflux for 2 hours under argon. The product was extracted by centrifuge, washed with MP H_2O and dried at 80 °C for 24 hours. The product was then annealed at 800 °C for 2 hours.

2.2.5 Preparation of Manganese Ferrite MNPs by Polyol ($MnFe_2O_4$)

The $MnFe_2O_4$ NP were prepared according to a previously reported procedure that was modified by us[9].

$FeCl_3.6H_2O$ (2.34 g, 8.7 mmol) and $MnCl_2.4H_2O$ (0.86 g, 4.3 mmol) were mixed in ethylene glycol (50 mL) and mechanically stirred until dissolved. Separately CH_3COONa (3.56 g, 43.4 mmol) was added to ethylene glycol (50 mL) and stirred until dissolved. The two solutions were mixed and set up for heating with mechanical stirring. The solution was refluxed (BP EG

is approx. 198 °C) for 20 hours with the condenser open to air. The solution was cooled to RT and the particles were extracted using a permanent neodymium magnet. The product was washed with MP H_2O (100 mL), MeOH (2 x 100 mL) and acetone (100 mL). The product was stored in EtOH for further use.

2.2.6 Preparation of Magnetite MNPs by Polyol (Fe_3O_4)

The Fe_3O_4 NP were prepared according to a previously reported procedure that was modified by us [9].

$FeCl_3.6H_2O$ (3.50 g, 12.9 mmol) was mixed in ethylene glycol (50 mL) and mechanically stirred until dissolved. Separately sodium acetate (3.54 g, 43.1 mmol) was added to ethylene glycol (50 mL) and stirred until dissolve. The two solutions were mixed and set up for heating with mechanical stirring. The solution was refluxed (BP EG is approx. 198 °C) for 20 hours under argon. The solution was cooled to RT and the particles were extracted using a permanent neodymium magnet. The product was washed with MP H_2O (100 mL), MeOH (2 x 100 mL) and acetone (100 mL). The product was stored in EtOH for further use.

2.3 Experimental Protocols for Chapter 4

2.3.1 Preparation of Citrate Stabilised Magnetite MNPs (Fe_3O_4@citrate)

The Fe_3O_4 (coprecipitated) magnetic nanoparticles were stabilised with citrate according to a previously reported procedure that was modified by us[10].

Magnetite nanoparticles (0.50 g, 2.1 mmol) prepared using coprecipitation were sonicated for 30 minutes in degassed MP water (100 mL) under argon. 0.5 molar equivalents of trisodium citrate, $Na_3C_6H_5O_7{\cdot}2H_2O$ (0.32 g, 1.1 mmol) was added to the sonicating solution. The solution was sonicated with heating (80 °C) under argon for 2 hours). The solution was allowed to cool to RT and the solution was brought to pH 7 with the addition of a citric acid solution (5.2 M, 1 g/mL). The Fe_3O_4@citrate were magnetically extracted from the solution by the addition of a

few drops of NaCl solution (4 M). The MNP were dispersed in degassed MP water (100 mL) and stored under argon.

2.3.2 Preparation of Citrate Stabilised Manganese Ferrite MNPs ($MnFe_2O_4$@citrate)

The $MnFe_2O_4$ (polyol) were stabilised with citrate using the same procedure as for magnetite above.

Manganese ferrite nanoparticles (0.50 g, 2.1 mmol) prepared using polyol synthesis were sonicated in degassed MP water (100 mL) for 30 minutes under argon. 0.5 molar equivalents of trisodium citrate, $Na_3C_6H_5O_7 \cdot 2H_2O$ (0.32 g, 1.1 mmol) was added to the sonicating solution. The solution was sonicated with heating (80 °C) under argon for 2 hours). The solution was allowed to cool to RT and the solution was brought to pH 7 with the addition of a citric acid solution (5.2 M). The $MnFe_2O_4$@citrate were magnetically extracted from the solution by the addition of a few drops of NaCl solution (4 M). The MNP were dispersed in degassed MP water (100 mL) and stored under argon.

2.3.3 Preparation of Silica Nanoparticles (SiO_2)

SiO_2 nanoparticles were synthesised using the Stober method[11].

EtOH (50 mL) was added to a RBF (100 mL) and magnetically stirred at RT. Tetraethyl orthosilicate (TEOS) (0.90 mL, 4.0 mmol) was added in bulk to the ETOH and stirred for 5 minutes. Stock (25%) ammonia solution (2.5 mL, 36.3 mmol) was added dropwise over 5 minutes. The solution was left stirring for 2 hours. The solution was brought to pH 7 with HCl solution (10 M). The product was separated by centrifugation and washed with MeOH (100 mL) and water (100 mL). The product was stored in H_2O (50 mL).

2.3.4 Preparation of Core@Shell Magnetite@Silica MNPs (Fe_3O_4@SiO_2)

The citrate stabilised magnetite nanoparticles (Fe_3O_4@citrate) were coated with silica using a modified previously reported procedure[12].

Fe_3O_4@citrate (0.1 g, 20 mL of previously made solution) was added to a RBF (1000 mL) with HPLC EtOH (400 mL), MP H_2O (80 mL) and stock (25%) ammonia solution (12.5 mL, 182 mmol). The solution was sonicated for 15 minutes to disperse the particles. The solution was set up for mechanical stirring at RT. TEOS (2.5 mL, 11.2 mmol) was added in batches (0.25 mL every 30 minutes in bulk). The solution was left stirring overnight. The solution was brought to pH 7 with HCl solution (10 M). The product was magnetically separated, washed with EtOH (2 x 100 mL). The product was stored in EtOH (100 mL).

2.3.5 Preparation of Core@Shell Manganese Ferrite@Silica MNPs ($MnFe_2O_4$@SiO_2)

The citrate stabilised manganese ferrite nanoparticles ($MnFe_2O_4$@citrate) were coated with silica using the same procedure as for the citrate stabilised magnetite nanoparticles.

$MnFe_2O_4$@citrate (0.1 g, 20 mL of previously made solution) was added to a RBF (1000 mL) with HPLC EtOH (400 mL), MP H_2O (80 mL) and stock (25%) ammonia solution (12.5 mL, 182 mmol). The solution was sonicated for 15 minutes to disperse the particles. The solution was set up for mechanical stirring at RT. TEOS (0.19 mL, 0.83 mmol) was added in 2 batches (0.095 mL every 30 minutes in bulk). The solution was left stirring overnight. The solution was adjusted to pH 7 with HCl solution (10 M). The product was magnetically separated, washed with EtOH (2 x 100 mL). The product was stored in EtOH (100 mL).

2.4 Experimental protocols for Chapter 5

2.4.1 Preparation of Manganese Dioxide Nanoparticles (MnO_2)

Manganese Dioxide nanoparticles have been prepared by reduction of $KMnO_4$ with an alcohol.

HPLC ethanol (100mL) was magnetically stirred in a RBF. To this $KMnO_4$ solution (0.1 M, 43 mL) was slowly added to the ethanol. After addition, the solution was heated to reflux (80 °C) with stirring for 1 hour. The product was separated by filtration and washed with MP H_2O several times. The MnO_2 product was dried in the oven (70 °C) overnight.

Manganese Dioxide nanoparticles have also been prepared by reaction of $KMnO_4$ with H_2SO_4.

$KMnO_4$ solution (0.1 M, 57 mL) was added to a RBF and heated (90 °C) with magnetic stirring. Stock H_2SO_4 (17.8 M, 0.17 mL) was added to MP H_2O (40 mL) and magnetically stirred for 5 minutes. The H_2SO_4 solution was added dropwise to the heating $KMnO_4$ solution. The solution was refluxed (100 °C) for 2 hours with condenser attached. The product was separated by filtration and washed with MP H_2O several times. The MnO_2 product was dried in the oven (70 °C) overnight.

2.4.2 Preparation of Manganese Ferrite@Manganese Dioxide core@shell MNPs ($MnFe_2O_4$@MnO_2)

The $MnFe_2O_4$@MnO_2 NPs were prepared according to a previously reported procedure that was modified by us [13].

$MnFe_2O_4$ MNP (1 g) were sonicated in MP H_2O (200 mL) in RBF (500 mL) with heating (75 °C) with condenser attached to disperse the MNP. $KMnO_4$ solution (0.2 M, 3.62 mL) was added in bulk to the sonicating solution. H_2SO_4 solution (0.2 M, 1.81 mL) was added dropwise to the sonicating heated solution and allowed to sonicate for 1 hour. The particles were magnetically extracted and washed once with water and EtOH. The MNP were transferred to EtOH (200 mL) in a RBF (500 mL). The solution was heated (70 °C) with condenser attached while sonicating. $KMnO_4$ solution (0.2 M, 3.62 mL) was added dropwise to the sonicating solution. The solution was sonicated for 1 hour. The particles were magnetically extracted and washed once with water and EtOH. This whole process was repeated 2 more times (6 separate sonicating sessions overall). The particles were dried in a vacuum oven (80 ^{o}C) and stored in sample tubes. These particles could readily be dispersed in solution with sonication.

2.4.3 Preparation of Cerium Dioxide Nanoparticles (CeO_2)

CeO_2 nanoparticles were synthesised using a previously reported procedure[14].

Cerium nitrate, $Ce(NO_3)_3{\cdot}6H_2O$ (3.71 g, 8.5 mmol) was dissolved in MP H_2O (230 mL) in a RBF (500 mL) with magnetic stirring. Hexamethylenetetramine $(CH_2)_6N_4$ (16.16g, 115.3 mmol) was added to the stirring solution. The solution was left stirring overnight (12 hr). The solution was

heated to 80 C for 2 hours while stirring. The product was separated by centrifugation and washed with MeOH (100 mL) and water (2 x 100 mL). The product was dried in a vacuum oven at 80 °C. The product was calcined at 800 °C for 2 hours.

2.4.4 Preparation of Manganese Ferrite@Silica@Cerium Dioxide MNPs ($MnFe_2O_4@SiO_2@CeO_2$)

$MnFe_2O_4@SiO_2$ MNPs (0.75 g) were sonicated in MP H_2O (200 mL) in RBF (500 mL) to disperse the MNP. Cerium nitrate, $Ce(NO_3)_3{\cdot}6H_2O$ (1.78 g, 4.1 mmol) was added to the solution and sonicated for 30 minutes. The solution was set up for mechanical stirring. The solution was cooled on ice while stirring. Hexamethylenetetramine $(CH_2)_6N_4$ (8.04g, 57.3 mmol) was added to the stirring solution. The solution was left stirring at RT for 16 hours. The solution was heated (70 °C) for 2 hours. The particles were magnetically extracted and washed once with MeOH (100 mL) and water (2 x 100 mL). The particles were stored in 200 mL of EtOH.

2.5 Experimental Protocols for Chapter 6

2.5.1 Procedure for Catalytic Oxidation of Benzyl Alcohol to Benzaldehyde

Benzyl alcohol (1 mL, 9.7 mmol) was placed in toluene (20 mL) in a RBF (100 mL). The required core@shell MNPs with catalytic shell (0.2g) were added and the solution was sonicated to disperse the MNPs. The solution was heated (with high efficiency condenser attached) at 100 °C (BP toluene = 110 °C) for 2 hours in a magnetic field free environment, with air bubbling through gently. The bubbling air mixed the solution and was the oxygen source for oxidation. The solution was cooled and the MNPs were separated. The solution was filtered through a 0.2 µm syringe filter. The solvent was evaporated. The product was stored in sample tubes. The MNPs were washed with acetone (100 mL), EtOH (100 mL) and water (100 mL). The particles were magnetically separated and dried in a vacuum oven (80 °C) before being recycled in next catalytic process.

2.5.2 Procedure for Catalytic Oxidation of Benzyl Alcohol to Benzylidene Alinine

Benzyl alcohol (0.5 mL, 4.8 mmol) and aniline (0.87 mL, 9.7 mmol) was placed in toluene (15 mL) in a RBF (100 mL). The required core@shell MNP with catalytic shell (0.2g) were added and the solution was sonicated to disperse the MNP. The solution was sonicated with heating (60 °C) with high efficiency condenser attached for 5 hours with air bubbling through gently. The bubbling air was the oxygen source for oxidation. The solution was cooled and the MNP were separated. The solution was filtered through a 0.2 µm syringe filter. The solvent was evaporated. The product was stored in sample tubes. The MNPs were magnetically separated and washed with acetone (100 mL), EtOH (100 mL) and water (100 mL). The particles were dried in a vacuum oven (80 °C) before being recycled in next catalytic process.

2.5.3 Procedure for Glue Inhibition and Reactivation Testing

Adhesive was prepared by mixing triethylene glycol dimethacrylate (5 mL, 19.1 mmol) and copper (ll) tetrafluoroborate (0.0025 g, 0.01 mmol)) by magnetic stirring until dissolved. Tert-butyl peroxybenzoate (2 µL, 0.01 mmol) was added to the solution and stirred for 30 minutes. This glue solution took 5 minutes to cure between metal plates. Addition of 150 mg of $MnFe_2O_4$@MnO_2 MNPs and sonicating the solution for 15 minutes gave a solution that was inhibited. The solution could be activated by magnetic removal of the MNPs and inhibited again by sonication for 15 minutes again.

2.5.4 Procedure for Dye Removal Testing

Solutions of dyes in water were made up to give an absorbance of between 1-2 AU (Methylene blue = 21.3 µM, Methyl Orange = 55.7 µM, Rhodamine B = 12.7 µM). Absorbance spectra of the dye solutions were recorded. MNPs with catalytic shell (100 mg) were added to the dye solution (50 mL) and the solution was sonicated at RT for 1 hour with samples taken at 5, 10, 15, 30, 45 and 60 minutes. Absorbance spectra of these samples were taken after the MNP were magnetically removed over 5 minutes. The MNPs were magnetically extracted from the

solution and place in the furnace for 3 hours at 300 °C. Then the MNPs were washed with MeOH (1x 100 mL) and MP H_2O (1x 100 mL). The particles were then recycled.

2.6 Experimental Protocols for Chapter 7

2.6.1 Preparation of Boron Nitride Nanosheets (BNNS)

BNNS were prepared from bulk BN following previous work with some modifications[15].

Bulk BN powder (300 mg) and MP H_2O (100 mL) was put in a RBF (150 mL). This solution was sonicated for 24 hours.

2.6.2 Preparation of Sodium Ethoxide (EtONa)

Dry EtOH (85 mL, 1.47 mol) was degassed and put under argon in a RBF (250 mL). NaOH (5.87 g, 0.15 mol) was added and magnetically stirred under argon until dissolved. Molecular Sieves (26.45 g, 300 mesh) were added and the RBF was sealed under argon. The solution was left for 48 hours. The liquid was separated from the molecular sieves under argon. The liquid was distilled (160 °C) under argon to remove excess EtOH leaving a dry white powder. Ethylene glycol (100 mL) was added to the EtONa (10 g) in preparation for further synthesis.

2.6.3 Transfer of BNNS from Water to Ethylene Glycol

BNNS (300 mg in 100 mL H_2O) were added to ethylene glycol (120 mL) in a RBF (500 mL) and magnetically stirred. The water was distilled off at 150 °C and collected. The distillation was stopped once 100 mL of water had been collected. The solution was cooled and sonicated for 1 hour.

2.6.4 Preparation of Boron Nitride Nanosheets Magnetite Nanocomposites (BNNS-Fe_3O_4)

BNNS (100 mg, 4 mmol of BN) in ethylene glycol (40 mL) was degassed and put under argon in a RBF (100 mL). $FeCl_3 \cdot 6H_2O$ (0.16 g, 0.60 mmol) and ethylenediamine (0.40 mL, 6.0 mmol) were added and sonicated for 30 minutes under argon. EtONa (0.55 g, 8 mmol) in ethylene glycol (5.5 mL) was added to the solution. The solution was set up for mechanical stirring under argon and stirred for 30 minutes at RT to mix. The solution was refluxed (200 °C) for 16 hours under argon. The solution was cooled to RT and the particles were magnetically separated and washed with water (2 x 100 mL) and EtOH (2 x 100 mL) and stored in EtOH (100 mL).

2.6.5 Preparation of Boron Nitride Nanosheets Cobalt Ferrite Nanocomposites (BNNS-$CoFe_2O_4$)

BNNS (100 mg, 4 mmol of BN) in ethylene glycol (40 mL) was put in a RBF (100 mL). $FeCl_3 \cdot 6H_2O$ (0.109 g, 0.40 mmol), $CoCl_2 \cdot 6H_2O$ (0.048 g, 0.3 mmol) and ethylenediamine (0.40 mL, 6.0 mmol) were added and sonicated for 30 minutes open to air. EtONa (0.55 g, 8 mmol) in ethylene glycol (5.5 mL) was added to the solution. The solution was set up for mechanical stirring and stirred for 30 minutes at RT to mix. The solution was refluxed (200 °C) for 16 hours open to air. The solution was cooled to RT and the particles were magnetically separated and washed with water (2 x 100 mL) and EtOH (2 x 100 mL) and stored in EtOH (100 mL).

2.6.6 Preparation of Boron Nitride Nanosheets - Magnetic Nanoparticle Nanocomposite Membranes

A solution of known concentration of the material was sonicated for 2 hours to disperse the material fully. The solution was filtered on a PVDF 0.45 µm filter to create the membrane. The membrane was used for filtration immediately after being created before it had dried out. For one of these membranes it was allowed to dry and the mass and thickness of the membrane was measured.

2.6.7 Testing of the Membrane for Extraction of Dye

A fresh membrane (40 mg) of the desired material (BNNS, BNNS-Fe_3O_4, BNNS-$CoFe_2O_4$) was made. A solution of MB (20 mL, 21 μM) was filtered through the membrane and the filtrate was collected and a UV-vis measurement taken. This was repeated with equal amounts of solution until the membrane became saturated.

2.6.8 Testing of the Membrane for Magnetic Nanoparticle Filtration

A fresh membrane (40 mg) of the desired material (BNNS, BNNS-Fe_3O_4, BNNS-$CoFe_2O_4$) was made. A solution (20 mL) of freshly sonicated MNPs at a concentration of 0.2 mg/mL was filtered. The filtrate was collected and left on a magnet overnight to see if any MNPs were extracted from the filtrate.

2.7 Instrumentation and Techniques used for Characterisation

2.7.1 Electron Microscopy

Optical microscopes have a theoretical optical resolution limit of approx. 0.250 µm, which is about half the wavelength of optical light. The resolving power limit on an optical microscope is caused by the wavelength of the light. To see objects below this limit one needs a smaller wavelength. Due to the wave-particle duality hypothesis first put forward by De Broglie, a particle with momentum *p* will have a wavelength λ, where *h* is Planks Constant, of

$$\lambda = \frac{h}{p}$$

Electrons can be accelerated in a potential field, E, thereby acquiring kinetic energy

$$eE = \frac{1}{2} m_0 v^2$$

Where m_0 is the electron mass at rest, v is the speed of the electron and e is the electron charge. This accelerated electron will have a momentum

$$p = m_0 v = \sqrt{2 m_0 eE}$$

Giving us

$$\lambda = \frac{h}{\sqrt{2 m_0 eE}}$$

Which gives the relationship between the acceleration voltage and the wavelength of an electron. In an accelerating potential of 200 keV the electron will have a wavelength of approximately 0.0025 nm, giving a theoretical resolving power of half this[16]. In practice, an electron microscope will have resolving power much less than this for a given potential because the limiting factor in an electron microscopes resolving power is from imperfections of the magnetic lenses. By using an electron source, known as the gun, a beam of Primary Electrons is produced which can be controlled and focused onto a sample with a series of magnetic lenses and apertures. In this work, two types of electron microscopy were used, the Transmission Electron Microscope (TEM) and the Scanning Electron Microscope (SEM).

Scanning Electron Microscope (SEM)

In a Scanning Electron Microscope (SEM) a focused incident beam of Primary Electrons is scanned over the surface of the sample. These electrons interact with the sample by backscattering, forming Secondary Electrons (SE) and by producing X-rays. Backscattered electrons (BSE) come from the electron being repelled by the electrons in the atoms of the material. SE are electrons that are knocked out from the outer shell of the atoms of the material by the beam. X-rays come from inner shell electron removal by the beam, with the X-ray emitted as the electron hole is filled by the outer shell electrons. The images in a SEM are formed by the BSE and SE at various detectors inside the SEM (Figure 2-1).

In this work, a Zeiss Ultra plus SEM was used capable of an accelerating potential of 30-1 keV. The SEM was operated at between 10-2 keV to form the images.

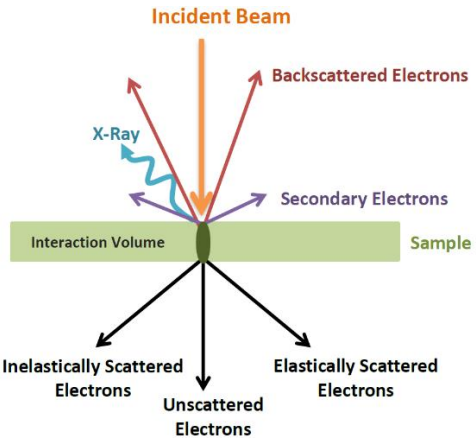


Figure 2-1: General overview of how an electron beam interacts with a sample.

Transmission Electron Microscope (TEM)

In a Transmission Electron Microscope (TEM) a beam of electrons is focused as a parallel beam on to the sample. A TEM works at a higher operating voltage than the SEM. This causes the electrons to penetrate the sample and the image is taken of the sample based on the amount of transmitted electrons, analogous to an X-ray image of a bone in the body. Contrast in the image is dependent on the amount of scattering where elastic scattering comes from interaction with the nuclei, with dense nuclei causing more scattering and inelastic scattering coming from interaction with the electrons of the atoms. Contrast can also be produced by diffraction of the electron beam by crystalline samples, known as Bragg scattering, and can

give crystallographic information about the sample. After the parallel beam interacts with the sample, lenses bring the image to a phosphor screen or image recording system for viewing.

In this work, the TEM used was a JEOL 2100 instrument operating at 200 kV with a LaB_6 electron source.

Energy-dispersive X-ray (EDX) Spectroscopy

The X-rays may be emitted by the electron beam interacting with the sample in either TEM or SEM instruments. The electron beam can knock out an inner shell electron to create an electron hole on the inner shell. This hole is immediately filled by an electron from an outer shell with the emission of an X-ray. The discrete energy level difference between the inner and outer shell for an atom gives the X-ray a specific energy, which is characteristic of that atom. All the elements have their characteristic energy levels and therefore the element can be identified. This analysis is known as Energy-Dispersive X-ray (EDX) spectroscopy and is a tool to identify what is the elemental composition of the sample.

EDX analysis has been done using the Oxford Inca EDX detector fitted to the JEOL 2100 TEM.

2.7.2 Vibrating Sample Magnetometer (VSM)

A vibrating-sample magnetometer is an instrument for measuring magnetic properties of a sample. The method is based on Faraday's Law of Induction where a magnetised material will induce an electromotive force in a conductive wire. A sample to be measured is placed in a uniform magnetic field, the strength of which can be controlled by an electromagnet. As the strength of this field is set at a particular value and does not change, the pickup coils have no EMF induced in them from the external field. The sample, which is connected to a piezoelectric material, is vibrated up and down. This will induce an EMF in the pickup coils, which can be read by the instrument. The instrument is calibrated by using a bulk sample of pure nickel of known mass, which has known magnetic properties. The electromagnet magnetises the sample across a range (from -1.1 T to 1.1 T) and the level of magnetism in the sample is measured by the pickup coils. A diagram of the setup is shown below (Figure 2-2).

The output as the sample is scanned for 1.1 T to -1.1 T and back to 1.1 T is known as a hysteresis loop. Certain magnetic properties of the sample can be found from the hysteresis loop such as saturation magnetisation (M_s), magnetic remanence (M_r) and the coercivity (H_c). An example of a hysteresis loop can be seen below (Figure 2-2).

Vibrating Sample Magnetometry measurements were carried out on an in-house assembled vibrating sample magnetometer, courtesy of the Coey research group. The instrument had a maximum field of 1.1 T.

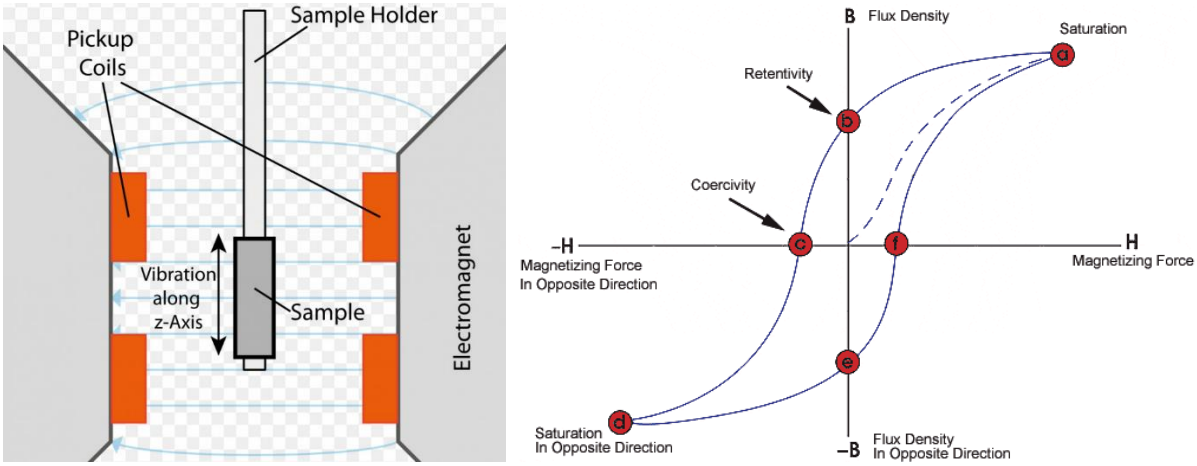


Figure 2-2: VSM setup showing the uniform magnetic field (blue lines) that induces the magnetism in the sample[17] **and the hysteresis loop with the saturation (M_s), retentivity (M_r) and coercivity (H_c)**[18]**.**

2.7.3 Fourier Transform Infrared (FTIR) Spectroscopy

Infrared (IR) Spectroscopy is bases on the phenomena that specific chemical bonds absorb specific frequencies of IR radiation. Therefore, an IR spectrum can give information of the chemical species and bonding present in a sample. IR Spectroscopy gives a transmittance profile over the IR range, which consists of the near-IR (14000-4000 cm^{-1}), mid-IR (4000-400 cm^{-1}) and far IR (400-10 cm^{-1}). This can be achieved by scanning over the individual wavelengths to build the profile, known as dispersive spectrometry but this method is time consuming. The Fourier Transform infrared spectrometry involves processing the data with a mathematical technique and thus enables simultaneous collection over a wide spectral range so the process is much faster. The technique involves measurements of the coherence of the radiative source to form an interferogram, which is then Fourier Transformed to give the spectrum over the IR range.

The IR spectrum can be formed by passing the IR light through the sample by forming a translucent matrix with KBr. The sample is lost by this process as it is contaminated with KBr. A more modern technique is Attenuated Total Reflectance (ATR) where the raw sample is held in direct contact with the surface of a crystal and the IR spectrum taken. The sample is not lost and can be recovered with this process. ATR uses a property of total internal reflection that produces evanescent waves that propagate into the sample and is absent from the exit beam as shown below (Figure 2-3). The spectrum of the sample can be obtained by this process. This only works if the crystal has a higher refractive index than the sample.

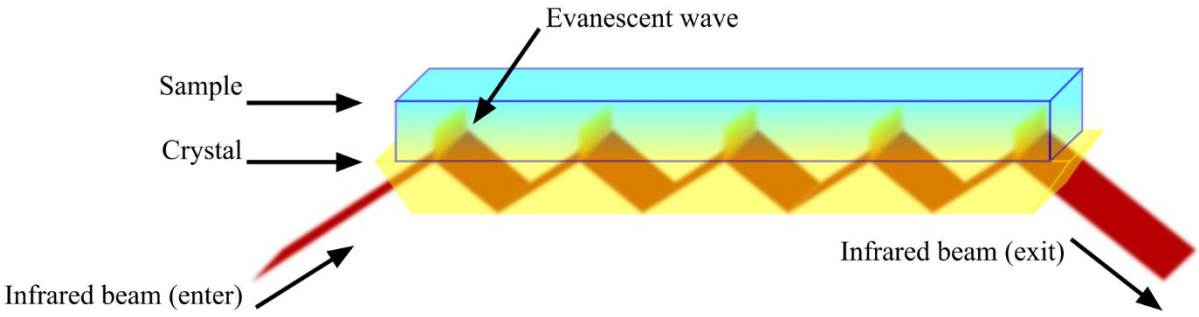


Figure 2-3: Setup of ATR attachment showing the Evanescent wave absorbed by the sample[19]**.**

Both the crystal and detector contribute to the effective range of an FTIR instrument. In this work FTIR spectra were recorded on a Perkin Elmer Spectrum 100 instrument, equipped with a Universal ATR Diamond/KRS-5 crystal window with an effective range of 4200-380 cm^{-1}.

2.7.4 Nuclear Magnetic Resonance (NMR)

Neutrons and protons have an intrinsic property known as spin angular momentum, which has a value of ±½. Nuclei are composed of neutrons and protons, which combine using quantum rules (Pauli Exclusion Principle, etc.) to give an overall spin S for a given nucleus, which can have value S = n/2 where n = 0, 1, 2, 3, etc. A nucleus will have 2S + 1 spin states which are degenerate in the absence of a magnetic field. In a magnetic field these spin states will split. For the ^{1}H nucleus, which has S = ½, this will give 2 spin states termed α and β or spin-up and spin-down. In a magnetic field, the energy difference between these states is

$$\Delta E = \gamma \hbar B_0$$

Where γ is the gyromagnetic ratio for the nucleus, $\hbar$ is the reduced Planck constant and $B_0$is the external magnetic field strength. A central concept to NMR is the precession of the spin vector (M_0) about the external field vector (B_0) with an angular frequency, ω_0, of

$$\omega_0 = 2\pi v_L = \gamma B_0$$

Where v_L is the Larmor frequency. A perturbation of nuclear spin orientations from equilibrium will occur when an oscillating magnetic field is applied whose frequency v_{rf} closely matches the Larmor precession frequency, v_L. Therefore, a second magnetic field (B_1) is applied perpendicular to the external field by applying an electromagnetic radiofrequency pulse of $v_{rf} = v_L$ along the x-axis. This causes the spin vectors to move to the x-axis, away from their equilibrium state (Figure 2-4).

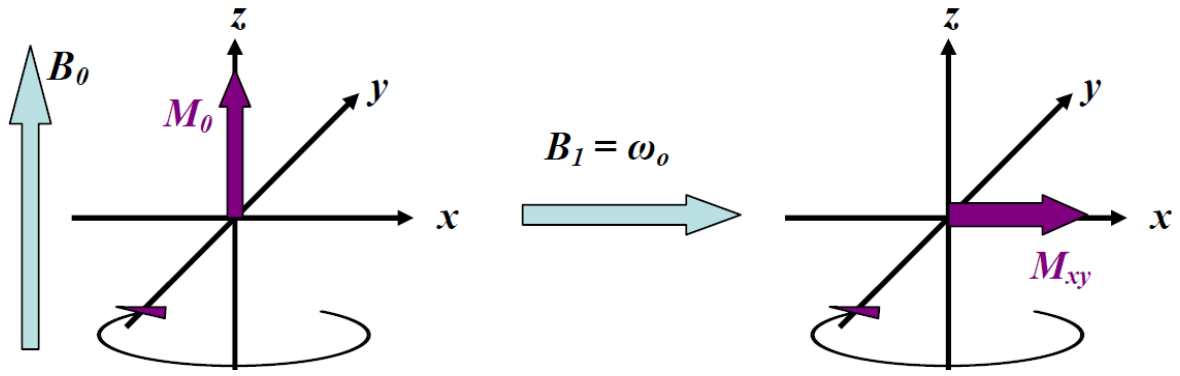


Figure 2-4: The applied radiofrequency (B_1) matches the Larmor frequency and perturbs the spin vector (M_0) to a transverse orientation to the applied external field (B_0).

Upon the removal of B_1, the nuclei relax to their previous equilibrium through precession, spiralling rotation about the z-axis at a frequency ω_0. This is referred to as longitudinal relaxation and the time it takes is T_1. The motion of the relaxing spin vector, which has a magnetic component, generates a current in a receiver coil in the x-axis, which is then used to construct a time domain NMR signal. A Fourier transform is then used to generate the typical frequency domain spectrum for the sample.

NMR spectra were recorded on Bruker AV-400 Advance (9.4 T) spectrometer (400.13 MHz for 1H NMR; 100.6 MHz for 13C NMR). Shifts are referenced to 25 internal solvent signals and data processed using MestraNova software.

2.7.5 Ultraviolet-Visible Spectroscopy (UV-vis)

UV-vis spectroscopy involves passing light through a sample in the UV-vis range (800-100 nm) and measures the absorbance at each wavelength. The UV-vis instrument uses a white light source (a xenon lamp) that is passed through a prism to split the light into its various wavelengths. This monochromatic beam is split in two with one beam going to the sample detector and the other to a reference detector (Figure 2-5). This procedure eliminates any fluctuations in intensity coming from the lamp. The sample absorbs different amounts of light at different wavelengths. The absorbance at any wavelength is proportional to the concentration of the absorbent in the solution according to the Beer-Lambert law:

$$A = \varepsilon C l$$

Where A is the absorbance with no units, ε is the molar extinction coefficient which is a constant related to how strongly a chemical species absorbs light at a given wavelength and has units, L mol^{-1} cm^{-1}. C is the concentration of the sample in the solvent, the molar concentration with units, mol L^{-1}. l is the pathlength of the light beam in the solution with units, cm. Using this equation the absorbance of a sample is directly related to the concentration of the absorbing species in the sample. This can be useful to measure a catalytic reactions concentration change over time as a chemical species is produced or the removal of a chemical species from solution over time by various processes such as adsorption or degradation.

UV-vis absorption spectra were recorded using an Agilent Cary 60 UV-vis spectrophotometer with a range of 1100 – 190 nm. All samples were recorded in a quartz cuvette with a pathlength of 1 cm.

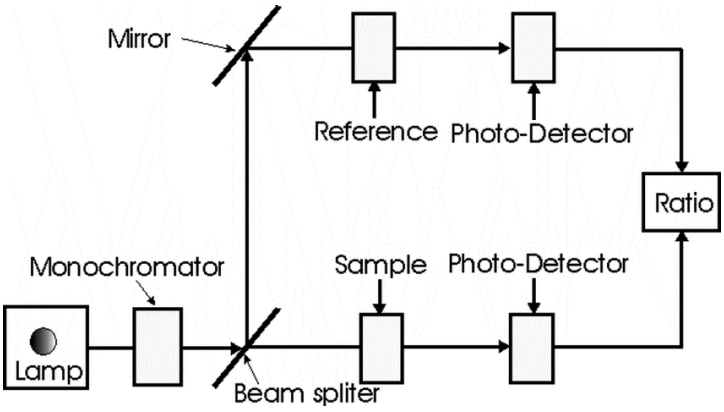


Figure 2-5: UV-vis spectrophotometer beam setup[20]**.**

2.7.6 Dynamic Light Scattering (DLS)

Dynamic Light Scattering (DLS) is a technique to determine the hydrodynamic diameter of sub-micron spherical particles. The hydrodynamic diameter is the size of the particle plus the bound layer of solution that moves with the particle due to surface electrostatic effects or the presence of surfactants or polymers on the surface. The technique is based on Brownian motion where suspended particles will move randomly, with larger particles moving slower than smaller ones. The hydrodynamic size is calculated using the Stokes-Einstein equation

$$d(H) = \frac{kT}{3\pi\eta D}$$

Where d(H) is the hydrodynamic diameter, k is Boltzmann's constant, T absolute temperature, η is the viscosity and D is the translational diffusion coefficient.

As the particles are suspended in solution, a laser shone at the suspension will be scattered. The scattered light at a given angle will have a given intensity that fluctuates with time because of the motion of the particles. Smaller particles will cause the intensity to fluctuate more rapidly. The rate of change of this intensity can be used to construct a correlogram, which is a graph of how closely the intensity after a time delay matches the intensity at time zero, with the correlation coefficient being 1 for perfect correlation and 0 for no correlation.

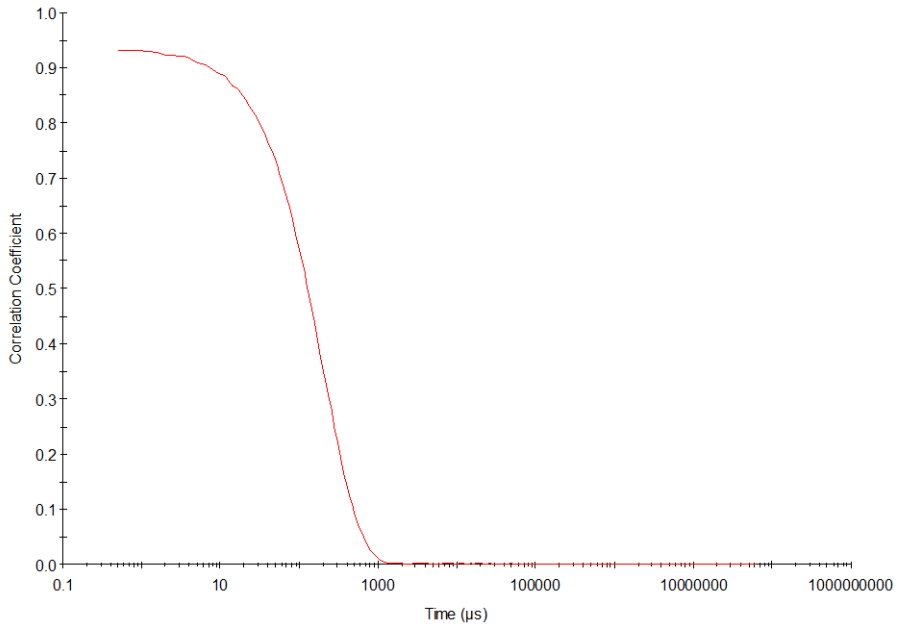


Figure 2-6: Correlogram showing the raw data output of a DLS measurement.

The correlogram (Figure 2-6) can give information about the sample such as the mean size of the sample (where significant decay starts) and the polydispersity of the sample (the rate of decay). The correlation function, G(τ), of the scattered intensity is

$$G(\tau) = A\left[1 + Be^{-2D\left(\frac{4\pi n}{\lambda}\sin\left(\frac{\theta}{2}\right)\right)^2\tau}\right]$$

Where A is the baseline of the correlation function, B is the intercept of the correlation function, D is the translational diffusion coefficient, n is the refractive index of the solution, λ is the wavelength of the laser, θ is the scattering angle and τ is the correlator time delay. The correlator in the DLS instrument will construct the correlation function from which the mean size of the ensemble and the polydispersity index (the width of the distribution) can be calculated. As DLS is a measure of the hydrodynamic radius, it will always be larger than the radius of the particle as measured by TEM or SEM

DLS measurements were taken on a Malvern Zeta-Sizer Nano series with a laser of 633 nm and scattering angle of 173°. Measurements were taken at 25 °C in MP H_2O unless otherwise stated.

2.7.7 Zeta Potential

Zeta Potential is a parameter of any colloidal solution and is a result of the existence of surface charge on the particle, which comes from the termination of the lattice, giving atoms that do not have their full complement of neighbours or from absorbed surfactant ions that coat the particle. Electroneutrality requirements require a compensation of the charge by an ion distribution in the area surrounding the particle, resulting in the electrical double layer (Figure 2-7). This consists of the Stern layer where the compensating ions are tightly bound and the diffuse layer where the ions are less bound. Within this diffuse layer exists a conceptual plane where the ions move with the particle when the particle moves because of an external field. This plane, known as the slipping plane or the surface of hydrodynamic shear, has a potential related to the surface and the potential at this point from the particle is the zeta potential. The zeta potential is a function of the surface charge density, the distance of the slipping plane from the surface and the surface structure[21]. Zeta potential can be calculated indirectly

from the electrophoretic mobility, which is the velocity of dispersed charged particles relative to the solution under the influence of an electric field, using the Henry equation:

$$U_E = \frac{2\varepsilon z\, f(\kappa a)}{3\eta}$$

Where U_E is the electrophoretic mobility, z is the zeta potential, ε is the dielectric constant, η is the viscosity and f(κa) is the Henry's function, with κ termed the Debye length, where κ^{-1} is a measure of the "thickness" of the electrical double layer and 'a' is the radius of the particle. Therefore, κa measures the ratio of the particle radius to electrical double layer thickness.

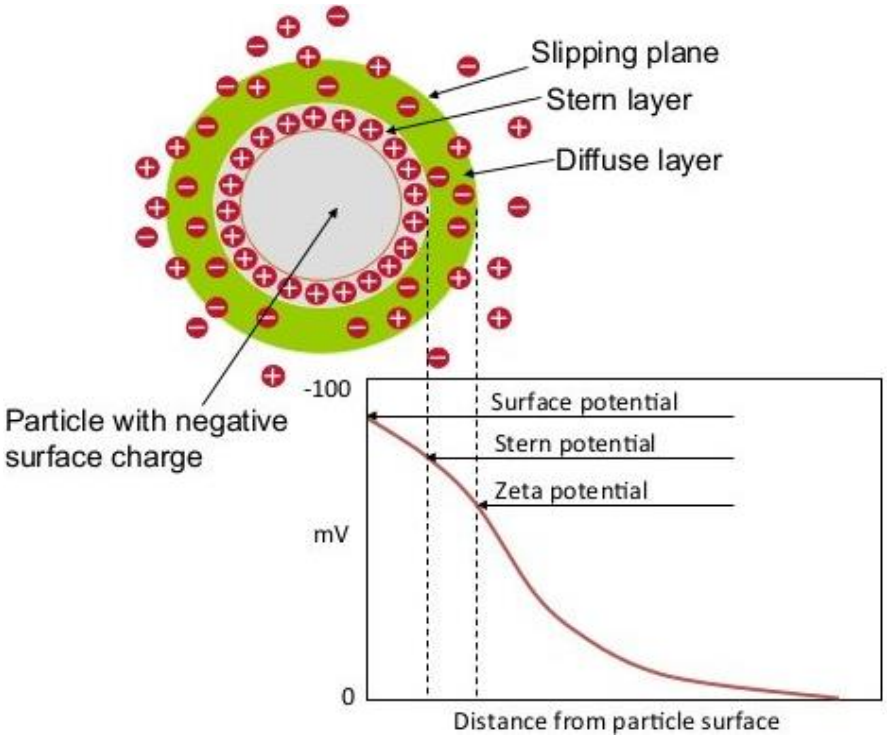


Figure 2-7: Concept of a negatively charged particle and its interactions with the surrounding solution.

Electrophoretic mobility can be measured by applying an electric field across a solution of suspended particles and measuring the Doppler shift of a scattered laser beam from the solution with respect to a split reference beam.

The zeta potential is indicative of the stability of colloidal particles in solution as higher zeta potentials will reduce particle contact because of electrostatic repulsion and minimise coagulation and sedimentation. Zeta potential measurements are useful for understanding how stability changes with the ionic strength of the solution, the pH of the solution and other

components in the solution. Zeta potential is also indicative of the surface charge of a particle with the sign of the zeta potential directly related to the surface charge.

Zeta potential measurements were performed on a Malvern Zeta-Sizer Nano series instrument with a laser of 633 nm and scattering angle of 13°. Measurements were taken at 25 °C in MP H_2O unless otherwise stated.

2.7.8 X-ray Diffraction (XRD)

Diffraction is a phenomenon that occurs when waves encounter an obstacle or an opening. It is defined as the bending of the waves around the corners of the obstacle or through the opening into the region of geometrical shadow of the obstacle or opening. The diffraction is most noticeable when the wavelength and the opening are of similar size.

Crystals are composed of regular arrays of atoms such that planes of atoms are formed. The spaces between these planes are analogous to openings and X-rays have wavelengths similar in size to the distance between these planes. X-ray diffraction is the scattering of the X-rays by the crystal due to these planes. The scattered rays can be used to reconstruct the position of atoms in the crystal lattice. Miller indices are used to describe planes in a crystal lattice using three integers (hkl). Braggs law defines the angle (θ) of a scattered X-ray in relation to its wavelength (λ) and the space between that plane (d_{hkl}) and the diffraction order (n). With a fixed wavelength, by measuring the scattering angle, the distance between planes can be calculated.

$$n\lambda = 2d_{hkl}\sin\theta$$

Powder XRD (pXRD) is a special case of XRD for samples with microcrystalline structure. In pXRD every possible crystalline orientation is represented in the sample. The sample is usually rotated while scanning to ensure crystal orientation isotropy. By measuring the scattering angle, a diffractogram is outputted with peaks of varying intensity at specific angles, which are characteristic of the sample. By comparison of these peaks with a database of known samples a match can be made and the phase (or phases) identified. If the unit cell of the crystal lattice is known, it is possible to calculate the pXRD pattern that will be produced from such a powder sample. For mixed samples, it is possible to quantify the phases of the various previously

identified phases, using software that calculates this from the intensities and shapes of the peaks.

Prior to any sample characteristics calculations using the outputted diffractogram, such as quantification, size and strain or lattice parameters, the instrumental effect on the diffractogram must be quantified so that the samples true output can be calculated. The instrument and the sample will create some peak broadening, so the sample broadening will be

$$B_{sample} = B_{diffactogram} - B_{instrument}$$

The instrument broadening is found by running standard samples that give known outputs and fitting the outputted diffractogram. Then the function variables of the fitting process will be known and can be used for a non-standard sample. Once this is done, the diffractogram can be used with the particular software to give results that are more accurate.

The broadening of peaks can be used to calculate the average crystallite size using the Williamson-Hall method. This is a combination of the Scherrer $\left(\frac{K\lambda}{L\cos\theta}\right)$ and Stokes & Wilson $(4\epsilon\tan\theta)$ methods for size and strain broadening respectively, where B_{sample} is the Full Width Half Maximum (FWHM) broadening of the peak, K is the shape factor, λ is the X-ray wavelength, L is the crystallite size, θ is the Bragg angle and ε is the strain.

$$B_{sample} = \frac{K\lambda}{L\cos\theta} + 4\epsilon\tan\theta$$

Using this equation a plot of $\left(B_{sample}\cos\theta\right)$ against $(4\varepsilon\sin\theta)$ for all the peaks gives a straight line with y-intercept of $\left(\frac{K\lambda}{L}\right)$. From this L, the crystallite size can be found. As this measures the crystallite size rather than the actual particle size (composed of a crystalline core and a surface layer) it will always be smaller than the size as measured by TEM and SEM.

The lattice constants for the sample can be calculated by doing a Rietveld refinement on the diffractogram. Rietveld refinement is a least-squares statistical fitting procedure that fits to the whole profile (diffractogram) rather than to the individual peaks. A profile shape constrained to the unit cell of a model of the sample, which is already known from knowledge of the sample, is fitted to the outputted diffractogram. The model is refined until the differences between the calculated and observed diffractogram are minimised, to give a

refined model of the sample. From the refined model, the lattice constants can be taken. Sample factors that determine a peak profile are the phase, mass absorption coefficient (sample transparency), size broadening, strain broadening, stacking faults and compositional inhomogeneity.

X-ray powder diffraction was carried out using a Bruker, D2 Phaser 2nd generation, pXRD machine with a copper X-ray source of wavelength 0.154 nm. All scans were over the range 15-85 °2θ and were run for 2.2 hours unless otherwise stated. The results were processed with Panalytical HighScore Plus software.

2.8 References

1 Neodymium Magnet - rectangle, https://www.first4magnets.com/rectangular-c35/50-x-25-x-10mm-thick-n42-neodymium-magnet-32-2kg-pull-p3611#ps_0_3761.

2 Neodymium Magnet - round, https://www.first4magnets.com/circular-disc-rod-c34/50mm-dia-x-30mm-thick-x-6mm-c-s-n42-neodymium-magnet-81kg-pull-p3535#ps_0_3641%7Cps_1_3425.

3 C. Blanco-Andujar, D. Ortega, Q. A. Pankhurst and N. T. K. Thanh, *J. Mater. Chem.*, 2012, **22**, 12498. https://doi.org/10.1039/c2jm31295f.

4 K. N. Jayaprabha and P. A. Joy, *RSC Adv.*, 2015, **5**, 22117–22125. https://doi.org/10.1039/c4ra16044d.

5 C. N. Chinnasamy, A. Yang, S. D. Yoon, K. Hsu, M. D. Shultz, E. E. Carpenter, S. Mukerjee, C. Vittoria and V. G. Harris, *J. Appl. Phys.*, 2007, **101**, 1–4. https://doi.org/10.1063/1.2710218.

6 G. L. Davies, J. Govan, R. Tekoriute, R. Serrano-García, H. Nolan, D. Farrell, O. Hajatpour and Y. K. Gun'Ko, *Chem. Sci.*, 2017, **8**, 7758–7764. https://doi.org/10.1039/c7sc03474a.

7 J. Zou, Y. G. Peng and Y. Y. Tang, *RSC Adv.*, 2014, **4**, 9693–9700. https://doi.org/10.1039/c3ra47043a.

8 E. Agouriane, B. Rabi, A. Essoumhi, A. Razouk, M. Sahlaoui, B. F. O. Costa and M. Sajieddine, *J. Mater. Environ. Sci.*, 2016, **7**, 4116–4120. https://doi.org/10.1016/j.jmmm.2019.03.128.

9 H. Deng, X. Li, Q. Peng, X. Wang, J. Chen and Y. Li, *Angew. Chemie - Int. Ed.*, 2005, **44**, 2782–2785. https://doi.org/10.1002/anie.200462551.

10 S. Nigam, K. C. Barick and D. Bahadur, *J. Magn. Magn. Mater.*, 2011, **323**, 237–243. https://doi.org/10.1016/j.jmmm.2010.09.009.

11 W. Stöber, A. Fink and E. Bohn, *J. Colloid Interface Sci.*, 1968, **26**, 62–69. https://doi.org/10.1016/0021-9797(68)90272-5.

12 Y. H. Deng, C. C. Wang, J. H. Hu, W. L. Yang and S. K. Fu, *Colloids Surfaces A Physicochem. Eng. Asp.*, 2005, **262**, 87–93. https://doi.org/10.1016/j.colsurfa.2005.04.009.

13 Y. Zhai, J. Zhai, M. Zhou and S. Dong, *J. Mater. Chem.*, 2009, **19**, 7030. https://doi.org/10.1039/b912767d.

14 P. -L Chen and I. -W Chen, *J. Am. Ceram. Soc.*, 1993, **76**, 1577–1583. https://doi.org/10.1111/j.1151-2916.1993.tb03942.x.

15 J. N. Coleman, M. Lotya, A. O'Neill, S. D. Bergin, P. J. King, U. Khan, K. Young, A. Gaucher, S. De, R. J. Smith, I. V. Shvets, S. K. Arora, G. Stanton, H. Y. Kim, K. Lee, G. T. Kim, G. S. Duesberg, T. Hallam, J. J. Boland, J. J. Wang, J. F. Donegan, J. C. Grunlan, G. Moriarty, A. Shmeliov, R. J. Nicholls, J. M. Perkins, E. M. Grieveson, K. Theuwissen, D. W. McComb, P. D. Nellist and V. Nicolosi, *Science*, 2011, **331**, 568–571. https://doi.org/10.1126/science.1194975.

16 Wavelength of an Electron, https://www.jeol.co.jp/en/words/emterms/search_result.html?keyword=wavelength of electron.

17 R0oland, VSM instument diagram, https://commons.wikimedia.org/wiki/File:VSM_en.svg.

18 Hysteresis Loop - labeled, https://www.nde-ed.org/Physics/Magnetism/HysteresisLoop.xhtml.

19 Fulvio314, ATR FTIR diagram, https://commons.wikimedia.org/w/index.php?curid=28499710.

20 W. Gong, M. Mowlem, M. Kraft and H. Morgan, *IEEE Sens. J.*, 2009, **9**, 862–869. https://doi.org/10.1109/JSEN.2009.2020659.

21 L. H. Reddy, J. L. Arias, J. Nicolas and P. Couvreur, *Chem. Rev.*, 2012, **112**, 5818–5878. https://doi.org/10.1021/cr300068p.

3 Synthesis of the Magnetic Core Nanoparticles

3.1 Introduction

There are a number of reports on the synthesis of metal oxide based MNPs by various techniques. The main techniques include thermal decomposition, coprecipitation, hydro/solvothermal and microemulsion as examples of bottom-up approaches[1][2][3].

In the case of thermal decomposition, there is more control over the size distribution outcome, with this synthesis giving the best examples to date of monodisperse samples with high crystallinity[4]. Also, there is some possibility for control of the size of the nanoparticles, which is temperature dependent[5], but there are issues with the high temperatures and non-aqueous solvents being needed for the synthesis. Furthermore, once the particles are formed they are frequently not transferable to aqueous medium without further modification steps that can affect the quality and stability of the particles.

Coprecipitation on the other hand is a facile synthesis in aqueous medium without any harsh conditions[6], but frequently it has issues with the size distribution of the final sample[7]. In the case coprecipitation, there is less control over the size, shape and crystallinity of the final particles. Modification of the synthesis particularly with the use of ligands in situ in the synthesis may enable some control over the final product to be achieved.

Hydrothermal or solvothermal synthesis involves the use of a high pressure vessel and either water based (hydro-)[8] or another solvent (solvo-)[9] as the reaction medium. These techniques frequently result in non-uniform nanoparticles and aggregates, but there is more control over the size of the particles[9] as a longer reaction time has been found to enable growth of the particles under these conditions.

Microemulsion involves the creation of micelles in an oil-water emulsion so they can be used as nanoreactors for the reaction to take place[10]. It allows for a good size control by varying the initial oil-water concentrations[11]. One issue with this synthetic method is that it is known to have lower yields comparing to other techniques.

MNPs have similar properties as other nanomaterials, such as a large specific surface area, but the primary property of MNPs is their ability to interact with a magnetic field. This enables a number of important applications such as materials for magnetic separation[12], magnetic heating[13], magnetic guidance in targeted drug delivery[14] and as contrast agents in MRI[15]. The magnetic characteristics of MNPs are strongly dependent on the nature of material being synthesised, with some materials having higher saturation magnetisation than others[16]. In addition, there are a number of various magnetic nanocomposites combining several materials. The classic example of this is a core@shell nanocomposite with the MNP at the core and the catalytic material as the shell which can then be magnetically extracted from the reaction mixture[17]. The effectiveness of the final nanocomposite and the suitability of the MNPs for further functionalisation is dependent on the quality of the initial cores produced. If the MNPs have high magnetisation then the magnetic properties will be transferred to the nanocomposite. Other properties apart from the magnetisation that are important in the initial MNP are size, size distribution, morphology and surface chemistry after the synthesis.

3.2 Aims

The aim of this part of our work is to prepare several different types of magnetic nanoparticles by two different synthetic methods. The MNPs to be prepared are magnetite, cobalt ferrite, manganese ferrite and copper ferrite, while the synthetic methods being used will be coprecipitation and polyol synthesis. It is expected that this work will allow us to develop highly reproducible syntheses that give consistent results with particles with narrow size distribution, good magnetic properties, uniform morphology and consistent size. One of the main goals of this work is to have reproducible results with a given set of starting materials and conditions. The magnetic nanomaterials will be characterised by TEM to confirm the consistent size, morphology and size distribution. XRD will be used to confirm that the correct material has been made and VSM will be use to assess the magnetic characteristics of the material. FTIR analysis will be done, as a supporting characterisation to investigate the MNPs. DLS will be used to quantify the stability and investigate the behaviour of the nanoparticles in solution while zeta potential will be used to assess the surface charge at neutral pH and to find the point of zero charge.

3.3 Results and Discussion

In this work, we will focus on two methods of synthesis of MNPs: coprecipitation and polyol synthesis. The coprecipitation method has been known for a long time as an effective way to prepare magnetite MNPs [18]. The method has also been used to produce many other magnetic spinels. The basic concept behind the method is the reaction of a +2 valent metal ion and +3 valent iron in stoichiometric ratio of 1:2 at basic pH in aqueous media to precipitate out the magnetic spinel particles.

$$M^{2+} + 2Fe^{2+} + 8OH^- \rightarrow MFe_2O_4 + 4H_2O$$

This method was used with a variety of bases and conditions to synthesise magnetite, manganese ferrite, cobalt ferrite and copper ferrite, to find the optimal conditions and starting materials for a highly reproducible syntheses of a monodisperse sample of the MNPs desired. These will be discussed individually in the following sections.

The polyol synthesis used in this work is a modification of the previously reported method for MNP preparation [19], which involves the reaction of the precursors in a polyol solvent at high pressure. The method here involves the mixing of a +2 valent metal ion and +3 valent iron in stoichiometric ratio of 1:2 in refluxing ethylene glycol, which is a higher boiling point solvent, at atmospheric pressure. Here the polyol acts as the solvent, a surfactant and sometimes as the reducing agent. In this case, the addition of sodium acetate is necessary to adjust the pH for the formation of the nanoparticles. The polyol method gives a larger size of particles that the coprecipitation method and so is useful depending on the further functionalisation and final application of the core MNPs.

3.3.1 Preparation of Magnetite NMPs (Fe_3O_4) by Coprecipitation

Magnetite nanoparticles were prepared by a modified coprecipitation method[6], where Fe^{+2} and Fe^{+3} ions in a stoichiometric ratio of 1:2 are precipitated out using base in aqueous media, as described in the experimental section (2.2.1). For this synthesis, there are many modifications of the basic procedure and all give similar results. In this work, different bases were used to precipitate the MNPs, various addition rates of the base to the metal ion solution, non-buffered solutions and mechanical vs magnetic stirring. These variations were

performed to find the optimal conditions for a monodisperse final magnetite sample. Using the procedure given we were able to get a highly reproducible result with a narrow size range as shown by characterisation of three repetitions of the exact procedure.

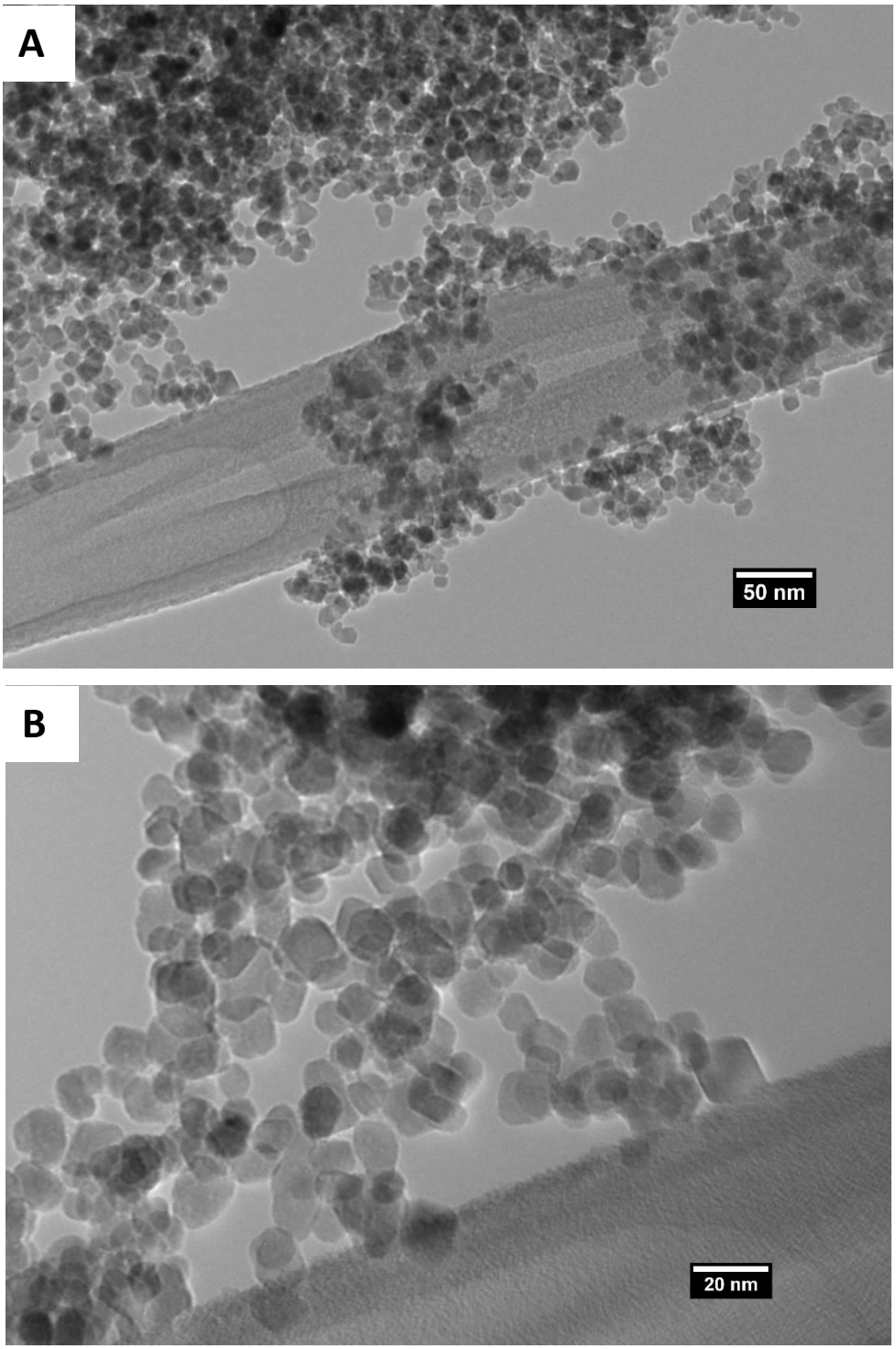


Figure 3-1: (A), (B) TEM images of Fe_3O_4 MNPs prepared by coprecipitation method.

The products were characterised by TEM, VSM, XRD and FTIR. The TEM images (Figure 3-1) have shown the monodisperse particles in the size range of 14±4 nm, but with significant

aggregation. Particle size distributions were calculated from 100 particles using ImageJ software (Figure A-1). The agglomeration was expected due to small size of the particles as the particles aggregate to reduce the surface energy. In addition, the sample had to be dried on the TEM grid and the drying process would cause some agglomeration.

VSM analysis of the sample gave the hysteresis loop shown below (Figure 3-2). The magnetisation was found to be 58 Am^2kg^{-1} at 1 T, which is typical for magnetite nanoparticles[20], while for bulk magnetite there is a reported specific magnetisation of 92 Am^2kg^{-1}[16]. The hysteresis loop had no remnant magnetisation at 0 T, that indicates on superparamagnetic behaviour of the samples. The shape of the curve was also indicative of superparamagnetic behaviour as there was no remnant magnetisation and the samples had not fully magnetically saturated at 1 T.

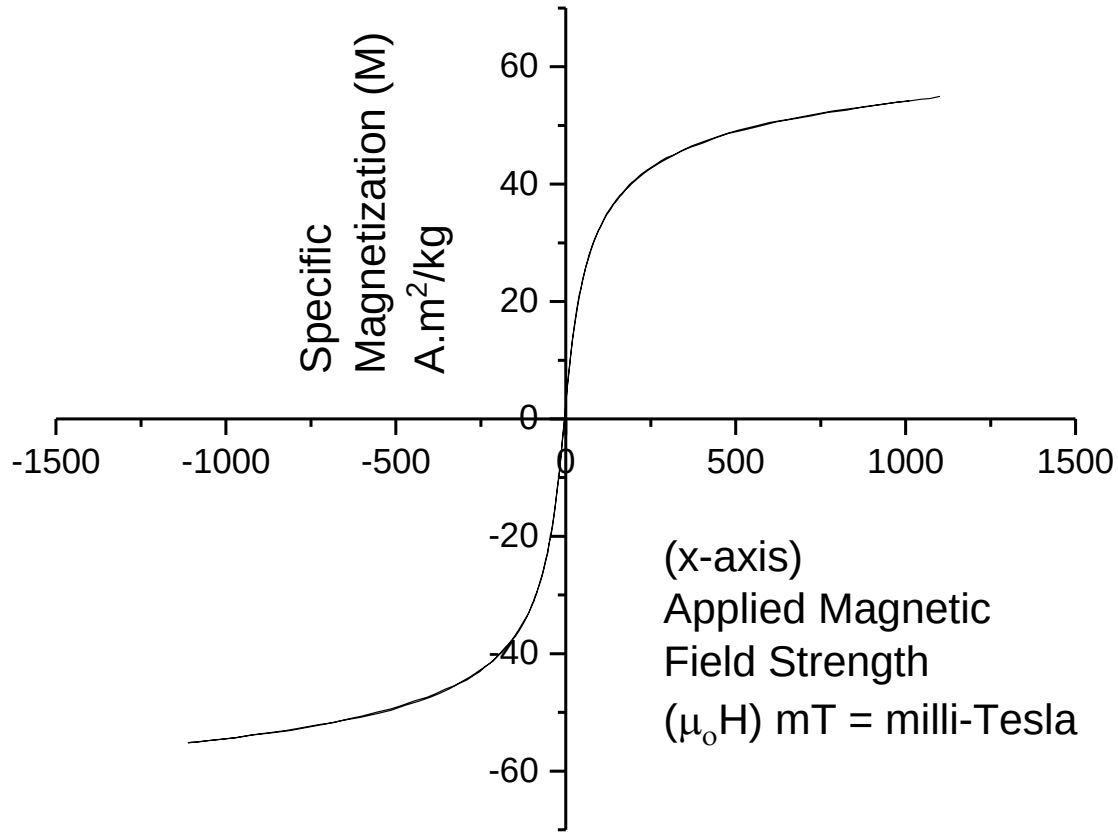


Figure 3-2: VSM curve for Fe_3O_4 prepared by coprecipitation.

XRD analysis confirmed that Fe_3O_4 was the product of the reaction, with it being a high match in the COD database for magnetite (Figure 3-3). The XRD pattern (red line) corresponds to the reference pattern (blue lines) of magnetite (COD 722-8111). A Williamson-Hall plot (Figure 3-4) for the peaks gave a crystallite size of 10.0±1.7 nm, which is in good agreement with the

TEM images above (Figure 3-1). Rietveld analysis on the output using this matched reference pattern for the structure fit gave a cubic crystal lattice with a lattice of a = 8.3441 Å.

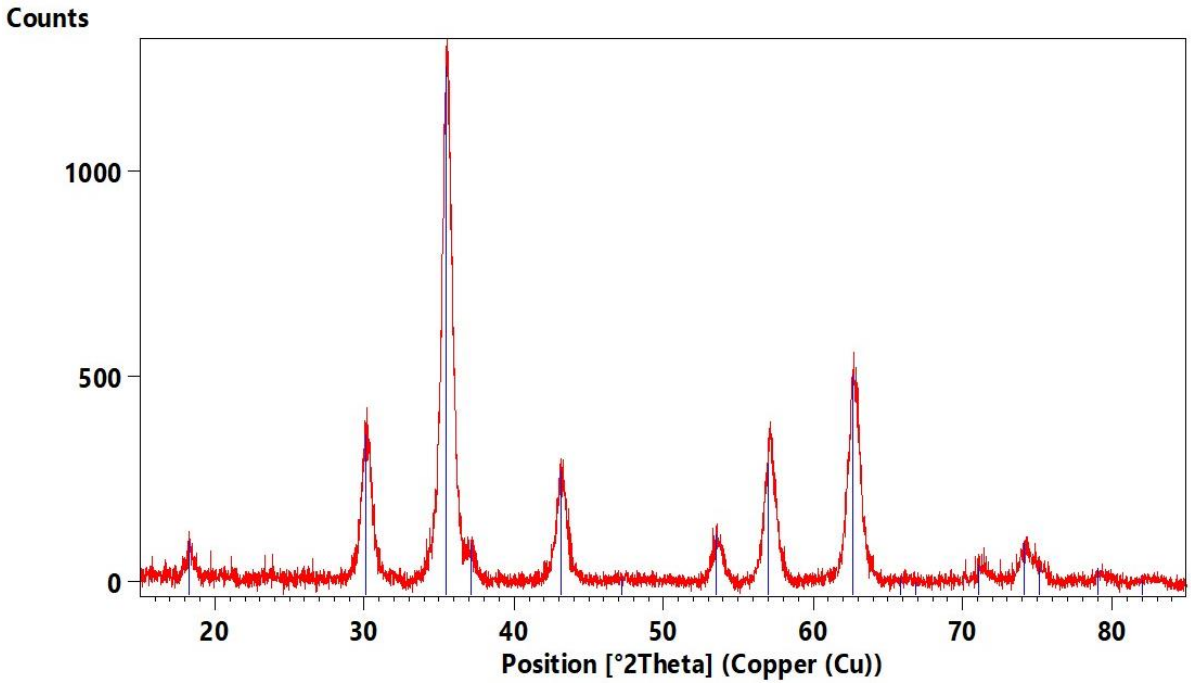


Figure 3-3: XRD pattern showing matched peaks for the Fe_3O_4 sample.

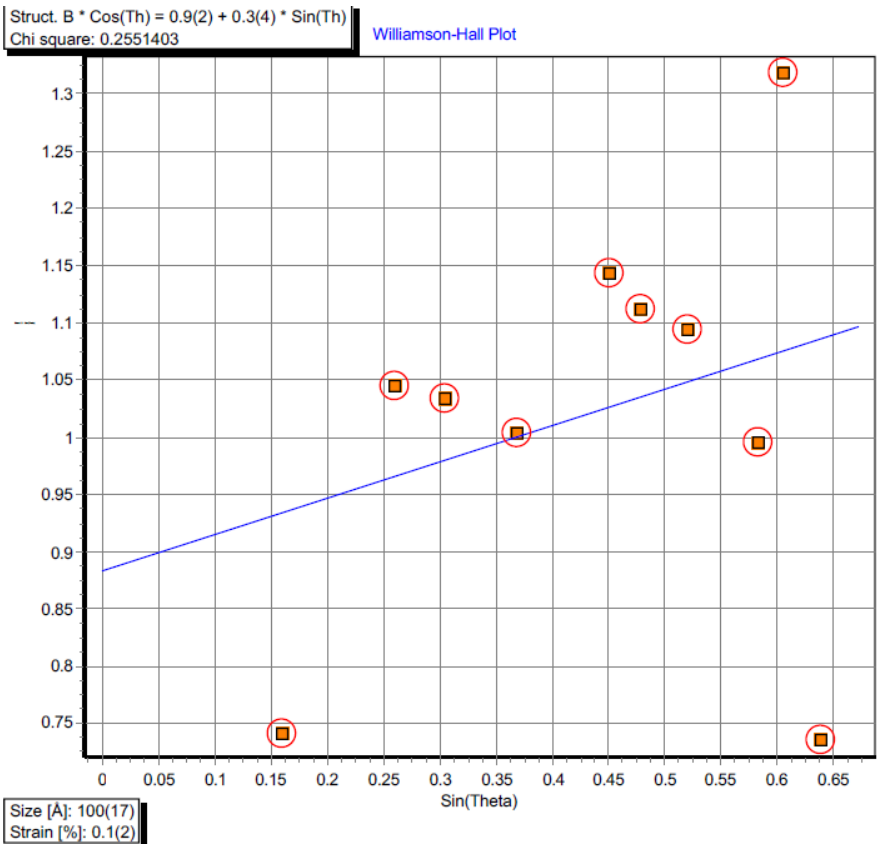


Figure 3-4: Williamson-Hall Plot for the peaks from XRD output.

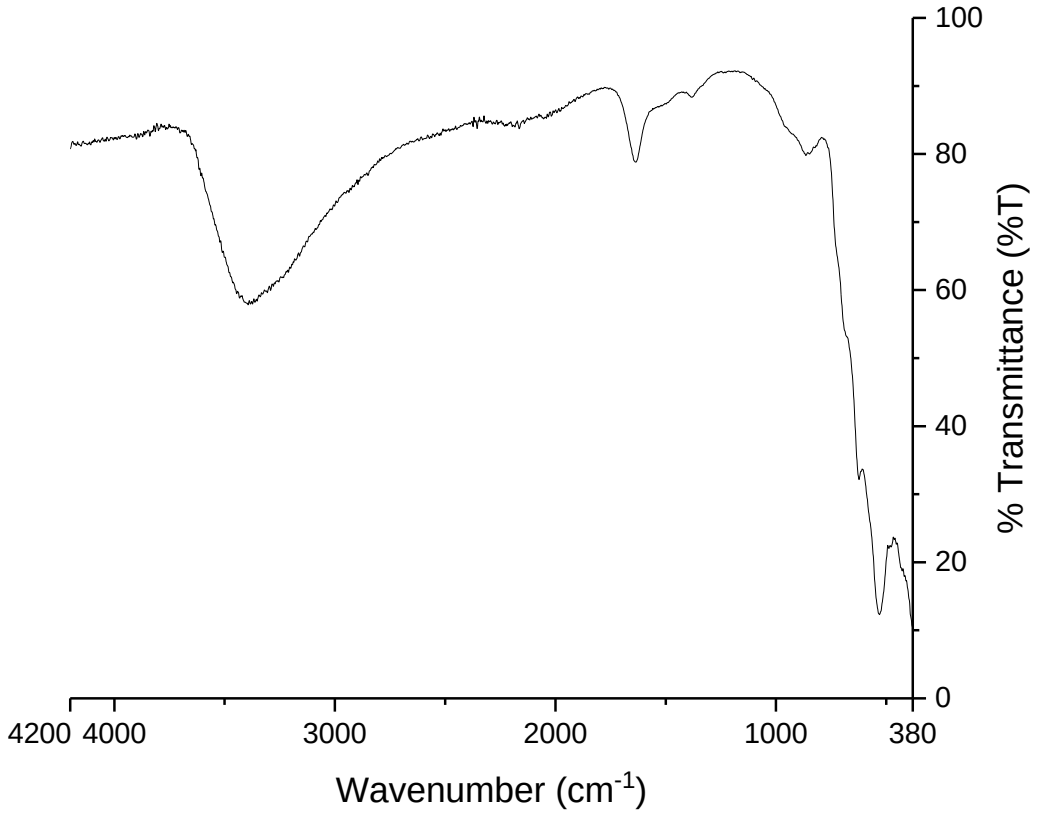


Figure 3-5: FTIR spectrum of Fe_3O_4 with its strong peak at 531 cm^{-1}.

FITR analysis above (Figure 3-5) of the sample gave the typical results[21] for Fe_3O_4 with a peak at 532 cm^{-1} corresponding to the Fe-O stretch[22]. The broad peak centred at approximately 3400 cm^{-1} and the peak at 1637 cm^{-1} corresponds to the O-H stretches and bending respectively of surface –OH groups or absorbed water[23][24].

The colloidal stability of the particles in solution was low which could be seen as the particles precipitated out of solution overnight. This stability could be quantified by DLS measurements over time. As can be seen in the table below (Table 3-1) the Z-average and PDI both increase over 24 hours indicating that the particles are aggregating in solution while the count rate decreases significantly over the 24 hours. After 24 hours the count rate of the solution had decreased by 99 %, particles could be seen to have formed a sediment at the bottom of the cuvette and the initial brown transparent solution was now clear.

It should be noted that uncoated magnetite nanoparticles are known not to be suitable for DLS measurements[25][26]. The DLS instrument gives a quality report with each measurement and for all but the first measurement here, the report said that the particles were unsuitable for DLS measurements because of aggregation. In addition, different samples from the same

batch of magnetite would give widely different results. The difficulty to get consistent results indicates the unsuitability of the bare MNPs for this type of analysis while also indicating the instability of the particles in solution themselves.

Table 3-1: DLS data of the bare Fe_3O_4 particles over 24 hours.

Time	Z-Average	PDI	PDI Width	Count Rate
	d.nm		d.nm	kcps
0 hr	178.6	0.202	80.2	23562
1 hr	920.9	0.525	667.5	19498
2 hr	1820	0.806	1633	9473
3 hr	2040	0.624	1611	3963
5 hr	1951	0.663	1588	3025
7 hr	2192	1	2192	1886
24 hr	4573	1	4573	291

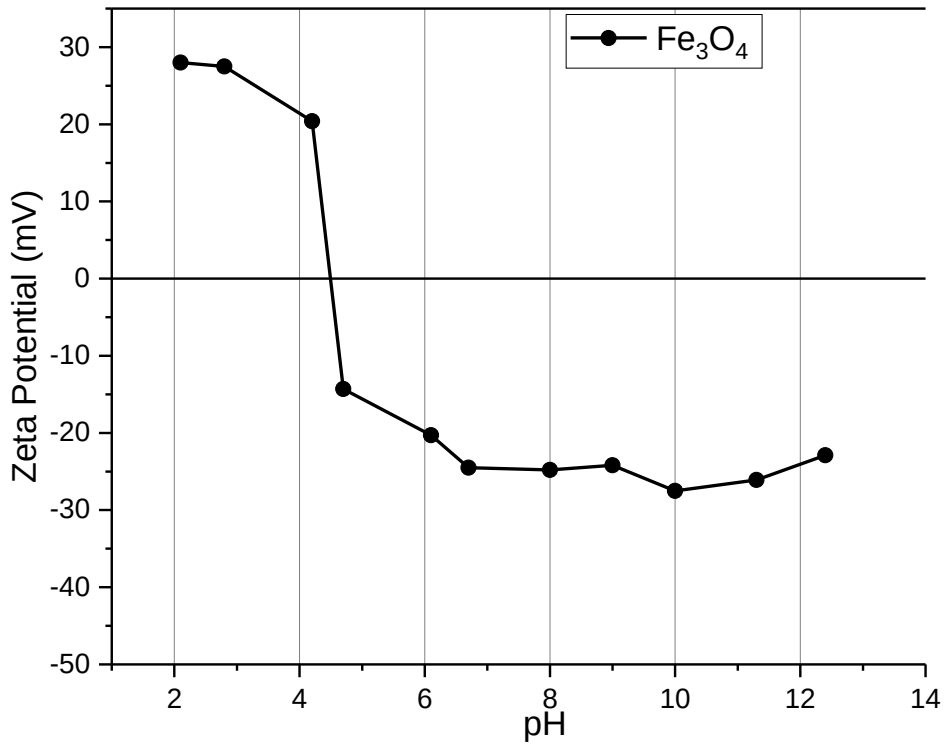


Figure 3-6: Zeta Potential measurements over a pH range showing the PZC.

Zeta potential measurements of the particles as seen above (Figure 3-6) also indicated that they had low colloidal stability at neutral pH with a value of -24.5 mV at pH 6.7. Zeta potential values between 0 and ±30 will have low colloidal stability in aqueous solution[27]. It should be noted here that the literature has conflicting reports for the zeta potential from +16 mV[25] to -31 mV[26]. By taking zeta potential measurements over a pH range of 2.1 – 12.4 the Point of Zero Charge (PZC) can be measures for the bare particles. It was found to be at approximately pH 4.5, although it should be noted that for pH 2.1 and 12.4, the conductivity was above 1 mS/cm when below that value is considered optimum for better measurements[27]. This PZC value is higher than a reported value for magnetite MNPs of 6.7[28]. It was noted that for the pH 2.1 sample, the MNP would dissolve in solution within 30 minutes but it was possible to get a measurement before this happened.

In coming to the final protocol for the synthesis of magnetite here, many variations were performed on the procedure to see if the outcome of the synthesis could be improved. One of the variations on the procedure that was done was changing from mechanical to magnetic stirring with all other conditions remaining the same. The TEM images (Figure 3-7) for this synthesis showed no major observable difference in the particle size distribution and morphology. Also the VSM, XRD and FTIR gave similar results as the mechanical stirring version with a specific magnetisation of 60 Am^2kg^{-1}, an XRD match for magnetite with crystallite size of 9.1 nm and a lattice constant of a = 8.3476 Å and an IR peak at 540 cm^{-1} for the Fe-O stretch.

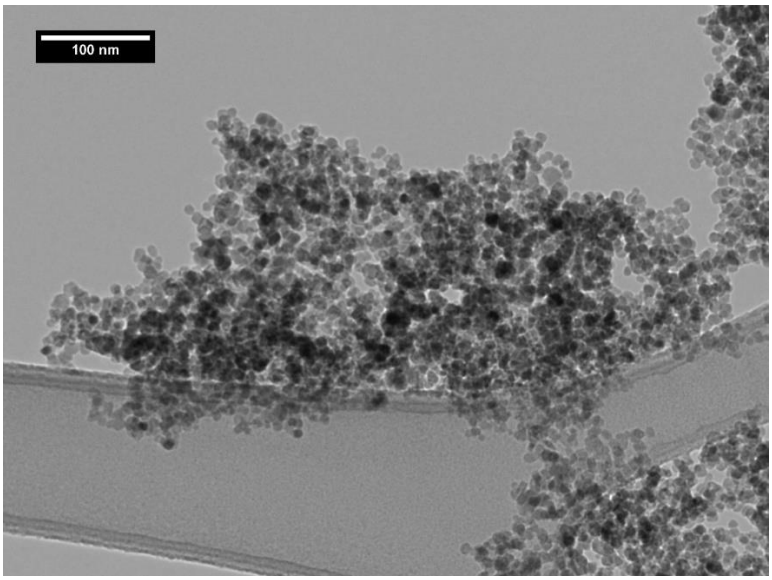


Figure 3-7: TEM images of Fe_3O_4 MNPs made with magnetic stirring.

The magnetisation was slightly higher (60 Am^2kg^{-1}) compared to the magnetic field free synthesis (58 Am^2kg^{-1}). The magnetic properties of a sample is related to its crystallinity[29], which is a factor that has low control by coprecipitation chemical synthesis. This was the only improvement with this variation but the slight increase is typical of a change in outcome between different batches in the synthesis. For this variation, the magnetic stirring *vs* mechanical stirring, it is considered that there is no major differences overall and the outcomes were within an acceptable range to say that this modification had no effect.

In another variation that was tried on the described procedure (2.2.1) was using a non-buffered base solution. It is reported in the literature that changing pH can have an effect on the outcome of the particles[3] and during the course of a non-buffered reaction the pH changes considerably. In the experimental describing our synthesis NH_4Cl was added to the ammonia solution to create a buffer so the pH will remain relatively constant as the metal ions are being added to the solution. In the synthesis, the initial pH of the buffered solution was 10.0 and the final pH was 9.6. Without a buffer, the initial pH was 12.6 and the final pH was 9.8. Using a small amount of NH_4Cl to create a buffer removes any effects that changing pH would have between the start and end of addition of the metal ions to create a more constant pH environment over the course of the reaction.

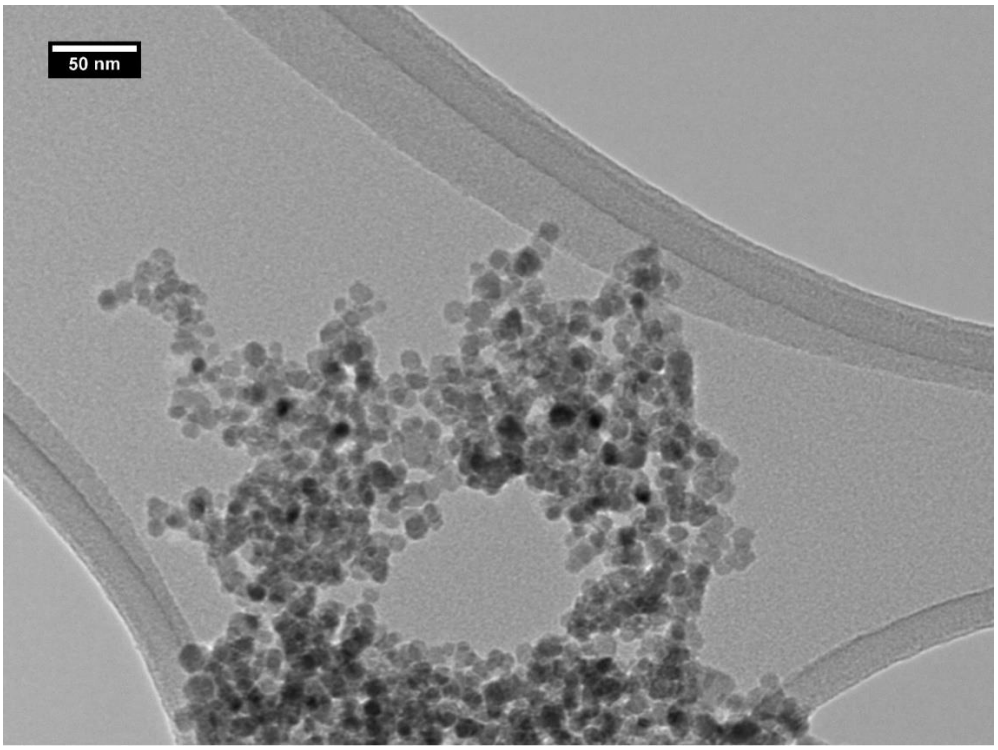


Figure 3-8: TEM images of the synthesised without a buffer Fe_3O_4 MNPs.

Again, a TEM image (Figure 3-8) for this synthesis showed no observable difference in the particle sizes and morphologies. Also the XRD and FTIR gave similar results as the experimental version with an XRD match for magnetite with crystallite size of 10.0 nm and a lattice constant of a = 8.3391 Å and an IR peak at 534 cm^{-1}. Interestingly the VSM gave a lower specific magnetisation of 54 Am^2kg^{-1}. This is inconclusive as to have been due to the change in the experimental procedure or because of the variation between batches.

Another variation on the standard procedure was adding the NH_4OH solution to the metal ion solution without a buffer. The freshly prepared degassed metal ion solution has a pH of 2.1 and after the addition of the excess base solution the pH was 10.2. The particles formed seemed to have a broader size range with some larger particles in the sample as seen with the TEM image below (Figure 3-9), although this was a small noticeable effect it would not be classed as having a major difference in the outcome of the reaction.

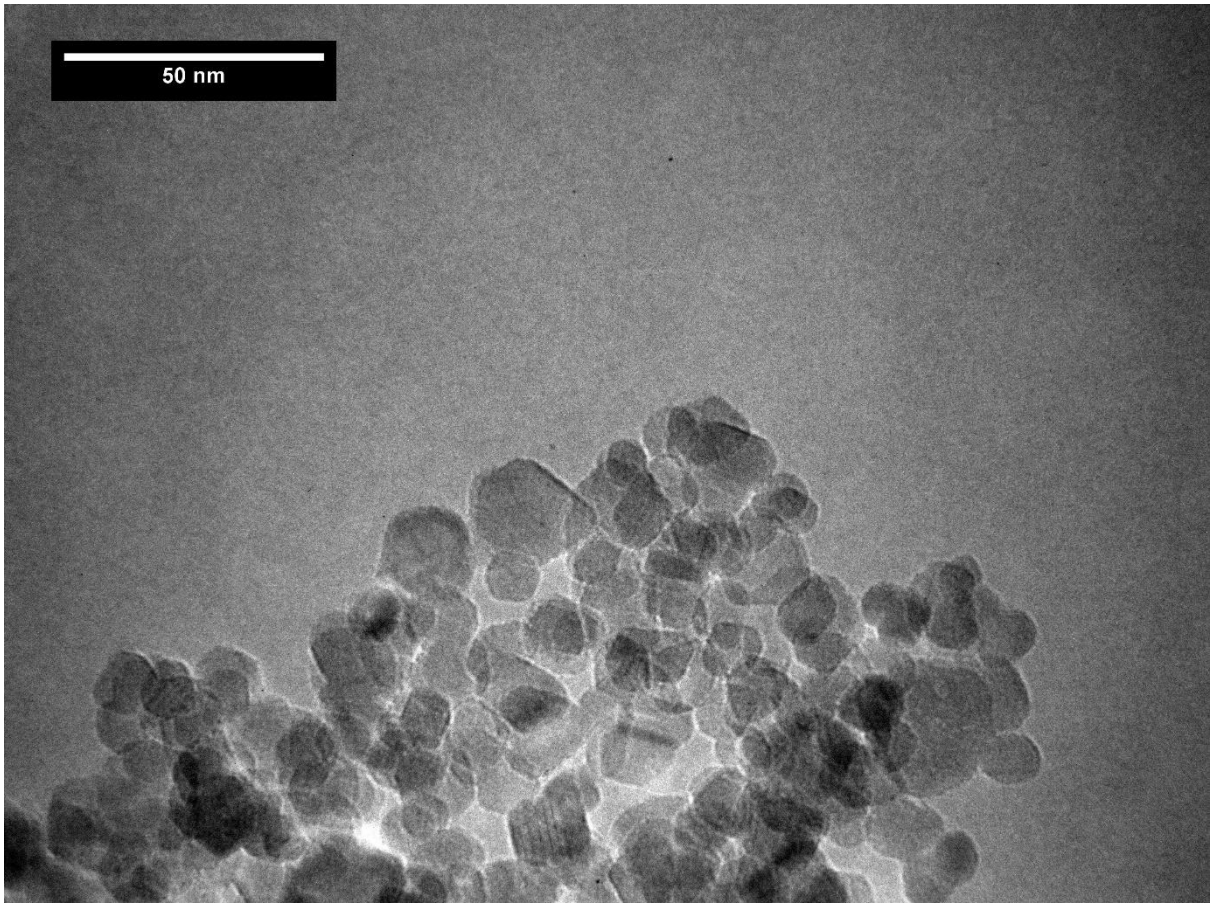


Figure 3-9: TEM images of Fe_3O_4 MNPs prepared by adding NH_4OH to the metal ions solution.

The VSM, XRD and FTIR gave similar results as the standard version with a specific magnetisation of 60 Am^2kg^{-1} at 1 T, an XRD match for magnetite with crystallite size of 9.1 nm

and a lattice constant of a = 8.3476 Å and an IR peak at 532 cm^{-1} for the metal-oxygen vibration.

Another variation that was tried was using different bases in the coprecipitation synthesis. The literature reports NaOH[6], Na_2CO_3[7] and NH_4OH[30] being used to precipitate out Fe_3O_4 from the solution. For using the Na_2CO_3, a buffer can be created to control the pH while with NaOH it was found that a buffer could not be created, as it is a strong base. A buffer is made from a weak acid or base and its conjugate base or acid. Using Na_2CO_3 both a buffered and non-buffered procedure was studied but showed no major difference. This variation, using different bases than NH_4OH, had a major effect on the outcome.

For the synthesis using NaOH as the base for precipitation of magnetite, the IR gave a peak at 540 cm^{-1} in the expected region. The VSM had a specific magnetisation of 77 Am^2kg^{-1} that was higher than for previous samples, while the TEM images showed a very polydisperse sample with some particles of around 100 nm (Figure 3-10).

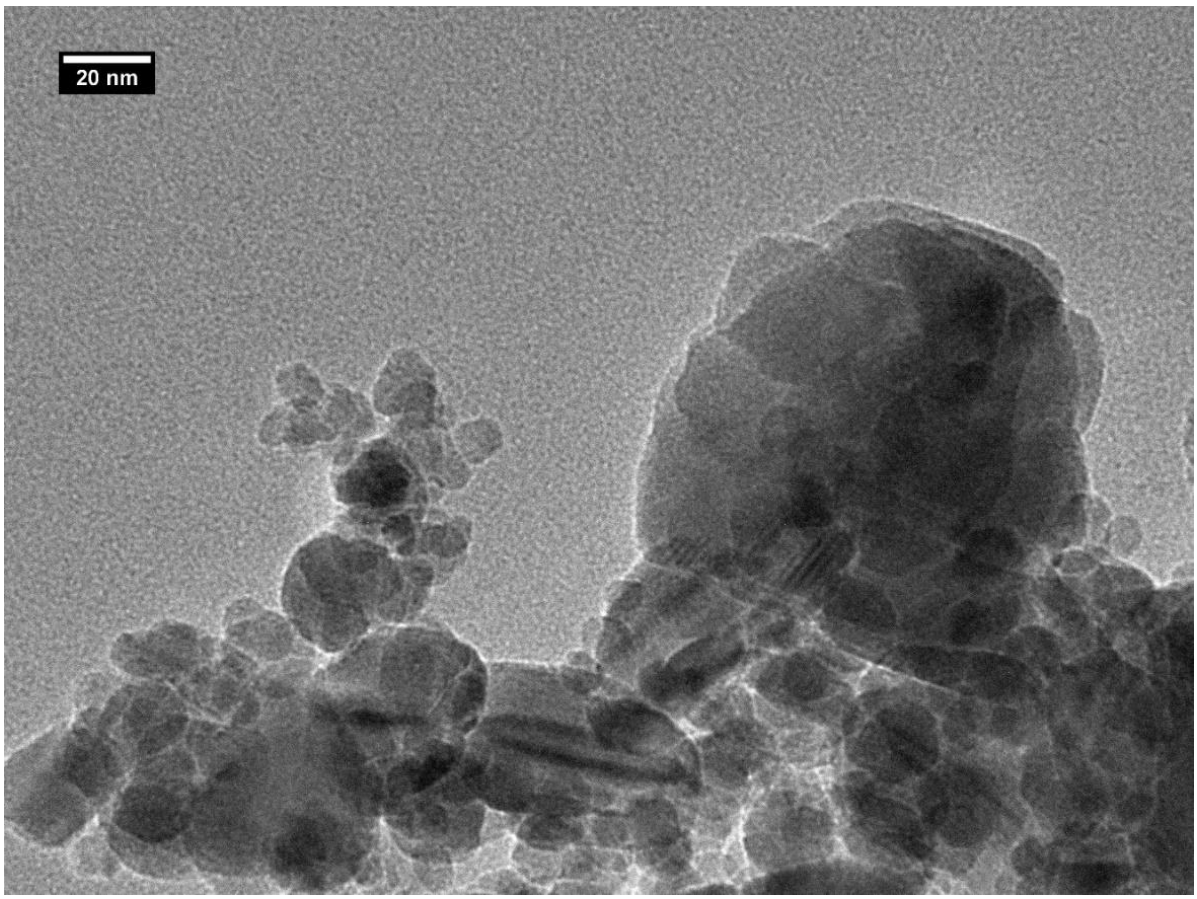


Figure 3-10: TEM images of coprecipitated Fe_3O_4 MNPs prepared using NaOH.

The higher magnetisation can be understood because of the larger crystalline particles in the sample, as surface effects are known to reduce the magnetisation[31].

XRD analysis confirmed that Fe_3O_4 was the product of the reaction with the material being a good match for that crystal structure as can be seen below (Figure 3-11). The XRD output gave a match for the reference pattern of magnetite (COD 210-1536). The XRD of the sample showed more narrow distinct peaks as is common when larger crystallites are present. The Scherrer equation, used for calculating crystallite size from diffraction data, is based on size broadening, that is where smaller crystallites induce peak broadening[32]. The Williamson-Hall method takes into account the size broadening and strain broadening for a more accurate estimation of crystallite size[33]. A Williamson-Hall plot for the peaks gave a crystallite size of 23.5 nm, which corresponds to the polydisperse sample as in the TEM images above (Figure 3-10). Rietveld analysis on the output using this matched reference pattern for the structure fit gave a cubic crystal lattice with a lattice of a = 8.38303 Å.

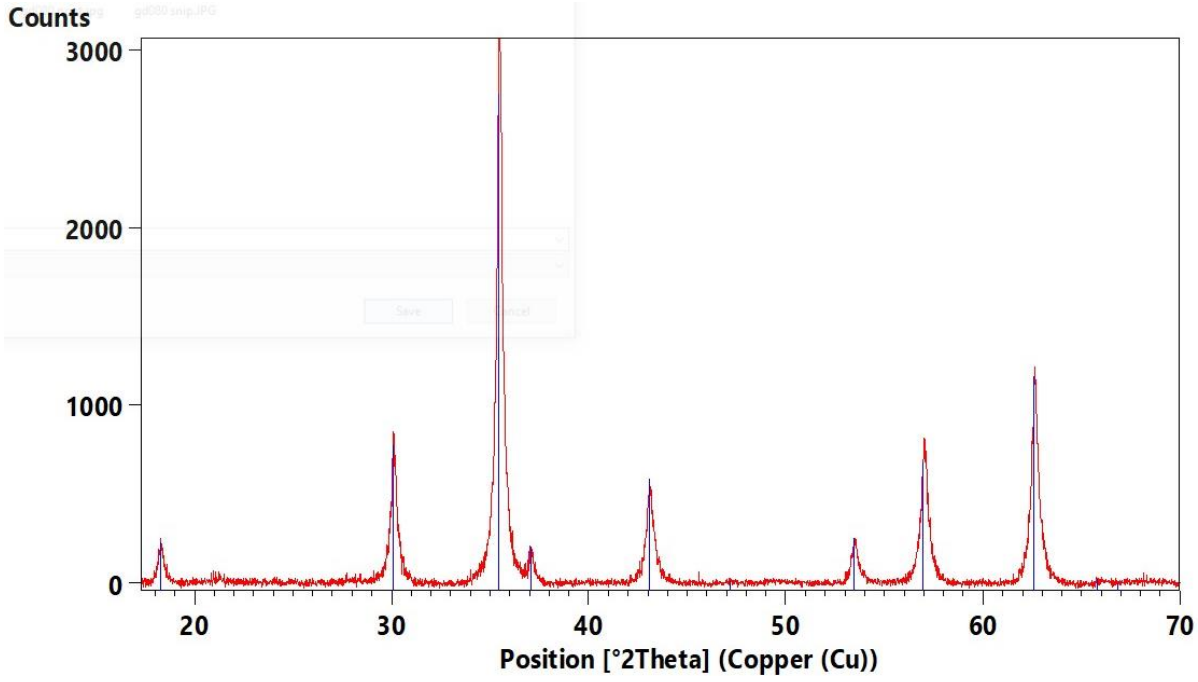


Figure 3-11: XRD pattern for Fe_3O_4 prepared using NaOH.

Similarly, changing the base to Na_2CO_3 and using $NaHCO_3$ salt to create a buffered solution with pH of 10.5 gave different results than the buffered NH_4OH version. The IR gave a peak at 537 cm^{-1} that is in the expected region. The VSM results showed a specific magnetisation of 60 Am^2kg^{-1}, which was slightly higher, while the TEM images showed a very polydisperse

sample with some particles of 100 nm, as seen below (Figure 3-12). It was surprising that the magnetisation was low as the sample had large particles.

The XRD again showed more narrow distinct peaks corresponding to larger crystallites present. XRD analysis confirmed that Fe_3O_4 was the product of the reaction with the material being a good match for that crystal structure, as can be seen below (Figure 3-13). The XRD corresponded well to the reference pattern of magnetite (COD 230-0617). A Williamson-Hall plot for the peaks gave a crystallite size of 15.0 nm, which is in line with the polydisperse sample shown in the TEM images below (Figure 3-12). Rietveld analysis using this matched reference pattern for the fit gave a cubic crystal lattice with a lattice of a = 8.35531 Å.

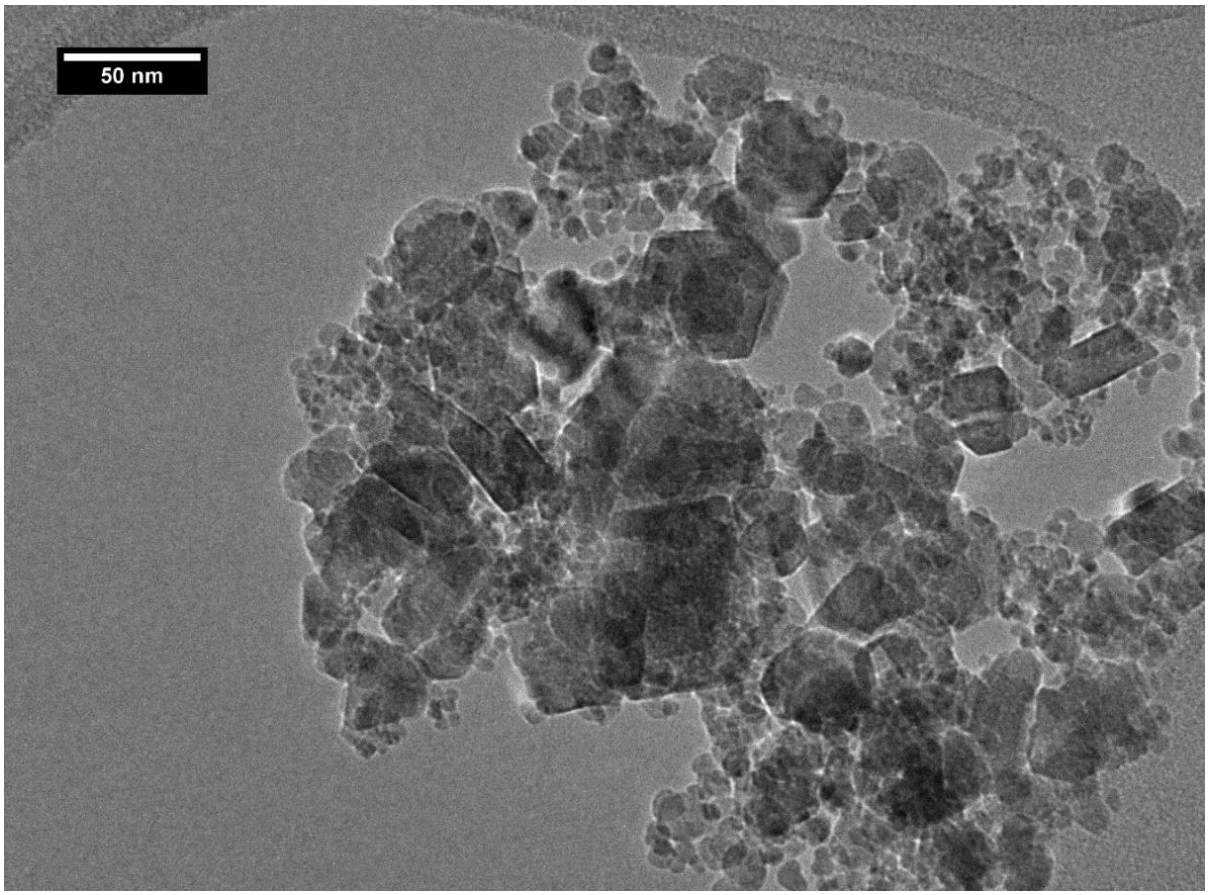


Figure 3-12: TEM images of Fe_3O_4 MNPs prepared using a buffered Na_2CO_3 solution.

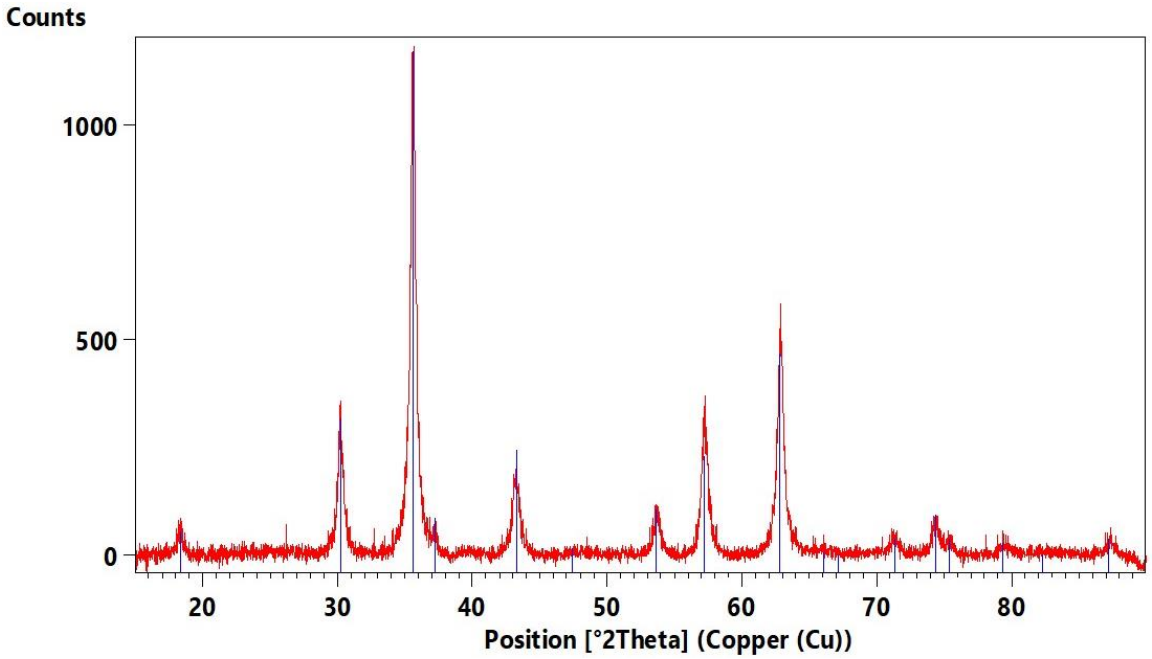


Figure 3-13: XRD pattern of magnetite prepared using Na_2CO_3 buffered synthesis.

From this, we can see that using NH_4OH instead of the other bases has a huge effect on the monodispersity of the final product. The reason behind this is not fully understood, as elucidating mechanisms at an atomic level is extremely difficult. Below is a table summarising these studies on optimisation of magnetite MNPs synthesis (Table 3-2).

Table 3-2: Summary of changing conditions to optimise synthesis of Fe_3O_4.

Coprecipitation synthesis detail	TEM particle sizes (nm)	XRD crystallite size (nm)	Magnetisation value (Am^2kg^{-1})	Comments
NH_4OH with buffer, mechanical stirring, metal ions added	11 ± 4	10.0	58	Best results, highly reproducible
NH_4OH without buffer	10 ± 5	10.0	54	Good result, reproducible
magnetic stirring	12 ± 5	9.1	60	good result
NH_4OH added to metal ions	14 ± 6	9.1	60	Some larger particles in images
NaOH as base	40 ± 30	23.5	77	polydisperse sample
Na_2CO_3 as base	40 ± 35	15.0	60	polydisperse sample

3.3.2 Preparation of Manganese Ferrite MNPs ($MnFe_2O_4$) by Coprecipitation

Magnetite MNPs have been used extensively in biomedical research and in some biomedical applications because of its excellent biocompatibility[34]. $MnFe_2O_4$ has also been used in biomedical research as it is relatively biocompatible, though not as much as Fe_3O_4. $MnFe_2O_4$ is also more stable to oxidation than Fe_3O_4 while having good magnetic properties[35].

There are not as many reports of $MnFe_2O_4$ synthesis comparing to Fe_3O_4 MNPs. Normally $MnFe_2O_4$ MNPs are prepared by coprecipitation syntheses using NaOH as the base in the reaction[36][37]. However, our initial attempts at synthesis of $MnFe_3O_4$ MNP using the coprecipitation method with NaOH were unsuccessful with the formation of particles with very low magnetisation values. Using the experience gained from our Fe_3O_4 research and considering the systems are similar with both being spinel ferrites, it was decided to try the same method as the iron oxide for the synthesis of the manganese ferrite. This procedure using NH_4OH with NH_4Cl to create a buffer solution to which the Mn^{2+} and Fe^{3+} ions are added is described in the experimental section (2.2.2), was successful in producing manganese ferrite MNPs and the product was characterised by TEM, VSM, XRD and FTIR.

The TEM images below (Figure 3-14) showed that the sample consisted of nanoparticles but that the product was not as monodisperse as the magnetite product had been for the same procedure. The size range was approx. between 3-40 nm.

VSM analysis gave a moderate magnetisation value of 38 Am^2kg^{-1} at 1 T as can be seen below (Figure 3-15). Manganese ferrite has a reported specific magnetisation of 77 Am^2kg^{-1} for the bulk material[16]. The hysteresis curve indicates that the particles have no remnant magnetisation and reached saturation in a low magnetic field. The particles could be quickly extracted from solution using a handheld neodymium magnet.

XRD analysis confirmed that $MnFe_2O_4$ phase had been made by a high match for that crystal structure as can be seen below (Figure 3-16). The XRD output corresponded well to the reference pattern of manganese ferrite (COD 152-8317). A Williamson-Hall plot for the peaks gave a crystallite size of 17.7 nm, which is consistent with the TEM images below (Figure 3-14). Rietveld analysis on the output using this matched reference pattern for the structure fit gave a cubic crystal lattice with a lattice of a = 8.41863 Å.

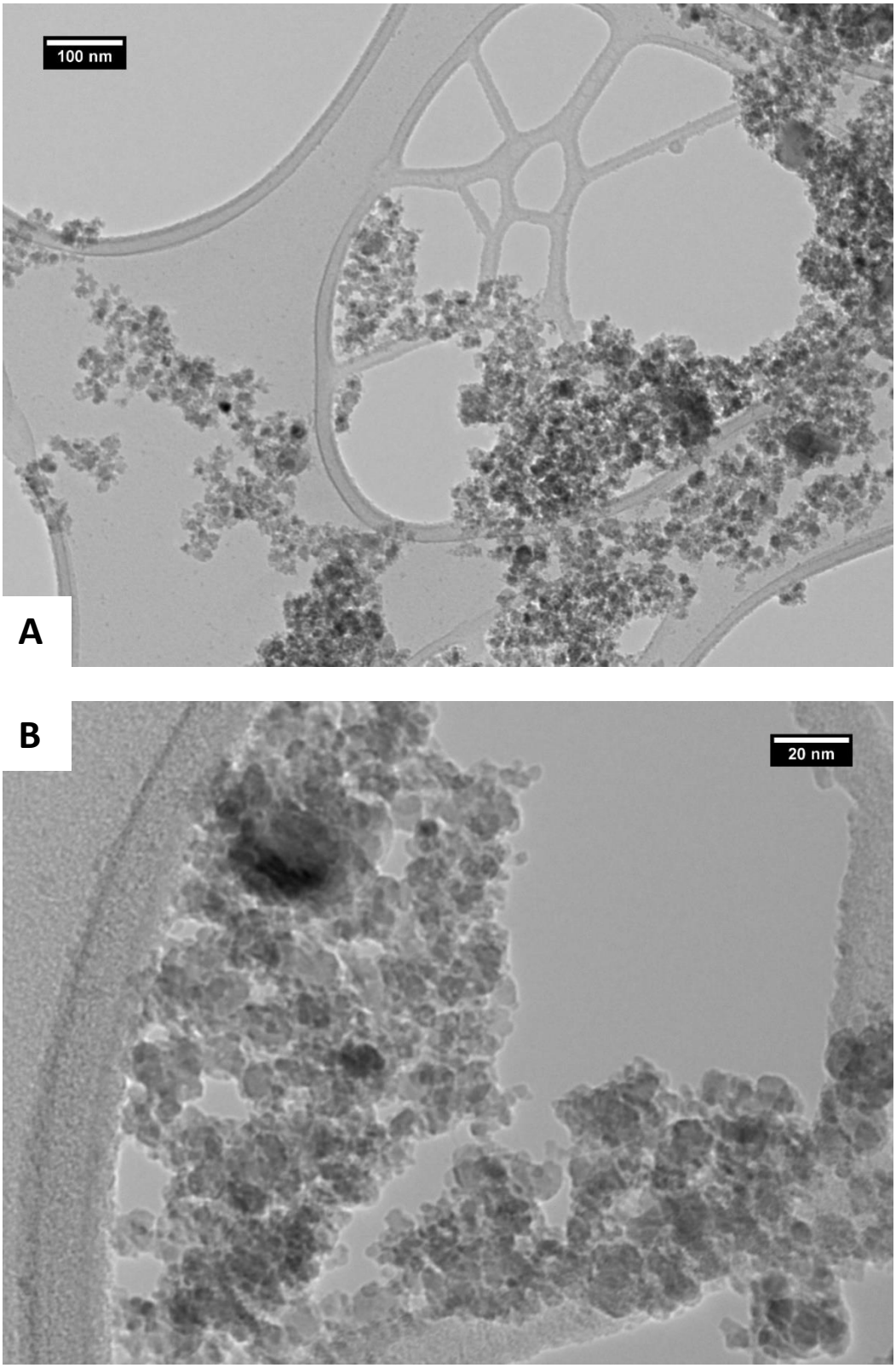


Figure 3-14: (A), (B) TEM images of coprecipitated $MnFe_2O_4$ MNPs.

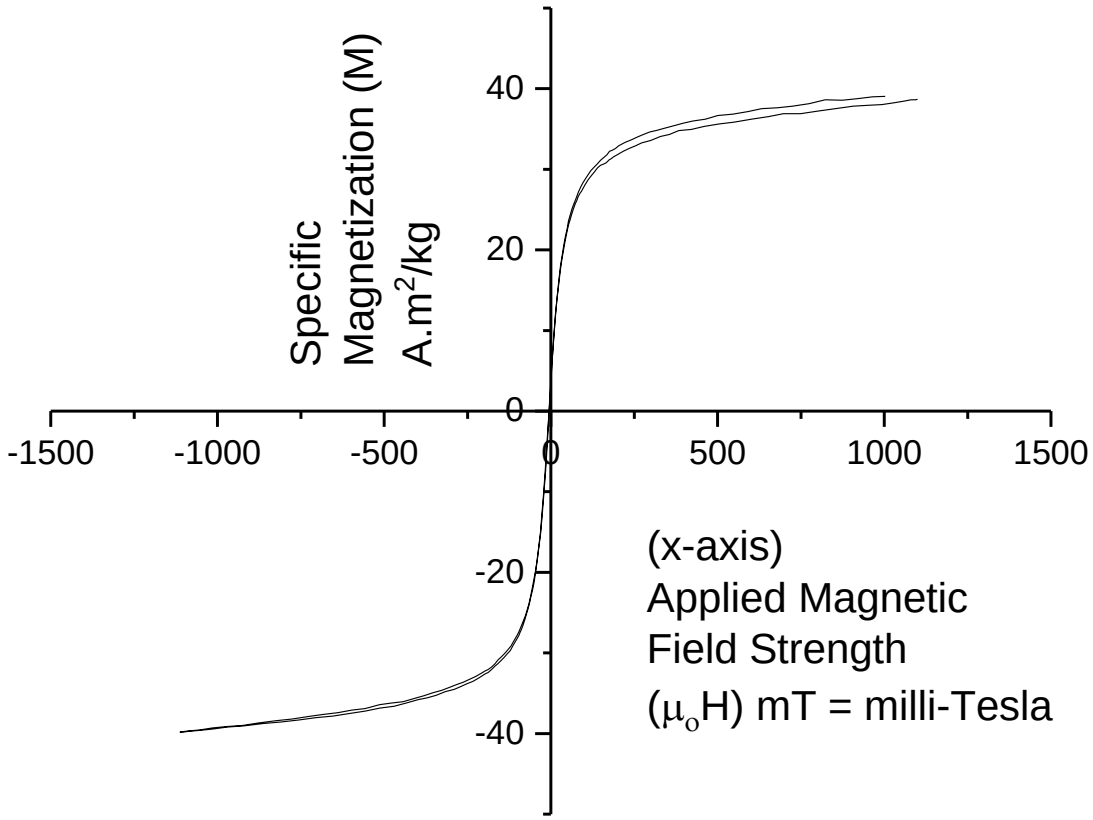


Figure 3-15: VSM curve of $MnFe_2O_4$ MNPs synthesised by coprecipitation.

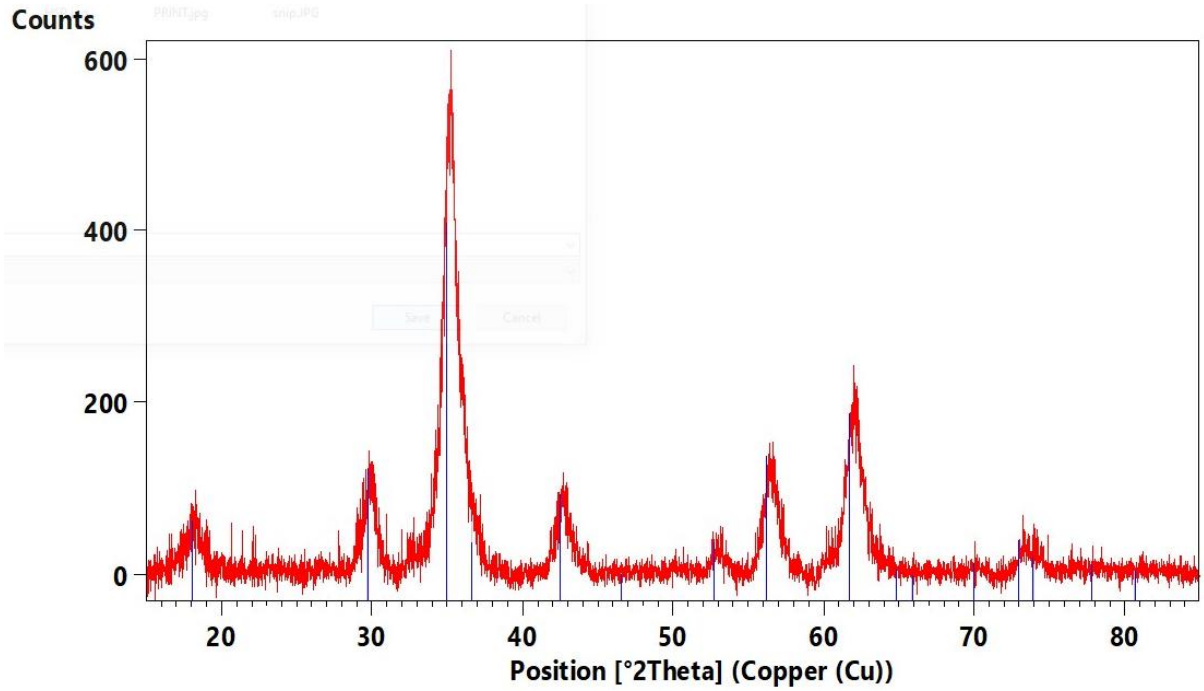


Figure 3-16: XRD pattern of $MnFe_2O_4$ MNPs synthesised by coprecipitation.

FITR analysis (Figure 3-17) of the $MnFe_2O_4$ sample gave the typical results with a peak at 536 cm^{-1} corresponding to metal-O stretching modes of tetrahedral and octahedral sites[38]. The broad peak centred at 3400 cm^{-1} and the peak at 1600-1500 cm^{-1} corresponds to the –OH stretches and bending respectively of surface –OH groups or absorbed water[23][24].

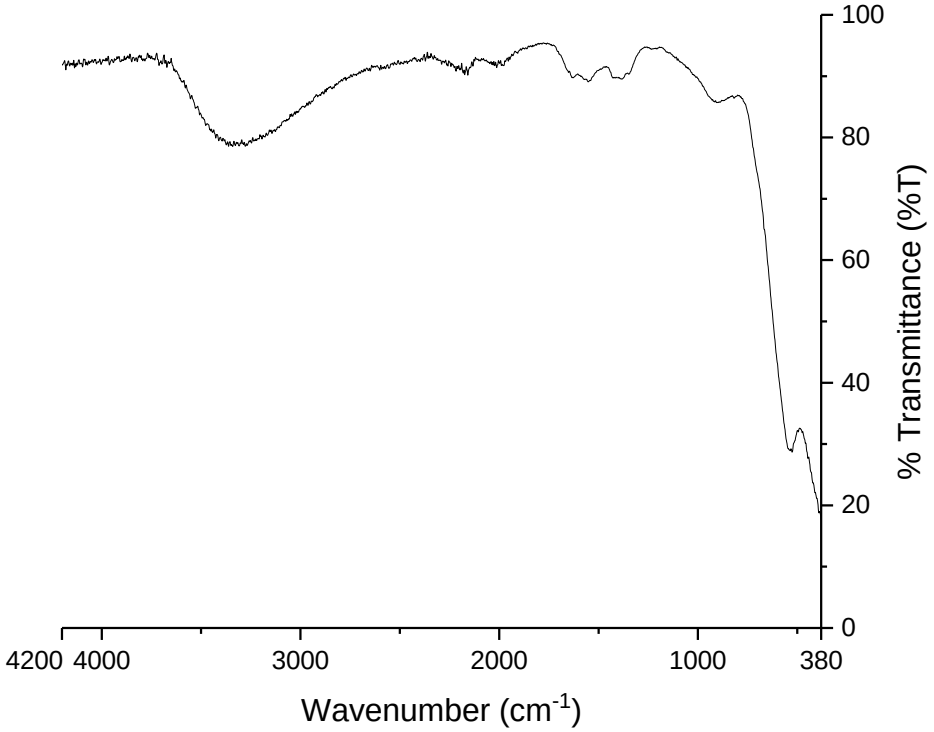


Figure 3-17: FTIR spectrumof $MnFe_2O_4$ particles synthesised by coprecipitation.

A variation on the basic procedure (2.2.2) was using magnetic stirring instead of mechanical while keeping all other conditions the same. A TEM image shown below (Figure 3-18) of the product of this reaction showed no major change in the sample with the sample still being polydisperse and with particles of a similar size. Also the VSM, XRD and FTIR gave similar results as the mechanical stirring version with a specific magnetisation of 46 Am^2kg^{-1}, an XRD match for manganese ferrite with crystallite size of 22.1 nm and a lattice constant of a = 8.46123 Å and an IR peak at 535 cm^{-1} for the metal-O stretch. Again, the slight increase in the magnetisation could be attributed to deviation between batches rather than a change due to the changing protocol. For this variation, the magnetic stirring *vs* mechanical stirring, it is considered that there are no major differences overall and the outcomes were within an acceptable range, so this modification had no effect.

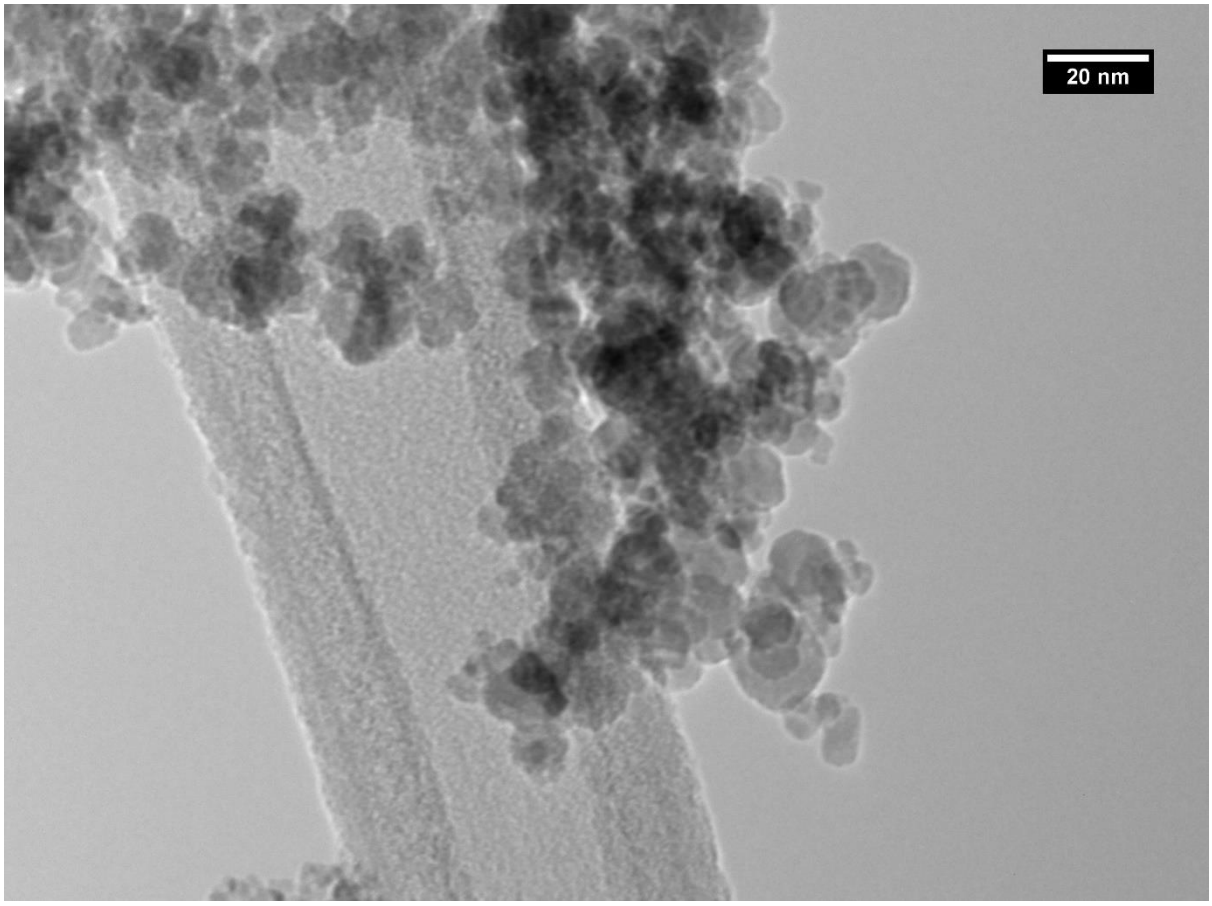


Figure 3-18: TEM images of $MnFe_2O_4$ prepared with magnetic stirring.

Another variation that was tried was changing the base used to initiate the precipitation of the ferrite nanoparticles from NH_4OH to NaOH. This variation had a major effect on the outcome of the reaction. A TEM image below (Figure 3-19) shows that some nanoparticles and some other structures were formed. The VSM result was very poor with a specific magnetisation of 5 Am^2kg^{-1} at 1 T. This was well below the value when using NH_4OH as the base. The XRD output below (Figure 3-20) showed that sample to be a mixture of several phases. Elucidation of this sample was not a simple process and the best fitting for phases using XRD software showed it to be composed of mainly Akaganeite, a chloride containing metal hydroxide (72.4 %, COD 900-2991) with some manganese ferrite phase (27.6 %, COD 101-0132) present. Solving the phases in complex mixtures is not a simple process and this analysis is not perfect as there are still some unexplained peaks in the XRD pattern.

This result was surprising as many papers use a similar procedure for the production of manganese ferrite nanoparticles[39][36]. It should be noted that this procedure had a only single iteration.

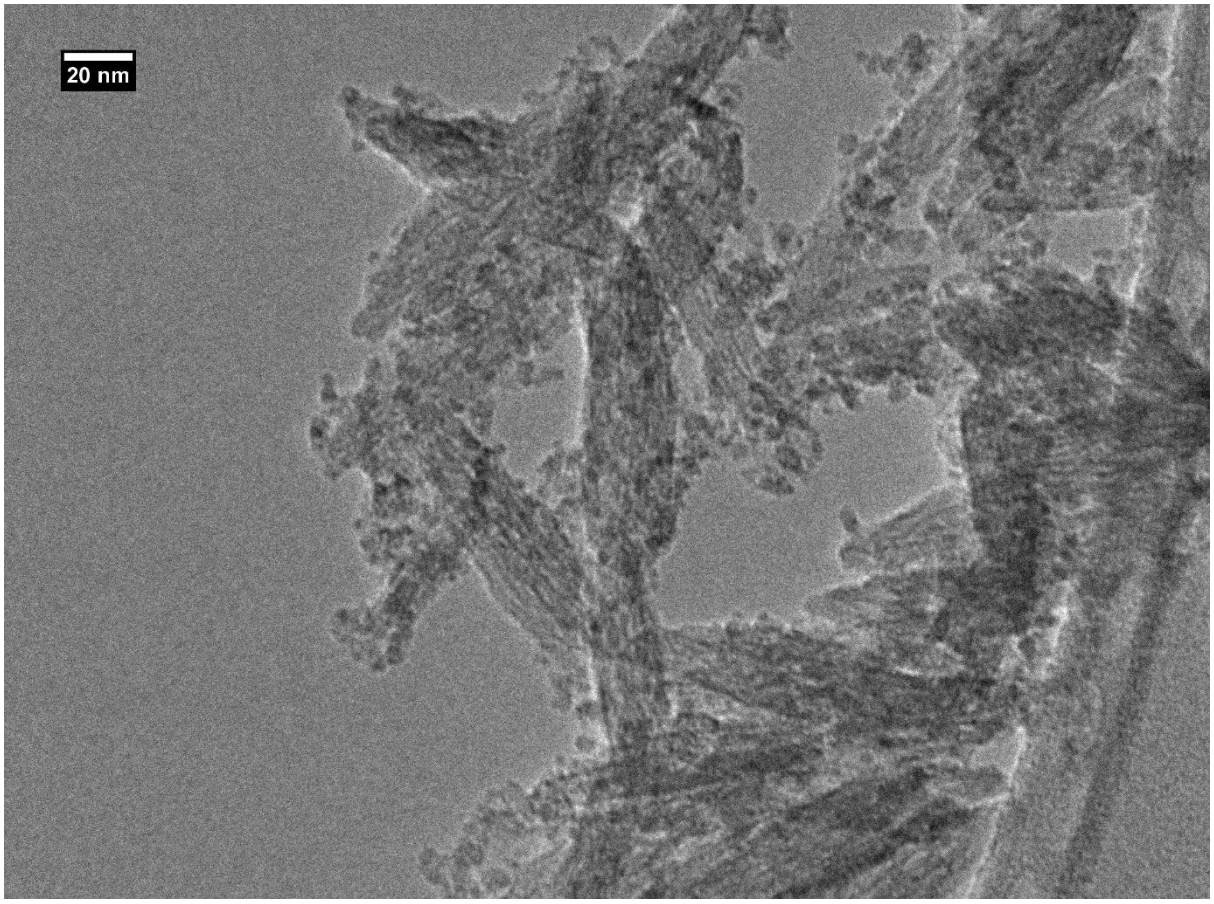


Figure 3-19: TEM image of Akaganeite and $MnFe_2O_4$ nanostructures prepared using NaOH as base.

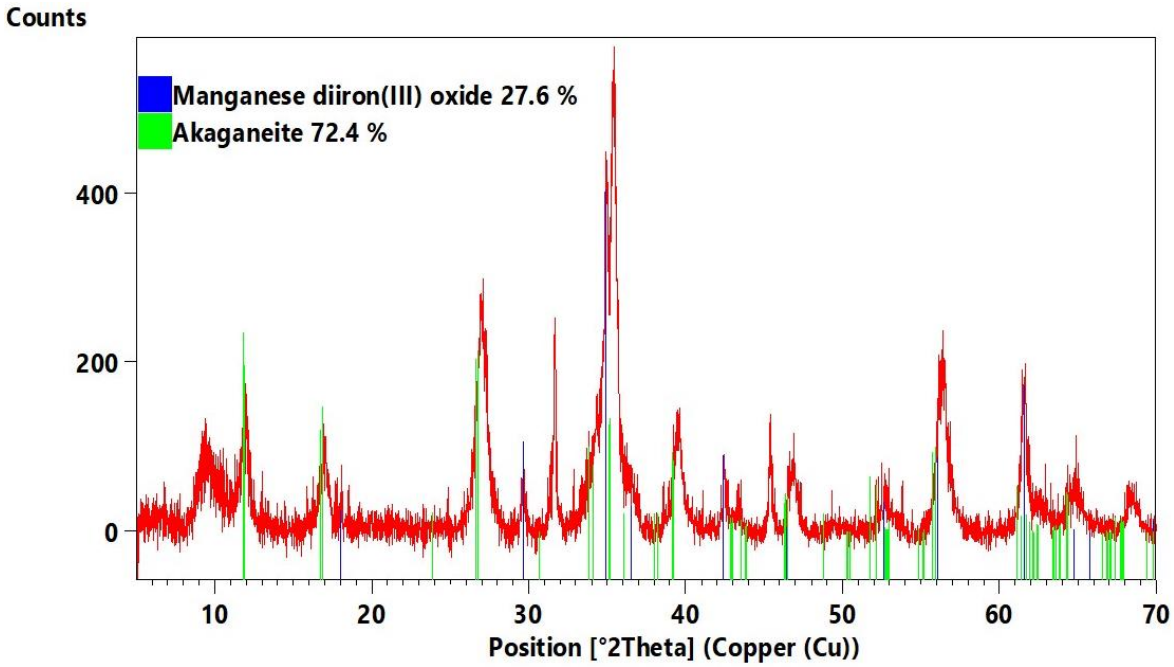


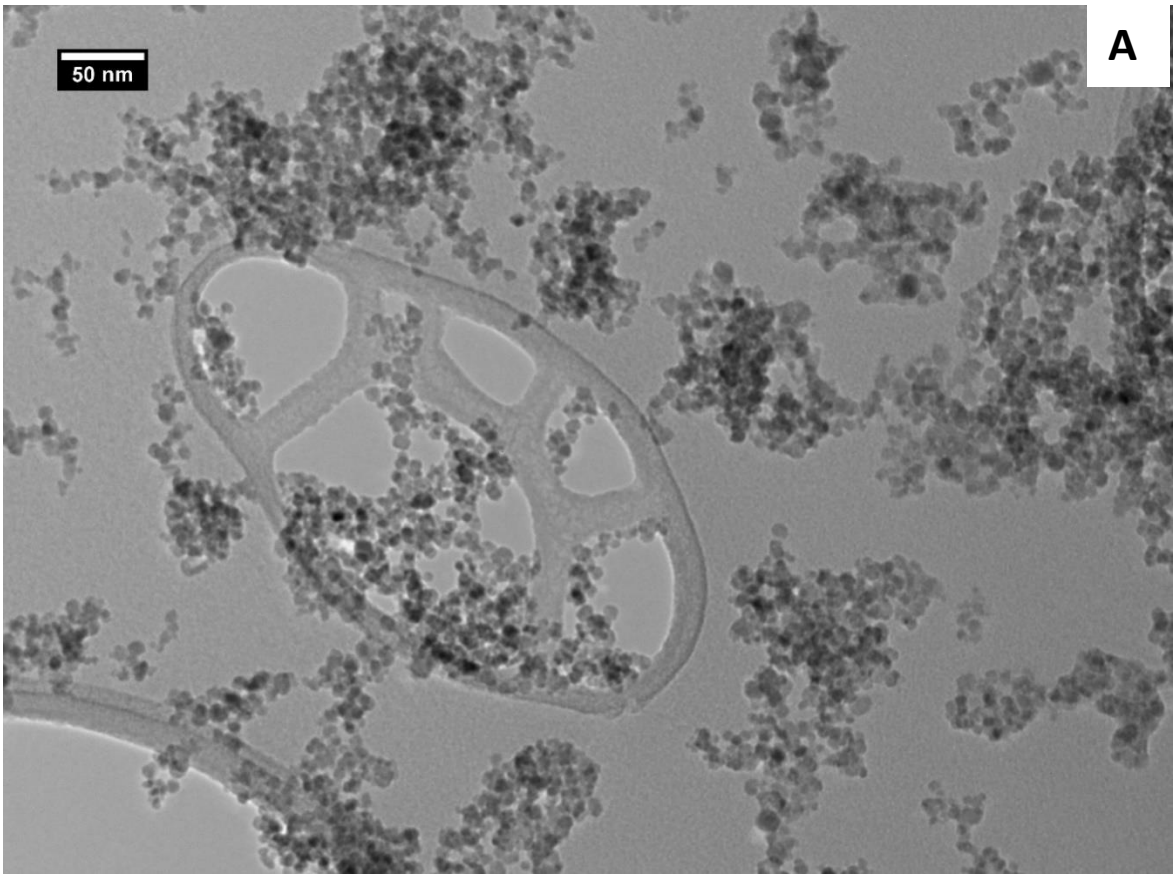
Figure 3-20: XRD patterns of Akaganeite and $MnFe_2O_4$ sample prepared by the coprecipitation using NaOH.

3.3.3 Preparation of Cobalt Ferrite MNPs ($CoFe_2O_4$) by Coprecipitation

The initial preparation of cobalt ferrite MNPs using the same method as for Fe_3O_4 and $MnFe_2O_4$ was unsuccessful with the formation of particles with very low magnetisation values. Several modifications were tried following procedures described in a variety of papers[40][41][42], with some modifications of procedures reported for magnetite synthesis[43]. The final procedure was similar to the synthesis for Fe_3O_4 and $MnFe_2O_4$ with the introduction of hydrazine being the major difference. This change was the major factor in the production of monodisperse superparamagnetic particles without any residual magnetism.

The procedure for the production of these $CoFe_2O_4$ MNPs is describe in the experimental section (2.2.3). Once again, the product was characterised by TEM, VSM, XRD and FTIR techniques.

The TEM images below (Figure 3-21) showed that the product was monodisperse with a size of 13±3 nm. The samples on the TEM grid showed it to be aggregated but this was most likely due to the sample preparation and drying technique.



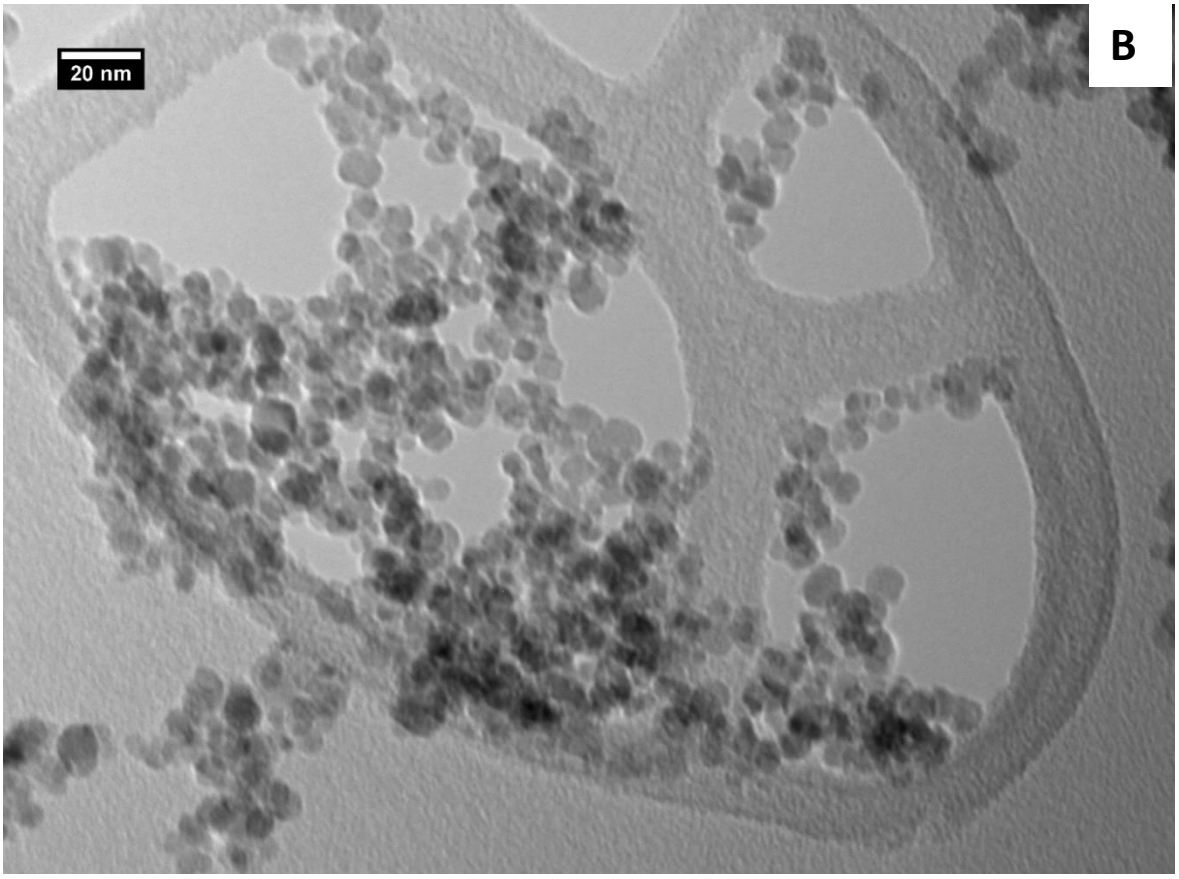


Figure 3-21: TEM images of as synthesised $CoFe_2O_4$ MNPs.

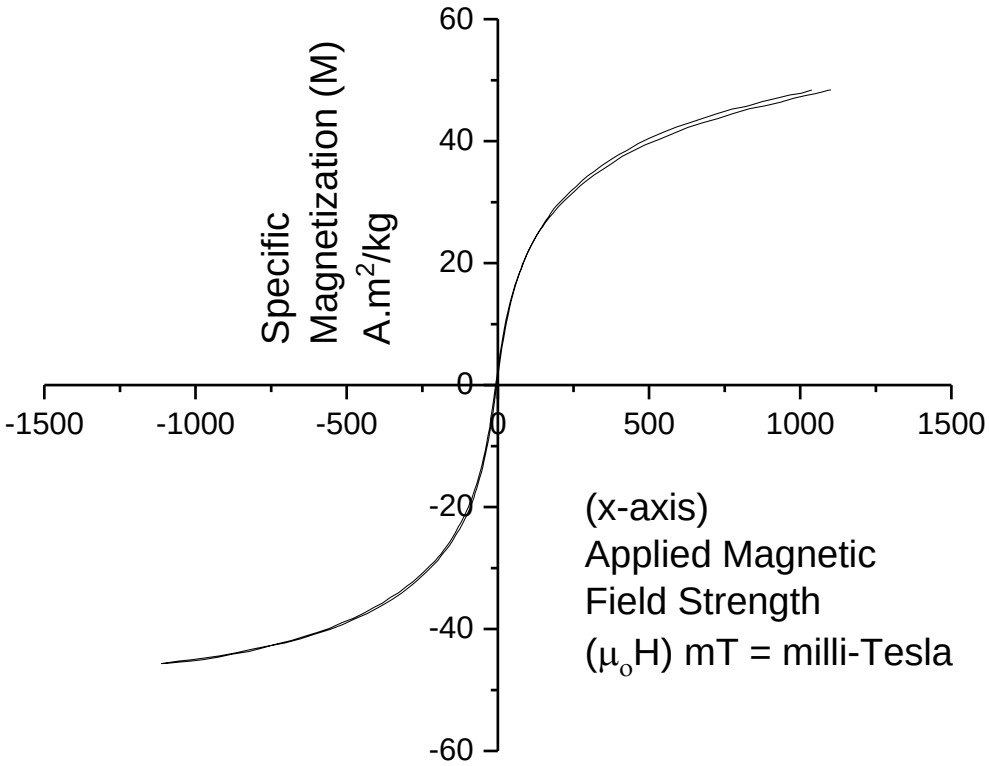


Figure 3-22: VSM curve of the synthesised $CoFe_2O_4$ MNPs.

VSM analysis have shown a moderate magnetisation of 48 Am^2kg^{-1} at 1 T as can be seen above (Figure 3-22). Cobalt ferrite has a reported specific magnetisation of 82 Am^2kg^{-1}[16]. The hysteresis curve indicates that the particles have no remnant magnetisation and have not reached saturation at 1 T which is indicative of superpararmagnetism.

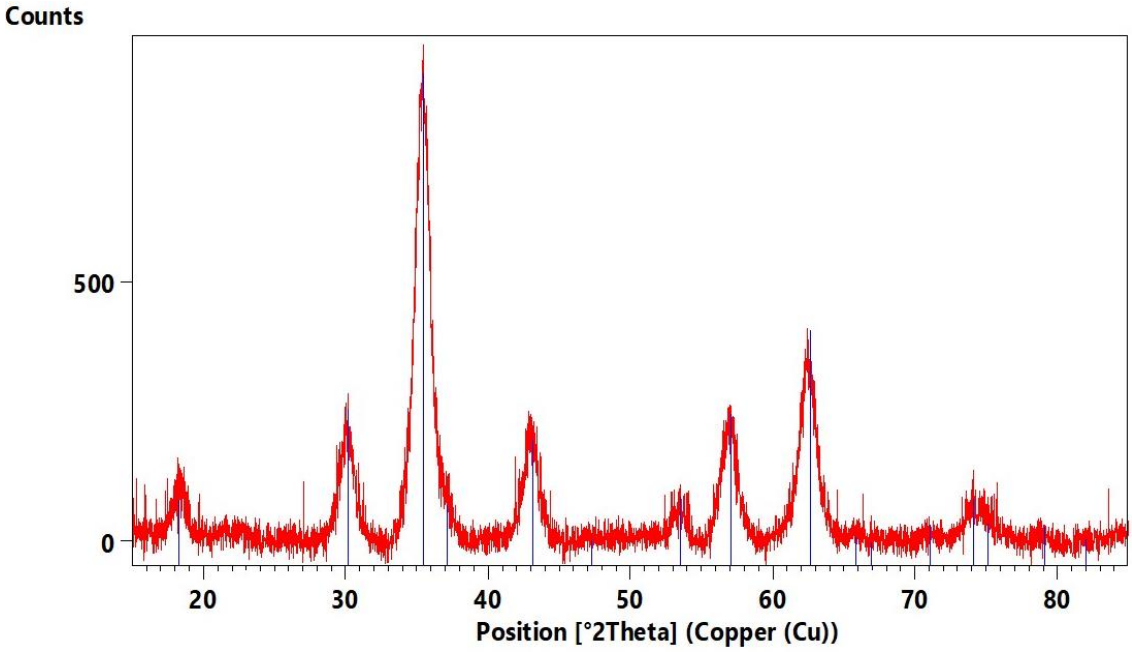


Figure 3-23: XRD pattern of the $CoFe_2O_4$ MNPs.

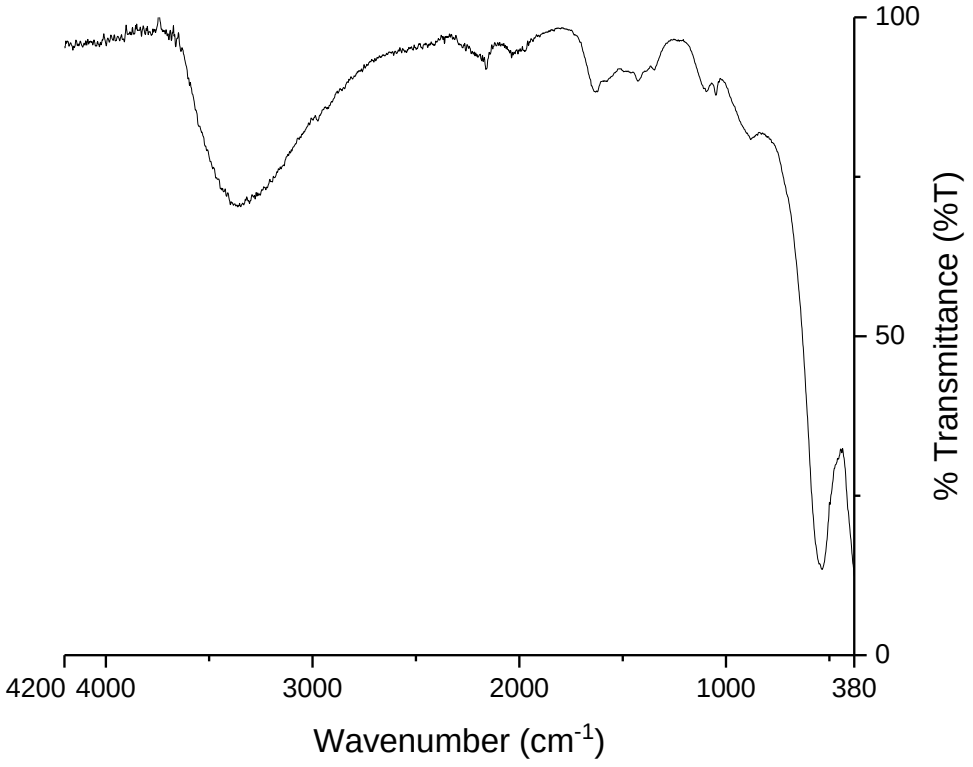


Figure 3-24: FTIR analysis of the $CoFe_2O_4$ MNPs.

XRD analysis confirmed that $CoFe_2O_4$ had been made by a high match for the standard crystal structure (Figure 3-23). The XRD output corresponded well to the reference pattern of cobalt ferrite (COD 153-3164). A Williamson-Hall plot for the peaks gave a crystallite size of 12.0 nm, which is in line with the TEM images above (Figure 3-21). Rietveld analysis on the output using this matched reference pattern for the structure fit gave a cubic crystal lattice with a lattice of a = 8.4142 Å.

FTIR analysis of the $CoFe_2O_4$ MNP gave the expected peak at 535 cm^{-1} corresponding to the metal-O stretching modes of tetrahedral and octahedral sites[38] (Figure 3-24).

One of the variations to this synthesis that was tried before the final version as described in the experimental section (2.2.3) was using a similar procedure to the synthesis of Fe_3O_4 and $MnFe_2O_4$ describe previously (2.2.1 and 2.2.2). That involved using a buffered solution of NH_4OH of effect the precipitation of the $CoFe_2O_4$ under inert conditions. The results of this procedure had a major change on the overall outcome.

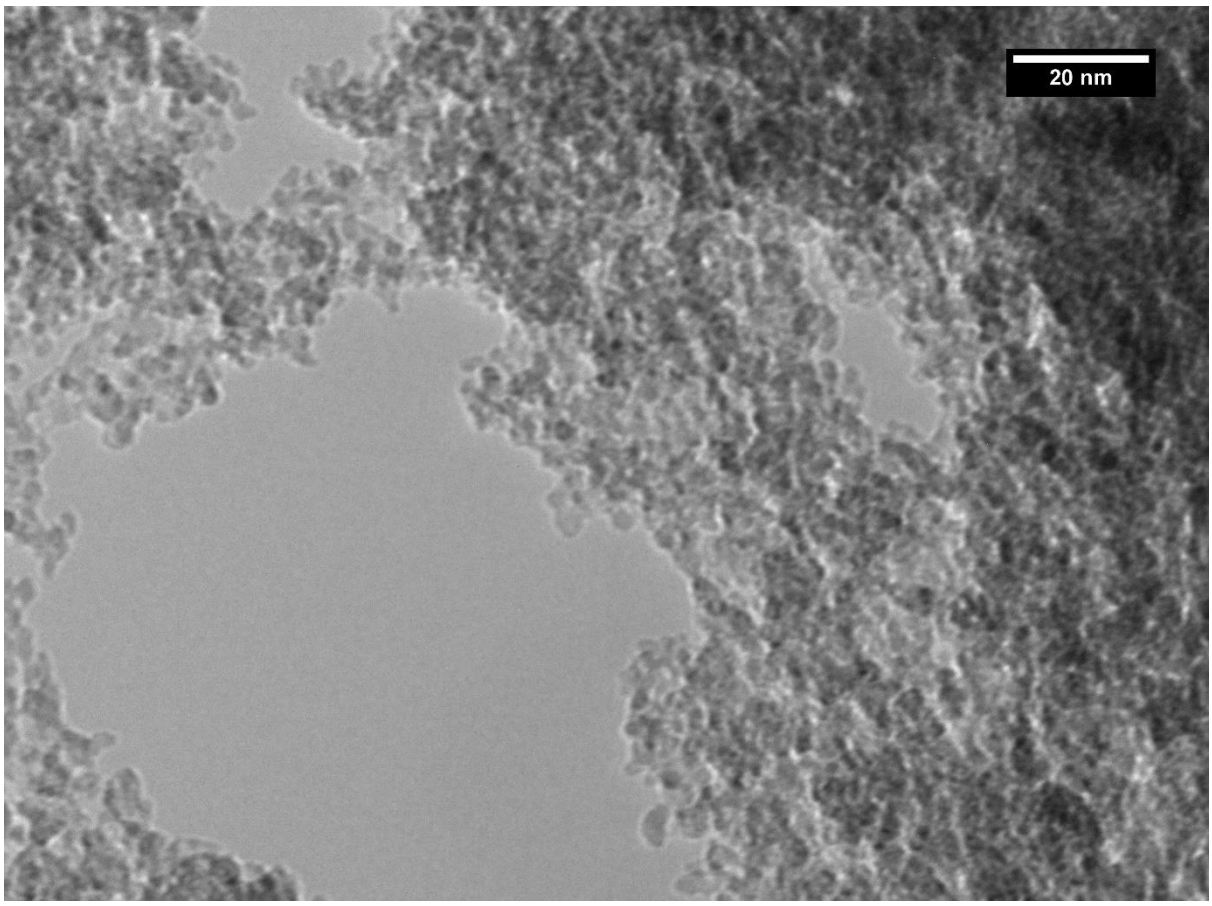


Figure 3-25: TEM images of $CoFe_2O_4$ MNPs synthesised using NH_4OH as base.

A TEM image above (Figure 3-25) showed that the particles were approximately 5±2 nm and were not well formed or distinct. The most observable change was the lower magnetisation when trying to extract the particles from solution. The magnetisation was much lower than expected giving a value of 7 $Am^2kg^{-}1$ at 1 T (Figure 3-26). FTIR gave a similar output but the peak at 600-500 cm-1 had now been reduced to a shoulder as can be seen below (Figure 3-27) while the XRD analysis, the red line in the graph below (Figure 3-29), gave a lower match for $CoFe_2O_4$ (COD 153-3164) with a crystallite size of 4.9 nm.

A common approach reported in the literature is the calcination of the product after coprecipitation[44]. These particles were calcined at 600 °C overnight to see the effect and indeed this had a major effect on the particles. The magnetisation increased to 43 Am^2kg^{-1} and the sample developed remnant magnetisation as can be seen below (Figure 3-26). The FTIR showed a change to a strong peak at 535 cm-1 (Figure 3-27). A TEM image of the particles below (Figure 3-28) showed that the particles had fused and grown in size to give a polydisperse sample with sizes from 10-70 nm.

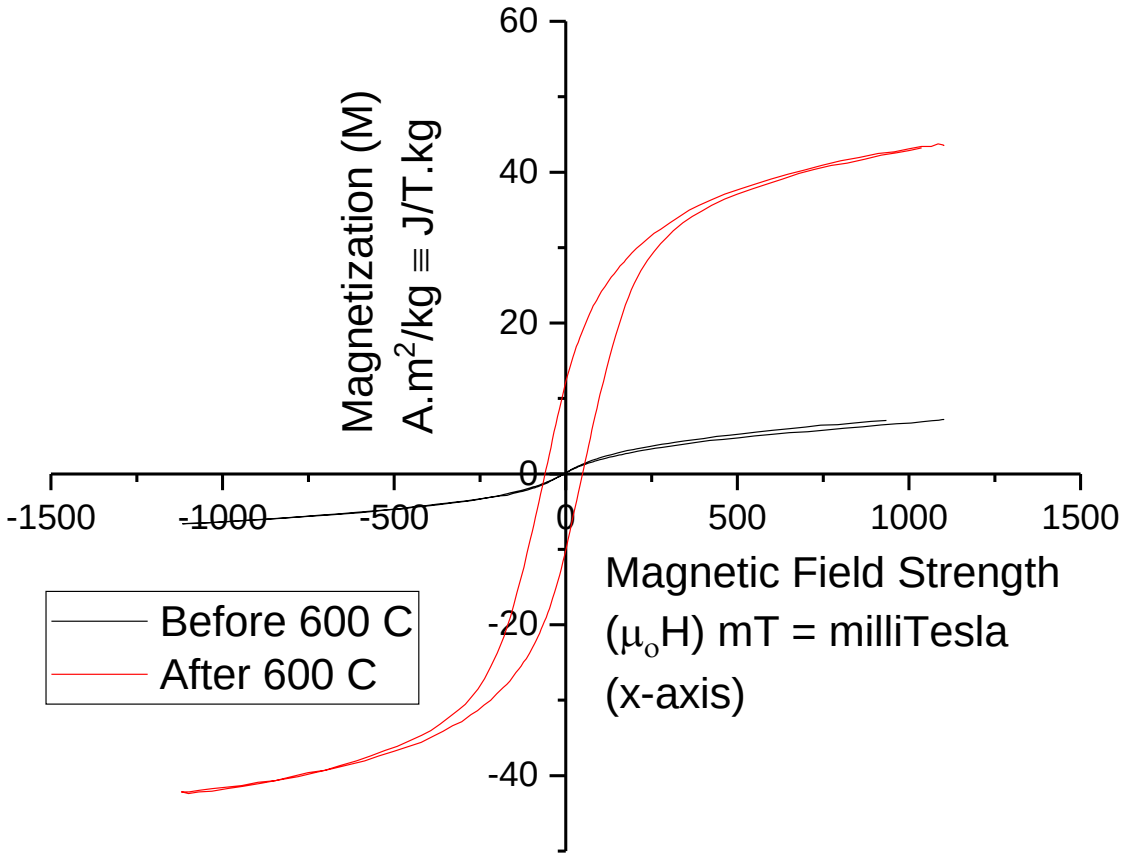


Figure 3-26: VSM curves of $CoFe_2O_4$ before and after calcination at 600 °C.

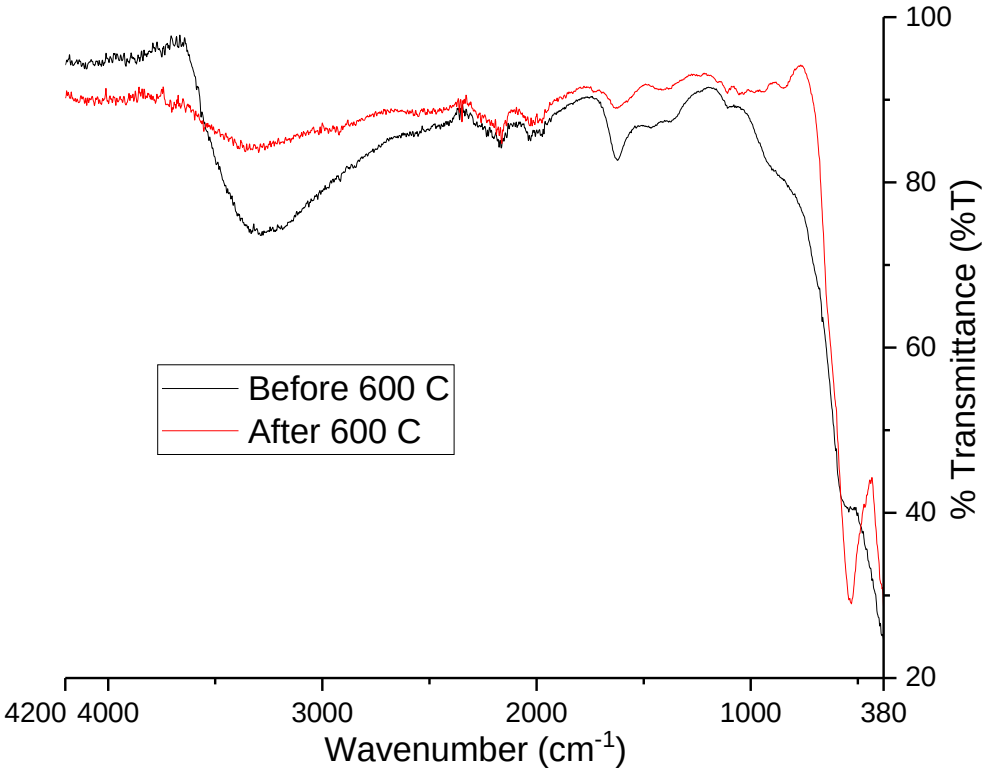


Figure 3-27: FTIR analysis of $CoFe_2O_4$ before and after calcination at 600 °C.

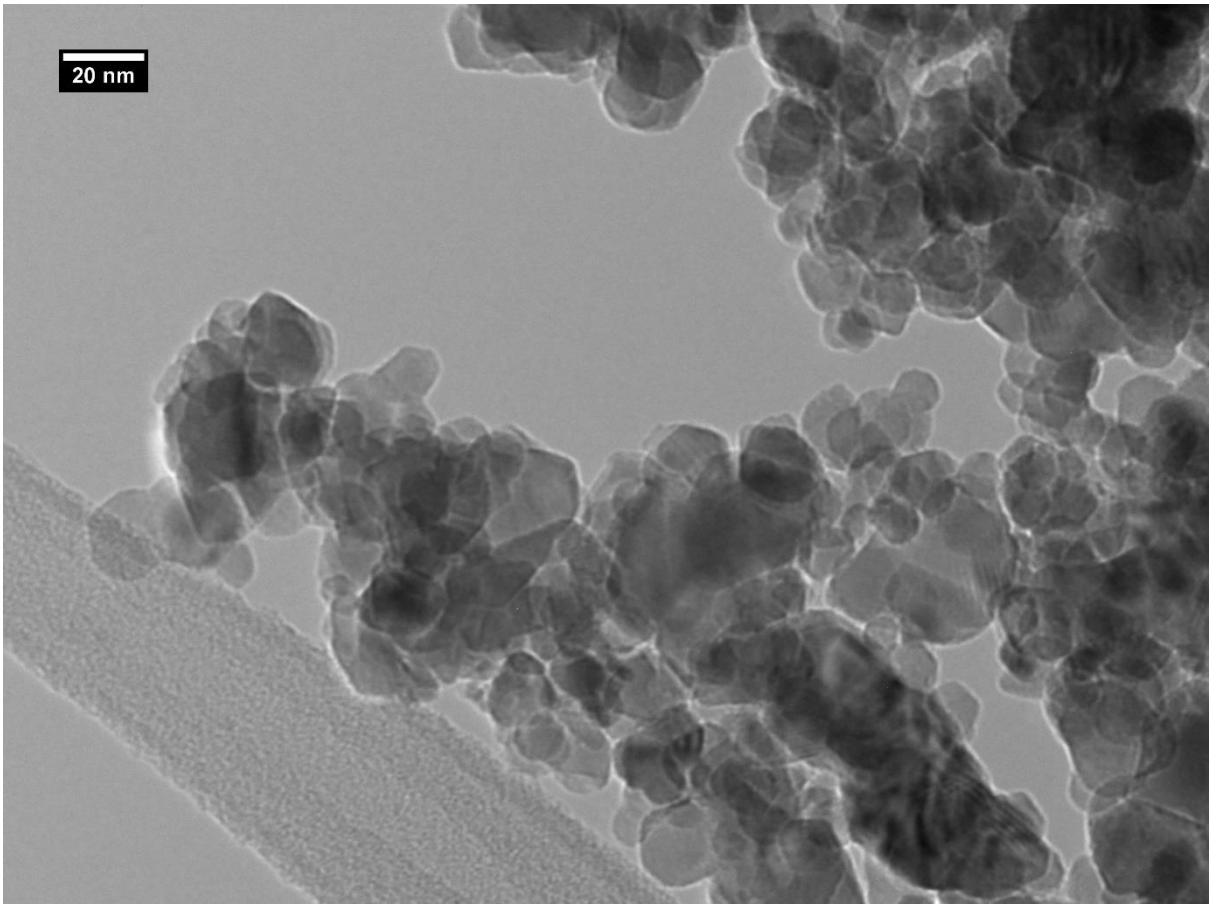


Figure 3-28: TEM image of the $CoFe_2O_4$ particles after calcination at 600 °C.

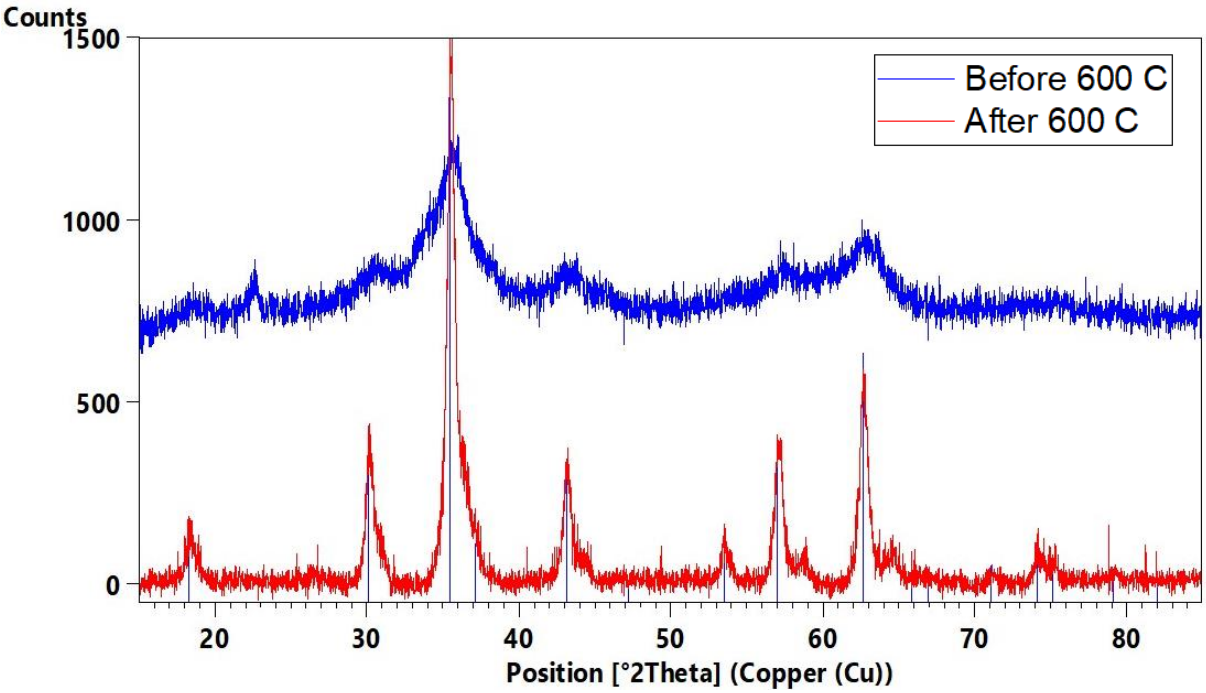


Figure 3-29: XRD patterns of the $CoFe_2O_4$ particles before (blue line) and after (red line) calcination.

The XRD pattern after calcination at 600 °C, blue line above (Figure 3-29), showed much clearer peaks which is an indication of larger crystallites in the sample. The pattern gave a high match for $CoFe_2O_4$ (COD 153-3164) with a crystallite size of 13.9 nm.

Another variation using a non-buffered NH_4OH solution to effect the precipitation gave similar results to the buffered NH_4OH version for before, after calcination at 600 °C. In another variation where a buffered NH_4OH solution was used without any hydrazine, with the only other change being that the solution was left open to air and not under inert gas, argon. The result was that the magnetisation was 32 Am^2kg^{-1} before calcination with an XRD crystallite size of 5.6 nm and a match for $CoFe_2O_4$, while after calcination the magnetisation was 49 Am^2kg^{-1} and the XRD crystallite size was 8.2 nm.

One variation that was tried early on in our work, following reports of previous group member[40], involved $Co(NO_3)_2{\cdot}6H_2O$ and $FeCl_2{\cdot}4H_2O$ as the metal ions sources and NH_4OH to precipitate out the ferrite with magnetic stirring. This synthesis involved magnetic stirring. TEM images showed that this synthesis produced a polydisperse sample with sizes 10-150 nm, while the hysteresis loop for magnetisation showed remnant magnetisation. Further work must be done to elucidate if it is the magnetic stirring or the change in precursors that was

responsible for the changes here and the effect of magnetic stirring versus mechanical in the basic procedure outlined in the experimental section (2.2.3).

As a side note, it should be pointed out that the redispersibility of the MNPs back into solution was reduced after drying out and seriously reduced after calcination. In the photos below (Figure 3-30) there is shown freshly prepared Fe_3O_4 nanoparticle suspension in MP H_2O on the left, a redispersed sample of Fe_3O_4 after having been dried in the oven overnight at 80 °C and sonicated back in to solution for 1 hour in the centre and MP H_2O on the right. As can be seen the solution shows visible signs of the reduction in redispersibility after 1 hour of settling. The result is even more pronounced after calcination (Figure 3-31) where the particles cannot be brought back into solution after sonication for an hour.

Due to this fact, whenever particles were going to be further functionalised they were stored in a solvent, usually EtOH or degassed H_2O. Dispersing of the MNPs into any other solvent was a simple process of magnetic extraction and sonication in the new solvent.

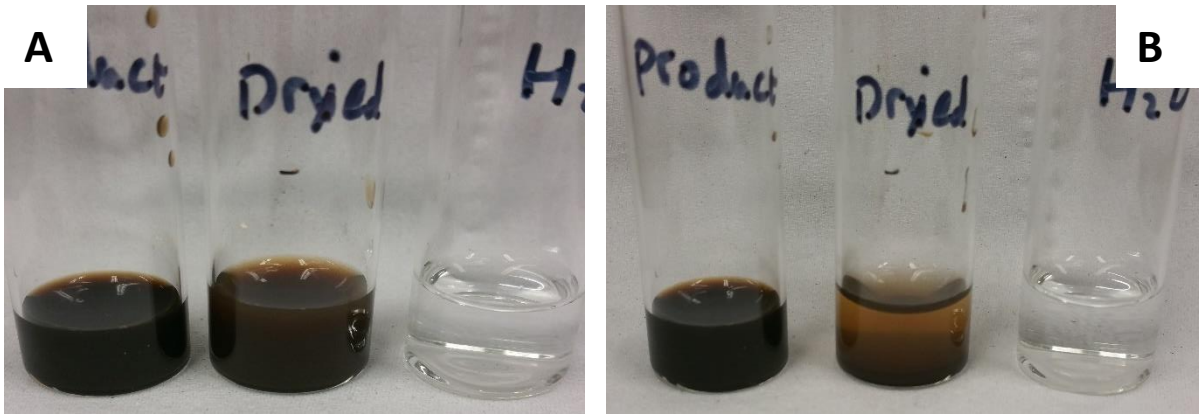


Figure 3-30: Effect of drying out on Fe_3O_4 in degassed MP H_2O at (A) 0 hours and (B) 1 hours after sonication.

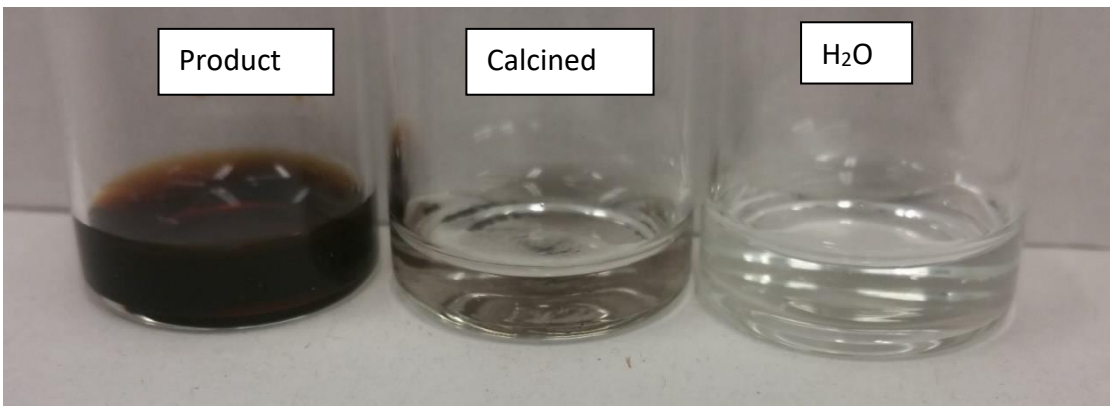


Figure 3-31: Effect of calcination on $CuFe_2O_4$ in degassed MP H_2O after 1 hour of sonication.

3.3.4 Preparation of Copper Ferrite MNPs ($CuFe_2O_4$) by Coprecipitation

Copper ferrite nanoparticles are reported to have catalytic activity in a one-pot three-component condensation of arylnaphtho-xazine-3-one derivative[45] and in a one-pot three-component synthesis of spirooxindole fused heterocycles[46]. Following on from the insights gained producing other ferrites, it was decided to explore the synthesis of these MNPs. A review of papers on the synthesis of $CuFe_2O_4$ indicated that calcination at 800 °C was a common step[45][46] with the reason for this being explained as the redistribution of cations in the spinel structure to enhance the magnetic properties as the spinel becomes a fully inverse spinel[47] (as opposed to a mixed spinel). As discussed previously (3.3.3) the drying out or calcination reduces the redispersibility of the MNPs back into solution.

The procedure for the formation, where NaOH is used with Cu^{2+} and Fe^{3+} ions to precipitate the $CuFe_2O_4$ MNPs, is described in the experimental section (2.2.4). The product was characterised by TEM, VSM, XRD and FTIR spectroscopy.

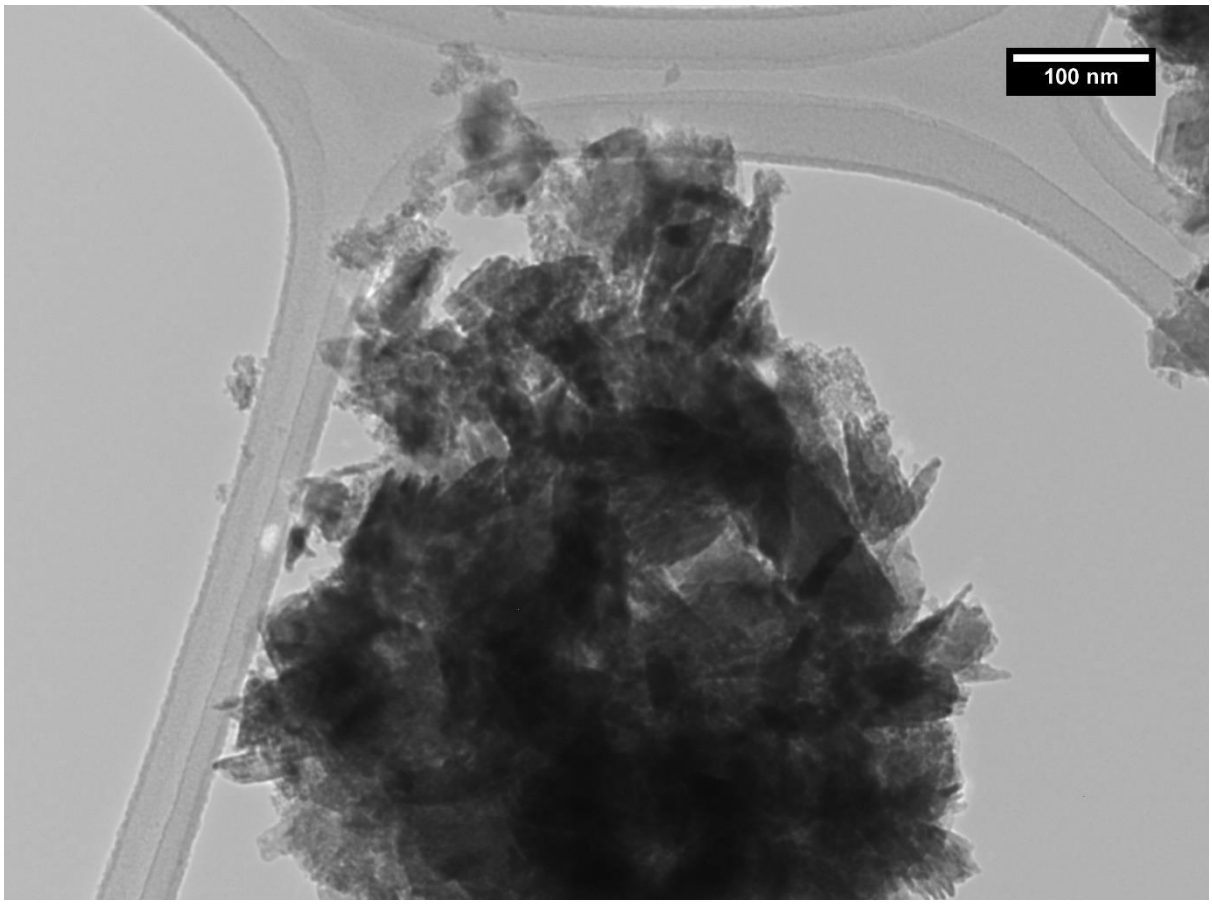


Figure 3-32: TEM image of synthesised $CuFe_2O_4$ MNPs before calcination at 800 °C.

A TEM image of the product above (Figure 3-32) shows the sample to be composed of highly aggregated particles of various morphologies and broad size distribution from 3-300 nm. After calcination of the product at 800 °C the smaller particles fused into much bigger ones with more narrow size distribution. The sample was still highly aggregated now composing of larger particles from >200 nm. The TEM image below (Figure 3-33) shows the fusing of the smaller particles to make much larger particles.

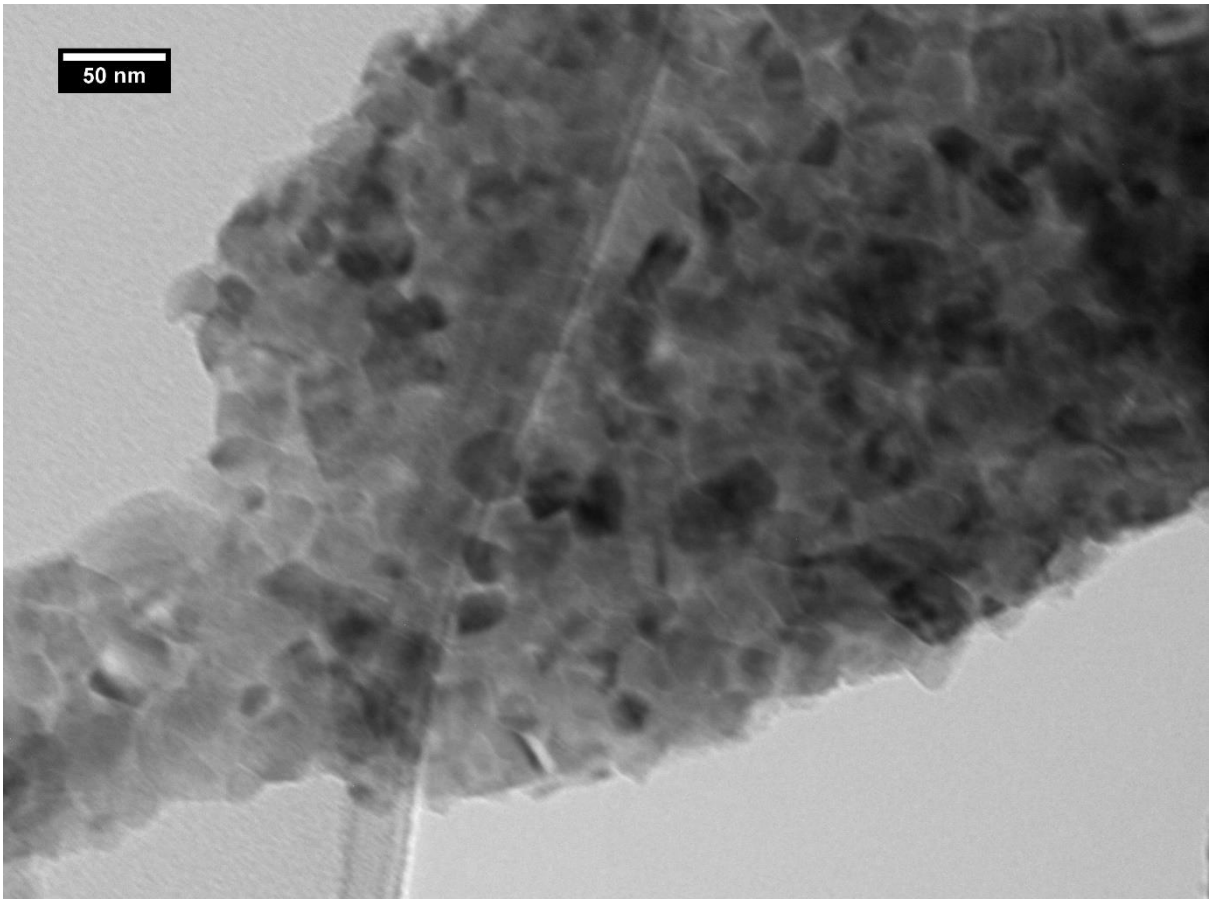


Figure 3-33: TEM image of synthesised $CuFe_2O_4$ MNP after calcination at 800 °C.

The VSM analysis below (Figure 3-34) of before and after calcination showed that the specific magnetisation increased from 1 Am^2kg^{-1} before to 25 Am^2kg^{-1} after calcination. However, copper ferrite has reported saturation magnetisation of up to 85 Am^2kg^{-1}[48]. The hysteresis curve showed a small remnant magnetisation after calcination.

XRD analysis of the product below (Figure 3-35) before calcination (blue line) showed an amorphous phase while after calcination (red line) it gave a high match for $CuFe_2O_4$ reference

pattern (COD 901-2439). A Williamson-hall plot for the peaks gave a crystallite size of 38.4 nm. Rietveld analysis on the output using this matched reference pattern for the structure fit gave a cubic crystal lattice with a lattice of a = 8.38224 Å.

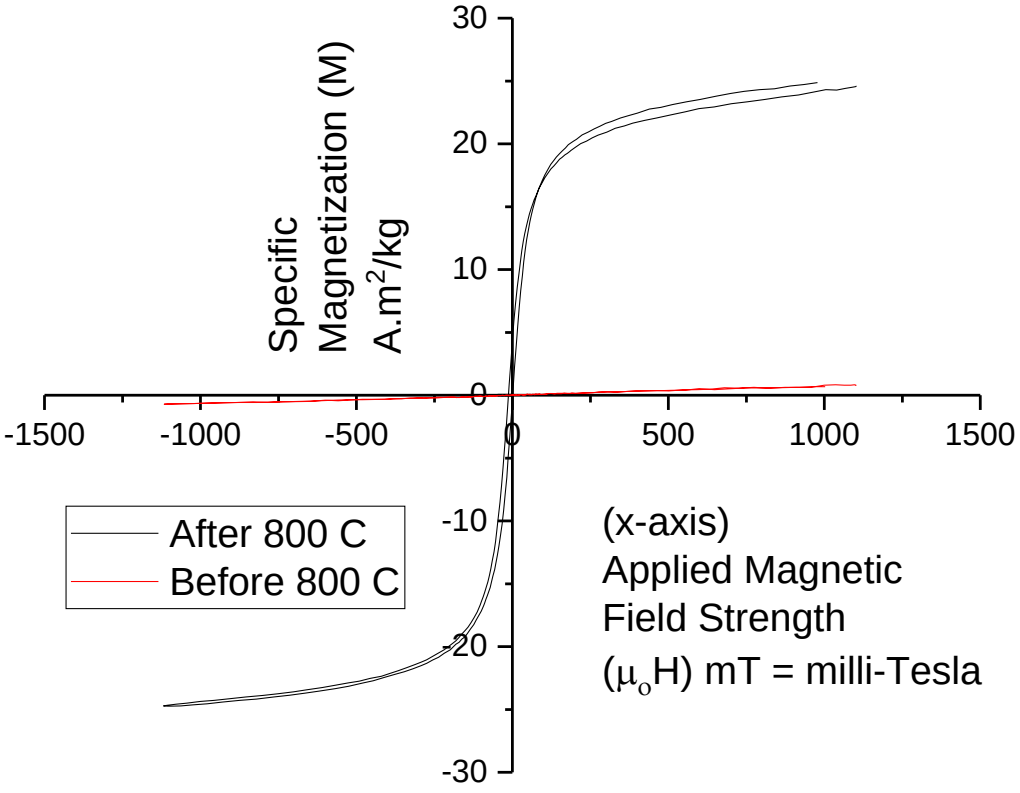


Figure 3-34: VSM curve for $CuFe_2O_4$ before and after calcination at 800 °C.

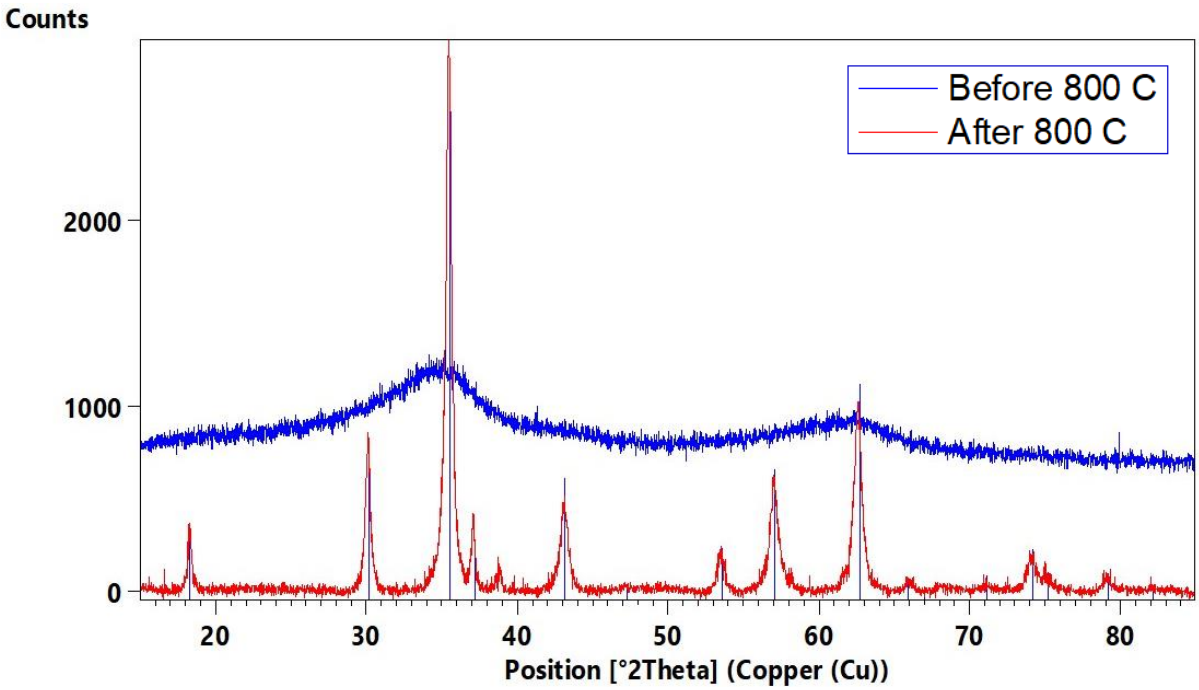


Figure 3-35: XRD patterns of $CuFe_2O_4$ before and after calcination at 800 °C.

FTIR analysis (Figure 3-36) showed no peak or shoulder around 540 cm^{-1} before calcination but showed a strong peak after calcination at 537 cm^{-1}, corresponding to the Fe-O stretch.

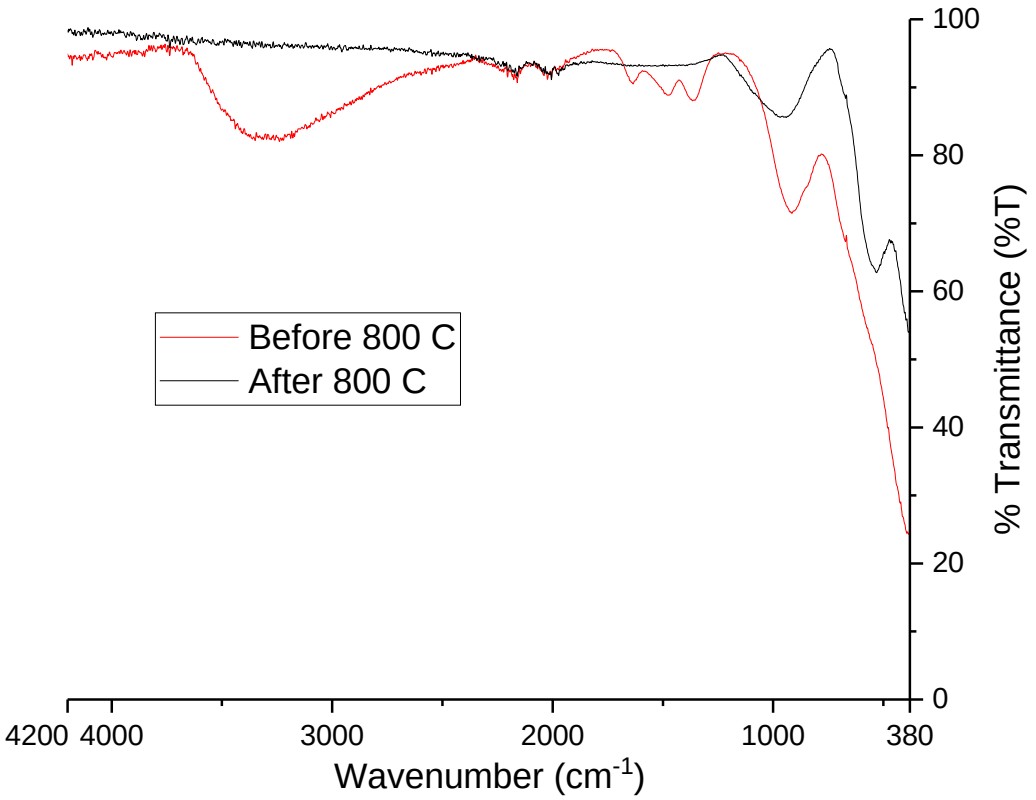


Figure 3-36: FTIR spectra of $CuFe_2O_4$ before and after calcination at 800 °C.

One variation that was tried on the described procedure (2.2.4) was applying a similar method as with Fe_3O_4 and $MnFe_2O_4$ where NH_4OH is used to precipitate out the ferrite. This was unsuccessful with the solution at the end of the reaction being a dark blue, most likely because of the formation of the copper-ammonia complex, $[Cu(NH_3)_4(H_2O)_2]^{2+}$, which remains in solution[49]. There was a precipitate and calcination of that solid gave a weakly magnetic material with magnetisation value of 4 Am^2kg^{-1}. XRD analysis of this material (Figure 3-37) gave a high match for hematite (COD 210-1169).

Another variation in synthesis was using extra base giving an excess ratio of 16 for NaOH to metal ions. This brought the pH of the final solution to over 14. Analysis of this sample by XRD before and after calcination showed that the sample contained a mixture of CuO and $CuFe_2O_4$. As can be seen below (Figure 3-38) the XRD pattern of the calcined product have shown that it was composed of 79.1% $CuFe_2O_4$. The magnetisation of the final product was 35 Am^2kg^{-1}. The XRD pattern was complex and it is possible that small amounts of iron oxides, which have

a higher magnetisation, are in the sample but are hidden by other stronger peaks. The TEM images of this product showed a polydisperse sample similar to the images above (Figure 3-32). In all cases the reactions failed to produce monodisperse well defined individual MNPs. A literature review of $CuFe_2O_4$ showed that this has not been achieved yet to the same degree as other coprecipitated MNPs and would be considered as future work.

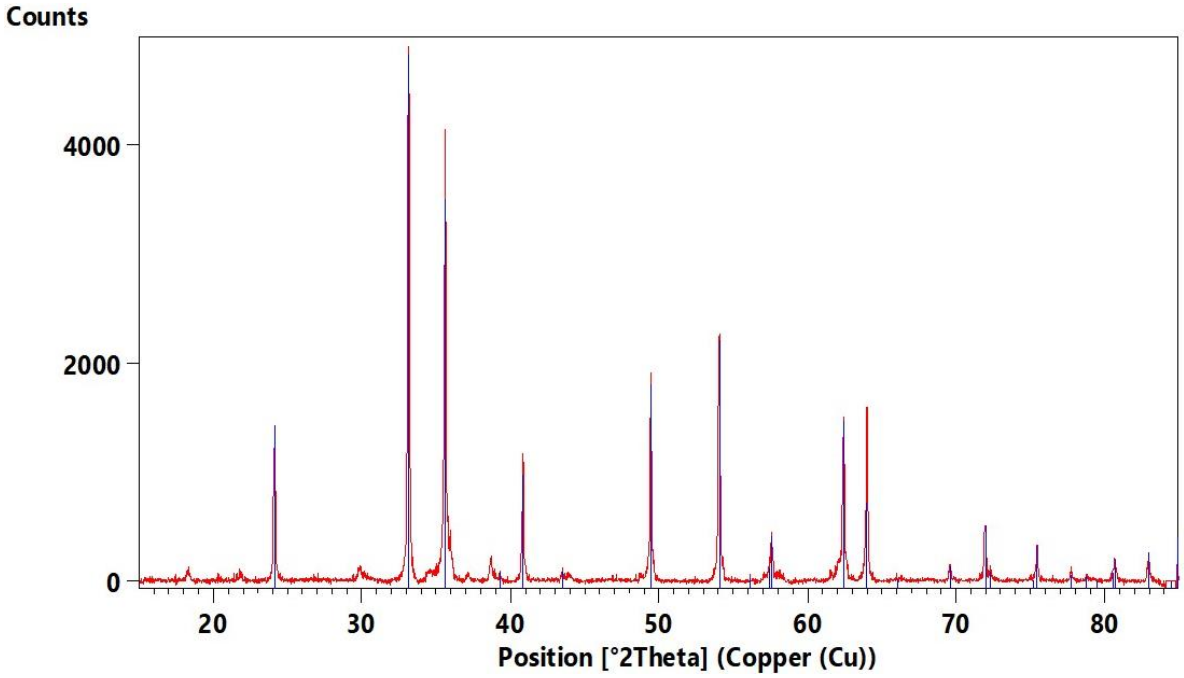


Figure 3-37: XRD pattern of the product produced using NH_4OH to precipitate.

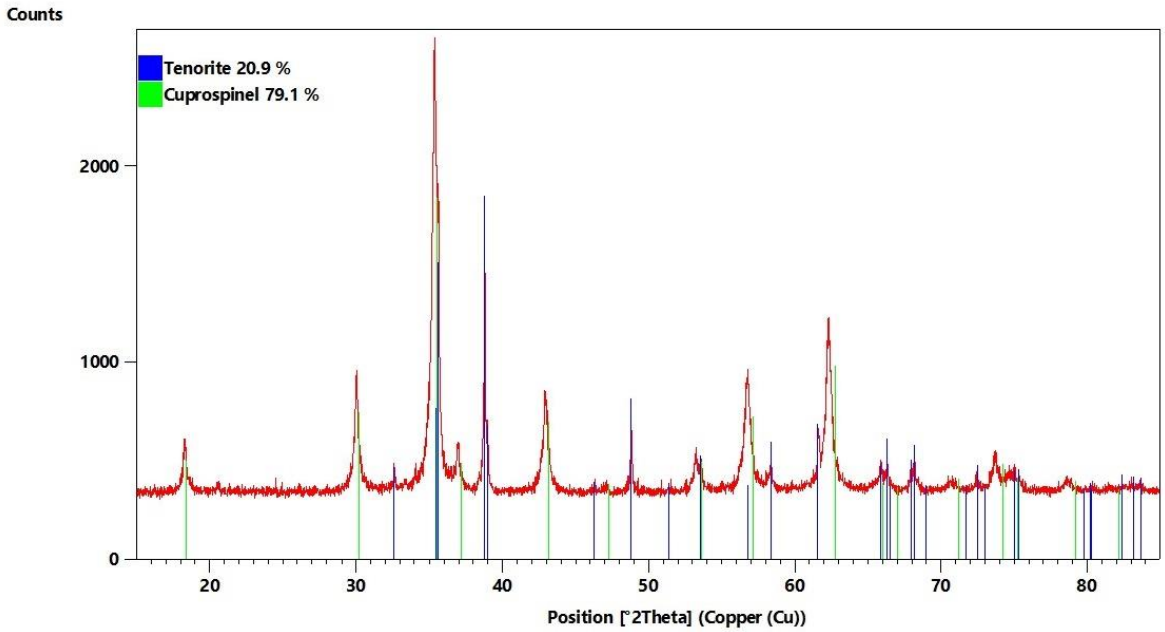


Figure 3-38: XRD pattern of product produced using an excess of NaOH.

3.3.5 Preparation of Manganese Ferrite MNPs ($MnFe_2O_4$) by Polyol Method

For monodisperse MNPs, coprecipitation was found to produce particles with sizes usually below 30 nm. For further functionalisation sometimes larger particles are required. A literature search showed that a solvothermal method could produce larger monodisperse particles[9]. The synthesis as described is performed in a high pressure vessel which commonly have a maximum volume of less than 50 mL for a general purpose lab versions[50]. This limits the volume of material that can be synthesised at one time. A modification of this synthesis, as describe in the experimental section (2.2.5), enabled the production of larger quantities and without the use of high-pressure vessels.

The basic procedure involved the refluxing of the Fe^{3+} and Mn^{2+} metal ions in a polyol solution with sodium acetate. It was found that despite the absence of the high pressure, as would be the case when this reaction is performed in a sealed high pressure vessel, the refluxing reaction at atmospheric pressure gave comparable results to the reported high pressure technique [9]. Some variations were performed on this basic procedure to see if any control of the final product, with respect to size and shape, could be found. The basic procedure was found to be highly reproducible with this synthesis being performed many times and the core MNPs being used for further functionalisation.

The product of the reaction was characterised by TEM, VSM, XRD and FTIR spectroscopy. The VSM analysis below (Figure 3-39) showed good magnetisation with a specific magnetisation of 60.1 Am^2kg^{-1} at 1 T with the sample beginning to saturate in a low magnetic field. This property and the larger size of the particles enabled fast magnetic extraction of the particles from solution.

TEM images of particles below (Figure 3-40) showed them to be monodisperse and composed of particles with sizes around 100±20 nm. Particle size distributions were calculated from 100 particles using ImageJ software (Figure A-2).There was some smaller particles and some fusing of the particles but most of the sample was composed of individual, well-defined particles, as can be seen below. The particles in the TEM images can be seen to be composed of “grains” that pack together to form the overall particle. Sonication of these particles for up to 2 hours showed that the particles do not disperse to give individual grains. This indicated that the

particles were fused into the grains consisting of single crystallites. XRD analysis discussed next confirmed this hypothesis.

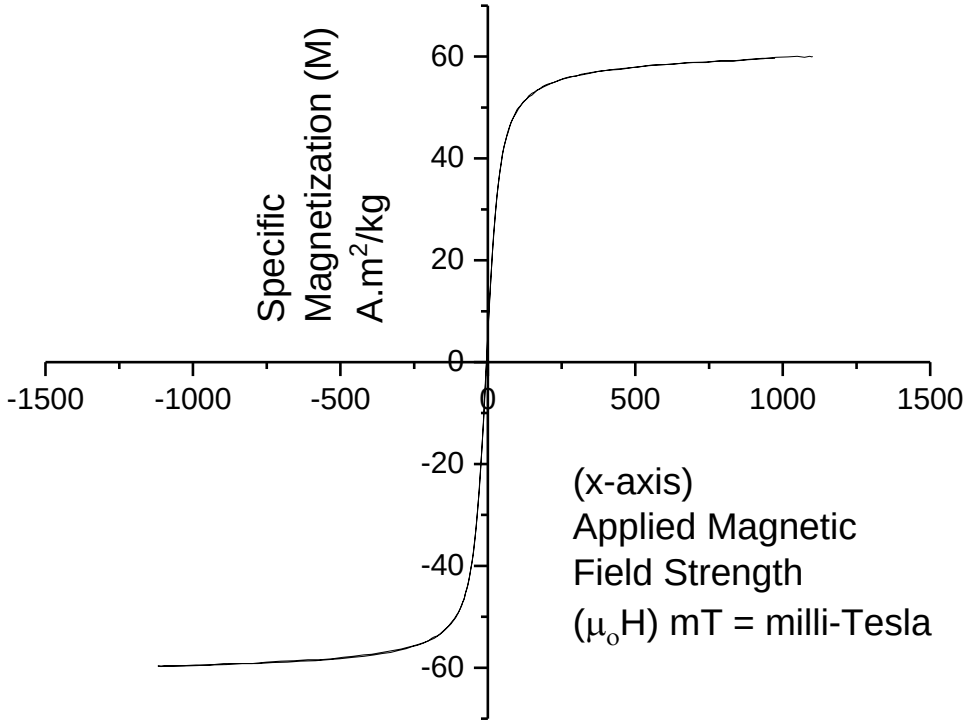
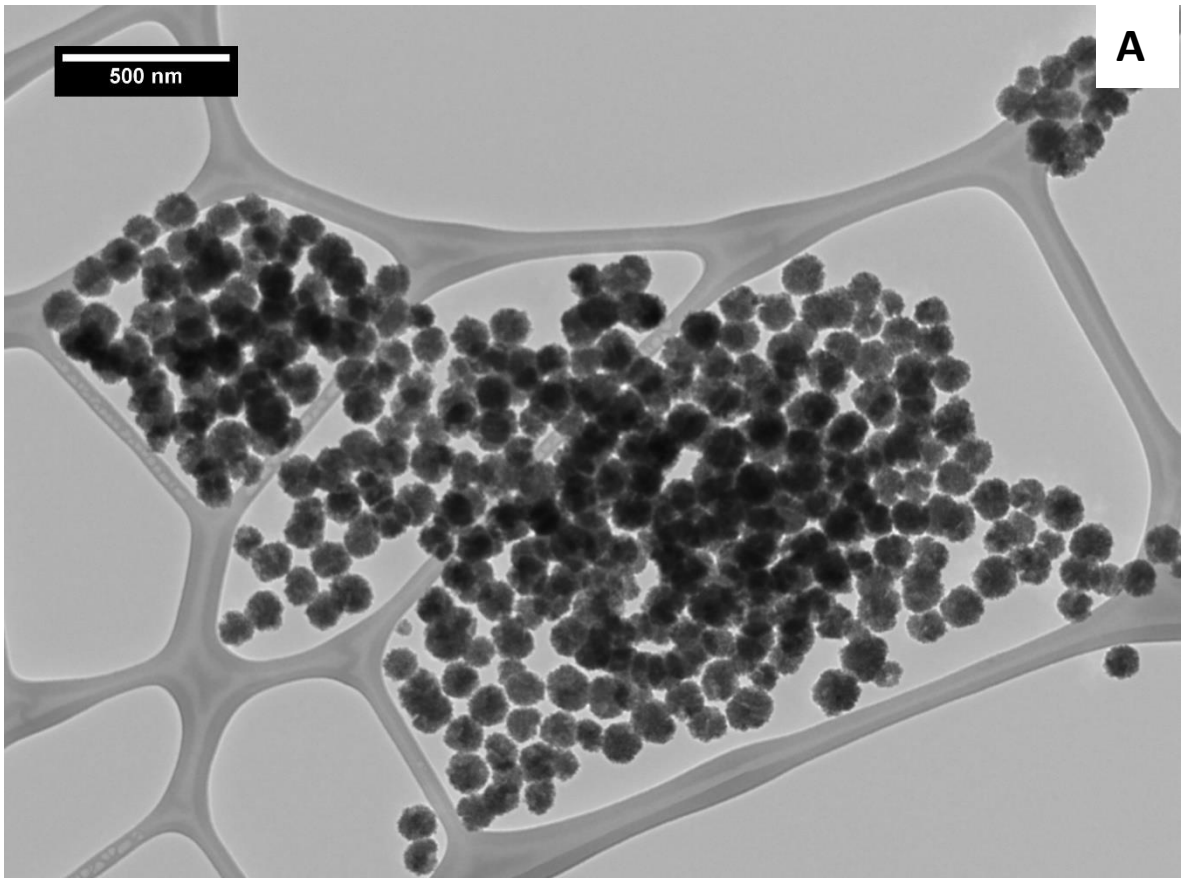


Figure 3-39: VSM curve of $MnFe_2O_4$ synthesised by polyol method.



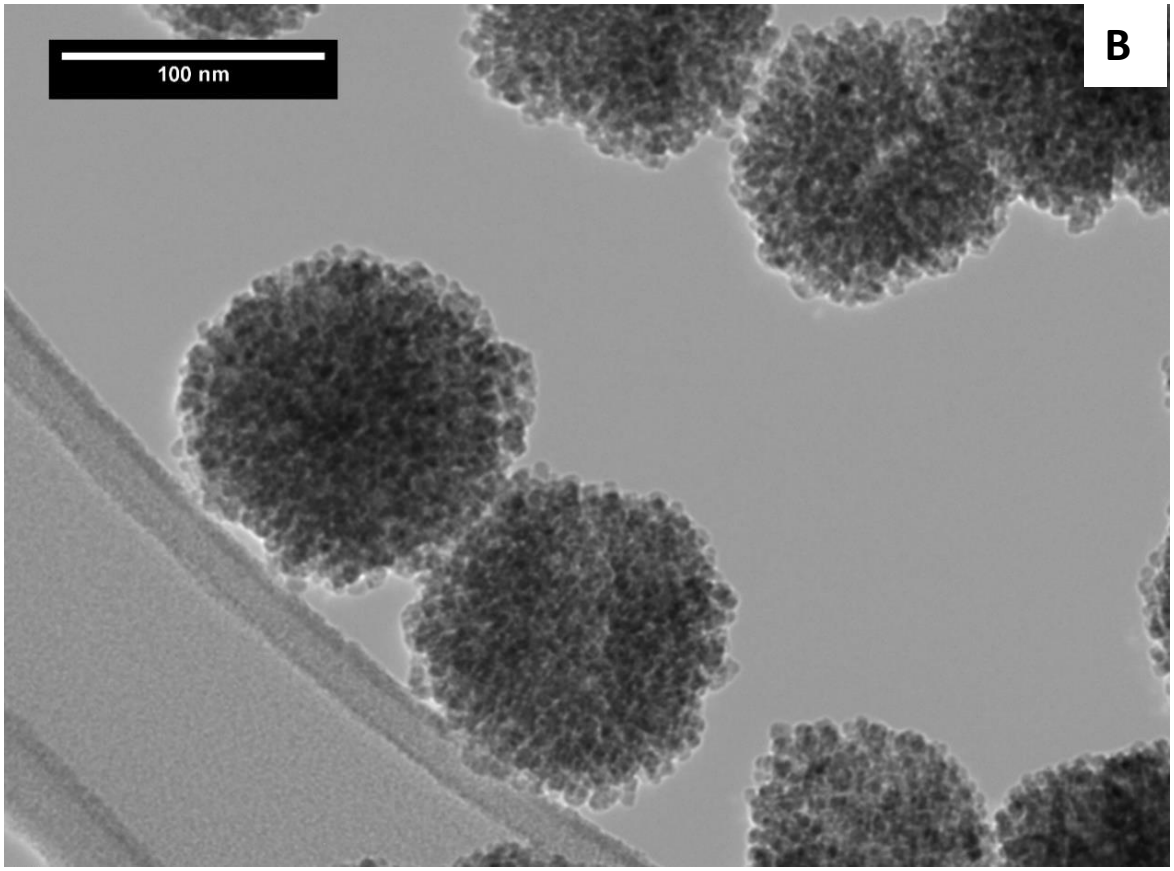


Figure 3-40: TEM images of $MnFe_2O_4$ particles synthesised by polyol method.

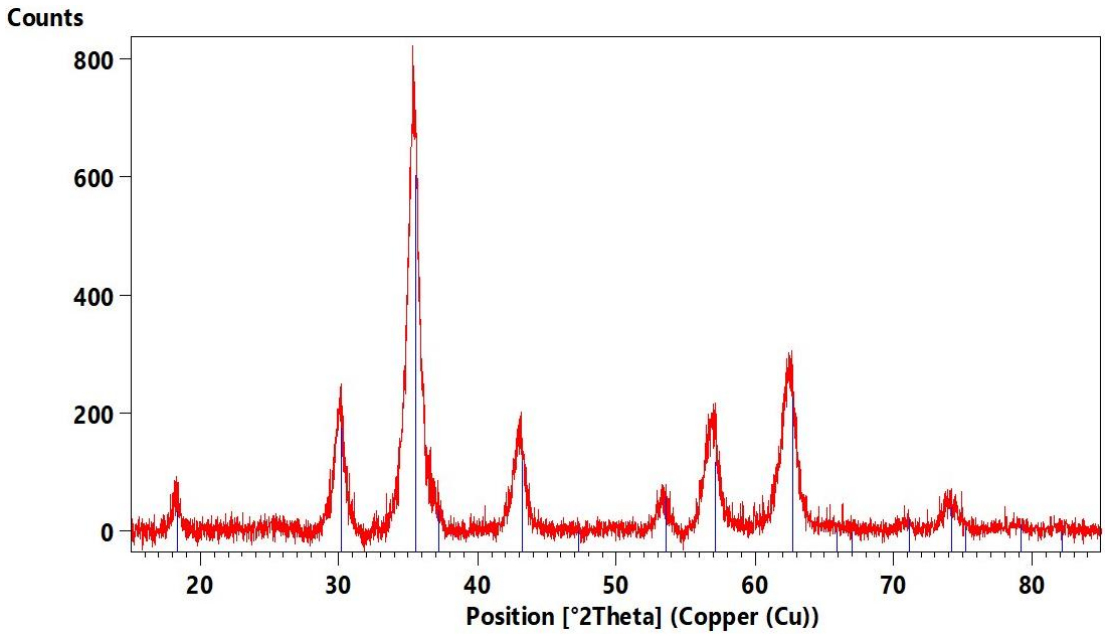


Figure 3-41: XRD pattern of the $MnFe_2O_4$ synthesised by polyol method.

XRD analysis confirmed that $MnFe_2O_4$ was the product of the reaction with the material being a high match for that crystal structure as can be seen above (Figure 3-41). The XRD gave a match for the reference pattern of magnetite (COD 230-0619). A Williamson-Hall plot for the

peaks gave a crystallite size of 8.0 nm. This is consistent with the TEM image above (Figure 3-40) where the particles are seen to be composed of small nanoparticles that coalesce to form the bigger particle aggregates, rather than a single crystallite that one gets with coprecipitation. Rietveld analysis with the matched reference pattern for the fit gave a cubic crystal lattice with a lattice of a = 8.37916 Å.

FTIR spectroscopy of these particles gave the expected peak for metal-O stretch at 530 cm^{-1}.

With the intention to getting a better understanding of the formation and growth of the particles over time, samples were taken from the reaction mixture at selected times and analysed by TEM, as are shown in the series of TEM images below (Figure 3-42). After 2 hours of the refluxing, it can be seen how the particles evolve during the synthesis with initial intermediate particles of various shapes and sizes that form first and then transform to the final large spherical nanoparticles over time. After 6 hours, usually the intermediate nanoparticles have been consumed and there are only the uniform spherical magnetic nanoparticles in the final suspension, although it was found that with some reactions it took up to 10 hours for the intermediates to disappear fully.

After 2 hours, it can be seen there is a mix of formed $MnFe_2O_4$ particles and an intermediate. These initial particles are about 70 nm and by the completion, the particles had grown to a stable size of approximately 100 nm. In the images below (Figure 3-42) we can see that that has happened by 6 hours with no intermediates in the images below at 6 hours. Leaving the reaction on overnight ensured complete conversion of the intermediates to the desired magnetic nanoparticles.

The intermediates were nanostructures that had an elliptical shape. They were up to 90 nm long and about 20 nm wide. As the images proceed from 2 to 6 hours it can clearly be seen how the intermediate is consumed as the ratio of $MnFe_2O_4$ MNPs to the intermediate grows until there is no intermediate nanoparticles left.

It should be noted that some synthesis gave slight variation is size of the final MNPs produced by the method for this section, but this was relatively small with the particle average size ranging from 90-120 nm as several repeats of the same procedure have shown. The reproducibility for this procedure was very high giving consistent results with regard to the morphology and size of the particles.

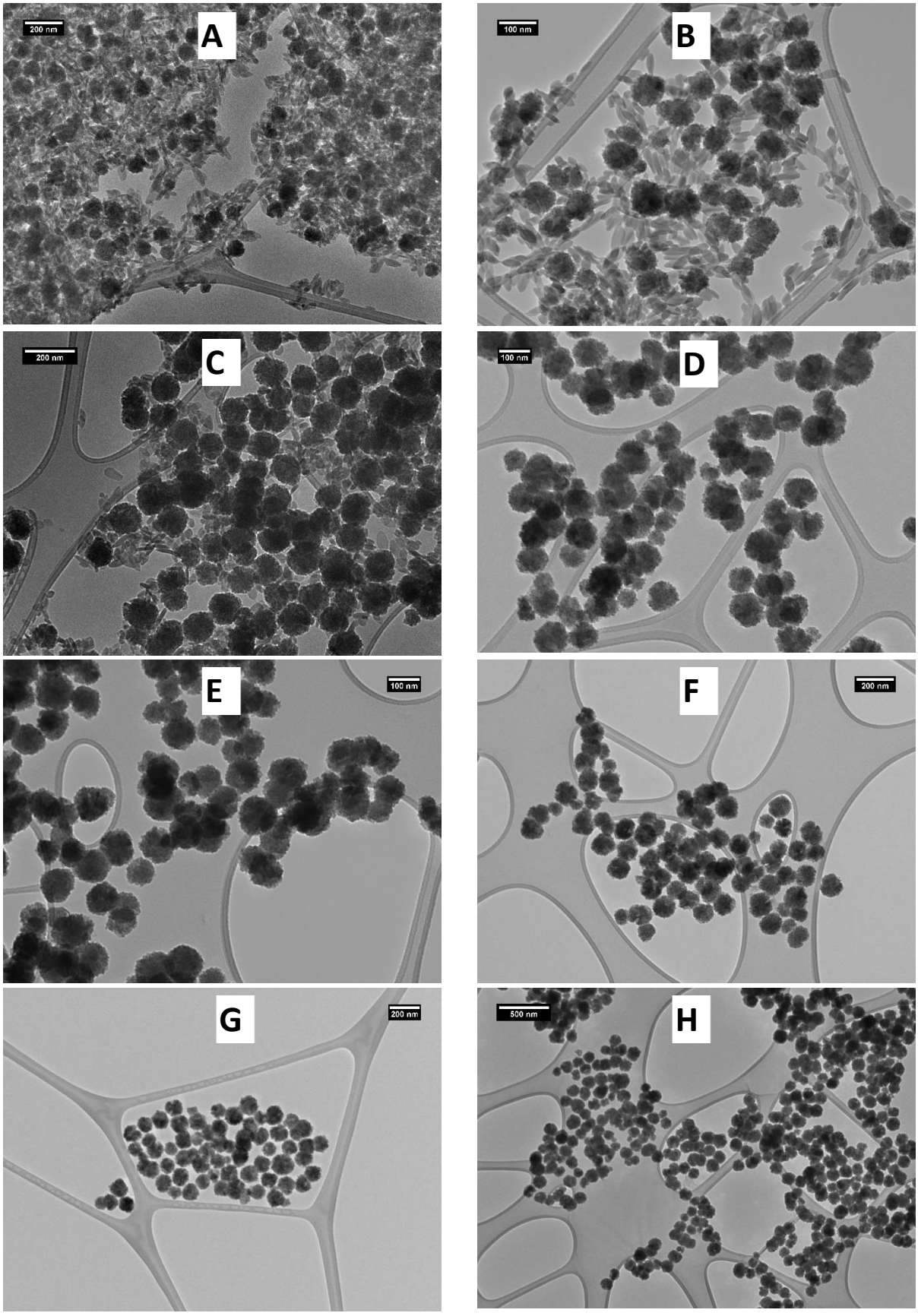


Figure 3-42: TEM images of samples taken at A-H = 2, 3, 4, 5, 6, 8, 10, 20 hr.

Once the particles had formed, leaving the reaction for longer times seemed to have no effect in terms of further particle growth, which was unexpected as the work that was the inspiration for this method[9] describes how longer reaction times gave larger particles with temperature and precursor concentrations held constant. The authors of this work mentioned that "the complex nature of the growth process makes it difficult to obtain a straightforward correlation between particle diameter and changes in reaction time or precursor concentration." In addition, their synthesis has been carried out in a high-pressure vessel.

VSM analysis of selected samples over the reaction time(Figure 3-43), showed that the magnetisation increased for the samples produced up to 6 hours after which there was no observable increase in magnetisation. Some samples took longer to reach full magnetisation. There could be some rearrangement of the cations in the lattice of the crystallite after this time but there is no major change in the magnetisation. It was because of this that to synthesis these particles the reaction was left on overnight even though the TEM indicated that the reaction was completed after 6 hours.

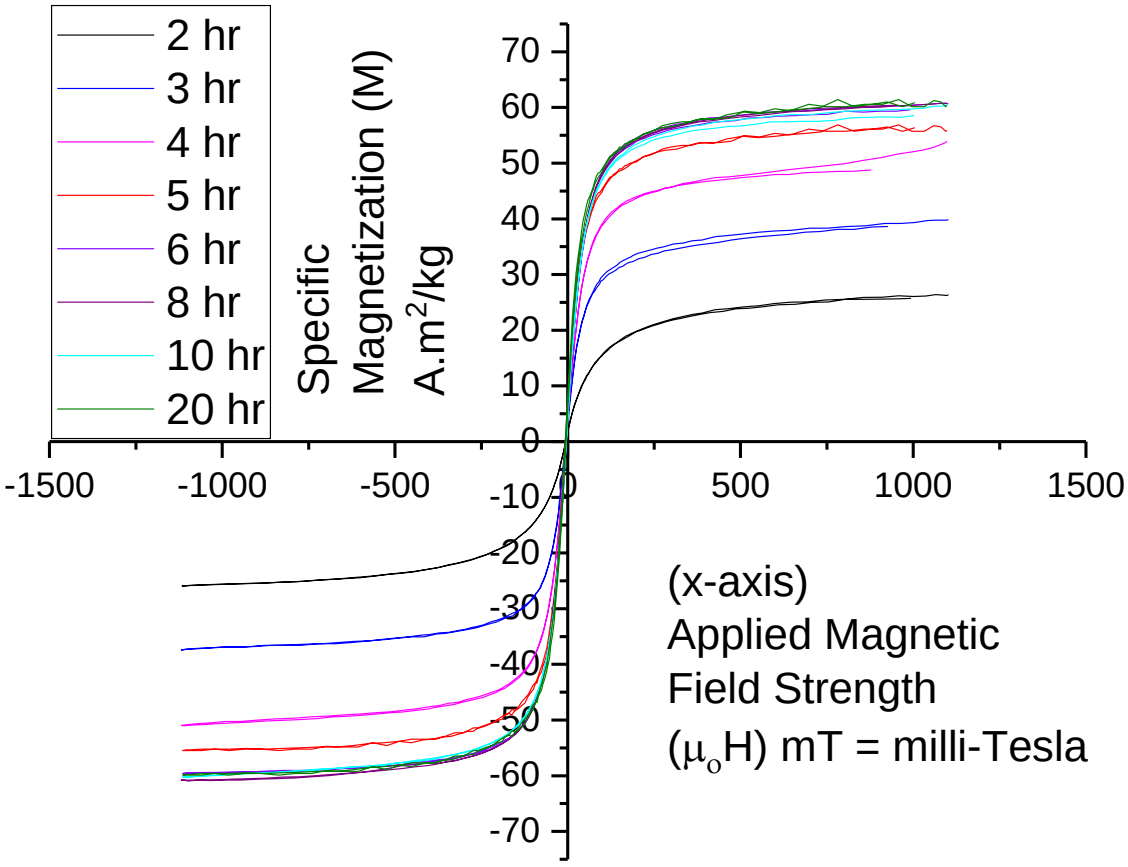


Figure 3-43: VSM analysis of particles prepared at different reaction times.

XRD analysis of selected samples over the reaction time (Figure 3-44), demonstrated that there were more than one phase at 2 hours but by 6 hours the only phase that remained was of $MnFe_2O_4$ as the peak as 26° disappears. The peak at 35.5° belonging to $MnFe_2O_4$ phase becomes stronger and more defined as the time proceeds indicating crystallite growth. A search of the database to find the other phase(s) apart from $MnFe_2O_4$ was inconclusive with several materials giving low matches. As such, the intermediate structures in the first few hours of the reaction have therefore not been identified. By the end of the reaction, after 20 hours, only the $MnFe_2O_4$ phase remained. This is consistent with the previous TEM and VSM data, which showed no visible change for samples refluxed for more than 6-10 hours.

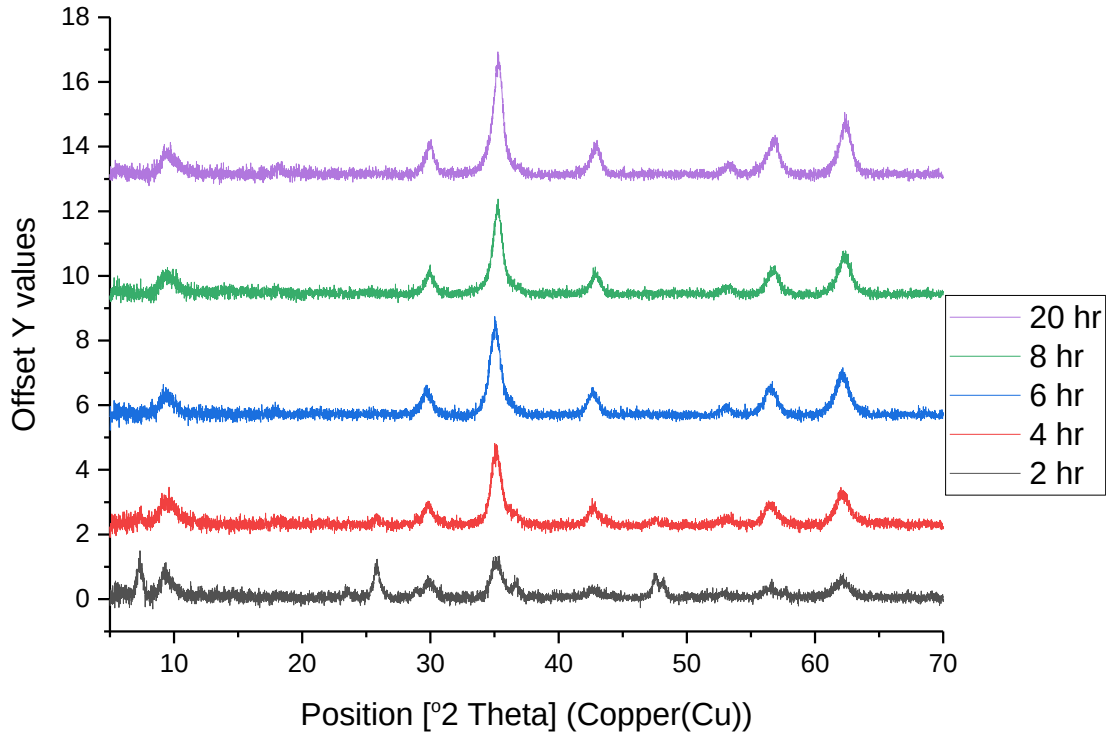


Figure 3-44: XRD analysis of selected samples prepared at different reaction times.

FTIR of selected samples over the timed period showed (Figure 3-45) the disappearance of peaks corresponding to the intermediate and the emergence of the strong peak at 535 cm^{-1} that would be assigned to the metal-O vibration for the octahedral and tetrahedral sites as before (3.3.2). The peaks at 2856, 1092, 1038 and 876 cm^{-1} disappeared over the time frame. These peaks which obviously came from the intermediate as seen in the TEM images, may have been from a metal acetate complex as acetate has peaks around 1000 cm^{-1}[51].

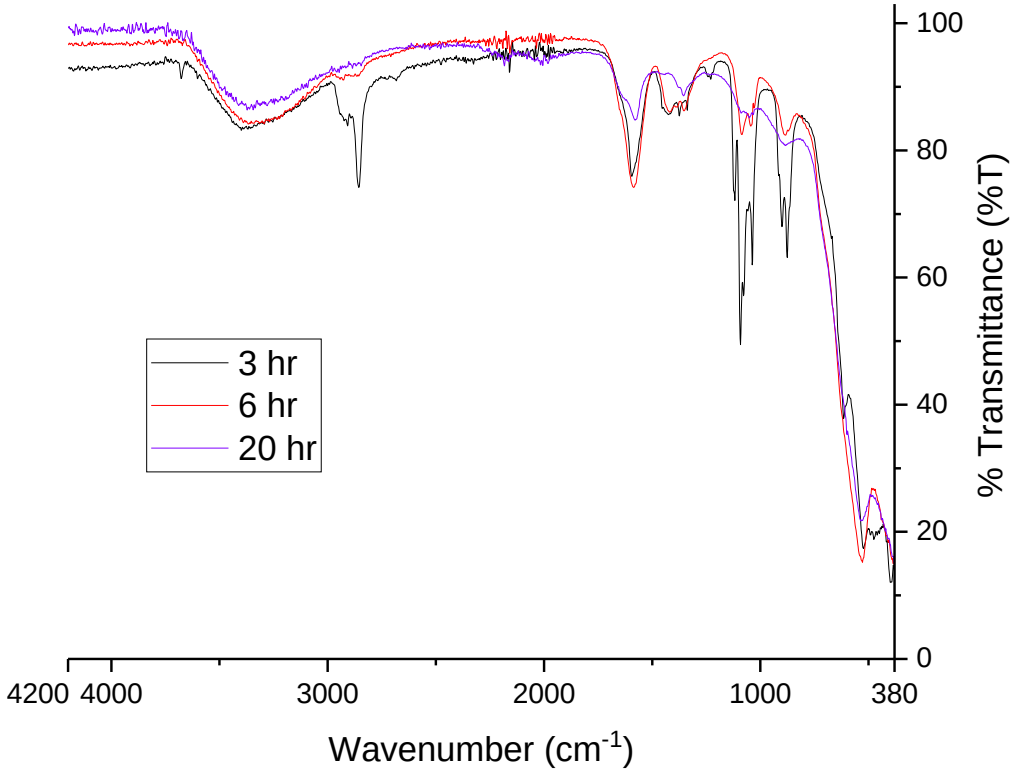


Figure 3-45: FTIR spectra for $MnFe_2O_4$ MNPs prepared at different reaction times.

The colloidal stability of the particles was surprisingly high despite them being larger particles for which precipitation would be expected. This may be because the slight excess of sodium acetate stabilises the particles through the carboxylic groups. The stability was quantified by DLS measurements over 7 days. As it is shown in the table below (Table 3-3) the Z-average and PDI both increase up to day 1-2 then by day 2 there is a large drop in the count rate. This indicates that by day 2 most of the particles have agglomerated and are beginning to precipitate out of solution. The count rate decreases by 88 % over the 7 days. This is because of the position of the laser in the instrument combined with the settling behaviour in solution.

Zeta potential measurements of the particles (Figure 3-46) also indicated that they had low colloidal stability at neutral pH with a value of -9.1 mV at pH 6.7. A zeta potential so close to zero at neutral pH indicates that the particles should precipitate out of solution rapidly[27], but the DLS results indicated slower precipitation than expected by these results. By taking zeta potential measurements over a pH range of 2.1 – 12.4 the point of zero charge (PZC) can be measures for the bare particles, although it should be noted that for pH 2.1 and 12.4, the conductivity was above 1 mS/cm and so above the optimum value for good measurements. The PZC was found to be at approximately pH 5.7. Again it was noted that the pH 2.1 sample

MNPs would dissolve in solution within 30 minutes but it was possible to get the measurement before this happened.

Table 3-3: DLS measurements for $MnFe_2O_4$ MNPs suspensions.

Time	Z-Average	PDI	PDI Width	Count Rate
	d.nm		d.nm	kcps
0 hr	221.3	0.197	98.2	215994
1 hr	242.7	0.242	119.4	227036
2 hr	258.9	0.272	135.1	224937
3 hr	236.4	0.21	108.4	198558
5 hr	255.2	0.254	128.7	189360
7 hr	257.2	0.258	130.7	185063
1 day	314.4	0.254	158.4	152362
2 day	290.6	0.25	145.4	106426
3 day	213.2	0.125	75.3	69809
5 day	217.1	0.097	67.8	45751
7 day	184.1	0.115	62.4	26553

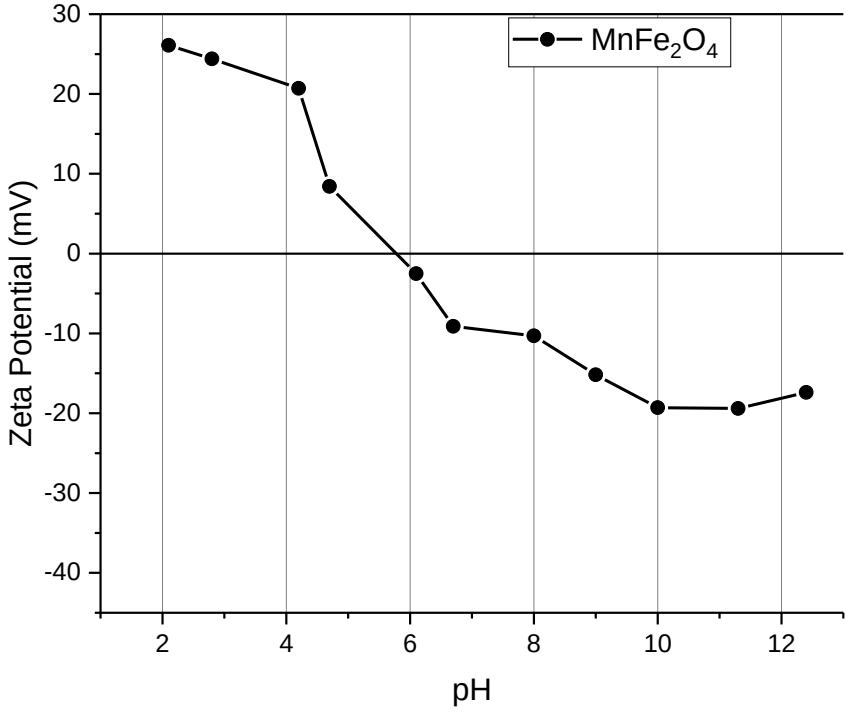


Figure 3-46: Zeta Potential measurements over a pH range showing the PZC for $MnFe_2O_4$ MNPs suspensions.

A few modifications on this basic procedure were tried. One modification involved carrying out the synthesis under argon as opposed to open to air. It was found that the reaction open air reached completion after 6-8 hours while the reaction under argon took slightly longer to reach completion at 8-10 hours. Despite these variations, the reaction always reached completion after an overnight run of 20 hours. There would be some variability between batches regarding the saturation magnetisation and the monodispersity of the batch, with some batches containing smaller fragmented particles while others composed mainly of well-formed individual particles in the 90 – 110 nm range. This is somewhat expected between batches and the research tries to narrow these variances. The magnetisation of batches varied between 55-65 Am^2kg^{-1} approximately. This variation in magnetisation would partially be due to the inherent difference between batches coming from the crystallinity. There is lack of control in the synthesis on this outcome.

Another variation was using magnetic stirring instead of mechanical. This change had no effect on the outcome of the reaction with particles of a similar size and dispersity formed with similar magnetic properties to the described basic procedure (see 2.2.5).

However, in this experiment where the particles were left magnetically stirring overnight to see if it affected the outcome of the reaction it was noted that there was a white flakes contamination floating on the surface of the solution in the vessel when the reaction was stopped. Further examination of the magnetic stirring bar showed that it had been grinded down (Figure 3-47) and therefore the white contamination was the PTFE coating. The reason for this can be understood because as the magnetic particles are formed, some will be attracted to the base of the vessel where the hot plates magnetic stirring element is. These nanoparticles will act as a grinding material on the PTFE coated magnetic stirrer, which is also pulled to the bottom of the vessel. Examination of other TEM images from other experiments where magnetic stirring was used showed traces of flakes in the images. On this basis, it was decided to use mechanical stirring during the PhD project to eliminate the possibility of micro- to nano- PTFE contaminants in the products of any of the reactions.

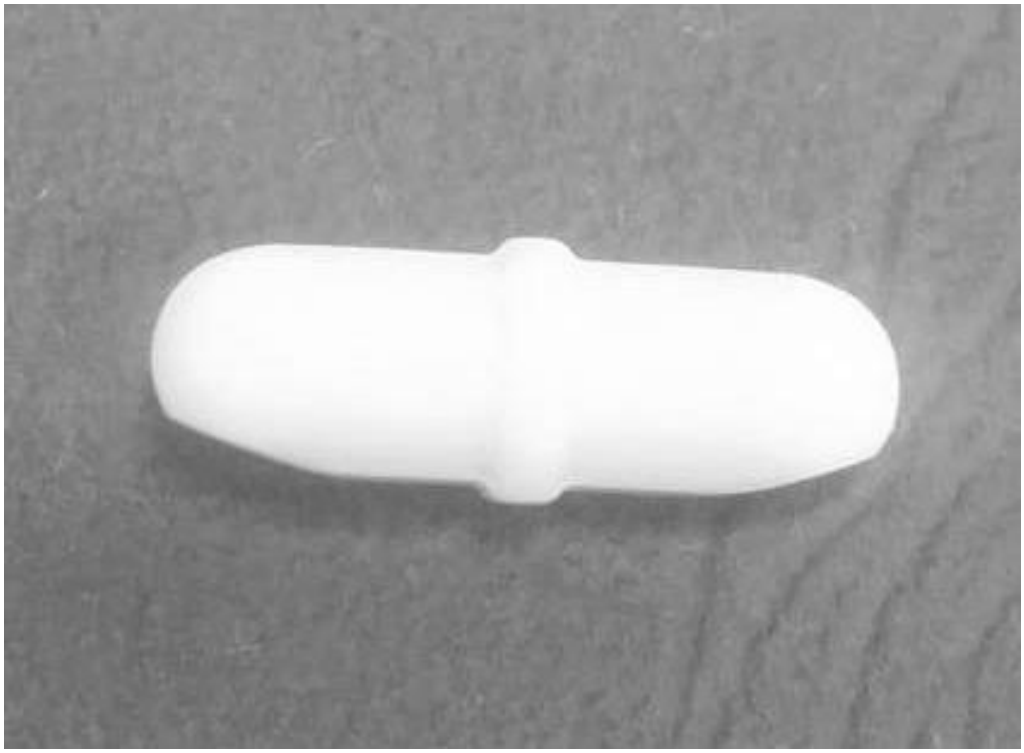


Figure 3-47: Photograph of PTFE stirring bar with ground edges visible.

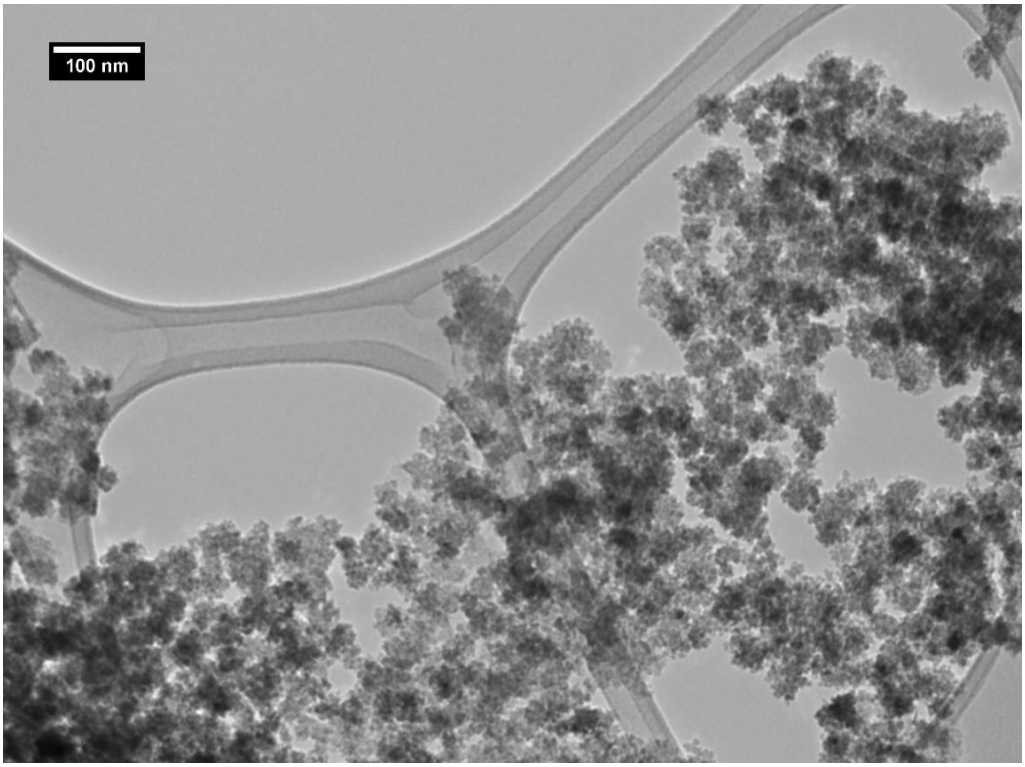


Figure 3-48: TEM image of the $MnFe_2O_4$ product of the reaction using NaOH as the base.

Another variation that was performed was using NaOH as the base instead of Na-acetate. The XRD of the product of this reaction again showed a match for $MnFe_2O_4$ (COD 230-0619)

confirming that the expected material had been made. The magnetisation values were lower than the Na-acetate version with a specific magnetisation of 41 Am^2kg^{-1} at 1 T. TEM images of the product showed that distinct particles had not been formed with the sample composed of aggregated grains as can be seen above (Figure 3-48).

Another variation was increasing the amount of Na-acetate by 50%. This had no effect on the outcome of the reaction with similar results as with the basic procedure in the experimental section (2.2.5). Decreasing the amount of Na-acetate was not tried as the balanced reaction for the reaction requires 8 Na atoms per unit of $MnFe_2O_4$ and the ratios described in the experimental has the ratio at 10 Na atoms. Decreasing the Na-acetate concentration by 50% it was therefore rationalised would negatively affect the yield of the ferrite.

One more variation was changing the amount of solvent (dilution factor). Halving the amount of solvent had a minor effect on the outcome of the reaction, in that the TEM images did show increased levels of aggregation. This however may be because of the preparation method of the TEM samples where the sample was not sonicated well enough before being dropped onto the TEM grid. A TEM image of the product of this reaction is shown below (Figure 3-49) and the slight increase in aggregation is evident.

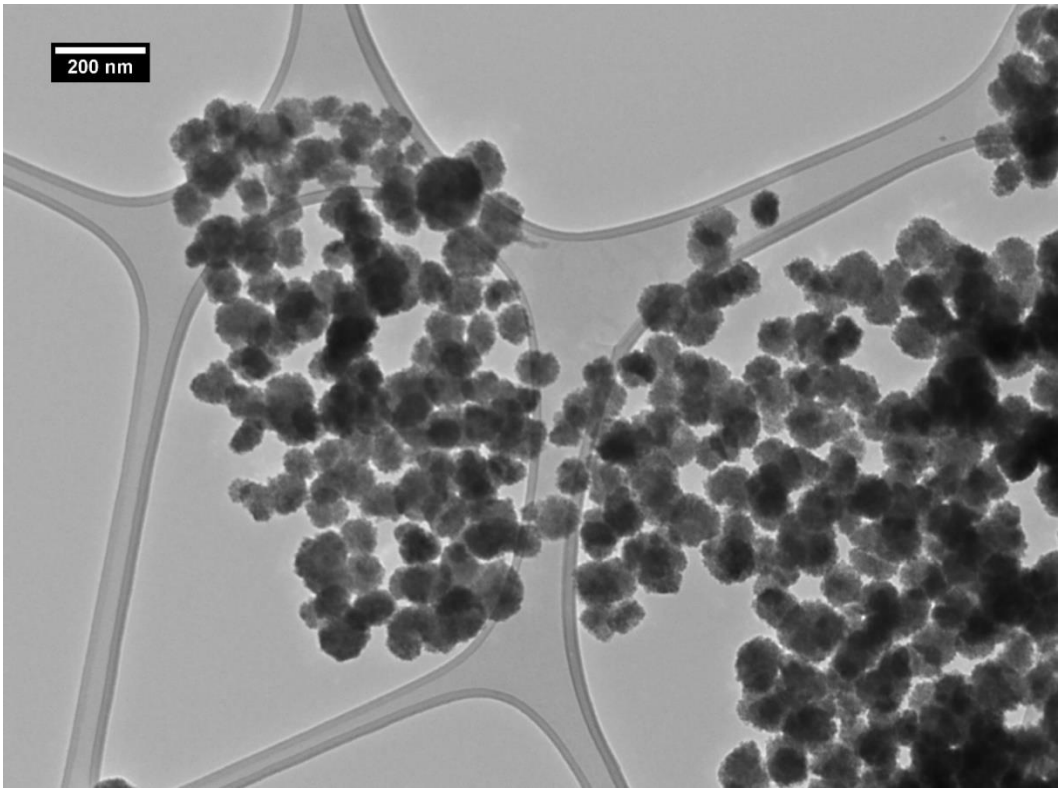


Figure 3-49: TEM image of $MnFe_2O_4$ produced using 50% the amount of solvent.

Doubling the amount of solvent caused the reaction to fail with no MNPs formed. This variation of the reaction was tried only once so there is the possibility that a contaminant or another error was the source of the failure. Considering that there was a version of the reaction that was working it was decided not to repeat this reaction, as there are always time consideration to be taken in to account in research.

One final variation was changing the solvent from ethylene glycol to diethylene glycol because it has a higher boiling point and it was considered that a higher boiling point polyol solvent might increase the grain and particle sizes. TEM images as seen below (Figure 3-51), of the product of this reaction showed only large aggregates and gave little information, as the aggregates were too big for this characterisation method. An SEM of the same grids used for TEM showed large aggregates giving cauliflower type structures as can be seen in the image below (Figure 3-50). The specific magnetisation for this material was 45 Am^2kg^{-1} at 1 T which was lower than expected. An XRD gave a good match for $MnFe_2O_4$ to show that manganese ferrite was indeed the product of the reaction.

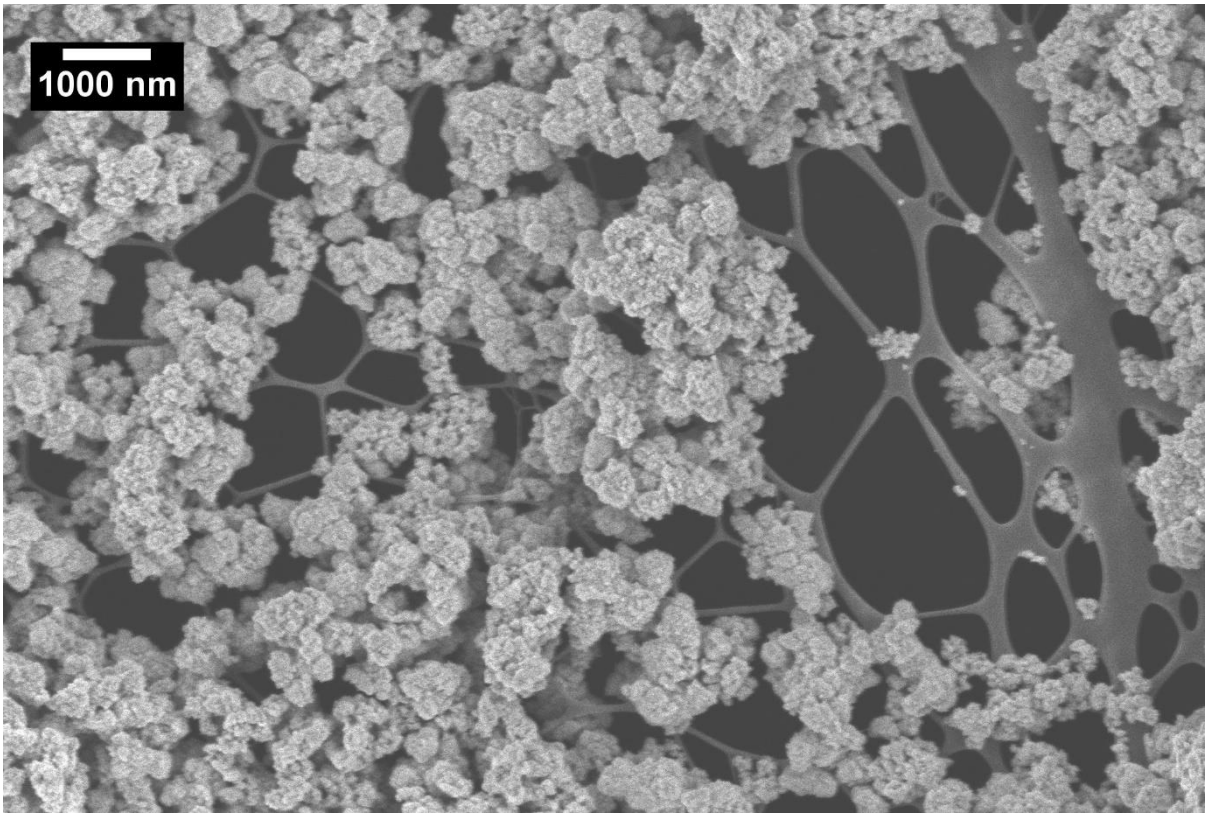


Figure 3-50: SEM image of cauliflower type structures when using diethylene glycol.

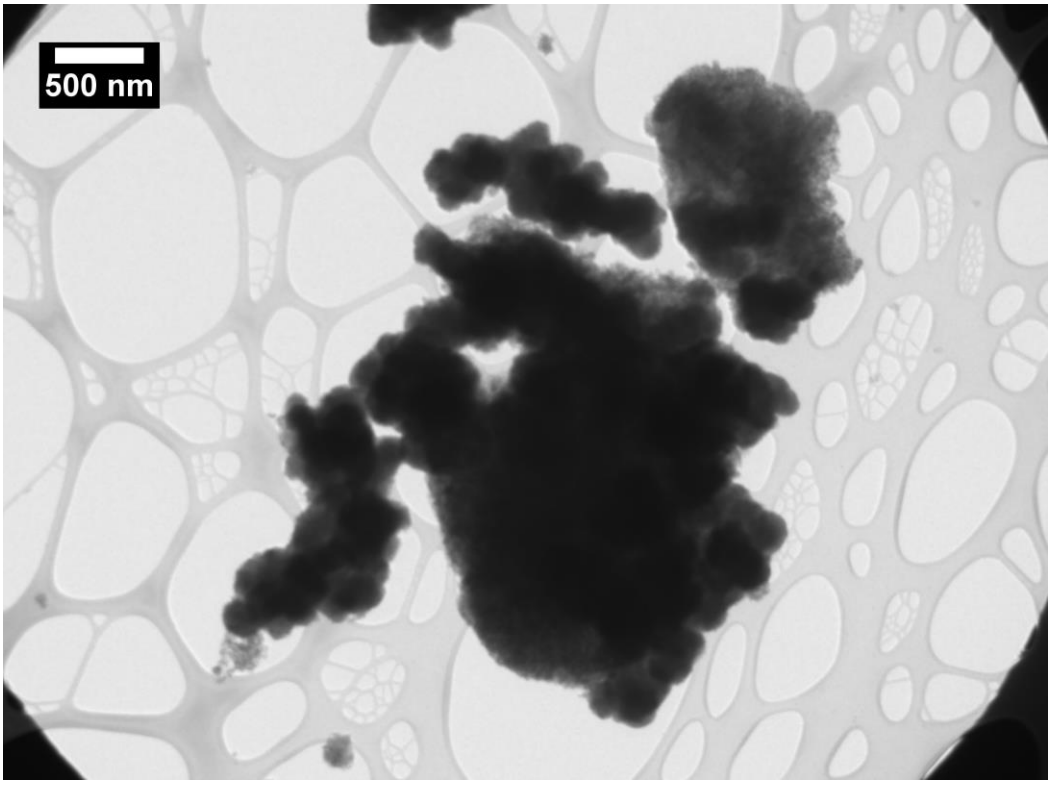


Figure 3-51: TEM image of cauliflower type structures when using diethylene glycol.

In the table below (Table 3-4), a summary of the studies on optimisation of the polyol manganese ferrite MNPs synthesise is given.

Table 3-4: Summary of variations for $MnFe_2O_4$ polyol synthesis.

Polyol synthesis detail	TEM sizes (nm)	XRD size (nm)	Magnetisation value (Am^2kg^{-1})	Comments
Ethylene glycol, Na-acetate mechanical stirring	100 ± 20	8.0	60.1	Best results, reproducible
under argon	100 ± 20	8.1	60	Reaction took longer to complete
magnetic stirring	100 ± 20	8.0	61	PTFE stirrer bar grinding
NaOH as base	14 ± 6	11.0	41	Aggregated smaller particles
50% more Na-acetate	100 ± 20	8.3	63	No major change
50% less solvent	100 ± 30	8.2	65	More aggregation
100 % more solvent	NA	NA	NA	No product isolated
diethylene glycol	NA	NA	45	No distinct particles

3.3.6 Preparation of Magnetite MNPs (Fe_3O_4) by Polyol Method

Having successfully produced larger particles of $MnFe_2O_4$ as discussed previously, it was decided to check if magnetite could also be produced using a similar method, as magnetite has a higher saturation magnetisation than manganese ferrite (92 Am^2kg^{-1} compared to 77 Am^2kg^{-1}). Therefore, to have the option to use these size MNPs composed of Fe_3O_4, with the increased magnetisation, was the main factors in pursuing this line of research. Not many variations were performed to the basic procedure as described in the experimental (2.2.6) to improve the core though.

For this procedure, similarly to the manganese ferrite polyol synthesis previously, the metal ion precursor was refluxed in a polyol solvent at atmospheric pressure in the presence of sodium acetate. For the magnetite polyol synthesis, only Fe(lll) ions were needed with no Fe(ll) ions in the precursors as glycol serves as a reducing agent for Fe(III).

The product of the reaction was characterised by TEM, VSM, XRD and FTIR. The VSM analysis showed reasonable magnetisation with a specific magnetisation of 61 Am^2kg^{-1} at 1 T. This was lower than expected but the particles were capable of fast magnetic extraction from solution.

The FTIR spectroscopy showed the strong peak at 533 cm^{-1} for the Fe-O stretch as expected.

XRD analysis proved that magnetite was the product of the reaction with a high match for its crystal structure (COD 900-2674). A Williamson-Hall plot for the peaks gave a crystallite size of 9.5 nm. Rietveld analysis using the matched reference pattern for the structure fit gave a cubic crystal lattice with a lattice of a = 8.37078 Å.

TEM analysis showed however that the particles of Fe_3O_4 formed were not as well defined as the $MnFe_2O_4$ discussed previously (3.3.5). As can be seen in a TEM image of the product of the reaction below (Figure 3-52) the sample was quite polydisperse being composed of particles in the range 90±40 nm. There also seems to be more agglomeration than with the $MnFe_2O_4$. With some modifications, the outcomes of this synthesis could be improved if the particles are to be used as magnetic cores and a well-defined core will lend itself to a well-defined core@shell structure after further functionalisation.

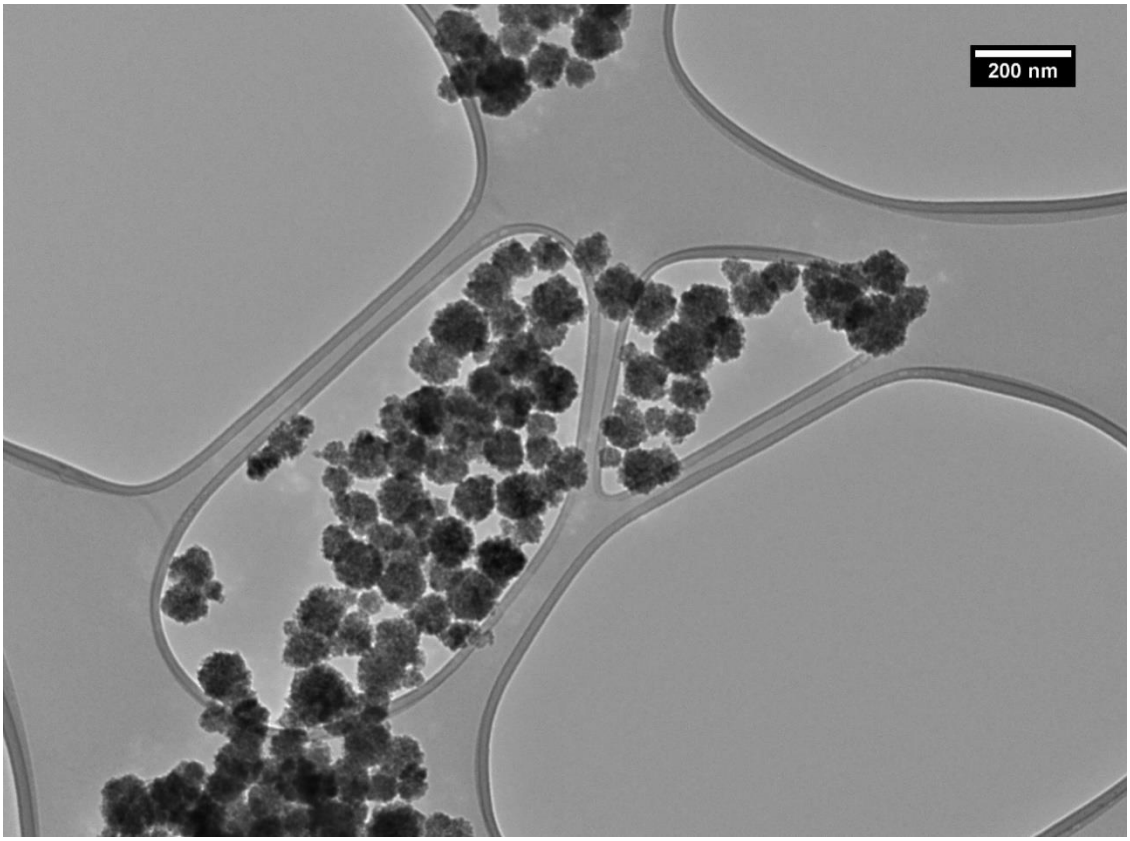


Figure 3-52: TEM image of Fe_3O_4 MNPs produced by polyol synthesis.

The formation of Fe_3O_4 using the described synthesis (2.2.6) with just Fe(lll) ions as precursors to form a lattice that contains Fe(ll) and Fe(lll) ions is because of the reaction in a polyol medium without an oxygen atmosphere. The reaction type is known as the "reduction by polyol" where the ethylene glycol, at high temperature, creates a reducing environment according to the proposed mechanism (Figure 3-53)[52].

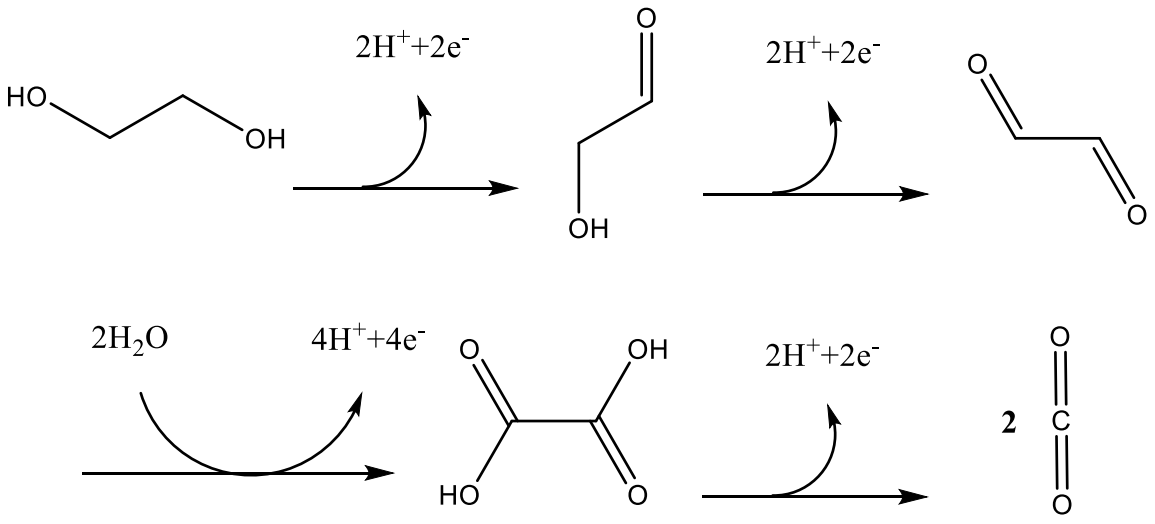


Figure 3-53: Proposed mechanism of the polyol oxidation process.

One variation that was done on the basic procedure as outlined in the experimental section (2.2.6) was using Fe(ll) and Fe(lll) ions in a ratio of 1:2, as was done for the synthesis of coprecipitated Fe_3O_4 previously (2.2.1). The TEM image below (Figure 3-54), using this method, showed a product where only grains were formed and none of the larger particles. VSM analysis of the product gave a specific magnetisation of 61 Am^2kg^{-1}. The XRD pattern of the product was also a high match for Fe_3O_4 (COD 101-0370). A Williamson-Hall plot for the peaks gave a crystallite size of 7.8 nm, which is in good agreement with the TEM image for the sample.

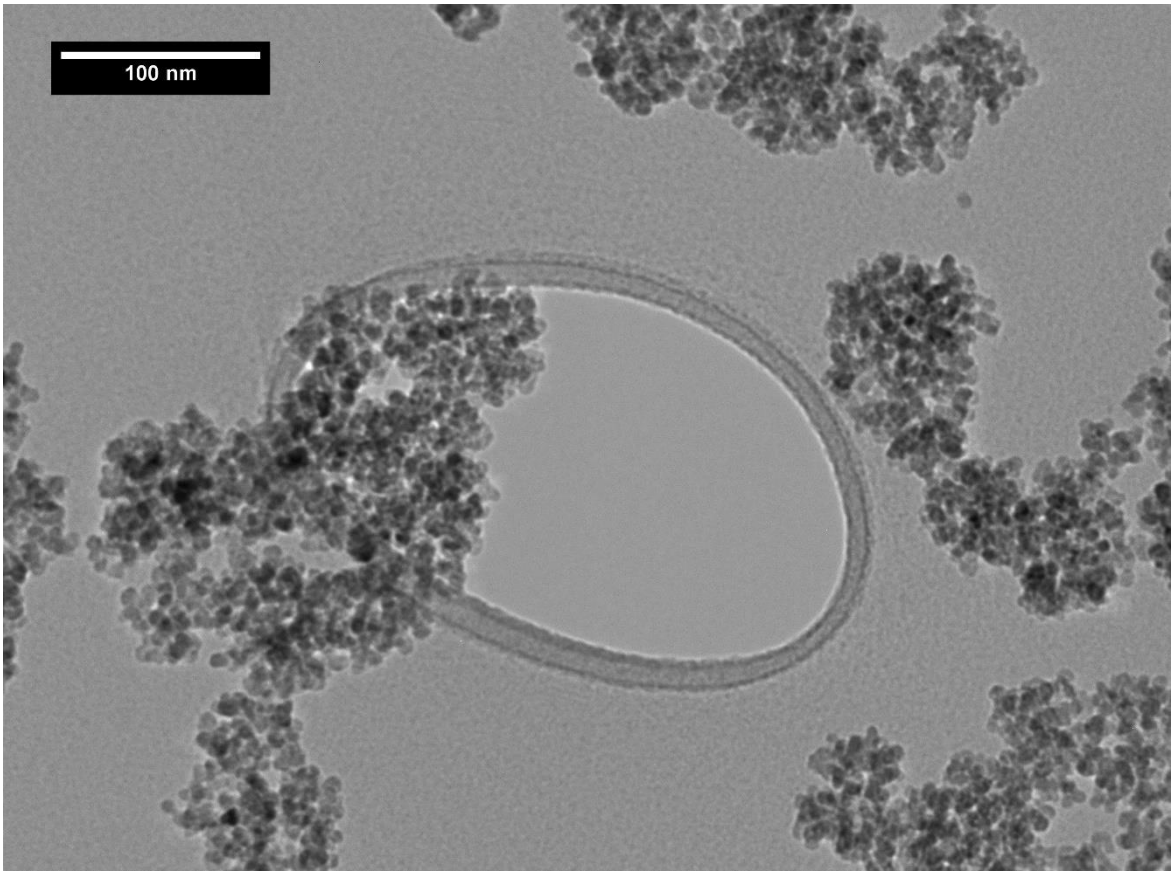


Figure 3-54: TEM image of the product of synthesis using Fe(ll) and Fe(lll) ions.

Another variation that was tried one time was substitution of NaOH for Na-acetate as the base in the basic procedure. This reaction gave a product that was not magnetic, so the reaction was deemed unsuccessful.

3.4 Conclusion

A variety of magnetic core nanostructures have been prepared and characterised. For the coprecipitated ferrites, it was found that the particles from the reaction could be produced as monodisperse samples with a narrow size distribution for magnetite and cobalt ferrite. For manganese ferrite and copper ferrite MNPs produced by coprecipitation the samples were not as monodisperse. For copper ferrite, the particles produced showed low magnetism values until after calcination but this calcination process fused the particles so they could not be dispersed back into solution.

XRD analysis of the samples demonstrated excellent matches for the materials produced which shows that the correct materials were made.

The magnetic properties for the produced particles, apart from copper ferrite, all indicated superparamagnetic behaviour with no remnant magnetisation when the external field was removed and good saturation magnetisation in a 1 T field.

The larger size of the cores for the polyol solvent produced particles, coupled with their good magnetic properties, enabled fast extraction from solution. The particles were also easily dispersed into solution with sonication. For the future applications as recyclable catalysts, this would be a requirement, easy dispersion in solution coupled with fast extraction from solution. These magnetic cores therefore have high potential for further applications in this area.

3.5 References

1 T. Hyeon, *Chem. Commun.*, 2003, **3**, 927–934. https://doi.org/10.1039/b207789b.

2 D. Huber, *Small*, 2005, **1**, 482–501. https://doi.org/10.1002/smll.200500006.

3 A.-H. Lu, E. L. Salabas and F. Schüth, *Angew. Chemie Int. Ed.*, 2007, **46**, 1222–1244. https://doi.org/10.1002/anie.200602866.

4 S. Sun and H. Zeng, *J. Am. Chem. Soc.*, 2002, **124**, 8204–5. https://doi.org/10.1021/ja026501x.

5 J.-H. J.-G. J. J.-H. Park, K. An, Y. Hwang, J.-H. J.-G. J. J.-H. Park, H.-J. Noh, J.-Y. Kim, J.-H. J.-G. J. J.-H. Park, N.-M. Hwang and T. Hyeon, *Nat. Mater.*, 2004, **3**, 891–895. https://doi.org/10.1038/nmat1251.

6 S. Riaz, M. Bashir and S. Naseem, *IEEE Trans. Magn.*, , DOI:10.1109/TMAG.2013.2277614. https://doi.org/10.1109/TMAG.2013.2277614.

7 C. Blanco-Andujar, D. Ortega, Q. A. Pankhurst and N. T. K. Thanh, *J. Mater. Chem.*, 2012, **22**, 12498. https://doi.org/10.1039/c2jm31295f.

8 H. Cai, X. An, J. Cui, J. Li, S. Wen, K. Li, M. Shen, L. Zheng, G. Zhang and X. Shi, *ACS Appl. Mater. Interfaces*, 2013, **5**, 1722–1731. https://doi.org/10.1021/am302883m.

9 H. Deng, X. Li, Q. Peng, X. Wang, J. Chen and Y. Li, *Angew. Chemie - Int. Ed.*, 2005, **44**, 2782–2785. https://doi.org/10.1002/anie.200462551.

10 V. Pillai and D. O. O. Shah, *J. Magn. Magn. Mater.*, 1996, **163**, 243–248. https://doi.org/10.1016/S0304-8853(96)00280-6.

11 C. Liu, B. Zou, A. J. Rondinone and Z. J. Zhang, *J. Phys. Chem. B*, 2000, **104**, 1143–1145. https://doi.org/10.1021/jp993552g.

12 Z. Y. Guo, Y. Zhang, D. D. Zhang, Y. Shu, X. W. Chen and J. H. Wang, *ACS Appl. Mater. Interfaces*, 2016, **8**, 29734–29741. https://doi.org/10.1021/acsami.6b11158.

13 R. T. Gordon, J. R. Hines and D. Gordon, *Med. Hypotheses*, 1979, **5**, 83–102. https://doi.org/10.1016/0306-9877(79)90063-X.

14 M. G. Krukemeyer, W. Wagner, M. Jakobs and V. Krenn, *Nanomedicine*, 2009, **4**, 875–

882. https://doi.org/10.2217/nnm.09.73.

15 J. W. M. M. Bulte and D. L. Kraitchman, *NMR Biomed.*, 2004, **17**, 484–499. https://doi.org/10.1002/nbm.924.

16 J. M. D. D. Coey, *Magnetism and magnetic materials*, Cambridge University Press, Cambridge, 2010, vol. 9780521816. https://doi.org/10.1017/CBO9780511845000.

17 S. Shylesh, V. Schünemann and W. R. Thiel, *Angew. Chemie Int. Ed.*, 2010, **49**, 3428–3459. https://doi.org/10.1002/anie.200905684.

18 J. Lefort, *CR Hebd Seances Acad Sci*, 1852, **34**, 488–491.

19 A. Bunge, A. S. Porav, G. Borodi, T. Radu, A. Pîrnău, C. Berghian-Grosan and R. Turcu, *J. Mater. Sci.*, 2019, **54**, 2853–2875. https://doi.org/10.1007/s10853-018-3030-9.

20 C. Y. Wang, J. M. Hong, G. Chen, Y. Zhang and N. Gu, *Chinese Chem. Lett.*, 2010, **21**, 179–182. https://doi.org/10.1016/j.cclet.2009.10.024.

21 R. D. Waldron, *Phys. Rev.*, 1955, **99**, 1727–1735. https://doi.org/10.1103/PhysRev.99.1727.

22 I. Chamritski and G. Burns, *J. Phys. Chem. B*, 2005, **109**, 4965–4968. https://doi.org/10.1021/jp048748h.

23 R. Safi, A. Ghasemi, R. Shoja-Razavi and M. Tavousi, *J. Magn. Magn. Mater.*, 2015, **396**, 288–294. https://doi.org/10.1016/j.jmmm.2015.08.022.

24 M. Darroudi, M. Hakimi, E. Goodarzi, R. Kazemi Oskuee and R. Kazemi, *Ceram. Int.*, 2014, **40**, 14641–14645. https://doi.org/10.1016/j.ceramint.2014.06.051.

25 A. Atrei, F. F. Mahdizadeh, M. C. Baratto and A. Scala, *Appl. Sci.*, , DOI:10.3390/app11156974. https://doi.org/10.3390/app11156974.

26 M. A. Dheyab, A. A. Aziz, M. S. Jameel, O. A. Noqta, P. M. Khaniabadi and B. Mehrdel, *Sci. Rep.*, 2020, **10**, 1–8. https://doi.org/10.1038/s41598-020-67869-8.

27 A. Kumar and C. K. Dixit, *Adv. Nanomedicine Deliv. Ther. Nucleic Acids*, 2017, 44–58. https://doi.org/10.1016/B978-0-08-100557-6.00003-1.

28 E. Amstad, T. Gillich, I. Bilecka, M. Textor and E. Reimhult, *Nano Lett.*, 2009, **9**, 4042–4048. https://doi.org/10.1021/nl902212q.

29 Q. Li, C. W. Kartikowati, S. Horie, T. Ogi, T. Iwaki and K. Okuyama, *Sci. Rep.*, 2017, **7**, 9894. https://doi.org/10.1038/s41598-017-09897-5.

30 M. Răcuciu, D. E. Creangă and A. Airinei, *Eur. Phys. J. E*, 2006, **21**, 117–121. https://doi.org/10.1140/epje/i2006-10051-y.

31 R. . Kodama, *J. Magn. Magn. Mater.*, 1999, **200**, 359–372. https://doi.org/10.1016/S0304-8853(99)00347-9.

32 J. I. Langford and A. J. C. Wilson, *J. Appl. Crystallogr.*, 1978, **11**, 102–113. https://doi.org/10.1107/s0021889878012844.

33 G. K. Williamson and W. H. Hall, *Acta Metall.*, 1953, **1**, 22. https://doi.org/10.1016/0001-6160(53)90006-6.

34 V. F. Cardoso, A. Francesko, C. Ribeiro, M. Bañobre-López, P. Martins and S. Lanceros-Mendez, *Adv. Healthc. Mater.*, 2018, **7**, 1–35. https://doi.org/10.1002/adhm.201700845.

35 T. Shanmugavel, S. G. Raj, G. R. Kumar and G. Rajarajan, *Phys. Procedia*, 2014, **54**, 159–163. https://doi.org/10.1016/j.phpro.2014.10.053.

36 Z. X. Tang, C. M. Sorensen, K. J. Klabunde and G. C. Hadjipanayis, *J. Colloid Interface Sci.*, 1991, **146**, 38–52. https://doi.org/10.1016/0021-9797(91)90004-R.

37 J. Chen, C. Sorensen and K. Klabunde, *Phys. Rev. B - Condens. Matter Mater. Phys.*, 1996, **54**, 9288–9296. https://doi.org/10.1103/PhysRevB.54.9288.

38 M. Ishii, M. Nakahira and T. Yamanaka, *Solid State Commun.*, 1972, **11**, 209–212. https://doi.org/10.1016/0038-1098(72)91162-3.

39 K. Zipare, J. Dhumal, S. Bandgar, V. Mathe and G. Shahane, *J. Nanosci. Nanoeng.*, 2015, **1**, 178–182.

40 R. Serrano-García, F. Purcell-Milton, S. McCarthy and Y. K. Gun'ko, *ChemistrySelect*, 2018, **3**, 4726–4729. https://doi.org/10.1002/slct.201800681.

41 B. Purnama, R. Rahmawati, A. T. Wijayanta and Suharyana, *J. Magn.*, 2015, **20**, 207–210. https://doi.org/10.4283/JMAG.2015.20.3.207.

42 C. N. Chinnasamy, B. Jeyadevan, O. Perales-Perez, K. Shinoda, K. Tohji and A. Kasuya, *IEEE Trans. Magn.*, 2002, **38**, 2640–2642. https://doi.org/10.1109/TMAG.2002.801972.

43 J. Zou, Y. G. Peng and Y. Y. Tang, *RSC Adv.*, 2014, **4**, 9693–9700. https://doi.org/10.1039/c3ra47043a.

44 M. Houshiar, F. Zebhi, Z. J. Razi, A. Alidoust, Z. Askari, Z. Jafari, A. Alidoust, Z. Askari, Z. J. Razi, A. Alidoust and Z. Askari, *J. Magn. Magn. Mater.*, 2014, **371**, 43–48. https://doi.org/10.1016/j.jmmm.2014.06.059.

45 M. Ghaani and J. Saffari, *Jns.Kashanu.Ac.Ir*, 2016, **6**, 172–178. https://doi.org/10.7508/JNS.2016.02.010.

46 A. Bazgir, G. Hosseini and R. Ghahremanzadeh, *ACS Comb. Sci.*, 2013, **15**, 530–534. https://doi.org/10.1021/co400057h.

47 E. Agouriane, B. Rabi, A. Essoumhi, A. Razouk, M. Sahlaoui, B. F. O. Costa and M. Sajieddine, *J. Mater. Environ. Sci.*, 2016, **7**, 4116–4120. https://doi.org/10.1016/j.jmmm.2019.03.128.

48 M. M. Rashad, R. M. Mohamed, M. A. Ibrahim, L. F. M. Ismail and E. A. Abdel-Aal, *Adv. Powder Technol.*, 2012, **23**, 315–323. https://doi.org/10.1016/j.apt.2011.04.005.

49 An equilibrium using copper(II) and ammonia, https://edu.rsc.org/experiments/an-equilibrium-using-copperii-and-ammonia/1711.article.

50 Parr Instrument High Pressure Vessels, https://www.parrinst.com/products/sample-preparation/acid-digestion/applications/hydrothermal-synthesis/.

51 Sodium Acetate FTIR, https://sdbs.db.aist.go.jp/sdbs/cgi-bin/direct_frame_top.cgi.

52 F. Fiévet, S. Ammar-Merah, R. Brayner, F. Chau, M. Giraud, F. Mammeri, J. Peron, J.-Y. Y. Piquemal, L. Sicard, G. Viau, F. Fievet, S. Ammar-Merah, R. Brayner, F. Chau, M. Giraud, F. Mammeri, J. Peron, J.-Y. Y. Piquemal, L. Sicard and G. Viau, *Chem. Soc. Rev.*, 2018, **47**, 5187–5233. https://doi.org/10.1039/C7CS00777A.

4 Stabilisation and Protection of the Magnetic Cores

4.1 Introduction

Bare MNP are not chemically inert with magnetite being prone to oxidation[1]. In solution, MNPs of the ferrite spinel type are prone to etching in low pH environments and the bare particles will precipitate out of solution as discussed in the chapter 3. Functionalisation of MNPs involves adding another material to impart a new function to the MNPs surfaces. A common purpose for a coating layer is to simply add stability[2] or protection[3]. Often in the process of forming a nanocomposite with a specific function or application, the first steps will involve the stabilisation or protection of the core. Protection of the core is especially important when dealing with highly reactive MNPs such as iron metal nanoparticles, which are pyrophoric[4].

Stabilisation of a MNP can be achieved by various methods, such as with citric acid[2], oleic acid[5], dextran[6] and other sugars[6], polyethylene glycol (PEG)[7] and polyelectrolytes[8]. Stabilisation of the MNPs in a solution results in a so-called ferrofluid, where the fluid can be manipulated by a magnetic field. A ferrofluid can be prepared in either a polar solvent such as hexane or a nonpolar solvent such as water [9]. For an iron oxide based MNPs in a polar organic solvent, a common surfactant used is oleic acid, giving the MNPs stability in the solvent without flocculation. With water based MNPs a common surfactant is citric acid to make an aqueous ferrofluid. All these types of surfactants have one major goal, that is the prevention of agglomeration of the individual MNP, and so the particles will become stabilised in the solution and will not precipitate out. The surface active molecule may also have other benefits of functions such as being biocompatible[10] or being able to bind other molecules[11]. Polymeric molecules are known to bind to MNPs more than single molecule surfactants with single molecule surfactants being described as labile, which means being easy to remove and replace with another surface active molecule.

Coating of the MNPs with a shell is another functionalisation approach that is commonly performed in MNPs synthesis. The coating is necessary because some of MNPs are very reactive and the coating enables usage of MNPs in a broader range of applications, such as

high pH environments. Surfactants of the polymeric type can be used for protection as they attach strongly to the MNP and thereby protect the surface to some degree. Protection of the core MNP with a more stable durable shell is desirable in many cases. A carbon coating is type of coating that has been used to protect MNP cores[12]. Carbon coating is biocompatible and can be easily functionalised. A carbon coating will also give the nanocomposite stability over a large pH range[13]. Probably the most well know coating for protection of MNPs is silica (SiO_2). The preparation of well-defined silica nanoparticles have been known since Stöber[14] and silica coated MNPs have been known since Philipse[15]. It has also been found that silica can be effectively functionalised further by APTES to become an effective surface for covalent coupling[16]. This has led to a vast body of research on these type of core@shell MNP nanostructures being used for targeted drug delivery[17] and as a supports for catalysts to enable magnetic separation of the catalyst after completion of the reaction[18]. These type of catalytic MNPs have been shown to be recyclable over 30 times without loss of activity[19], although sometimes the recyclability was much lower, with one group finding a decrease from 80 to 42% yield after just 4 cycles[20].

4.2 Aims

This chapter explores the stabilisation and protection of selected MNPs, discussing variations that were tried in the synthesis and the outcomes. This is a necessary step for further functionalisation with a catalytic shell. The magnetic cores that will be used in this chapter are the magnetite prepared by coprecipitation and the manganese ferrite prepared in polyol solvent as these particles had the best characteristic, in terms of magnetic properties and morphology, from the particles prepared previously. These cores will be stabilised by citric acid and protected with a SiO_2 shell. Much of this work is well established in the literature but some exploration of these processes will be done here. The synthesised nanoparticles will be characterised by TEM to confirm the consistent size, morphology and shell thickness, with EDX confirming the elements present, while VSM will be use to assess the magnetic characteristics. FTIR spectroscopy will be used to investigate functional groups on the surface. DLS and zeta potential measurements will be employed to assess the solution behaviour and colloidal stability of the particles.

4.3 Results and Discussion

Having made several types of MNPs previously, it was decided to functionalise the coprecipitated magnetite MNPs and the manganese ferrite MNPs prepared by polyol method. One of the basic functionalisation methods for bare MNP is coating of the bare particles with a surfactant, such as citric acid[21][11][2]. As mentioned previously there are various surfactants with some being more displaceable[22]. Citric acid is a well-known surfactant that is readily displaced at the MNP surface by another binding material. Citric acid binds to the surface through one or two of the carboxylic residue to the Fe atoms on the surface of the MNP as an electrostatic interaction[11]. The remaining carboxylic residues are now interacting with the solution and give the particle a higher zeta potential at neutral pH than the bare MNP. This causes less agglomeration and better stability in solution as the negatively charged carboxylic residues repel each other. Further functionalisation with other materials, such as SiO_2, should therefore give well-dispersed individual particles as the particles are well separated in solution. SiO_2 coating to the surface of MNPs forms an amorphous shell structure whereas citrate molecules form a layer on the surface. A SiO_2 shell protects the MNP from the environment while also creating a surface for further attachment[23]. The surface chemistry of binding for each material is different with some materials favouring attachment. However, surface effects like lattice mismatch can hinder growth of shell materials[24].

4.3.1 Preparation of Citrate Stabilised Magnetite MNPs

Citric acid stabilisation for the bare coprecipitated magnetite MNPs was performed by using a procedure as described in the experimental section (2.3.1). There are several modifications in the literature for citric acid stabilisation[2][25]. Here sodium citrate is used for functionalisation and citric acid for neutralisation of the solution, so a minimum of complexity is involved at the surface of the nanoparticles.

The functionalised magnetite MNPs were characterised by VSM, FTIR, XRD, TEM, DLS and Zeta Potential. VSM results (Figure 4-1) show a very small reduction in magnetisation from 54.2 Am^2kg^{-1} at 1 T for the bare particles to 51.7 Am^2kg^{-1} for the citrate functionalised particles. Several repeats of this synthesis and comparison of the bare to the functionalised particles showed that the change in magnetism was consistently small. A larger change was expected,

as a monolayer of citrate would have added approximately 12-23 % to the mass of the particle for a NP of 12 nm when a calculation is done assuming 1-2 binding sites on the citrate molecule. However, magnetite would have absorbed water at the surface and this would be replaced by the citrate explaining to some degree the negligible change in magnetisation. It could also be explained by not all binding sites being saturated due to steric and electrostatic hindrance considerations.

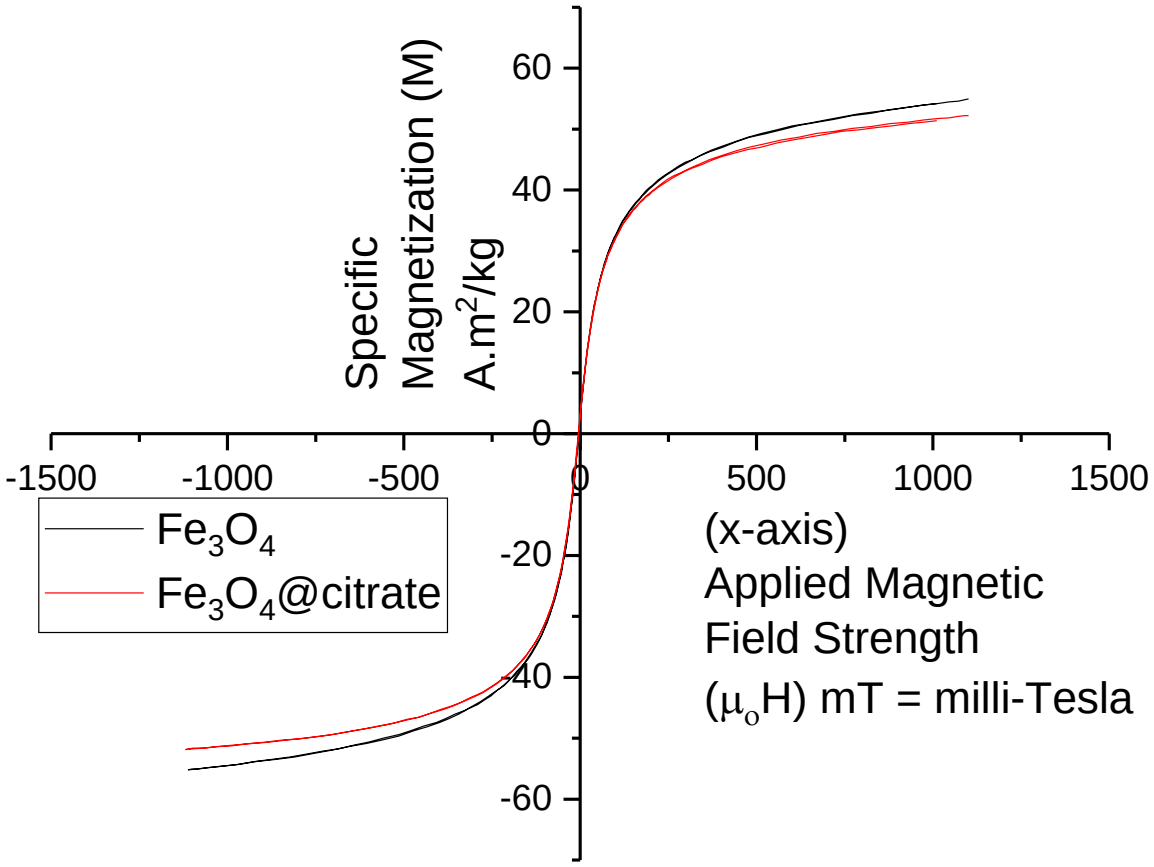


Figure 4-1: VSM curves of citrate functionalised magnetite, Fe_3O_4@citrate.

FTIR spectra as shown below (Figure 4-2) indicated that the MNP now had citrate groups bound to the surface with the appearance of the peaks at 1616 cm^{-1} and 1387 cm^{-1} which are characteristic of the symmetric and asymmetric stretching of the COOH group[26]. Again, we see the broad peak at 3400 cm^{-1} of the –OH groups and the peak for Fe-O is at 535 cm^{-1}.

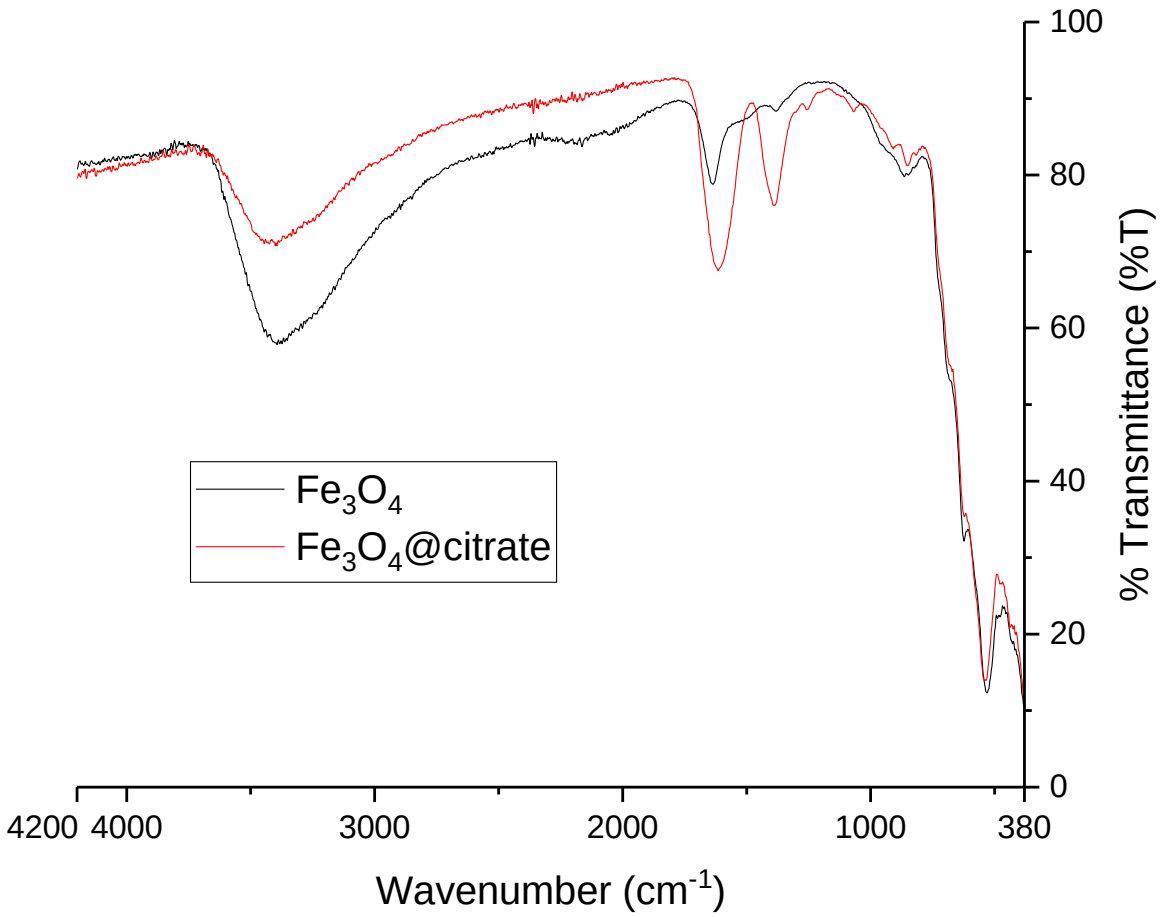


Figure 4-2: FTIR spectra of bare Fe_3O_4 and Fe_3O_4-citrate.

XRD analysis (Figure 4-3) of the Fe_3O_4@citrate particles showed no major change as would be expected with a high match for the reference pattern of magnetite (COD 900-5839). A Williamson-Hall plot for the peaks gave a crystallite size of 9.7 nm, which is in excellent agreement with the TEM images below (Figure 4-4). Rietveld analysis on the output using this matched reference pattern for the structure fit gave a cubic crystal lattice with a lattice of a = 8.35417 Å.

The FTIR and XRD data clearly indicate the formation of citrate-coated magnetite MNPs. The fact that in the XRD we only have a signal for Fe_3O_4 while the FTIR spectrum has changed to include the carboxylate groups indicates that a citrate coating is now on the surface of the Fe_3O_4 nanoparticles.

The TEM results (Figure 4-4) showed a monodisperse sample of particles with an average diameter in the range 14±1 nm. Particle size distributions were calculated from 100 particles

using ImageJ software (Figure A-3). There is no visible change in the core regarding size or morphology with the citrate functionalisation but the images show significant agglomeration.

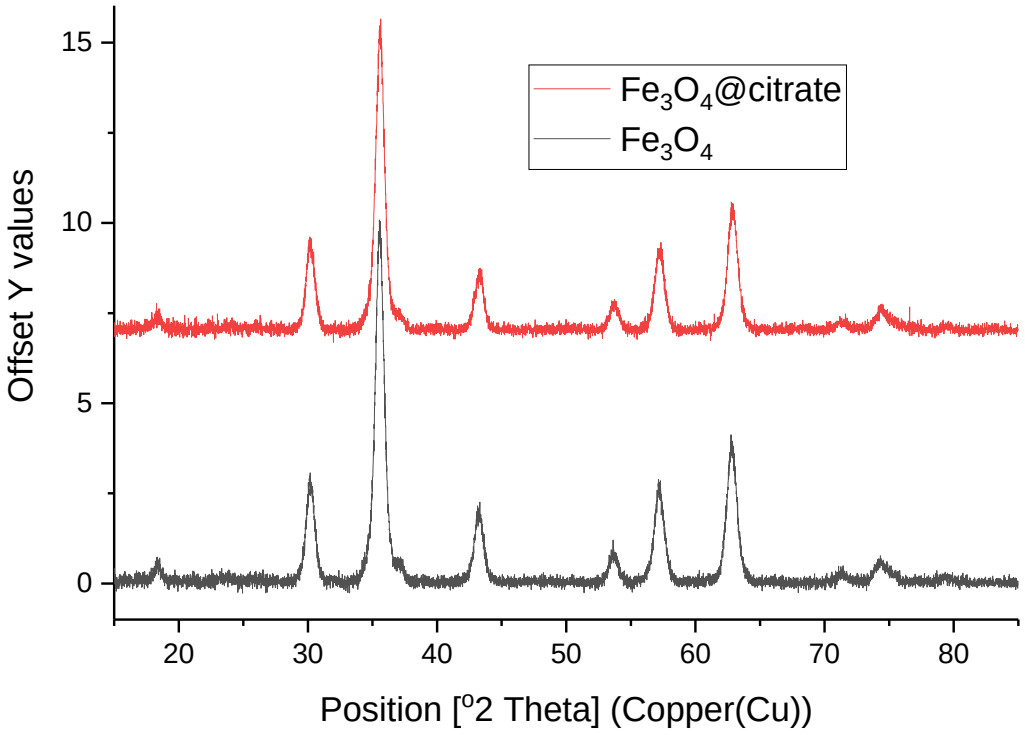


Figure 4-3: XRD pattern of Fe_3O_4 and Fe_3O_4@citrate.

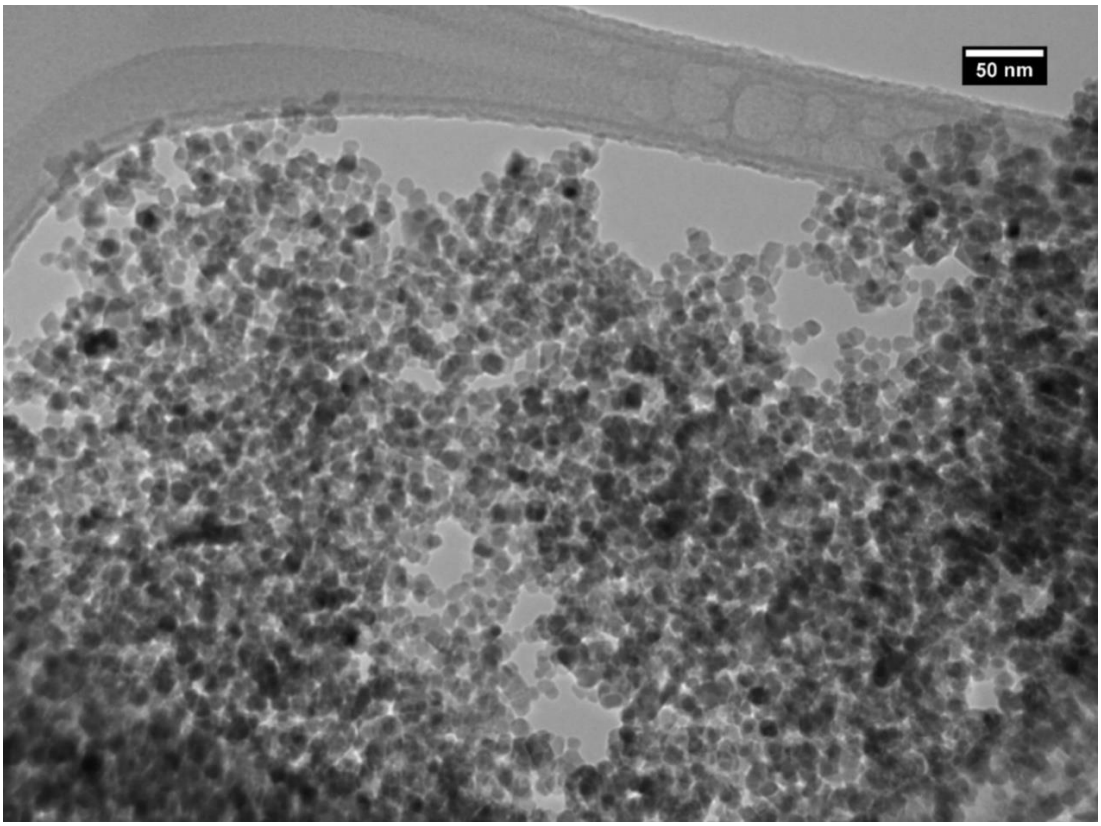


Figure 4-4: TEM image of Fe_3O_4@citrate.

The stability of the particles in solution can be quantified by a Zeta Potential of the product, which had a value of -36.7 mV at pH 6.7 in aqueous solution indicating that the nanoparticles should have high colloidal stability in water. Furthermore, as seen in the table below (Table 4-1), DLS measurements of the sample taken at intervals over several days show that Z-average does not increase so the particles are not agglomerating, while the count rate decreases by 27 % over 7 days, indicating that the particles are slowly precipitating out of solution. These result show that the citrate functionalised particles are more stable than the bare particles. The quality report for all measurements were good and repeats from the same batch gave consistent results.

The DLS result can be compared to the results for the bare MNP (Table 3-1) where we observe a reduction in count rate over hours, indicating that the particles are precipitating out of solution, while we also see the Z-average and PDI increases, which indicates the particles are agglomerated in the solution. For the citrate-stabilised particles, the Z-average is much smaller indicating well-separated individual particles while the Z-average and the PDI does not increase over time indicating no aggregation. In addition, the count rate decreases over 7 days but is still high indicating some precipitation but higher stability than the bare MNPs.

Table 4-1: DLS data of the citrate stabilised magnetite MNPs over several days.

Time	Z-Average	PDI	PDI Width	Count Rate
	d.nm		d.nm	kcps
0 hr	85.2	0.198	38	26893
1 hr	86.0	0.189	37	25256
2 hr	88.2	0.204	40	26408
3 hr	85.9	0.201	38	24313
5 hr	86.1	0.219	40	24709
24 hr	84.7	0.19	36.9	24807
2 days	83.3	0.134	30.5	24793
3 days	82.3	0.128	29.5	22206
5 days	85.0	0.141	31.9	20553
7 days	80.4	0.138	30	19660

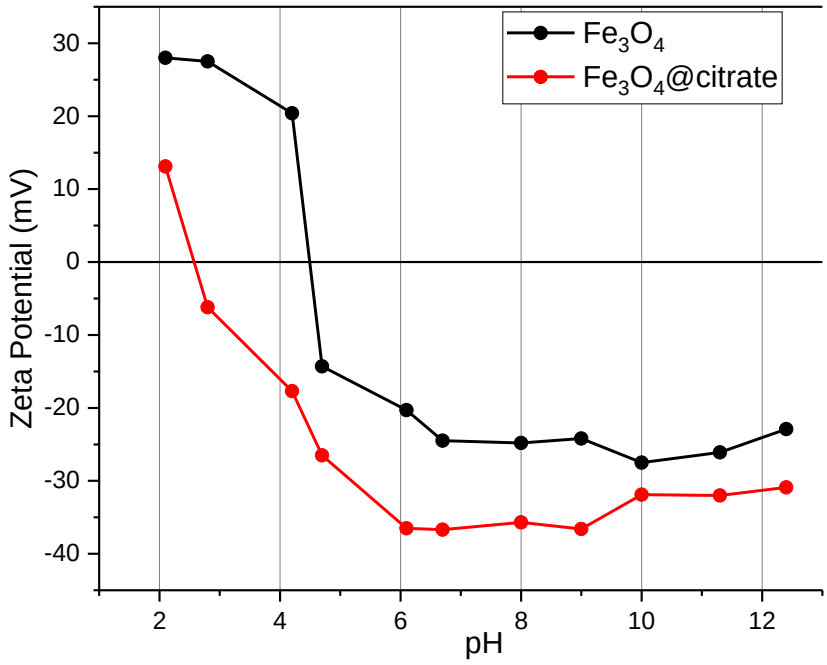


Figure 4-5: pH Dependence of Zeta Potential and PZC for Fe_3O_4 and Fe_3O_4@citrate MNPs.

Zeta potentials over the pH range 2.1-12.4 for the bare and citrate-stabilised particles indicate how the point of zero charge changes for the bare to the citrate particles. The citrate-stabilised particles now having a PZC of pH 2.6, similar to previous reports[27], while the bare particles have PZC of pH 4.5, as can be seen above (Figure 4-5). As with the bare MNP, for the pH2.1 sample the citrate-capped particles would dissolve in solution within 30 minutes but it was possible to get a measurement before this happened.

It can also be seen how at greater than pH 5 the citrate particles have a larger zeta potential with up to -36.6 mV at pH 9. Generally particles that have a zeta potential of greater than 30 mV or less than -30 mV they are considered to have moderate colloidal stability, although it should be noted that for pH 2.1 and 12.4, the conductivity was above 1 mS/cm which is considered the optimum value for better measurements[28]. Overall, it can be seen from the graph that that the citrate-stabilised particles have a higher magnitude zeta potential at neutral and mild pH values (pH 6-8). The Zeta potential for the bare particles has a value of -24.5 mV at pH 7 indicating that the bare particles would have less colloidal stability in water.

The procedure for the synthesis of Fe_3O_4@citrate as described in the experimental section (2.3.1) is a relatively facile method and as such does not lend itself to many practical modifications. One modification that was tried was using citric acid for the coating process and tetraethylammonia hydroxide for the neutralisation step. This method showed no major

differences in the TEM images, the FTIR results or the VSM analysis. DLS and Zeta potential measurements were not performed for the sample, but the particles showed good stability in solution. In one iteration of this with a hot solution of excess citric acid to which the magnetite was added, the MNPs dissolved in solution because of the acidic environment. This is why sodium citrate was considered as a better option in the final procedure.

Finally, we have also performed the synthesis by adding the citric acid in situ in the reaction mixture while coprecipitating out the Fe_3O_4 nanoparticles. This gave significantly smaller particles as seen below (Figure 4-6) of 6±3 nm while also giving a lower magnetisation value of 15.1 Am^2kg^{-1}.

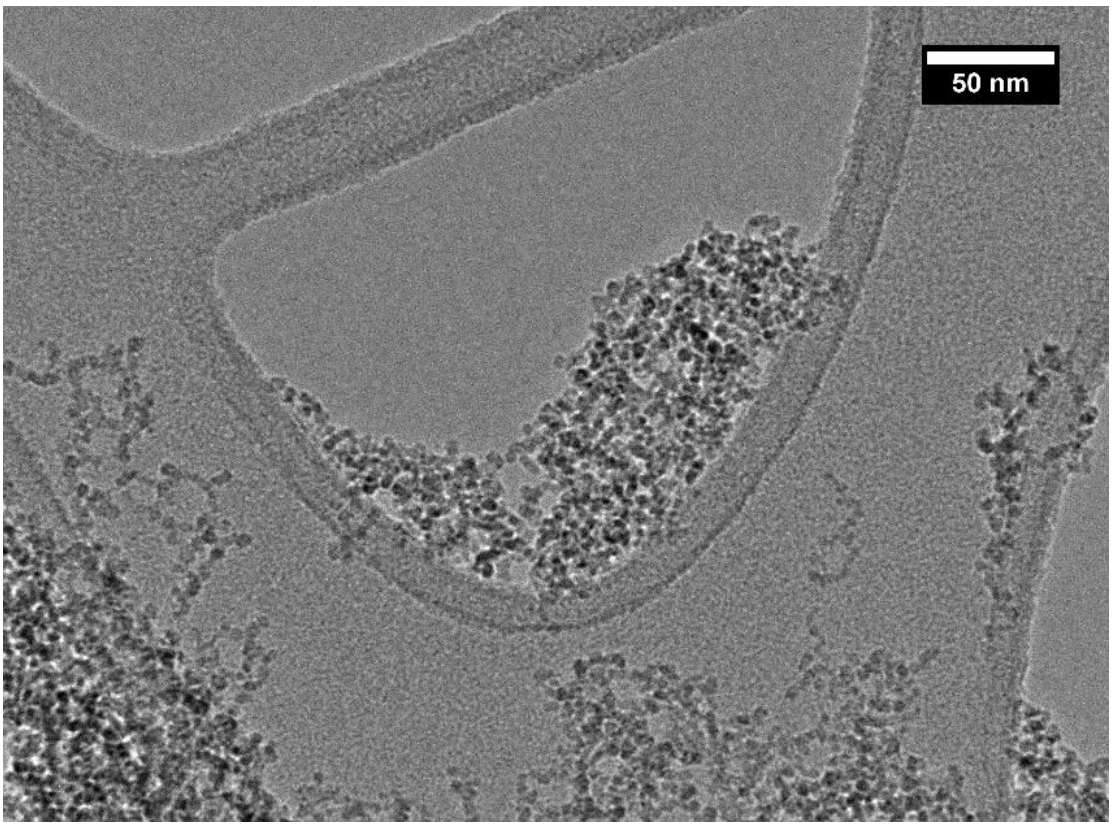


Figure 4-6: TEM image of Fe_3O_4@citrate MNPs when coprecipitated in situ with citric acid.

4.3.2 Preparation of Citrate Stabilised Manganese Ferrite MNPs

In a similar fashion, the larger manganese ferrite cores were also citrate stabilised using the same method as for the smaller magnetite cores. The procedure is described in the experimental section (2.3.2). This step was necessary for further functionalisation of these particles and so characterisation was done for these citrate-stabilised particles. Because of the

larger cores with less of a surface area to volume ratio, it should be theoretically possible to use less Na-citrate per unit mass but excess ensures complete coverage.

The citrate functionalised manganese ferrite MNPs were characterised by VSM, FTIR, XRD, TEM, DLS and Zeta Potential. VSM results as shown below (Figure 4-7) show a very small change in magnetisation from 59.9 Am^2kg^{-1} at 1 T for the bare particles to 56.5 Am^2kg^{-1} for the citrate functionalised particles. Again, a negligible change is expected as these core particles are much larger and so the citrate monolayer is expected to add approximately 2-5% mass of a non-magnetic material to the particle when a calculation is done assuming 1-2 binding sites on the citrate molecule, in conjunction with replacing any absorbed water on the surface.

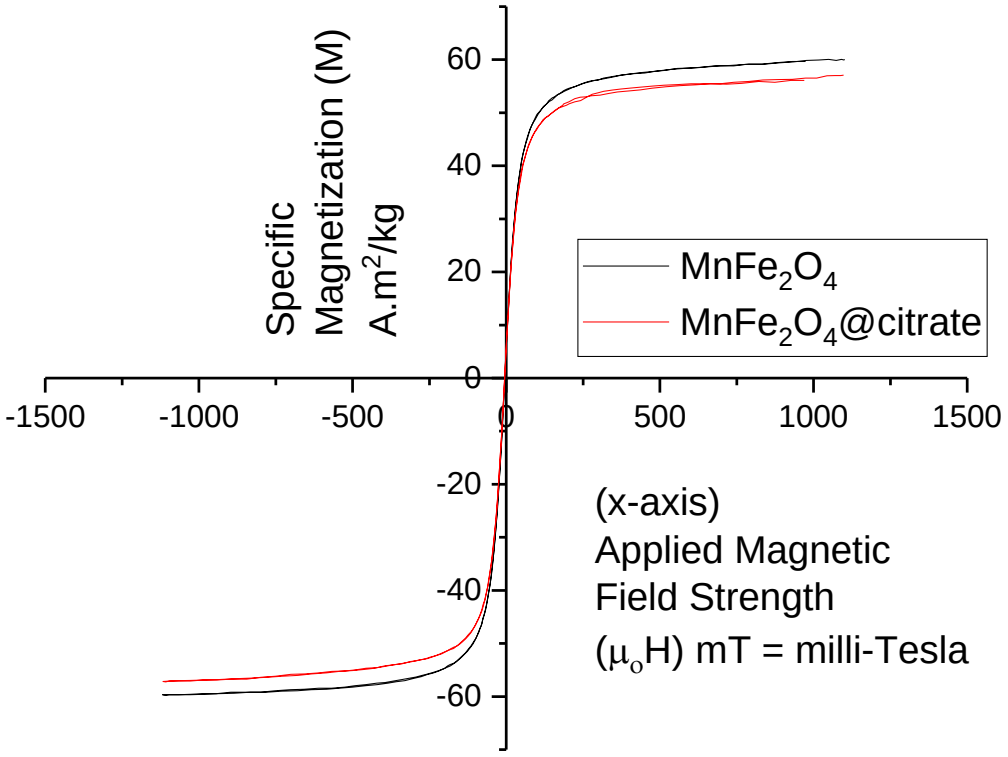


Figure 4-7: VSM curves of the citrate stabilised $MnFe_2O_4$ MNP from polyol reaction.

FTIR analysis as shown below (Figure 4-8) indicated that the MNPs now had citrate groups bound to the surface with the appearance of the peaks at 1579 cm^{-1} and 1392 cm^{-1} that are characteristic of the symmetric and asymmetric stretching of the COOH group. Again, we see the broad peak at 3400 cm^{-1} of the -OH groups and the peak for Fe-O is at 533 cm^{-1}.

XRD analysis (Figure 4-9) of the $MnFe_2O_4$@citrate particles again showed no major change as would be expected with a high match for manganese ferrite (COD 230-0619). A Williamson-Hall plot for the peaks gave a crystallite size of 7.9 nm as the particle is composed of coalesced

grains. The bare particle had a size of 8.0 nm indicating negligible changes have taken place. Rietveld analysis on the output using this reference pattern for the structure fit gave a cubic crystal lattice with a lattice of a = 8.40375 Å.

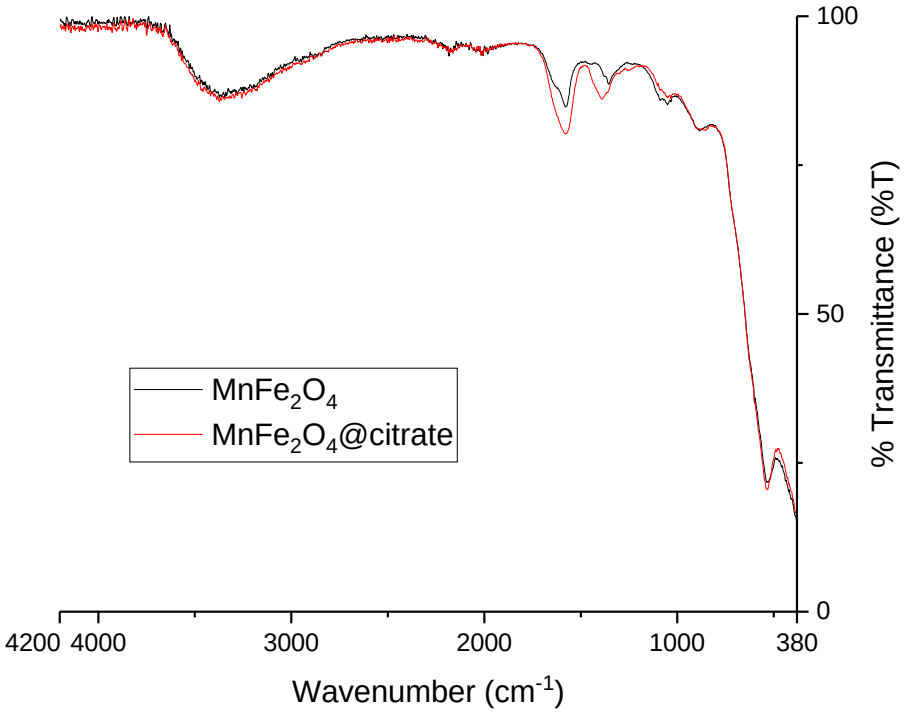


Figure 4-8: FTIR spectra of the bare and citrate stabilised $MnFe_2O_4$ MNPs.

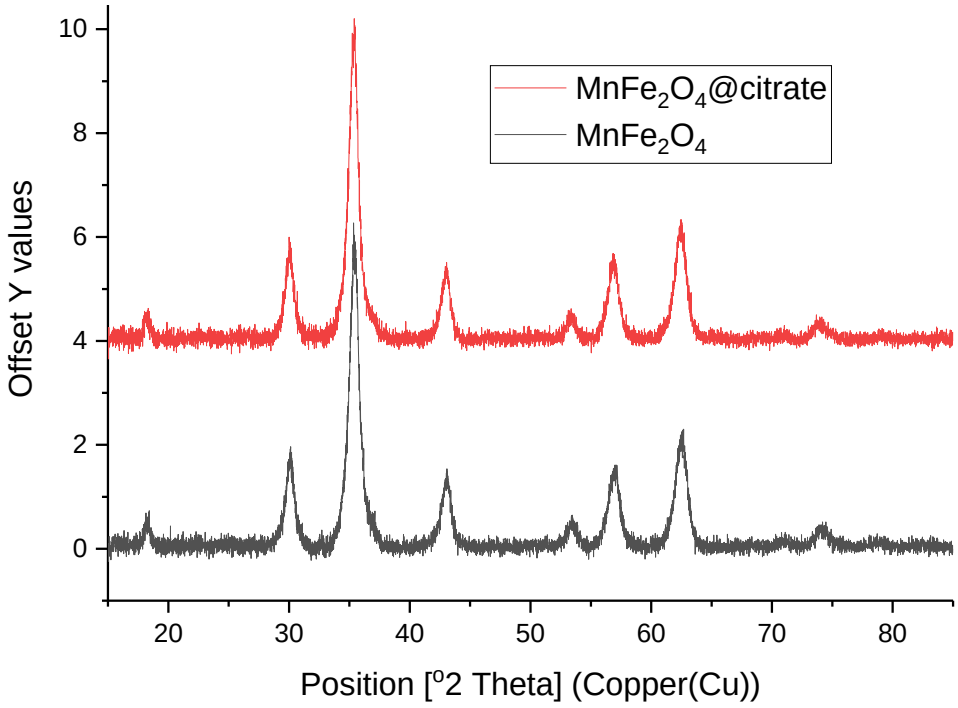


Figure 4-9: XRD patterns of $MnFe_2O_4$ and $MnFe_2O_4$@citrate MNPs.

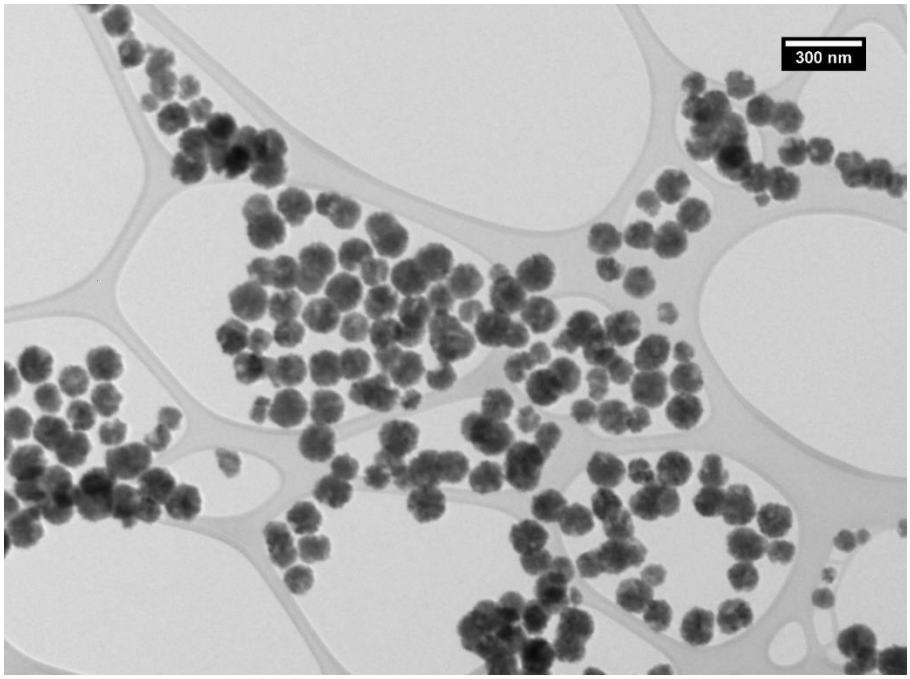


Figure 4-10: TEM image of the citrate stabilised $MnFe_2O_4$ particles.

The TEM results above (Figure 4-10) showed a relatively monodisperse sample of particles with an average diameter of 104±10 nm with no discernible change from the bare particles. This is to be expected as the citrate surface coating would not change the bulk particles and so there would be no visible morphological change observable using the TEM.

The DLS result below (Table 4-2) can be compared to the results for the bare MNPs (Table 3-3). Here we see the Z-average is relatively stable over 7 days where the PDI is low, indicating well-dispersed particles which are not agglomerated. The slight decrease in the Z-average and PDI over the analysis time will be because the larger particles in the ensemble precipitate out first thereby lowering both these values slightly. In the bare particles we seen the Z-average increased and that the PDI was much larger and grew over time. The count rate in the bare particles changes considerably over the 7 days with a 88 % decrease while here the count rate decreases by 64 %. Overall, by comparison with the DLS results of the unstabilised to the stabilised particles we can see the effect of the citrate coating in decreasing the agglomeration while also increasing their stability so to remain suspended in solution.

Zeta potentials over the pH ranges 2.1-12.4 for the bare and citrate stabilised particles indicate that the point of zero charge for both the bare and citrate particles, as can be seen below (Figure 4-11), are at pH 5.7 for the bare particles and at pH 3.0 for the citrate stabilised particles. For the pH 2.1 sample the $MnFe_2O_4$@citrate would dissolve in solution within 30

minutes but it was possible to get a measurement before this happened. The Zeta Potential of the citrate stabilised MNPs at pH 6.7 had a value of -34.8 mV, which indicates that the particles should be stable in solution. Stability is related to several factors including surface effects such as steric and electrostatic properties, size and concentration of particles and temperature[29]. The larger size of the particles would have lower colloidal stability.

Table 4-2: DLS data of the citrate stabilised $MnFe_2O_4$.

Time	Z-Average	PDI	PDI Width	Count Rate
	d.nm		d.nm	kcps
0 hr	184.1	0.082	52.8	78296
1 hr	187.5	0.062	46.9	77056
2 hr	181.9	0.043	37.9	80535
3 hr	182.9	0.086	53.8	72957
5 hr	184.4	0.093	56.3	74890
24 hr	180	0.072	48.1	72701
2 days	180.6	0.086	53.0	63751
3 days	175.6	0.071	46.9	48604
5 days	172.3	0.074	46.9	34912
7 days	176.3	0.044	36.9	28191

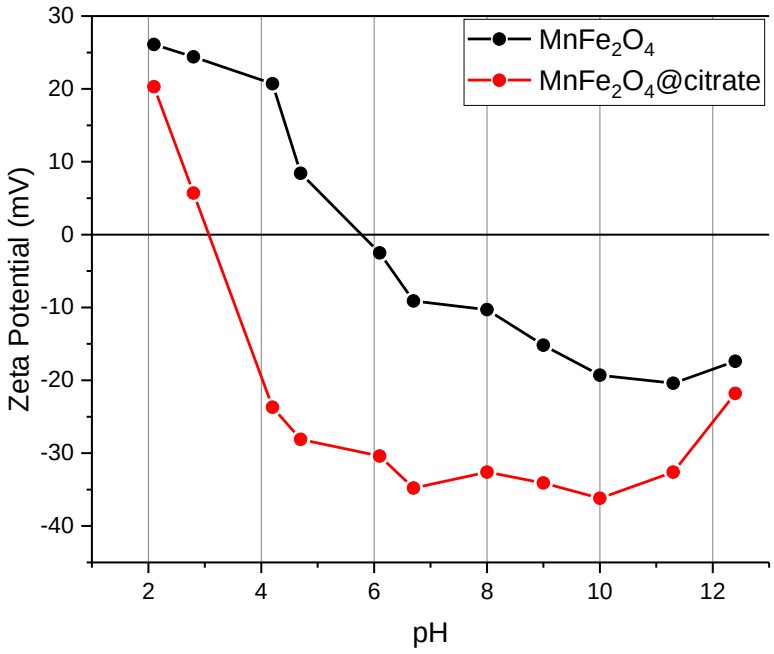


Figure 4-11: Zeta Potential and PZC for $MnFe_2O_4$ and $MnFe_2O_4$@citrate over pH range.

4.3.3 Preparation of SiO_2 Nanoparticles

With the intention of coating the MNPs with a layer of silica to both protect and stabilise the cores it was decided to synthesise some silica particles using the process that will be used to coat the magnetic nanoparticles. This was done to verify that the synthesis conditions and then this material could be characterised and used as reference for the characterisation of the core@shell particles. The preparation of silica particles have a long history since the seminal paper in 1968 by Stöber and Fink[14]. Much work has been done in elucidating the synthesis[30] and in finding methods to make SiO_2 particles[31][32]. Considering the previous works using the Stöber method and the reported reliability of the synthesis, our SiO_2 particles were made using this protocol as a guide as described in the experimental section (2.3.3).

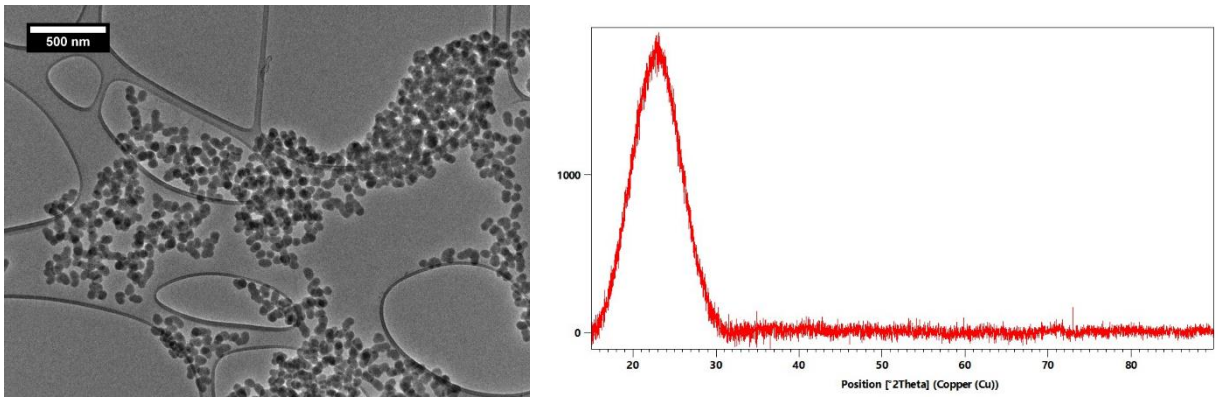


Figure 4-12: TEM image and XRD analysis of the SiO_2 nanoparticles.

The TEM images of the silica sample above (Figure 4-12) have shown spherical particles with sizes 80±30 nm with some aggregation and fusing. As a test run for the silica coating of the MNPs these results were promising showing that indeed the silica NPs are made according to the published literature with good reproducibility[30]. The XRD result above (Figure 4-12) showed a broad peak centred at 22 °2θ. A broad peak is common for an amorphous material which shows that an amorphous phase of SiO_2 was made[33].

FTIR analysis (Figure 4-16) of the particles showed the broad peak at 3400 cm^{-1} would be from absorbed –OH on the surface, a large peak at 1058 cm^{-1} for the SiO_2 stretch and another peak at 441 cm^{-1} corresponding to the Si-O-Si bending mode[34].

DLS results below (Table 4-3) showed a very stable monodisperse sample with stable Z-average and PDI results. The increase in count rate and then reduction was to do with the

unusual settling of the particles in the solution where they did not precipitate out but concentrated at the bottom of the cuvette as seen below (Figure 4-13).

Table 4-3: DLS results for the SiO_2 NPs.

Time	Z-Average	PDI	PDI Width	Count Rate
	d.nm		d.nm	kcps
0 hr	127.7	0.088	37.8	72685
1 hr	126.4	0.093	38.5	74889
2 hr	126	0.087	37.0	74893
3 hr	125.3	0.088	37.0	76816
5 hr	125.4	0.081	35.6	79485
24 hr	128.9	0.092	39.2	82886
2 days	127.6	0.075	34.8	81415
3 days	127.5	0.096	39.5	83422
5 days	127.6	0.07	33.8	93144
7 days	126.9	0.089	37.8	57751

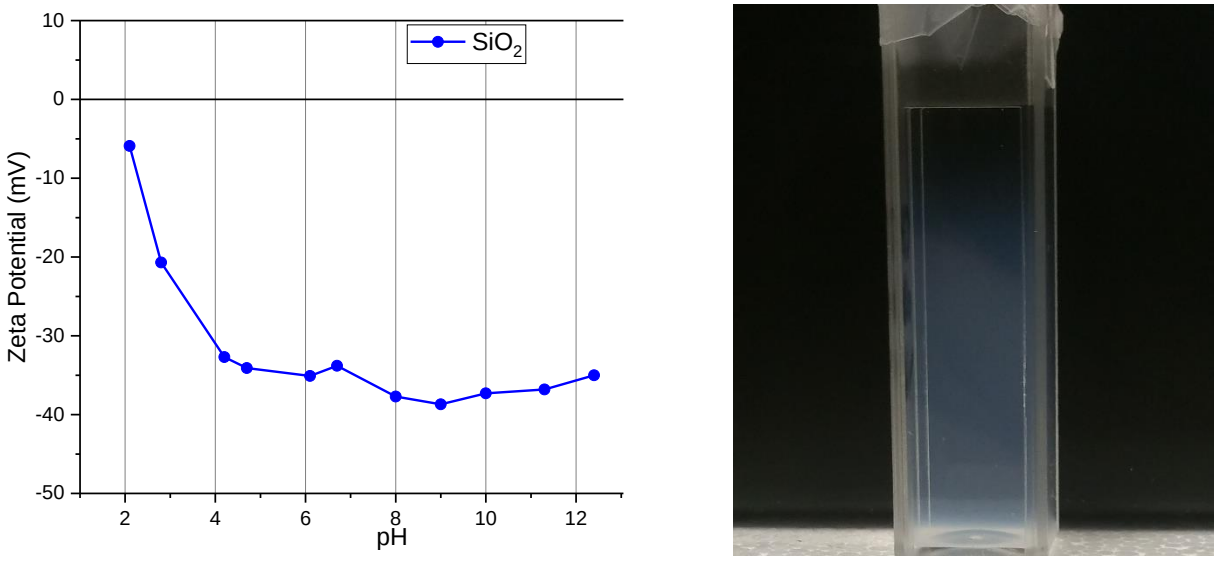


Figure 4-13: Zeta Potential behaviour over pH 2-12 for SiO_2 NPs and settling behaviour of SiO_2 solution.

The zeta potential (Figure 4-13) showed very stable NPs over a large pH range with a surface charge of -33.8 mV at pH 6.7. These characterisations will aid in the studies of the MNP@SiO_2 nanostructures as they are characterised and discussed in the following sections.

4.3.4 Preparation of SiO_2 shell on Magnetite Core MNPs

Coating of the citrate stabilised magnetic cores with silica shell was performed using the procedure described in the experimental section (2.3.4). Silica coating is well established but it was a necessary step for further functionalisation so characterisation was performed here with some variation to examine control of the shell thickness. The literature contains several modifications of this method [17][25], but we used a basic procedure that was optimised by us which is described in the experimental. The procedure involved stirring citrate-stabilised magnetite in an ethanol-water-ammonia solution at RT in the presence of tetraethyl orthosilicate (TEOS) to effect the precipitation of the silica (SiO_2), following a previously published method[3] which built on Stöbers work[14].

The amount of TEOS necessary for a shell of certain thickness could be calculated with reasonable accuracy prior to the reaction. The process for calculating the amount of shell material is as follows. Knowing the yields of the reactions for both core and shell (from previous reactions), the size of the core (from TEM images), the density of the core (from references), the amount of the core put into the reaction, the density of the shell material (from references), and the molar masses of the materials and precursors.

Firstly, the ratio of the volume of the core to the volume of the shell for one MNP is calculated

$$\frac{\left(\frac{core\ diameter}{2} + shell\ thickness\right)^3 - \left(\frac{core\ diameter}{2}\right)^3}{\left(\frac{core\ diameter}{2}\right)^3} = volume\ shell{:}\,core$$

From this ratio the ratio of the mass of the shell to the mass of the MNP is calculated knowing the densities of each material

$$volume\ shell{:}\,core\ \left(\frac{density\ of\ shell\ material}{density\ of\ core\ material}\right) = mass\ shell{:}\,core$$

From this, we can calculate the ratio of the number of moles of shell to core

$$mass\ shell{:}\,core\ \left(\frac{molar\ mass\ of\ core\ material}{molar\ mass\ of\ shell\ material}\right) = moles\ of\ shell{:}\,core$$

Now if we know the mass of core material as precursor in the reaction we know the number of moles and so we now know the number of moles of shell material from the above ratio.

Knowing the number of moles of shell material, we can calculate the amount of precursors from the balanced chemical reaction equation and the known yield of the reaction to produce the shell. It was found that the shell was always bigger, as observed by TEM, than the calculated value. In addition, some variations to the basic procedure were done with a view to understanding the process. The silica-coated magnetite were characterised by TEM, VSM, FTIR, XRD, DLS and Zeta Potential measurements.

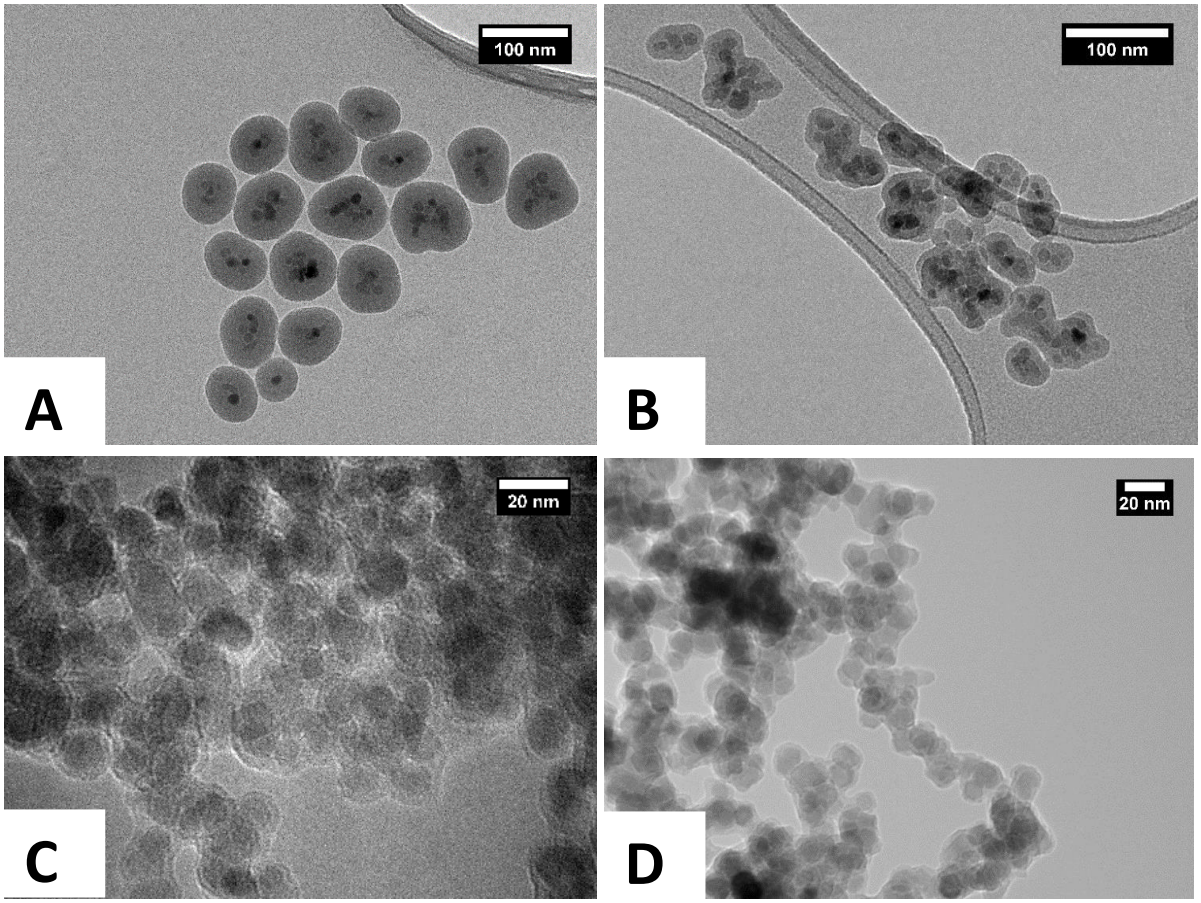


Figure 4-14: TEM images of Fe_3O_4@SiO_2 samples, (A) sample A, (B) sample B, (C) sample C, (D) sample D.

Using the calculation method above different amounts of TEOS were added to the reaction to observe the outcome of the reaction, with shell thickness and magnetisation being the primary characteristics of interest. TEOS amounts for a calculated shell of 15, 10, 5 and 1 nm were added to the reaction with the citrate-capped magnetite core particles and these were labelled samples **A**, **B**, **C** and **D** respectively. This gave particles with a shell of approximately 20, 13, 7 and 3 nm for the samples **A**, **B**, **C** and **D** as observed by TEM, as can be seen above (Figure 4-14). The addition of a shell of non-magnetic material reduced the magnetisation in the samples as the shell thickness increased, as expected. For the samples **A**, **B**, **C** and **D** the

magnetisations were 8.5, 15.4, 23.2 and 44.9 Am^2kg^{-1} respectively. For comparison, the VSM of sample **A** is shown against the VSM of the bare Fe_3O_4 and the Fe_3O_4@citrate below (Figure 4-15). The graphs clearly show the reduction in magnetisation. The reduction in magnetisation, the small size of the particles and the SiO_2 shell resulted in a very stable nanoparticle suspension and the extraction from solution with a neodymium magnet was very slow and took more than 24 hours, even for the particles with the thinnest shell.

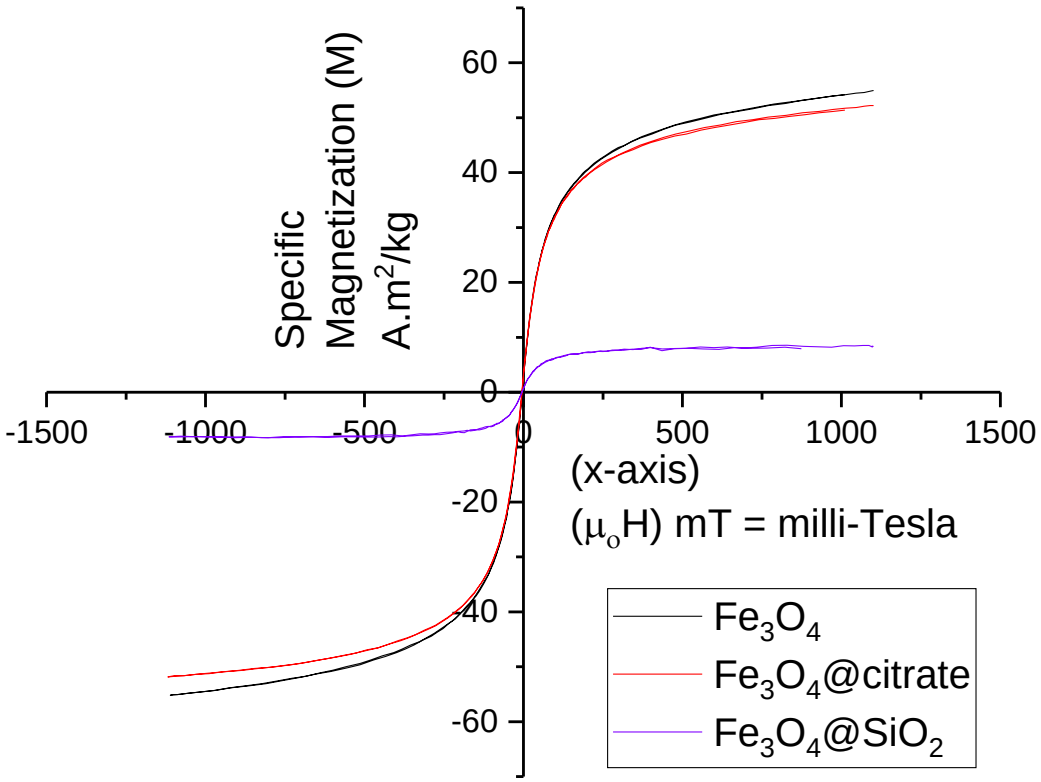


Figure 4-15: VSM curves of Fe_3O_4@SiO_2 MNP sample A compared with the bare and citrate-capped MNPs.

As can be seen in the image above (Figure 4-14) the particles with the thickest silica shell, sample **A**, are approximately 62 ± 15 nm in diameter with a shell of approximately 20 nm with the sample being relatively monodisperse. Size distribution and shell thicknesses were calculated for 100 particles using ImageJ (Figure A-5). This sample, sample **A**, showed little agglomeration and no separate pure SiO_2 particles present. Some particles with a single magnetic core were also observed in the sample but most of the nanoparticles were multicore. Thus, further work has to be done to optimise the synthesis in order to produce core@shell nanostructures with a single core. It was found that as we tried to reduce the thickness of the silica shell so as the have better magnetisation the particles began to agglomerate more with

no individual particles found in samples **C** and **D**. The results of these explorations are summarised in the table below (Table 4-4).

Table 4-4: Table with summary of results for the samples A, B, C and D of Fe_3O_4@SiO_2.

Sample	Calculated shell (nm)	TEOS : MNP Molar Ratio	Shell from TEM (nm)	VSM (Am^2kg^{-1})	Comment on synthesis outcome
A	15	50 : 1	20	8.5	No agglomeration; Multi-core particles
B	10	23 : 1	13	15.4	Some agglomeration; Multi-core particles
C	5	7 : 1	7	23.2	Major agglomeration; Single-core particles
D	1	1 : 1	3	44.9	Major agglomeration; Single-core particles

The FTIR results for the bare, citrate functionalised, sample **A** of the silica coated MNPs and silica nanoparticles are presented below (Figure 4-16) to compare the nanoparticles and see the changes over the course of the functionalisation. FTIR analysis indicated that the MNP now had silica bound to the surface with the appearance of the strong peaks at 1016 cm^{-1} that is characteristic for the Si-O bond. The broad peak at 3400 cm^{-1} for the -OH groups is still visible now coming from Si-OH terminal groups on the surface. The peak for Fe-O is not visible in the spectra indicating that they are occluded by the SiO_2 spectra. The citrate peaks at approximately 1700 cm^{-1} are not visible either because they are occluded or more likely because they were replaced at the surface by the SiO_2.

XRD analysis (Figure 4-17) of sample **A** of the Fe_3O_4@SiO_2 particles showed the appearance of a broad peak centred at 22 °2θ for the SiO_2 shell. This type of broad peak is common for amorphous material indicating the SiO_2 shell is amorphous[35]. For the other samples (sample B, C and D) with the thinner shells, the broad peak was less visible as would be expected when less of the material is in the sample. The peaks for the Fe_3O_4 core are still visible in the same positions giving a high match for the reference pattern of magnetite (COD 900-2675). A Williamson-Hall plot for the peaks gave a crystallite size of 7.0 nm, which is smaller than the citrate stabilised core used in the synthesis (9.7 nm). The peak broadening is used to calculate the crystallite size while the peak positions are used to verify the phase of the material.

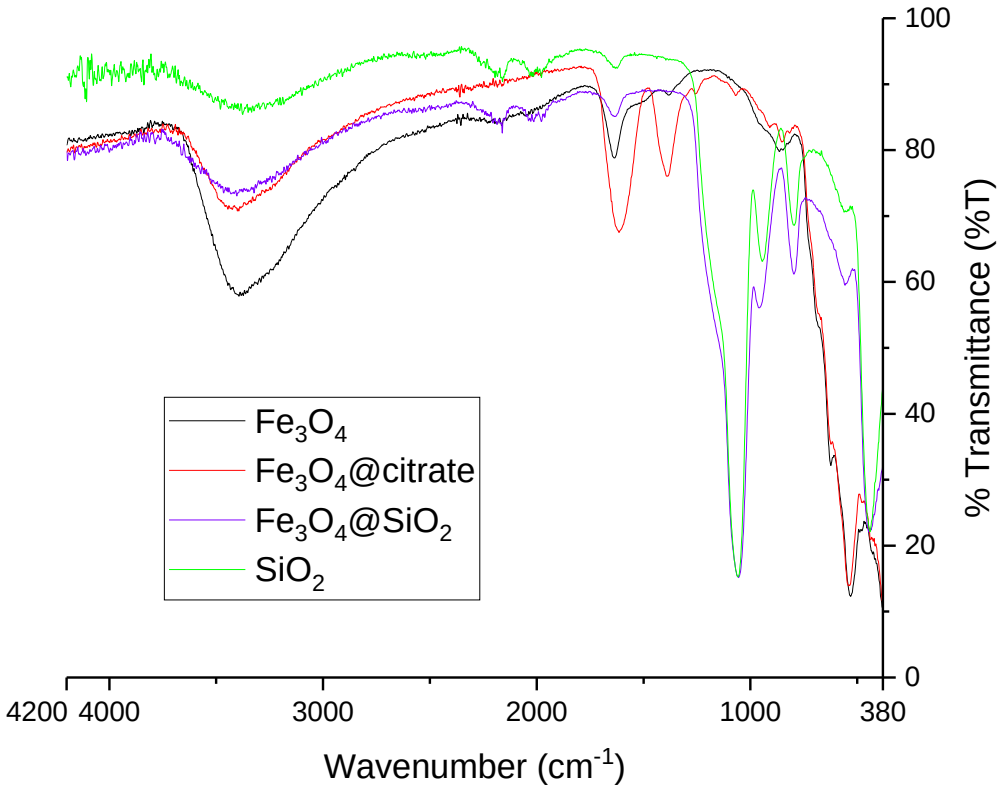


Figure 4-16: FTIR spectra of various nanoparticles for comparison.

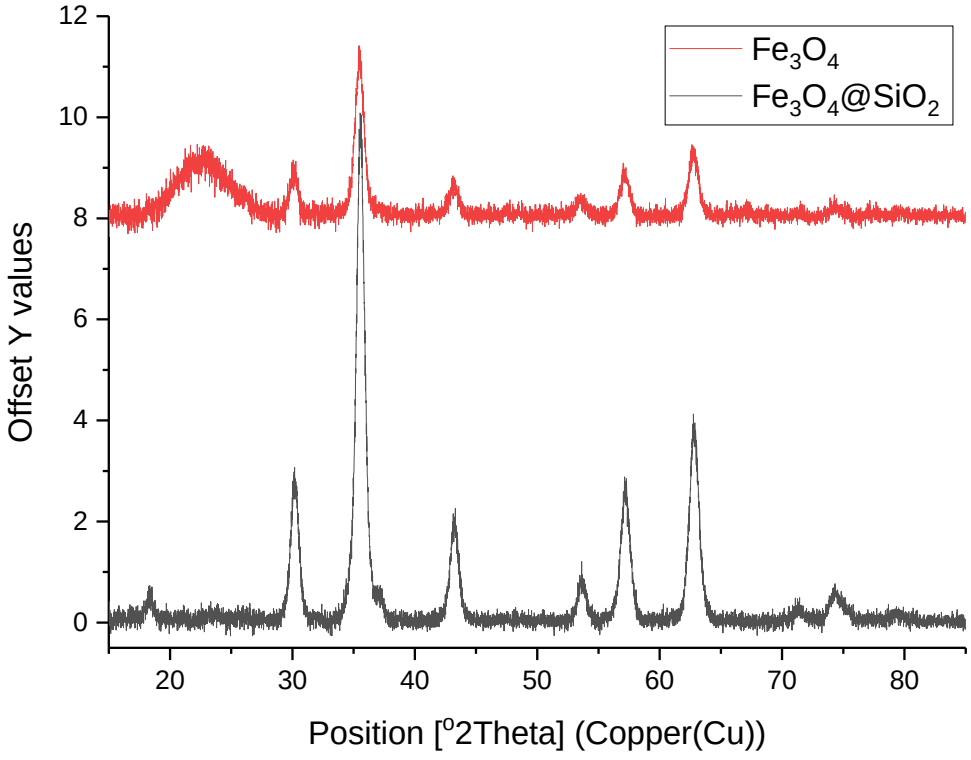


Figure 4-17: XRD patterns of Fe_3O_4@SiO_2.

The DLS (Table 4-5) of sample **A** of the silica-coated magnetite MNPs showed that the Z-average and PDI do not vary significantly over 7 days. This indicates no aggregation, while the

count rate decreases by 17 % over the course of 7 days but to a lesser extent than the citrate stabilised particles indicating that they are more stable in solution. The stability in solution was evidenced when trying to extract them from solution using a magnet, with all 4 samples taking over 24 hours to extract while sample **A**, with the thickest shell, took 48 hours to extract. However, the addition of a few drops of NaCl solution (4 M) caused destabilisation of the suspension and then the particles could be extracted with a magnet in under 3 hours.

Table 4-5: DLS data for sample 1 of the Fe_3O_4@SiO_2 MNPs over several days.

Time	Z-Average	PDI	PDI Width	Count Rate
	d.nm		d.nm	kcps
0 hr	124.4	0.083	35.8	22808
1 hr	124.7	0.086	36.5	22005
2 hr	123.7	0.082	35.4	21853
3 hr	125.4	0.112	42.0	21853
5 hr	124.7	0.097	38.9	21938
24 hr	124.1	0.111	41.3	22059
2 days	125.3	0.068	32.76	21903.5
3 days	124.1	0.069	32.5	20340
5 days	120.2	0.058	28.8	19726
7 days	120.2	0.077	30.3	19001

Zeta potentials over the pH ranges 2.1-12.4 for the bare, citrate stabilised and silica-coated particles can be compared below (Figure 4-18). The PZC for the silica coated MNPs is pH 2.2 which is similar to previous reported results[25]. The stability of the particles over the pH ranges is similar to the citrate particles. The Zeta potential value at pH 6.7 for the silica coated MNPs is -38.3 mV. The particles have good stability over a large pH range, as the Zeta potential is greater than -30 mV from pH 4.4 to 12.1. A negative zeta potential means the surface of the particle has a negative charge[11]. At pH 2.1 the silica particles did not dissolve showing that the silica shell protects the core, whereas the bare and citrate-capped particles did dissolve at this pH as discussed previously.

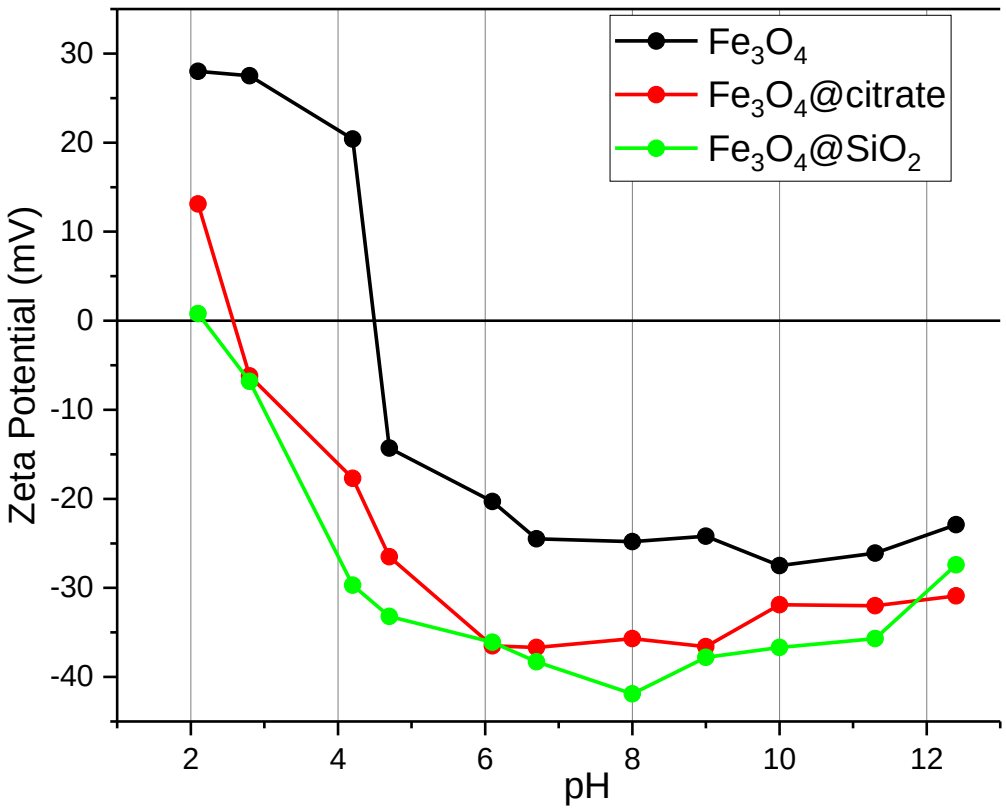


Figure 4-18: Zeta Potential for Fe_3O_4@SiO_2 nanoparticles over pH range 2.1-12.4.

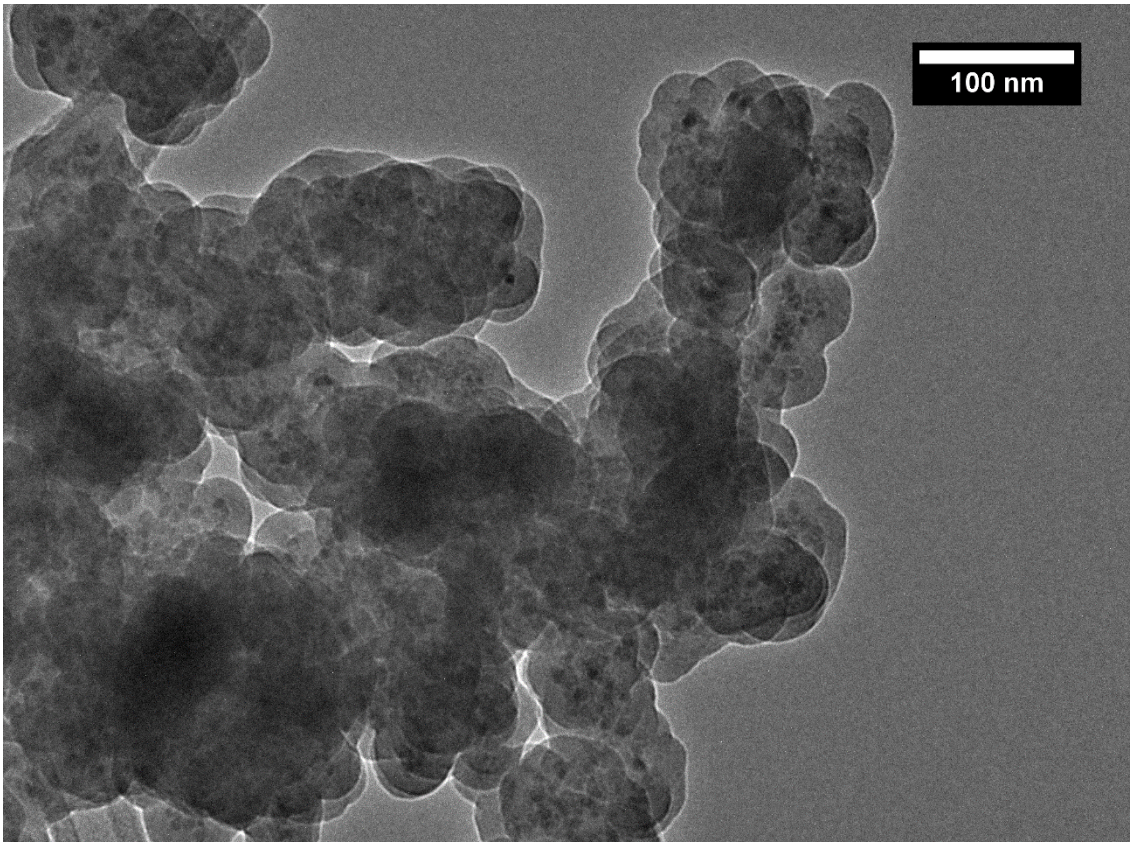


Figure 4-19: TEM images of silica coated Fe_3O_4 MNPs produced using bare Fe_3O_4 as the precursor.

One variation that was done was using the bare magnetite particles in the described protocol instead of the citrate-stabilised particles. This gave large agglomerated particles of the core shell structures as can be seen above (Figure 4-19). This was not appropriate for our applications, as it did not give individual particles. The VSM measurements have shown a quite low magnetisation value of 10 Am^2kg^{-1}. The initial shell thickness calculated in this case was for 10 nm while in fact the resulting shell here can be seen to be much thicker in the TEM images. Interestingly, a DLS result for these particles gave a Z-average 518.6 nm immediately after synthesis, which corresponds to the TEM image. This shows the need for stabilisation of the particles prior to further functionalisation if our target to produce discreet individual silica coated magnetic nanoparticles.

Another variation involved the use of sonication in an ice bath[36]. This procedure was found to be more inconsistent than with the procedure described in the experimental section and after several tries was abandoned because of the poor reproducibility of the results. Although in some cases a shell would form, repeating the exact procedure may not form any shell. Many times no visible shell was formed. Several attempts were tried to get a good consistent result but the variations between batches were considerable. The next most common method from a literature review was a reverse micelle procedure[37]. This reverse micelle procedure was not used in our work as the procedure following Stöbers work[14] was found to give suitable results.

As an endnote on this section, the protocol described in the experimental section was the most suitable procedure to date. However, it was found that there were some reproducibility issues with this procedure, where sometimes agglomeration would result. Other times separate small SiO_2 particles would form and then other times the shell deviated significantly from the calculated thickness. Further work would need to be done for a more complete analysis to establish all factors that result in deviations to be able to have consistent reproducibility. It can be concluded that stabilisation of the particles before SiO_2 coating, with mechanical stirring, while following Stöbers method for solution based SiO_2 NP synthesis are necessary to produce good quality silica coated magnetite nanostructures as these explorations here have shown.

4.3.5 Preparation of SiO_2 shell on Manganese Ferrite Core MNPs

The larger manganese ferrite MNPs were also coated with silica using the procedure described in the experimental section (2.3.5). Again, an initial calculation based on the size of the particles and the density of silica using the method describe earlier for the Fe_3O_4@SiO_2 could be performed to estimate the amount of TEOS for a shell of a certain thickness. These calculations had good correlation with the produced shell according to TEM measurements. It was found that the silica coating of the larger polyol MNPs gave better and more consistent results than the smaller MNPs produce by coprecipitation. The method for coating the $MnFe_2O_4$ polyol particle with silica involved as similar method as with the Fe_3O_4 particles, where the citrate-capped manganese ferrite were mechanically stirred in an ethanol-water-ammonia solution at RT in the presence of tetraethyl orthosilicate (TEOS) to effect the precipitation of the silica (SiO_2), following a previous work[3]. In addition, much was learned with the earlier work producing the silica-coated magnetite that was useful and was applied here. The silica coated manganese ferrite was characterised by TEM, VSM, FTIR, XRD, DLS and Zeta potential measurements.

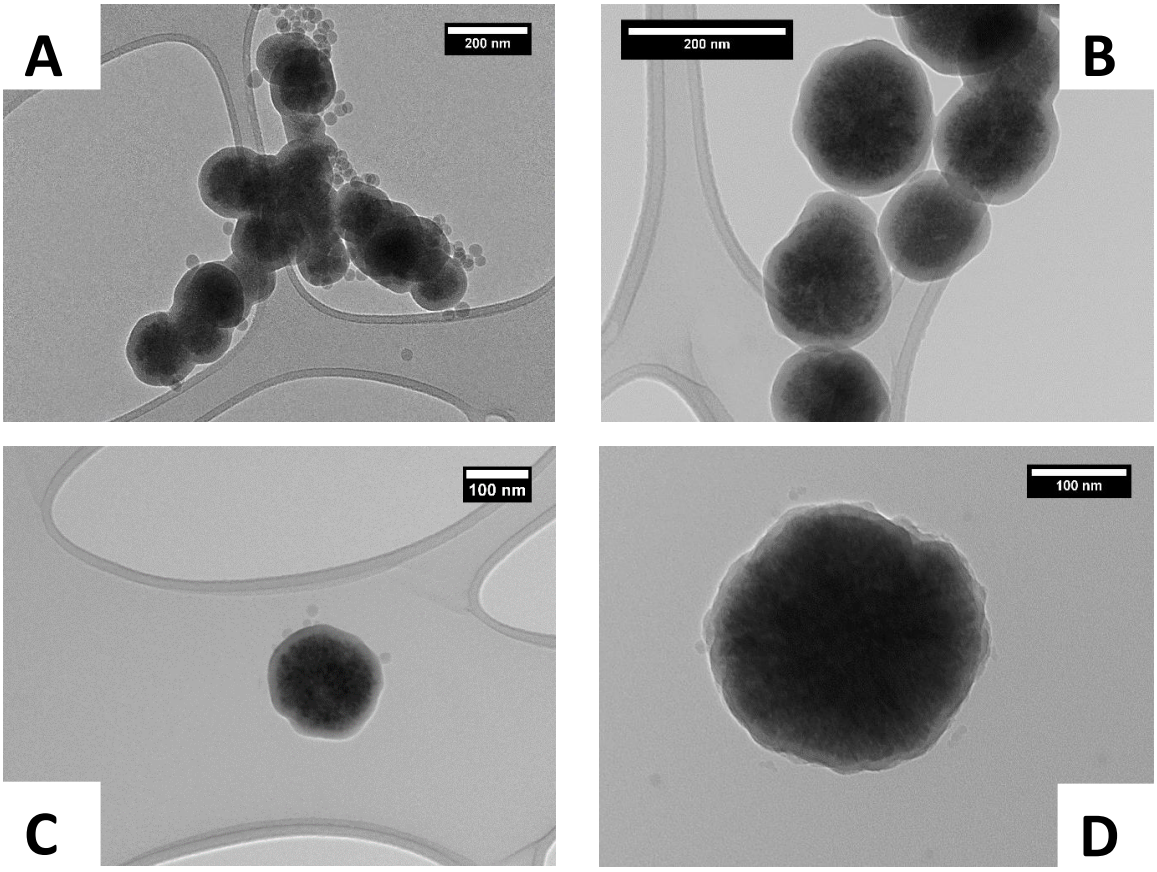


Figure 4-20: TEM images of $MnFe_2O_4$@SiO_2 (A) sample A, (B) sample B, (C) sample C, (D) sample D.

Using the calculation method described previously, different amounts of TEOS were added to the reaction mixture containing the citrate-capped manganese ferrite nanoparticles to produce silica shells of different thickness. The TEOS amounts added were for calculated shells of 20, 15, 10 and 5 nm for sample **A**, sample **B**, sample **C** and sample **D** respectively. This this produces shell of 30, 20, 13 and 8 nm approximately for the respective samples, as can be seen in the TEM images above (Figure 4-20). As with the smaller coprecipitated magnetite cores, the silica shell was always larger than the calculated values on the manganese ferrite cores. As can be seen in the image above (Figure 4-20) the particles with the thinest silica shell, sample **D**, are approximately 170 ± 20 nm in diameter with a shell of approximately 20 nm with the sample being relatively monodisperse. Size distribution and shell thicknesses were calculated for 100 particles using ImageJ (Figure A-6). One outcome that was observed was that there was not as much aggregation, especially with a thinner shell when compared with the smaller silica-coated magnetite MNPs. This could be related to the larger size where for the smaller particles the larger surface energy would cause more aggregation as the system tries to lower that energy. The larger particles have a smaller surface area to volume ratio and so a lower surface energy, so effects like aggregation and fusing would be reduced.

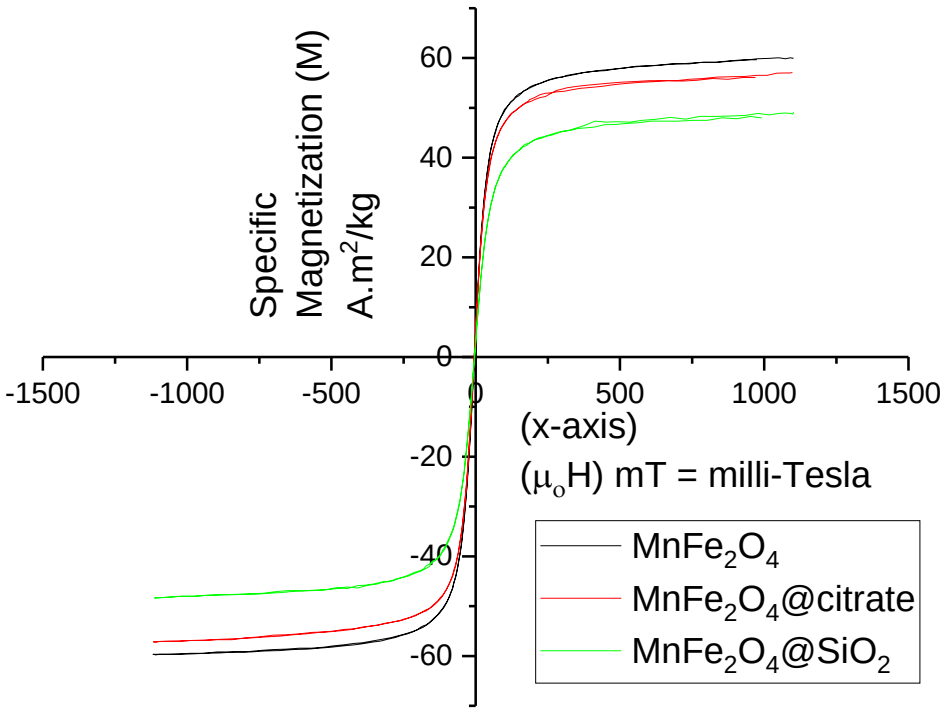


Figure 4-21: VSM curves of $MnFe_2O_4$@SiO_2 Sample D compared with the bare and citrate-stabilised core.

The reduction in magnetisation was not as drastic as with the silica-coated magnetite previously. There was some reduction in magnetisation because of the addition of a non-magnetic shell material but as the magnetic cores here were bigger, the majority of the mass of the final particle was from the magnetic core and so the magnetisation change was less. As can be seen in the graph above (Figure 4-21), for sample **D** with the thinnest silica shell, the magnetisation of the sample is 49.2 Am^2kg^{-1}. The graph shows the magnetisation of the core particle and the citrate-coated core for comparison. The magnetisation of the 4 samples with different thickness of silica shell were 23.0, 32.3, 40.2 and 49.2 Am^2kg^{-1} for samples **A**, **B**, **C** and **D** respectively. In general, there was less agglomeration in all the samples, even with a thin shell. The samples with higher molar ratios of TEOS:MNP showed some separate SiO_2 particles. A table outlining these results can be seen below (Table 4-6).

Table 4-6: Table with summary of results for the samples A, B, C and D of $MnFe_2O_4$@SiO_2.

Sample	Calculated shell (nm)	TEOS : MNP Molar Ratio	Shell from TEM (nm)	VSM (Am^2kg^{-1})	Comment on synthesis outcome
A	20	3.5 : 1	30	23.0	Some agglomeration; Separate SiO_2 particles
B	15	2.4 : 1	20	32.3	Less agglomeration; No SiO_2 particles
C	10	1.5 : 1	13	40.2	No agglomeration; Some SiO_2 particles
D	5	0.7 : 1	8	49.2	No agglomeration; No SiO_2 particles

FTIR analysis below (Figure 4-22) for sample **D** indicated that the MNP now had silica bound to the surface with the appearance of the strong peaks at 1016 cm^{-1} that is characteristic for the Si-O bond. The broad peak at 3400 cm^{-1} for the -OH groups on the surface of the silica is still visible. The peak for Fe-O is at 543 cm^{-1} as expected. The graphs below shows the FTIR results for the bare, citrate functionalised and silica coated particles where the change as the particle is functionalised can clearly be seen. The ferrite peak is visible, not occluded by the SiO_2 spectrum because the ferrite makes up a larger percentage of the particle in these core@shell structures compared with the coprecipitated magnetite core@shell structures.

XRD analysis (Figure 4-23) of sample **D** for the $MnFe_3O_2$@SiO_2 particles showed no major changes from the citrate stabilised cores with a high match for the reference pattern of manganese ferrite (COD 230-0619). The amorphous SiO_2 shell did not show up in the XRD because as most of the structure is made up of the ferrite core and the background calculation by the software would absorb small broad peaks. A Williamson-Hall plot gave a crystallite size of 13.4 nm, which is larger than the citrate stabilised cores used in the synthesis of 7.9 nm.

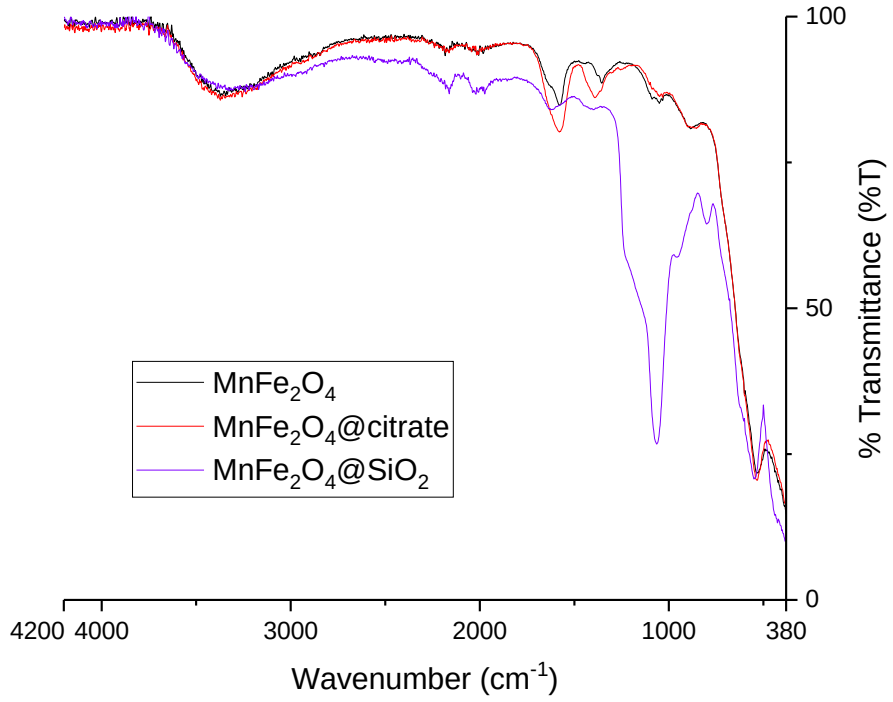


Figure 4-22: FTIR spectra of $MnFe_2O_4$ based nanostructures at various stages of synthesis.

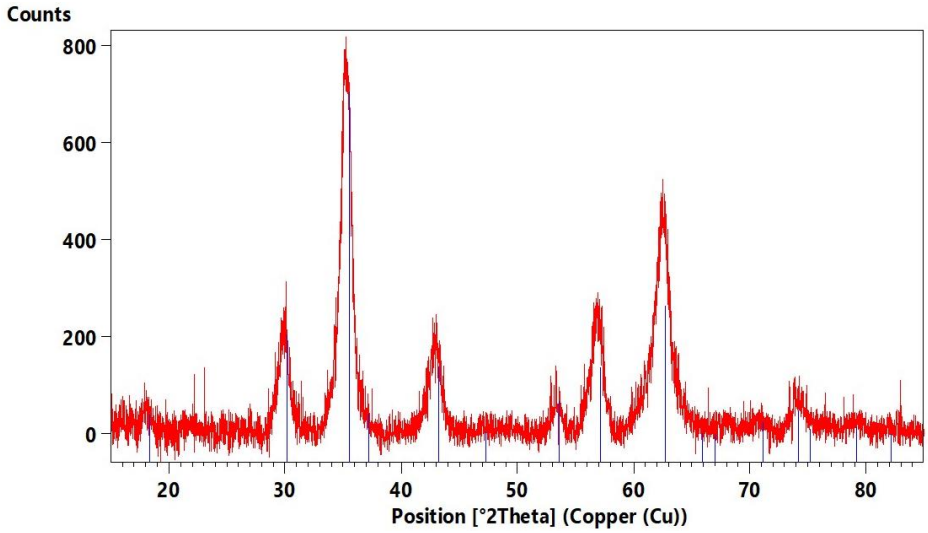


Figure 4-23: XRD pattern of $MnFe_2O_4$@SiO_2 nanoparticles.

As can be seen in the table below (Table 4-7), DLS analysis over 7 days showed that the particles are not agglomerating in solution as the Z-average and PDI do not vary considerably. However, the particles are precipitating out of solution slowly with a 65 % decrease over 7 days of the count rate. This is comparable with the citrate-stabilised particles (64 %) and the bare particles (88 %). These particles could be readily extracted in under 2 hours by magnet from solution and redispersed with sonication back into solution.

Table 4-7: DLS data for the $MnFe_2O_4$@SiO_2 MNPs over several days.

Time	Z-Average	PDI	PDI Width	Count Rate
	d.nm		d.nm	kcps
0 hr	221.8	0.023	33.8	50651
1 hr	219.0	0.028	36.3	50098
2 hr	221.4	0.065	56.5	49719
3 hr	221.2	0.054	51.6	49009
5 hr	221.3	0.007	18.9	48675
24 hr	224.3	0.002	10.0	48329
2 days	217.4	0.003	11.2	59226
3 days	218.5	0.056	51.6	59780
5 days	210.7	0.008	18.4	44100
7 days	212.9	0.03	37.0	17870

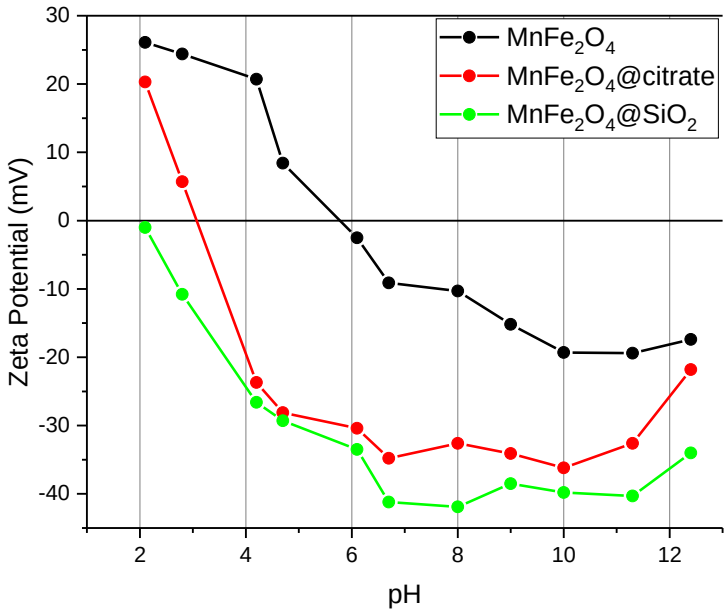


Figure 4-24: Zeta potential behaviour over 2.1-12.4 pH range for various MNPs.

The zeta potential results over the pH range 2.1-12.4 for the bare, citrate stabilised and silica coated particles are shown in (Figure 4-24). It can be seen that the zeta potential for the silica coated manganese ferrite nanoparticles at pH 6.7 is -41.2 mV indicating that they should have good stability at neutral pH in aqueous solution. According to the graph above, the stability should be as good as or better than the citrate-stabilised particles over a large pH range. The PZC for the silica coated MNP's is approximately pH 2.0 when the graph is extrapolated beyond the pH of our lowest pH solution.

One variation that was tried was to use the bare particles before citrate stabilisation leaving all other factors in the synthesis the same. The outcome as can be seen in the TEM images below (Figure 4-25) there was more agglomeration than with the citrate-stabilised particles. The agglomeration was not as high as when using the bare magnetite nanoparticles, which showed severe agglomeration (Figure 4-19) but it was found that using the citrate-stabilised particles gave better outcomes. The DLS results for the bare particles previously (Table 3-3) shows that some agglomeration happened shortly after the synthesis while for the citrate-stabilised particles (Table 4-2) no agglomeration happens.

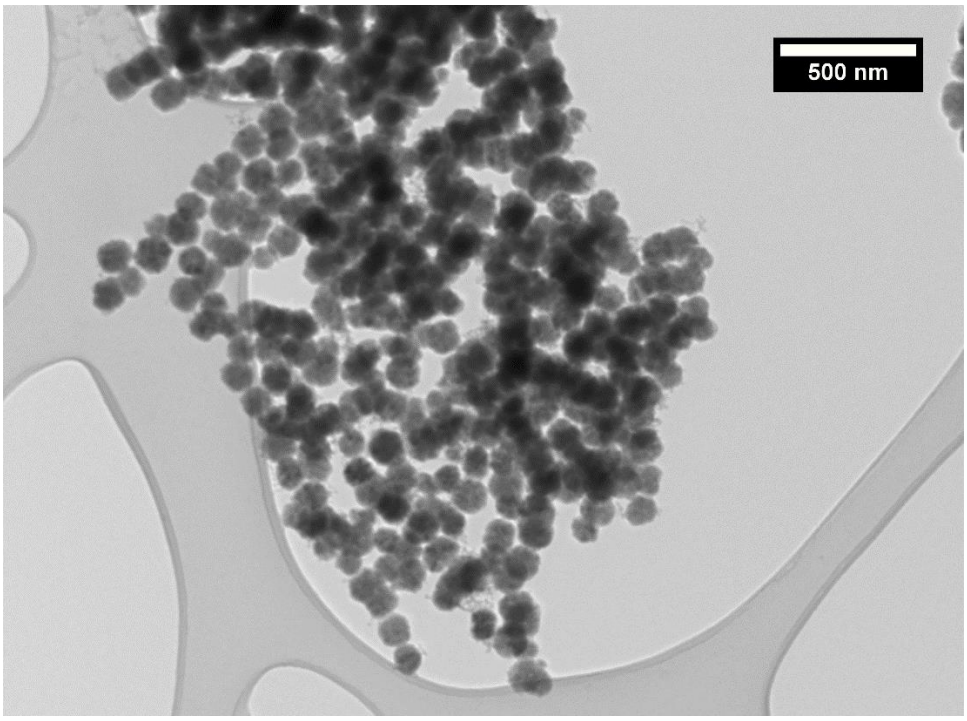


Figure 4-25: TEM image of $MnFe_2O_4$@SiO_2 using bare particles in synthesis.

Another variation that was tried was using magnetic stirring instead of mechanical in the synthesis. This had a major effect resulting in necklace-like linear assemblies of silica

nanoparticles being formed and can be seen in the TEM image below (Figure 4-26). Several iterations of this variation gave the same bead structures, sometimes with significant agglomeration. These bead structures may be useful in other future work but this work was focused on individual well-dispersed nanoparticles.

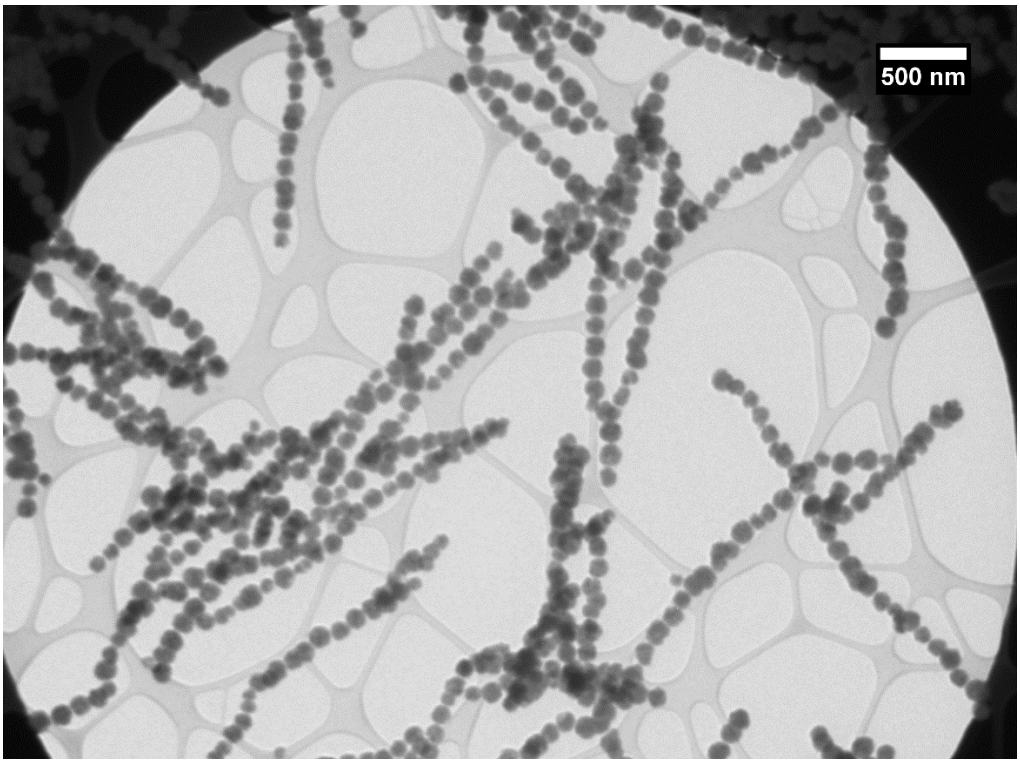


Figure 4-26: TEM image of $MnFe_2O_4$@SiO_2 formed using magnetic stirring.

As a final note on this section, it should be mentioned that there was one outstanding issue in some syntheses to varying degrees. It was found that separate small pure SiO_2 particles would form and the exact source of this issue has not been found. The protocol modifications that would be a solution have yet to be fully elucidated and this would be considered future work here. However, because of the larger size of these particles and the relative ease of magnetic extraction it was found that several washing cycles of magnetic extraction and dispersing in fresh solvent, would remove most of the SiO_2 residue particles. It should however be possible to develop a protocol that does not produce these separate particles and indeed some of the many synthesis that were done had none of these particles in the mixture with only the silica coated magnetic nanoparticles visible in the TEM images. Future work needs to be done in this area to get consistent reproducibility with no residual SiO_2 NPs. However, this is beyond the scope of this project as the goal was to prepare functional MNPs that can be used in applications but this is recommended for future work.

4.4 Conclusions

Selected magnetic cores, such as magnetite and manganese ferrite nanoparticles, have been initially functionalised with citrate to increase their colloidal stability. The characterisation for these particles indicated that the particles had been successfully capped with citrate molecules. The FTIR for the magnetite clearly showed the presence of carboxylate groups while the XRD patterns showed only one phase corresponding to the MNP core material in the sample. For the manganese ferrite, the FTIR signals were not as strong but the appropriate peaks were present. The reduction in magnetisation was slight for both samples with citrate capping. The Fe_3O_4@citrate were not extractable from solution with a magnet while the $MnFe_2O_4$@citrate could be extracted relatively easily. TEM images of both particles showed that there was no morphological change upon addition of the citrate to the particles surface. DLS analysis showed the effect of the citrate in increasing the colloidal stability of the particles with a major change for the smaller magnetite particles. Zeta potential analysis showed the Point of Zero Charge for the particles and indicated their stability in solution.

The coprecipitated magnetite and the polyol manganese ferrite cores were also functionalised with silica to protect the cores and prepare them for further functionalisation. DLS and Zeta potential results for the silica-coated particles showed they had increased in stability, when compared with the bare cores, after silica functionalisation. TEM images clearly showed the silica shell on the particles. FTIR analysis supported this result. XRD patterns also confirmed this result but only where the ratio of silica to ferrite material was large when the amorphous SiO_2 peak could be seen. VSM measurements showed a huge reduction in magnetisation for the smaller magnetite core with the addition of a shell while for the larger manganese ferrite cores the reduction was not as drastic. Magnetic extraction from aqueous solution was fast for the silica coated manganese ferrite MNPs but took much longer for the silica-coated magnetite MNPs. It was found that the larger cores were easier to coat in a more controlled fashion than the smaller cores, with more reproducible results.

Thus, in this section we have successfully citrate-stabilised the selected MNP cores and successfully created a SiO_2 shell on the selected cores.

4.5 References

1 S. P. Schwaminger, D. Bauer, P. Fraga-García, F. E. Wagner and S. Berensmeier, *CrystEngComm*, 2017, **19**, 246–255. https://doi.org/10.1039/c6ce02421a.

2 M. Răcuciu, D. E. Creangă and A. Airinei, *Eur. Phys. J. E*, 2006, **21**, 117–121. https://doi.org/10.1140/epje/i2006-10051-y.

3 Y. H. Deng, C. C. Wang, J. H. Hu, W. L. Yang and S. K. Fu, *Colloids Surfaces A Physicochem. Eng. Asp.*, 2005, **262**, 87–93. https://doi.org/10.1016/j.colsurfa.2005.04.009.

4 D. Huber, *Small*, 2005, **1**, 482–501. https://doi.org/10.1002/smll.200500006.

5 C. Y. Wang, J. M. Hong, G. Chen, Y. Zhang and N. Gu, *Chinese Chem. Lett.*, 2010, **21**, 179–182. https://doi.org/10.1016/j.cclet.2009.10.024.

6 H. K. Can, S. Kavlak, S. ParviziKhosroshahi and A. Güner, *Artif. Cells, Nanomedicine Biotechnol.*, 2018, **46**, 421–431. https://doi.org/10.1080/21691401.2017.1315428.

7 W. Xue, Y. Liu, N. Zhang, Y. Yao, P. Ma, H. Wen, S. Huang, Y. Luo and H. Fan, *Int. J. Nanomedicine*, 2018, **13**, 5719–5731. https://doi.org/10.2147/IJN.S165451.

8 G. L. Davies, S. A. Corr, C. J. Meledandri, L. Briode, D. F. Brougham and Y. K. Gun'Ko, *ChemPhysChem*, 2011, **12**, 772–776. https://doi.org/10.1002/cphc.201000853.

9 V. Patsula, M. Moskvin, S. Dutz and D. Horák, *J. Phys. Chem. Solids*, 2016, **88**, 24–30. https://doi.org/10.1016/j.jpcs.2015.09.008.

10 M. Peng, H. Li, Z. Luo, J. Kong, Y. Wan, L. Zheng, Q. Zhang, H. Niu, A. Vermorken, W. Van De Ven, C. Chen, X. Zhang, F. Li, L. Guo and Y. Cui, *Nanoscale*, 2015, **7**, 11155–11162. https://doi.org/10.1039/c5nr01382h.

11 S. Nigam, K. C. Barick and D. Bahadur, *J. Magn. Magn. Mater.*, 2011, **323**, 237–243. https://doi.org/10.1016/j.jmmm.2010.09.009.

12 S. J. Lee, J. H. J. J. H. J. Cho, C. Lee, J. H. J. J. H. J. Cho, Y. R. Kim and J. K. Park, *Nanotechnology*, , DOI:10.1088/0957-4484/22/37/375603. https://doi.org/10.1088/0957-4484/22/37/375603.

13 A.-H. Lu, X.-Q. Zhang, Q. Sun, Y. Zhang, Q. Song, F. Schüth, C. Chen and F. Cheng, *Nano Res.*, 2016, **9**, 1460–1469. https://doi.org/10.1007/s12274-016-1042-9.

14 W. Stöber, A. Fink and E. Bohn, *J. Colloid Interface Sci.*, 1968, **26**, 62–69. https://doi.org/10.1016/0021-9797(68)90272-5.

15 A. P. Philipse, M. P. B. van Bruggen and C. Pathmamanoharan, *Langmuir*, 1994, **10**, 92–99. https://doi.org/10.1021/la00013a014.

16 J. Govan and Y. Gun'ko, *Nanomaterials*, 2014, **4**, 222–241. https://doi.org/10.3390/nano4020222.

17 M. A. Agotegaray and V. L. Lassalle, *Silica-coated Magnetic Nanoparticles - An Insight into Targeted Drug Delivery and Toxicology*, 2017.

18 R. B. Nasir Baig, M. N. Nadagouda and R. S. Varma, *Coord. Chem. Rev.*, 2015, **287**, 137–156. https://doi.org/10.1016/j.ccr.2014.12.017.

19 C. Ó Dálaigh, S. A. Corr, Y. Gun'ko and S. J. Connon, *Angew. Chemie Int. Ed.*, 2007, **46**, 4329–4332. https://doi.org/10.1002/anie.200605216.

20 B. G. Wang, B. C. Ma, Q. Wang and W. Wang, *Adv. Synth. Catal.*, 2010, **352**, 2923–2928. https://doi.org/10.1002/adsc.201000508.

21 Y. A. Gromova, V. G. Maslov, M. A. Baranov, R. Serrano-García, V. A. Kuznetsova, F. Purcell-Milton, Y. K. Gun'Ko, A. V. Baranov and A. V. Fedorov, *J. Phys. Chem. C*, 2018, **122**, 11491–11497. https://doi.org/10.1021/acs.jpcc.8b00829.

22 Surface Coatings, https://nanocomposix.com/pages/nanocomposix-university.

23 K. Cendrowski, P. Sikora, B. Zielinska, E. Horszczaruk and E. Mijowska, *Appl. Surf. Sci.*, 2017, **407**, 391–397. https://doi.org/10.1016/j.apsusc.2017.02.118.

24 S. Stafford, R. Serrano Garcia and Y. Gun'ko, *Appl. Sci.*, 2018, **8**, 97. https://doi.org/10.3390/app8010097.

25 J. Zou, Y. G. Peng and Y. Y. Tang, *RSC Adv.*, 2014, **4**, 9693–9700. https://doi.org/10.1039/c3ra47043a.

26 D. Singh, R. K. Gautam, R. Kumar, B. K. Shukla, V. Shankar and V. Krishna, *J. Water Process Eng.*, 2014, **4**, 233–241. https://doi.org/10.1016/j.jwpe.2014.10.005.

27 R. De Palma, S. Peeters, M. J. Van Bael, H. Van Den Rul, K. Bonroy, W. Laureyn, J. Mullens, G. Borghs and G. Maes, *Chem. Mater.*, 2007, **19**, 1821–1831. https://doi.org/10.1021/cm0628000.

28 A. Kumar and C. K. Dixit, *Adv. Nanomedicine Deliv. Ther. Nucleic Acids*, 2017, 44–58. https://doi.org/10.1016/B978-0-08-100557-6.00003-1.

29 B. V. Derjaguin, *Pure Appl. Chem.*, 1976, **48**, 387–392. https://doi.org/10.1351/pac197648040387.

30 G. H. Bogush, M. A. Tracy and C. F. Zukoski IV, *J. Non. Cryst. Solids*, 1988, **104**, 95–106. https://doi.org/10.1016/0022-3093(88)90187-1.

31 J. M. Fedeyko, J. D. Rimer, R. F. Lobo and D. G. Vlachos, *J. Phys. Chem. B*, 2004, **108**, 12271–12275. https://doi.org/10.1021/jp047623+.

32 K. Suzuki, K. Ikari and H. Imai, *J. Am. Chem. Soc.*, 2004, **126**, 462–463. https://doi.org/10.1021/ja038250d.

33 P. Deshmukh, J. Bhatt, D. Peshwe and S. Pathak, *Trans. Indian Inst. Met.*, 2012, **65**, 63–70. https://doi.org/10.1007/s12666-011-0071-z.

34 T. N. Tran, T. Van Anh Pham, M. L. Phung Le, T. P. Thoa Nguyen and V. M. Tran, *Adv. Nat. Sci. Nanosci. Nanotechnol.*, 2013, **4**, 045007. https://doi.org/10.1088/2043-6262/4/4/045007.

35 M. Zhang, B. L. Cushing and C. J. O'Connor, *Nanotechnology*, , DOI:10.1088/0957-4484/19/8/085601. https://doi.org/10.1088/0957-4484/19/8/085601.

36 P. I. Girginova, A. L. Daniel-da-Silva, C. B. Lopes, P. Figueira, M. Otero, V. S. Amaral, E. Pereira and T. Trindade, *J. Colloid Interface Sci.*, 2010, **345**, 234–240. https://doi.org/10.1016/j.jcis.2010.01.087.

37 J. Lee, Y. Lee, J. K. Youn, H. Bin Na, T. Yu, H. Kim, S.-M. Lee, Y.-M. Koo, J. H. Kwak, H. G. Park, H. N. Chang, M. Hwang, J.-G. Park, J. Kim and T. Hyeon, *Small*, 2008, **4**, 143–152. https://doi.org/10.1002/smll.200700456.

5 Coating of MNPs with Catalytic Shells

5.1 Introduction

Incorporation of a MNP core within another nanomaterial is frequently used to introduce magnetic modality to that material. There are many examples in the literature where catalysts are attached to the surface of a MNP and the MNP@catalyst nanocomposite being used for catalysis and then magnetically recycled [1][2][3][4][5]. Absorbent layers can also be attached to the MNPs and then the resulting nanocomposite can be used for magnetic separation of small organic molecules[6], heavy metal ions[7], larger biomolecules such as DNA and chiral compounds[8]. Other functional molecules, such as drugs, can be bound to the MNP surface and then the MNP@drug conjugates can be directed to the site of interest in the body for a targeted delivery of specific dose of the drug[9]. This is particularly useful in the area of cancer treatment where the drug itself can be toxic to the body, such as in the case of doxorubicin[10], a well-known drug used for cancer treatment[11] and so a lower dose of the drug can be used with targeted drug delivery using MNPs. Often a functional layer will add stability[12] and/or protection[13] in tandem with a functionality, such as plasmonic resonance. Usually in the process of forming a nanocomposite with a function or application, the first steps will involve the stabilisation or protection of the core.

One of the most useful coatings that can be applied to a MNP is a catalytic shell, as this will give a magnetic retrievable catalyst. This approach has been widely used to immobilise and magnetically retrieve homogeneous catalysts. When the catalyst is in the same phase as the reactants, separation can be a tedious and expensive process[14]. The strategy of a catalyst being attached to a MNP that is dispersible into solution and then extractable from solution with a magnet is very promising. One method to do this for homogeneous catalysts is by covalent bonding the catalyst to the silica shell of core@shell MNPs, by functionalising the silica shell with APTES to introduce surface amino groups that can be used for further covalent binding of the homogeneous catalyst for catalytic application[15][16]. However, one issue with this type of covalent attachment to a silica shell is the loss of catalytic activity with repeated recycling. Although there are examples of magnetically retrievable catalysts which are recyclable over 30 times without loss of activity[16], usually the recyclability is much lower.

For example it was shown that the catalytic activity can decrease from 80 to 42% yield after just 4 cycles[15]. Other covalent linkers that can be created on the silica surface include thiol, carboxyl, phosphonate and phenyl groups[17][18], to which a variety of catalysts, metal based, organcocatalyst or enzyme based, can be attached[4]. Common problems with these methods include leaching of the metal catalysts and reduction in catalytic activity with recycling of the catalyst[19][4].

There are also a number of examples when catalytic shells on MNPs were produced from noble metals, such as Au[20], Ag[21] and Pd[22], to be used as magnetically retrievable catalysts. In addition many catalytically metal oxides have been used for coating of MNPs including MnO_2[23], TiO_2[24] and Al_2O_3[25] resulting in magnetically removable catalytic core@shell nanostructures. Some of these catalysts showed good recyclability with small reductions in yields after several recycles[24]. These types of nanocatalysts are still poorly explored and not very well covered in literature due to great challenges associated with their synthesis and reproducibility of their catalytic activity.

5.2 Aims

The aims of this part of our work is to develop new MNPs coated with catalytic manganese dioxide (MnO_2) and cerium dioxide (CeO_2) shells. These metal oxides have been selected, as they are well known catalysts that are readily synthesised and cheap to produce. It is expected that these nanocatalysts will not suffer from the decrease in activity that is frequently observed for the homogeneous catalysts immobilised on MNPs with repeated recycling. The metal oxide nanocatalysts will also be synthesised in a pure form on their own by the same process that will be used create a shell on the MNPs so that they can be used as controls for testing catalytic activity. The surface chemistry of attachment for each material is different though and the colloidal stability of the starting MNP is one of the factors in a complex system. Other surface effects like lattice mismatch can affect attachment of materials, especially metal oxides. In this section, we will explore the possibilities of obtaining controlled, reproducible shells of MnO_2 and CeO_2 and discuss the outcomes.

5.3 Results and Discussion

In this work, we have used the magnetic nanoparticles described in previous chapters as precursors for catalytic core@shell nanostructures. These nanomaterials have been characterised by a range of instrumental methods and we have selected nanoparticles with optimal magnetic properties, which demonstrated the best responses to magnetic fields because for a magnetically recyclable catalyst fast removal from solution with a magnet is necessary. Therefore, we have selected the magnetite MNPs and the polyol $MnFe_2O_4$ that have been functionalised with silica shell. The bare $MnFe_2O_4$ polyol nanoparticles were also used for further coating with catalytic shells as it was found to be amenable to coating with MnO_2 due to Mn and O being part of the core. These selected MNPs have been coated with catalytic CeO_2 and MnO_2 oxides, characterised by various methods and tested in selected catalytic processes. The outcomes of these studies are discussed for each core@shell nanostructure individually in the following sections.

5.3.1 Preparation of MnO_2 Nanoparticles

To coat MNPs with MnO_2 it was necessary to test the procedure for the synthesis of MnO_2 to see if the correct material was made and to test the catalytic activity without any MNPs. In addition, the characterisation of this material will aid with the further studies of the core@shell MNP@MnO_2 nanostructures. There are several methods for the synthesis of MnO_2[26]. In this work, two methods were used. One where the manganese is reduced from the Mn^{+7} state to Mn^{+2} in the presence of H_2SO_4

$$4KMnO_4 + 2H_2SO_4 \rightarrow 4MnO_2 + 2K_2SO_4 + 2H_2O + 3O_2$$

And another one is the reaction of $KMnO_4$ with a primary alcohol, where EtOH was used as a reducing agent:

$$2KMnO_4 + 3CH_3CH_2OH \rightarrow 3CH_3CHO + 2KOH + 2MnO_2 + 2H_2O$$

Both procedures are described in the experimental section (2.4.1) and resulted in a black solid precipitates, which were characterised, by TEM, EDX, XRD and FTIR. For both procedures, the results for all characterisation were similar apart from the TEM images.

For the reaction of $KMnO_4$ with H_2SO_4, the TEM image below (Figure 5-1 A) shows the product of the reaction as nanoflakes that are aggregated. Many of the MnO_2 polymorphs have layered structures and here we can see how the synthesis has created individual layers that can be seen as the flakes in the TEM image that have aggregated into flower type structures. The reaction of $KMnO_4$ with EtOH in the TEM image below (Figure 5-1 B) shows flakes again but this time there is more layering of the individual flakes. The flakes however are still separate; they have not formed into larger crystals. In both cases as can be seen in the images, nanoflakes of 20-40 nm in diameter were produced.

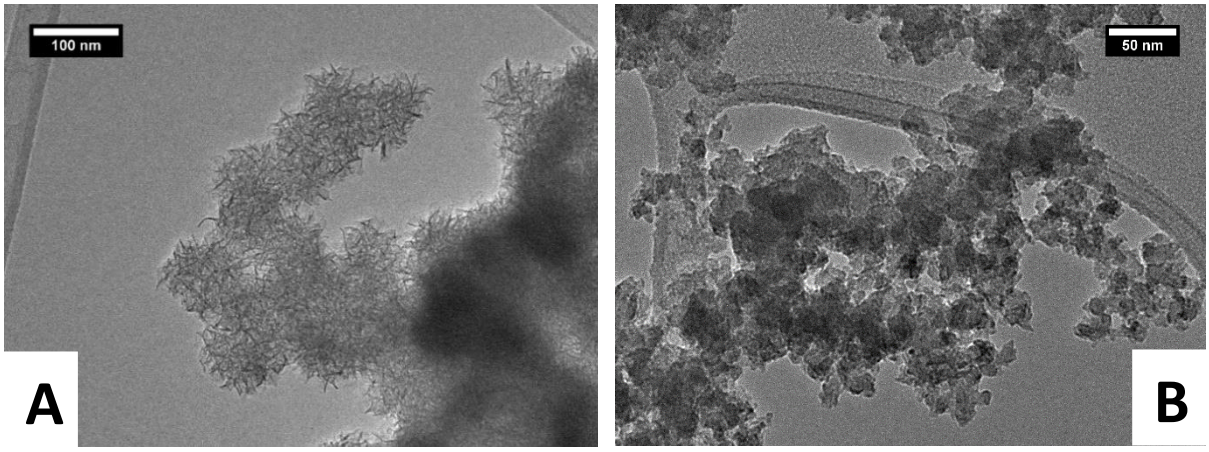


Figure 5-1: TEM images of the as synthesised MnO_2 (A) from H_2SO_4 route, (B) from EtOH route.

EDX of both of these samples (Figure A-9 & Figure A-10) confirmed that the product was composed of Mn and O with traces of K in both samples and some traces of S in the H_2SO_4 route sample. The majority of the peaks, however, corresponded to Mn and O. This is strong evidence that MnO_2 has been made. Manganese oxides however exist in both a number of polymorphs of MnO_2 and other oxides of manganese, such as Mn_2O_3, MnO and Mn_3O_4.

FTIR spectra of both samples (Figure A-11 & Figure A-12) were similar with each showing a broad band at 3400 cm^{-1} for absorbed water and a peak at exactly 401 cm^{-1} in both cases, which can be attributed to the Mn-O vibration. This value was however lower than previously reported values for MnO_2[27]. Both samples had small peaks in the 1700-1500 cm^{-1} that could be attributed to absorbed water on the MnO_2 surface.

XRD pattern of both samples shown below (Figure 5-2) gave similar results with broad peaks at 37 and 67 °2θ approximately and a small peak visible at 25 °2θ for the EtOH sample. These broad peaks are common for an amorphous material, which has not fully formed into a 3D

crystal structure. These XRD patterns were an excellent match for a previously reported data for δ-MnO_2[26].

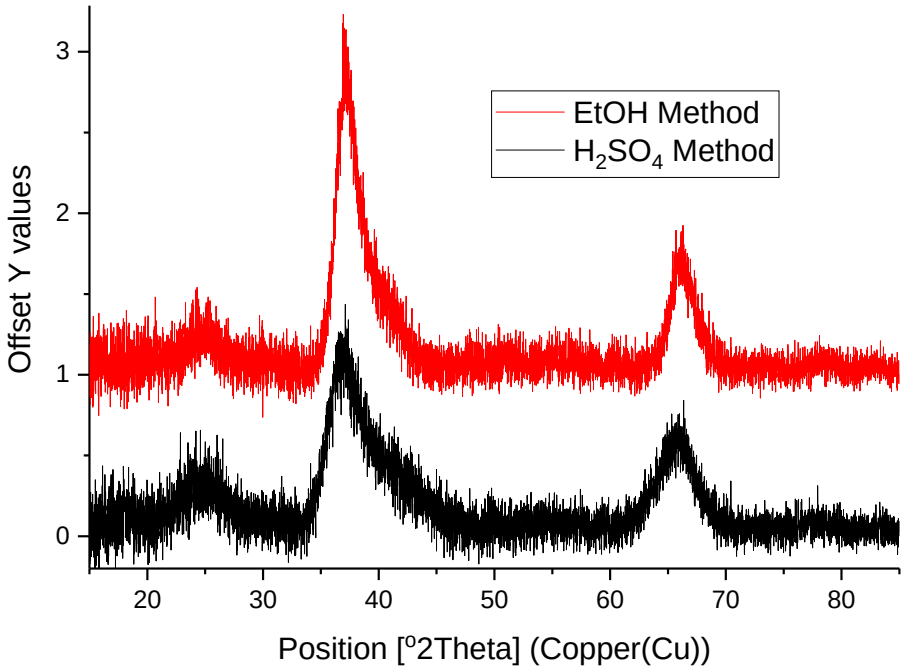


Figure 5-2: XRD patterns of both samples of MnO_2 showing similar peaks.

5.3.2 Preparation of MnO_2 Shell on MNP Cores

Manganese dioxide is a well-known oxidation catalyst. For example, it can readily catalyse decomposition of hydrogen peroxide. It has also been used for removal of pollutants as some of its polymorphs have a very large surface area[28]. There are some examples in the literature of manganese dioxide coated magnetite MNPs[29][6] but our attempts to reproduce one of the synthesis from these reports resulted in poor structures with much lower coverage than was reported[23]. A modified version of this synthesis, using $MnFe_2O_4$ MNPs for an in situ reaction with $KMnO_4$ being reduced by H_2SO_4 and then by EtOH, with several cycles to build up a coating, as described in the experimental section (2.4.2), gave reproducible results with good coverage. It should be noted that it was found it was necessary to wash the initial MNPs with acetone, as described in the experimental, for the coating to be successful. In some syntheses where the core $MnFe_2O_4$ from the polyol synthesis were used having only been washed with water and alcohol several times, the coating procedure failed to coat the particle as TEM images of the product showed. FTIR analysis showed no difference between the acetone washed and unwashed particles. One reason for this lack of coating with the

unwashed particles could be a monolayer of ethylene glycol bound to the surface that is washed away with the acetone.

The coating procedure involved 6 cycles to produce the MnO_2 coating. A single cycle was found to coat the particles a little but after several repeated alternating cycles a good coating was formed as can be seen in the TEM images below. A molar ratio 1:1 for MnO_2 to $MnFe_2O_4$ was found to give the best coating using this procedure. The method of calculation used previously for the SiO_2 shell was not used for these particles as the shell here was composed of flakes of MnO_2 material rather than a compact shell and so such a calculation would not be accurate and should always give a shell that would be larger than the calculated value. Some variation on this ratio of shell to core will be discussed below.

Small amount of unbound individual MnO_2 flakes were also observed in initial samples, but continuous washing of the sample with water, sonication and magnetic extraction did remove most of the residue of unbound MnO_2. The overall coating procedure was effective and reproducible. Manganese dioxide layers were successfully applied to the manganese ferrite cores synthesised by the polyol method to give the $MnFe_2O_4$@MnO_2 nanoparticles, which were characterised by VSM, FTIR, XRD, and TEM.

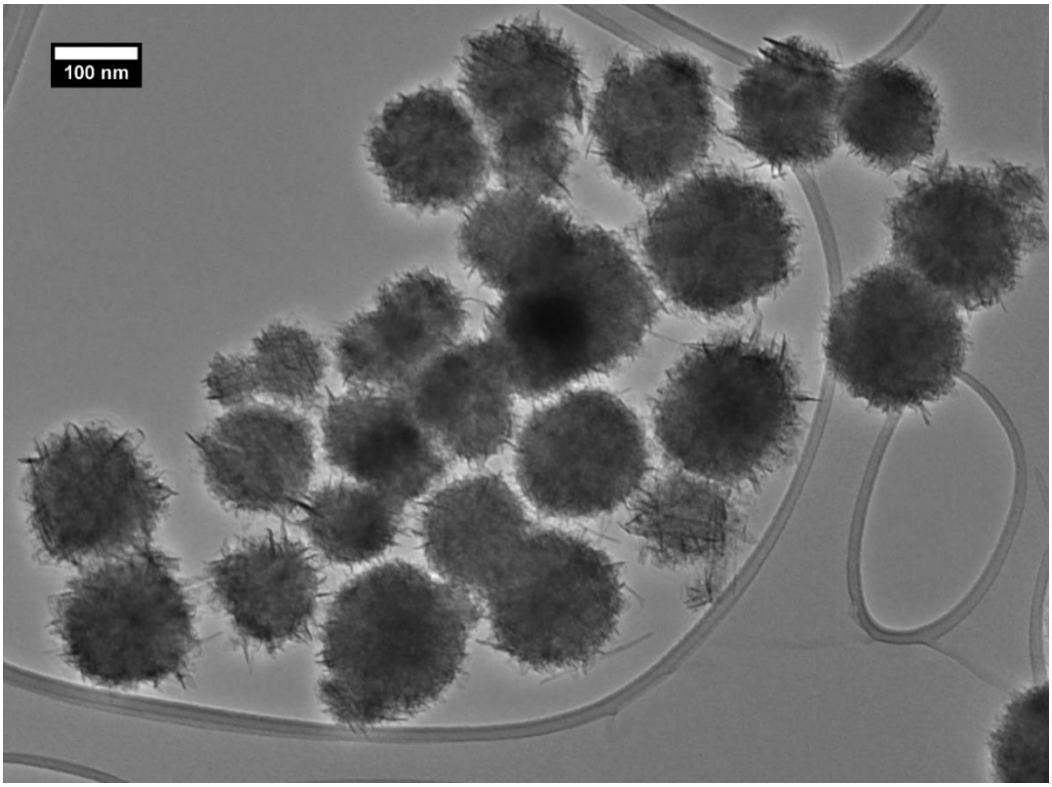


Figure 5-3: TEM image of the $MnFe_2O_4$@MnO_2 MNPs.

A TEM image above (Figure 5-3) of the $MnFe_2O_4$@MnO_2 sample showed hedgehog-like nanoparticles with a diameter of 164±30 nm. Size distribution were calculated for 100 particles using ImageJ (Figure A-7). The bare $MnFe_2O_4$ particles used here had an average size of 120±30 nm giving a shell of approximately 25±15 nm. The shell is composed of flakes that extend out from the surface of the $MnFe_2O_4$ core, being denser closer to the surface. As can be seen, there are no bare particles in the sample but some separate MnO_2 flakes.

FTIR of the $MnFe_2O_4$@MnO_2 nanocomposites below (Figure 5-4) showed a peak at 532 cm^{-1} for the Fe-O stretch in $MnFe_2O_4$ which was occluded by a peak beyond 380 cm^{-1}. Other than this change, there was only the similar peaks for absorbed water between 1600-1300 cm^{-1} and the broad peak at 3400 cm^{-1} for surface –OH groups. FTIR analysis showed no difference between the acetone washed and unwashed particles (Figure A-13). One reason for this lack of coating with the unwashed particles could be a monolayer of ethylene glycol bound to the surface that does not show up in the FTIR but is washed away with the acetone.

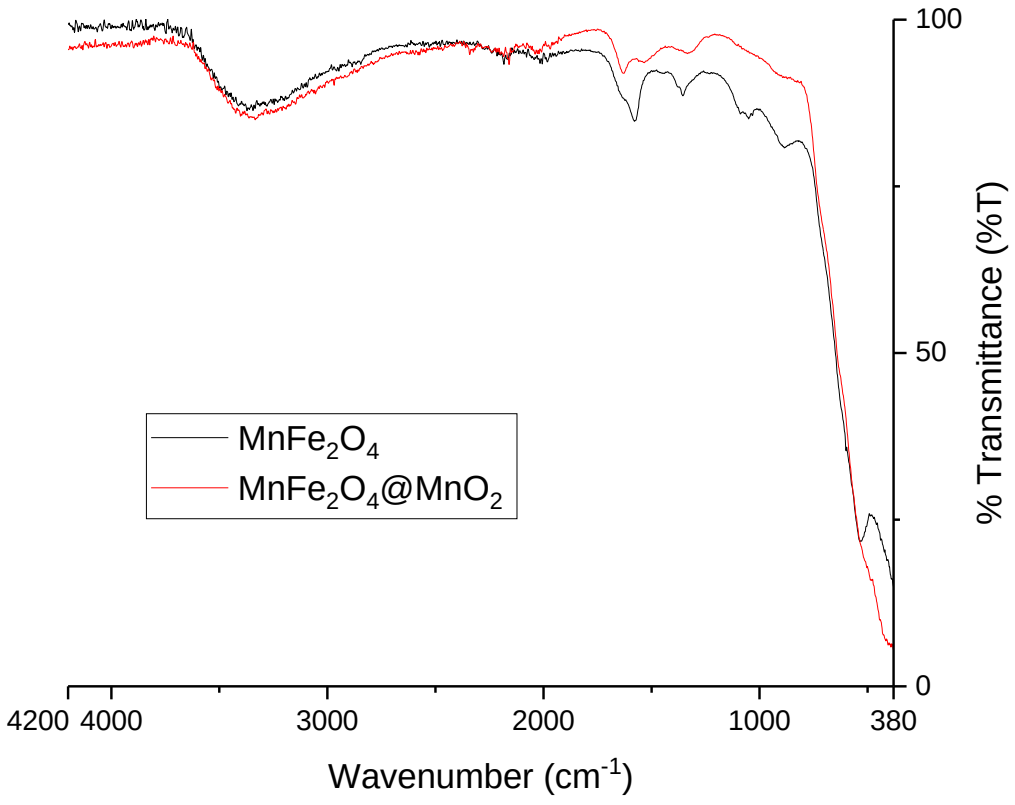


Figure 5-4: FTIR spectra of $MnFe_2O_4$@MnO_2 MNPs.

VSM curves (Figure 5-5) showed a change in magnetisation from 60.1 Am^2kg^{-1} for the pure $MnFe_2O_4$ to 27.4 Am^2kg^{-1} for the $MnFe_2O_4$@MnO_2 core@shell nanostructures. This reduction

in magnetisation is expected as the MnO_2 layer is a non-magnetic material and is adding mass to the magnetic particles. As the core is larger for the polyol particles, the reduction in magnetisation upon addition of the shell would not be as drastic as with smaller coprecipitated MNPs. The magnetisation curve showed that the particles reach saturation in a low magnetic field and that they have no remanence magnetisation when the applied field is removed. These particles showed relatively fast removal from solution with a handheld neodymium magnet, the particles could be removed in under 1 hour.

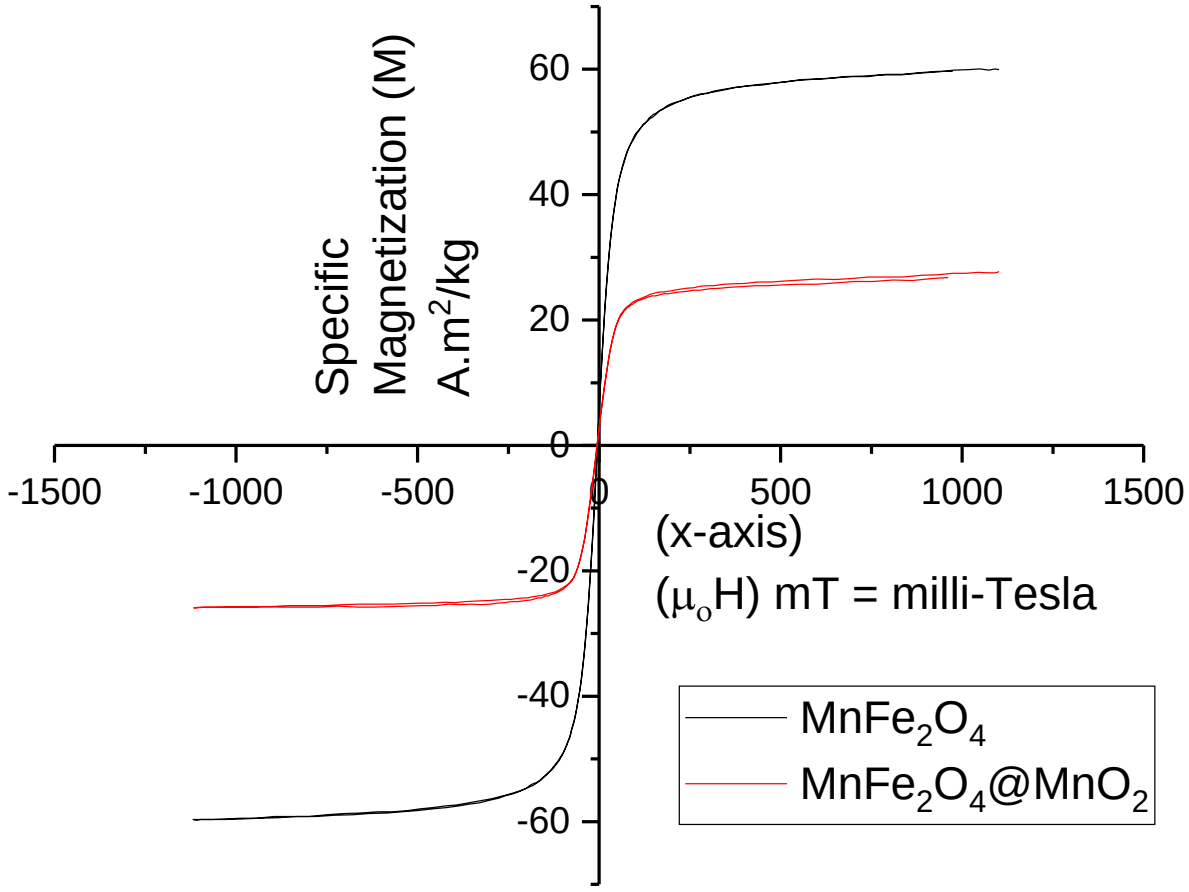


Figure 5-5: VSM curves for the $MnFe_2O_4$@MnO_2 MNPs.

XRD pattern of the $MnFe_2O_4$@MnO_2 sample below (Figure 5-6) has shown a combination of the $MnFe_2O_4$ and MnO_2 patterns as expected. This shows that no structural or phase changes have taken place with the procedure of coating the MNPs.

The zeta potential of these particles over the pH range 4.2-9 as can be seen below (Figure 5-7). It shows that the surface charge of the nanoparticles are negative over this pH range

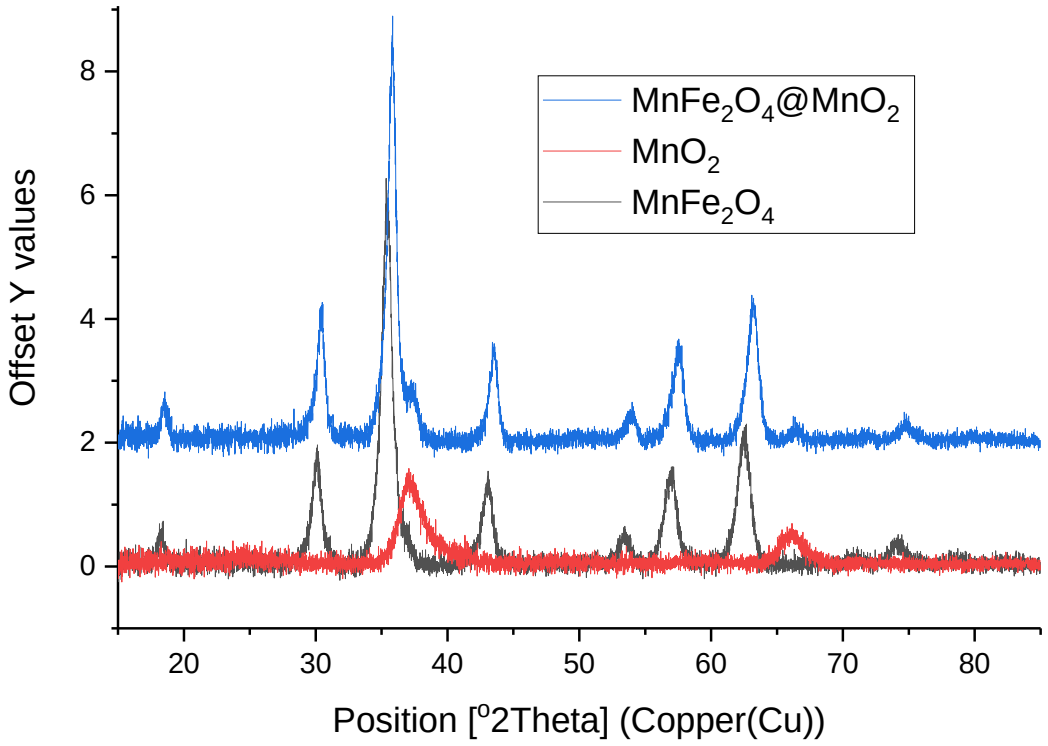


Figure 5-6: XRD patterns of the $MnFe_2O_4$@MnO_2 shown as a combination of the core and shell phases.

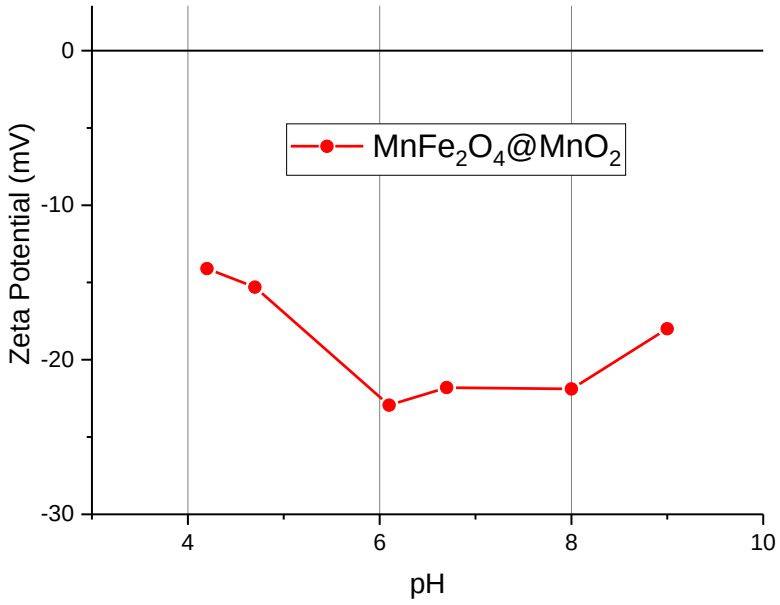


Figure 5-7: Zeta potential over pH range for $MnFe_2O_4$@MnO_2.

The process described in the experimental section (2.4.2) did not result in all the MnO_2 produced coating the MNPs because with the magnetic extractions during the procedure the reaction solution did not go clear but remained a slight brown opaque solution, which was discarded. This would be the non-magnetic MnO_2 remaining in solution. In addition, there were some unbound excess of MnO_2 was observed in the TEM images after 5 washes.

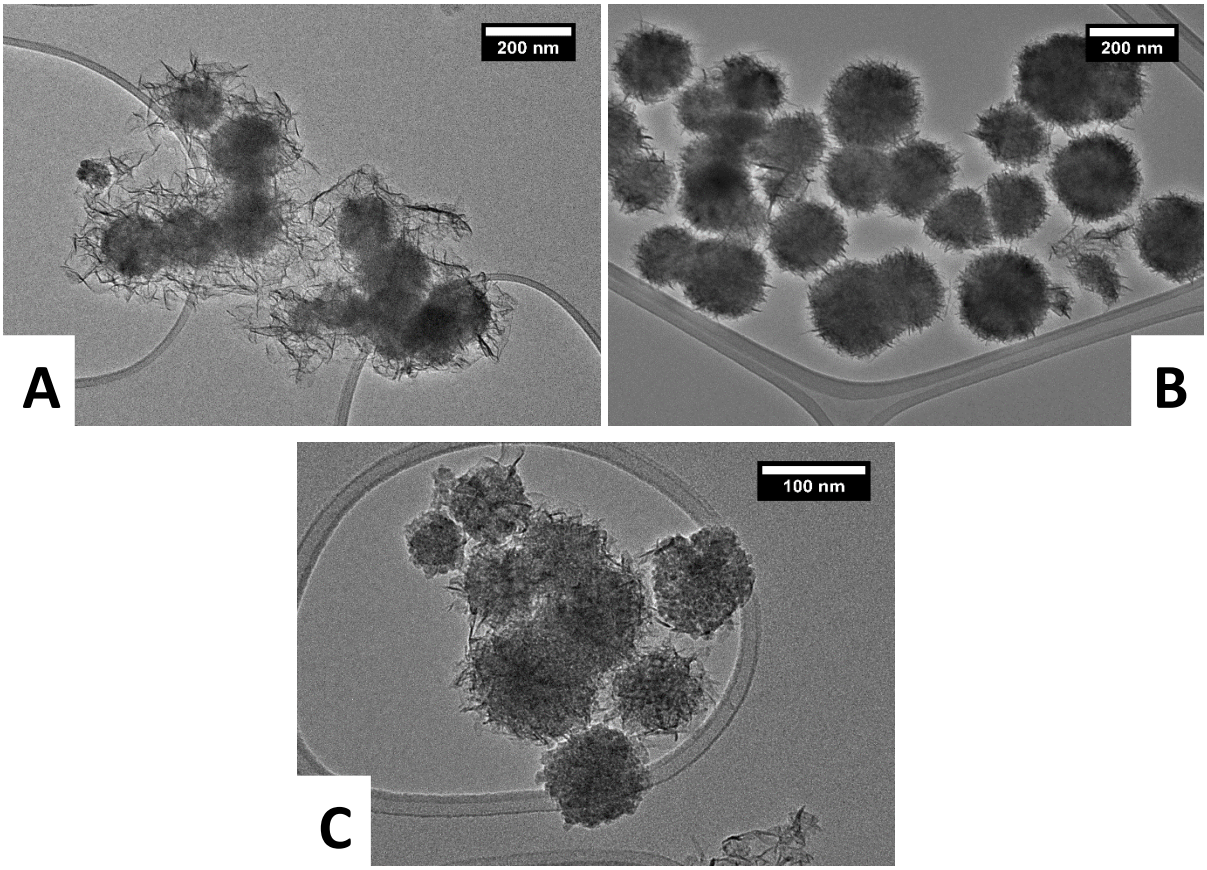


Figure 5-8: TEM images showing MNPs with different molar ratios of MnO_2 coating (A) 2 molar ratio (B) 1 molar ratio (C) 0.5 molar ratio.

To find if less MnO_2 could be used so that there would be no excess MnO_2 the same procedure was performed with 50% of the starting $KMnO_4$, giving a MnO_2 to MNPs molar ratio of 0.5. Again the reaction solution was brown opaque after the first magnetic extraction, although less so. TEM images of the product of this reaction after 5 washes as can be seen in **C** above (Figure 5-8). It showed particles that were not coated as much with some uncoated particles also. As can be seen a molar ratio of 1 gave a better result.

In another variation, the amount of MnO_2 was increased by 100 %, giving a MnO_2 to MNPs molar ratio of 2:1, to see if a more dense coating could be achieved. As can be seen in the image **A** above (Figure 5-8) the effect was to produce large clusters of multicore particles surrounded by excess MnO_2. There were few individual particles with the sample composed mainly of these clusters of multicore particles. The MnO_2 flakes attached to these particles extended out by 100 nm from the cores. As large cluster were formed because of the excess MnO_2 it was considered that a 1 molar ratio gave a better result. It can be seen in **B** above (Figure 5-8) that the particles with a molar ratio of 1 are well coated and the sample is

composed of individual particles with small amounts of excess MnO_2. The following table (Table 5-1) summarised these results with a brief description of the shell.

Table 5-1: Table describing the images in (Figure 5-8) and the molar ratio of coating.

	Molar Ratio of MnO_2 : $MnFe_2O_4$	Approximate Shell Size (nm)	Effects from TEM results
A	2 : 1	100	Aggregated MnO_2 with multicore particles
B	1 : 1	50	Good uniform coating of particles
C	0.5 : 1	20	Some uncoated particles and thinner coating

It was found that the coating was additive, which is that the coating on the MNP could be increased by repeating the procedure with more of MnO_2 precursors and following the procedure described previously (2.4.2). This effect can be seen in the images below (Figure 5-9), where sample **A** was processed with 0.5 molar ratio of MnO_2 precursors and gave a partial coating. This sample was then processed with another 0.5 molar ratio of the MnO_2 precursors again to give fully coated particles, which can be seen in **B**. This indicates that a coating of a specific thickness can be made by continuous cycling of the procedure until a coating of the desired thickness is achieved.

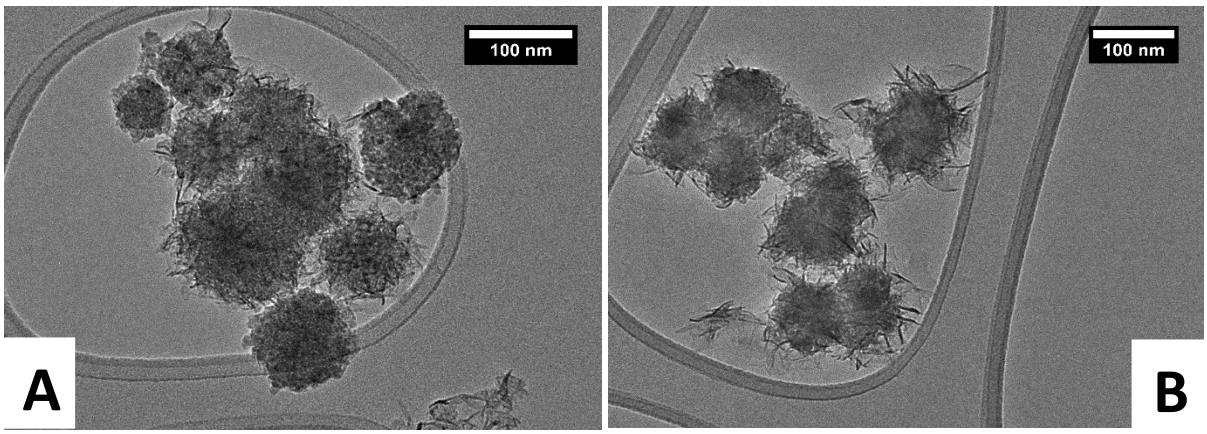


Figure 5-9: TEM images of (A) 0.5 molar ratio coating (B) A after another 0.5 molar ratio coating.

Following the procedure described in the literature[23], for the formation of the same $MnFe_2O_4$@MnO_2 nanoparticles to the ones produced here, did not give the expected results. The results of this reaction as can be seen in the TEM image below (Figure 5-10) were of needles of MnO_2 and separate MNPs. No core@shell structures were found in the product of

this reaction. This outcome is different than that reported in the paper, where the paper has core@shell nanoparticles similar to above (Figure 5-3), which they describe as layered birnessite-type manganese oxides on the MNP core. The paper had a quite simple procedure and this would have been more favourable than our procedure in the experimental section (2.4.2), as that was very involved with several cycles of sonication, washing and extraction but our procedure in the experimental section does give reproducible results. The morphology and density of the coating from our procedure can vary between batches but in general, there is a good degree of similarity between batches as seen in TEM images.

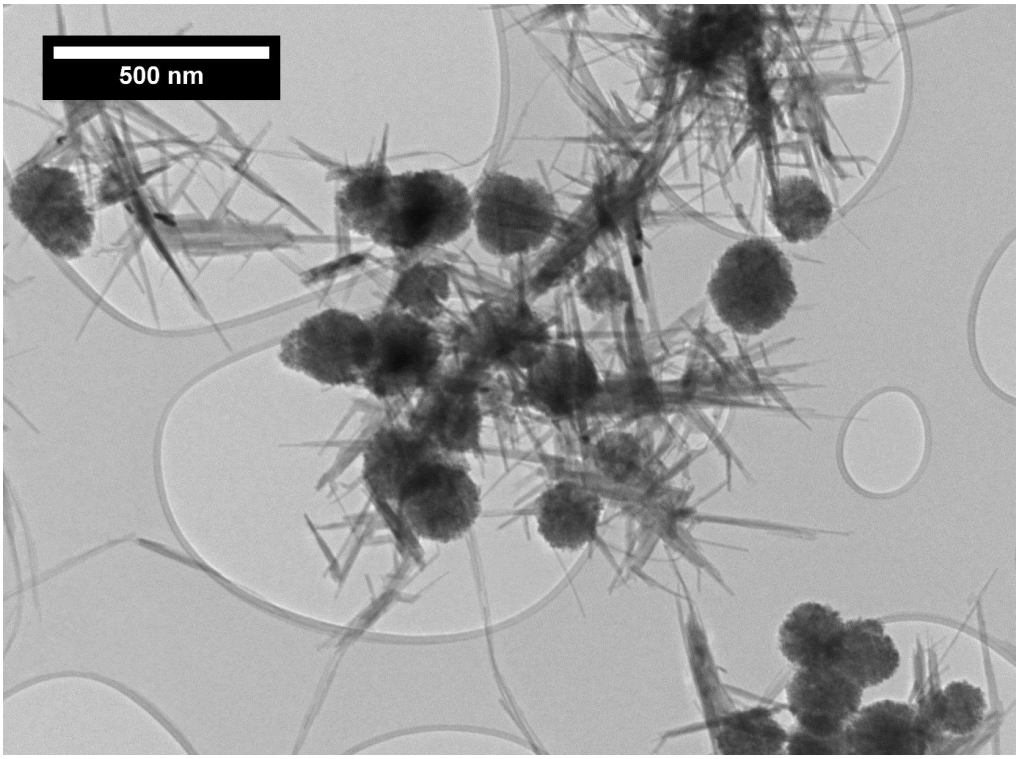


Figure 5-10: TEM image of coating obtained by following the procedure from reference [23]**.**

The procedure for this section as outlined earlier involves several cycles of sonication with $KMnO_4$ being reduced by H_2SO_4 and EtOH in each cycle with the MNP in situ in the reaction. It is described in detail in the experimental section (2.4.2). This procedure involved several cycles of sonication, washing and extraction to get good quality $MnFe_2O_4$@MnO_2 nanoparticles. It involved 1 molar ratio of MNP:MnO_2 being used overall in 6 cycles of sonication (0.17 molar ratio each cycle) using a mixture of the H_2SO_4 method and EtOH, method used to create the MnO_2 nanoflakes (2.4.1). The procedure took a day and involved a lot of hands-on manipulation. Efforts to simplify this procedure were tried. These variations are summarised in the table below (Table 5-2)

Table 5-2: Description of variations to simplify the procedure.

	Method	Brief Description of Procedure
A	$KMnO_4 + H_2SO_4$	1 molar ratio MNP:MnO_2 with one sonication cycle of 5 hours
B	$KMnO_4 + H_2SO_4$	1 molar ratio MNP:MnO_2 with 5 sonication cycles of 1 hr each
C	$KMnO_4$ + EtOH	1 molar ratio MNP:MnO_2 with one sonication cycle of 5 hours
D	$KMnO_4$ + EtOH	1 molar ratio MNP:MnO_2 with 5 sonication cycles of 1 hr each

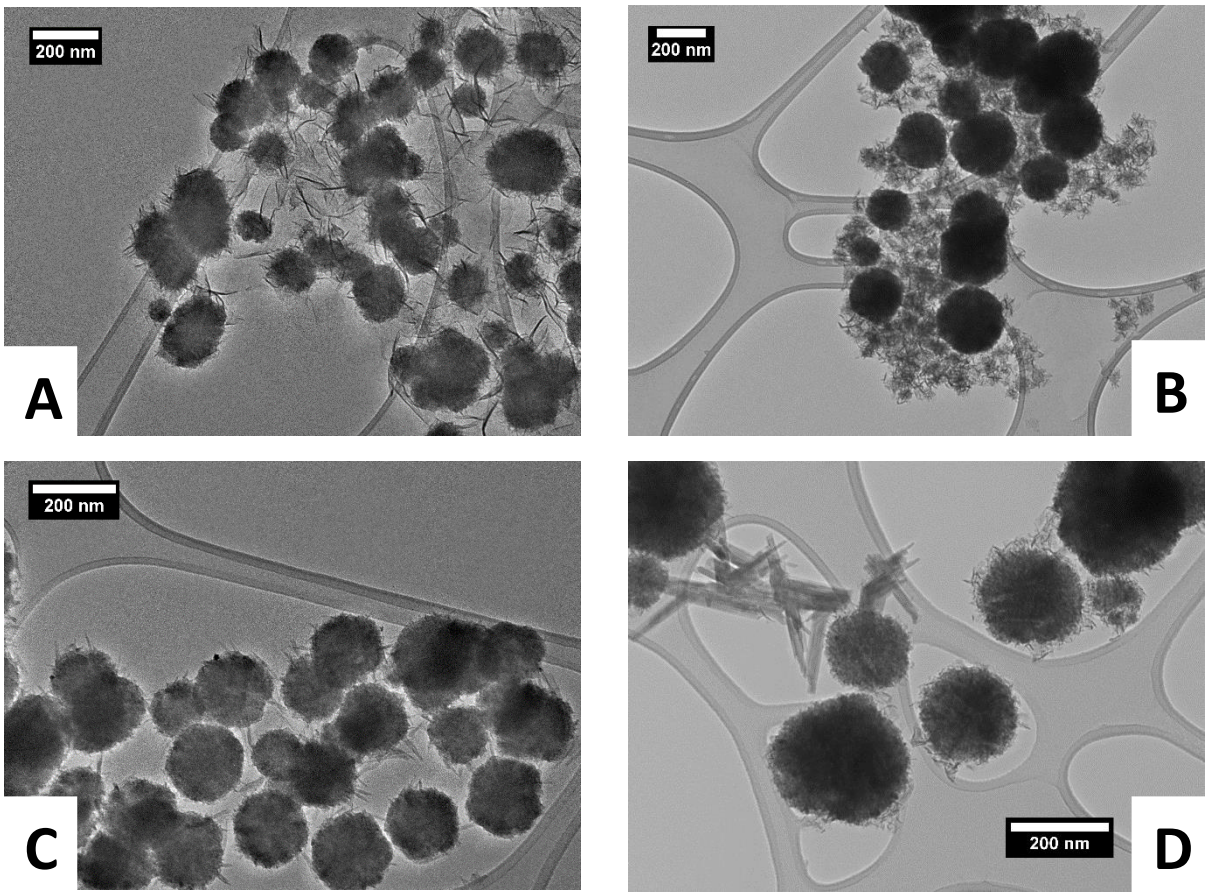


Figure 5-11: TEM images of different methods to coat the MNPs. (A) H_2SO_4 method with 1 molar ratio MNP:MnO_2 with one sonication cycle of 5 hours. (B) H_2SO_4 method with 1 molar ratio MNP:MnO_2 with 5 sonication cycles of 1 hr each. (C) EtOH method with 1 molar ratio MNP:MnO_2 with one sonication cycle of 5 hours. (D) EtOH method with 1 molar ratio MNP:MnO_2 with 5 sonication cycles of 1 hr each.

Method **A** and **C** here would have been favourable to work as they meant leaving the process running without need for manipulation through the procedure until the very end. **B** and **D** here were performed to find the effect of that type of procedure in isolation, the H_2SO_4 method and the EtOH method.

The TEM images of the products produced in these experiments are shown above (Figure 5-11). As can be seen method **A** resulted in some core@shell particles but also some large sheets of MnO_2 that seemed to be interacting with the MNPs. In addition, some uncoated particles were visible in the images for this sample. The shell on the particles was approximately 20 nm. Method **B** gave a result where some of the particles were coated and others were not, there were no large sheets of separate MnO_2 but there was excess MnO_2 in the form of small flakes of approximately 10-20 nm. Method **C** gave thicker coated particles of approximately 30 nm with small needle like structures but with some uncoated particles too. Method **D** gave some sparsely coated particles of with needle like structures unbound to the MNPs too.

From these investigations in could be concluded that the alternating of the H_2SO_4 and the EtOH methods allows the slow build-up of the MnO_2 filling the gaps on the shell that the previous coating left. This results in good quality coating of the core MNPs. The table above (Table 5-3) summarises the results.

Table 5-3: Summary of results for variations in procedure corresponding to images in (Figure 5-11).

	Brief Description of Procedure	**Summary of Result**
A	KMnO4 + H_2SO_4 method with 1 molar ratio MNP:MnO_2 with one sonication cycle of 5 hours	Large sheets of MnO_2 causing aggregation with coated particles.
B	$KMnO_4$ + H_2SO_4 method with 1 molar ratio MNP:MnO_2 with 5 sonication cycles of 1 hr each	Sparsely coated particles with lots of separate MnO_2 flakes.
C	$KMnO_4$ + EtOH method with 1 molar ratio MNP:MnO_2 with one sonication cycle of 5 hours	Some uncoated particles with needle like structures too.
D	$KMnO_4$ + EtOH method with 1 molar ratio MNP:MnO_2 with 5 sonication cycles of 1 hr each	Sparsely coated particles with separate needle like structures.

Some other variations that deserve a mention were the use of the coprecipitated MNPs. Attempts were made to form nanocomposites with the coprecipitated Fe_3O_4 and the $MnFe_2O_4$ with MnO_2. TEM images of these products are shown below (Figure 5-12). For the Fe_3O_4 it seems there was no MnO_2 coating on the MNPs as after magnetic extraction no MnO_2 was present as seen in image **A**. After magnetic extraction of materials produced with the

coprecipitated $MnFe_2O_4$ cores there was some interaction with MnO_2 sheets visible in the TEM, see image **B**. The images have shown that large size MnO_2 nanosheets where interacting with the spherical core nanoparticles but no proper core@shell structures have been produced. The interaction is quite random with both the MnO_2 and the $MnFe_2O_4$ surfaces exposed. It is possible that with continuous sonication and magnetic extraction that the materials would separate but this experiment was not performed.

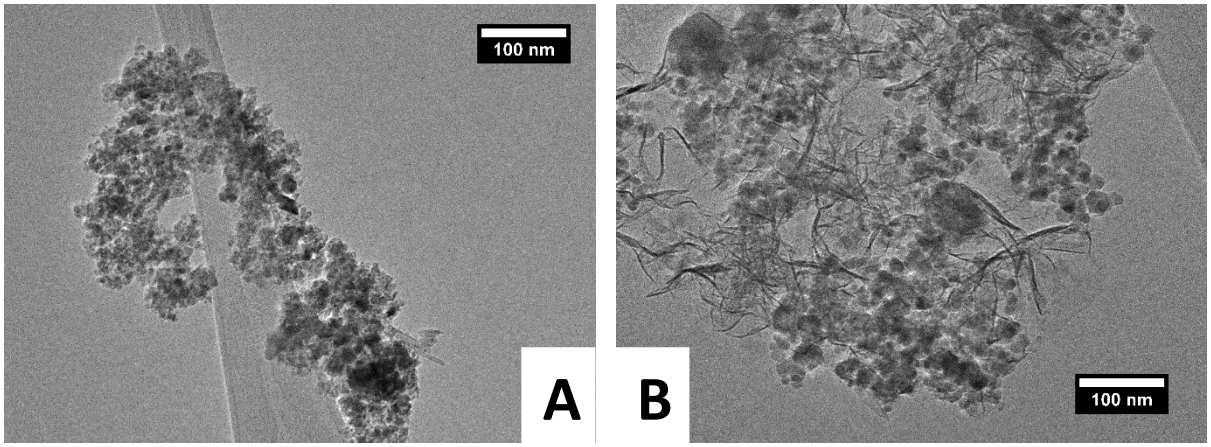


Figure 5-12: TEM images of functionalised with MnO_2, (A) coprecipitated Fe_3O_4 and (B) $MnFe_2O_4$ MNPs.

One final variation was to functionalise the core@shell $MnFe_2O_4$@SiO_2 particles with MnO_2. This experiment did not give good core@shell nanostructures either. TEM images of the results of this reaction can be seen below (Figure 5-13). Separate MnO_2 sheets and MNPs are visible in the image.

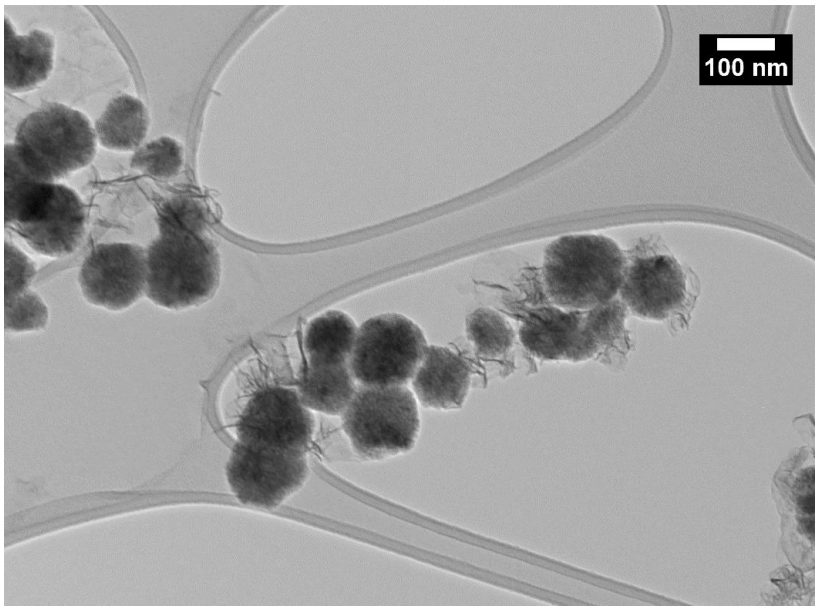


Figure 5-13: TEM image of $MnFe_2O_4$@SiO_2@MnO_2 showing no core@shell structures.

5.3.3 Preparation of CeO_2 Nanoparticles

In a similar fashion to the MnO_2 shell, synthesis of CeO_2 nanoparticles was performed for characterisation to confirm the correct material was made and to help with understanding the results of the MNP@CeO_2 nanoparticles. The procedure described in the experimental section (2.4.3) follows a previously reported method for synthesis of CeO_2[30]. The HMTA hydrolyses slowly to produce ammonia, which will then react with the cerium nitrate according to the following proposed equation:

$$3Ce(NO_3)_3 + 8NH_4OH \rightarrow 3CeO_2 + 8NH_4NO_3 + NO + 4H_2O$$

The synthesis resulted in a pale yellow powder, which became bright yellow after calcination at 800 °C. In our lab inventory, we also had a commercial sample of CeO_2, which was used for comparison of the synthesised product. The commercial CeO_2 was a similar bright yellow. The product was characterised by TEM, EDX, XRD and FTIR. TEM results below (Figure 5-14) showed agglomerated nanoparticles of 8 ± 5 nm approximately. EDX (Figure A-14) showed that the sample contained Ce and O. This indicates the product of the reaction was CeO_2.

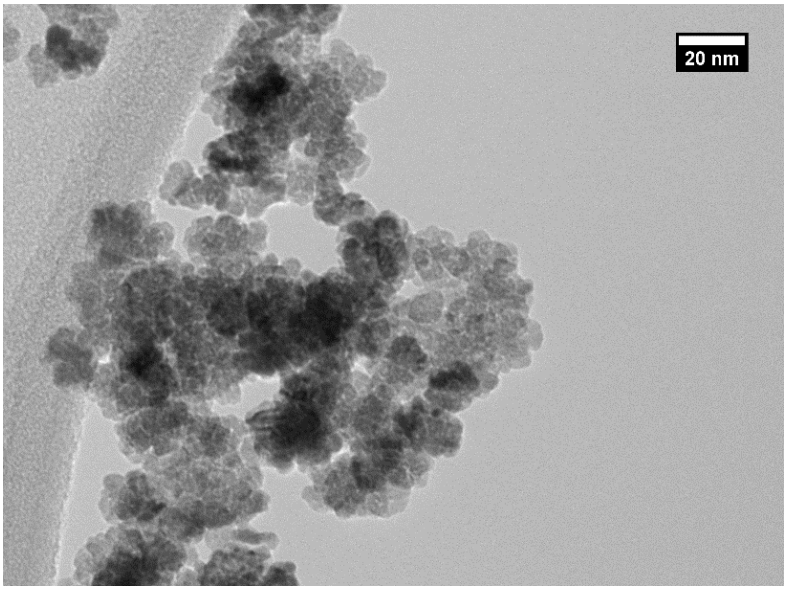


Figure 5-14: TEM image of the prepared CeO_2 NPs.

FTIR spectra in Figure 5-15 showed a developing peak below 380 cm^{-1}. There were the peaks due to absorbed water, 1534 and 1337 cm^{-1}, and surface –OH group, 3400 cm^{-1}. The synthesised material was an exact match with the commercial sample. Interestingly the literature[31][32][33] describes peaks at 840 and 554 cm^{-1} for pure ceria which were not in our synthesised sample nor in the commercial sample spectrum.

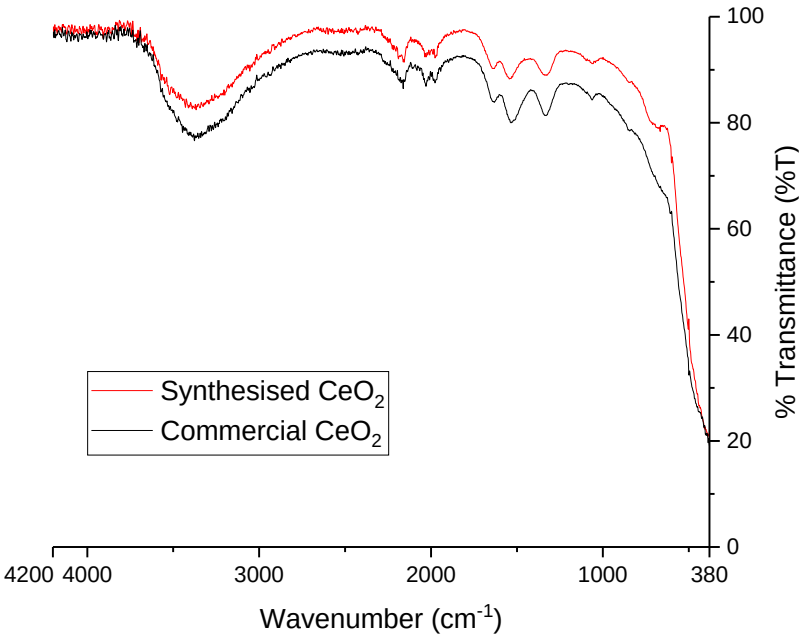


Figure 5-15: FTIR of CeO_2 NPs.

XRD results as shown in Figure 5-16 demonstrate the patterns of the synthesised material and the commercial material. The synthesised nanoparticles gave an excellent match for cerium dioxide in the COD database (COD 900-9009). A Williamson-Hall plot for the peaks gave a crystallite size of 8.3 nm, which is in excellent agreement with the TEM images above (Figure 5-14). An XRD of the commercial showed no difference in the peaks to our synthesised sample as could be seen in the XRD results confirming that our product was identical.

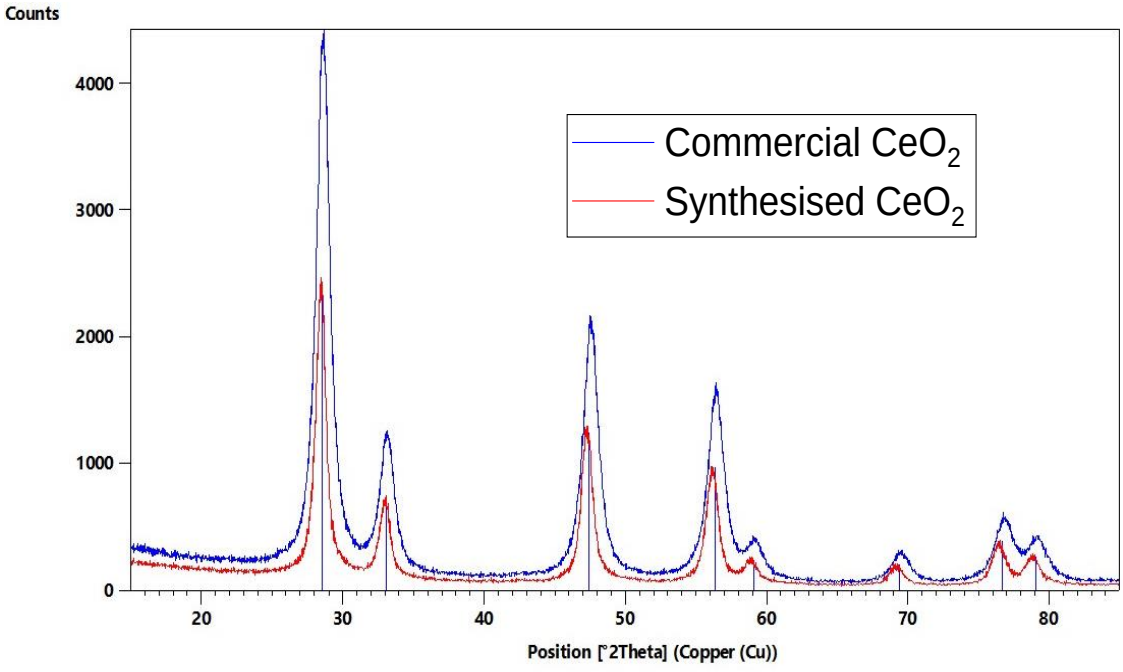


Figure 5-16: XRD pattern of the synthesised CeO_2 and the commercial CeO_2.

5.3.4 Preparation of CeO_2 shell on MNP Cores

Cerium dioxide is a well know catalyst. Amorphous silicon dioxide is known to be a good surface for attachment of metal oxides[5]. Therefore, cerium dioxide was deposited onto the silica coated manganese ferrite core@shell nanoparticles according to the procedure described in the experimental section (2.4.4). The procedure involved the precipitation of the CeO_2 out of solution, using cerium nitrate and hexamethylenetetramine, in the presence of the MNPs to be coated. As the CeO_2 forms in the aqueous solution it will precipitate onto surface of the MNPs provided the surface is favourable to the growth of the CeO_2 crystallites.

The amount of material needed in the reaction can be calculated knowing the size of the core@shell1 precursor (from TEM images), the density of the core@shell1 (from references and a calculation), the amount of the core@shell1 precursor put into the reaction, the density of the second shell material (from references), and the molar masses of the materials and precursors.

Similar to previously for the first shell, the ratio of the volume of the core (which now has a first shell or now the "core" = MNP core + shell1)) to the volume of the shell2 is

$$\frac{\left(\frac{core\ diameter}{2} + shell2\ thickness\right)^3 - \left(\frac{core\ diameter}{2}\right)^3}{\left(\frac{core\ diameter}{2}\right)^3} = volume\ shell2{:}\,core$$

From this the ratio of the mass of the shell2 to the mass of the "core" (MNP core + shell1) is calculated knowing the densities of each material

$$volume\ shell2{:}\,core\ \left(\frac{density\ of\ shell2\ material}{calculated\ density\ of\ core}\right) = mass\ shell2{:}\,core$$

The calculated density of the core here is found from the TEM images of the initial core@shell precursor, knowing the diameter of the core and the thickness of the shell from the images, the density of an individual core@shell MNP can be calculated as follows

$$\frac{volume\ of\ core(density\ of\ core) + volume\ of\ shell1(density\ of\ shell1)}{volume\ of\ core + volume\ of\ shell1}$$

Now if we know the mass of core@shell1 material as precursor in the reaction we know the mass of shell2 material needed. Knowing the mass of shell2, the mass of the second shell, that

is needed we can calculate the amount of precursors needed in the reaction for a shell of certain thickness.

This calculation makes some assumptions, such as all the particles in the ensemble are the same core size, that all particles are coated evenly with shell1 and will be coated evenly with shell 2, and that the solution of the precursor core material (the core@shell1) is of known concentration. The nanoparticles were kept in solutions throughout the various stages because it was found that after drying out the nanoparticles and then redispersing them back into solution by sonication was problematic with noticeable differences regarding stability after drying out, this would be because of agglomeration of the particles and then fusing of the surfaces while drying out.

The $MnFe_2O_4@SiO_2@CeO_2$ core@shell nanoparticles were characterised by VSM, FTIR, XRD, TEM and EDX. VSM results shown below (Figure 5-17) show a change in magnetisation from 31.9 Am^2kg^{-1} for the $MnFe_2O_4@SiO_2$ to 18.3 Am^2kg^{-1} for the $MnFe_2O_4@SiO_2@CeO_2$. The reduction in magnetisation was expected with the addition of a non-magnetic shell. Although there was a reduction, it was found that the particles could still be extracted from solution in a reasonable time of under 3 hours with a handheld neodymium magnet. The particles could also be easily dispersed back into solution by sonication of the solution.

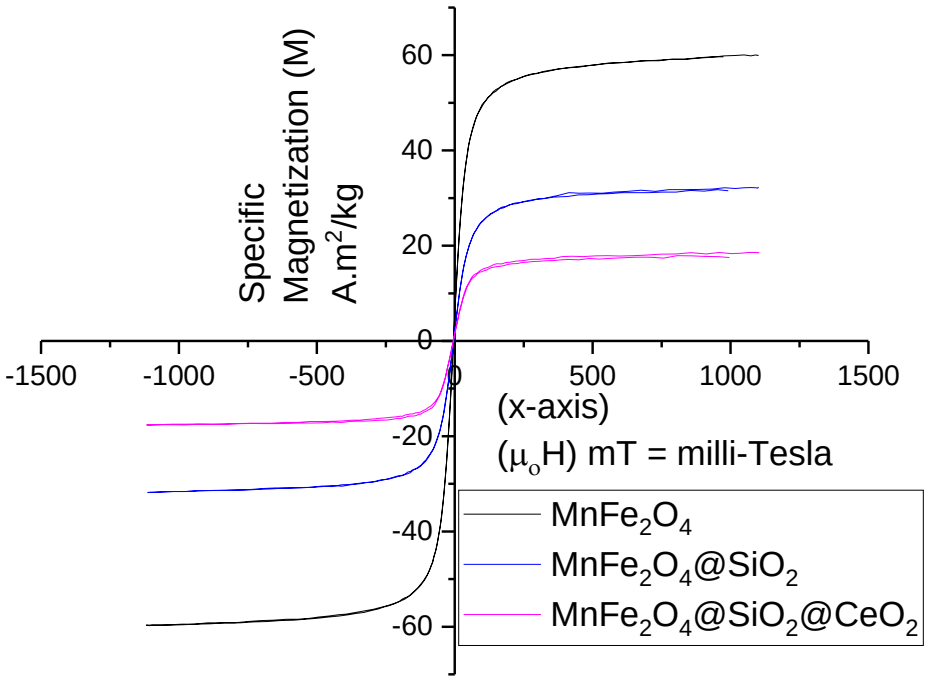


Figure 5-17: VSM results for $MnFe_2O_4$, $MnFe_2O_4@SiO_2$ and $MnFe_2O_4@SiO_2$ CeO_2 samples showing changes.

FTIR spectra of the nanoparticles below (Figure 5-18) showed the peak for SiO_2 at 1000 cm^{-1} but the peak for the metal-O stretch of the ferrite was now occluded by the spectra for CeO_2 in that region. The spectra also showed a broad peak at 3400^{-1} for the bound –OH groups.

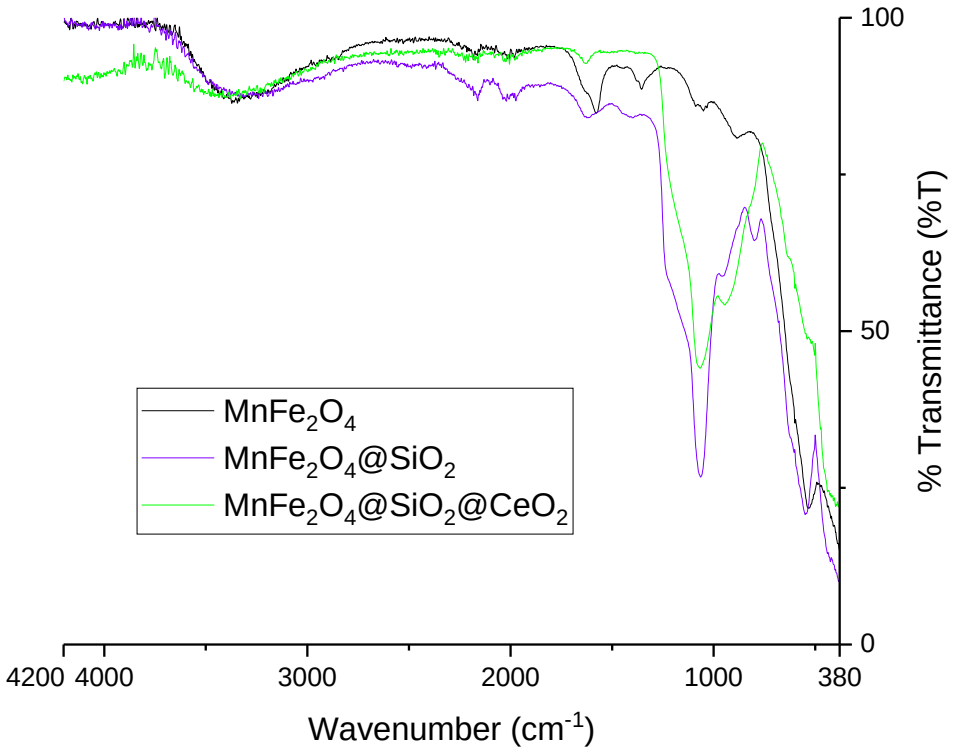


Figure 5-18: FTIR spectra of the CeO_2 shelled MNP showing stages of development.

TEM images of the particles below (Figure 5-19) showed the silica shell completely covered with CeO_2 nanoparticles that have coalesced on the surface of the SiO_2, forming a shell approximately 20 nm thick. The images showed some free CeO_2 particles but the majority of the sample was composed of the $MnFe_2O_4@SiO_2@CeO_2$ nanoparticles. There was some aggregation of the particles but this came from the fusing of the SiO_2 shell to create larger multicore particles rather than from the CeO_2 shell causing the issue. In the TEM image, there are some multicore particles, but the sample is mainly composed of individual particles. Repeated washing, sonication and magnetic extraction does remove some of the unbound CeO_2 but even after 5 of these cycles, it was found that some residual CeO_2 remained. The images show a CeO_2 shell approximately 20 nm thick, the SiO_2 inner shell approximately 30 nm thick and the $MnFe_2O_4$ core of approximately 120 nm diameter, giving overall particles of 219±20 nm. Size distribution were calculated for 100 particles using ImageJ (Figure A-8). The variation in sizes comes mostly from the variation in the initial $MnFe_2O_4$ core size. Overall, the coating procedure had been very successful.

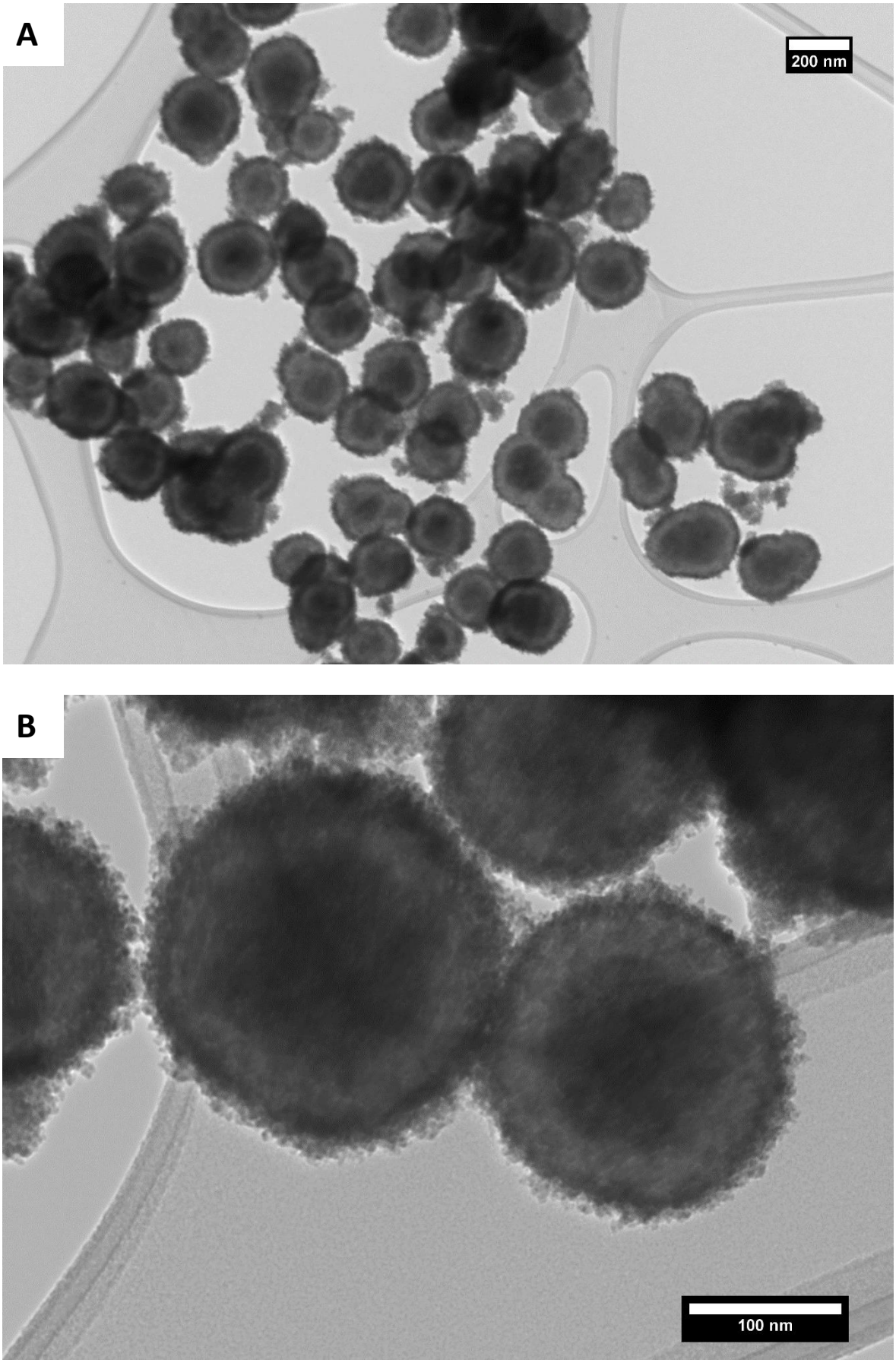


Figure 5-19: (A), (B) TEM images of the $MnFe_2O_4$@SiO_2@CeO_2 MNPs.

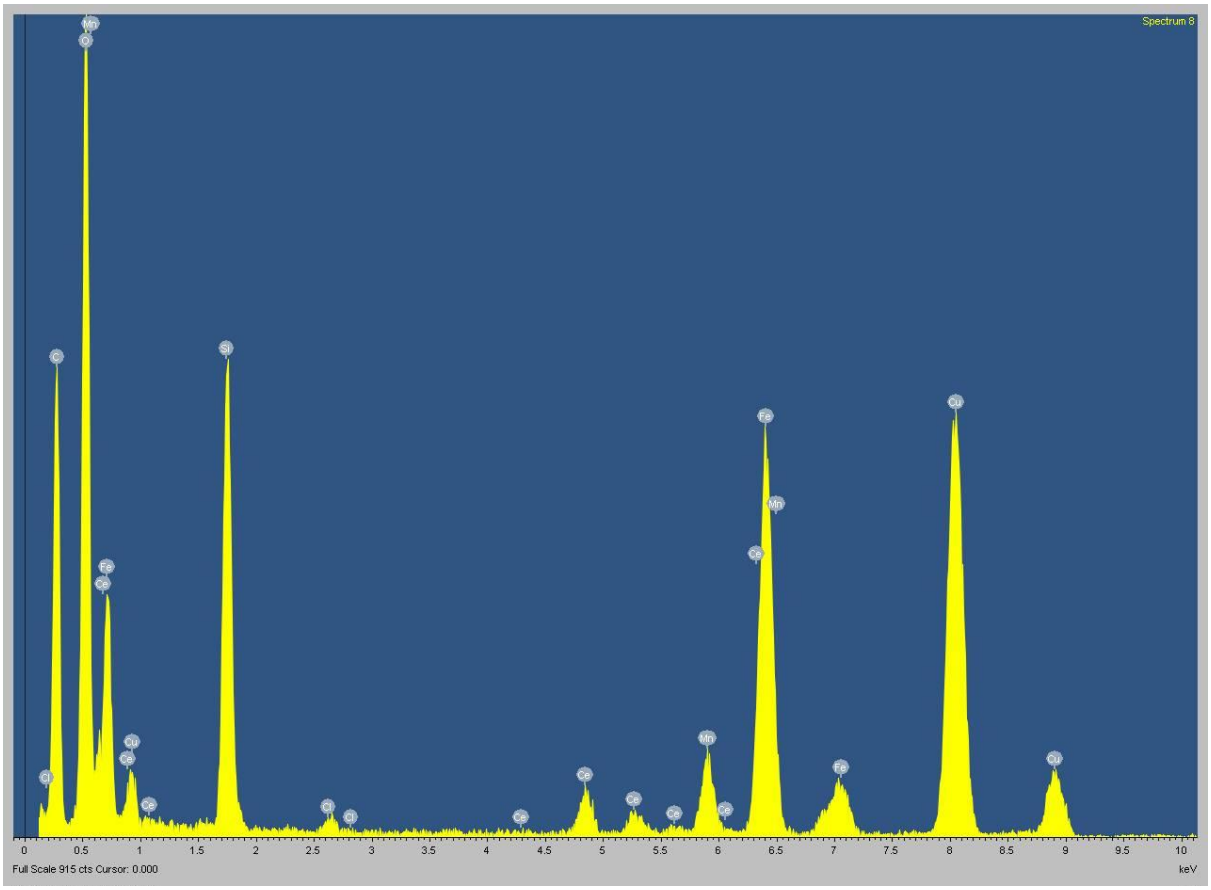


Figure 5-20: EDX of the $MnFe_2O_4$@SiO_2@CeO_2 nanoparticles.

EDX of the nanoparticles above (Figure 5-20) showed them to be composed of Fe, Mn, O, Si and Ce. There was some small contamination of Cl. The Ce peaks show that cerium had deposited on the particle surface. The EDX results confirm the results of the TEM images.

XRD of the sample shown below (Figure 5-21) gave a high match for the reference patterns of $MnFe_2O_4$ (COD 230-0619) and CeO_2 (COD 434-3162). A phase quantification performed by the *HighScore Plus* software package indicated that the sample contained 90.8 % of crystalline $MnFe_2O_4$ and 9.2 % CeO_2. Phase quantification does not take into account amorphous material so the actual ratio of CeO_2 and $MnFe_2O_4$ may be different but the results are indicative of a particle composed of more magnetic core material than the non-magnetic shell material. The results confirm that the nanostructure had a phase of CeO_2 coating the surface.

Being a mixture of phases a Williamson-Hall plot to calculate crystallite size may not give accurate results as many of the peaks overlap. Pure CeO_2 was synthesised for comparison using the same synthesis that precipitated the NP on to the surface of the silica coated MNP

here and it indicated that crystallites of 8.3 nm were produced by this synthesis. In the various TEM images, the CeO_2 NP had similar sizes.

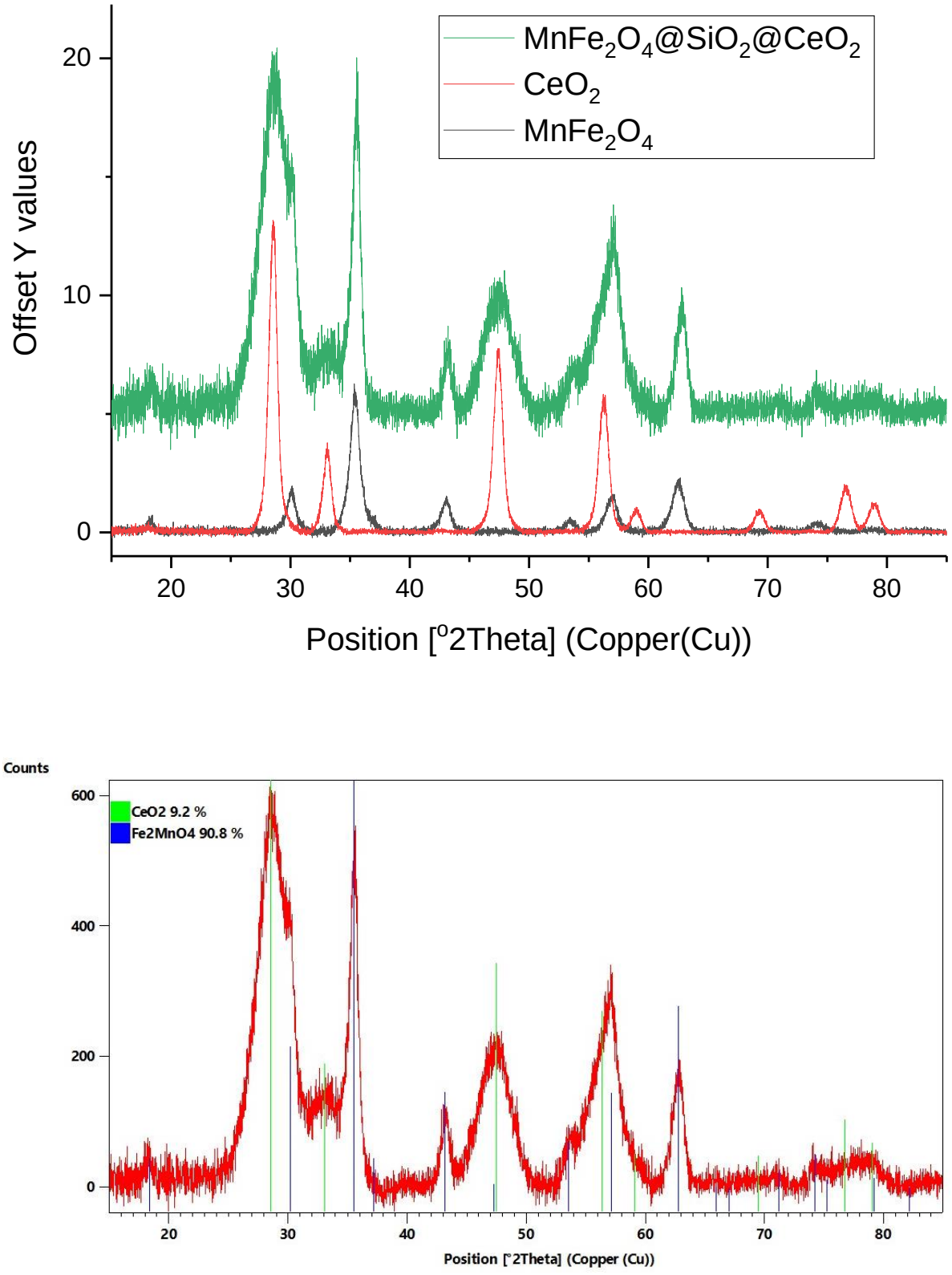


Figure 5-21: XRD patterns showing the result as a combination of CeO_2 and $MnFe_2O_4$ and the match for $MnFe_2O_4$ and CeO_2 with the phase quantification.

The amount of precursors for the reaction in the experimental section was determined by a calculation as described earlier, involving the known size of the silica coated MNPs from TEM data and the densities of the materials involved. The procedure as described in the experimental section (2.4.4) calculated for a CeO_2 shell of 10 nm. The TEM results indicate a shell of 20 nm was formed however. The shell can be seen to be composed of aggregations of crystallites rather than a single crystalline layer so the packing of these crystallites would increase the volume compared with the packing of a single crystal layer.

One of the variations that was tried was changing the thickness of the shell to see the results.

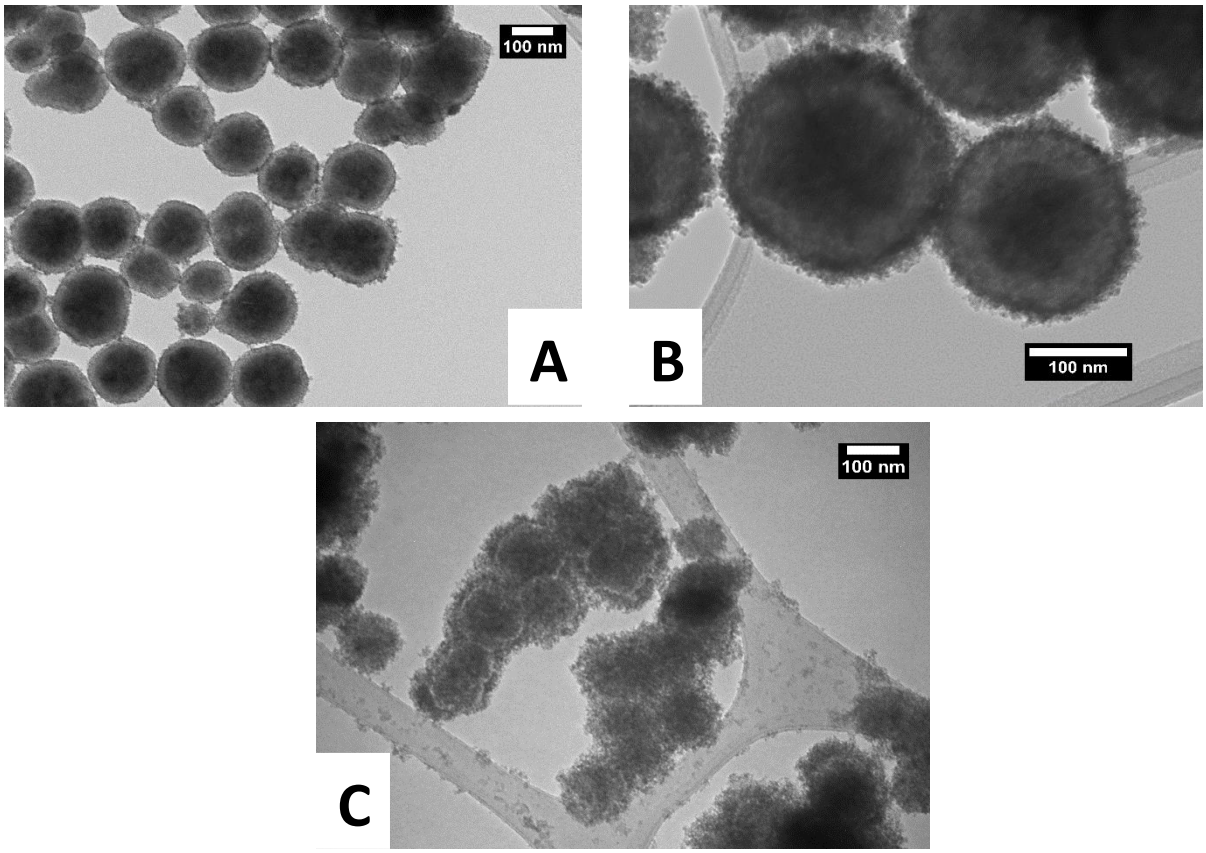


Figure 5-22: TEM images with different calculated for shell thicknesses (A) 5 nm (B) 10 nm (C) 20 nm.

As can be seen in the images above (Figure 5-22) there was some correlation between the shell thickness as calculated for and the thickness of the shell on the surface observed by TEM. Attempts to create a thicker shell caused more agglomeration of the particles as the high levels of CeO_2 began to cause multicore particles coated by a shell of CeO_2 as can be seen in image **C** above. The synthesis for a thinner shell produced good results with separate particles coated with a thick shell of CeO_2 as can be seen in image **A** above. The optimal result was found to be for a calculated shell of 10 nm given a shell of 20 nm, as can be seen in image **B**

above. The coating is thicker but the particles are still individual and not fused together. A summary of these results is given in the table below (Table 5-4).

Table 5-4: Table giving summary of result of different shell thicknesses.

	Calculated for a shell of (nm)	Shell thickness from TEM (nm)	Comment
A	5	6±2	Thin CeO_2 shell
B	10	20±5	Thick CeO_2 shell
C	20	35±10	Agglomeration

One interesting variation result was that after stirring overnight, following the experimental procedure (2.4.4), a sample of the mixture was taken prior to the heating for 2 hours to precipitate out the CeO_2 onto the MNPs. A TEM image of this sample as can be seen below (Figure 5-23) showed that the particle was already thinly coated with a layer of CeO_2 approximately 2 nm thick. This layer would offer excellent nucleation points for the remainder CeO_2 that has to precipitate out of solution upon heating.

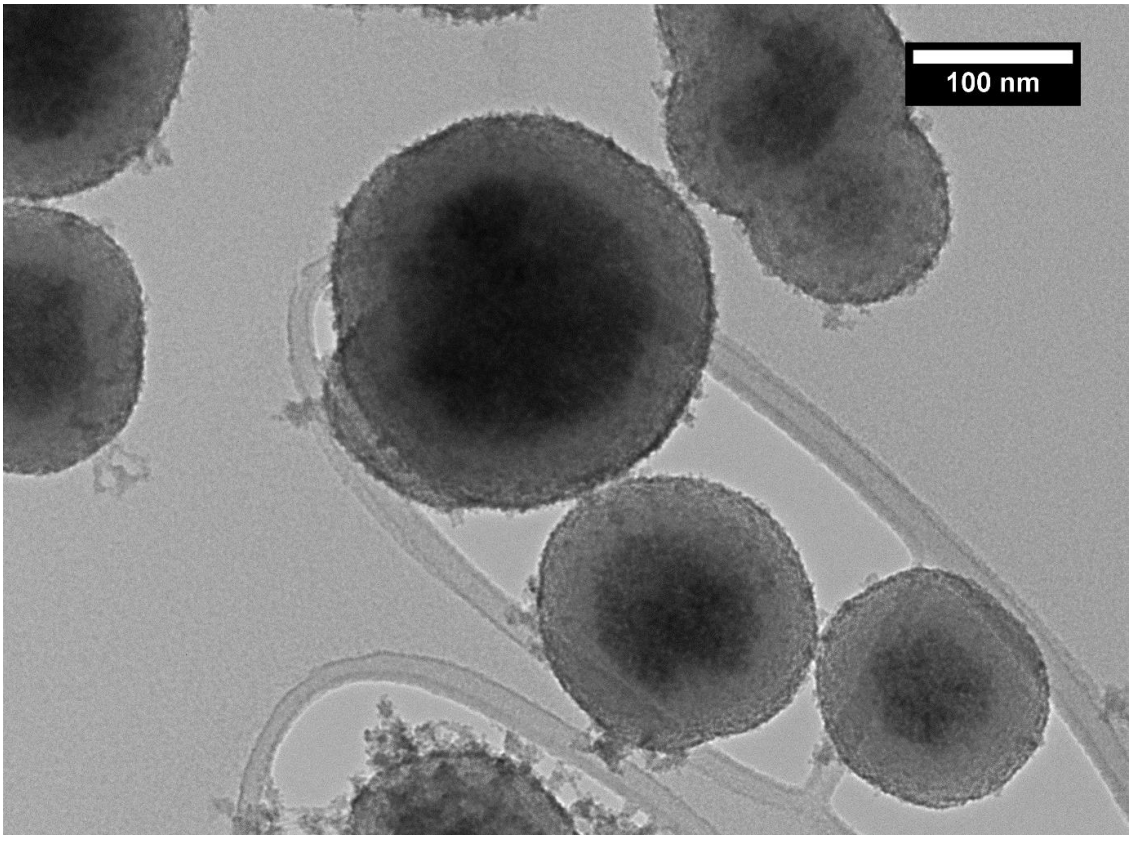


Figure 5-23: TEM images of the $MnFe_2O_4$@SiO_2@CeO_2 after stirring overnight, before heating for 2 hours.

Previously Fe_3O_4@SiO_2 coming from coprecipitated Fe_3O_4 with smaller cores had been synthesised and discussed above (4.3.4). This type of magnetic nanostructures were found to be very stable in solution and not easily extracted with a neodymium magnet. In addition, it was more difficult to get individual core@shell particles without fusing of the SiO_2 shell when it was attempted to reduce the thickness of the shell. A sample of the Fe_3O_4@SiO_2 was also coated with CeO_2. The sample used had a Fe_3O_4 core of 14 ± 4 nm. This core had a SiO_2 shell of 5 nm attached. There was significant aggregation in the MNP@silica precursor as can be seen below (Figure 5-24). This was because of the attempt at a thinner shell synthesis. This sample was chosen because a thicker shell significantly reduces the magnetisation. Adding a CeO_2 shell will further reduce the magnetisation so it was a choice here of a balance between a thick shell with well-defined individual particles but with low magnetisation or higher magnetisation values but with some fusing of the silica shell between particles.

The TEM images of the nanostructures produced in this study are shown below (Figure 5-24). We can see the silica coated particles used as the precursor in **A** and then these MNPs coated with CeO_2 in **B**. The particles can be seen to have a 14 nm core with a 5 nm SiO_2 shell and an approximately 5 nm CeO_2 shell. This gives a final Fe_3O_4@SiO_2@CeO_2 particle of approximately 24 ± 4 nm from the TEM images. The coating was successful but not as clear and uniform as with the larger $MnFe_2O_4$@SiO_2 particles. The magnetisation of these particles was 37.8 Am^2kg^{-1} for the Fe_3O_4@SiO_2 and 22.6 Am^2kg^{-1} for the Fe_3O_4@SiO_2@CeO_2 at 1 T. Extraction of these particles with a neodymium magnet though took 16 hours, which was considered too long for a useful magnetically recyclable catalyst.

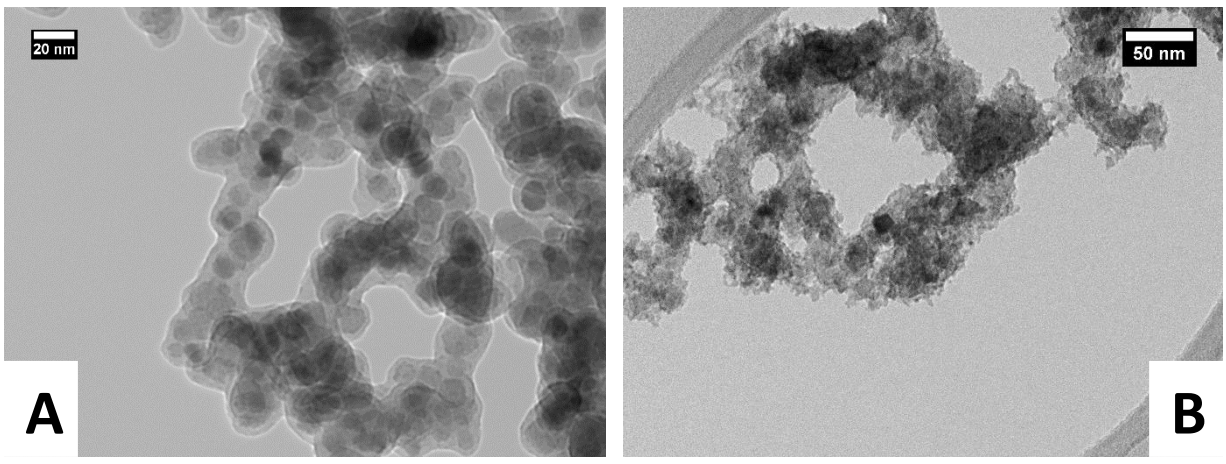


Figure 5-24: TEM images of (A) Fe_3O_4@SiO_2 and (B) Fe_3O_4@SiO_2@CeO_2 particles.

A calculation of the surface area was performed for the final CeO_2 coated particle coming from the larger $MnFe_2O_4$ core and the smaller Fe_3O_4 core, to understand the theoretical amount of CeO_2 surface available as a catalytic surface. This calculation gives the area of surface available per mass of the material. The calculation assumes a uniform CeO_2 surface on spheres that are all of the same size. From our images, the CeO_2 on the surface can be seen not to create a perfectly even surface so the actual surface area would probably be larger than these values. These values are a good guide though towards understanding the catalytic activity when we test these particles. The results of these calculations are given in the table below (Table 5-5). The extraction times are the times for extraction with a magnet.

Table 5-5: Calculated Surface Area and actual extraction times for the various core@shell particles.

MNP type	Diameter of particle (nm)	Calculated Surface Area (m^2g^{-1})	Extraction Time
$MnFe_2O_4$@SiO_2@CeO_2	140	11.6	under 3 hours
Fe_3O_4@SiO_2@CeO_2	24	51.0	over 12 hours

We have also attempted to coat the bare MNP with CeO_2. Coprecipitated magnetite that was prepared with NaOH was used for this synthesis. The sample was not as monodisperse as the magnetite prepared using the coprecipitation with ammonium but it would be sufficient to test the possibility for CeO_2 coating. In addition, the extraction of these particles with a neodymium magnet was relatively fast. If these smaller particles could be directly coated with CeO_2 this would give a larger surface area sample with hopefully quick extraction with a handheld neodymium magnet. This approach was unsuccessful though with separate Fe_3O_4 and CeO_2 particles forming as can be seen below (Figure 5-25).

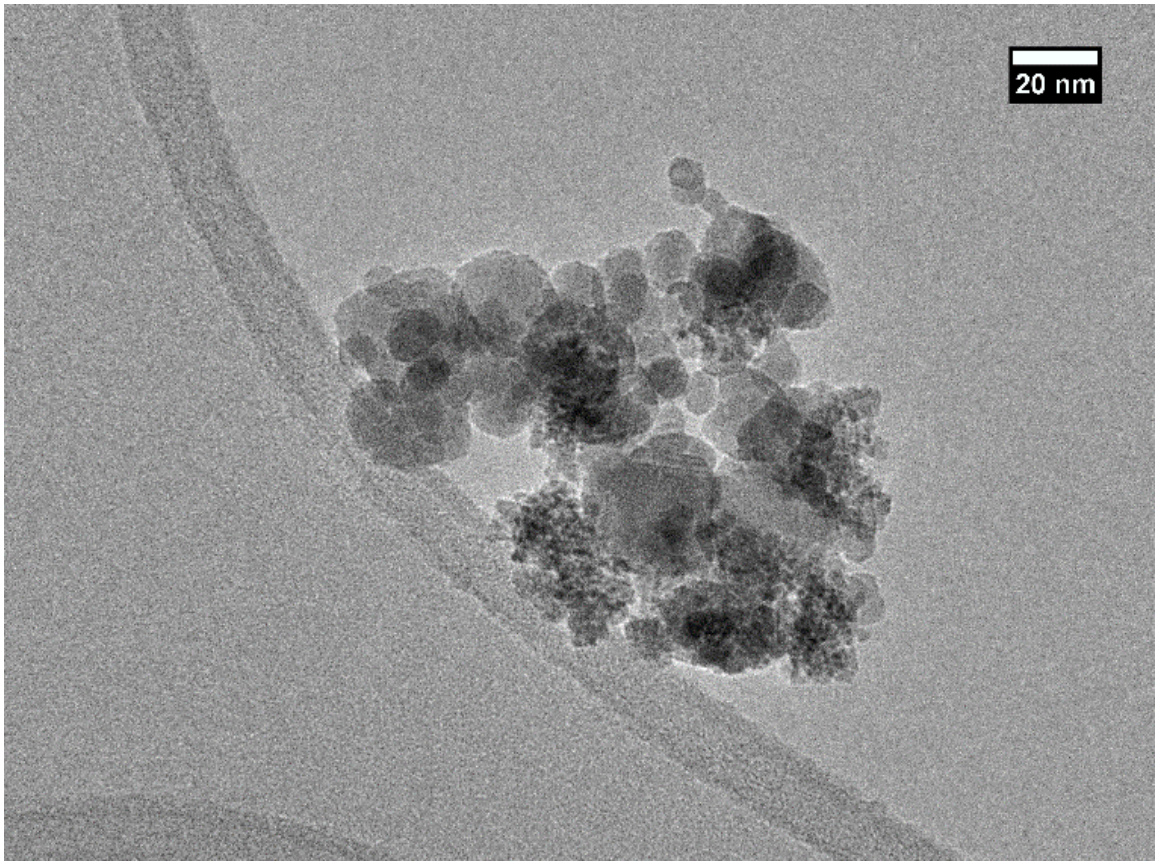


Figure 5-25: TEM image of the bare Fe_3O_4 with the smaller CeO_2 particles.

5.4 Conclusions

Magnetic core nanoparticles have been coated with shells of known catalytic materials, namely cerium dioxide and manganese dioxide. It was found that the manganese dioxide had a favourable interaction and binding with manganese ferrite cores and that there was a favourable size match for the polyol synthesised manganese ferrite cores and the nanosheets of manganese ferrite to give good core shell structures of $MnFe_2O_4$@MnO_2. The reason for the good attachment to the $MnFe_2O_4$ cores was probably the Mn and O on the surface creating preferential binding sites for the MnO_2 precipitating out of solution. For the cerium dioxide, attachment directly to the magnetic nanoparticle was not possible probably because of a lattice mismatch between the two crystal structures. However, it was found that a silica shell on the MNPs core provide a good surface for attachment. Amorphous silica has variable lattice parameters and some of these sites would be a good match for the lattice of ceria, giving sites for the growth of ceria on the surface of the silica.

As a result, good quality core@shell structures of both particles, the $MnFe_2O_4$@MnO_2 and the $MnFe_2O_4$@SiO_2@CeO_2, were created. These nanostructures have been characterised by TEM to show the core@shell structures had been created and by XRD to show that the correct phases had been created. VSM analysis showed appropriate magnetic properties where the particles saturated in a low magnetic field and it was observed that the particles could be extracted from solution in a reasonably short timeframe. These particles will next be further tested for various applications.

5.5 References

1 J. Govan and Y. Gun'ko, *Nanomaterials*, 2014, **4**, 222–241. https://doi.org/10.3390/nano4020222.

2 S. Shylesh, V. Schünemann and W. R. Thiel, *Angew. Chemie Int. Ed.*, 2010, **49**, 3428–3459. https://doi.org/10.1002/anie.200905684.

3 A.-H. Lu, E. L. Salabas and F. Schüth, *Angew. Chemie Int. Ed.*, 2007, **46**, 1222–1244. https://doi.org/10.1002/anie.200602866.

4 R. Dalpozzo, *Green Chem.*, 2015, **17**, 3671–3686. https://doi.org/10.1039/C5GC00386E.

5 R. Ghosh Chaudhuri and S. Paria, *Chem. Rev.*, 2012, **112**, 2373–2433. https://doi.org/10.1021/cr100449n.

6 H. Shayesteh, A. Ashrafi and A. Rahbar-Kelishami, *J. Mol. Struct.*, 2017, **1149**, 199–205. https://doi.org/10.1016/j.molstruc.2017.07.100.

7 P. I. Girginova, A. L. Daniel-da-Silva, C. B. Lopes, P. Figueira, M. Otero, V. S. Amaral, E. Pereira and T. Trindade, *J. Colloid Interface Sci.*, 2010, **345**, 234–240. https://doi.org/10.1016/j.jcis.2010.01.087.

8 X. Chen, J. Rao, J. Wang, J. J. Gooding, G. Zou and Q. Zhang, *Chem. Commun.*, 2011, **47**, 10317. https://doi.org/10.1039/c1cc13734d.

9 M. Y. Hua, H. W. Yang, C. K. Chuang, R. Y. Tsai, W. J. Chen, K. L. Chuang, Y. H. Chang, H. C. Chuang and S. T. Pang, *Biomaterials*, 2010, **31**, 7355–7363. https://doi.org/10.1016/j.biomaterials.2010.05.061.

10 K. Chatterjee, J. Zhang, N. Honbo and J. S. Karliner, *Cardiology*, 2010, **115**, 155–162. https://doi.org/10.1159/000265166.

11 M. Peng, H. Li, Z. Luo, J. Kong, Y. Wan, L. Zheng, Q. Zhang, H. Niu, A. Vermorken, W. Van De Ven, C. Chen, X. Zhang, F. Li, L. Guo and Y. Cui, *Nanoscale*, 2015, **7**, 11155–11162. https://doi.org/10.1039/c5nr01382h.

12 M. Răcuciu, D. E. Creangă and A. Airinei, *Eur. Phys. J. E*, 2006, **21**, 117–121.

https://doi.org/10.1140/epje/i2006-10051-y.

13 E. A. Kwizera, E. Chaffin, X. Shen, J. Chen, Q. Zou, Z. Wu, Z. Gai, S. Bhana, R. Oconnor, L. Wang, H. Adhikari, S. R. Mishra, Y. Wang and X. Huang, *J. Phys. Chem. C*, 2016, **120**, 10530–10546. https://doi.org/10.1021/acs.jpcc.6b00875.

14 D. J. Cole-Hamilton, *Science*, 2003, **299**, 1702–1706. https://doi.org/10.1126/science.1081881.

15 B. G. Wang, B. C. Ma, Q. Wang and W. Wang, *Adv. Synth. Catal.*, 2010, **352**, 2923–2928. https://doi.org/10.1002/adsc.201000508.

16 C. Ó Dálaigh, S. A. Corr, Y. Gun'ko and S. J. Connon, *Angew. Chemie Int. Ed.*, 2007, **46**, 4329–4332. https://doi.org/10.1002/anie.200605216.

17 D. K. Yi, S. S. Lee and J. Y. Ying, *Chem. Mater.*, 2006, **18**, 2459–2461. https://doi.org/10.1021/cm052885p.

18 B. Chang, J. Guo, C. Liu, J. Qian and W. Yang, *J. Mater. Chem.*, 2010, **20**, 9941. https://doi.org/10.1039/c0jm01237h.

19 M. B. Gawande, Y. Monga, R. Zboril and R. K. Sharma, *Coord. Chem. Rev.*, 2015, **288**, 118–143. https://doi.org/10.1016/j.ccr.2015.01.001.

20 E. A. Kwizera, E. Chaffin, Y. Wang and X. Huang, *RSC Adv.*, 2017, **7**, 17137–17153. https://doi.org/10.1039/C7RA01224A.

21 A. Najafpoor, R. Norouzian-Ostad, H. Alidadi, T. Rohani-Bastami, M. Davoudi, F. Barjasteh-Askari and J. Zanganeh, *J. Mol. Liq.*, 2020, **303**, 112640. https://doi.org/10.1016/j.molliq.2020.112640.

22 M. Nasrollahzadeh, *Advances in magnetic nanoparticles-supported palladium complexes for coupling reactions*, 2018, vol. 23. https://doi.org/10.3390/molecules23102532.

23 Y. Zhai, J. Zhai, M. Zhou and S. Dong, *J. Mater. Chem.*, 2009, **19**, 7030. https://doi.org/10.1039/b912767d.

24 P. M. Álvarez, J. Jaramillo, F. López-Piñero and P. K. Plucinski, *Appl. Catal. B Environ.*,

2010, **100**, 338–345. https://doi.org/10.1016/j.apcatb.2010.08.010.

25 J. Chen, Y. G. Wang, Z. Q. Li, C. Wang, J. F. Li and Y. J. Gu, *J. Phys. Conf. Ser.*, 2009, **152**, 012041. https://doi.org/10.1088/1742-6596/152/1/012041.

26 H. Chen, Y. Wang and Y. K. Lv, *RSC Adv.*, 2016, **6**, 54032–54040. https://doi.org/10.1039/c6ra10103h.

27 H. Kumar and P. Sangwan, *Int. J. Chem. Chem. Eng.*, 2013, **3**, 155–160.

28 S. Zhou, Z. Du, X. Li, Y. Zhang, Y. He and Y. Zhang, *R. Soc. Open Sci.*, 2019, **6**, 190351. https://doi.org/10.1098/rsos.190351.

29 X. Liu, N. Wu, C. Cui, N. Bi and Y. Sun, *RSC Adv.*, 2015, **5**, 24016–24022. https://doi.org/10.1039/c4ra14753g.

30 P. -L Chen and I. -W Chen, *J. Am. Ceram. Soc.*, 1993, **76**, 1577–1583. https://doi.org/10.1111/j.1151-2916.1993.tb03942.x.

31 K. K. Babitha, A. Sreedevi, K. P. Priyanka, B. Sabu and T. Varghese, *Indian J. Pure Appl. Phys.*, 2015, **53**, 596–603.

32 S. B. Khan, M. Faisal, M. M. Rahman and A. Jamal, *Sci. Total Environ.*, 2011, **409**, 2987–2992. https://doi.org/10.1016/j.scitotenv.2011.04.019.

33 M. Palard, J. Balencie, A. Maguer and J. F. Hochepied, *Mater. Chem. Phys.*, 2010, **120**, 79–88. https://doi.org/10.1016/j.matchemphys.2009.10.025.

6 Testing the core@shell MNPs in Applications

6.1 Introduction

A catalyst speeds up chemical reactions enabling the process to be completed within a reasonable time and with high yields. The correct choice of reagents, catalyst and solvents gives an opportunity to minimize the environmental impact and reduce waste and costs in chemical industry [1]. In terms of catalysts, two types are defined, homogeneous and heterogeneous. Homogeneous catalyst are catalysts that are in the same phase as the reagents whereas heterogeneous catalysts are in a different phase (usually on a solid support)[2]. Homogeneous catalysts are needed in lower concentrations as more active sites are available and have very high reactivity and selectivity. In addition, there is the possibility of easy modification of the catalysts. Many efficient homogeneous catalysts have been developed but only a limited number of these catalysts have been used in industry because of difficulties associated with catalyst separation and recycling [1][3][4]. Heterogeneous catalysts are needed in higher concentrations and have lower selectivity frequently resulting in unwanted side products. Modification of the heterogeneous catalyst is difficult as the processes occurring on the surface of heterogeneous catalysts in often obscure but separation of heterogeneous catalyst is much easier, so heterogeneous catalyst are used more in industry[4][5]. Magnetic core@shell nanoparticles with a catalytic shell give the unique possibility to bring together some of the advantages of these two different catalyst types[3]. They have large surface areas for immobilisation of a catalytic shell giving more sites available to the reaction and separation of the catalyst can be easily achieved using a magnet. Manganese dioxide is a well-known catalyst for oxidation[6] and is often used for demonstration purposes in teaching about catalysts [7]. Cerium dioxide is another well-known catalyst which is widely used in catalytic converters for exhaust gases[8]. The development of magnetic core@shell nanostructures with catalytic metal oxide coating should enable their use in catalytic reactions with easy magnetic recovery and recycling.

Activation of chemical reactions is an important area in chemistry. There are a number of processes, which can be heat or light activated. However, magnetic activation of a chemical reaction is a new area with a very limited number of examples of reactions triggering[9].

Remote magnetic activation using MNPs with magnetic hyperthermia is another important area of interest [10]. The use of coated MNPs that inhibit a reaction and the magnetic removal then causing the reaction to initiate could find application in many areas where remote triggering is necessary[11]. It is expected that this field can be further developed using magnetic core@shell nanostructures that have been produced in our work.

Magnetic extraction of pollutants from water is another emerging area of interest. Removal of toxic metals ions[12] and organic pollutants[13] are currently of high importance for wastewater remediation. Dye pollutants are produced by many industries, particularly in printing and textile manufacture. These pollutants often end up in wastewater and methods to degrade, adsorb and remove these pollutants are of great interest for water security. The high surface area of MNPs combined with their magnetic modality makes them very attractive materials for immobilisation of adsorbents materials for water purification applications. MnO_2 is also known to be an effective adsorbent[14] aside from its use as an oxidation catalyst. Having made good quality MnO_2 coated magnetic nanoparticles these will be tested for removal of various dyes.

6.2 Aims

The main aim of this part of our work is to test selected core@shell nanoparticles described in previous chapters, namely the $MnFe_2O_4@SiO_2@CeO_2$, the $MnFe_2O_4@MnO_2$ and the $Fe_3O_4@SiO_2@CeO_2$ for catalytic activity in selected oxidation reactions, with magnetic extraction and recycling of the catalyst. We tested our nanostructures in catalytic oxidation of benzyl alcohol to benzaldehyde. After several recycles, the magnetic core@shell nanostructures are to be isolated and characterised again for any changes to be noted. The $MnFe_2O_4@MnO_2$ nanostructures will also be tested for use as an inhibitor in a selected glue formulation, to see if the glue can be firstly inhibited by the presence of the coated MNPs and then the glue reactivated by magnetic removal of the core@shell MNPs. The $MnFe_2O_4@SiO_2@CeO_2$ and $MnFe_2O_4@MnO_2$ particle are also going to be tested for removal of dyes from water with potential regeneration of the particles after magnetic extraction. They are to be recycled several times to see if they remain effective at pollutant removal.

6.3 Results and Discussion

The magnetic core@shell nanoparticles discussed in the previous chapters have been characterised by a variety of techniques. We have selected the best core@shell nanostructures coated with the functional catalytic shell with reasonably good magnetic properties, which could be magnetically extracted from solution in under 3 hours. These nanostructures have been chosen for testing for various application in this part of our work. The selected core@shell magnetic nanostructures are first to be tested for catalytic activity in oxidation of benzyl alcohol, which is a known standard reaction for testing of catalytic materials. By comparison of our results with previously reported examples of each catalytic material, we will be able to judge the efficacy of the nanostructures. The reports in the literature do not use MNP core@shell structures but use the catalytic materials usually supported on another non-magnetic material. We will also use magnetic core@shell nanostructures to produce new glue formulations, which could be magnetically activated by magnetic removal of the nanostructures. Finally, the particles will also be tested and quantified for the removal of selected pollutant dyes from water. This will be done by UV-vis analysis of the water to quantify removal of the specific dye. These studies will be presented and discussed in detail in the following sections.

6.3.1 Testing of $MnFe_2O_4$@MnO_2 Nanostructures in Catalytic Oxidation of Benzyl Alcohol to Benzaldehyde

The oxidation of benzyl alcohol to benzaldehyde reaction was chosen as the test reaction as there are several literature reports on the use of supported MnO_2 catalysts in this process showing high yields[2][5]. The oxygen source used in our reaction was atmospheric oxygen with air bubbling through the reaction mixture in a similar fashion to previous work[2] but it is also possible to use a peroxide as the oxygen source with benzyl peroxide or tert-butyl hydrogen peroxide[15] commonly used. Previous reports have yields of up to 90 % [2][15].

The reaction was carried out in toluene at 100 °C, with the $MnFe_2O_4$@MnO_2 or MnO_2 nanocatalysts in the reaction mixture. Air was bubbled through the reaction mixture and a high efficiency condenser was attached to capture the evaporated toluene and return it to the reaction solution. Even with the high efficiency condenser, there was some loss of toluene

because of the bubbling air evaporating the solution. The process was tried with no catalyst, with the core $MnFe_2O_4$ MNP on their own and with pure MnO_2 nanoparticles as controls. The accepted mechanism for oxidation on MnO_2 has been described by Goldman[16] where the alcohol is adsorbed on the MnO_2 surface , coordinates the Mn(IV), then radical formation on the alcohol-aldehyde transition state causes the formation of aldehyde and $Mn(II)(OH)_2$ which is quickly oxidised back to MnO_2 with the formation of H_2O by-product. The outline of the mechanism of this process is given in below (Figure 6-1).

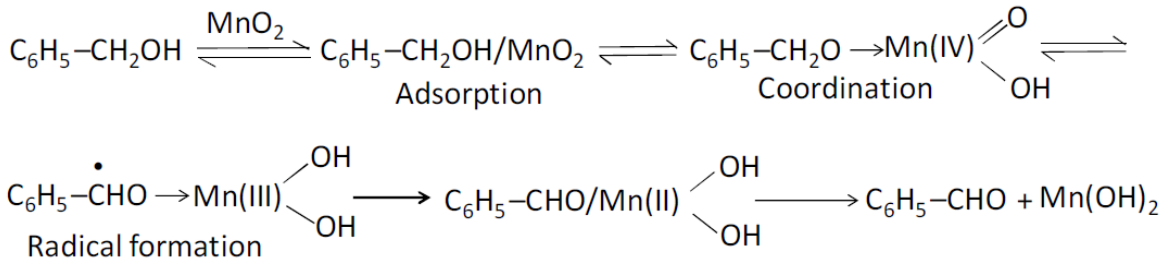


Figure 6-1: Proposed mechanism for the oxidation of benzyl alcohol with MnO_2[17]**.**

After the reaction was completed, the particles were magnetically extracted, washed several times with alcohol, acetone and water and then dried in a vacuum oven at 80 °C. They were then used in a repeat reaction with up to 6 reactions cycles done. The reaction mixture had the toluene removed by rotary evaporation and the crude product was studied by NMR. Integration of the peaks from NMR was used to calculate the conversion. The results from these explorations are summarised in the table below (Table 6-1).

Table 6-1: Results for the conversion of benzyl alcohol to benzaldehyde using $MnFe_2O_4$@MnO_2.

Entry Run	Catalyst	Conversion (%)
	No MNP, only air	0
	$MnFe_2O_4$	0.4
	Synthesised MnO_2 (5% mol. ratio)	34.3
1	$MnFe_2O_4$@MnO_2	1.4
2	$MnFe_2O_4$@MnO_2	2.4
3	$MnFe_2O_4$@MnO_2	2.0
4	$MnFe_2O_4$@MnO_2	1.8
5	$MnFe_2O_4$@MnO_2	1.9
6	$MnFe_2O_4$@MnO_2	1.7

The conversion was monitored by NMR analysis of the product, where the transformation of the two hydrogens peak at 4.7 ppm on the benzyl alcohol, to a single hydrogen peak at 10.0 ppm for the aldehyde, gives clear results. In the spectra below (Figure 6-2), we see the HNMR output after the reaction with MnO_2 on its own, as it gave the highest yield. The pertinent peaks for the conversion calculation are labelled at the top, 4.7 for benzyl alcohol and 10.0 for benzaldehyde. The benzene ring is in the region 7-8 ppm. The peak at 2.4 ppm comes from toluene, which was the reaction solvent. We can see in this spectrum the integrated peak values of 1.00 and 3.83 at the bottom. These values are used for the conversion calculation.

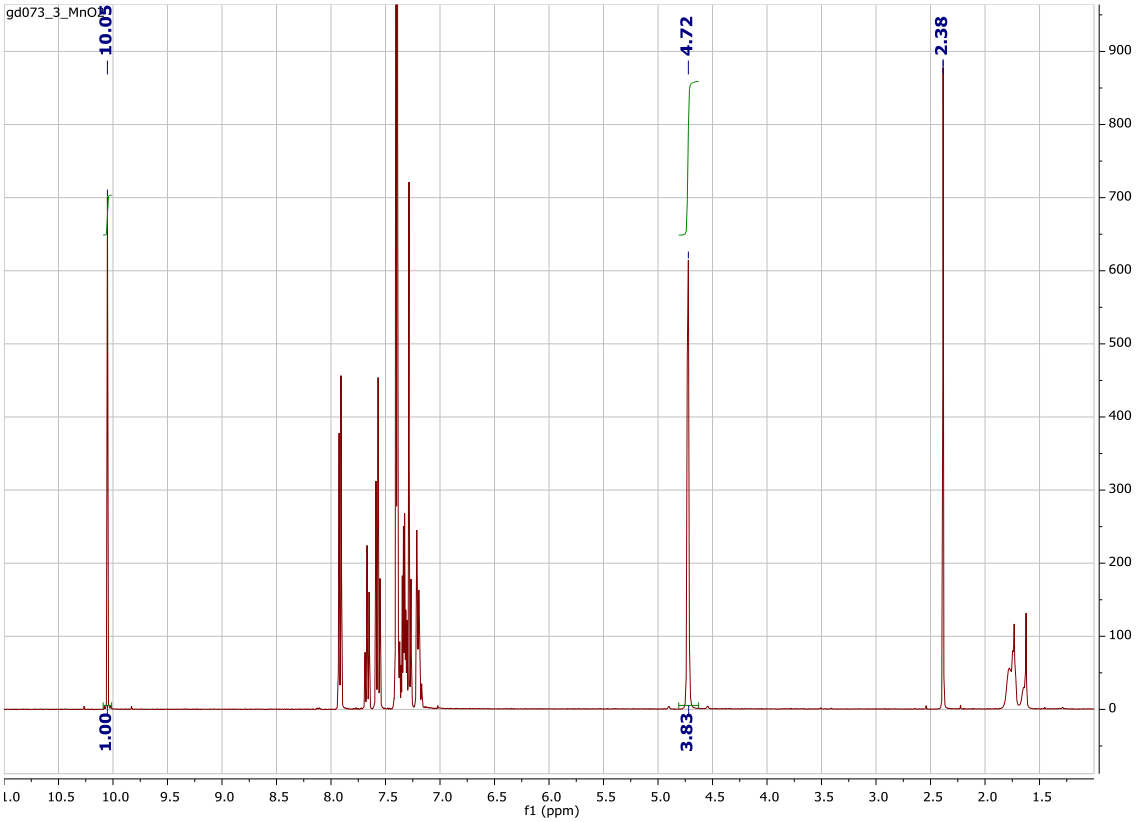


Figure 6-2: ^{1}H NMR (400 MHZ, $CDCl_3$) spectrum of the products for catalysis using MnO_2 only.

The catalytic activity of the nanocatalyst was much lower than expected. Several polymorphs of MnO_2 are known to exist and some have better catalytic activity[18]. The XRD analysis of the MnO_2 shell synthesis on its own (Figure 5-2) indicated that the δ-MnO_2 phase was produced which has been reported to have a lower catalytic activity than other phases[18][19]. The 5 % molar ratio of MnO_2 (42 mg of MnO_2) was chosen following a previously reported result with 90% yield using MnO_2 for comparison[2]. For the $MnFe_2O_4$@MnO_2, 200 mg was used, as most of the mass of the particle would have been

coming from the $MnFe_2O_4$ core. A literature search did not reveal these type of MNPs being used for catalysis for comparison of yields and conversion rates.

The initial NMR results of the product were not well defined with broad and skewed peaks in the spectra even after the solution had gone clear after magnetic extraction. It was also found that to get good NMR results, the reactant solution needed to be filtered through a 0.2 µm syringe filter. This indicates that the presence of some residual MnO_2 flakes left in the solution were affecting the quality of NMR spectra resulting in broadening of the peak. After filtering all solid residues were removed giving good quality NMR spectra.

Before the experimental run 6, the particles were placed in the furnace at 400 °C to burn off any material that may be blocking the active sites on the surface of the nanocatalyst. XRD of the particles were taken after the particles had been in the furnace prior to the catalytic reaction to see if any changes had taken place. The XRD results can be seen below (Figure 6-3) and showed no change to the particles. As can be seen from the results of run 6 above (Table 6-1) no observable change in catalytic behaviour was noticed.

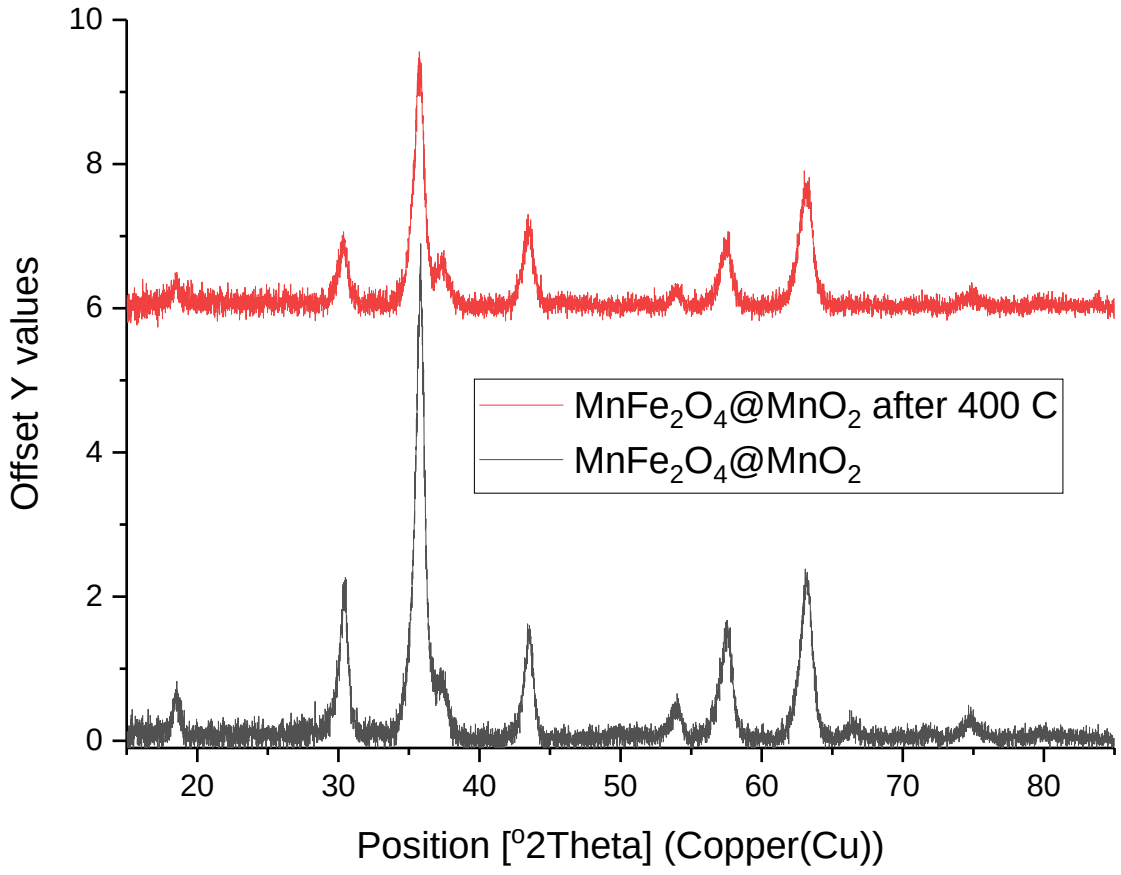


Figure 6-3: XRD patterns of $MnFe_2O_4$@MnO_2 before and after furnace at 400 °C.

Unfortunately, the results for the conversion percentages were low and the magnetic removal was not very effective as evidenced by the NMR. The most possible causes for the low conversion efficiency could be explained by low concentration of MnO_2, the δ polymorph being less catalytic[18], and low access of active species at the surface of the magnetic core@shell nanoparticles as the surface reactive sites may be blocked during the reaction by side products. With the reasonable yield of 34.3 % for the MnO_2 on its own, it would be expected there would be a reasonable result for the core@shell nanoparticles. Much more work would needs to be done here to fully elucidate this reaction but given time constraints and the poor initial results, our exploration of this catalytic process was stopped.

6.3.2 Testing of $MnFe_2O_4$@SiO_2@CeO_2 Nanostructures in Catalytic Oxidation of Benzyl Alcohol to Benzaldehyde

Similar to $MnFe_2O_4$@MnO_2 nanoparticles the $MnFe_2O_4$@SiO_2@CeO_2 core@shell nanostructures were also tested in catalytic conversion of benzyl alcohol to benzaldehyde. Previous work has shown that CeO_2 supported Au catalyst could oxidise benzyl alcohol but the reported yields were low at 3.4 %[20]. Another group found that Au and CeO_2 nanocomposites could give up to 23.5 % conversion with 100 % selectivity[21].

The oxidation reaction was again carried out in toluene with an oxygen source of air bubbling through the reaction mixture similar to the previous experiment (6.3.1). Again, the reaction mixture was stirred for 2 hours. As a control, the silica-coated MNPs were tested and as expected, they showed no catalytic activity. The pure CeO_2 that had been synthesised by the same process as was used to coat the MNPs were also tested at a 5 % molar ratio (28 mg of CeO_2). After the process was finished, the particles were magnetically extracted and washed with alcohol, acetone and water and dried in a vacuum oven at 80 °C.

A summary of the results can be seen in the table below (Table 6-2). As can be seen the results for the conversion were even lower than for the MnO_2 coated particles. As with the MnO_2 coated MNP previously, there was need to syringe filter the reaction solution after the particles had been removed to obtain good quality NMR spectra for the conversion to be calculated, indicating residual metal ions or nanoparticles left behind in the solution.

Table 6-2: Results for the conversion of benzyl alcohol to benzaldehyde using $MnFe_2O_4@SiO_2@CeO_2$.

Entry Run	Catalyst	Conversion (%)
	No MNP, only air	0
	$MnFe_2O_4@SiO_2$	0
	Synthesised CeO_2 (5% mol. ratio)	1.0
1	$MnFe_2O_4@SiO_2@CeO_2$	< 1
2	$MnFe_2O_4@SiO_2@CeO_2$	< 1
3	$MnFe_2O_4@SiO_2@CeO_2$	< 1

6.3.3 Testing of $Fe_3O_4@SiO_2@CeO_2$ for Catalytic Oxidation of Benzyl Alcohol to Benzaldehyde

As discussed earlier in a previous chapter (5.3.4), the $Fe_3O_4@SiO_2@CeO_2$ particles have a larger specific surface area than the $MnFe_2O_4@SiO_2@CeO_2$ particles. It was also decided to test these particles for catalytic oxidation of benzyl alcohol to benzaldehyde. Again, the same procedure was used where the reaction was carried out in toluene at 100 °C, with atmospheric oxygen bubbling through the mixture, with 200 mg of MNP catalytic particles in the solution. After the reaction, the particles were magnetically extracted and washed with alcohol, acetone and water before being dried in a vacuum oven at 80 °C. Again the magnetic extraction was not 100 % perfect as the NMR spectra were of poor quality initially but after filtering with a 0.2 µm syringe filter the results improved, showing that there is most likely some residual CeO_2 particles or metal ions left in the reaction mixture.

Table 6-3: Results for the conversion of benzyl alcohol to benzaldehyde using $Fe_3O_4@SiO_2@CeO_2$.

Entry Run	Catalyst	Conversion (%)
	$Fe_3O_4@SiO_2$	0
1	$Fe_3O_4@SiO_2@CeO_2$	< 1
2	$Fe_3O_4@SiO_2@CeO_2$	< 1
3	$Fe_3O_4@SiO_2@CeO_2$	< 1

As can be seen in the table above (Table 6-3) the particles performed poorly for the catalytic conversion with the conversion rates much lower than expected, despite having a larger surface area available.

6.3.4 Testing of $MnFe_2O_4@SiO_2@CeO_2$ for Catalytic Conversion of Benzyl Alcohol to Benzylidene Aniline

Previously it was reported that CeO_2 was used as a catalyst for the conversion of benzyl alcohol to benzylidene aniline at temperatures of 60 °C giving yields of up to 99 % with >99 % selectivity[22]. It was decided to test if the CeO_2 coated MNPs above could be used as catalysts in this type of reaction.

With the aniline and benzyl alcohol in the reaction mixture from the beginning of the reaction, the reaction proceeds through a 2-step process as it is shown below (Figure 6-4), where first the benzyl alcohol is converted to the benzaldehyde by oxidation involving the cerium dioxide. Then the benzaldehyde reacts with the present aniline to create the imine, benzylidene aniline. The conversion of the aldehyde to the imine proceeds readily with no need for the catalyst as our investigations showed. The conversion of the alcohol to the aldehyde however is catalysed by the presence of the cerium dioxide, without which no reaction occurs.

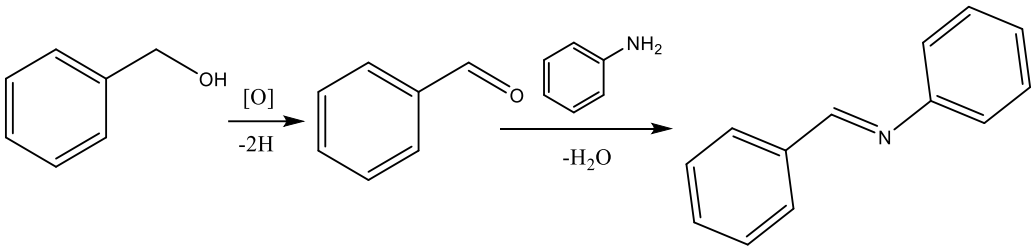


Figure 6-4: Scheme for the reaction showing the two steps involved.

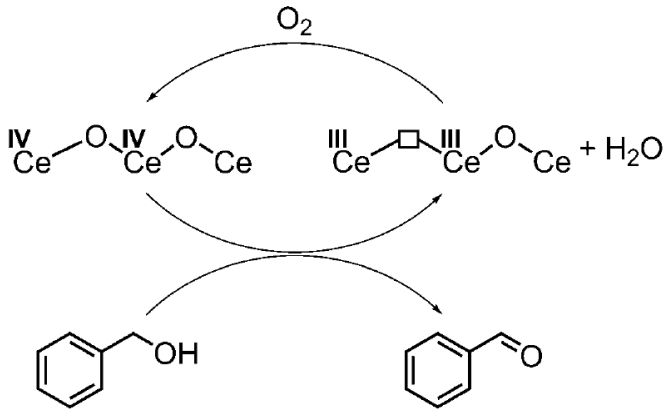


Figure 6-5: Proposed mechanism for oxidation on the CeO_2 surface[19].

The reaction mechanism that has been proposed for the oxidation step involves the reduction of the Ce^{+4} to Ce^{+3} with the oxidative dehydrogenation of benzyl alcohol with oxygen at the CeO_2 surface[22]. CeO_2 is then regenerated by oxidation of the reduced Ce(lll) with O_2. The outline of this mechanism can be seen above (Figure 6-5).

With some modifications to the described procedure, the process was performed where the reaction solution was heated to 60 °C and sonicated for 6 hours with air bubbling through the reaction solution, which consisted of toluene with the reactants and the CeO_2 coated MNPs. Again, a high efficiency condenser was attached as the bubbling air caused evaporation of the toluene but even with the condenser because of the longer reaction time, it was needed to add a few drops of toluene at intervals through the reaction to prevent drying out.

After the reaction was finished, the particles were magnetically extracted, washed several times with alcohol, acetone and water and then dried in a vacuum oven at 80 °C. The same catalytic MNP were then recycled and used in the reaction again. The results from these explorations are summarised in the table below (Table 6-4).

Table 6-4: Results for the production of benzylidene aniline using Fe_3O_4@SiO_2@CeO_2.

Entry Run (starting material)	Catalyst	Conversion (%)
(benzyl alcohol)	No MNP, only air	0
(benzyl alcohol)	$MnFe_2O_4$@SiO_2	0.4
(benzyl alcohol)	Synthesised CeO_2 (5% mol. ratio)	9.8
1 (benzyl alcohol)	$MnFe_2O_4$@SiO_2@CeO_2	4.2
2 (benzyl alcohol)	$MnFe_2O_4$@SiO_2@CeO_2	4.0
3 (benzyl alcohol)	$MnFe_2O_4$@SiO_2@CeO_2	3.8
4 (benzyl alcohol)	$MnFe_2O_4$@SiO_2@CeO_2	4.0
(benzyaldehyde)	No MNP, only air	99
(benzyaldehyde)	$MnFe_2O_4$@SiO_2@CeO_2	> 99

As can be seen the reaction with benzaldehyde proceeds readily with or without the catalyst, with the conversion of the benzyl alcohol being the limiting step. One reason for the low yields

could be the surface reactive sites can be blocked during the reaction by side products. Control reactions were performed with no catalyst and with the SiO_2 coated MNP to see if any conversion took place. The conversion of the benzyl alcohol to benzylidene aniline was followed by NMR analysis of the crude product, where the transformation of the two hydrogens peak at 4.7 ppm on the benzyl alcohol to the hydrogen peak at 8.5 ppm for the benzylidene aniline gives clear results for the level of conversion as can be seen below (Figure 6-6). The integration values of these peaks was used for the conversion calculation.

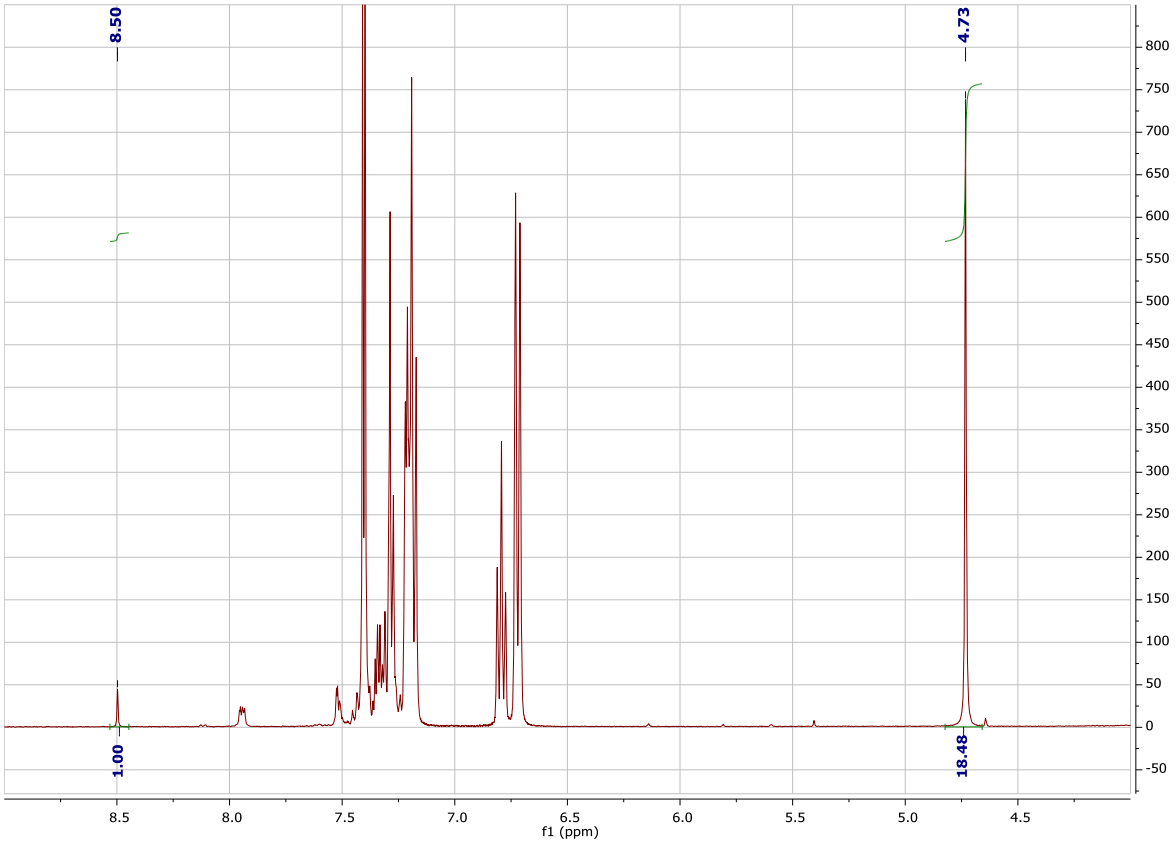


Figure 6-6: ^{1}H NMR (400 MHZ, $CDCl_3$) spectrum for benzylidene aniline product using CeO_2 (5% mol ratio).

6.3.5 Testing of $MnFe_2O_4$@MnO_2 in the Activation of an Anaerobic Glue Formulation

Anaerobic adhesives are among the most widely used types of glue formulations[23]. Anaerobic adhesives are mixtures of compounds that creates a system that cures due to a redox-initiated free radical polymerisation reaction. At ambient temperatures and in the presence of oxygen, such anaerobic adhesives remain stable and un-reacted for extended

periods. Normally, very fast polymerisation is initiated when oxygen is excluded upon assembly of suitably active substrates (i.e. redox agents) with the adhesive. The basic components of these adhesive formulations are the monomer that polymerises, an initiator that starts the polymerisation and a metal ion with adjacent oxidation states. The basic concept behind the process involves the metal ion with adjacent oxidation states will cause the initiator to decompose to produce a radical and then that radical will start the polymerisation of the monomer to cure the glue. The curing process is inhibited by oxygen with anaerobic adhesives[23]. The lower oxidation state metal ion will produce the radical by scavenging an electron from the peroxide to produce a radical while the metal ion changes to the higher oxidation state. While the metal ion is in the higher oxidation state, the glue solution is stable. The metal ion in the glue solution changes to the lower oxidation state once contact has been made with a metal surface, where free electrons on the surface of the metal are absorbed to initiate the redox-initiated free radical polymerisation. The glue will then seal or fasten the various metal parts.

The glue formulation used in our work consisted of triethylene glycol dimethacrylate as the monomer, tert-butyl peroxybenzoate as the initiator and Cu(II) tetrafluororborate as the metal ion. Once this formulation was placed between metal (aluminium or stainless steel) plates the Cu(II) ions were reduced to become Cu(I) which were then oxidised by the peroxide decomposition producing a radical necessary for polymerisation of the triethylene glycol dimethacrylate monomer. The glue solution was stable but upon contact with the metal the reaction begins, when the metal is sealed, creating an anaerobic environment, the reaction proceeds rapidly and the separate metal parts are glued by the curing of the solution after 5 minutes. The diagram below gives a simplified outline of this process (Figure 6-7).

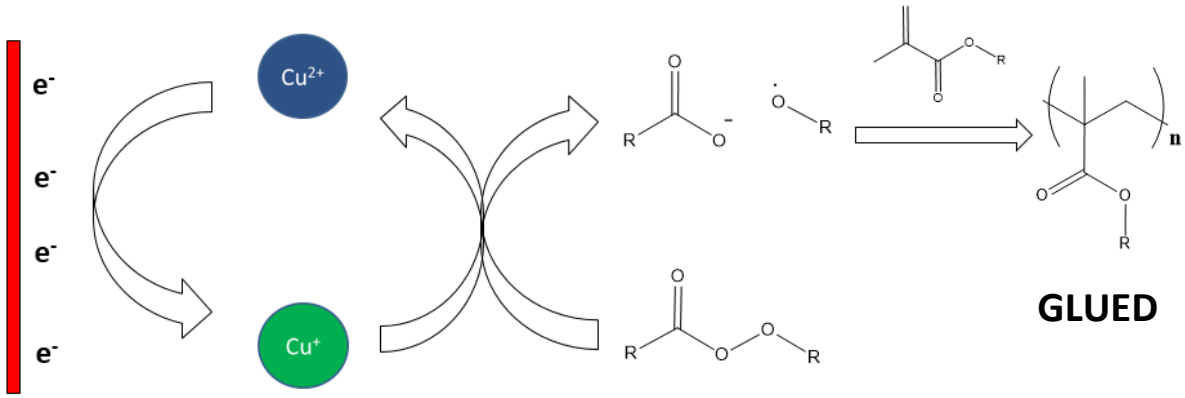


Figure 6-7: The metal plate (red) reduces Cu(II) to Cu(I) which produces a radical from the peroxide to polymerise the methacrylate. The Cu(I) is regenerated back to Cu(II) in the process.

The glue solution consisted of the triethylene glycol dimethacrylate monomer, with 0.00063 molar equivalents of the peroxide and 0.00055 molar equivalents of the Cu(II) ions. We have modified this formulation using our $MnFe_2O_4$@MnO_2 MNPs, which were mixed with the glue solution at 30 mg/mL. Our goal was to inhibit the polymerisation reaction and prevent sealing of the metal plates. This formulation demonstrated successful inhibition of the glue solution. It was also noticed that a lower content of $MnFe_2O_4$@MnO_2 MNPs (below 30 mg/mL) did not inhibit the polymerisation reaction and glue curing. Favourably, the MnO_2 coated MNPs were quite stable in the glue solution and did not precipitate out of the solution as observed for at least one week. However, it was found that when our MNPs were magnetically extracted from the glue solution, the glue polymerisation was no longer inhibited and the glue formulation was cured after 5 minutes upon application between metal plates. This showed clear inhibition of a chemical reaction and magnetic reactivation by magnetic removal of the inhibitor, the $MnFe_2O_4$@MnO_2 MNPs.

A proposed mechanism for the inhibition was that the MnO_2 absorbed the electrons before the Cu(ll) ions. Manganese dioxide has a standard reduction potential of E° = +1.23 V whereas Cu(ll) has a reduction potential of E° = +0.15 V. This means that the manganese dioxide will scavenge the electrons from the surface of the metal before the Cu(ll), preventing the formation of Cu(l) species and thereby stopping the redox-initiated free radical polymerisation. Since the MnO_2 was bound to a MNP core they could be removed by simply placing the glue solution next to a neodymium magnet and observe the glue solution go clear as the particles are magnetically extracted. Once the solution was clear, the glue was reactivated and was found to cure between the metal plates again.

This work showed very promising results with inhibition and reactivation of a chemical reaction by magnetic removal of the inhibitor. Application of this concept to other chemical processes has a great potential. Our group is currently following this line of research with the hope of finding other similar reactions where inhibition and magnetic reactivation of chemical processes using magnetic core@shell nanostructures could be applied.

6.3.6 Testing of $MnFe_2O_4$@MnO_2 for Methylene Blue Dye Removal

Our next aims were to test the $MnFe_2O_4$@MnO_2 for removal of various dyes from water. Previously it was reported that manganese dioxide can be used as an adsorbent[24] for dye removal. Another paper also described that manganese dioxide was causing a chemical degradation of the methylene blue dye [25]. It is possible that these two processes are at play during a given reaction, as will be discussed.

The investigations here were done with MB at a concentration of 21.3 µM in aqueous solution as this concentration was found to give an absorbance of approximately 1.5 AU at 662 nm. This gives a calculated molar attenuation coefficient of 65761 mol^{-1} L cm^{-1}. This value is slightly lower than a previous reported value of 95000 mol^{-1} L cm^{-1} [26] but higher than another reported value of 54912 mol^{-1} L cm^{-1} [27]. MB has an absorption peak at 662 nm and the change in intensity of this peak can be used to calculate the removal efficiency of the MNPs.

The testing of the manganese dioxide coated MNPs for removal of the MB involved sonication of 50 mL of the 21.3 µM MB solution with 100 mg of the MNP for one hour with samples taken at various time intervals throughout. These samples had the MNP magnetically extracted for 5 minutes and then a UV-vis spectrum of the sample were recorded. As a control, the MB solution was sonicated on its own with no MNP and with the $MnFe_2O_4$ core with no MnO_2 shell, the results of which can be seen below (Figure 6-8). As can be seen the MB solution on its own shows no change after 1 hour of sonication, while the MNP cores causes a small decrease in concentration of the MB solution equating to a 7 % removal of the MB over the hour.

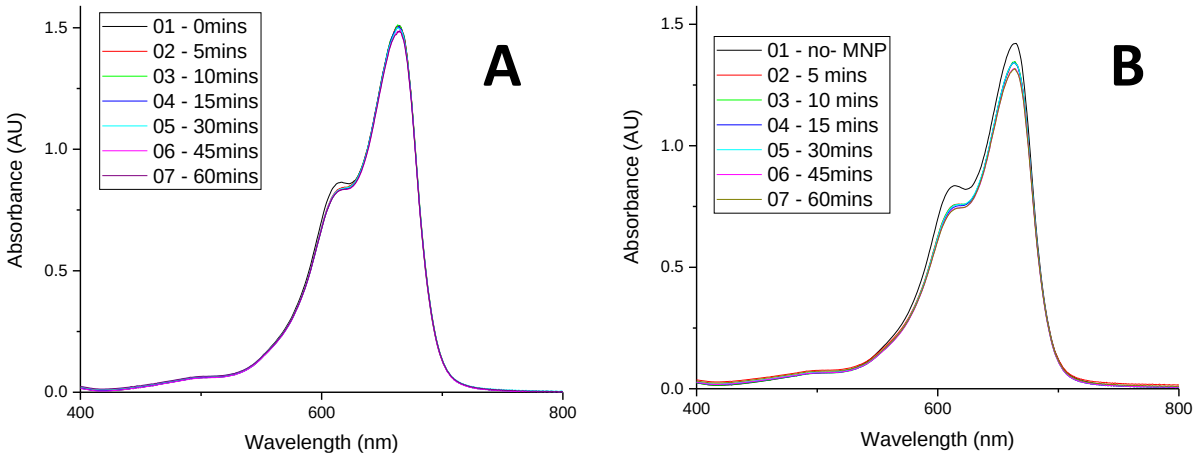


Figure 6-8: UV-vis results of (A) MB solution only and (B) MB solution with $MnFe_2O_4$ cores.

The testing of the $MnFe_2O_4$@MnO_2 particles for MB removal was then performed and monitored by UV-Vis spectroscopy. After testing, the $MnFe_2O_4$@MnO_2 nanoparticles were magnetically extracted. Then the MNPs were placed in a furnace at 300 °C for 3 hours to burn off any MB on the surface after which they were washed with methanol and MP water. Then the particles were ready to be reused in the next MB extraction, so they had been recycled.

To compare the above graph of the core alone in **A** Above (Figure 6-8) with a run using the MnO_2 coated nanoparticles, the graphs of the absorbance over 1 hour for run 1 and run 8 are shown below (Figure 6-9) as **A** and **B** respectively. It should be noted that these graphs have been baseline subtracted. For the 1st experiment with the MnO_2 coated nanoparticles, there is immediate removal of the MB with no development of other peaks. This type of behaviour is consistent with adsorption, as seen in **A** below (Figure 6-9). After the same nanoparticles have been recycled 7 times, for the 8th dye extraction, the peak at 662 nm reduces over the hour, while a 610 nm peak begins to develop as can be seen in **B** below (Figure 6-9). This would be characteristic of degradation rather than adsorption because the development of the peak at 610 nm indicates an increase in concentration of a compound in the solution. This is what would be expected with degradation as the MB is converted to another material over the course of the experiment, as will be discussed more below. Close examination of absorbance profile for run 8 shows that over the first 5 minutes the peak at 610 nm drops by approximately the same factor as the initially larger peak at 662 nm. After this the peak at 610 nm drops very little while the peak at 662 nm continues to fall. After the hour the peak at 610 nm is now larger than the peak at 662 nm. This behaviour indicates initial absorption, as the intensity of all peaks are reducing together, indicating a lowering in concentration of the MB. Then degradation begins as we can see the different peaks no longer reduce by the same factor with the development of the peak at 610 cm $^{-1}$ indicating the development of a degradation product.

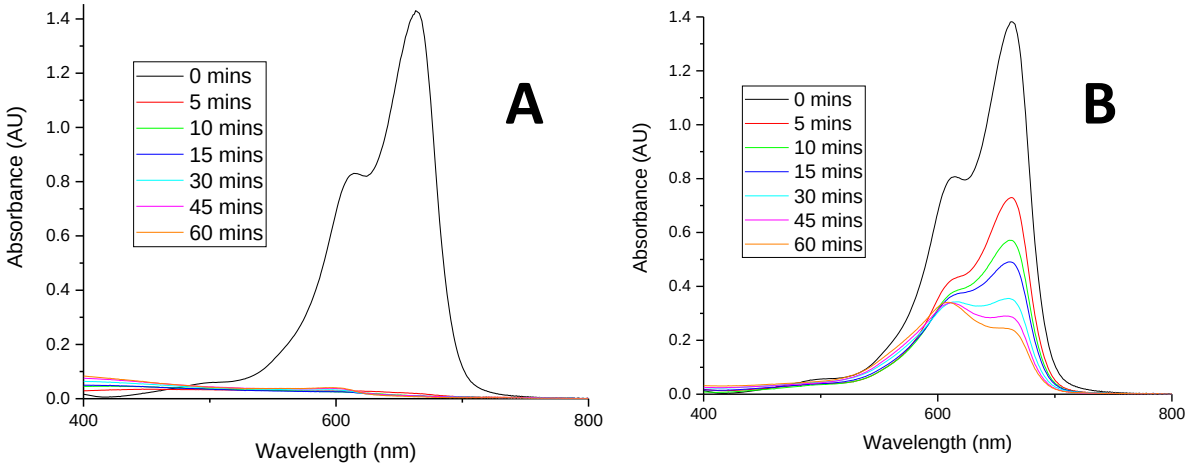


Figure 6-9: UV-Vis spectral absorbance profiles over 1 hour for (A) run 1 and (B) run 8 using the MnO_2 coated MNPs.

The first two experiments with MB showed initial rapid extraction of the dye from solution. The particles showed dye extraction even after 9 recycles. There was some variability between runs, with run 4 and run 8 showing less dye removal than then final run 10. This can be put down to experimental errors because the position of the solution in the sonic bath and the extraction on the magnet were parts of the experiment that would bring extraction efficiency variation into the different runs. The fitting of the graphs can be done with a variety of mathematical approximations but our choice was to use the one-phase exponential decay function with time constant parameter that was fit using Origin graphing software, with one example of the fitted parameters given for run 6. The results of these experiments are shown below (Figure 6-10).

The efficiency of the dye removal by the MnO_2 coated nanoparticles can be quantified with run 1 showing a >99 % removal of the dye. For run 8, which has the lowest removal of the 10 runs, the value is 83 % of the MB removed. For run 10, which was the final run, the removal efficiency was 92%. These results show that the MnO_2 coated magnetic nanoparticles are effective at removing the MB dye from solution and the MNPs are recyclable. More work needs to be done to find out if the particles lose their efficiency after several more runs but the results here indicate that the removal efficiency remains high.

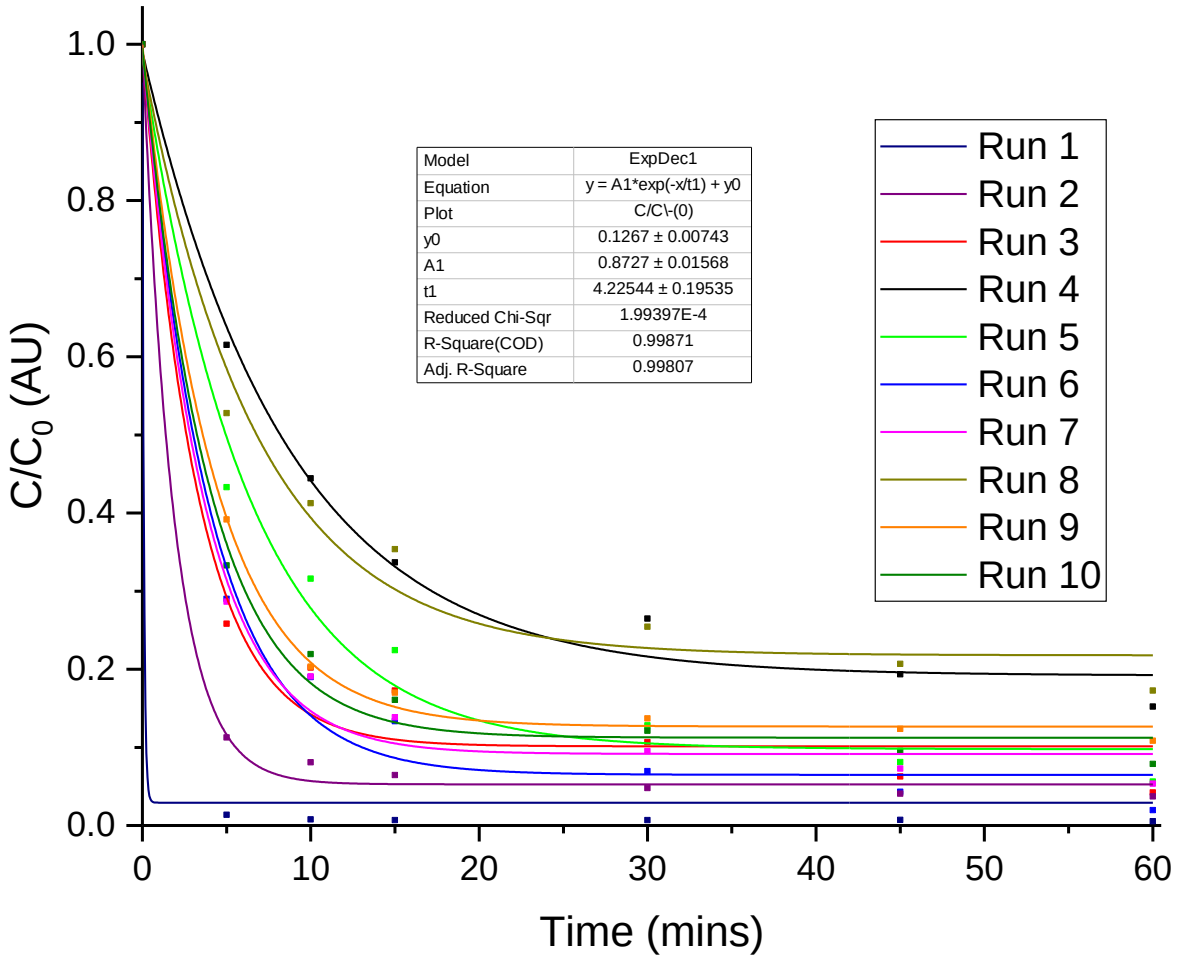


Figure 6-10: Fitted exponential decay graphs for the 10 runs of the MnO_2 coated MNPs.

The results for the 10 runs after the hour is outlined in the table below (Table 6-5). As can be seen the removal efficiency fluctuates but is high throughout the 10 runs. The first run has a removal of greater than 99 %, which is excellent, and the tenth run had a removal of 93% showing the particles were still effective even after 9 recycles.

In an effort to understand the process, mass spectrometry (MS) analysis was done of the MB solution before and after run 8. The MS graph for the extracted solution is shown below (Figure 6-11). The circled peak corresponds to 284.121 m/z for MB. As can be seen the largest peak is at 228.06 m/z, which indicated the major product after 1 hour. For the initial MB solution, there is a strong peak at 284.121 m/z corresponding to the MB molecule. After the extraction, the solution shows a diminished peak at 284.121 m/z for MB but other peaks at 228.056, 242.070, 256.086 and 270.098 m/z, with the peak at 228.056 m/z being the largest. These masses correspond to the degradation of the MB molecule as it loses methyl groups. The outline of the process is shown below (Figure 6-12).

Table 6-5: Percent Removal of MB from the solution with MnO_2 coated MNP.

Run	% Removal
1	>99
2	97
3	96
4	85
5	95
6	98
7	95
8	83
9	90
10	93

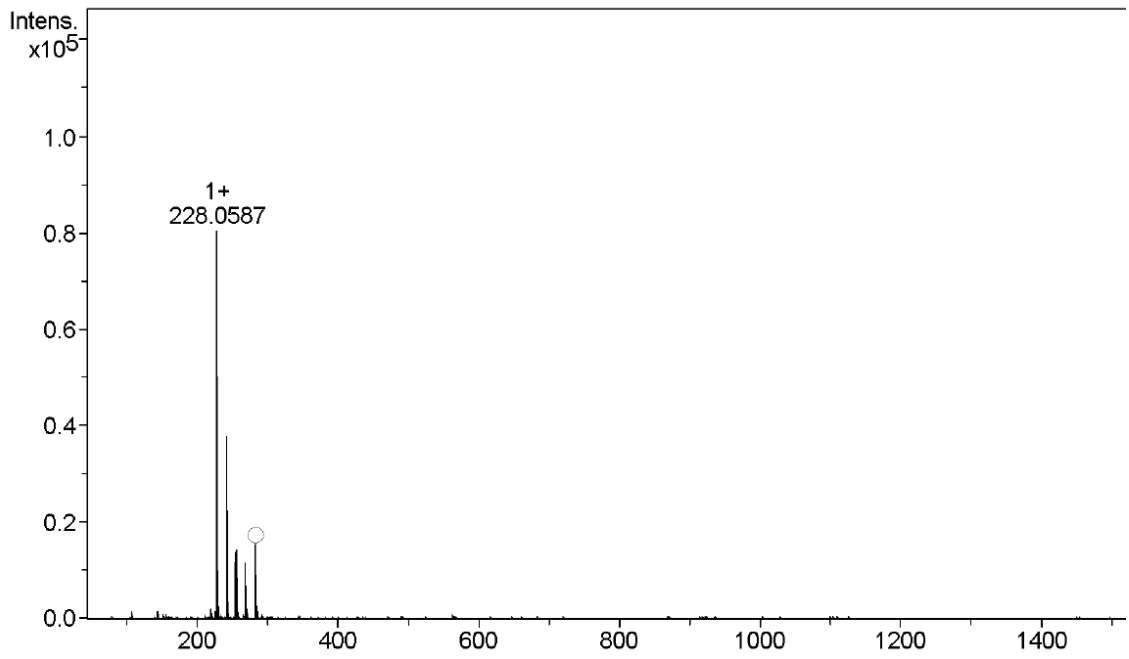


Figure 6-11: Mass Spectrometry output of the extracted solution.

The bond energies for the MB molecule indicated that the methyl bond is the weakest and so it will break first[28]. Further degradation of the molecule would be expected with the reaction being left for a long period as this work has similar outcomes to a previously reported example for degradation. However, this was not done because of time constraints. In this paper, after 7.5 hours ring opening degradation was observed but the peak at 270 m/z was

unusually large compared to other peaks[25]. This paper itself contained contradictions about the extraction times however. Other papers also indicated that MB is degraded by loss of the methyl groups initially before further fragmentation of the structure through breaking of the centre ring at the S and N[29][30].

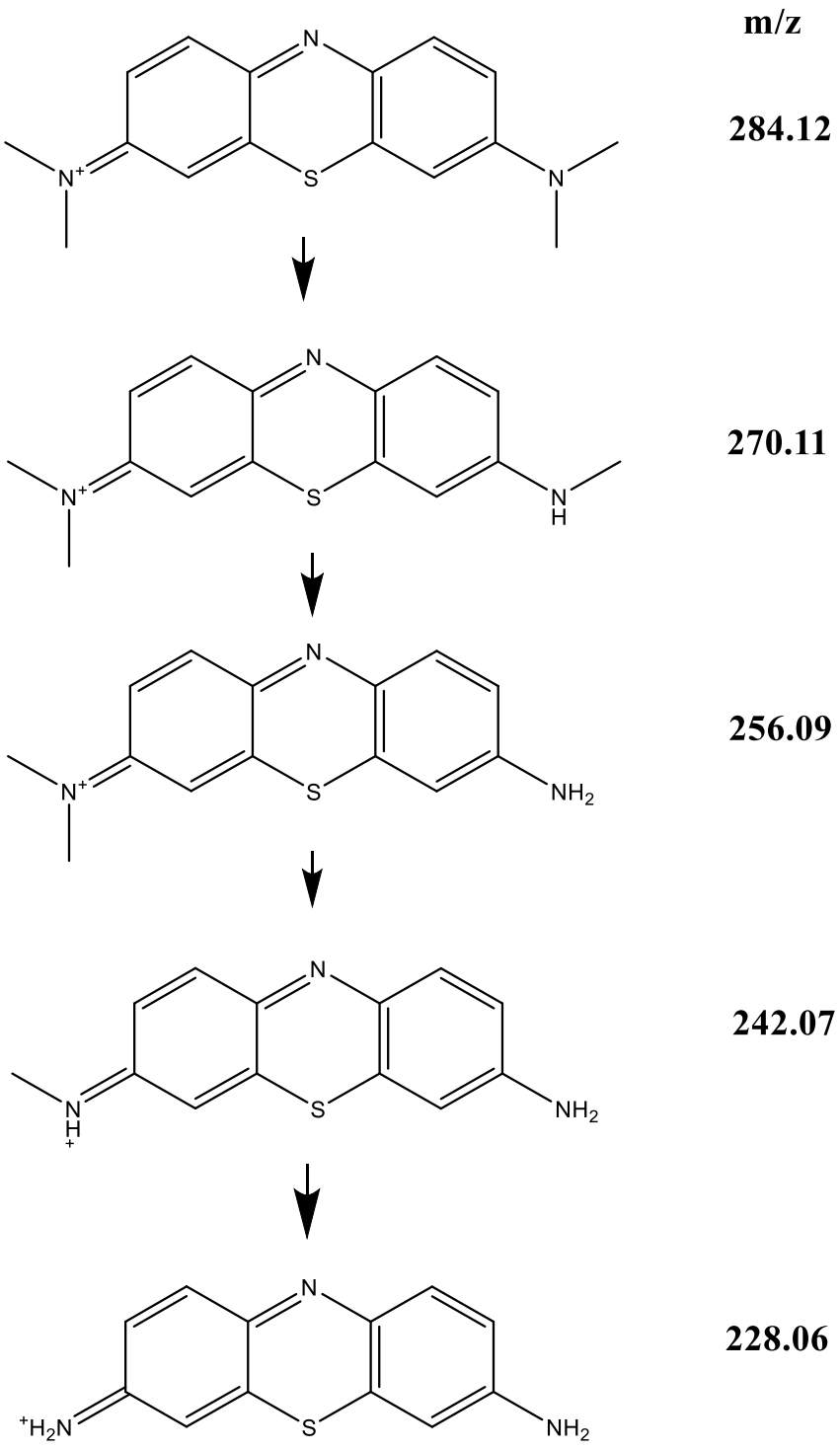


Figure 6-12: Proposed MS products for the extracted solution.

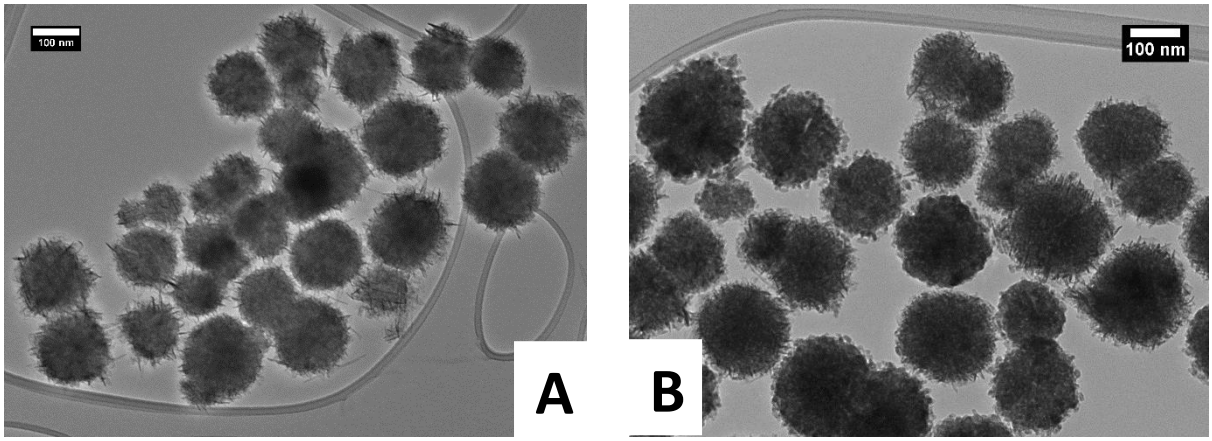


Figure 6-13: MnO_2 coated MNP (A) before and (B) after 10 recycles.

Finally, after the 10 runs the particles were imaged with TEM to see if there were any significant changes in their morphology or the shell. The images above (Figure 6-13) are of the particles before and after 10 recycles. There is some small loss of the shell but the particles can be seen to have MnO_2 still on their surface indicating they are robust to sonication. XRD of the particles after the 10 recycles below (Figure 6-14) showed no major changes but a reduction in intensity of the peaks was observed indicating reduction in crystallite size in the particle.

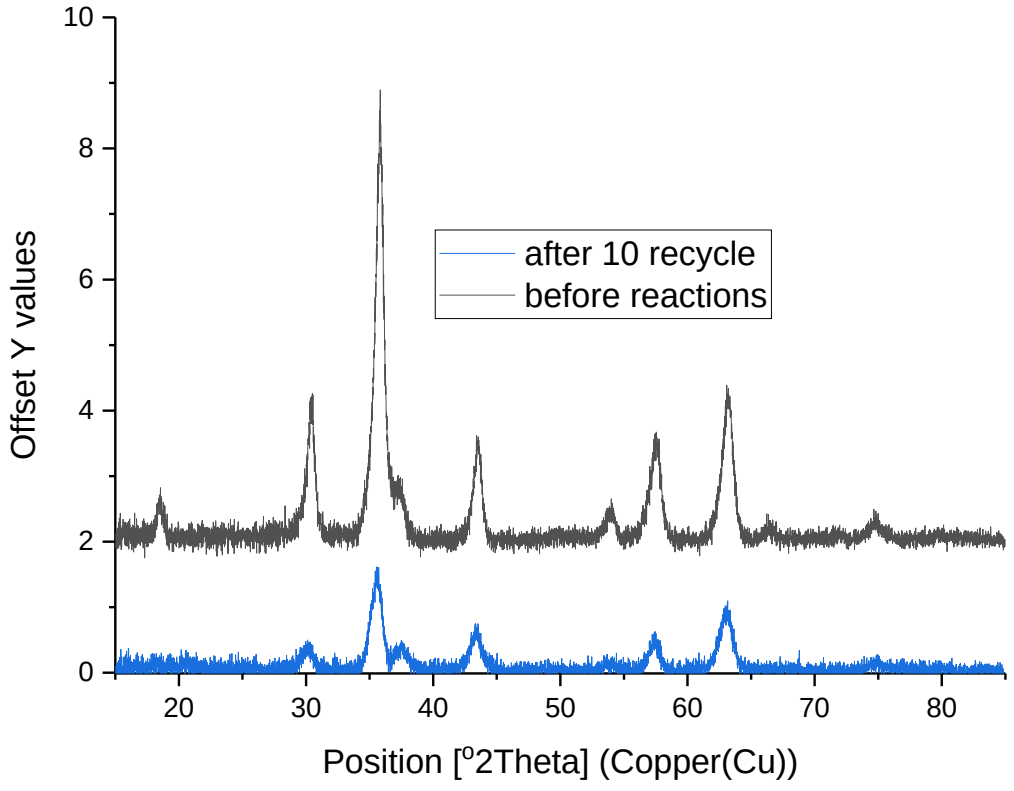


Figure 6-14: XRD pattern of the $MnFe_2O_4$@MnO_2 particles before and after the 10 recycles.

6.3.7 Testing of $MnFe_2O_4$@MnO_2 for Methyl Orange Dye Removal

For the methyl orange (MO) solution the initial concentration was 55.7 µM at which the absorbance was approximately 1.4 AU giving a molar attenuation coefficient of 25114 mol^{-1} L cm^{-1} which was similar to a previously reported value[27]. MO has an absorption peak at 464 nm that can be used to assess the removal efficiency of the MnO_2 coated MNP.

The testing of the nanoparticles with MO again involved sonication of 50 mL of the 55.7µM MO solution with 100 mg of the MNPs for one hour. After the hour of sonication, the MNPs were magnetically extracted, put in a furnace at 300 °C for 3 hours and then washed with methanol and MP water. Then the particles were recycled and the process repeated. As a control, the MO solution was sonicated with no MNP and with only the $MnFe_2O_4$ cores for 1 hour each. These reactions showed no reduction in the MO absorbance for the MO solution on its own and a 1% removal for the MO solution with the $MnFe_2O_4$ cores, in line with the results for the MB dye previously.

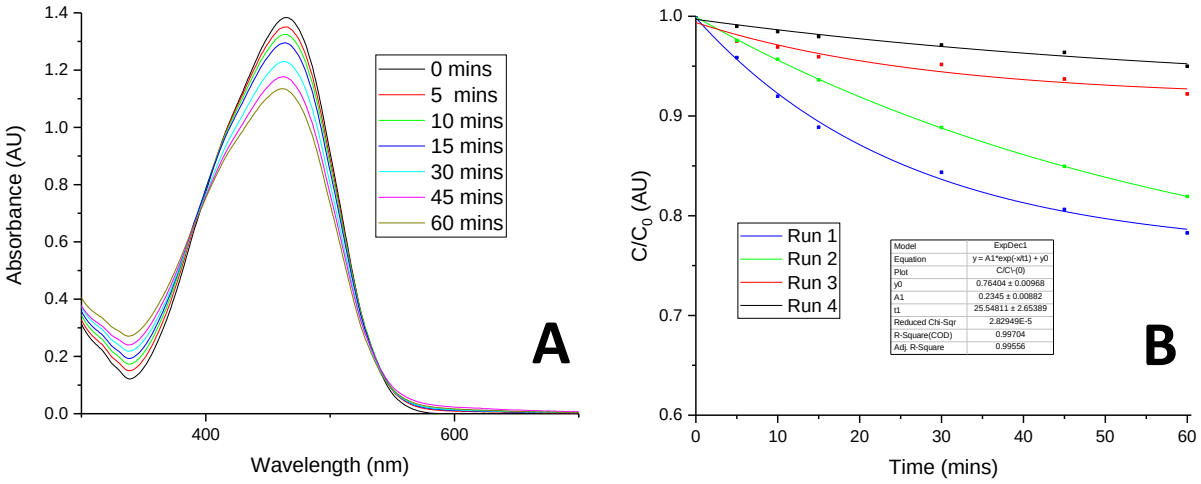


Figure 6-15: UV-Vis spectra for MO removal (A) absorbance over 1 hour for run 2 and (B) the decay curves for four runs using the MnO_2 coated MNPs.

When the MO removal reaction was done with the MnO_2 coated MNPs there was a reduction in absorbance as can be seen for run 2 in **A** above (Figure 6-15). For the MO removal, 4 runs were done and the removal efficiency was not as good as with MB with a maximum removal of 22 % for the first run but reducing to 5 % for the final run. In the graph above (Figure 6-15), in **B** the decay curves for the four runs can be seen. The decays were fitted again with a simple one-phase exponential decay function with time constant parameter. The output parameters for run 2 can be seen on the graph.

As can be seen the absorbance over the hour in **A** above (Figure 6-15), the peak at 464 nm is reduced over the time while a trough at 339 nm grows. This is indicative of degradation rather than adsorption of the dye because with adsorption one would expect the absorbance to fall at the same rate at all points in the absorbance curve. Degradation involves the breakdown of the molecule to form the products, which have absorbance peaks that will increase as their concentration grows in line with the reduction of the absorbance peak for the MO. For methyl orange, the results of extraction were very poor with the particles showing reduced ability to extract the MO with each run, unlike the MB, which showed good recyclability.

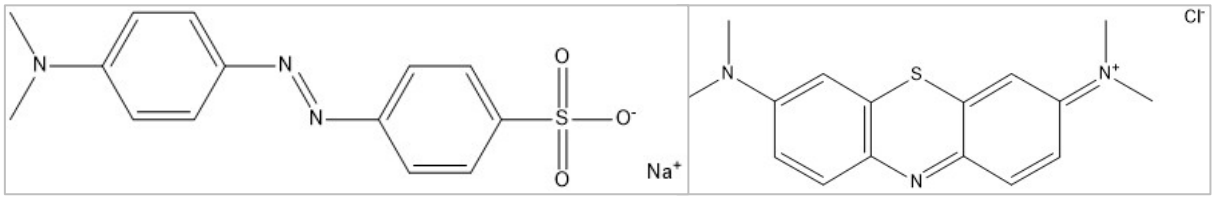


Figure 6-16: Methyl Orange (left) and Methylene Blue (right).

The reason for the low extraction efficiency when compared to MB can be explained by looking at the structures of both molecules above (Figure 6-16). MB is a cationic dye with a chloride counter ion whereas MO is an anionic dye with a sodium counter ion. Previously it has been shown that the MnO_2 coated particles have a negative surface charge (Figure 5-7). This then would causes the MB to bind more strongly to the surface of the particles in solution. With MO, the negative charge on the molecule would cause electrostatic repulsion causing the dye to approach the surface less in solution and so there would be less binding.

Table 6-6: Percent Removal of MO from the solution with MnO_2 coated MNP.

Run	% Removal
1	22
2	19
3	8
4	5

The results for the 4 runs after the hour are summarised above (Table 6-6). As can be seen the removal efficiency reduces after each run. For the removal of MO, it can be seen that these

nanoparticle are not as effective as with MB. The percentage of MO dye removal was lower than expected.

6.3.8 Testing of $MnFe_2O_4$@MnO_2 for Rhodamine B Dye Removal

Our next goal was to test the dye Rhodamine B (RB) for removal with the MnO_2 coated MNPs. For RB the concentration of the aqueous solution used was 12.7 µM, which gave an absorbance peak at 548 nm of approximately 1.35 AU giving a molar attenuation coefficient of 106689 mol^{-1} L cm^{-1}, which was similar to a previous reported value[31]. The reduction of the peak at 548 nm can be used to assess the removal of the dye from the solution.

The testing of the MnO_2 coated particles involved sonication of 50 mL of the 12.7µM solution with 100 mg of the MNPs for one hour with the absorbance of the solution measured at time intervals. After the dye removal reaction, the MNPs were magnetically extracted, placed in a furnace at 300 °C for 3 hours and then washed with methanol and MP water. Then the particles were recycled and the process repeated. As a control, the RB solution was sonicated with no MNPs and with only the $MnFe_2O_4$ cores for 1 hour each. These reactions showed no reduction for the RB solution on its own and a 3 % reduction for the RB solution with the $MnFe_2O_4$ cores.

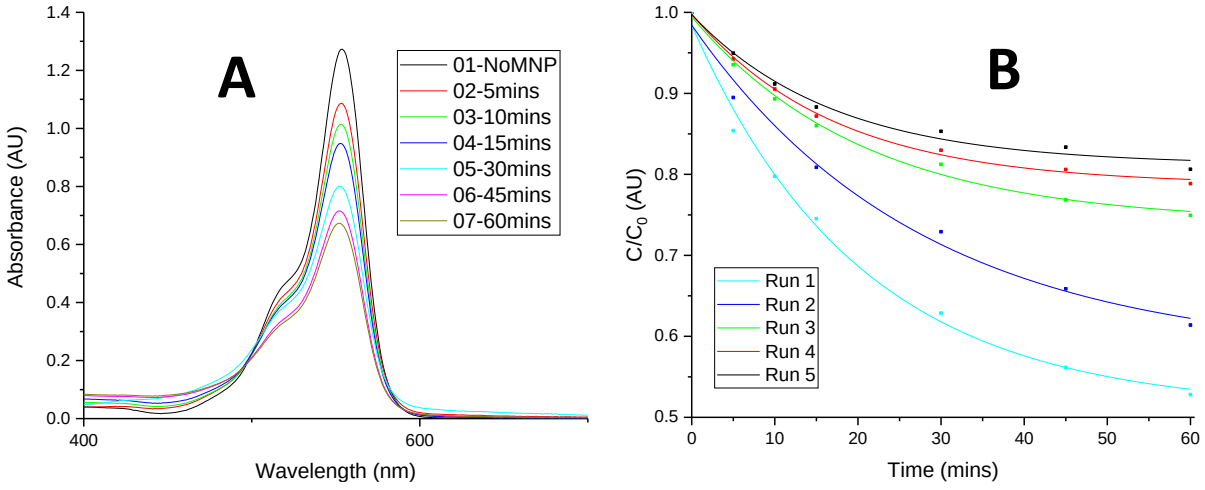


Figure 6-17: UV-Vis spectra for RB removal (A) absorbance over 1 hour for run 1 and (B) the decay curves for the 5 runs using the MnO_2 coated MNPs.

For the RB removal reaction with the MnO_2 coated nanoparticles there was a reduction in the absorbance at the 548 nm peak for each of 5 runs with an initial reduction of 48 % for run 1

and a final reduction of 20 % for run 5. This shows that the MnO_2 coating is more effective at removing the RB dye than the $MnFe_2O_4$ cores alone. The removal efficiency is reducing with each recycle though. The absorbance profile for run 1 in **A** and the decay curves in **B** can be seen above (Figure 6-17). For the absorbance spectra for run 1, they were baseline subtracted to give a more accurate representation. The results for the 5 runs are summarised below (Table 6-7). As can be seen the removal efficiency reduces after each run.

Table 6-7: Percent Removal of RB from the solution with MnO_2 coated MNP.

Run	% Removal
1	48
2	39
3	26
4	22
5	20

The results for RB were better than MO but not as good as for MB. The reason for this could be to due to larger size of RB molecule comparing to MB that results is sterical hinderance and limited access to reactive sites in the MnO_2 shell structures. RB is also a cationic molecule like MB with a chloride counter ion. As such, it would be expected to perform better than MO, which is an anionic molecule. The reduction in the efficiency as the particles are recycled with the RB was not observed for the MB. More studies are necessary to elucidate the reason behind this observation.

6.3.9 Testing of $MnFe_2O_4$@SiO_2@CeO_2 for Methylene Blue Dye Removal

Taking into account the reasonably good efficiencies for MB removal by the MnO_2 coated MNP previously it was decided to test the CeO_2 coated MNP for MB dye removal. The peak at 662 nm for MB can again be used to assess the removal efficiency for these nanoparticles. The aqueous MB solution had a concentration of 21.3 μM giving an absorbance of approximately 1.4 AU as before. For this experiment, the reaction was both illuminated with a UV lamp and performed in daylight in the fumehood. No significant difference between these reactions was found as shall be seen.

The testing of these particles involved sonication of 50 mL of the MB solution with 100 mg of the CeO_2 coated MNP for one hour with samples taken at various time intervals throughout. After the reaction, the particles were magnetically extracted, put in a furnace at 300 °C for 3 hours and then washed with methanol and water. A control had been done previously of the MB on its own and no significant change was found. A control with the $MnFe_2O_4$@SiO_2 cores also showed no reduction in the adsorption peak at 662 nm as expected.

For the CeO_2 coated nanoparticles 4 runs were performed. Below (Figure 6-18) as can be seen in **B**, the decay curves show good removal of the MB for each of the 4 runs. Run 2 and run 4 were performed under UV illumination while run 1 and run 3 were in daylight. As can be seen this had no major effect on the outcome. The absorbance profile for run 4 can be seen in **A** below (Figure 6-18). The removal efficiency for the four runs has been quantified in the table below (Table 6-8).

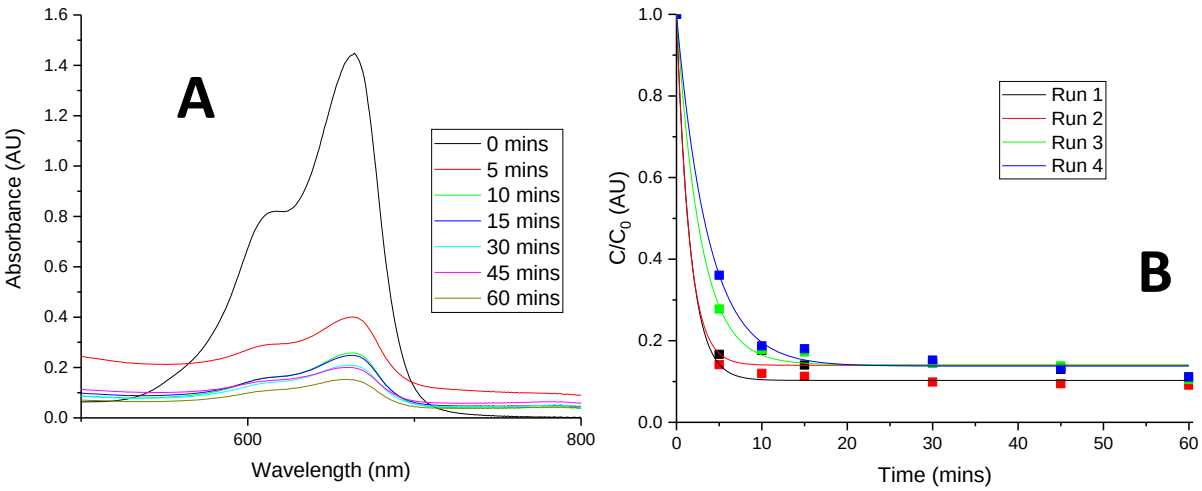


Figure 6-18: For MB removal (A) absorbance over 1 hour for run 4 and (B) the decay curves for the 4 runs using the CeO_2 coated MNPs.

Table 6-8: Percent Removal of MB from the solution with CeO_2 coated MNPs.

Run	% Removal
1	91
2	90
3	89
4	89

As can be seen the CeO_2 particles showed high efficiency in removal of the MB dye from the solution with a very small reduction in efficiency after 4 runs.

6.4 Conclusions

The magnetic core@shell nanoparticles were tested for a variety of potential applications. It was found that the MnO_2 coated magnetic nanoparticles showed low yields in the catalytic reaction for the oxidation of benzyl alcohol to benzaldehyde. The CeO_2 coated magnetic nanoparticles showed very low yields in the same reaction. These results, especially for the MnO_2 coated MNP were disappointing and lower than expected. The formation of the δ polymorph may be one explanation for the low activity, as this polymorph has a lower activity than other polymorphs of MnO_2. Another reason could be the blocking of sites as the reaction proceeds by side products, which are washed away when the particles are recycled. In addition, the amount of MnO_2 in the core shell particles may be very small and the majority of the mass may come from the MnF_2O_4 core. In a similar catalytic reaction but with different reaction conditions the CeO_2 coated MNP performed slightly better but still with very low yields. Similar reasons for the CeO_2 yields could be the blocking of active sites and the very low level of CeO_2 in the catalyst as the majority of the catalyst is made from the $MnFeO_4$@SiO_2 core, giving a small molar ratio of CeO_2 available.

For the anaerobic glue formulation inhibition and activation, the MnO_2 coated MNP performed very well demonstrating that the glue formulation can be efficiently re-activated by magnetic removal of the core@shell MNPs with a permanent magnet. It is expected that this study will find other potential applications in using the concept of inhibition and reactivation upon magnetic removal of the functionalised MNPs.

For the dye removal, application the MnO_2 coated MNP performed very well with MB showing over 90 % efficiency in removal even after 9 recycles. For RB the removal efficiencies were poor and for MO the results were lower too. The most likely explanation for this is the cationic (MB & RB) and anionic (MO) nature of the dyes and their interaction with the negatively charged surface of the MnO_2. MB and RB would have better surface attachment to the surface due to electrostatic forces. For the CeO_2 coated MNP the removal efficiencies were good for MB with consistent results over 4 runs.

6.5 Reference

1 D. J. Cole-Hamilton, *Science*, 2003, **299**, 1702–1706. https://doi.org/10.1126/science.1081881.

2 A. Shaabani, M. Borjian Boroujeni and M. S. Laeini, *Appl. Organomet. Chem.*, 2016, **30**, 154–159. https://doi.org/10.1002/aoc.3412.

3 S. Shylesh, V. Schünemann and W. R. Thiel, *Angew. Chemie Int. Ed.*, 2010, **49**, 3428–3459. https://doi.org/10.1002/anie.200905684.

4 J. Hagen, *Industrial Catalysis*, Wiley, 2005, vol. 2017. https://doi.org/10.1002/3527607684.

5 J. D. Lou, X. L. Lu, L. H. Huang, Q. Wang and X. N. Zou, *Synth. React. Inorganic, Met. Nano-Metal Chem.*, 2011, **41**, 1342–1345. https://doi.org/10.1080/15533174.2011.609216.

6 M. Hirano, S. Yakabe, H. Chikamori, J. H. Clark and T. Morimoto, *J. Chem. Res.*, 1998, 770–771. https://doi.org/10.1039/a805342a.

7 J. J. Dolhun, *J. Chem. Educ.*, 2014, **91**, 760–762. https://doi.org/10.1021/ed4006826.

8 L. Vivier and D. Duprez, *ChemSusChem*, 2010, **3**, 654–678. https://doi.org/10.1002/cssc.201000054.

9 G. L. Davies, J. Govan, R. Tekoriute, R. Serrano-García, H. Nolan, D. Farrell, O. Hajatpour and Y. K. Gun'Ko, *Chem. Sci.*, 2017, **8**, 7758–7764. https://doi.org/10.1039/c7sc03474a.

10 O. Azie, Z. F. Greenberg, C. D. Batich and J. P. Dobson, *Int. J. Mol. Sci.*, 2019, **20**, 1–12. https://doi.org/10.3390/ijms20133190.

11 R. Göstl, A. Senf and S. Hecht, *Chem. Soc. Rev.*, 2014, **43**, 1982–1996. https://doi.org/10.1039/c3cs60383k.

12 J. Chen, F. He, H. Zhang, X. Zhang, G. Zhang and G. Yuan, *Ind. Eng. Chem. Res.*, 2014, **53**, 18481–18488. https://doi.org/10.1021/ie502967a.

13 Y. Zhai, J. Zhai, M. Zhou and S. Dong, *J. Mater. Chem.*, 2009, **19**, 7030.

https://doi.org/10.1039/b912767d.

14 C. A. Calderon Rosas, M. Franzreb, F. Valenzuela and W. H. Höll, *React. Funct. Polym.*, 2010, **70**, 516–520. https://doi.org/10.1016/j.reactfunctpolym.2010.03.011.

15 A. R. Massah, R. J. Kalbasi and M. Azadi, *Comptes Rendus Chim.*, 2012, **15**, 428–436. https://doi.org/10.1016/j.crci.2012.03.001.

16 I. M. Goldman, *J. Org. Chem.*, 1969, **34**, 3289–3295. https://doi.org/10.1021/jo01263a015.

17 A. Chakravarty, D. Sengupta, B. Basu, A. Mukherjee and G. De, *RSC Adv.*, 2015, **5**, 92585–92595. https://doi.org/10.1039/C5RA17777D.

18 H. Chen, Y. Wang and Y. K. Lv, *RSC Adv.*, 2016, **6**, 54032–54040. https://doi.org/10.1039/c6ra10103h.

19 D. M. Robinson, Y. B. Go, M. Mui, G. Gardner, Z. Zhang, D. Mastrogiovanni, E. Garfunkel, J. Li, M. Greenblatt and G. C. Dismukes, *J. Am. Chem. Soc.*, 2013, **135**, 3494–3501. https://doi.org/10.1021/ja310286h.

20 D. I. Enache, D. W. Knight and G. J. Hutchings, *Catal. Letters*, 2005, **103**, 43–52. https://doi.org/10.1007/s10562-005-6501-y.

21 S. Miao, Z. Liu, Z. Miao, B. Han, K. Ding, G. An and Y. Xie, *Microporous Mesoporous Mater.*, 2009, **117**, 386–390. https://doi.org/10.1016/j.micromeso.2008.07.014.

22 M. Tamura and K. Tomishige, *Angew. Chemie*, 2015, **127**, 878–881. https://doi.org/10.1002/ange.201409601.

23 A. Pizzi and K. L. Mittal, *Handbook of Adhesive Technology, Third Edition*, CRC Press, 2017. https://doi.org/10.1201/9781315120942.

24 H. Shayesteh, A. Ashrafi and A. Rahbar-Kelishami, *J. Mol. Struct.*, 2017, **1149**, 199–205. https://doi.org/10.1016/j.molstruc.2017.07.100.

25 S. Zhou, Z. Du, X. Li, Y. Zhang, Y. He and Y. Zhang, *R. Soc. Open Sci.*, 2019, **6**, 190351. https://doi.org/10.1098/rsos.190351.

26 J. Cenens and R. A. Schoonheydt, *Clays Clay Miner.*, 1988, **36**, 214–224.

https://doi.org/10.1346/CCMN.1988.0360302.

27 N. O. Mainya, P. Tum and T. M. Muthoka, *Int. J. Sci. Res.*, 2015, **4**, 3185–3189.

28 F. Huang, L. Chen, H. Wang and Z. Yan, *Chem. Eng. J.*, 2010, **162**, 250–256. https://doi.org/10.1016/j.cej.2010.05.041.

29 Y. He, D. Bin Jiang, D. Y. Jiang, J. Chen and Y. X. Zhang, *J. Hazard. Mater.*, 2018, **344**, 230–240. https://doi.org/10.1016/j.jhazmat.2017.10.018.

30 M. A. Rauf, M. A. Meetani, A. Khaleel and A. Ahmed, *Chem. Eng. J.*, 2010, **157**, 373–378. https://doi.org/10.1016/j.cej.2009.11.017.

31 Extinction Coefficient [Rhodamine B], https://www.aatbio.com/resources/extinction-coefficient/Rhodamine_B#:~:text=The molar extinction coefficient (ε,1M-1 in Methanol.

7 Boron Nitride - Magnetic Nanoparticle Composites

7.1 Introduction

Up to now, a significant amount of work has been done in developing core@shell MNPs with the magnetic functionality at the core[1][2][3]. Another approach to introduce magnetic functionality is to coat the surface of another material with a magnetic material. Hexagonal boron nitride (h-BN) is a well-known layered 2D material analogous to graphite[4]. The layered materials can be exfoliated to give boron nitride nanosheets (BNNS) as with graphite giving graphene[5]. h-BN has anisotropic properties due to it being a 2D material, it has high mechanical strength and high thermal conductivity similar to graphene but unlike graphene, it is electrically insulating. BN also has high thermal and chemical stability[6].

BN coated with magnetite has already been reported for a variety of applications such as toxic heavy metal ion removal form water[7][8], enhancing the thermal conductivity of an interfacial material when used in composite[9][10] and as an electromagnetic wave-absorbing composite[11]. In all these cases, the coating of the BNNS with the magnetic material was an important factor in contributing to the added functionality; it was not a simple case of the mixing of the two materials. So increasing the surface coverage to get a more uniform coating should improve composite properties in these applications. Previous groups have tried to functionalise BN prior to attachment of MNPs by various methods. One method reported to functionalise the BN surface was using a 5 M NaOH solution at 120 °C for 48 hours to create hydroxide functional groups on the surface[9]. Another approach was reacting h-BN in the presence of di-tert-butyl peroxide, which decomposes at 120 °C by homolytic fission to produce oxygen radicals. These reactive species will then attack the BN structure. Further modification finally produces hydroxyl-functionalised BNNS[12]. These harsh methods have been understood to be necessary for attachment of other species as BN is quite inert.

Other groups have reported attachment of iron oxide directly onto the BN surface without any modification of the surface. One example is with BN nanotubes (BNNT) coated with Fe_3O_4. The study indicated the likely sites that the Fe ions would bind to the bare BN surface through electrostatic interaction[7]. Another report claimed to have created BNNS-Fe_3O_4

nanocomposites without functionalisation of the BN surface by in situ coprecipitation of Fe_3O_4 with BNNS. However, the TEM images in the paper are inconclusive and unclear regarding the attachment and coverage of the magnetic material[8].

BNNS are thermally and chemically stable and has been used for nanofiltration previously[13]. Attachment of MNPs to the surface of BNNS will give the possibility of magnetic inductive heating. This would give the opportunity of using magnetic heating to burn off retained organic pollutants on the surface of the BNNS-MNPs nanocomposite potentially enabling an efficient regeneration of the nanofiltration membrane.

An overall review of the literature shows that surface coverage of BNNS with magnetic materials has not been really explored. In this part of our project, we show that excellent coverage of BNNS with MNPs is possible without need for functionalisation prior to attachment of the MNPs and that this method has high reproducibility. In addition, this method is shown to be transferable to other spinel type MNPs with the fabrication of a BNNS-$CoFe_2O_4$ nanocomposite. This material has been reported only recently and has been shown to be an effective flame retardant[14].

7.2 Aims

The main aim of this part of our work is to develop a new method for coating BNNS with spinel ferrites. The coated BNNS are to be characterised by TEM, SEM, VSM, FTIR and XRD techniques to understand the properties and coverage of the final material. The spinel ferrites that are to be used to coat the BNNS are Fe_3O_4 and $CoFe_2O_4$. The coating of the BNNS will be done without any functionalisation of the BNNS and the aim is to get high coverage with magnetic material using new methods developed by us. Once coated and characterised the BNNS-MNP nanocomposites will be used to produce new membranes and these membranes will be tested for removal of selected dyes. It is envisaged that if the membrane is successful in removing dyes, that it could be easily regenerated and recycled by magnetic induction heating to burn off the captured pollutants. The membranes will also be tested for filtering MNPs solutions to see if this approach can be used for removal of any larger particles as well as potential purification of MNPs using magnetic membranes.

7.3 Results and Discussion

Initially our work was focused on the development of a new way to coat BNNS with magnetic iron oxide to create BNNS-Fe_3O_4. The process involves the use of BNNS, which have been exfoliated in water from bulk boron nitride similar to previously reported procedures[15]. The BNNS have then been transferred to a polyol solvent for the further coating with MNPs. A variety of different modifications was tried for coating the BNNS and these will be discussed from the perspective of creating a membrane for filtration out of the coated BNNS. These included changing the amounts of precursor and changing the base used in the polyol synthesis.

The method was also found to be effective with $CoFe_2O_4$ coatings with some modification. $CoFe_2O_4$ is more chemically and thermally stable than Fe_3O_4 and does not oxidize as easily. Also at temperatures >585 °C [16], the magnetite oxides irreversibly losing its magnetism as the material is transformed to hematite. $CoFe_2O_4$ however is able to be heated to 1000 °C[17] without loss of its magnetism. For the creation of a membrane that can be recycled in situ by magnetic induction heating to burn off collected organic residue, $CoFe_2O_4$ may be a more promising option and so this line of research was followed.

7.3.1 Preparation of BNNS

BNNS could be made from bulk BN by sonication in water for 24 hours as described in the experimental section (2.6.1).

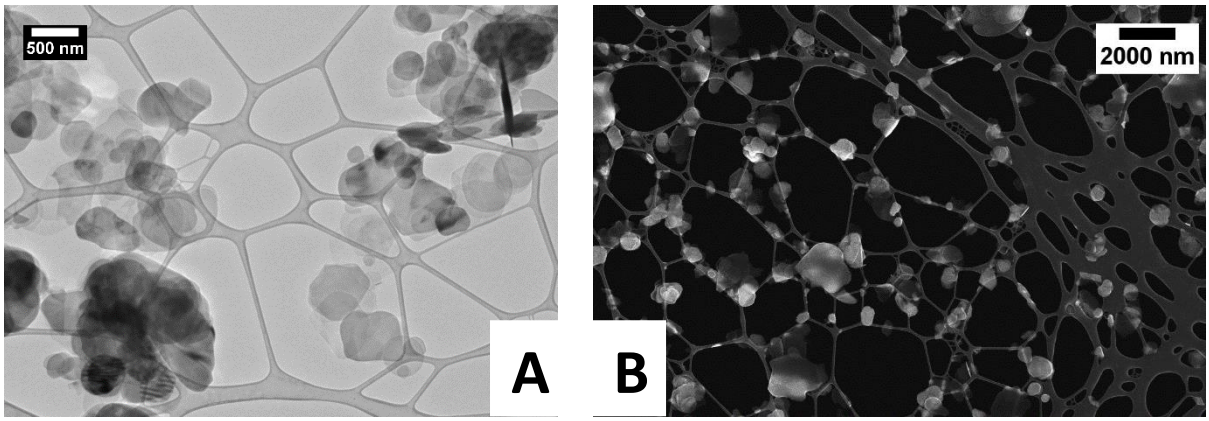


Figure 7-1: (A) TEM and (B) SEM images of BNNS on a TEM grid.

TEM and SEM images above (Figure 7-1) show the nanosheets of BNNS. As can be seen the sample consists mainly of individual nanosheets with some aggregation due to sample drying

for the TEM characterisation. SEM images of BNNS on the TEM grid show similar outcomes with the individual sheets visible on the TEM grid. As can be seen the individual flakes vary in size greatly with dimensions ranging from 50 nm to 1000 nm in width.

XRD of the BNNS gave an exact match for BN in the COD database (COD 201-6171) with the major peak at 26.7 2θ as can be seen below (Figure 7-2). There was no difference to an XRD of the powder BN.

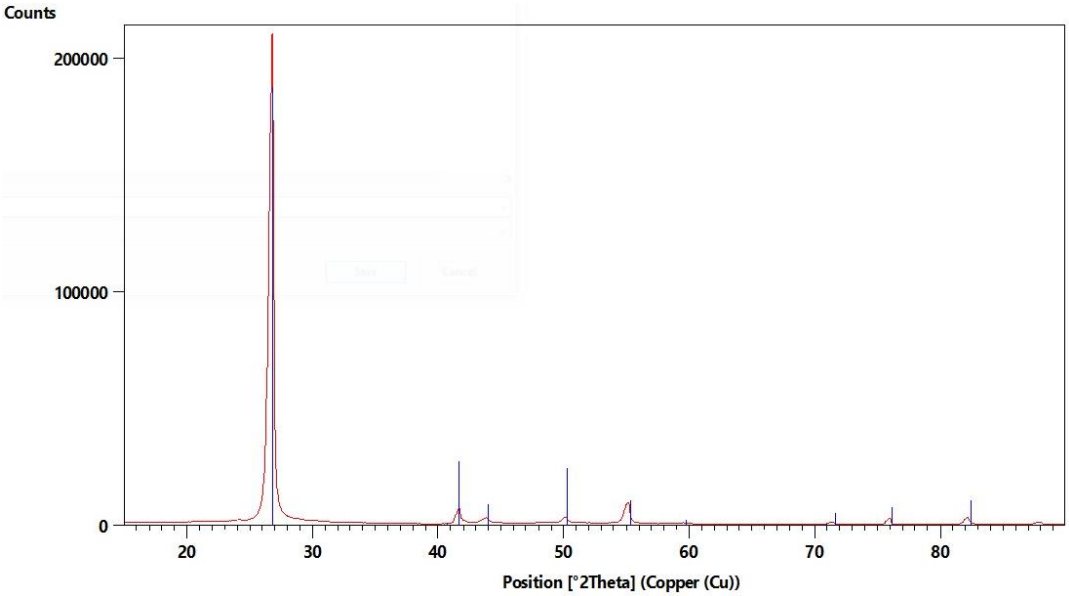


Figure 7-2: XRD pattern of exfoliated BNNS.

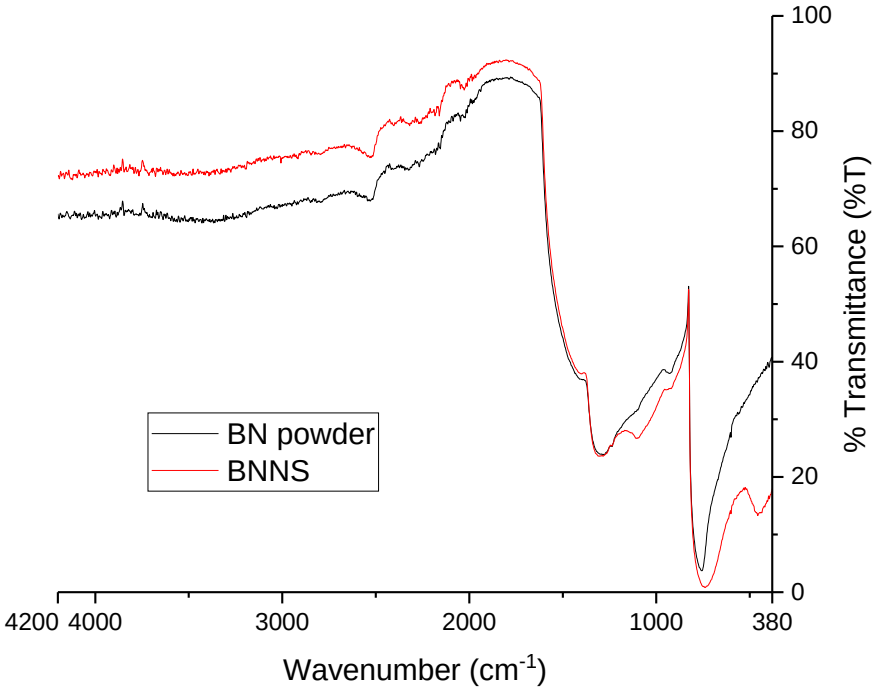


Figure 7-3: FTIR spectra of BN powder and exfoliated BNNS.

FTIR spectra of the BNNS above (Figure 7-3) showed strong peaks at 740 and 1300 cm^{-1} where previous work has attributed these peaks to the out-of-plane vibration of B−N−B and the in-plane vibration of B−N−B respectively[12]. These peaks were also in the powder BN prior to exfoliation as would be expected.

This initial characterisation for the BNNS will be used for reference as we discuss the MNP coated BNNS in the following sections.

7.3.2 Preparation of BNNS-Fe_3O_4 Nanocomposites

BNNS-Fe_3O_4 nanocomposites were prepared according to a new procedure, which is described in detail in the experimental section (2.6.4). The procedure involves transfer of the exfoliated BNNS to ethylene glycol so that a polyol type reaction to produce MNPs can be performed in situ with the BNNS. A molar ratio for BNNS:Fe_3O_4 of 1:0.05 was chosen to make sure there was no excess Fe_3O_4. This ratio gives 1 Fe atom per 6 BN rings This method was found to give well-coated BNNS that could be used to form a membrane. This approach was tried several times and was found to be highly reproducible. The BNNS-Fe_3O_4 nanocomposites and the corresponding membranes were characterised by SEM, TEM, FTIR, VSM and XRD.

The TEM and SEM images below (Figure 7-4) of the BNNS-Fe_3O_4 nanocomposites show BN nanosheets well coated with MNPs. It should be noted that no separate MNPs were found in the images with all the MNP on the surface of the BNNS. Some BNNS were more heavily coated than others were though but in general, there was consistent and uniform coverage of the BN flakes across the sample. The iron oxide coverage consisted mainly of particles of approximately 6 ± 3 nm but with some larger particles of approximately 40 ± 20 nm too.

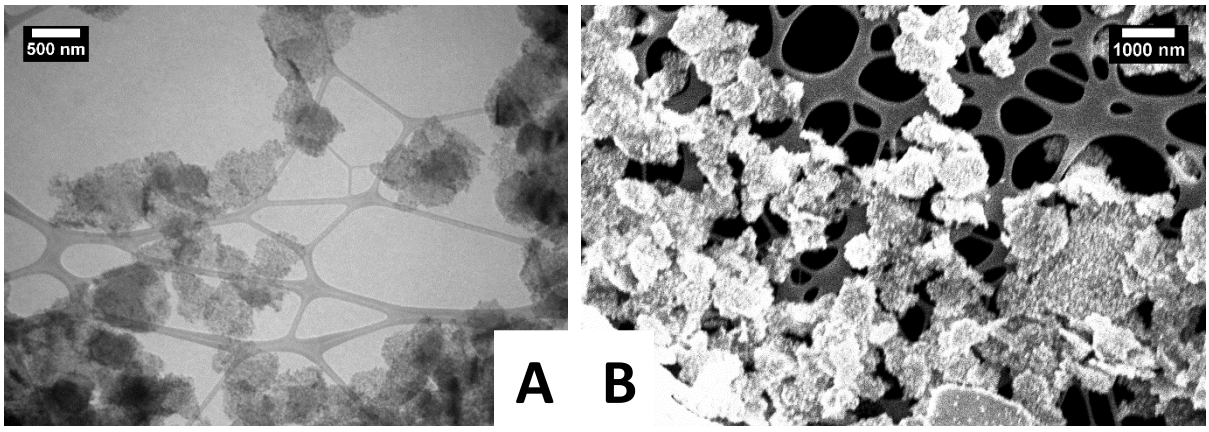


Figure 7-4: (A) TEM and (B) SEM images of the Fe_3O_4 coated BNNS.

FTIR analysis of the samples shown below (Figure 7-5) gave peaks at 552 cm^{-1} corresponding to the Fe-O stretch of the iron oxide. The peaks at 740 and 1300 cm^{-1} have both shifted slightly to 790 and 1350 cm^{-1} respectively as would be expected with the Fe-O interacting with the flakes of B-N. The observed almost complete coverage would be expected to produce some change in the BN peaks. These shifts indicate a new interaction resulting in changes in the out-of-plane and the in-plane vibration. Previous work has looked at the binding of iron oxides[8] and Fe ions[7] to the surface of BN. In the Fe ion study, the group looked at how Fe ions interacted with the surface of BN and found that the optimal binding site was at the centre of the BN ring. They proposed the formation of borazine metal complex bonds, which would result in the changes in the IR spectra of the BN similar to what is observed here. As the BN was sonicated with the Fe ions prior to the reaction, it is likely that this enabled the formation of these bonds. This then gives the excellent coverage seen as the Fe ions were in place as seeds for the growth of iron oxide when the reaction took place. The study used DFT calculations to show the optimised binding of iron oxide with the BN sheet with a view for increased adsorption of contaminants[8].

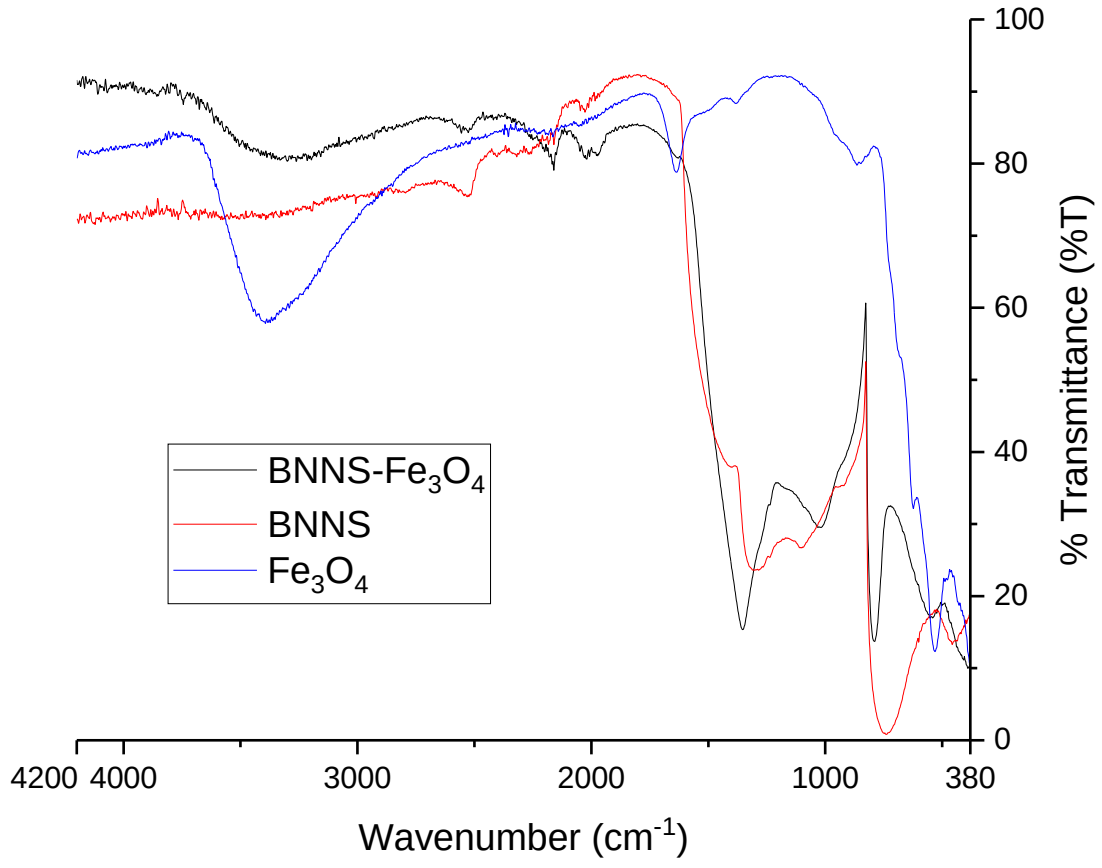


Figure 7-5: FTIR spectra of BNNS-Fe_3O_4, BNNS and Fe_3O_4 for comparison.

XRD analysis showed that the BNNS-Fe_3O_4 had a combination of the patterns of BNNS and Fe_3O_4 made previously and matched to the COD database, (COD 201-6171) and (COD 722-8111) respectively, as shown below (Figure 7-6). It should be noted that these patterns had to be adjusted for intensities but not peak positions.

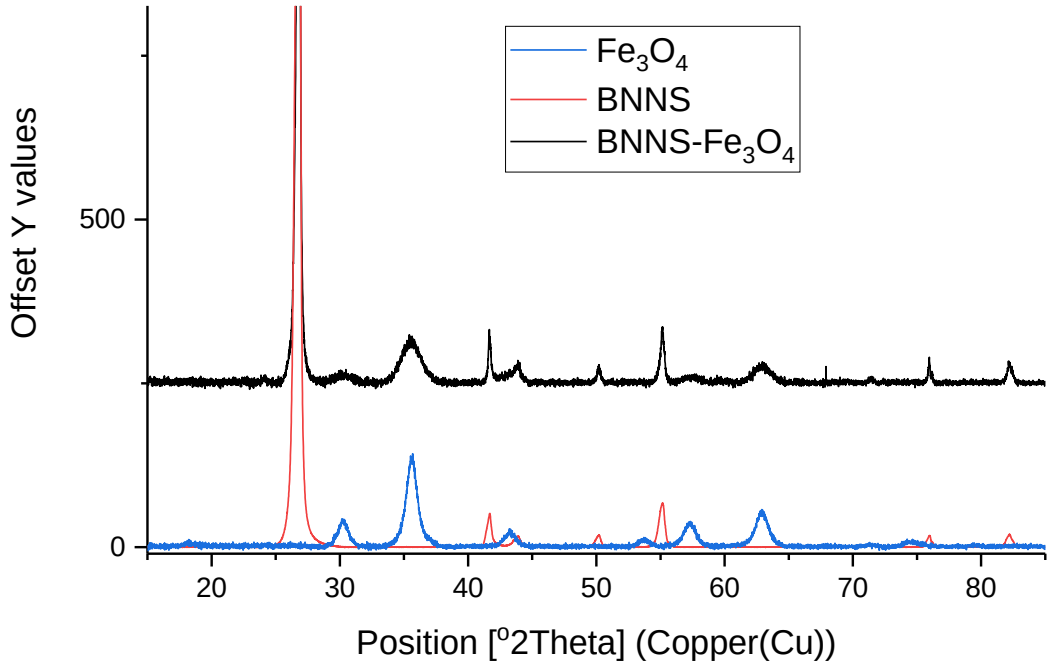


Figure 7-6: XRD patterns of BNNS-Fe_3O_4 shown to be a combination of BNNS and Fe_3O_4.

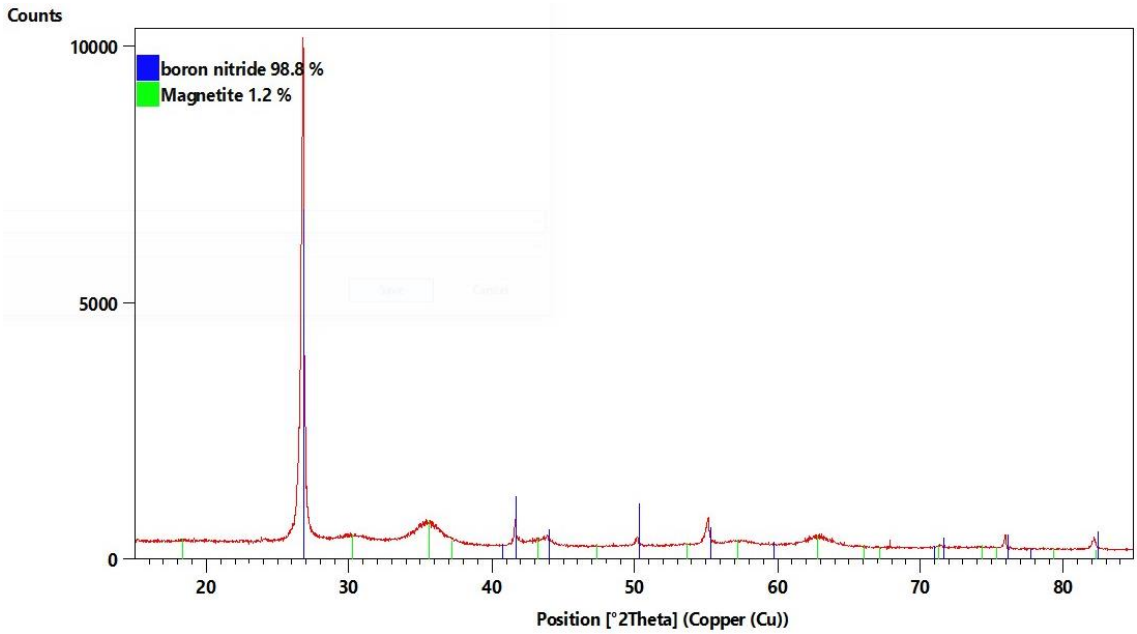


Figure 7-7: XRD phase quantification of the BNNS-Fe_3O_4 nanocomposite.

A phase quantification analysis (Figure 7-7) of the XRD result gave boron nitride as 98.8 % of the sample with Fe_3O_4 as 1.2 %. This is reasonably close to the 1:0.05 ratio of the precursors.

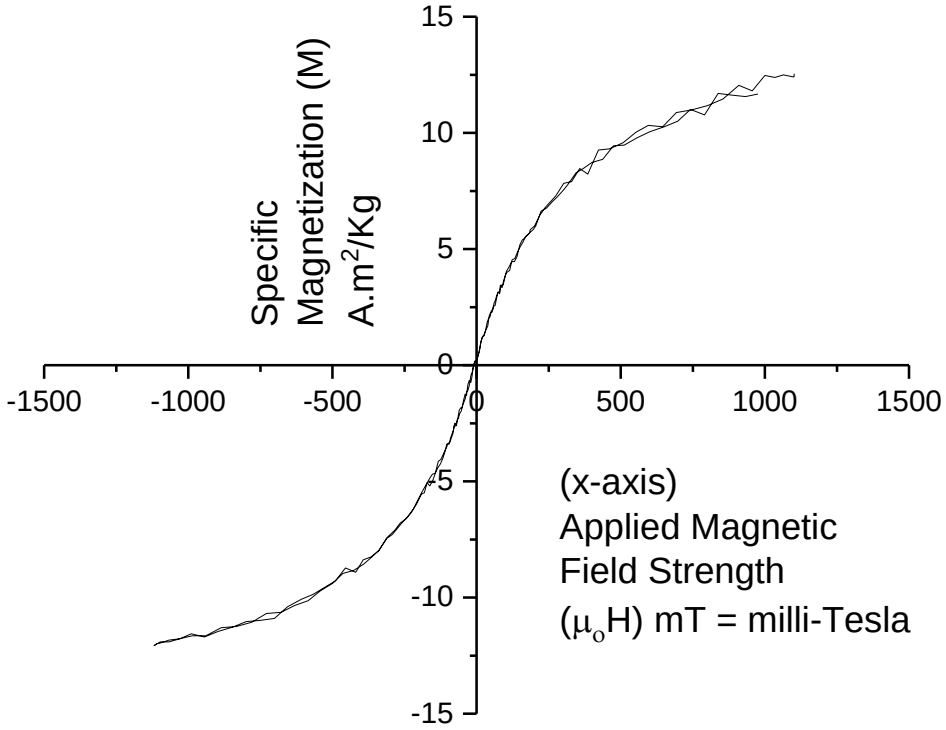
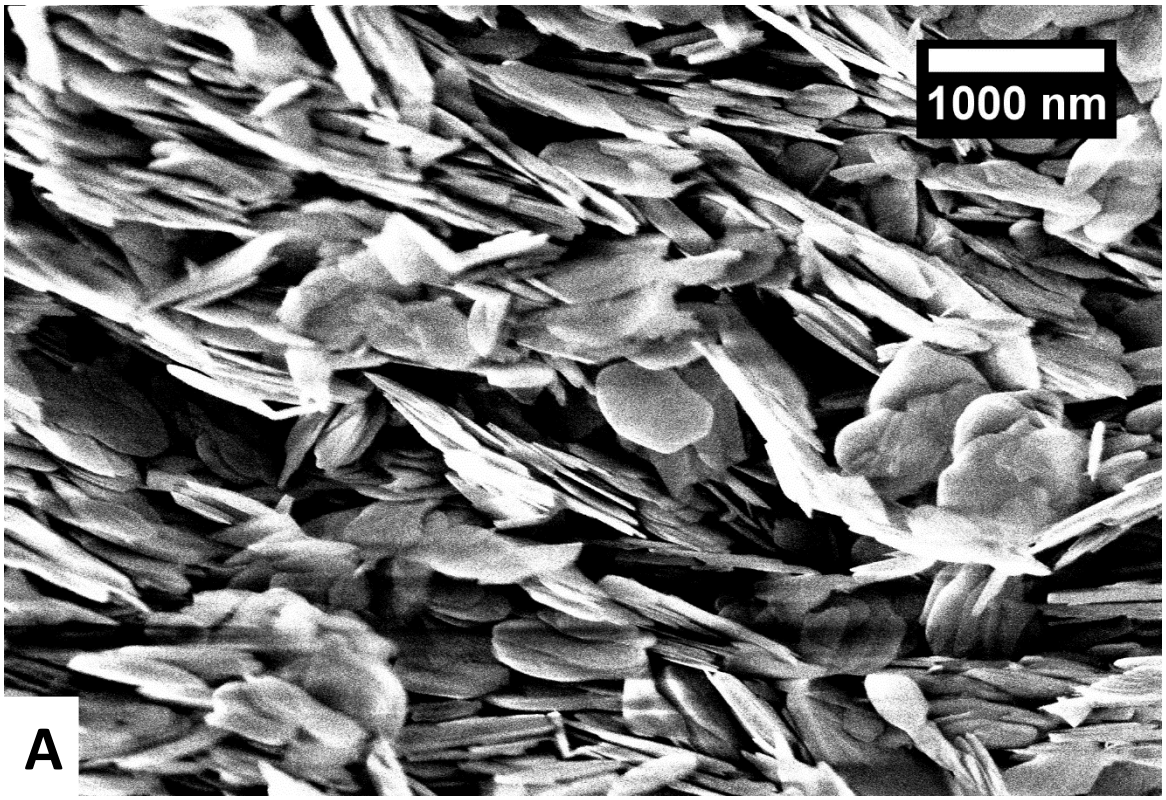


Figure 7-8: VSM curve of the BNNS-Fe_3O_4 nanocomposites.

VSM analysis gave a magnetisation value of 13 Am^2kg^{-1} at 1 T. There was no residual magnetism when the field was 0 T and the shape of the magnetisation curve indicated superparamagnetism as there was no hysteresis loop and the magnetisation has not saturated at 1 T, as can be seen above (Figure 7-8).



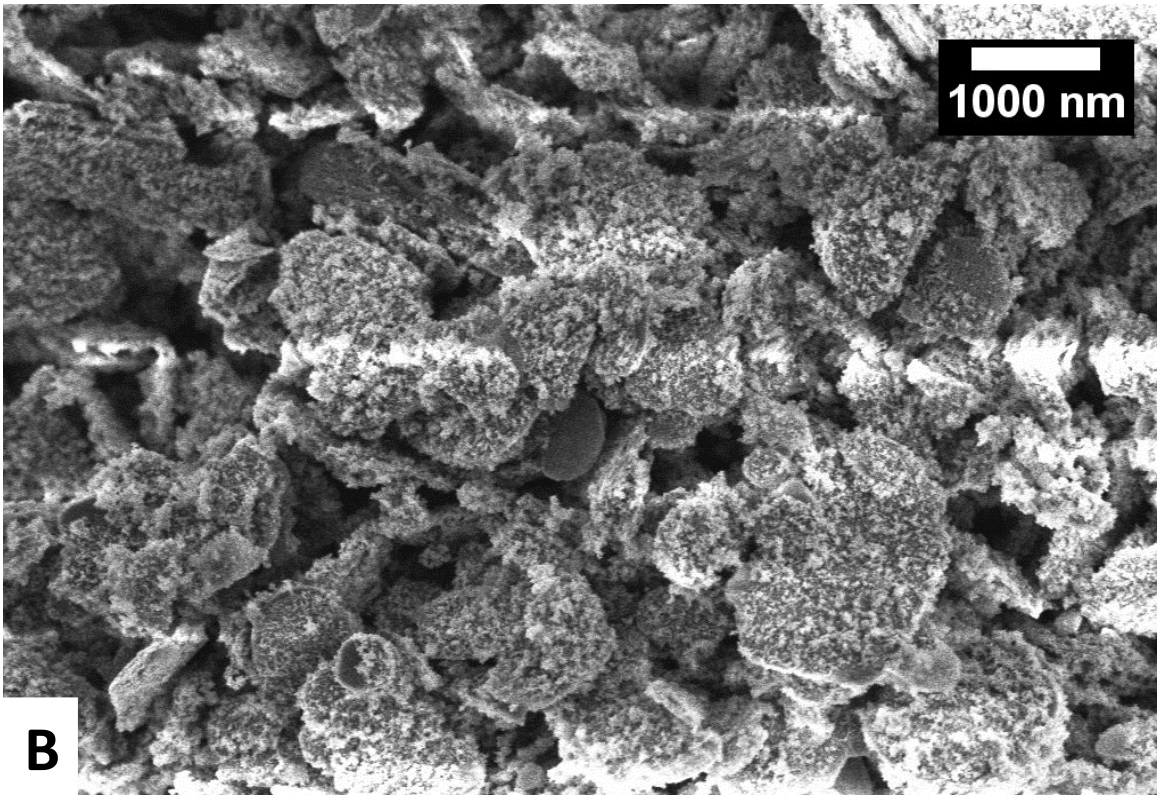


Figure 7-9: SEM cross-sections images of (A) Bare BNNS membrane and (B) Fe_3O_4 coated BNNS membrane.

A membrane of these materials was made by filtering an aqueous suspension on a polyvinylidene fluoride (PVDF) 0.45 µm filter on a fritted glass filtering apparatus. This process captured the nanosheets forming a membrane in the process with the PVDF as the support. Once made, SEM images of the edge profile of a membrane were taken to show the layering. For comparison, a membrane of uncoated BNNS was made as well. The above images (Figure 7-9) show the change from the uncoated BN in **A** to the Fe_3O_4 coated BNNS in **B**. As can be seen, excellent coverage has been achieved.

Some variations to the procedure were done in order to optimise the coating. Instead of using EtONa as the base, NaOH was used instead. This gave good coverage too but slightly lower than with EtONa as can be seen in **A** below (Figure 7-10). This may be because of variations between experiments rather than because of using a different base though. Another variation that was tried was doing the synthesis without EDA. This gave an outcome of larger particles on the surface of the BNNS as can be seen in **B** below (Figure 7-10) with areas of the BNNS that were not fully covered. These particles were approximately 40 ± 20 nm with very few of the smaller particles when using EDA. Using EDA in the reaction gave more uniform coverage

overall. The coverage was very good though with no separate MNPs observed in the TEM images.

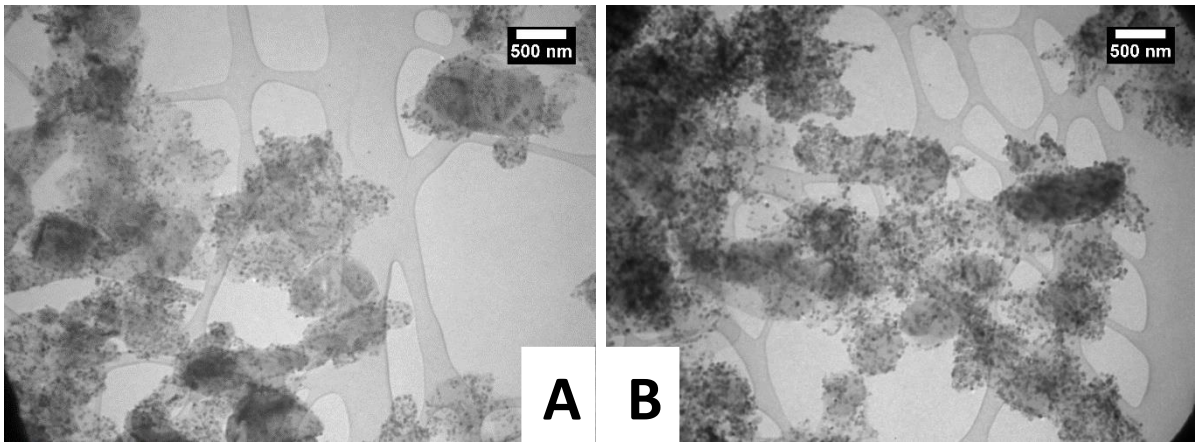


Figure 7-10: TEM images of outcome when (A) using NaOH and (B) without EDA.

The membranes that were made on the PDVF support were very fragile and there was difficulty in removing them from the PVDF. Also by using Fe_3O_4, which is prone to oxidation and is more reactive than other magnetic spinels, there was the possibility of the magnetism and coating degrading with time and heating. $CoFe_2O_4$ is another magnetic spinel with similar saturation magnetisation to Fe_3O_4 but is more chemically inert and retains its magnetism after heating to over 600 °C. On this basis, it was decide to see if similar coated nanocomposites could be created using $CoFe_2O_4$ as the coating magnetic spinel.

7.3.3 Preparation of BNNS-$CoFe_2O_4$ Nanocomposites

BNNS-$CoFe_2O_4$ nanocomposites were prepared by the new procedure used to produce the BNNS-Fe_3O_4. The procedure involved the transfer of the exfoliated BNNS to ethylene glycol for a polyol type of reaction to take place to form $CoFe_2O_4$ MNPs with the BNNS in situ enabling the formation on the surface of the BNNS. $CoFe_2O_4$ is not as biocompatible as Fe_3O_4 with Co being relatively toxic, but $CoFe_2O_4$ is more chemically robust than Fe_3O_4 and can be heated to higher temperatures while retaining its magnetic properties. In addition, the knowledge and techniques learned in the formation of the BNNS-Fe_3O_4 were useful in the preparation of this nanocomposite. The BNNS-$CoFe_2O_4$ nanocomposites and the membranes were characterised by SEM, TEM, FTIR, VSM and XRD techniques.

A TEM image below (Figure 7-11) of the BNNS-$CoFe_2O_4$ show that the BNNS were coated with $CoFe_2O_4$ particles but not as uniformly as with the Fe_3O_4. As can be seen larger $CoFe_2O_4$ particles had formed on the surface of the BNNS of approximately 40±20 nm. Although the coverage was not as good as with the Fe_3O_4, there were no separate $CoFe_2O_4$ particles in the images. This indicated that all the particles had formed on the BNNS.

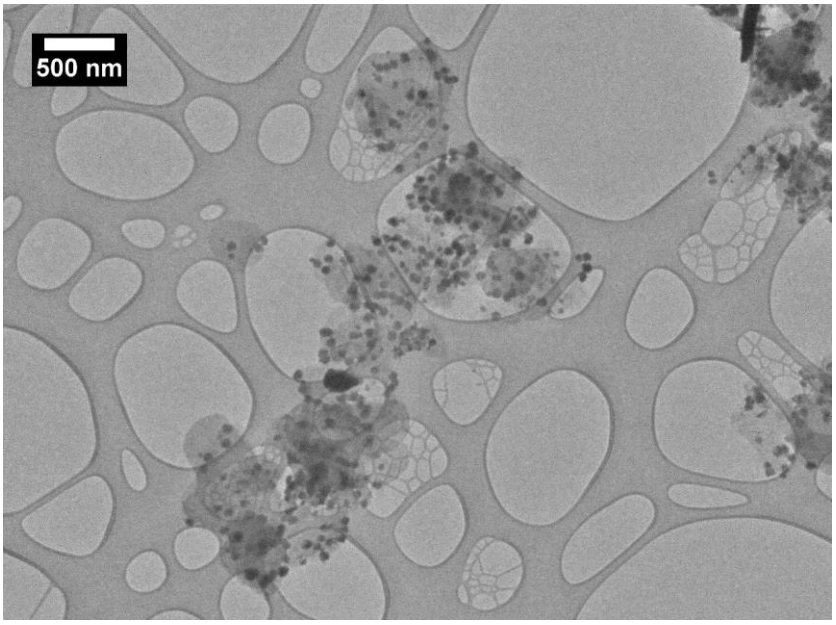


Figure 7-11: TEM image of the BNNS-$CoFe_2O_4$ showing larger $CoFe_2O_4$ particles on BNNS surface.

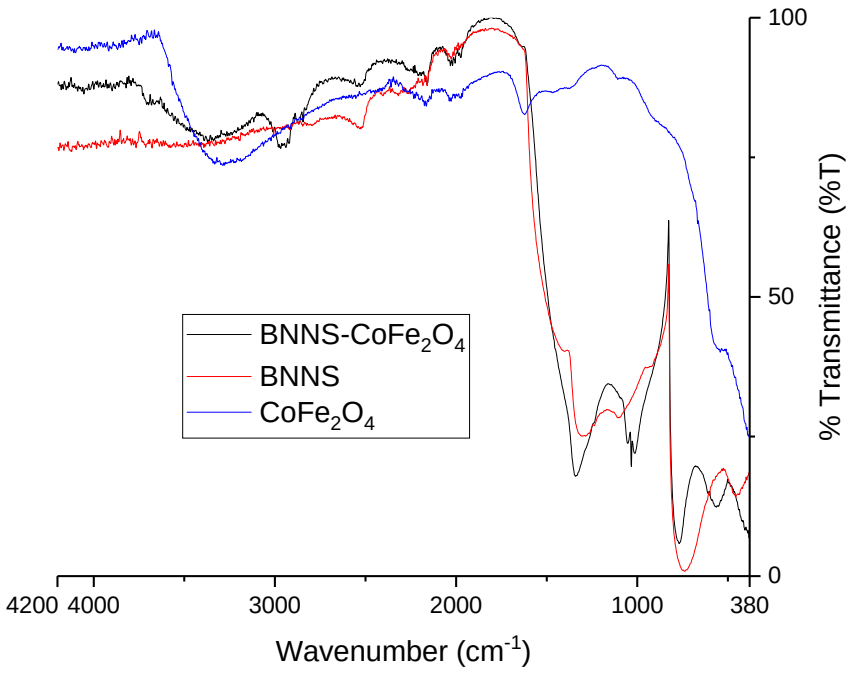


Figure 7-12: FTIR spectra of BNNS-$CoFe_2O_4$ with BNNS and $CoFe_2O_4$ for comparison.

FTIR spectra above (Figure 7-12) have shown bands at 563 cm^{-1} corresponding to the metal-oxygen stretch of the $CoFe_2O_4$. The peaks at 740 and 1300 cm^{-1} have both shifted slightly to 770 and 1340 cm^{-1} respectively. This shift was not as much for the BNNS-Fe_3O_4 as there was not as much coverage. The shifts however indicate interaction of the $CoFe_2O_4$ with the BNNS.

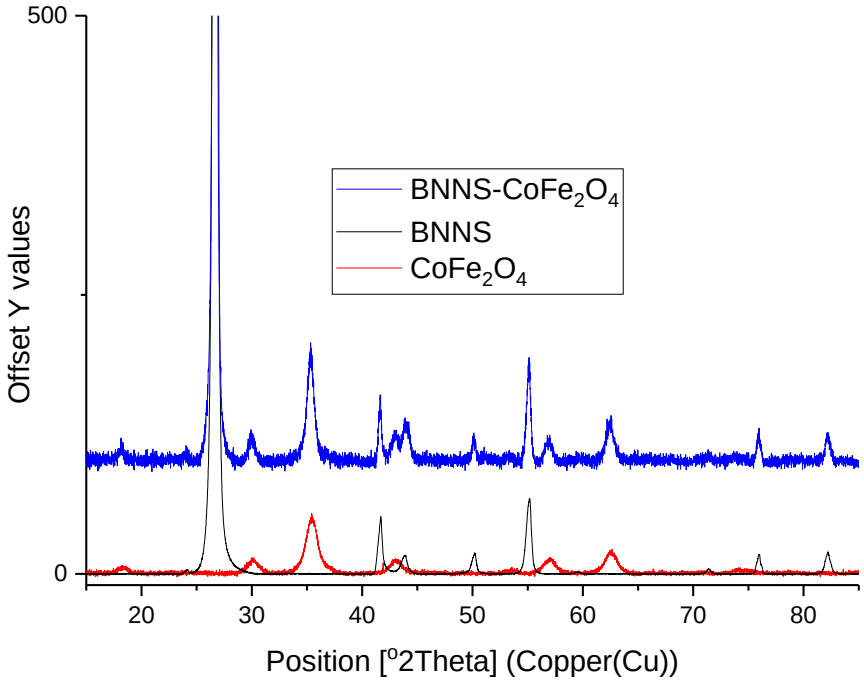


Figure 7-13: XRD pattens of BNNS-$CoFe_2O_4$ shown to be a combination of BNNS and $CoFe_2O_4$.

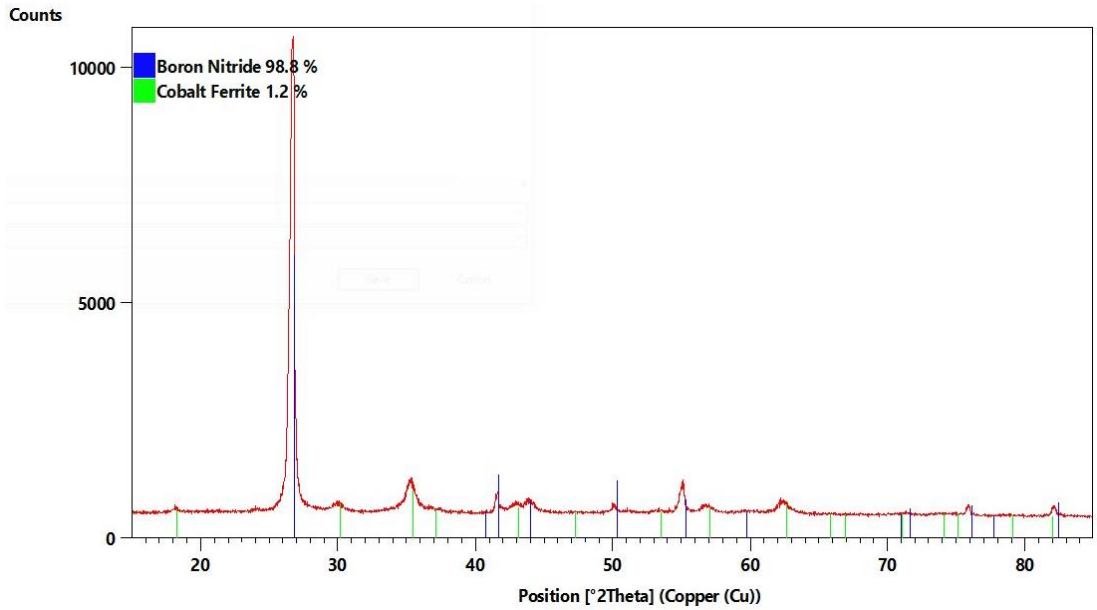


Figure 7-14: Phase quantification of the BNNS-$CoFe_2O_4$.

XRD analysis showed that the BNNS-$COFe_2O_4$ was a combination of the BNNS and $CoFe_2O_4$ made previously and matched to the COD database (COD 201-6171) and (COD 153-3164)

respectively as shown above (Figure 7-13). The graphs were adjusted for intensities but not peak positions because without adjustment the peaks for BNNS-$CoFe_2O_4$ specifically would not be visible as its intensity was much lower than the others were. A phase quantification analysis (Figure 7-14) of the XRD result gave boron nitride as 98.8 % of the sample with $CoFe_2O_4$ as 1.2 %. Again, this is reasonable close to the 1:0.05 ratio of the precursors.

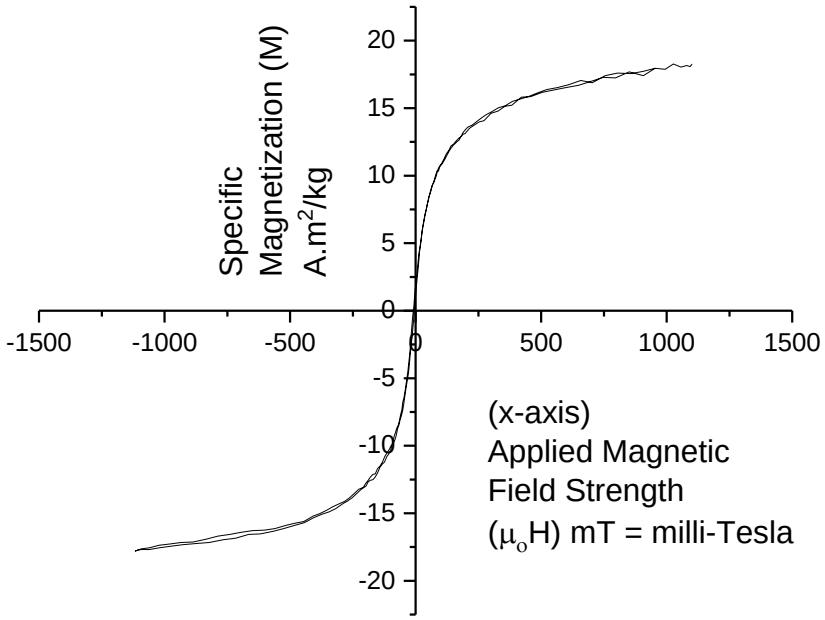


Figure 7-15: VSM curve of the BNNS-$CoFe_2O_4$ nanocomposites.

VSM analysis above (Figure 7-15) gave a magnetisation value of 17.0 Am^2kg^{-1} at 1 T. There was no hysteresis loop and no residual magnetisation when the field was 0 T and indicated superparamagnetism.

One variation that was tried in the synthesis of this material was to use different ratios of BNNS to $CoFe_2O_4$. The sample above had a molar ratio for BN:$CoFe_2O_4$ of 1:0.05. Samples were also made having ratios of 1:0.1 and 1:0.01 to see the effect on coverage and magnetic properties. As expected, the coverage of the MNPs on the BNNS was dependent of the ratio with the larger molar ratio giving high coverage and the lower ratio giving less coverage. The effect of this can be seen in the TEM images below (Figure 7-16) where there is high coverage with the 0.1 ratio with some separate individual MNPs in the images. For the other two ratios, there is a decreasing level of coverage and no separate MNPs were observed in the images. The size of the MNPs on the surface remained constant with the changing molar ratio at approximately 40±20 nm as can be seen in the images.

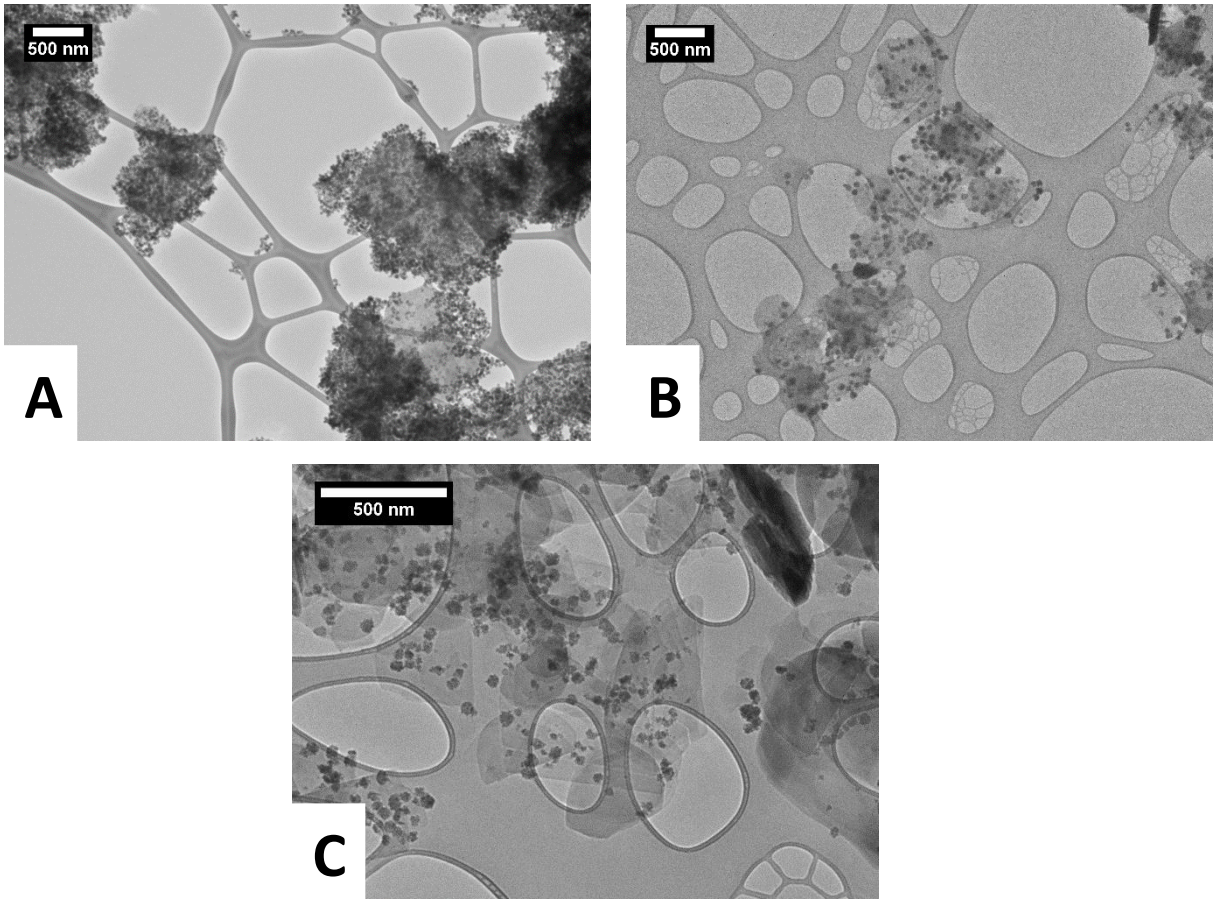
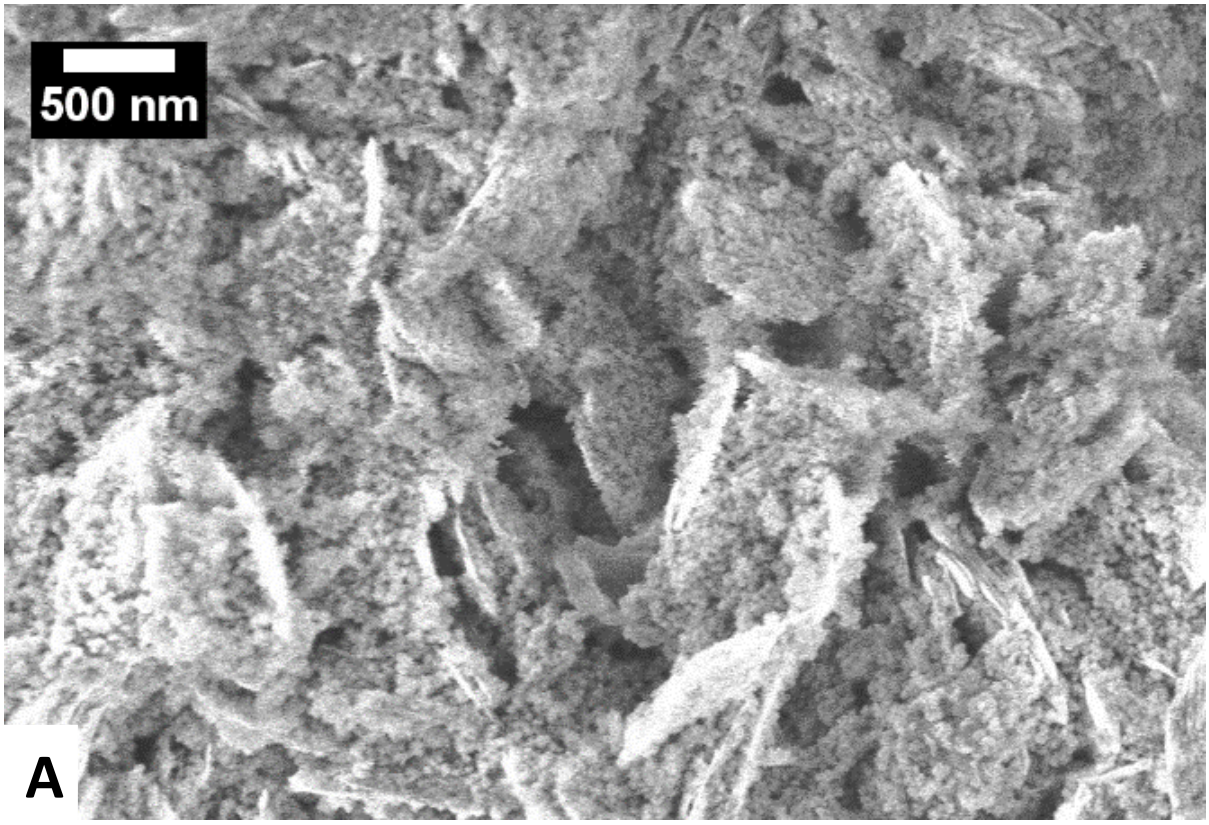


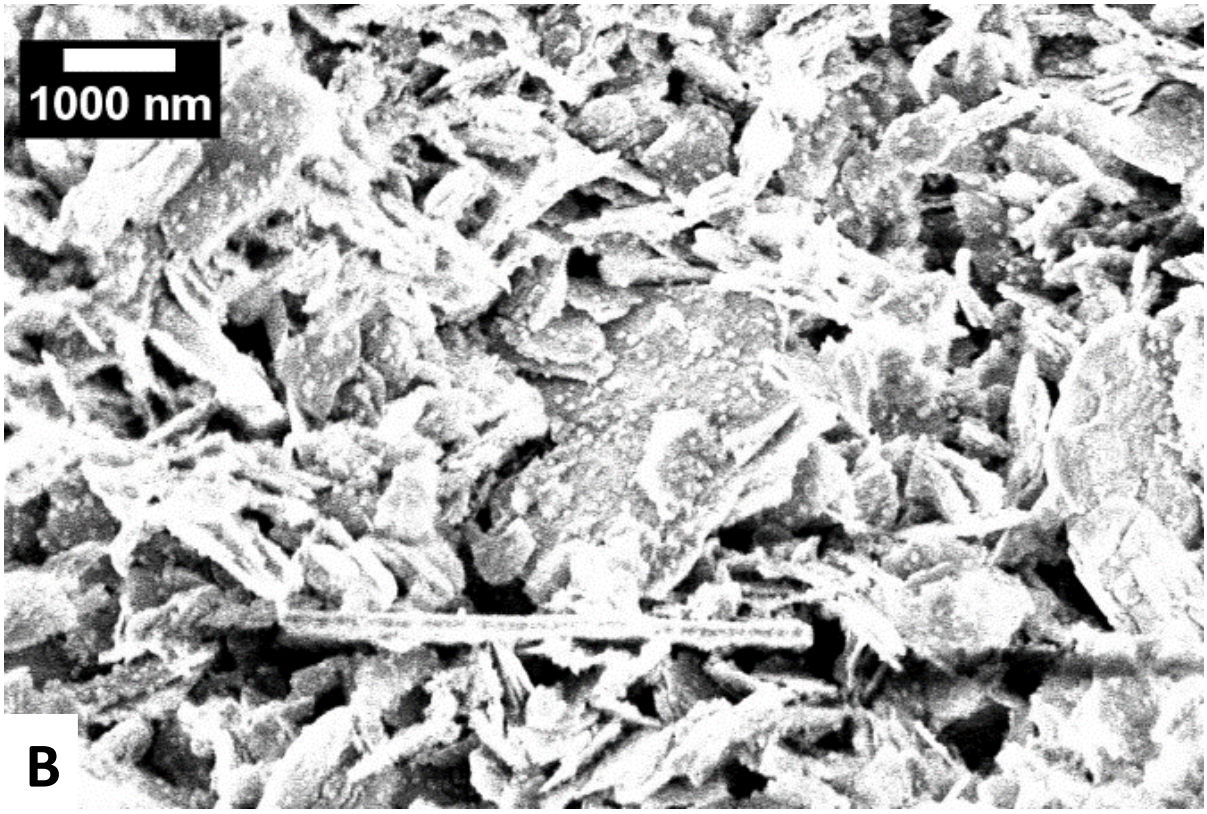
Figure 7-16: TEM images of the composites with different molar ratios of $CoFe_2O_4$ (A) 0.1 (B) 0.05 (C) 0.01.

The magnetic properties were also dependent on the molar ratio of the non-magnetic BNNS and the magnetic $CoFe_2O_4$ with the magnetisation being 27, 13 and 6 Am^2kg^{-1} for the 0.1, 0.05 and 0.01 ratios respectively. The results of these observations are summarised in the table below (Table 7-1). These results demonstrated that a ratio between 1:0.1 and 1:0.05 would give the optimum coverage with no separate MNP in the sample. Optimisation studies to find this ratio were not performed. However, this may be done as future work dependent on the outcome of the research to create a recyclable filter.

Table 7-1: Summary of outcomes for different molar ratios of BNNS:$CoFe_2O_4$.

BNNS:$CoFe_2O_4$ molar ratio	Coverage of BNNS	Magnetisation (Am^2kg^{-1})
1:0.1	high, some separate MNP	27
1:0.05	medium; no separate MNP	17
1:0.01	low; no separate MNP	6


500 nm
A


1000 nm
B

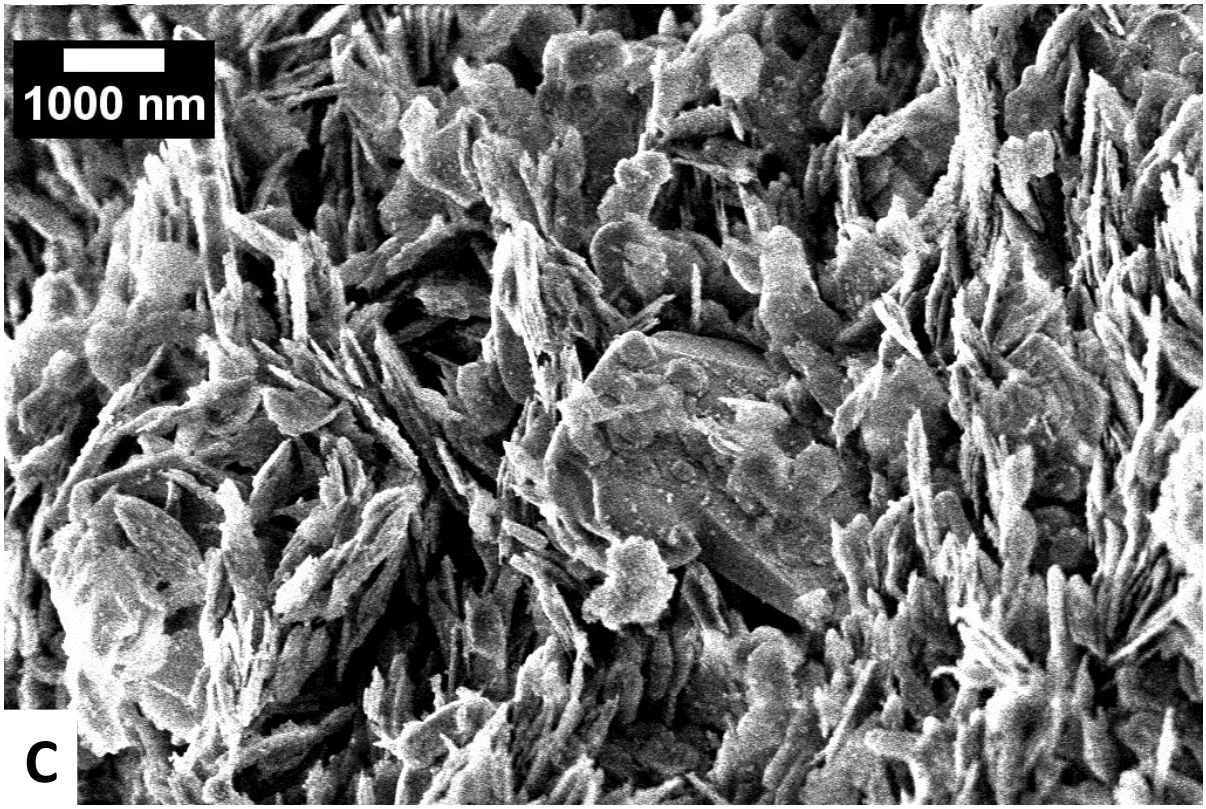


Figure 7-17: SEM cross-section images of membranes with BNNS:$CoFe_2O_4$ ratios of (A) 1:0.1 (B) 0.05 (C) 0.01.

Membranes were made from these three samples and their SEM images are shown above (Figure 7-17). It was found that there was increased shrinkage leading to cracking as the ratio of $CoFe_2O_4$ increased, with the 1:0.1 sample showing considerable cracking as the membrane was dried. The 1:0.05 showed some cracking but to a lesser extent while the 1:0.01 sample showed no cracking. A membrane without any cracks is necessary for an appropriate filter.

On this basis, some optimisation was done to find the optimal level to create a membrane that did not crack when dried. It was found that with a molar ratio of 1:0.4 it was possible to create a membrane without cracks after drying, as can be seen below (Figure 7-18 B).

The membrane with no cracking was still very fragile and could not be lifted as a whole piece without breaking although it was possible to remove it from the PVDF filter. Previous work[17] has shown the calcination of $CoFe_2O_4$ at between 800-1000 °C causes fusion of the $CoFe_2O_4$ and in a previous section (3.3.3) calcination at 600 °C showed fusion of the nanoparticles. Boron nitride begins oxidation at above 900 °C in air[18]. To see if calcination would help to improve the mechanical strength of the BNNS-$CoFe_2O_4$ membrane, it was calcined in the furnace for 12 hours at 800 °C. An improvement in the mechanical strength was observed as

the membrane could now be lifted in one piece, although it was easily broken if pressure was applied. Having made this progress, the next goal was to test the membranes for nanofiltration.

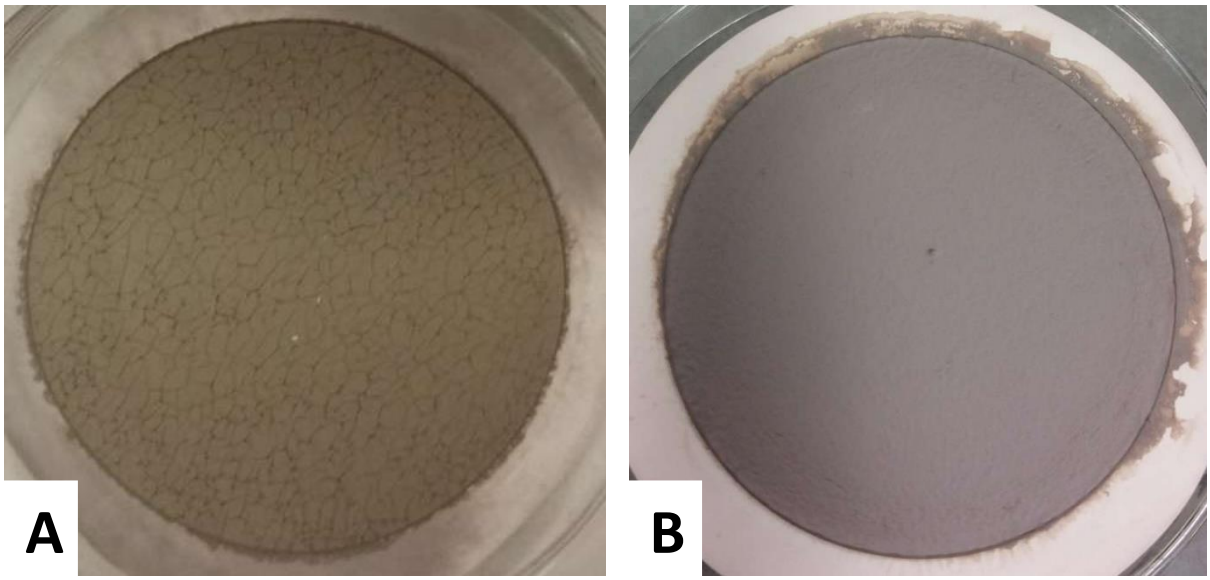


Figure 7-18: Photographs of membranes produced with BNNS:$CoFe_2O_4$ ratios (A) 1:0.05 (see cracking) (B) 1:0.04 (no cracking).

7.3.4 Testing the Membranes for Filtration Applications

In the previous section membranes of BNNS-Fe_3O_4 and BNNS-$CoFe_2O_4$ were made. The BNNS-$CoFe_2O_4$ was calcined in the furnace to improve its mechanical strength. The testing here with the BNNS-$CoFe_2O_4$ was done on a membrane that had not been in the furnace as the idea of improving its mechanical strength by this method was came upon after these tests were done.

The created membranes were to be tested for retention of MB, coprecipitated Fe_3O_4 and Fe_3O_4@citrate nanoparticle samples to see the ability of the membranes to filter nanoparticles and small molecules. As a reference the PVDF membrane on its own was used to filter MB, coprecipitated Fe_3O_4 and Fe_3O_4@citrate and it showed no ability to capture the MNP or the MB as expected. The PDVF membrane used to create the BNNS membrane and used in combination with the BNNS for filtration had a thickness of 0.105 mm and a mass of 125 mg.

The creation of the membrane for testing is described in the experimental section (2.6.6). This gave a membrane with a surface area of 0.001018 m^2. For each of the membranes, the BNNS membrane, the BNNS-Fe_3O_4 and the BNNS-$CoFe_2O_4$ membrane, a mass of 40 mg of the

material was used to create the membrane. The thickness of the membrane in all cases was similar with 0.050 mm for the BNNS, 0.052 mm for the BNNS-Fe_3O_4 and 0.053 mm for the BNNS-$CoFe_2O_4$ as measured using a micrometre screw gauge.

Table 7-2: Physical characteristics for a membrane of 0.001018 m^2 operating at 1 bar.

	BNNS	**BNNS-Fe_3O_4**	**BNNS-$CoFe_2O_4$**
Mass	40 mg	40 mg	40 mg
Thickness	0.050 mm	0.052 mm	0.053 mm
Flow rate	620 $Lm^{-2}hr^{-1}$	343 $Lm^{-2}hr^{-1}$	492 $Lm^{-2}hr^{-1}$

Flow rates for the prepared membranes were calculated at 1 bar pressure. The PVDF membrane had a flow rate of 26700 $Lm^{-2}hr^{-1}$, which is higher than a specified value from a manufacturer of these membranes[19]. The BNNS membrane in combination with the PVDF had a flow rate of 620 $Lm^{-2}hr^{-1}$. The BNNS-Fe_3O_4 membrane in combination with the PVDF had a flow rate of 343 $Lm^{-2}hr^{-1}$. The BNNS-$CoFe_2O_4$ membrane in combination with the PVDF had a flow rate of 492 $Lm^{-2}hr^{-1}$. The reduction in flow rates for the Fe_3O_4 and $CoFe_2O_4$ coated BNNS is indicative of smaller pores in the membrane, as the particles on the surface would create smaller pores for the liquid to filter through, thereby decreasing the flow rates. These membrane characteristics are summarised in the table above (Table 7-2).

The prepared membranes were tested for retention of MB. These were the BNNS membrane on its own, the BNNS-Fe_3O_4 membrane and the BNNS-$CoFe_2O_4$ membrane. It was found that prior to becoming saturated the membrane retained >99% of the MB dye from solution. This is an excellent performance. In addition, the magnetic modality allows for the magnetic heating of the membrane that could be used for membrane regeneration once it has become saturated or blocked. The saturation point is easily observed for MB using UV-vis analysis. For the testing of the membranes, a 40 mg membrane was made on the PVDF support. Then 20 mL aliquots of a 21 µM solution were filtered through the prepared membrane using vacuum filtration, giving an effective membrane pressure of 1 bar approximately. The initial deep blue solution was observed to become clear as the filtrate was collected, as can be seen in the image below (Figure 7-19) of the collected liquid of each successive filtration. As can be seen

in the image, after the 5th aliquots the filtrate begins to show the blue of the MB as the membrane becomes saturated.

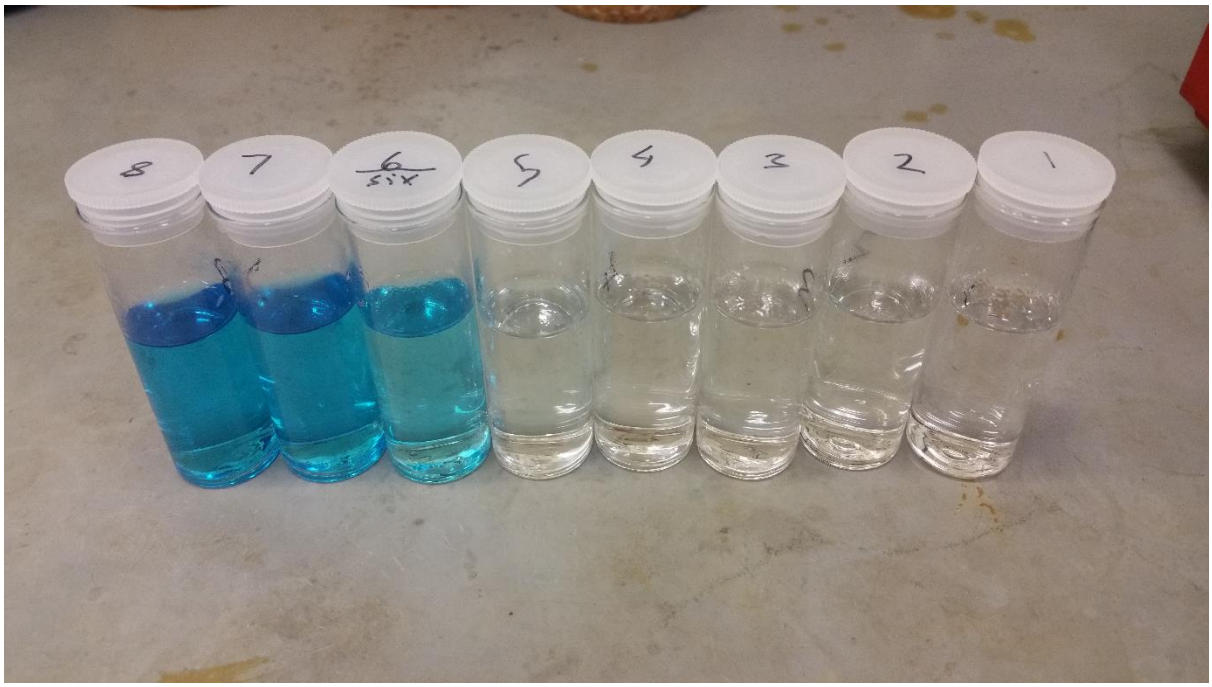


Figure 7-19: Successive filtrates showing MB after the fifth aliquot for BNNS membrane.

These results were quantified with UV-vis analysis as can be seen below (Figure 7-20). It can be seen that for the first 4 runs there >99% removal of the dye then at the fifth run MB begins to pass through the membrane as the membrane is getting saturated. By the eighth filtrate, the solution is approaching the concentration of the original MB solution before filtration.

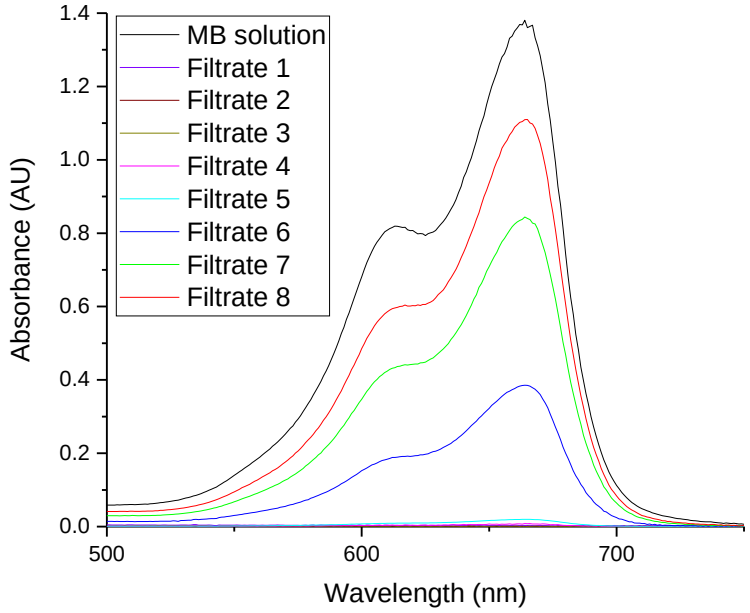


Figure 7-20: UV-vis analysis of successive 20 mL aliquots of MB solution for BNNS membrane.



Figure 7-21: Successive filtrates showing MB after the fourth aliquot for BNNS-Fe_3O_4 membrane.

The same procedure was applied to the BNNS-Fe_3O_4 membrane with successive 20 mL aliquots of the 21 µM MB solution. These filtered aliquots were collected as can be seen above (Figure 7-21). It can clearly be seen how the initial clear filtrate begins to have MB in it with successive filtrations through the same membrane. These results again were quantified with UV-vis spectroscopy analysis, as can be see below (Figure 7-22).

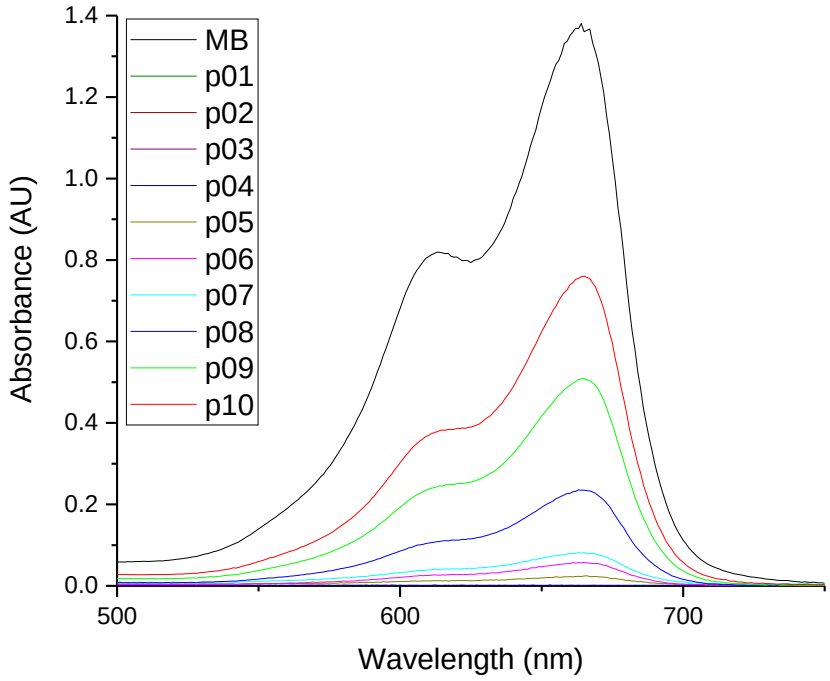


Figure 7-22: UV-vis analysis of successive 20 mL aliquots of MB solution for BNNS-Fe_3O_4 membrane.

A 40 mg of the BNNS-Fe_3O_4 membrane was used and 20 mL aliquots of a 21 µM MB solution of MB which has a molar mass of 373.9 g mol^{-1}. Each 20 mL will contain 157 µg of MB (0.02 L x 21 µM x 373.9 g mol^{-1}) that will be absorbed until the membrane is saturated. The graph below (Figure 7-23) shows this and the beginning of the plateau of the curve, which will plateau at approximately 1.5 mg. This give a capture of 1.5 mg for 40 mg of membrane or 37.5 mg g^{-1}, which is lower than other reported values for adsorbance of MB with BN[20].

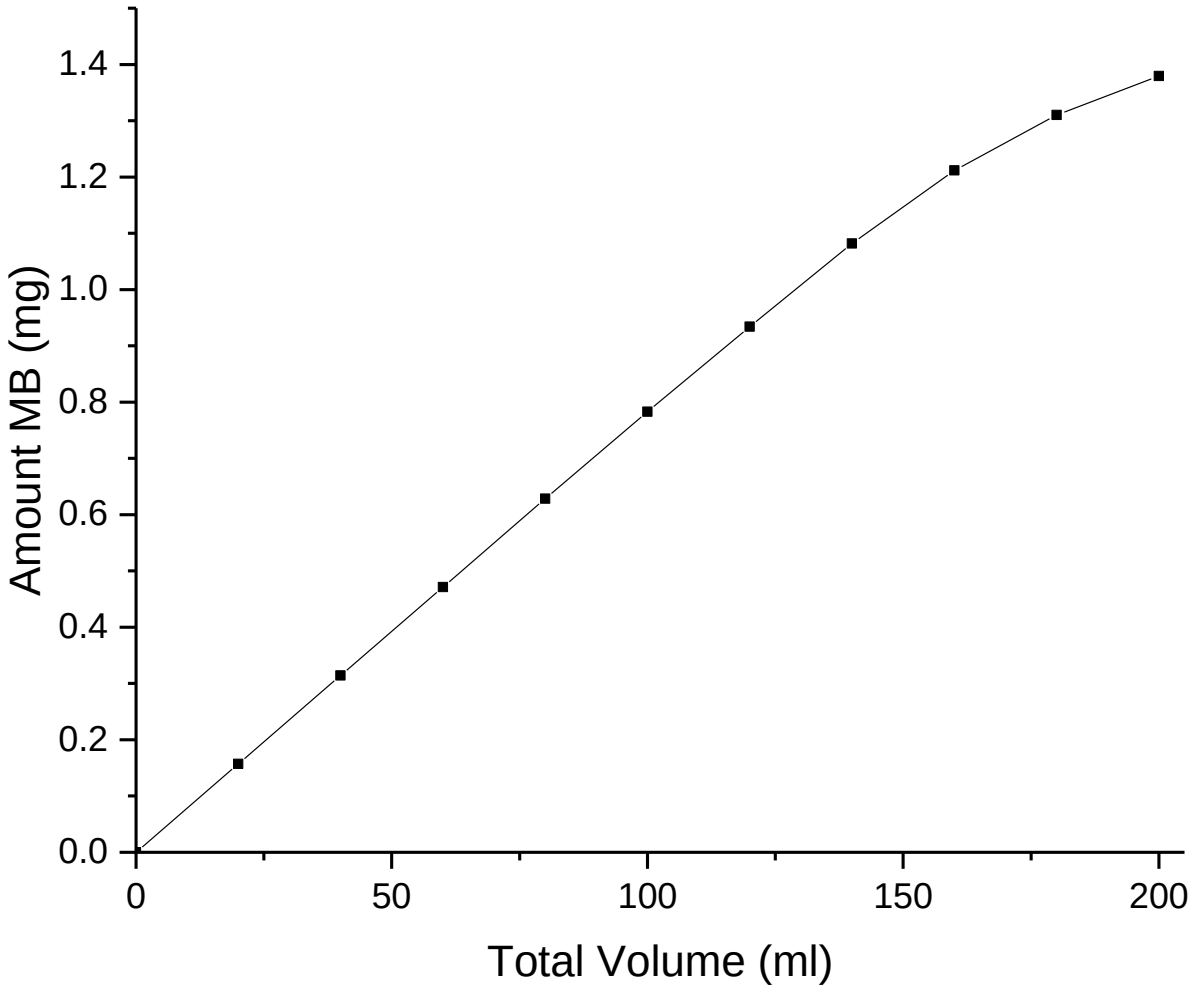


Figure 7-23: Accumulation of MB on BNNS-Fe_3O_4 membrane until saturation develops.

A similar calculation for the BNNS membrane show that the 40 mg of BNNS adsorbs 1.0 mg when plateauing, giving 25 mg g^{-1}, which again is lower than other reported values[20].

The same procedure done for the BNNS-$CoFe_2O_4$ membrane with successive 20 mL aliquots of the 21 µM MB solution These results again were quantified with UV-vis spectroscopy analysis, as can be seen below (Figure 7-24). The calculation for saturation for this material gave a value of 21.5 mg g^{-1}.

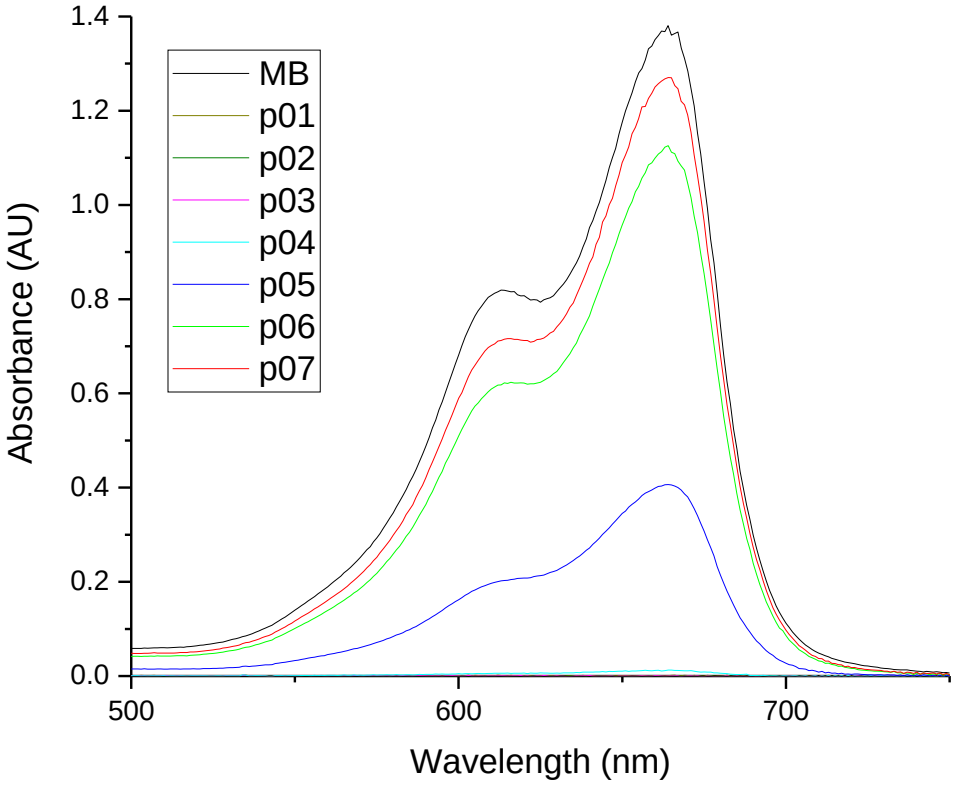


Figure 7-24: UV-vis analysis of successive 20 mL aliquots of MB solution for BNNS-$CoFe_2O_4$ membrane.

What can be seen from the UV-vis analysis is that the BNNS membrane captures more MB from solution initially as the fifth filtrate for this has the lowest absorbance at 0.019 AU in comparison with the BNNS-Fe_3O_4 and BNNS-$CoFe_2O_4$ for their fifth filtrate, 0.025 AU and 0.406 AU respectively. Then the BNNS membrane saturates quickly while the BNNS-Fe_3O_4 saturates slowly and so adsorbs more MB overall. Apart from this, all membranes showed a tendency toward saturation and then letting the MB through the filter. With the MNPs as part of the membrane, the potential for magnetic heating and regeneration is possible, as the MB is captured by the membrane as this work shows.

It was also decided to test the BNNS membrane, the BNNS-Fe_3O_4 membrane and the BNNS-$CoFe_2O_4$ membrane for filtration of 14 nm bare MNP and 14 nm citrate stabilised MNP with a measured hydrodynamic radius measure in MP H_2O of approximately 80 nm (Table 4-1). The bare MNPs are prone to agglomeration due the lack of a surfactant and the tendency of the particle to reduce the surface energy as discussed previously (3.3.1). The citrate-stabilised MNPs will have a hydrodynamic radius larger than 14 nm, as discussed previously (4.3.1). The procedure involved sonication of a 0.2 mg/mL solution of each of the MNPs to create well-dispersed solutions. Then 20 mL of each solution was filtered at approximately 1 bar pressure.

The filtrate was then left on a magnet overnight to see if any particles came out of solution. For each of the membranes there was no particles extracted on the magnet indicating that no particles passed the membrane. The membranes had captured the all MNPs. The surface of the membranes could be seen to have the MNPs on them. This was most visible for the BNNS membrane as it was white in the beginning but after filtration was brown-black, as can be seen in the images below (Figure 7-25). When the membranes dried out the bare Fe_3O_4 were seen as brown layer on the surface, while the citrate-stabilised Fe_3O_4 looked black. The citrate-stabilised MNPs caused the BNNS layer to crumple as it dried while the bare MNPs did not. This could indicate stronger bonding from the citrate to the BN surface as the membrane dried.

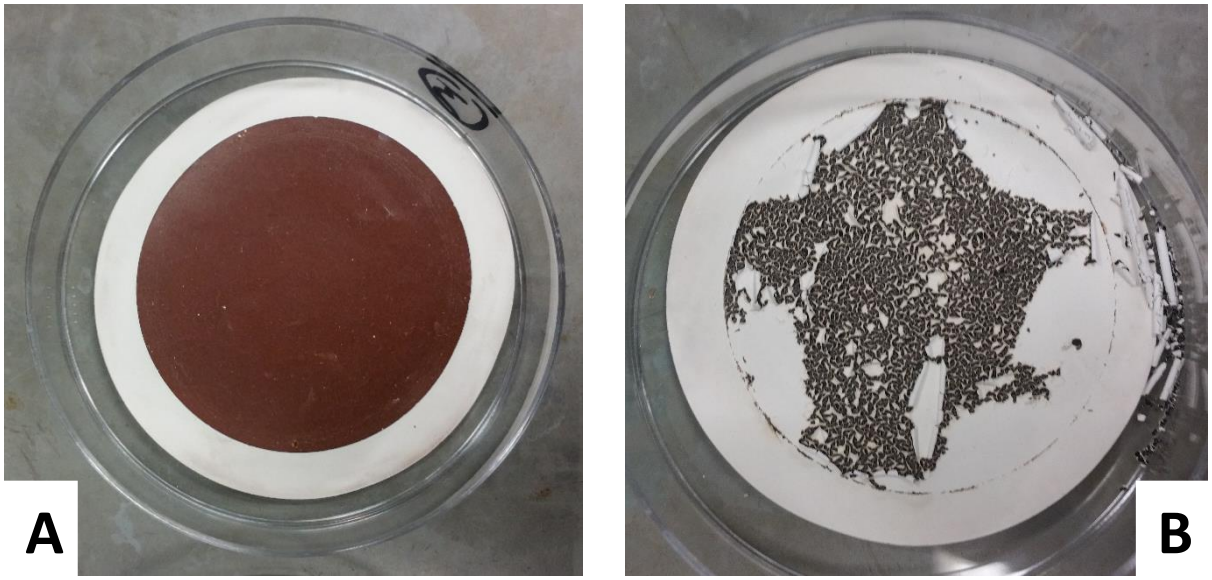


Figure 7-25: BNNS membranes with (A) Fe_3O_4 MNP on surface (B) Fe_3O_4 @citrate on surface.

7.4 Conclusions

In this chapter, we have shown that BNNS can be coated with MNPs to give excellent coverage that is robust and stable to sonication. The bulk BN was easily exfoliated giving 2D BNNS as seen by SEM and TEM. After the transfer of these sheets to ethylene glycol and reaction with the metal precursors, the MNP of Fe_3O_4 and $CoFe_2O_4$ could clearly be seen on the surface with TEM and SEM imaging. The magnetic properties of the nanocomposites were reasonable with the nanosheets being capable of extraction from solution with a neodymium magnet. The coverage achieved for the BNNS-Fe_3O_4 material as observed by TEM and SEM was higher than any previous reported case in the literature that we could find. Changing the ratio of the MNP to the BNNS causes more or less coverages depending on the ratio. The synthesised nanocomposites were made in to a membrane with a view to filtration and magnetic induction heating.

The membranes were tested for filtration of MB and it was found that the membranes absorb the MB until it saturates at which point the MB is found in the filtrate. The membranes were also tested for filtration of bare and citrate-stabilised magnetite with a 14 nm core approximately. No MNP were found in the filtrate.

The capture of the MB blue, at >99% prior to saturation beginning, with the MNPs coated BNNS is a promising result as they will shortly be tested for magnetic induction heating to see if the MB can be burned out to recycle the filter. This is ongoing work in our research group.

7.5 References

1 R. Ghosh Chaudhuri and S. Paria, *Chem. Rev.*, 2012, **112**, 2373–2433. https://doi.org/10.1021/cr100449n

2 A.-H. Lu, E. L. Salabas and F. Schüth, *Angew. Chemie Int. Ed.*, 2007, **46**, 1222–1244. https://doi.org/10.1002/anie.200602866

3 J. Govan and Y. Gun'ko, *Nanomaterials*, 2014, **4**, 222–241. https://doi.org/10.3390/nano4020222

4 H. Ribeiro, P. von Cardoso Randow, D. N. Vilela, M. Adriane Luciano and L. Maria de Andrade, *Recent Adv. Boron-Containing Mater.*, 2020, **i**, 13. https://doi.org/10.5772/intechopen.80849

5 J. N. Coleman, M. Lotya, A. O'Neill, S. D. Bergin, P. J. King, U. Khan, K. Young, A. Gaucher, S. De, R. J. Smith, I. V. Shvets, S. K. Arora, G. Stanton, H. Y. Kim, K. Lee, G. T. Kim, G. S. Duesberg, T. Hallam, J. J. Boland, J. J. Wang, J. F. Donegan, J. C. Grunlan, G. Moriarty, A. Shmeliov, R. J. Nicholls, J. M. Perkins, E. M. Grieveson, K. Theuwissen, D. W. McComb, P. D. Nellist and V. Nicolosi, *Science (80-.).*, 2011, **331**, 568–571. https://doi.org/10.1126/science.1194975

6 D. Golberg, Y. Bando, Y. Huang, T. Terao, M. Mitome, C. Tang and C. Zhi, *ACS Nano*, 2010, **4**, 2979–2993. https://doi.org/10.1021/nn1006495

7 R. Chen, C. Zhi, H. Yang, Y. Bando, Z. Zhang, N. Sugiur and D. Golberg, *J. Colloid Interface Sci.*, 2011, **359**, 261–268. https://doi.org/10.1016/j.jcis.2011.02.071

8 R. S. Bangari, V. K. Yadav, J. K. Singh and N. Sinha, *ACS Omega*, 2020, **5**, 10301–10314. https://doi.org/10.1021/acsomega.9b04295

9 K. Kim, H. Ju and J. Kim, *Polymer (Guildf).*, 2016, **91**, 74–80. https://doi.org/10.1016/j.polymer.2016.03.066

10 M. Salehirad, M. M. Alavi Nikje and L. Ahmadian-Alam, *Ind. Eng. Chem. Res.*, 2018, **57**, 1803–1814. https://doi.org/10.1021/acs.iecr.7b03540

11 W. Ye, Q. Sun, X. Long and Y. Cai, *RSC Adv.*, 2020, **10**, 11121–11131. https://doi.org/10.1039/d0ra00785d

12 T. Sainsbury, A. Satti, P. May, Z. Wang, I. McGovern, Y. K. Gun'ko and J. Coleman, *J. Am. Chem. Soc.*, 2012, **134**, 18758–18771. https://doi.org/10.1021/ja3080665

13 N. García Doménech, F. Purcell-Milton and Y. K. Gun'ko, *Mater. Today Commun.*, 2020, **23**, 100888. https://doi.org/10.1016/j.mtcomm.2019.100888

14 Q. Zhang, Z. Li, X. Li, L. Yu, Z. Zhang and Z. Wu, *Nano*, 2019, **14**, 1950063. https://doi.org/10.1142/S1793292019500632

15 V. Nicolosi, M. Chhowalla, M. G. Kanatzidis, M. S. Strano and J. N. Coleman, *Science (80-.).*, 2013, **340**, 72–75. https://doi.org/10.1126/science.1226419

16 S. S. Pati and J. Philip, in *Proceedings of the International Conference on Nanoscience, Engineering and Technology, ICONSET 2011*, IEEE, 2011, pp. 323–325. https://doi.org/10.1109/ICONSET.2011.6167973

17 B. Purnama, A. T. Wijayanta and Suharyana, *J. King Saud Univ. - Sci.*, 2019, **31**, 956–960. https://doi.org/10.1016/j.jksus.2018.07.019

18 V. A. Lavrenko and A. F. Alexeev, *Ceram. Int.*, 1986, **12**, 25–31. https://doi.org/10.1016/S0272-8842(86)80006-2

19 PVDF Membrane Specifications, https://www.sterlitech.com/media/wysiwyg/Data_Sheet_PVDF_Membrane_Filters.pdf

20 S. Yu, X. X. Wang, H. Pang, R. Zhang, W. Song, D. Fu, T. Hayat and X. X. Wang, *Chem. Eng. J.*, 2018, **333**, 343–360. https://doi.org/10.1016/j.cej.2017.09.163

8 Conclusion and Future Work

8.1 Conclusions

In this work, a number of magnetic nanoparticle cores were synthesised using the coprecipitation and polyol methods. Selected cores were stabilised and protected using citrate and silica coatings. These were then further functionalised with a catalytic shell of two well-known catalysts, manganese dioxide and cerium dioxide, giving excellent quality nanoparticles with distinct shells. These nanoparticles were then tested for catalytic activity and for dye pollutant removal with the recyclability of the particles examined too. The manganese dioxide coated nanoparticles were also tested as a chemical reaction inhibitor and activator after magnetic removal of the particles. A nanocomposite was also made with magnetic nanoparticles on the surface of a 2D nanomaterial with excellent coverage with a view to creating a recyclable nanofiltration system.

The initial focus of this work was on creating the magnetic cores. For the coprecipitated cores four different spinel materials were looked at, namely magnetite, manganese ferrite, cobalt ferrite and copper ferrite. For magnetite and cobalt ferrite, the outcomes were excellent with good quality nanoparticles produced with monodisperse samples as observed under TEM analysis. The magnetic properties of these two materials were excellent too, showing superparamagnetic behaviour. For the manganese ferrite, the sample was not monodisperse showing a broad size distribution but the magnetic properties were good. The copper ferrite synthesis did not produce good results because of the need to calcine the product as part of the synthesis. This caused fusing of the nanoparticles, which then could not be dispersed into solution with sonication. For the polyol method, manganese ferrite and magnetite nanoparticles were produced. The quality of both nanoparticle samples were good, but the manganese ferrite nanoparticles synthesis gave a slightly better result with regard to the consistent morphology of the particles. The coprecipitated magnetite, the cobalt ferrite and the polyol manganese ferrite results were excellent in terms of the magnetic properties, size distribution and the reproducibility of the syntheses. For the copper ferrite and coprecipitated manganese ferrite, the results were lower than expected in terms of size distribution. The magnetic properties of copper ferrite only improved after calcination but this procedure

caused fusing of the particles so that they were no longer dispersible in solution. Further research is needed here to improve the size distribution of the coprecipitated manganese ferrite MNPs and to have good magnetic properties with the copper ferrite without the need for calcination. The polyol magnetite gave a reasonable result in terms of the size distribution of the particles but could be improved in my opinion, while the magnetic properties were good for this synthesis.

Then selected magnetic nanoparticles were stabilised with citrate and protected with silica as necessary steps for further functionalisation. Some exploration for control of the silica shell was examined and it was found to be a process that needed more exploration to gain full control of the outcomes. Although this is a well-established procedure, we found the reproducibility was not high as expected and more work needs to be done here for consistent reproducibility. I found the citrate procedure to be easy and reproducible according to previous reported results and resulted in nanoparticles with good stability. However, there were difficulties to produce good quality reproducible silica coating.. Following protocols exactly from papers gave widely different results and so the reproducibility was poorer than expected for this procedure. Silica coating of magnetic nanoparticles to give highly reproducible results with controllable shell thickness and single core nanoparticles is an area of research that is highly important for potential commercialisation of this desired product.

After that, catalytic shells of manganese dioxide and cerium dioxide were created on selected magnetic nanoparticles. For both of these catalytic shells excellent results were achieved with well-defined shells on individual particles observed with TEM analysis. Attempts were done to try to modify the synthesis of the manganese dioxide shelled particles in an effort to simplify the protocol but these explorations were unsuccessful. Explorations were also done to control the amount of manganese dioxide on the shell with the optimal ratio for the polyol cores found to be a one molar ratio. It was found to be necessary to wash the manganese ferrite polyol synthesised particles with acetone for the manganese dioxide coating to be achieved. For the cerium dioxide coated particles, explorations were also done to control the shell thickness. There was more success here but at high ratios of cerium dioxide to the core, agglomeration was found to happen. In the TEM images of these particles it was possible to see the core of manganese ferrite, the inner shell of silica and the outer shell of cerium dioxide clearly. Efforts to coat bare nanoparticles with cerium dioxide were unsuccessful with

separate particles forming as seen under the TEM, showing the need for the amorphous silica shell. The coating of the magnetic nanoparticles with the catalytic shells was very successful as the characterisation by the TEM images showed. The target structures that we had planned for, core-shell structures with the desired catalytic shell were made successfully. The fast magnetic extraction was achieved for these nanoparticles because of the larger magnetic core, which was a positive result from this research.

Then the nanoparticles with the catalytic shell were tested for a variety of applications, with the first being as magnetically removable catalysts. The results here were disappointing with very low conversion rates and yields for both particle types. The manganese dioxide coated particles were expected to perform better as the shell material on its own gave better yields. The catalyst was magnetically removed easily form the solution, but it was found that it was necessary to filter the solution to get reliable NMR results. The same was found with the cerium dioxide coated nanoparticles, in that they could be removed from solution effectively with a magnet but the solution needed to be filtered to clean up the NMR spectra. The manganese dioxide coated $MnFe_2O_4$ particles performed well for the glue inhibition with reactivation of the glue after magnetic removal. It is expected that this work can be expanded to find other areas where this inhibition with magnetic reactivation can be achieved. These nanoparticles were also tested for the application of pollutant removal from water, with organic dyes being used as the pollutant in this case. The manganese dioxide coated particles showed excellent removal of methylene blue dye from the solution with excellent recyclability. After 10 recycles the particles still performed well and showed minimal change with XRD and TEM analysis after the 10 runs. The extraction efficiency was above 83% in all cases. The efficiencies were lower in the cases of methyl orange and Rhodamine B with decreasing efficiencies with each recycle. The cerium dioxide coated MNPs also showed excellent removal of the methylene blue dye from solution. The extraction efficiency was above 89% in all cases with little loss of efficiency over the four runs.

Finally, magnetic nanoparticles - boron nitride nanocomposites were created with excellent coverage of the surface of the boron nitride nanosheets with MNPs. The nanocomposites were formed into membranes that demonstrated an efficient (over 99%) removal of methylene blue dye from the solution until the membrane was saturated. The membranes also captured 14 nm bare and citrate-stabilised magnetite nanoparticles from a solution that

was filtered, indicating their effectiveness for nanofiltration. The coating of the BNNS with the Fe_3O_4, as viewed by TEM and SEM was better than anything reported in the literature to date, to the best of our knowledge. This method of attaching magnetite and cobalt ferrite to BN worked very well and gave an excellent result as the TEM and SEM images showed for coverage on and attachment to the BNNS. The method was also found to be reproducible with several repeat syntheses done.

Overall, the project was a success as the target nanostructures were created with excellent morphologies as observed with electron microscopy images. Unfortunately, the performance of some of these nanostructures was lower than expected in selected applications, namely catalysis. However, the nanostructures showed great potential in pollutant extraction and removal.

8.2 Future Work

This project resulted in development of good quality core@shell nanoparticles with a desired shell, which can be extracted easily and quickly, from solution with a magnet. It was also shown that magnetic nanoparticles can be bound to the surface of boron nitride with excellent coverage and that organic dye can be absorbed onto these nanocomposites. We believe that following further studies should be performed in the future work:

1. Improving the syntheses of manganese ferrite coprecipitated nanoparticles to get a lower polydispersity index. The use of hydrazine as the base may achieve this outcome, as it was successful with cobalt ferrite.
2. Improving the synthesis of copper ferrite so there is no need for calcination as this causes fusing and loss of dispersion into solution. Again, the use of hydrazine here as the base to precipitate the ferrite may achieve this outcome, as it was successful for cobalt ferrite.
3. Gain control over the size of the manganese ferrite nanoparticles produced by the polyol method. There was some difference in sizes between batches with the source of this change not understood. There are many options to achieve this goal, such as optimisation of the temperature and time to achieve the best outcomes. This use of various regimes including heating rates may have an effect on the nucleation and

growth mechanism. Other possible future studies could involve using different bases or different precursors such as sulphates or nitrate instead of chlorides.

4. Improve the shell of SiO_2 as there was a lot of variability between batches. Problems were the formation of separate silica particles for the polyol method and agglomeration with a thin shell for the coprecipitated method. As this is meant to be a well-established procedure it should be easy to reproduce the procedures in the literature but the reproducibility was not consistent we found. Again, here several possible future avenues could be explored to achieve these goals, such as controlled addition of the TEOS over a longer period of time. In addition, other precursors for SiO_2 growth could be tried such as sodium silicate or tetramethylorthosilicate.
5. Detailed studies of nanoparticles with the catalytic shells are necessary to understand the reasons for low catalytic activity and to find the way to optimise these nanostructures in order to achieve highest conversion rates in selected oxidation reactions. Particular attention should be paid to an exploration to see if other manganese dioxide polymorphs coating could be attached, which may demonstrate higher catalytic activities.
6. The boron nitride magnetic nanoparticle nanocomposites should be tested for magnetic induction heating to see if they can burn off the absorbed dyes and regenerate the membranes. In addition, the calcined membrane with better mechanical properties should be tested for filtration and then magnetic heating.
7. Finally, many of the developed nanocomposite structures could find applications in water purification (dyes and poisonous metal removal) and bioseparation. Further studies are needed to develop these important applications.

Appendix

A.1 Supplementary Information

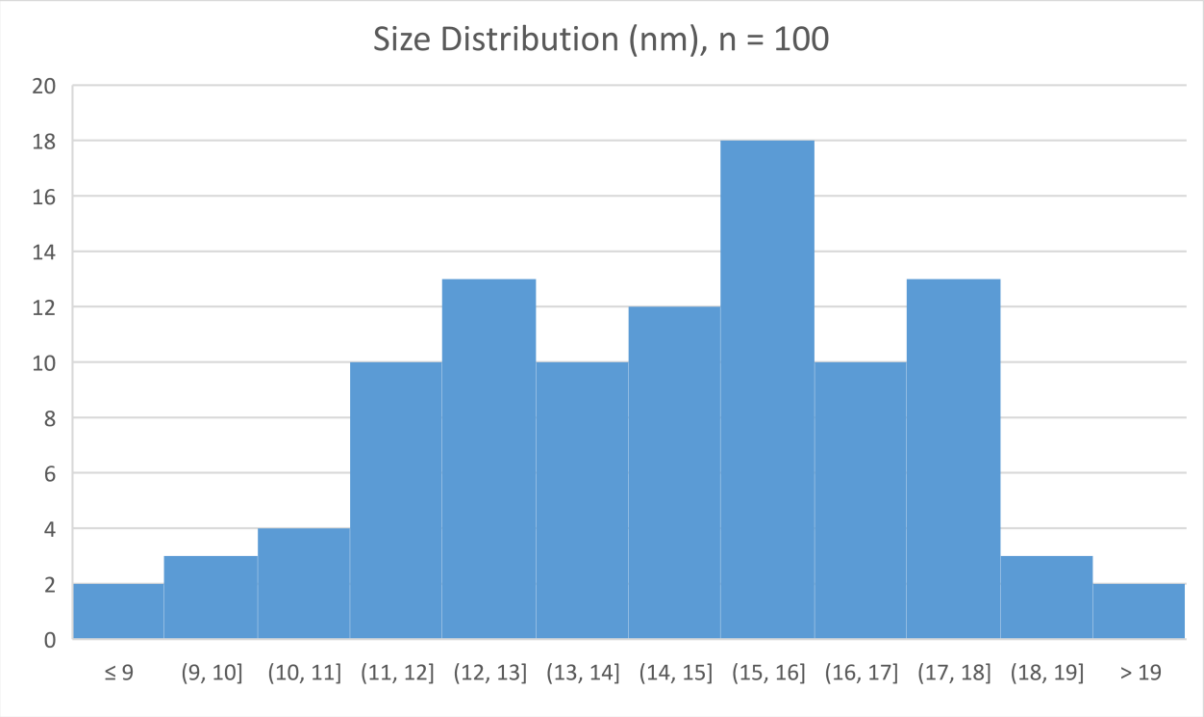


Figure A-1: Size distribution histogram for the coprecipitated Fe_3O_4 nanoparticles.

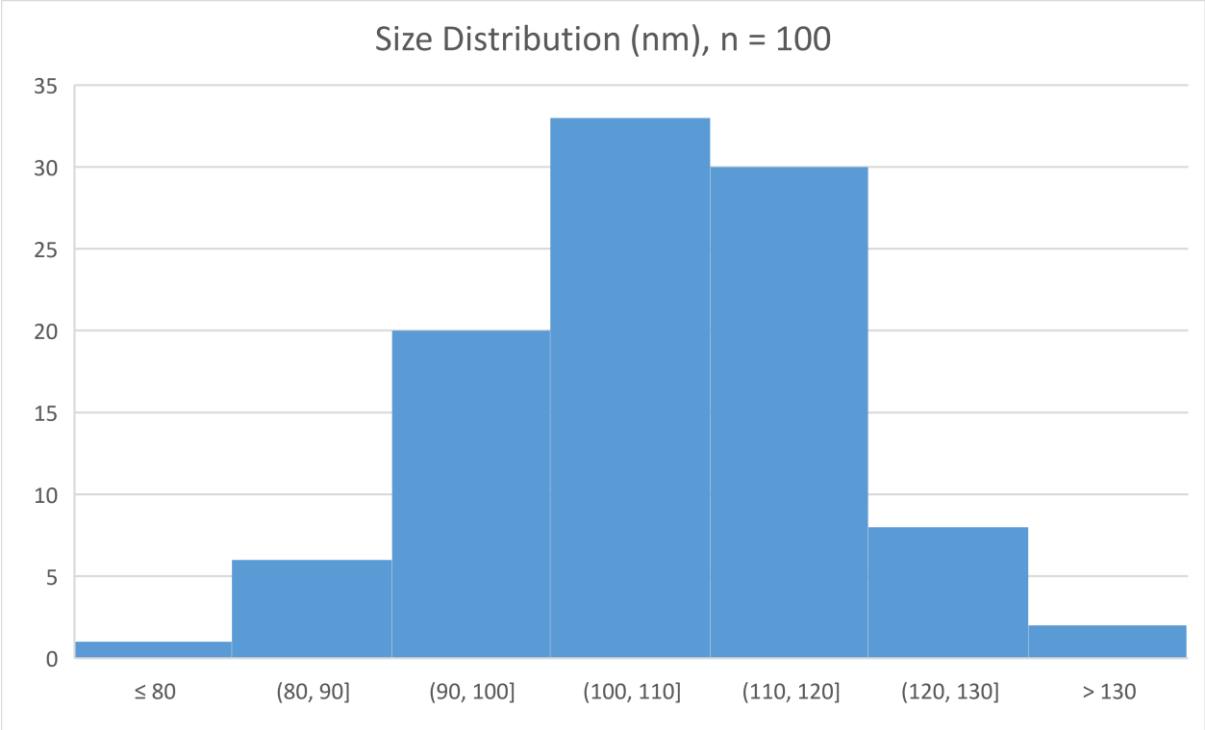


Figure A-2: Size distribution histogram for the polyol $MnFe_2O_4$ nanoparticles.

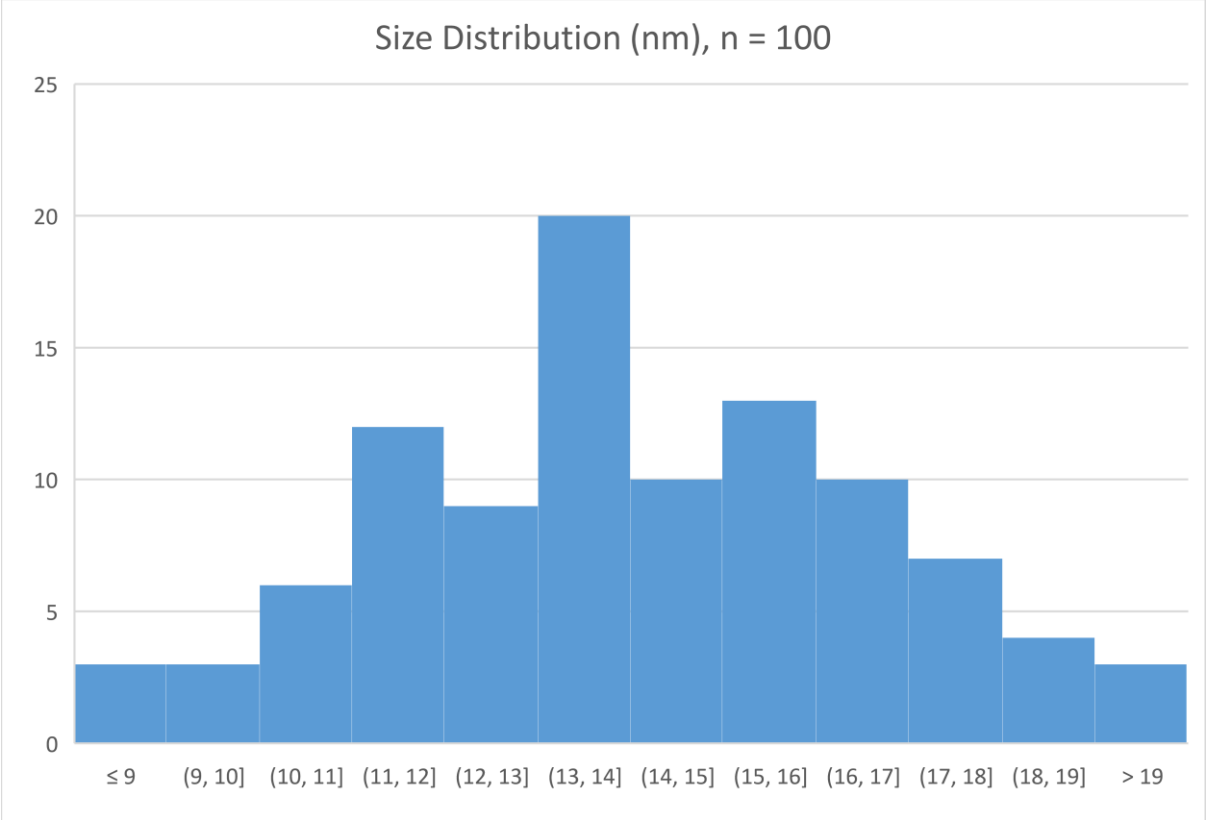


Figure A-3: Size distribution histogram for the citrate stabilised coprecipitated Fe_3O_4 nanoparticles.

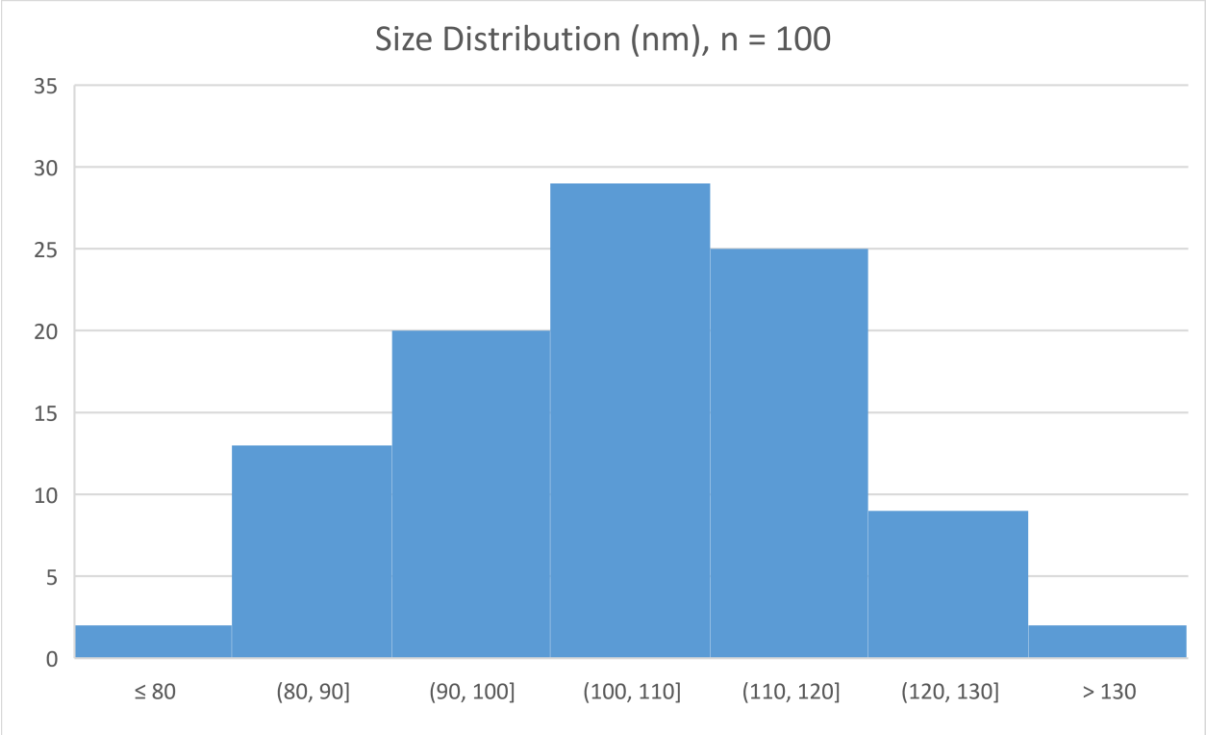


Figure A-4: Size distribution histogram for the citrate stabilised polyol $MnFe_2O_4$ nanoparticles.

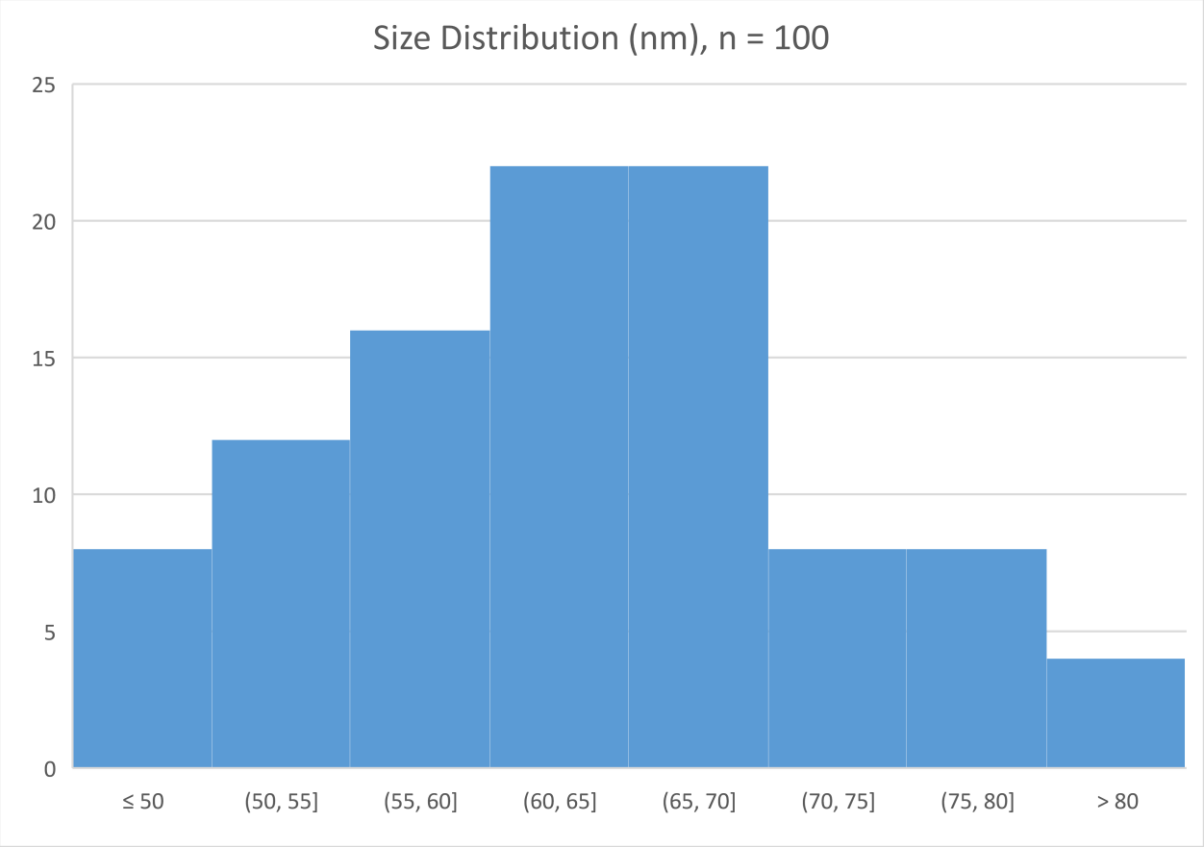


Figure A-5: Size distribution histogram for the SiO_2 coated Fe_3O_4 nanoparticles.

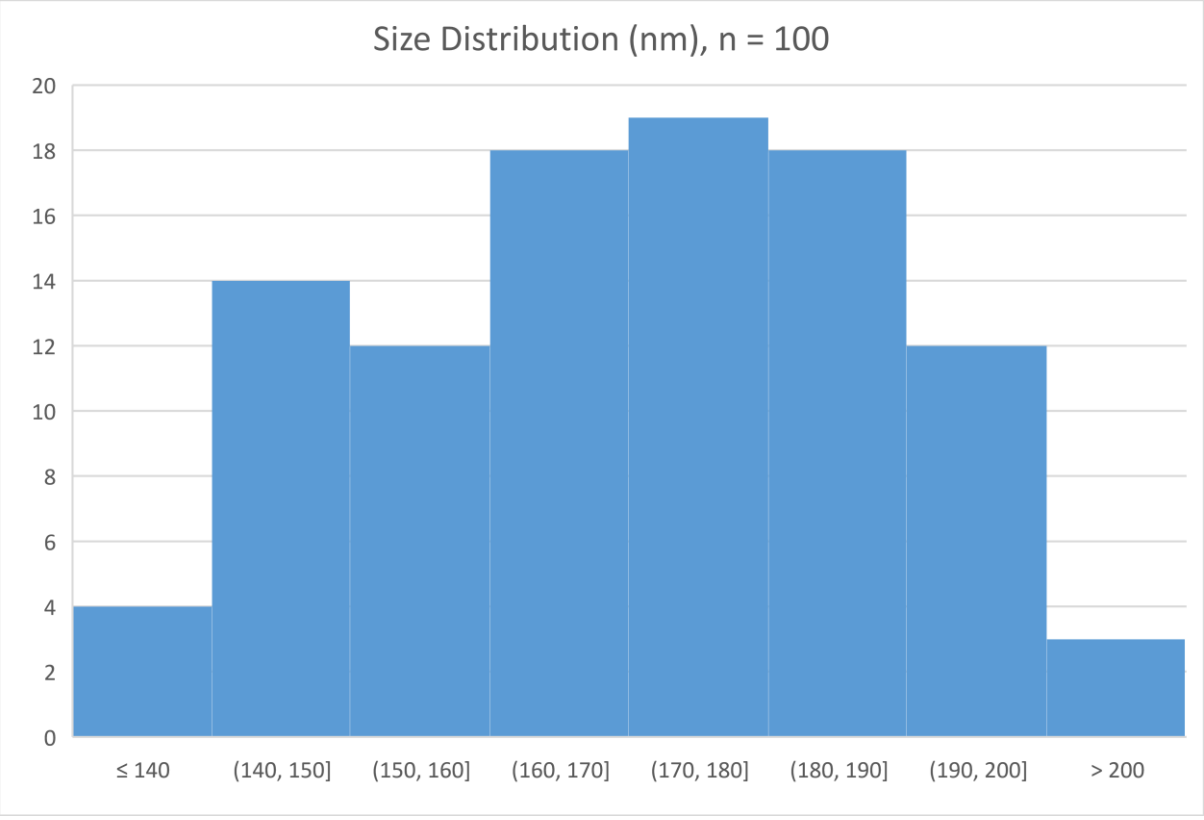


Figure A-6: Size distribution histogram for the SiO_2 coated $MnFe_2O_4$ nanoparticles.

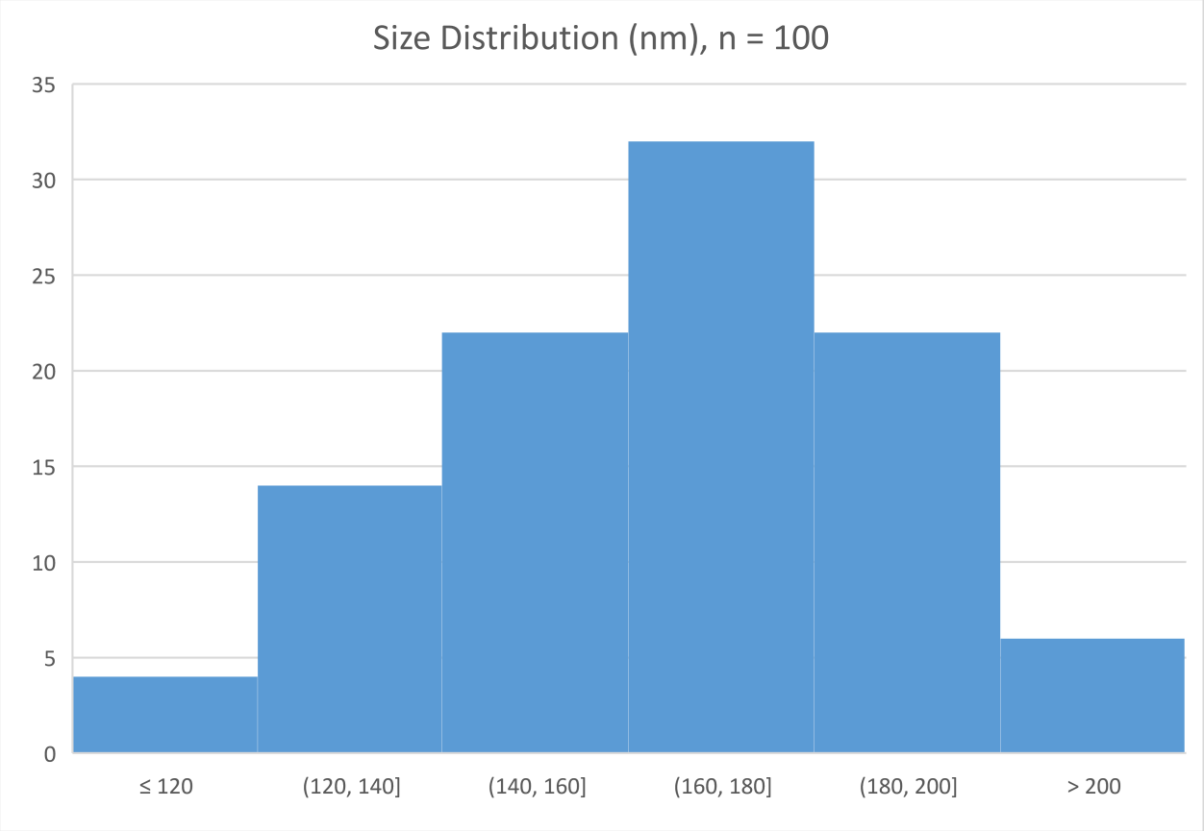


Figure A-7: Size distribution histogram for the MnO_2 coated $MnFe_2O_4$ nanoparticles.

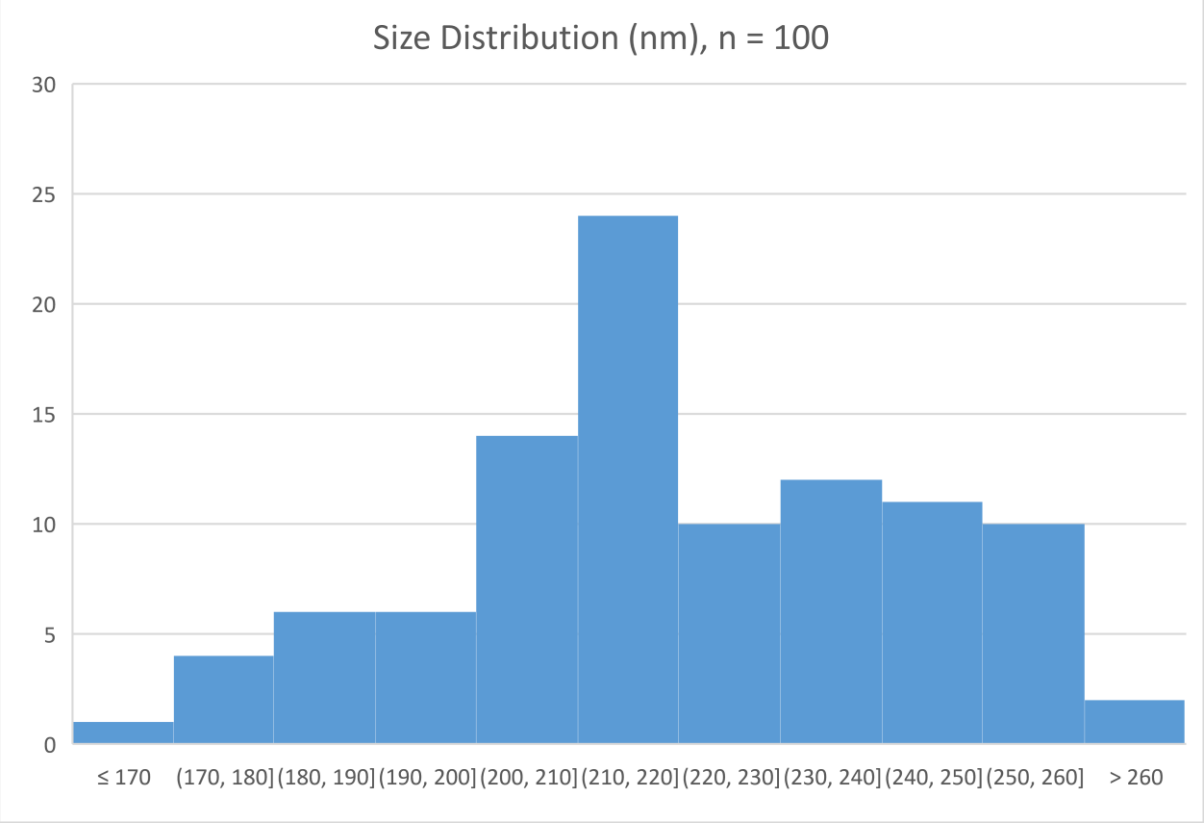


Figure A-8: Size distribution histogram for the CeO_2 coated $MnFe_2O_4$@SiO_2 nanoparticles.

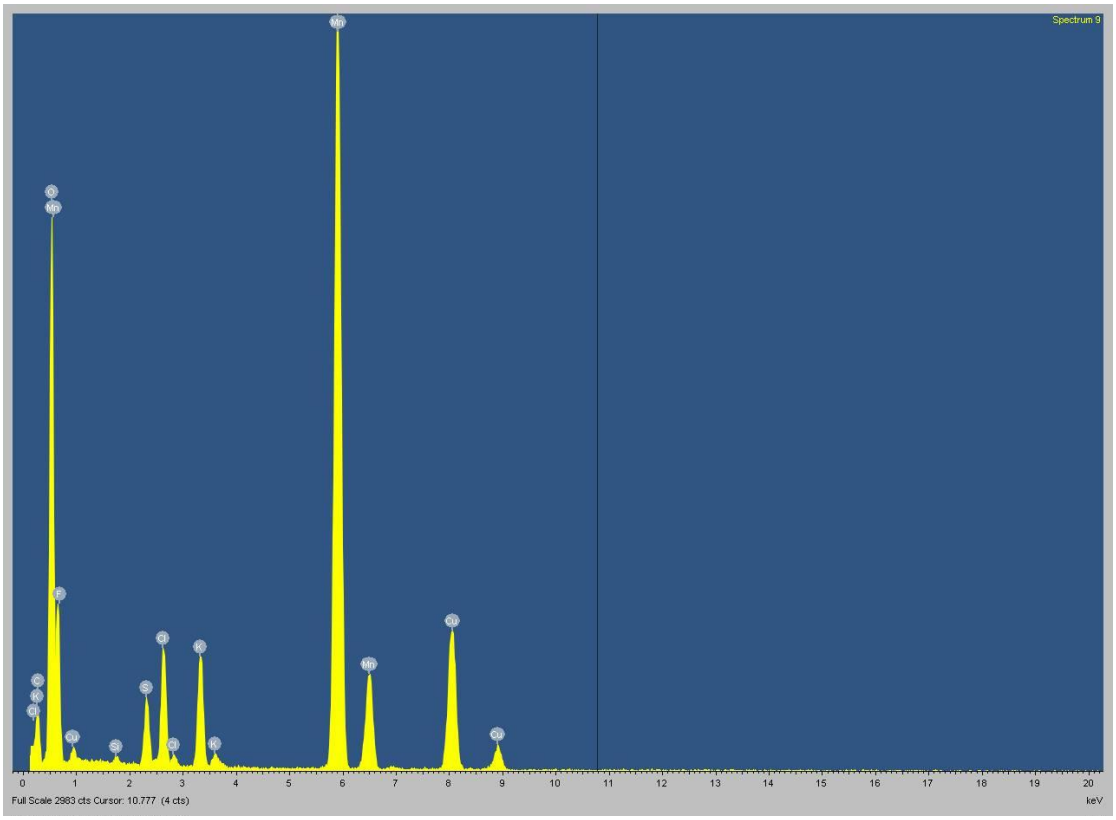


Figure A-9: EDX of synthesised MnO_2 using H_2SO_4 route.

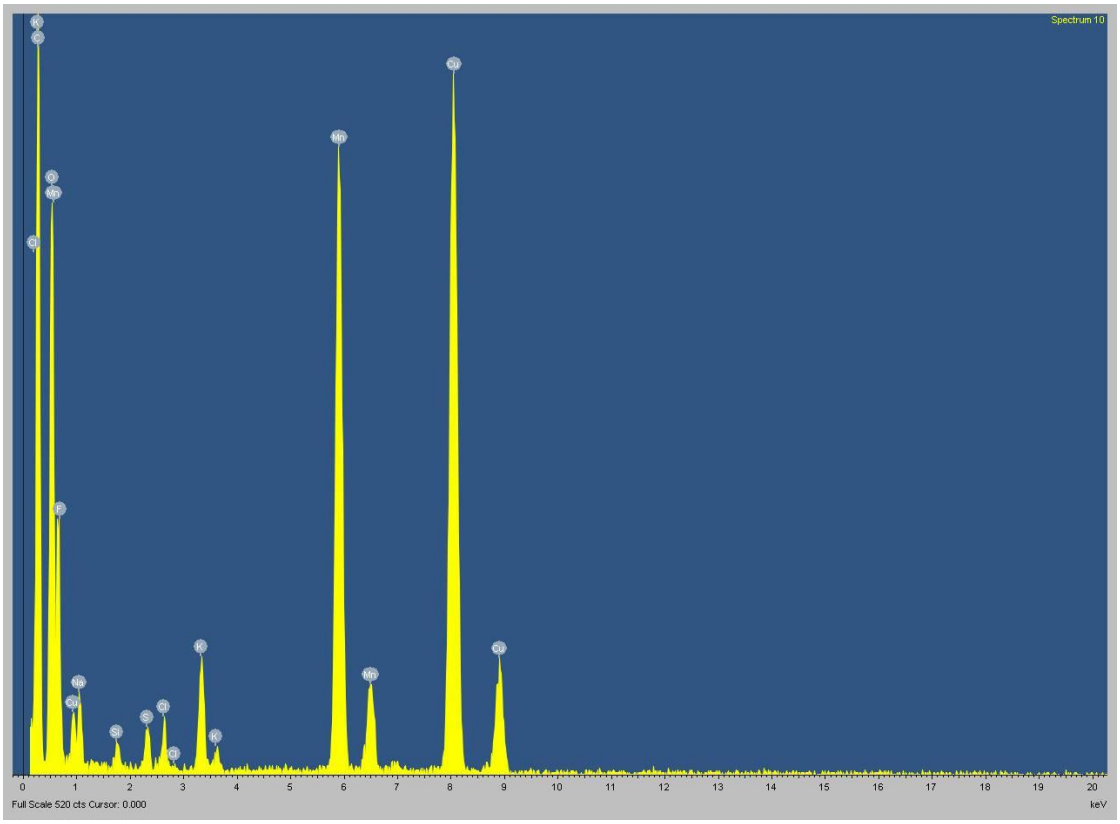


Figure A-10: EDX of MnO_2 synthesised by EtOH route.

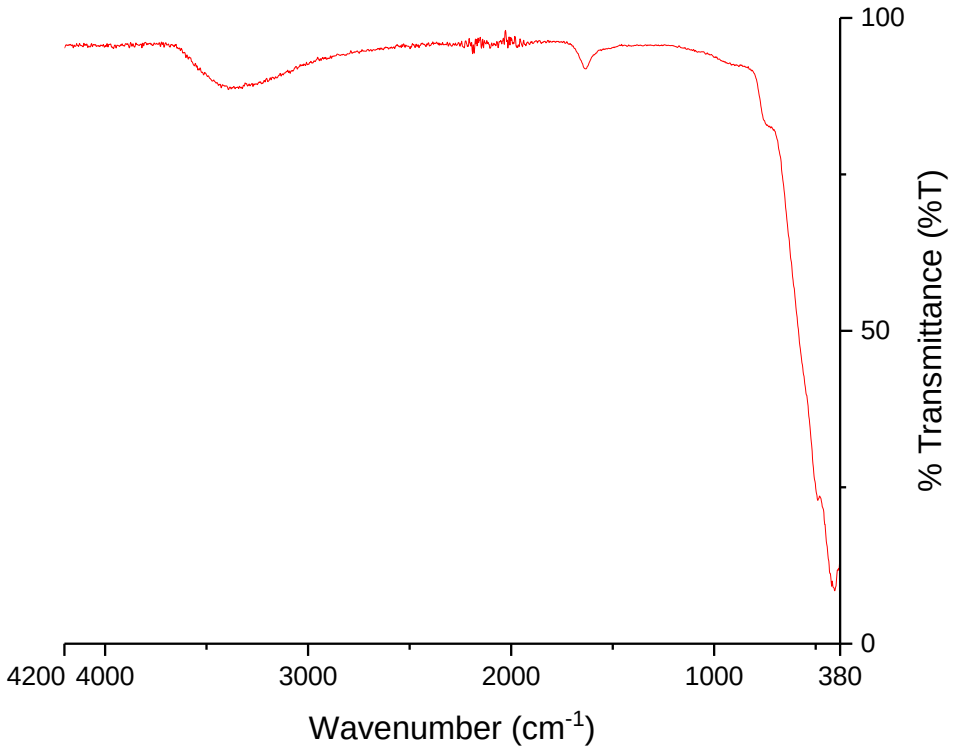


Figure A-11: FTIR of synthesised MnO_2 using H_2SO_4 route.

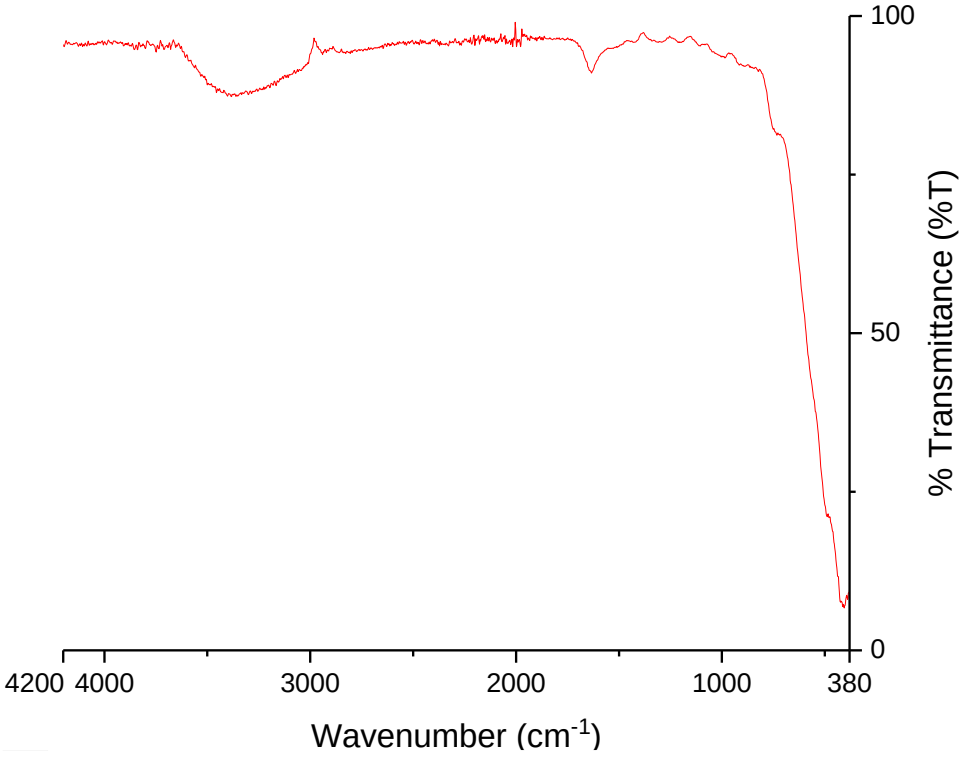


Figure A-12: FTIR of synthesised MnO_2 using EtOH route.

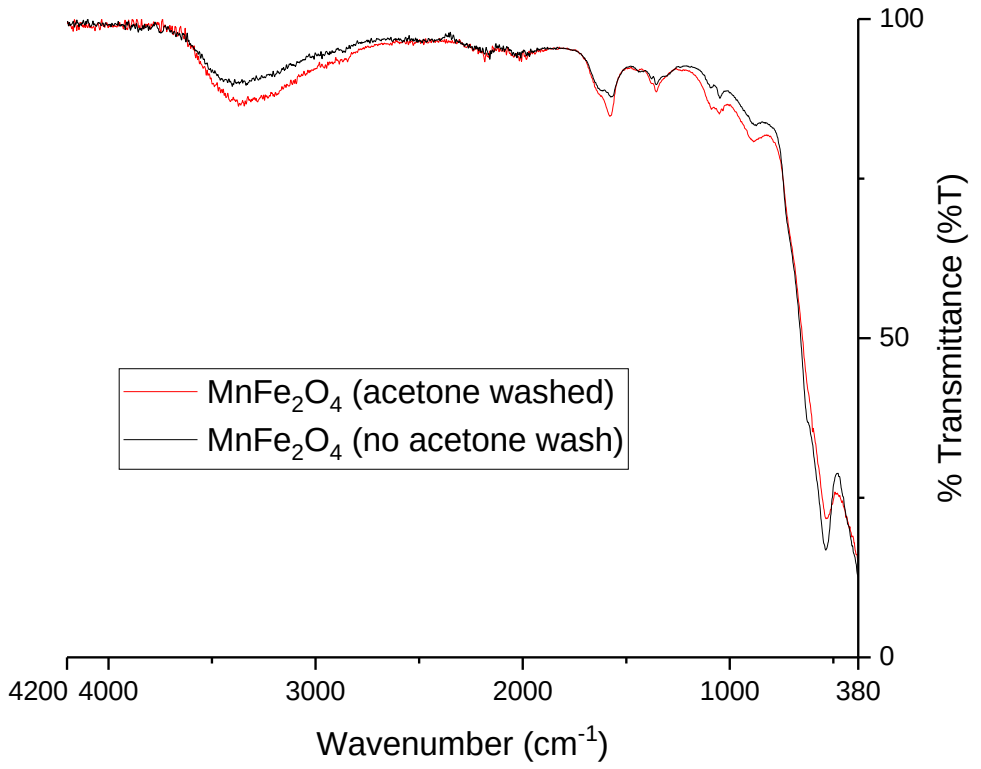


Figure A-13: FTIR spectra of $MnFe_2O_4$ washed with acetone and with only EtOH and water.

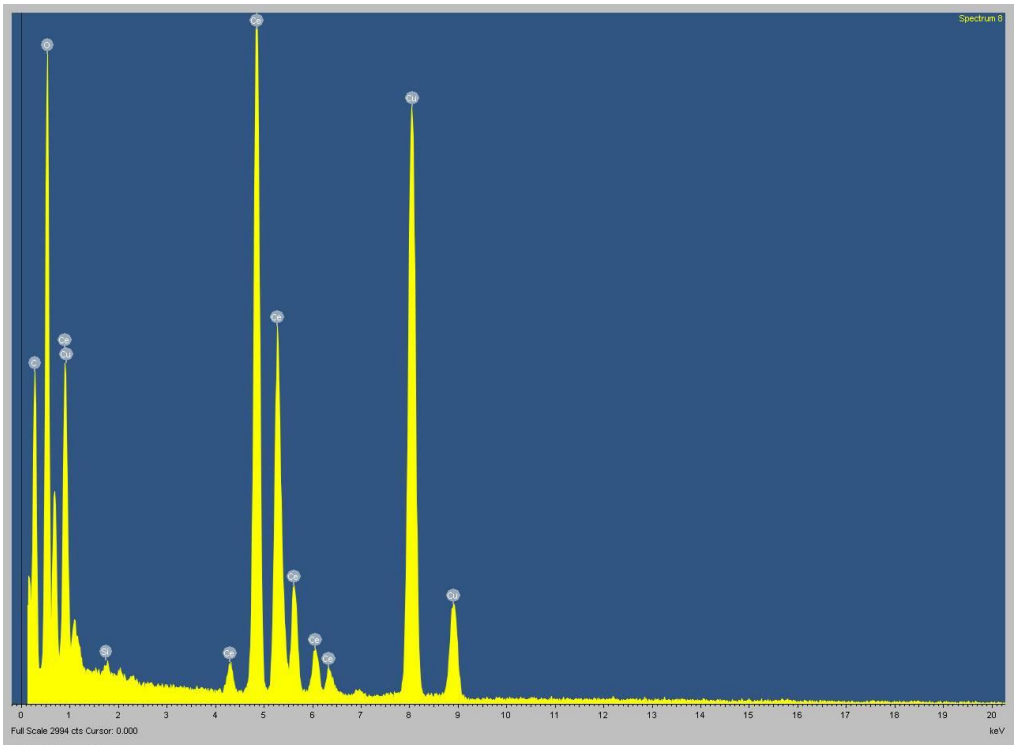


Figure A-14: EDX of synthesised CeO_2 nanoparticles.

A.2 List of Figures

Figure 1-1: Types of magnetism[15]. 3
Figure 1-2: General hysteresis loop showing magnetic saturation (a, d) and coercivity (c, f)[16]. 4
Figure 1-3: Hysteresis loops for a soft and hard magnetic material[17]. 5
Figure 1-4: The qualitative behaviour of the size-dependent coercivity of magnetic particles. The magnetic behaviour of superparamagnetic (SPM) nanoparticles is demonstrated by the solid line, while ferromagnetic (FM) particles are presented by dashed lines in the hysteresis loops. Here H denotes the applied magnetic field strength and M is the measured magnetisation[19]. 6
Figure 1-5: Normal spinel structure showing red balls as the B octahedral sites and blue balls as the A tetrahedral sites and white balls as the FCC lattice of oxygen atoms[21]. 9
Figure 1-6: Thermal decomposition synthesis basic procedure[41]. 13
Figure 1-7: Hydrothermal synthesis concept showing the pressure vessel[46]. 14
Figure 1-8: Schematic presentation of the structure of reverse micelles formed by dissolving the surfactant AOT in n-hexane. The inner core of the reverse micelle is hydrophilic and can dissolve water-soluble compounds. The size of these inner aqueous droplets can be modulated by controlling the parameter w/o (w/o = [water]/ [surfactant])[47] 15
Figure 1-9: Iron oxide MNP showing citric acid binding to surface to create a monolayer[63]. 17
Figure 1-10: The two Ni-based catalysts attached to the silica shell of the MNP[87]. 19
Figure 1-11: Structural models of 2D, 1D and 0D BN nanostructures[133]. 24
Figure 1-12: Schematic of the interaction mechanism of pollutants with BN-based materials[143]. 25
Figure 1-13: Raw BN (a) and BN with Fe_3O_4 on surface (b)[144]. 25
Figure 2-1: General overview of how an electron beam interacts with a sample. 55
Figure 2-2: VSM setup showing the uniform magnetic field (blue lines) that induces the magnetism in the sample[17] and the hysteresis loop with the saturation (M_s), retentivity (M_r) and coercivity (H_c)[18]. 57
Figure 2-3: Setup of ATR attachment showing the Evanescent wave absorbed by the sample[19]. 58

Figure 2-4: The applied radiofrequency (B_1) matches the Larmor frequency and perturbs the spin vector (M_0) to a transverse orientation to the applied external field (B_0). 59
Figure 2-5: UV-vis spectrophotometer beam setup[20]..... 60
Figure 2-6: Correlogram showing the raw data output of a DLS measurement. 61
Figure 2-7: Concept of a negatively charged particle and its interactions with the surrounding solution. 63
Figure 3-1: (A), (B) TEM images of Fe_3O_4 MNPs prepared by coprecipitation method. 72
Figure 3-2: VSM curve for Fe_3O_4 prepared by coprecipitation. 73
Figure 3-3: XRD pattern showing matched peaks for the Fe_3O_4 sample. 74
Figure 3-4: Williamson-Hall Plot for the peaks from XRD output. 74
Figure 3-5: FTIR spectrum of Fe_3O_4 with its strong peak at 531 cm^{-1}. 75
Figure 3-6: Zeta Potential measurements over a pH range showing the PZC. 76
Figure 3-7: TEM images of Fe_3O_4 MNPs made with magnetic stirring. 77
Figure 3-8: TEM images of the synthesised without a buffer Fe_3O_4 MNPs. 78
Figure 3-9: TEM images of Fe_3O_4 MNPs prepared by adding NH_4OH to the metal ions solution. 79
Figure 3-10: TEM images of coprecipitated Fe_3O_4 MNPs prepared using NaOH. 80
Figure 3-11: XRD pattern for Fe_3O_4 prepared using NaOH. 81
Figure 3-12: TEM images of Fe_3O_4 MNPs prepared using a buffered Na_2CO_3 solution..... 82
Figure 3-13: XRD pattern of magnetite prepared using Na_2CO_3 buffered synthesis..... 83
Figure 3-14: (A), (B) TEM images of coprecipitated $MnFe_2O_4$ MNPs..... 85
Figure 3-15: VSM curve of $MnFe_2O_4$ MNPs synthesised by coprecipitation. 86
Figure 3-16: XRD pattern of $MnFe_2O_4$ MNPs synthesised by coprecipitation. 86
Figure 3-17: FTIR spectrumof $MnFe_2O_4$ particles synthesised by coprecipitation. 87
Figure 3-18: TEM images of $MnFe_2O_4$ prepared with magnetic stirring. 88
Figure 3-19: TEM image of Akaganeite and $MnFe_2O_4$ nanostructures prepared using NaOH as base. 89
Figure 3-20: XRD patterns of Akaganeite and $MnFe_2O_4$ sample prepared by the coprecipitation using NaOH..... 89
Figure 3-21: TEM images of as synthesised $CoFe_2O_4$ MNPs. 91
Figure 3-22: VSM curve of the synthesised $CoFe_2O_4$ MNPs..... 91
Figure 3-23: XRD pattern of the $CoFe_2O_4$ MNPs. 92

Figure 3-24: FTIR analysis of the $CoFe_2O_4$ MNPs. 92
Figure 3-25: TEM images of $CoFe_2O_4$ MNPs synthesised using NH_4OH as base. 93
Figure 3-26: VSM curves of $CoFe_2O_4$ before and after calcination at 600 °C. 94
Figure 3-27: FTIR analysis of $CoFe_2O_4$ before and after calcination at 600 °C. 95
Figure 3-28: TEM image of the $CoFe_2O_4$ particles after calcination at 600 °C. 95
Figure 3-29: XRD patterns of the $CoFe_2O_4$ particles before (blue line) and after (red line) calcination 96
Figure 3-30: Effect of drying out on Fe_3O_4 in degassed MP H_2O at (A) 0 hours and (B) 1 hours after sonication 97
Figure 3-31: Effect of calcination on $CuFe_2O_4$ in degassed MP H_2O after 1 hour of sonication. 97
Figure 3-32: TEM image of synthesised $CuFe_2O_4$ MNPs before calcination at 800 °C. 98
Figure 3-33: TEM image of synthesised $CuFe_2O_4$ MNP after calcination at 800 °C. 99
Figure 3-34: VSM curve for $CuFe_2O_4$ before and after calcination at 800 °C. 100
Figure 3-35: XRD patterns of $CuFe_2O_4$ before and after calcination at 800 °C. 100
Figure 3-36: FTIR spectra of $CuFe_2O_4$ before and after calcination at 800 °C. 101
Figure 3-37: XRD pattern of the product produced using NH_4OH to precipitate. 102
Figure 3-38: XRD pattern of product produced using an excess of NaOH. 102
Figure 3-39: VSM curve of $MnFe_2O_4$ synthesised by polyol method. 104
Figure 3-40: TEM images of $MnFe_2O_4$ particles synthesised by polyol method. 105
Figure 3-41: XRD pattern of the $MnFe_2O_4$ synthesised by polyol method. 105
Figure 3-42: TEM images of samples taken at A-H = 2, 3, 4, 5, 6, 8, 10, 20 hr. 107
Figure 3-43: VSM analysis of particles prepared at different reaction times. 108
Figure 3-44: XRD analysis of selected samples prepared at different reaction times. 109
Figure 3-45: FTIR spectra for $MnFe_2O_4$ MNPs prepared at different reaction times. 110
Figure 3-46: Zeta Potential measurements over a pH range showing the PZC for $MnFe_2O_4$ MNPs suspensions. 111
Figure 3-47: Photograph of PTFE stirring bar with ground edges visible. 113
Figure 3-48: TEM image of the $MnFe_2O_4$ product of the reaction using NaOH as the base. . 113
Figure 3-49: TEM image of $MnFe_2O_4$ produced using 50% the amount of solvent. 114
Figure 3-50: SEM image of cauliflower type structures when using diethylene glycol. 115
Figure 3-51: TEM image of cauliflower type structures when using diethylene glycol. 116

Figure 3-52: TEM image of Fe_3O_4 MNPs produced by polyol synthesis. 118
Figure 3-53: Proposed mechanism of the polyol oxidation process. 118
Figure 3-54: TEM image of the product of synthesis using Fe(ll) and Fe(lll) ions. 119
Figure 4-1: VSM curves of citrate functionalised magnetite, Fe_3O_4@citrate. 128
Figure 4-2: FTIR spectra of bare Fe_3O_4 and Fe_3O_4-citrate. 129
Figure 4-3: XRD pattern of Fe_3O_4 and Fe_3O_4@citrate. 130
Figure 4-4: TEM image of Fe_3O_4@citrate. 130
Figure 4-5: pH Dependence of Zeta Potential and PZC for Fe_3O_4 and Fe_3O_4@citrate MNPs. 132
Figure 4-6: TEM image of Fe_3O_4@citrate MNPs when coprecipitated in situ with citric acid. 133
Figure 4-7: VSM curves of the citrate stabilised $MnFe_2O_4$ MNP from polyol reaction. 134
Figure 4-8: FTIR spectra of the bare and citrate stabilised $MnFe_2O_4$ MNPs. 135
Figure 4-9: XRD patterns of $MnFe_2O_4$ and $MnFe_2O_4$@citrate MNPs. 135
Figure 4-10: TEM image of the citrate stabilised $MnFe_2O_4$ particles 136
Figure 4-11: Zeta Potential and PZC for $MnFe_2O_4$ and $MnFe_2O_4$@citrate over pH range. 137
Figure 4-12: TEM image and XRD analysis of the SiO_2 nanoparticles. 138
Figure 4-13: Zeta Potential behaviour over pH 2-12 for SiO_2 NPs and settling behaviour of SiO_2 solution. 139
Figure 4-14: TEM images of Fe_3O_4@SiO_2 samples, (A) sample A, (B) sample B, (C) sample C, (D) sample D. 141
Figure 4-15: VSM curves of Fe_3O_4@SiO_2 MNP sample A compared with the bare and citrate-capped MNPs. 142
Figure 4-16: FTIR spectra of various nanoparticles for comparison. 144
Figure 4-17: XRD patterns of Fe_3O_4@SiO_2. 144
Figure 4-18: Zeta Potential for Fe_3O_4@SiO_2 nanoparticles over pH range 2.1-12.4. 146
Figure 4-19: TEM images of silica coated Fe_3O_4 MNPs produced using bare Fe_3O_4 as the precursor. 146
Figure 4-20: TEM images of $MnFe_2O_4$@SiO_2 (A) sample A, (B) sample B, (C) sample C, (D) sample D. 148
Figure 4-21: VSM curves of $MnFe_2O_4$@SiO_2 Sample D compared with the bare and citrate-stabilised core. 149

Figure 4-22: FTIR spectra of $MnFe_2O_4$ based nanostructures at various stages of synthesis. 151
Figure 4-23: XRD pattern of $MnFe_2O_4$@SiO_2 nanoparticles. 151
Figure 4-24: Zeta potential behaviour over 2.1-12.4 pH range for various MNPs. 152
Figure 4-25: TEM image of $MnFe_2O_4$@SiO_2 using bare particles in synthesis. 153
Figure 4-26: TEM image of $MnFe_2O_4$@SiO_2 formed using magnetic stirring. 154
Figure 5-1: TEM images of the as synthesised MnO_2 (A) from H_2SO_4 route, (B) from EtOH route. 162
Figure 5-2: XRD patterns of both samples of MnO_2 showing similar peaks. 163
Figure 5-3: TEM image of the $MnFe_2O_4$@MnO_2 MNPs. 164
Figure 5-4: FTIR spectra of $MnFe_2O_4$@MnO_2 MNPs. 165
Figure 5-5: VSM curves for the $MnFe_2O_4$@MnO_2 MNPs. 166
Figure 5-6: XRD patterns of the $MnFe_2O_4$@MnO_2 shown as a combination of the core and shell phases. 167
Figure 5-7: Zeta potential over pH range for $MnFe_2O_4$@MnO_2. 167
Figure 5-8: TEM images showing MNPs with different molar ratios of MnO_2 coating (A) 2 molar ratio (B) 1 molar ratio (C) 0.5 molar ratio. 168
Figure 5-9: TEM images of (A) 0.5 molar ratio coating (B) A after another 0.5 molar ratio coating. 169
Figure 5-10: TEM image of coating obtained by following the procedure from reference [23]. 170
Figure 5-11: TEM images of different methods to coat the MNPs. (A) H_2SO_4 method with 1 molar ratio MNP:MnO_2 with one sonication cycle of 5 hours. (B) H_2SO_4 method with 1 molar ratio MNP:MnO_2 with 5 sonication cycles of 1 hr each. (C) EtOH method with 1 molar ratio MNP:MnO_2 with one sonication cycle of 5 hours. (D) EtOH method with 1 molar ratio MNP:MnO_2 with 5 sonication cycles of 1 hr each. 171
Figure 5-12: TEM images of functionalised with MnO_2, (A) coprecipitated Fe_3O_4 and (B) $MnFe_2O_4$ MNPs. 173
Figure 5-13: TEM image of $MnFe_2O_4$@SiO_2@MnO_2 showing no core@shell structures. 173
Figure 5-14: TEM image of the prepared CeO_2 NPs. 174
Figure 5-15: FTIR of CeO_2 NPs. 175
Figure 5-16: XRD pattern of the synthesised CeO_2 and the commercial CeO_2. 175

Figure 5-17: VSM results for $MnFe_2O_4$, $MnFe_2O_4$@SiO_2 and $MnFe_2O_4$@SiO_2 CeO_2 samples showing changes. 177
Figure 5-18: FTIR spectra of the CeO_2 shelled MNP showing stages of development. 178
Figure 5-19: (A), (B) TEM images of the $MnFe_2O_4$@SiO_2@CeO_2 MNPs. 179
Figure 5-20: EDX of the $MnFe_2O_4$@SiO_2@CeO_2 nanoparticles. 180
Figure 5-21: XRD patterns showing the result as a combination of CeO_2 and $MnFe_2O_4$ and the match for $MnFe_2O_4$ and CeO_2 with the phase quantification. 181
Figure 5-22: TEM images with different calculated for shell thicknesses (A) 5 nm (B) 10 nm (C) 20 nm. 182
Figure 5-23: TEM images of the $MnFe_2O_4$@SiO_2@CeO_2 after stirring overnight, before heating for 2 hours. 183
Figure 5-24: TEM images of (A) Fe_3O_4@SiO_2 and (B) Fe_3O_4@SiO_2@CeO_2 particles. 184
Figure 5-25: TEM image of the bare Fe_3O_4 with the smaller CeO_2 particles. 186
Figure 6-1: Proposed mechanism for the oxidation of benzyl alcohol with MnO_2[17]. 194
Figure 6-2: ^{1}H NMR (400 MHZ, $CDCl_3$) spectrum of the products for catalysis using MnO_2 only. 195
Figure 6-3: XRD patterns of $MnFe_2O_4$@MnO_2 before and after furnace at 400 °C. 196
Figure 6-4: Scheme for the reaction showing the two steps involved. 199
Figure 6-5: Proposed mechanism for oxidation on the CeO_2 surface[19]. 199
Figure 6-6: ^{1}H NMR (400 MHZ, $CDCl_3$) spectrum for benzylidene aniline product using CeO_2 (5% mol ratio). 201
Figure 6-7: The metal plate (red) reduces Cu(ll) to Cu(l) which produces a radical from the peroxide to polymerise the methacrylate. The Cu(l) is regenerated back to Cu(ll) in the process. 203
Figure 6-8: UV-vis results of (A) MB solution only and (B) MB solution with $MnFe_2O_4$ cores. 204
Figure 6-9: UV-Vis spectral absorbance profiles over 1 hour for (A) run 1 and (B) run 8 using the MnO_2 coated MNPs. 206
Figure 6-10: Fitted exponential decay graphs for the 10 runs of the MnO_2 coated MNPs. 207
Figure 6-11: Mass Spectrometry output of the extracted solution. 208
Figure 6-12: Proposed MS products for the extracted solution. 209
Figure 6-13: MnO_2 coated MNP (A) before and (B) after 10 recycles. 210

Figure 6-14: XRD pattern of the $MnFe_2O_4$@MnO_2 particles before and after the 10 recycles. 210
Figure 6-15: UV-Vis spectra for MO removal (A) absorbance over 1 hour for run 2 and (B) the decay curves for four runs using the MnO_2 coated MNPs. 211
Figure 6-16: Methyl Orange (left) and Methylene Blue (right). 212
Figure 6-17: UV-Vis spectra for RB removal (A) absorbance over 1 hour for run 1 and (B) the decay curves for the 5 runs using the MnO_2 coated MNPs. 213
Figure 6-18: For MB removal (A) absorbance over 1 hour for run 4 and (B) the decay curves for the 4 runs using the CeO_2 coated MNPs. 215
Figure 7-1: (A) TEM and (B) SEM images of BNNS on a TEM grid. 222
Figure 7-2: XRD pattern of exfoliated BNNS. 223
Figure 7-3: FTIR spectra of BN powder and exfoliated BNNS. 223
Figure 7-4: (A) TEM and (B) SEM images of the Fe_3O_4 coated BNNS. 224
Figure 7-5: FTIR spectra of BNNS-Fe_3O_4, BNNS and Fe_3O_4 for comparison. 225
Figure 7-6: XRD patterns of BNNS-Fe_3O_4 shown to be a combination of BNNS and Fe_3O_4. ..226
Figure 7-7: XRD phase quantification of the BNNS-Fe_3O_4 nanocomposite. 226
Figure 7-8: VSM curve of the BNNS-Fe_3O_4 nanocomposites. 227
Figure 7-9: SEM cross-sections images of (A) Bare BNNS membrane and (B) Fe_3O_4 coated BNNS membrane. 228
Figure 7-10: TEM images of outcome when (A) using NaOH and (B) without EDA. 229
Figure 7-11: TEM image of the BNNS-$CoFe_2O_4$ showing larger $CoFe_2O_4$ particles on BNNS surface. 230
Figure 7-12: FTIR spectra of BNNS-$CoFe_2O_4$ with BNNS and $CoFe_2O_4$ for comparison. 230
Figure 7-13: XRD pattens of BNNS-$CoFe_2O_4$ shown to be a combination of BNNS and $CoFe_2O_4$. 231
Figure 7-14: Phase quantification of the BNNS-$CoFe_2O_4$. 231
Figure 7-15: VSM curve of the BNNS-$CoFe_2O_4$ nanocomposites. 232
Figure 7-16: TEM images of the composites with different molar ratios of $CoFe_2O_4$ (A) 0.1 (B) 0.05 (C) 0.01. 233
Figure 7-17: SEM cross-section images of membranes with BNNS:$CoFe_2O_4$ ratios of (A) 1:0.1 (B) 0.05 (C) 0.01. 235

Figure 7-18: Photographs of membranes produced with BNNS:$CoFe_2O_4$ ratios (A) 1:0.05 (see cracking) (B) 1:0.04 (no cracking)..... 236
Figure 7-19: Successive filtrates showing MB after the fifth aliquot for BNNS membrane. . 238
Figure 7-20: UV-vis analysis of successive 20 mL aliquots of MB solution for BNNS membrane. 238
Figure 7-21: Successive filtrates showing MB after the fourth aliquot for BNNS-Fe_3O_4 membrane..... 239
Figure 7-22: UV-vis analysis of successive 20 mL aliquots of MB solution for BNNS-Fe_3O_4 membrane..... 239
Figure 7-23: Accumulation of MB on BNNS-Fe_3O_4 membrane until saturation develops. ... 240
Figure 7-24: UV-vis analysis of successive 20 mL aliquots of MB solution for BNNS-$CoFe_2O_4$ membrane..... 241
Figure 7-25: BNNS membranes with (A) Fe_3O_4 MNP on surface (B) Fe_3O_4 @citrate on surface. 242
Figure A-1: Size distribution histogram for the coprecipitated Fe_3O_4 nanoparticles. 251
Figure A-2: Size distribution histogram for the polyol $MnFe_2O_4$ nanoparticles. 251
Figure A-3: Size distribution histogram for the citrate stabilised coprecipitated Fe_3O_4 nanoparticles..... 252
Figure A-4: Size distribution histogram for the citrate stabilised polyol $MnFe_2O_4$ nanoparticles. 252
Figure A-5: Size distribution histogram for the SiO_2 coated Fe_3O_4 nanoparticles. 253
Figure A-6: Size distribution histogram for the SiO_2 coated $MnFe_2O_4$ nanoparticles. 253
Figure A-7: Size distribution histogram for the MnO_2 coated $MnFe_2O_4$ nanoparticles..... 254
Figure A-8: Size distribution histogram for the CeO_2 coated $MnFe_2O_4$@SiO_2 nanoparticles.254
Figure A-9: EDX of synthesised MnO_2 using H_2SO_4 route. 255
Figure A-10: EDX of MnO_2 synthesised by EtOH route. 255
Figure A-11: FTIR of synthesised MnO_2 using H_2SO_4 route..... 256
Figure A-12: FTIR of synthesised MnO_2 using EtOH route. 256
Figure A-13: FTIR spectra of $MnFe_2O_4$ washed with acetone and with only EtOH and water. 257
Figure A-14: EDX of synthesised CeO_2 nanoparticles. 257

A.3 List of Tables

Table 1-1: Néel relaxation times for cobalt particles of different sizes and at different temperatures[18]. 8

Table 1-2: Various magnetic materials showing the saturation magnetisation (σ_s), Curie temperature (T_C) and structure (the most common crystal structure of the material). 10

Table 3-1: DLS data of the bare Fe_3O_4 particles over 24 hours. 76

Table 3-2: Summary of changing conditions to optimise synthesis of Fe_3O_4. 83

Table 3-3: DLS measurements for $MnFe_2O_4$ MNPs suspensions 111

Table 3-4: Summary of variations for $MnFe_2O_4$ polyol synthesis 116

Table 4-1: DLS data of the citrate stabilised magnetite MNPs over several days. 131

Table 4-2: DLS data of the citrate stabilised $MnFe_2O_4$. 137

Table 4-3: DLS results for the SiO_2 NPs. 139

Table 4-4: Table with summary of results for the samples A, B, C and D of Fe_3O_4@SiO_2 143

Table 4-5: DLS data for sample 1 of the Fe_3O_4@SiO_2 MNPs over several days. 145

Table 4-6: Table with summary of results for the samples A, B, C and D of $MnFe_2O_4$@SiO_2. 150

Table 4-7: DLS data for the $MnFe_2O_4$@SiO_2 MNPs over several days 152

Table 5-1: Table describing the images in (Figure 5-8) and the molar ratio of coating. 169

Table 5-2: Description of variations to simplify the procedure. 171

Table 5-3: Summary of results for variations in procedure corresponding to images in (Figure 5-11) 172

Table 5-4: Table giving summary of result of different shell thicknesses. 183

Table 5-5: Calculated Surface Area and actual extraction times for the various core@shell particles. 185

Table 6-1: Results for the conversion of benzyl alcohol to benzaldehyde using $MnFe_2O_4$@MnO_2. 194

Table 6-2: Results for the conversion of benzyl alcohol to benzaldehyde using $MnFe_2O_4$@SiO_2@CeO_2. 198

Table 6-3: Results for the conversion of benzyl alcohol to benzaldehyde using Fe_3O_4@SiO_2@CeO_2. 198

Table 6-4: Results for the production of benzylidene aniline using Fe_3O_4@SiO_2@CeO_2 200

Table 6-5: Percent Removal of MB from the solution with MnO_2 coated MNP. 208
Table 6-6: Percent Removal of MO from the solution with MnO_2 coated MNP. 212
Table 6-7: Percent Removal of RB from the solution with MnO_2 coated MNP. 214
Table 6-8: Percent Removal of MB from the solution with CeO_2 coated MNPs. 215
Table 7-1: Summary of outcomes for different molar ratios of BNNS:$CoFe_2O_4$. 233
Table 7-2: Physical characteristics for a membrane of 0.001018 m^2 operating at 1 bar. 237